UNIVERSITY
OF TASMANIA

Establishing the value of an integrated geochemistry-mineralogy-texture approach for acid rock drainage prediction

by

Anita Parbhakar-Fox
MSci. (Hons), Imperial College, London, UK

Submitted in fulfilment of the requirements for the degree of Doctor of Philosophy

University of Tasmania, September 2012

Declaration of originality

This thesis contains no material which has been accepted for the award of any other degree or diploma in any tertiary institution and, to the best of my knowledge and belief, contains no copy or paraphrase of material previously published or written by another person, except where due reference is made in the text of this thesis.

Signature: Date:

Authority of access

This thesis is not to be made available for loan or copying for 24 months from the date this statement was signed; after that time limited copying is permitted in accordance with the Copyright Act 1968.

Signature: Date:

Abstract

The total estimated cost for worldwide liability associated with current and future ARD (acid rock drainage) remediation is approximately US $100 billion (Tremblay and Hogan, 2001 *in* Hudson-Edwards et al., 2011). Such liabilities are partly due to the limitations of existing predictive protocols, highlighting the importance of using appropriate and accurate methodologies. Current protocols for ARD risk assessment follow the wheel approach (Morin and Hutt, 1998) or the AMIRA P387A Handbook (Smart et al., 2002). However, the accuracy of these protocols solely relies on geochemical tests and, there is a clear absence of detailed mineralogical and textural characterisation in the applied methodologies. Consequently, inappropriate decisions can be made, either by not allocating the necessary resources when the ARD risk is underestimated, or by wrongly not pursuing development when ARD risk overestimated. Therefore, an improved predictive methodology based on ARD characteristics must be developed and implemented at early-stages of the mine life cycle. Additionally, such a methodology should have applications at historic mine sites to identify acid forming samples and guide site rehabilitation strategies.

The potential for improvement in ARD prediction methodology needs to consider mineralogical and textural characteristics as well as geochemical analyses. Therefore, this thesis has developed an improved and integrated protocol for classifying solid mine waste in terms of acid forming potential. The geochemistry-mineralogy-texture, or GMT approach, consists of three stages which involve a parallel use of geochemical, mineralogical and textural analyses:

- *Stage-one:* Low-cost pre-screening geochemical, mineralogical and textural tests and evaluations are performed on the largest number of samples.
- *Stage-two:* Routine geochemical tests are performed on fewer samples, using more expensive tests.
- *Stage-three*: Advanced geochemical tests and microanalytical techniques are performed on well selected samples.

Results are cross-checked at the end of each stage to provide an accurate sample classification in terms of acid forming potential. The advantage of the proposed GMT methodology relative to those currently used (e.g., the wheel approach, AMIRA P387A Handbook) is its structured approach, as evaluations of problematic samples are focused upon, thereby increasing technical accuracy of predictions, and reducing total number of samples analysed by routine tests, and overall costs. The acid rock drainage index (ARDI) forms part of the GMT approach as a stage-one test, and was developed to evaluate intact rock texture in terms of five key parameters (A: sulphide contents; B: sulphide alteration; C : sulphide morphology; D: content of neutralising minerals; and E: sulphide mineral associations), which influence acid formation. The GMT approach was tested on waste material from the historic Croydon gold-lode mines, and drill

core samples from the operational Ernest Henry iron-oxide copper gold (IOCG) deposit, both located in Queensland, Australia. The geology (including style of mineralisation and texture) differed between the two sites, allowing for critical assessment of both the GMT approach and the ARDI.

A mesotextural classification method (using geological logging, field portable X-Ray fluorescence and short-wave Infrared techniques) for grouping waste materials was developed and tested at the historic Croydon-gold mining operations. Through undertaking mesotextural classification, ten groups (A to J) were identified, and systematically characterised by the GMT approach. At the end of stage-one, five groups (C: porphyritic rhyolite containing disseminated pyrite in quartz veins; E: porphyritic rhyolite containing disseminated pyrite in the groundmass; G: semi-massive quartz-sphalerite-galena-pyrite; H: massive arsenopyrite-quartz; and J: semi-massive quartz- pyrite) were identified as potentially acid forming and required stage-two testing. However, all samples were tested at stage-two to check the accuracy of stage-one results, and were in agreement thus validating stage-one classifications. Samples from mesotextural groups C, E, G, H and J were subjected to stage-three analyses which utilised advanced geochemical tests, and microtextural analyses (i.e., mineral liberation analysis, laser ablation-ICP-MS and scanning electron microscopy). Stage-three geochemical analyses demonstrated that NAG testing results on samples containing <0.3 wt. % sulphide were inaccurate (i.e., underestimated acid forming potential), with the multi-addition NAG test instead recommended for use. Microtextural studies indicated that trace element distribution; contents of micro-inclusions and mineral association were significant controls on sulphide oxidation. Final GMT approach classifications identified groups H and J as extremely acid forming; and groups E and G as potentially acid forming.

Croydon waste materials representative of mesotextural groups E, G, H and J were selected for thirty-week column leach kinetic testing following the recommendations of the GMT approach. Twelve columns were established, with two size fractions (-10 mm and -4 mm) prepared from each sample, to investigate the effects of grain size on pH, metal elution and secondary mineral precipitation. The mineralogy and microtexture of the column feed material were examined routinely (i.e., every five weeks) through quantitative X-Ray diffractometry, scanning electron microscopy and laser ablation ICP-MS studies. These data were directly compared with leachate chemistry (pH, EC, SO_4 and cation contents) to identify the controls on sulphide oxidation and trace element liberation. Material representative of mesotextural group H was the most acid forming, with lower pH values and higher cumulative mass release of elements calculated for the -4 mm fraction. Mineralogical data showed progressive replacement of arsenopyrite to trace element rich (i.e., Cu, Pb and Zn) scorodite. Pyrite in material representative of mesotextural groups E and J was As-rich, with greater quantities of pyrite weathering products (i.e., rhomboclase, jarosite, alunite) and textures identified over time. Generally, lower pH and higher dissolved metals and arsenic were measured in leachate from the -4 mm fraction. Values of pH were particularly sensitive to the development of fine hydrous ferric oxide coatings on pyrite in groups E and J. Galena was also identified in material representative of groups E and J and was observed to weather rapidly to anglesite over the duration of these tests. Whilst sphalerite present in material representative of mesotextural group G was Cd- and Fe-rich and contained Cu micro-inclusions (factors which increase

oxidation rate), overall it was the least weathered of the sulphides. However, the leachate pH values measured from group G indicated that this material is acid forming as a consequence of the oxidation of pyrite which was also identified in this group. The highest cumulative mass release of Zn relative to the other groups was measured from the -4 mm fraction. However, very low cumulative mass release rates of Cd were calculated from both grain size fractions. Kinetic test results confirmed that mesotextural groups G, H and J pose the greatest environmental risk in terms of ARD and potential metal/metalloid leaching. Consequently, a rehabilitation strategy focusing on individual segregation and treatment of material representative of groups G, H and J from non-acid forming mesotextural groups is recommended.

The application of geometallurgical techniques for predicting acid formation was demonstrated using samples from the Ernest Henry IOCG deposit. Samples from two drill holes were initially subjected to GMT analyses with results compared against geometallurgical data sets collected by mineral liberation analysis (MLA), HyLogger and EQUOtip. Modal mineralogy data collected by MLA allowed for the carbonate:sulphide ratio to be examined down hole as is required by stage-one of the GMT approach. Relative carbonate contents determined from the HyLogger allowed for acid neutralising capacity (ANC) values to be critically evaluated in terms of effective ANC. Finally, relationships between mineral hardness measured using EQUOtip and lag-time to acid formation were identified. This study identifies the potential for integrating geometallurgical techniques and data into the GMT approach, as a means of allowing for ARD characterisation to be routinely undertaken at the early stages of mine operations.

Results from the two case study sites (Croydon, Ernest Henry) demonstrate that the geochemistry-mineralogy-texture (GMT) approach represents a significant improvement to existing ARD predictive protocols (e.g., the wheel approach, AMIRA P387A Handbook), by providing a structured methodology to more efficiently identify problematic samples. Stage-one of the GMT approach allows best practice sample numbers to be realistically achieved through cost-effective pre-screening tests, thus improving ARD risk assessment. Furthermore, selection of samples for testing based on mesotextural grouping, rather than lithology, allows for deposit wide ARD domaining to be effectively undertaken, particularly when integrated with geometallurgical data. The presented methodology effectively integrates existing geochemical tests with novel mineralogical and textural characterisation techniques. This in turn leads to maximisation of knowledge, cost savings, and a more detailed characterisation of the most acid forming samples. Therefore, the GMT approach represents a fundamental step-change in how ARD should be predicted.

Acknowledgments

This research was funded by the Centre of Excellence in Ore Deposits (CODES), the AMIRA P843/843A GeM project, and CRC ORE Ltd. So I thank them for the logistical and financial support throughout the research programme. I must also thank the Society of Economic Geologists for the provision of a Graduate Research Fellowship in 2008.

I first would like to thank my primary supervisor, Professor Bernd Lottermoser for his encouragement and guidance from 2011 onwards. It was no small challenge taking on a PhD candidate a significant way through the research programme, and I cannot thank him enough for reviewing this thesis and guiding it towards submission. I would also like to thank my former supervisors (2007-2010) Dr. Steve Walters and Dr. Mansour Edraki, who provided me with the opportunity to undertake this research and gave me much freedom to explore my ideas. My deepest thanks go to my advisor, Professor Dee Bradshaw, who has been a real inspiration to me since the start, and has provided valuble comments, ideas, and opportunities throughout this research programme. Additional thanks go to Associate Professor Jeff Foster and Professor Tim Napier-Munn.

I would like to extend my gratitude to the staff at CODES and UTAS who have directly and indirectly provided assistance with this research. Many thanks go to Karsten Goemann, Sandrin Feig, Ian Little, Sarah Gilbert, Katie McGoldrick, Phil Robinson, Thomas Rodemann, Jay Thompson and Maya Kamenetsky for analytical assistance, and Simon Stephens and Al Cuison for lapidary work. Thank you to Simon Michaux, Pat Walters, Esther Soden and Andrew Fletcher at the University of Queensland for sample preparation and laboratory assistance. Additional thanks are extended to Helen Scott, Keith Dobson, Christine Higgins, Karen Mollross, Dianne Steffens, Caroline Mordant, June Pongratz and Nilar Hlaing for help with all matters relating to finance, travel, computing and printing over the years.

I would like to also thank Simon Cottier and Tania Hall from the Queensland Government Department of Employment, Economic Development and Innovation for providing funding to undertake site work at Croydon, and passing on additional site data and samples when required.

The people who have been so important throughout are my family and friends. I thank my parents, Shashi and Santosh, my sister Sonia, and my in-laws Bev, Helen and Paul for providing love, support and patience throughout the research programme. My closest friends Phil (thank you too for taking the time to review this thesis), Hayley, Steph and Natalie, your friendship has been so precious; your frequent calls and e-mails listening to me talk at length about the latest hurdle or significant finding,

as well keeping me included in your own personal milestones. You've been such a huge part of this, and even though you are all thousands of miles away, it never felt like there was any distance at all. Thanks to new friends: Jeff (for the many entertaining conversations), Joe (your kindness has been immeasurable), Taryn (for keeping me so motivated), Andrea, Helen, Wojtek, Natalee, Heidi, Sang, Steve, Sophia, Julie, Dave, Sam, Amy and Hugo. Thanks are also extended to my very patient office mates Olga, Guan and Daniele, you have been exceptionally understanding over these past couple of years, for which I am truly grateful.

However, the biggest thanks go to the two most important people in my life, my wonderful husband Nathan and my beautiful son Cohen. Nathan you have been simply the best friend and companion I could ask for. These past years have been so exciting to be alongside you, both personally and professionally. Your love, support, wisdom and encouragement have meant everything to me. Your enthusiasm for my research and your willingness to discuss it at length have really given me the confidence to produce this thesis, and I am so proud of you for recently completing your own. I am so honoured to be by your side, now and forever. Cohen, you are the most precious thing to me, many people thought I'd quit when you arrived unexpectedly halfway through the research programme, but instead you motivated me to the end equipping me with focus, purpose and immense joy. For that, I cannot thank you enough.

Table of contents

Chapter 1: Introduction

Chapter 2: Proposed methodology for waste rock classification

Chapter 3: Waste rock classification at the historic Croydon mine operations using the GMT approach

Chapter 4: Mineralogical and chemical evolution of sulphidic mine wastes (Croydon gold mines, Australia) upon kinetic testing

Chapter 5: Applications of geometallurgical data for predicting ARD: Examples from the Ernest Henry IOCG deposit, Queensland

Chapter 6: Conclusions and further research

References

Appendices (on accompanying CD)

Appendix 1.1 Parbhakar-Fox, A., and Lottermoser, B., 2011. Predictive Environmental Indicators in Mining: Review of the literature and current best practices. CRC ORE Technical Report 2, CRC for Optimising Resource Extraction, Brisbane, Australia, pp.1-142.

Appendix 2.1 Parbhakar-Fox, A.K., Edraki, M., Bradshaw, D. and Walters, S. 2011. Development of a textural index for the prediction of acid rock drainage. Minerals Engineering, v.24 (12), p.1277-1287.

Appendix 2.2 Micro X-Ray Fluorescence method development report, Parbhakar, A.K., 2008 (Unpublished).

Appendix 3.1 Geochemical, mineralogical and textural characterisation of heap leach material from the historic Croydon mine operations. Parbhakar-Fox, A.K., 2010 (Unpublished).

Appendix 3.2 Geochemical test results from the Croydon waste rock materials.

Appendix 3.3 Element maps of sulphides from Croydon mesotextural groups G, H and J mapped using laser ablation ICP-MS.

Appendix 4.1 Geochemical results of first flush tests performed on Croydon waste rock materials from mesotextural groups E, G, H and J.

Appendix 4.2 Geochemical results of stream sediment and surface water sampling performed in the Croydon mine District.

Appendix 4.3 Total-metal contents of Croydon waste rock materials at the start of the kinetic trials.

Appendix 4.4 Geochemical, mineralogical and LA-ICP-MS element mapping data from mesotextural group E.

Appendix 4.5 Geochemical, mineralogical and LA-ICP-MS element mapping data from mesotextural group G.

Appendix 4.6 Geochemical, mineralogical and LA-ICP-MS element mapping data from mesotextural group H.

Appendix 4.7 Geochemical and LA-ICP-MS element mapping data from mesotextural group J.

Appendix 4.8 Mineralogical QXRD data from three mesotextural group J samples (3, 15 and 19).

Appendix 5.1 Geometallurgical techniques: Summary Report. Parbhakar-Fox, A.K 2011 (Unpublished).

Appendix 6.1 Calculated GMT Costings.

List of Figures

Chapter 1: Introduction

Chapter 2: Proposed methodology for waste rock classification

Chapter 3: Waste rock classification at the historic Croydon mine operations using the GMT approach

Chapter 4: Mineralogical and chemical evolution of sulphidic mine wastes (Croydon gold mines, Australia) upon kinetic testing

Chapter 5: Applications of geometallurgical data for predicting ARD: Examples from the Ernest Henry IOCG deposit, Queensland

Chapter 6: Conclusions and further research

List of Tables

Chapter 1: Introduction

Chapter 2: Proposed methodology for waste rock classification

Chapter 3: Waste rock classification at the historic Croydon mine operations using the GMT approach

Chapter 4: Mineralogical and chemical evolution of sulphidic mine wastes (Croydon gold mines, Australia) upon kinetic testing

Chapter 5: Applications of geometallurgical data for predicting ARD: Examples from the Ernest Henry IOCG deposit, Queensland

Chapter 6: Conclusions and further research

List of Abbreviations

ABA: acid base accounting, of which NAPP is an example
ABCC: acid buffering characteristic curve
AF: acid forming classification
AMIRA: Australian Mineral Industries Research Association Limited
ANC: acid neutralising capacity in kg H_2SO_4/t calculated from titration methods (e.g., Sobek)
ARDI: acid rock drainage index
EAF: extremely acid forming classification
EC: electrical conductivity
CODES, UTAS: ARC Centre of Excellence in ore deposits, University of Tasmania
CSL, UTAS: central science laboratory, University of Tasmania
EA: elemental microanalysis
EDS: energy dispersive spectroscopy
EPMA: electron-probe microanalysis
Eq: equation
FP-XRF: field portable X-Ray fluorescence
GMT approach: geochemistry-mineralogy-texture approach
kNAG: Kinetic NAG test (a single addition NAG test in which temperature and pH are measured)
LA-ICP-MS: laser-ablation inductively coupled plasma spectrometry
MPA: maximum potential acidity, calculated from total S in kg H_2SO_4/t
MLA: mineral liberation analysis
MMWI: modal mineralogy weathering index
mNAG: multi addition NAG test
NAF: non acid forming classification
NAG to pH 4.5: NAG acidity titrated to pH 4.5 in kg H_2SO_4/t
NAG to pH 7.0: NAG acidity titrated to pH 7.0 in kg H_2SO_4/t
NAG pH: pH of NAG solution at room temperature after application of the standard heating step and before titration, also referred to as post-boil NAG pH
NAPP: net acid producing potential, calculated from ANC and total S (or MPA) in kg H_2SO_4/t
NP: neutralisation potential, normally reported in units of $CaCO_3$
PAF: potentially acid forming classification
Paste pH: pH of a sample slurry with a solid to water ratio of 1:2 (w/w)
PIMA: portable infrared mineral analyser
PNC: potential neutralising capacity
Single Addition NAG: single addition of 250ml of 15% H_2O_2 to a sample.
SEM: scanning electron microscopy
sNAG: sequential additions of 250ml of 15% H_2O_2 to a sample with pH and acidity measured
S_{Total}: Total sulphur contents (wt. %)
$S_{Sulphide}$: Total sulphide contents (wt. %)
QXRD: quantiative X-Ray diffractometry

Chapter 1
Introduction

1.1 Preamble

Oxidation of sulphidic mine waste (e.g., waste rock, tailings) and the consequent release of acid rock drainage (ARD) waters is a significant environmental challenge (Harris, 1997; Dold, 2008; Hansen et al., 2008; Broadhurst and Petrie, 2010; Hudson-Edwards et al., 2011). As a result, ARD liability costs are high, with the total worldwide liability cost associated with the current and future ARD remediation estimated as approximately US$100 billion (Tremblay and Hogan, 2001). In North America alone they are estimated as between $2 and 5 billion for Canada (Feasby and Tremblay, 1995), and between $32 and $72 billion for the US (Strong and Flores, 2008). These costs are a consequence of historical mining, for example, in western US, there are 500,000 abandoned mines of which 15,000 actively produce ARD and require rehabilitation (Strong and Flores, 2008).

In Australia too, there are many thousands of abandoned mines (Figure 1.1); in Queensland alone there are 18,000 abandoned sites, 10,000 of which are managed by the state government (Franco et al., 2010). Harris (1997) estimated that rehabilitation costs are >AUD $100,000 per hectare for these sites, which is approximately five times greater than the cost of managing potentially acid forming wastes during mine operation (AUD $20,000-50,000 per hectare). Quantities of solid mine waste being produced are increasing too, with the average grade of Australian ore bodies being mined halved, and waste removed to access the minerals doubled over the past thirty years (Mudd, 2007; ABARE, 2008; Figure 1.2).

Published evidence for failing to predict and manage ARD is plentiful (i.e., Fillpek et al., 1987; Ashley and Lottermoser, 1999; Nordstrom et al., 2000; Hudson-Edwards, 2003; Harris et al., 2003; Gault et al., 2005; da Silva et al., 2009), consequences of which include unplanned spending on remedial measures (Dowd, 2005). As a result of inadequate predictive test work undertaken at the early stages of mine operations (e.g., pre-feasibility/feasibility), it is widely recognised that a proactive approach to ARD management should be adopted (Harris et al., 2003; Aykol et al., 2003; Ashley et al., 2004; Lottermoser et al., 2005; Marescotti et al., 2008; Tarras-Wahlberg and Nguyen, 2008).

The challenge therefore posed, is to develop predictive ARD protocols that can be used to effectively characterise waste material at historic mine sites, and can also be implemented at new ventures in the early stages of operation in order to minimise potential ARD liabilities. This would allow for a detailed understanding of the ARD characteristics of a deposit to be well established prior to mine operation.

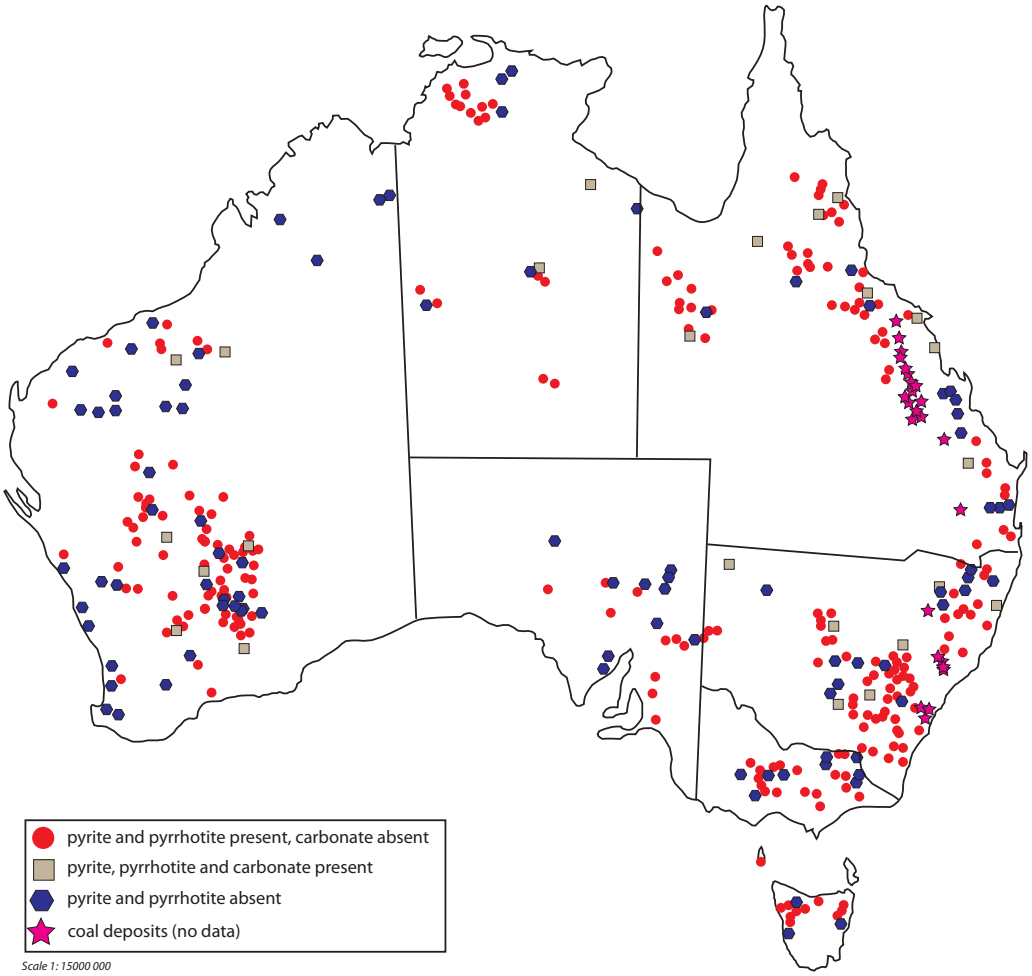

Figure 1.1 Major operating and historical mines sites in Australia: mines with pyrite/pyrrhotite present and without carbonate gangue are indicated, from which ARD is expected (data from OZMIN database, redrawn from ACMRR/OSS acid mine drainage study, 1997).

1.2 Acid rock drainage: the problems and processes

An up-to-date review of sulphide oxidation and acid rock drainage formation (including tables and figures) is documented in Parbhakar-Fox and Lottermoser (2011; Appendix 1.1), with a summary given here. Acid rock drainage is produced by oxidation of sulphide minerals, particularly pyrite (FeS_2), and occurs via inorganic and biologically-mediated pathways (Evangelou and Zhang, 1995; Egiebor and Oni, 2007; Lottermoser, 2010). Solutions are characterised by low pH and high metal concentrations, and pose significant environmental problems because ARD chemistry can be harmful to humans and other life forms (Ma and Banfield, 2011). General oxidation reactions for pyrite (FeS_2) are given in *equations 1.1 to 1.5*. The initial step in the presence of atmospheric oxygen is described in *equation 1.1* (Evangelou and Zhang, 1995). Oxygen also directly reacts with pyrite and forms Fe^{2+}, which is subsequently oxidised to Fe^{3+} (*equation 1.2*). Ferric iron has a low solubility around neutral pH but as oxidation proceeds with oxygen, the pH decreases until *equation 1.3* is triggered at around pH 4.5 (Dold, 2010). As the concentration of dissolved Fe^{3+} decreases with increasing pH, Fe^{3+} solubility is limited by the precipitation of Fe^{3+} hydroxides ($Fe(OH)_3$) and oxy-hydroxides (FeOOH; Evangelou and Zhang, 1995). Therefore, if the pH increases to >3 then reactions shown in *equations 1.4* and *1.5* occur (Lottermoser, 2010).

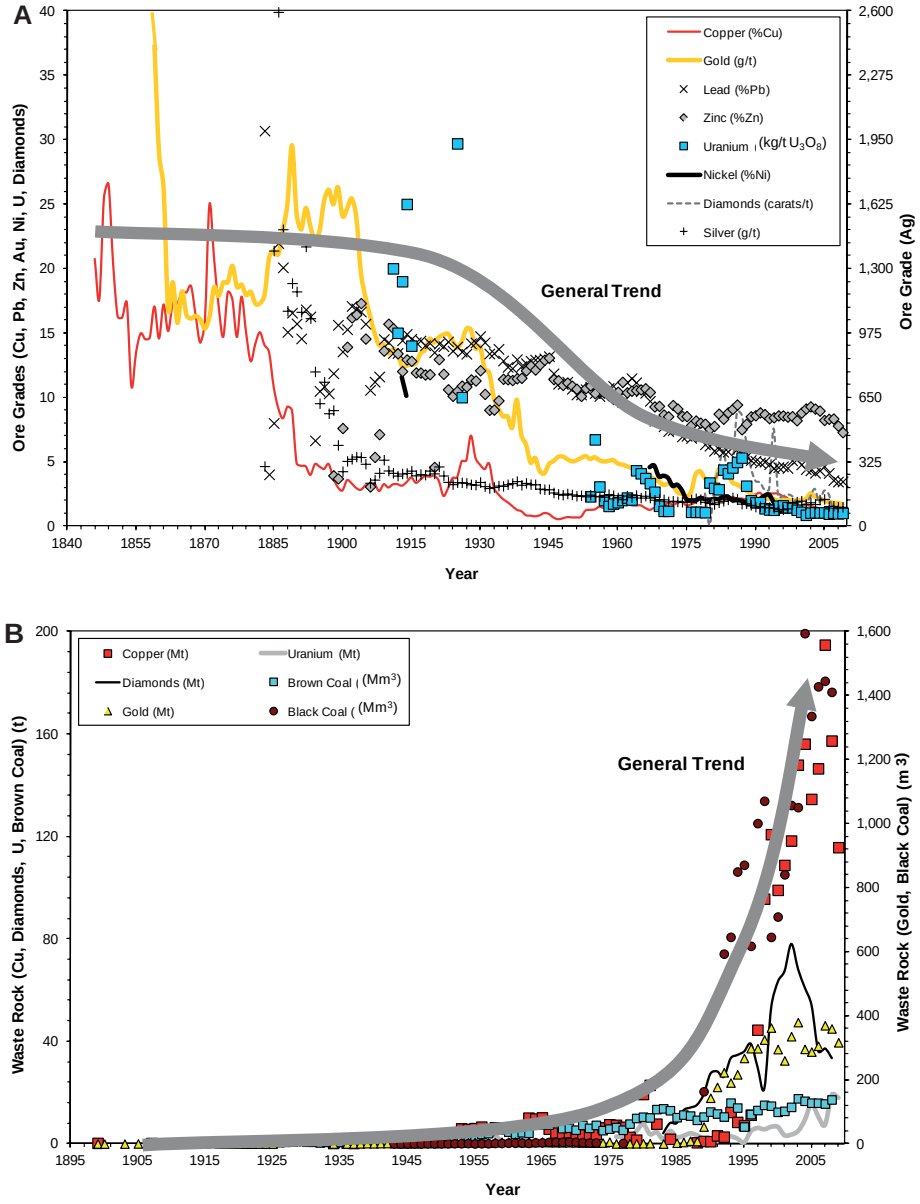

Figure 1.2 Trends in Australian mining: **(A)** Average ore grades in g/t (1840 to 2007) and; **(B)** Quantity of waste rock and overburden (1895 to 2007; Mudd, 2007).

$$FeS_2 + 7/2O_2 + H_2O \rightarrow Fe^{2+} + 2SO_4^{2-} + 2H^+ \quad (1.1)$$

$$Fe^{2+} + ¼O_2 + H+ \rightarrow Fe^{3+} + ½H_2O \quad (1.2)$$

$$FeS_2 + 14Fe^{3+} + 8H_2O \rightarrow 15Fe^{2+} + 2SO_4^{2-} + 16H^+ \quad (1.3)$$

$$Fe^{3+} + 3H_2O \rightarrow Fe(OH)_3 + 3H^+ \quad (1.4)$$

$$Fe^{3+} + 2H_2O \rightarrow FeOOH + 3H^+ \quad (1.5)$$

Processes of pyrite oxidation are generally controlled by several factors including pH (Evangelou and Zhang, 1995; Dold, 2010), oxidant type (O_2 or Fe^{3+}; Moses and Herman, 1991; Moses et. al., 1987; Hustwit et al., 1992), oxidant concentration (Lottermoser, 2010), morphology (Weber et al.,

2004; Lottermoser, 2010), microbial populations (Evangelou and Zhang, 1995; Bond et al., 2000; Baker and Banfield, 2003), and trace element contents (Kwong, 1993, 1995; Jambor, 1994; Plumlee, 1999; Blanchard et al., 2007). Oxidation is further complicated by the electrochemical nature of pyrite (Evangelou and Zhang, 1995; Rimstidt and Vaughan, 2003; Egiebor and Oni, 2007; Savage et al., 2008; Chandra and Gerson, 2010).

Other sulphides have differing acid-forming potential and rates of reaction. This is dependent on the amount of Fe present, with Fe-sulphides generating the most acidity (Plumlee, 1999; Dold, 2010). Sulphides, which do not contain Fe in their crystal lattice (e.g., galena, Fe-poor sphalerite), do not have the capacity to generate large amounts of acid, but can be sources of potentially deleterious metals such as Cd, Pb and Zn (Dold, 2010; Lottermoser, 2010). General oxidation reactions for pyrrhotite ($Fe_{(1-x)}S$), arsenopyrite (FeAsS), chalcopyrite ($CuFeS_2$), sphalerite (ZnS) and galena (PbS) are given in *equations 1.6* to *1.10* (Lottermoser, 2010; Nicholson and Scharer, 1994; Corkhill and Vaughan, 2009; Thurston et al., 2010; Abbassi et al., 2009). Oxygen is the oxidant shown in *equations 1.6* to *1.8*, and iron in *equations 1.9* and *1.10*.

$$Fe_{(1-x)}S + (2-x/2)O_2 + xH_2O \rightarrow (1-x)Fe^{2+} + SO_4^{2-} + 2xH^+ \quad (1.6)$$

$$4FeAsS + 11O_2 + 6H_2O \rightarrow 4\,Fe^{2+} + 4H_2SO_4^{2-} + H_3AsO_3 \quad (1.7)$$

$$2CuFeS_2 + 17/2O_2 + 5H_2O \rightarrow 2Cu^{2+} + 2Fe(OH)_3 + 4SO_4^{2-} + 4H^+ \quad (1.8)$$

$$ZnS + 8Fe^{3+} + 4H_2O \rightarrow Zn^{2+} + SO_4^{2-} + 8Fe^{2+} + 8H^+ \quad (1.9)$$

$$PbS + 8Fe^{3+} + 4H_2O \rightarrow Pb^{2+} + SO_4^{2-} + 8Fe^{2+} + 8H^+ \quad (1.10)$$

Sulphide reactivity is generally in the order of: pyrrhotite > galena - sphalerite > pyrite - arsenopyrite > chalcopyrite (Keith and Vaughan, 2000; Moncur et al., 2009). Product layers can develop on oxidation which can control the rate of diffusion and thus the overall rate of oxidation (Blowes and Jambor, 1990; Garcia et al., 1995; Weisner et al., 2003; Harvey et al., 2006; Lottermoser, 2010; Murceigo et al., 2011). Additionally, secondary efflorescent minerals may form, particularly in semi-arid and arid regions (Jambor et al., 2000; Harris et al., 2003; Nordstrom, 2009). These represent temporary stores of sulphate and metals and possibly hydrogen ions, which on dissolution will be released as detailed in Appendix 1.1 (Section 3.2.8). A significant source of acidity in mine waste is also the precipitation of Fe^{3+} and Al^{3+} hydroxides (Lottermoser, 2010).

Acid formed by sulphide oxidation can be consumed through reaction with gangue minerals. Neutralisation is primarily offered by dissolution of carbonate minerals of which calcite is the most effective (Sherlock et al., 1995; White et al., 1999; Lapakko, 2002; Frostad et al., 2002; Lottermoser, 2010). Some neutralisation is offered from silicate mineral dissolution, particularly olivine, wollastonite and serpentine phases (Jambor et al., 2002, 2007). However, the rate of dissolution is much slower than that of carbonates. Additionally, clay minerals and Al and Fe hydroxides have a neutralisation capacity, but the likely net-neutralising contribution is small compared to that of calcite (Lottermoser, 2010).

1.3 Current predictive techniques

In countries including Australia, Canada, Europe and the US, mine regulators will only permit mining if robust waste management plans have been developed. Mine wastes are to be fully characterised as part of the environmental impact assessment, with the future performance of the materials predicted. Environmental mine management strategies have evolved over the past two decades resulting in publication of Australian government-funded best practice guidelines in 2007, and the industry-funded Global Acid Rock Drainage (GARD) guide in 2009. Similarly in Canada an updated MEND prediction manual for drainage chemistry from sulphidic geological materials was recently published (Price, 2009).

Whilst these up-to-date handbooks provide information on how to undertake site-by-site ARD prediction, they do not deviate too far from the 'wheel approach' to prediction of drainage chemistry developed by Morin and Hutt (1998) and shown in Figure 1.3. This approach comprises a variety of tests (dominately geochemical) which are either laboratory or field based.

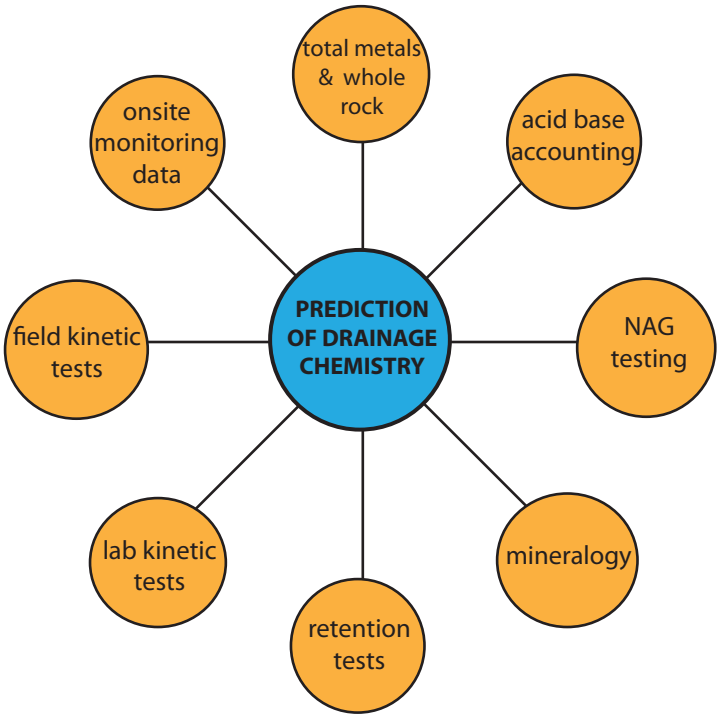

Figure 1.3 The 'wheel approach', for predicting drainage chemistry and the likelihood of ARD (redrawn from Morin and Hutt, 1998).

Due to site-specific limitations and method weaknesses, not all techniques under the 'wheel' are required or are even possible at a mine site depending on the stage of mine operations (Morin and Hutt, 1998). For example, a mine at the pre-feasibility stage would not yet have full-scale monitoring data, so this category of the 'wheel' would be discounted. Furthermore, if test method inaccuracies have been identified, that particular category of the wheel can be omitted. In spite of this, it is recommended that as many of the techniques should be conducted, with the results compared to deduce the drainage chemistry. A summary of tests used in each category as per the wheel approach is given in the following sections, with full descriptions of all methods referred to given in Appendix 1.1.

1.3.1 Total metals and whole rock

Geochemical characterisation typically includes the measurement of sulphur, carbon, metals and metalloids in a sample. Total sulphur and carbon are commonly measured using combustion of sample powders and infrared spectrometry of evolving gases. Methods for measuring sulphide contents include the modified Leco furnace and the chromium reducible sulphur methods. Sulphur and carbon values are used in calculations of acid producing/neutralising potential (Downing and Giroux, 1993; Borden, 2003; Weber et al., 2005a; Hakkou et al., 2009). Measurement of total-metals/metalloids is commonly through XRF or ICP methods. Field portable XRF devices allow for rapid measurement of these, however, the quality of data is poorer. Whilst lithogeochemical models for predicting ARD using whole-rock XRF data have been developed (e.g., Downing and Madeisky, 1997; Lawrence and Scheske, 1997; Paktunc, 1999a), they have limited application.

1.3.2 Acid base accounting

Acid base accounting is the most widely used of all static tests and involves the determination of maximum potential acidity (MPA) and the acid neutralising capacity (ANC) from which the net acid producing potential (NAPP) is calculated. Values can be expressed in either kg H_2SO_4/t as in Australia and Asia Pacific, or kg $CaCO_3$/t as in North America. MPA or acid potential (AP) is calculated directly from total sulphur (S_{Total}) or sulphide-sulphur ($S_{Sulphide}$) values. The S_{Total} or $S_{Sulphide}$ value is multiplied by the stoichiometric factor of 30.6 to give the MPA value in kg H_2SO_4/t (Weber et al., 2005a; Stewart, 2005). A factor of 31.25 is used to give MPA in kg $CaCO_3$/t (White et al., 1999). However, the inaccuracy of using these factors for samples containing sulphides other than pyrite has long since been recognised. Paktunc (1999a) stated that if the sample being tested contains pyrrhotite in addition to pyrite, then overestimation of MPA/AP values may occur up to 1.5 times. Considering this, he proposed a mineralogical method of determining MPA/AP. Weber et al. (2004) explained that this method requires detailed knowledge of the sulphide contents, mineralogy and the corresponding oxidation reactions, potentially limiting its application. However, it can be argued that basing MPA/AP on S_{Total} only makes for cautious, and therefore more effective waste management plans.

The ANC (or neutralising potential: NP) is a quantitative measurement of a solid phase sample's capacity to neutralise aqueous acidity (Morin and Hutt, 2009). It is typically calculated by a titration method. The most widely used is the Sobek method (White et al., 1999; Bezaazoua et al., 2004; Jambor et al., 2006). This method has subsequently been modified, and several additional methods exist. There is no standard method; rather one is used in accordance with environmental legislation in that particular country. For example, the U.S. EPA-600-compliant Sobek et al. (1978) NP method is the standard method in the United States (Morin and Hutt, 2009). In Australia, the Sobek and modified Sobek methods are the most widely used in accordance with legislation specified by Commonwealth, state and local Governments (Comarmond, 1997). Alternative methods to ANC calculations were presented in Bucknam (1997) and Hutt and Morin (2000), who proposed ANC calculations based on carbonate contents. Methods to determine silicate ANC are presented in Nesbitt and Jambor (1998), Jambor et

al. (2002, 2007) and Miller et al. (2010), but these have limited application at the early stages of mine operations.

Calculations for NAPP, net neutralising potential (NNP), and the neutralising potential ratio (NPR) are shown in *equations 1.11*, *1.12* and *1.13*. NNP and NPR are commonly used in North America.

Net Acid Producing Potential or NAPP = MPA - ANC *(1.11)*

Net Neutralising Potential or NNP = ANC - MPA *(1.12)*

Neutralising Potential Ratio or NPR = ANC / MPA *(1.13)*

NAPP values >20 kg H_2SO_4/t indicate that the rock unit has acid forming potential (Skousen et al., 2002). If the NNP is >20 kg/t $CaCO_3$, then the material is non-acid producing. However, if NNP is lower than -20 kg/t $CaCO_3$, then the material is acid forming. Values between -20 and +20 kg/t $CaCO_3$ are considered to require kinetic tests to clarify their NNP (Fey, 2003; Bezaazoua et al., 2004). Often it is easier to use NPR values; when the value is <1 the material is considered acid forming, and non-acid forming if the NPR is >3 (Fey, 2003).

1.3.3 pH methods

Whilst determining pH is sometimes regarded as part of acid base accounting (e.g., Siddharth et al., 2002), it is summarised independently here. Measuring paste pH is the simplest of all static methods, and provides an indication of the inherent acidity (and salinity) of a sample (Weber et al., 2006; Hughes et al., 2007). Minerals assumed to be assessed by paste pH tests include acid forming sulphate salts such as melanterite, reactive sulphides such as greigite, and high surface area pyrite and carbonates (Weber et al., 2006). Paste pH tests vary in the ratio of solid to water used, for example, Sobek et al. (1978) recommend a 2:1 test and Miller et al. (1997) a 1:2 test. Samples which return a paste pH value >4.5, are generally considered non-acid forming, and those <4.5 are potentially acid forming. Variations of the paste pH test include the abrasion pH (Stevens and Carron, 1948), rinse pH (Price et al., 1997) and dynamic pH tests (Rossiter et al., 2008).

1.3.4 Net acid generation tests

Net acid generation (NAG) tests evaluate the acid forming potential of a sample without separate estimation of MPA and ANC. This is achieved by using H_2O_2 to rapidly oxidize sulphide minerals, allowing the product to react with any acid neutralising minerals present (Miller et al., 1997; Smart et al., 2002). These tests do not require S_{Total} or $S_{Sulphide}$ calculation and are therefore more readily conducted in a field laboratory than ABA (White et al., 1999; Lei and Watkins, 2005). There are six main types of NAG tests (single addition, sequential, multi addition, kinetic, field and extended boil), with single addition the most commonly used. Two values are obtained, a NAG pH and a final NAG value (kg H_2SO_4/t).

1.3.5 Mineralogy

Mineralogy can be assessed using a range of tools ranging from the simple (e.g., optical microscopy) to the advanced (e.g., laser ablation-inductively coupled plasma-mass spectrometry or LA-ICP-MS). Selection of the most appropriate tools for the evaluation of mineralogy is dependent on the objective of the study (e.g., is the bulk mineralogical composition required for calculating the calcite: sulphide ratio (e.g., Paktunc, 1999a), or is the elemental composition of a specific mineral required to understand its relative susceptibility to oxidation (e.g., iron in sphalerite?). Mineralogical evaluations and tools used in ARD studies are outlined.

1.3.5.1 Drill core evaluation

Interpretation of the nature and relationships of sulphide and carbonate mineralogy on a core-scale is by far the most efficient way to gather a deposit-scale understanding of the potential for acid formation. However, it is often the case that when logging is undertaken, the motives are for metallurgical, geotechnical and resource evaluation purposes. The GARD Guide (2010) summarised parameters to observe for understanding the potential for ARD formation whilst logging. However, guidelines of how to evaluate these were not given.

1.3.5.2 Optical microscopy

No standard approach for undertaking optical microscopy for predictive ARD assessment exists. However, Mills et al. (2011) recommended that transmitted light and reflected light microscopy techniques should be performed: (a) to examine sulphide and carbonate mineralogy; (b) to determine primary and secondary neutralisation mineralogy; (c) to examine alteration variations; (d) to determine modal mineralogy; and (e) to examine grain size boundaries as reaction sites for acid. Examples of ARD focussed optical mineralogy studies are given in Blowes and Jambor (1990), Gunsinger et al. (2006) and Moncur et al. (2009), in which the sulphide alteration index (SAI), primarily developed for tailings classification, is used. However, the SAI is limited by the lack of consideration given to the dissolution of adjacent metal sulphides (and release of metals) under acid conditions (i.e., sulphide mineral-associations not considered). Despite this, with modification, it has application at the pre-feasibility/feasibility stage as a semi-quantitative petrographic index (Parbhakar-Fox and Lottermoser, 2011).

1.3.5.3 Bulk mineralogy

Bulk mineralogy is routinely assessed by powder X-ray diffractometry (XRD) with examples given in Dold and Fontbote (2001), Marescotti et al. (2008) and Moricz et al. (2009). However, amorphous minerals such as iron oxyhydroxides, aluminium and aluminosilicates commonly associated with ARD cannot be readily identified unless the Rietveld Method is used (Lapakko, 2002; Raudsepp and Pani, 2003). Additionally, the results are only qualitative. Other XRD techniques include quantitative XRD, whereby the modal mineralogy is deduced, and differential XRD (Dold, 2003a). However, these are less frequently used due to the high cost per sample. Methods to estimate modal mineralogy using XRD and whole-rock data are presented in Paktunc (2001) and Posch and Kurz (2007), with examples given in Weber et al. (2005a) and McLemore et al. (2009). A method of assessing modal mineralogy of an intact

rock sample (thus relating this to texture) would be of greater use in understanding the potential for ARD formation. Such a method exists using mineral-liberation analysis-scanning electron microscopy (MLA-SEM).

1.3.5.4 Mineral form and composition

Electron probe microanalysis (EPMA) and scanning electron microscopy (SEM) with energy X-ray dispersion (EDS) are the two most commonly used techniques to resolve mineralogical composition and undertaking surface analysis (Rollinson, 1993; Goldstein, 2003). A complimentary tool to these techniques is LA-ICP-MS. Examples of the application of these techniques for sulphide characterisation and ARD studies are given in: Muller et al. (2002); Chappell and Craw (2002); Jambor (2003); Hudson-Edwards and Edwards (2005); Al et al. (2007); Diehl et al. (2007); Ohlander et al. (2007); Savage et al. (2008); Haffert et al. (2010); and Weisner and Weber (2010). Generally, their application is confined to sulphide minerals where compositional abnormalities affect ARD test work interpretation (Mills et al., 2011). Whilst high-resolution techniques such as LA-ICP-MS are effective in quantifying trace elements and mapping their distribution, they are costly. Either a protocol which guides sample selection for this analysis is required, or alternative instrumentation should be utilised; e.g., Micro-Particle Induced X-ray Emission (Cabri and Campbell, 1998; Belcher et al., 2004; Jamieson et al., 2005) or Micro-XRF (Adams et al., 1998; Katsuta et al., 2007).

1.3.6 Retention tests

Retention tests target sulphide weathering reaction products stored on the surface of mined materials. Retention tests range from simple washing with water to sequential-extraction tests (Morin and Hutt, 1998). Examples of sequential extraction test protocols are given in Tessier et al. (1979), Li et al. (1995), Margui et al. (2004) and Dold (2003b). Retention tests have limited application in deposit-wide predictive ARD test work as results reflect short-term dissolution of minerals, and sequential extraction procedures have several problems including readsorption and precipitation, non-selective dissolution, transformation of labile phases to more stable phases during drying (cf. Rendell et al., 1980; Tipping et al., 1985). Reaction rates of primary minerals are more reliably obtained from kinetic tests (Morin and Hutt, 1998).

1.3.7 Laboratory based kinetic tests

In general, kinetic tests involve: (a) the subjection of samples to periodic leaching; (b) collection of drainage for analysis; (c) calculation of rates of acid formation and neutralisation capability depletion; (e) calculation of rates of metal release; and (f) the prediction of water quality (Mills et al., 2011). This is generally undertaken by accelerating the natural weathering rate of a sample under closely controlled laboratory conditions. However, a drawback of these tests is the extended amount of time required to perform the tests, as it is not uncommon for these to continue for at least 20 weeks (White et al., 1999). The two main types used are humidity cell tests (Lapakko, 2003; Frostad et al., 2003; Bezaazoua et al., 2004; Mills et al., 2011) and column leach tests (Shaw et al., 1998; Smart et al., 2002; Weber et al., 2004; Bezaazoua et al., 2004; Stewart et al., 2009; Miller et al., 2010; Mills et al., 2011). The GARD Guide

(2010) recommends that all materials involved in kinetic testing undergo comprehensive characterisation before the test begins, including surface area, particle size distribution, mineralogy, chemical composition and MPA and ANC determination. At completion of testing, the interpretive value of the kinetic testing program is greatly enhanced by repeating the determination of mineralogy, chemical composition, and acid-forming potential.

1.3.8 Field based kinetic tests

Undertaking of field-based kinetic tests more closely approximates the evolution of ARD as they permit accurate replication of the local climate and allow for the selection of appropriate sample material and volume (Smith et al., 1992, Morin and Hutt, 1997, Bethune et al., 1997 *in* Lottermoser, 2010). Therefore, field based pilot waste rock piles allow the determination of acid forming parameters under actual field conditions (Lottermoser, 2010). Small scale field kinetic tests are routinely undertaken and scaled up from these are pilot waste rock piles with examples given in Andrina et al. (2006), Blowes et al. (2006) and Smith et al. (2009). These are constructed with appropriate liners and various instrumentation is installed to allow for the analysis of leachate, run-off and pore waters (Lottermoser, 2010).

1.3.9 Onsite monitoring data

If the mine site is in operation, onsite monitoring of water quality is undertaken (Morin and Hutt, 1998). However, if the site is in pre-feasibility/feasibility stages, water quality predictions are made based on the data obtained from the techniques described in Sections 1.3.1 to 1.3.8. Additionally, data from geochemical and physical modelling can be used (e.g., PHREEQC, MINTEQ). Water quality predictions are compared against relevant water quality standards such as those published in ANZECC (2000) or WHO (2006).

1.3.10 Waste classification

Sulphide and calcite contents can be used to classify samples based on mineralogy, with examples shown in Paktunc (1999a). However, classifications are more commonly based on static geochemical results. The convention is to use NAPP versus NAG pH data to classify samples as either PAF (potentially acid forming: when NAPP >0 kg H_2SO_4/t and pH < 4.5); NAF (non-acid forming: when NAPP <0 kg kg H_2SO_4/t and pH > 4.5); or UC (uncertain: when NAPP <0 kg H_2SO_4/t but pH < 4.5 or NAPP >0 kg H_2SO_4/t and pH > 4.5). Classification examples are shown in Stewart et al. (2006), and Hesketh et al. (2010). Total sulphur values are also consulted to evaluate these classifications. Miller (1996) and Smart et al. (2002) recommend the use of addition waste categories (potentially acid forming-high capacity and potentially acid forming-low capacity). However on review of recent publications, these terms are infrequently applied. Additional classification methods using paste pH values are proposed in Price et al. (1997) and Hughes et al. (2007), but again these are not widely used.

1.4 Limitations of ARD prediction

ARD prediction and waste classification are affected by two major factors. Firstly, predictions are largely

based on geochemical analyses with static testing the most commonly used (i.e., ABA). These screening tests have been accurate in some cases and misleading in others. Reasons for failure are due to inherent limitations of static tests as detailed in White et al. (1999), Dobos (2000), Jambor (2003) and Weber et al. (2005a), and summarised in Section 1.4.1. Secondly, waste classification protocols do not require the assessment of parameters with direct influence on sulphide oxidation and ARD formation such as texture and micro-scale mineralogy. Additionally, protocols do not provide enough test selection guidelines as discussed in Section 1.4.2.

1.4.1 Test limitations

Total sulphur values may not account for different acid yields from species such as non-ferrous sulphides, chalcopyrite and arsenopyrite and in the absence of mineralogical data, the general assumption is that all sulphur represents pyrite (White et al., 1999). Thus, the calculated value represents the acid yield based on pyrite oxidation, and therefore potentially inaccurate depending on the sulphide mineralogy. In real samples that are partly or completely oxidised, sulphate sulphur is treated as sulphide sulphur, even though acid yields may be zero (from mineral species such as gypsum), or different from pyrite (such as from jarosite; Dobos, 2000).

Acid base accounting (ABA) assumes that ferrous iron is oxidised to ferric iron (that is, precipitated as ferric hydroxides), that iron sulfosalts and other iron salts are not produced, and that all sulphides are oxidised to sulphates (White et al., 1999). Acid base accounting also predicts the final result of completed reactions with the assumption that no significant chemical species are lost during the 'reactions' (Dobos, 2000). On a mine site, intermediate products may be removed from the reacting solids, such as by leachates. All available carbonates are assumed to react in the presence of excess acid by ABA (Dobos, 2000). This may not be realistic, since coarse-grained calcite in waste-rock piles may be coated or 'armoured' by precipitated gypsum during early neutralisation reactions (Jambor, 2003). Subsequently, acid will not directly contact the armoured calcite, leading to acidic leachates where none were predicted. This may be a signficiant long-term issue. Acid base accounting is largely concerned with the balance between acid-producing and acid-consuming minerals. In many instances, determining the concentration of potentially delterious elements (e.g., As, Cd, Pb, Zn) is far more important, and yet ABA offers no information on this (Dobos, 2000).

Acid neutralising capacity (ANC) titration tests utilise fixed reaction stoichiometries to calculate acidity yield. However, for minerals such as pyrrhotite, a number of reaction pathways are available and not all produce the same acid yields (Jambor, 2003). Additionally, ANC values are affected by differences in titration protocols, chiefly the sample particle size, amount of acid added, back titration endpoint and digestion duration. Errors may arise from deducing carbonate concentrations from total carbon values, as presence of organic carbon and/or graphite in the sample leads to overestimation of mineral carbonate and hence ANC (Weber et al., 2005b). Siderite is often added to the ANC budget, which for many coal and gold deposits is of significance as it is the dominate carbonate material. Comparisons of ANC

titration methods are often presented (Adam et al., 1997; White et al., 1999; Capanema and Ciminelli, 2003). However, Morin and Hutt (2009) argue that no one method is superior or inferior, despite claims in the GARD Guide (2010) that the Modified Sobek method prevents overestimation of ANC or MPA relative to the Sobek method, or the draft EU standard recommending a unique NP method. They also raise the point as to which method is actually accurate; if a method provides a lower ANC value - is it inherently better? Their wheel approach (Morin and Hutt, 1998) recommends that cross checks are made. This applies too to ANC titration methods, which also need to be cross referenced with sample mineralogy.

Screening static tests do not consider important variables that control sulphide oxidation and ARD formation in the long term (including weathering reaction rates of individual minerals, presence or absence of particular micro-organisms, mineral and waste particle size, mineral chemistry or formation of secondary minerals). Kinetic tests provide some information on these variables, by identifying dominant chemical-weathering reactions, acid-formation rates and temporal variation in leachate water quality (White et al., 1999). However, as kinetic tests elapse over a longer time scale (months to years), data which could influence ARD management may not be available at the mine planning stages. Additionally, these tests are expensive, with a twenty week experiment costing between US $3,000-5,000 (Lengke et al., 2010).

In general, too few static (and kinetic) tests are performed (e.g., Robertson, 2005; Akabzaa et al., 2007). Despite this, ARD waste block models are formulated using this limited information resulting in the definition of few (e.g., <6) waste categories as summarised in Table 1.1. This raises the question as to whether the inherent geological and mineralogical variability of the mineral deposit is accurately accounted for (Jambor, 2003).

Recent attempts to improve ARD classification have focussed on developing new short-term geochemical tests. Examples of these include the net carbonate value test (Bucknam, 1997; Lengke et al., 2010) and dynamic pH test (Rossiter et al., 2008). However, their application is questionable, as they do not consider the complexity required to test for ARD generation. Instead, the objective should be on obtained the most value from established tests and routinely collected data such as paste pH testing, assay values and geometallurgical data (e.g., Downing and Giroux, 1993; Borden, 2003; Hughes et al., 2007).

1.4.2 Protocol limitations

Despite the limitations of geochemical tests, waste rock classification protocols are strongly biased towards their use. This is evident in the wheel approach (Morin and Hutt, 1998), where seven of the eight categories of tests are geochemically focussed. Bias towards geochemical testing remains in updated protocols such as the AMIRA P387A approach (Smart et al., 2002; Figure 1.4). Mineralogical evaluations are recommended only to define the nature of samples geochemically classified as 'uncertain'. The advantage of the AMIRA P387A approach (Smart et al., 2002) over the wheel approach (Morin and Hutt, 1998) is that improved classification guidelines and reasoning for tests are given. Additionally, the

Table 1.1 Examples of the number of solid waste categories identified at operational mine sites.

Mine/Location	No. of waste categories	Reference
PT Freeport Au-Cu, Indonesia	2	Andrina et al. (2006)
Diavik Diamond mine, Canada	3	Blowes et al. (2006)
Antamina Cu-Zn-Mo, Peru	3	Brown et al. (2006)
Savage River Fe, Australia	4	Hutchinson and Brett (2006)
Svartliden Au, Sweden	3	Linklater et al. (2005)
Akara Au, Thailand	6	Changul et al. (2010)

use of advanced geochemical tests is recommended (e.g., advanced net acid generation and acid buffering characterisation curve tests). However, the wheel approach (Morin and Hutt, 1998) assigns the same importance to mineralogy and whole-rock geochemical tests as static geochemical tests. Advantages of both approaches must be adopted into an improved protocol which also systematically incorporates texture.

Mills et al. (2011) summarised the need for textural analyses when presenting four scenarios for sulphide mineral liberation from non-sulphides minerals (i.e., silicates, oxides or carbonates) as shown in Figure 1.5. Scenarios A and D contain a sulphide that is liberated with respect to atmospheric leaching. The second and third particles contain a grain or grains of a sulphide mineral that are not liberated with respect to atmospheric leaching. It is possible that the same total sulphur value could be assigned to all scenarios, with the same MPA calculated. Therefore, static tests would rate the four grains equally with respect to potential acid formation. However, in a kinetic test, only A and D would have the potential to form acid, as they would in the field (Mills et al., 2011).

In geological studies, texture is commonly defined as the smaller features of a rock which relate to the size, shape and arrangement of its constituent minerals (Bastin, 1950; Pryor, 1963; Gove, 1965; Nelson and Nelson, 1967; Thrush, 1968; Whitten and Brooks, 1972; Collott and Dobson, 1974; Dictionary of Geological Terms, 1976; Bates and Jackson, 1984; Wyatt, 1986 *in* Vink, 1997). Additional definitions refer to the megascopic and microscopic appearance demonstrated in a smooth surface of a homogenous rock (Rice, 1963 *in* Vink, 1997). Considering these definitions, texture in the context of ARD prediction must be clearly defined and must focus upon evaluating sulphide and carbonate mineralogy by parameters including size, shape and mineral association. Additionally, a scaled approach must be adopted as demonstrated in Bonnici et al. (2009) when characterising ore prior to mineral processing. This approach is becoming commonplace in the field of geometallurgy (Walters, 2008), and is supported by automated mineralogical platforms such as MLA-SEM, QEMSCAN® and automated optical microscopy (Gottlieb et al., 2000; Gu, 2003; Fandrich et al., 2007; Berry, 2008). Examples of the application of these technologies in ARD studies focussed on the characterisation of reaction products (i.e., tailings, hardpan) are given in Aranda et al. (2009) and Redwan et al. (2012).

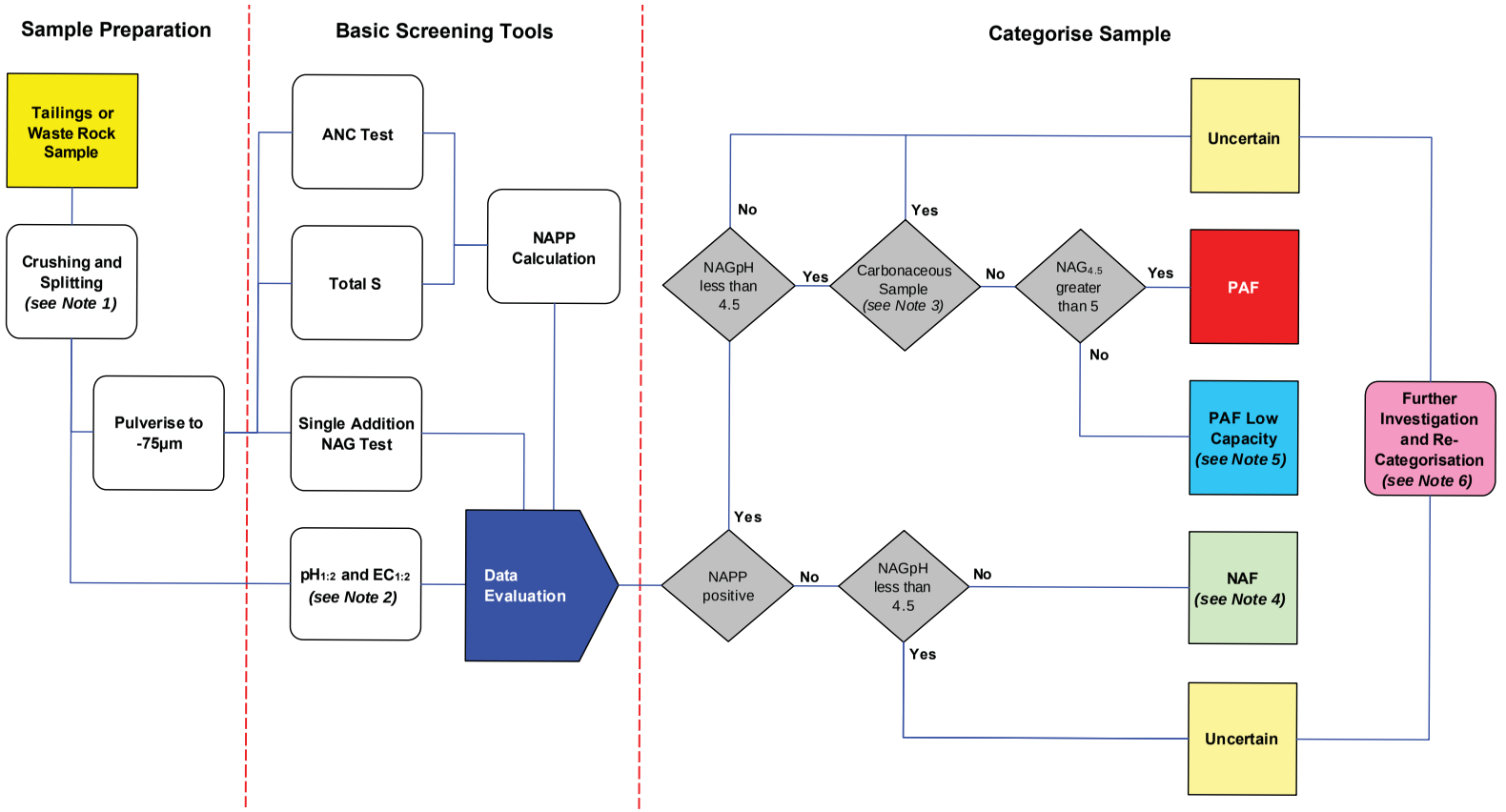

Note 1: Sample preparation may include crushing to nominal -4mm and splitting of a representative sub sample from the bulk. Core and rock samples require crushing before splitting. Drill chips and tailings do not normally require crushing.

Note 2: pH and EC measurements provide a measure of immediately available acidity and salinity. This information may influence the final categorisation of the sample due to potential short term effects of a given material on rehabilitation, drainage etc. Measurements are best carried out on the crushed sample rather than the pulverised sample where possible.

Note 3: The occurrence of organic compounds in some materials may interfere with NAG tests. In particular samples from coal deposits with more than about 5% TOC.

Note 4: Further evaluation is recommended to confirm classification on samples with High Sulphur and High ANC. There is a risk of incomplete sulphide oxidation during the NAG test on high sulphur samples Selected samples of High S and High ANC material should be subjected to Sequential NAG and ABCC determinations. Samples with more than 2% S and ANC/MPA ratios less than 1.5 should be evaluated.

Note 5: Further investigation is recommended to determine acid forming capacities of samples with high S values(>1%S) and low NAG/NAPP ratios (<0.5). Low NAG/NAPP ratios indicate either non-acid producing S forms or incomplete oxidation in the NAG test, and additional testing would be required to determine which applies in a particular case.

Note 6: Further investigations are required to determine:
-Classification of samples with conflicting NAPP and NAG results.
-Magnitude of acid forming capacity for PAF samples with low NAG/NAPP ratios.
-Availability of ANC for neutralisation of acid produced in samples with moderate to high S.

Figure 1.4 Flow chart showing ARD screening tests, decision nodes and ARD rock type categories (taken from Smart et al., 2002).

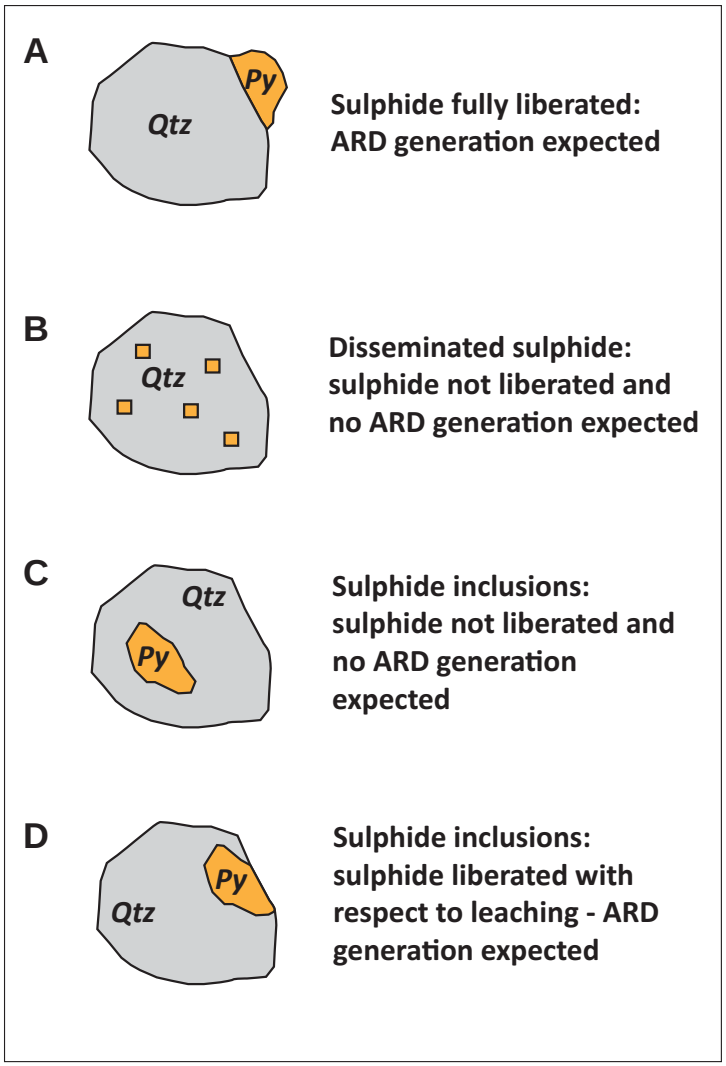

Figure 1.5 Four possible scenarios for sulphide liberation, modified from Mills et al. (2011). Abbreviations: Py, pyrite; Qtz, quartz.

Recent examples of ARD predictive protocols are given in Hansen et al. (2008), the GARD Guide (2010) and Broadhurst and Petrie (2010). Hansen et al. (2008) aimed to increase the understanding of the role of ore type and composition in determining waste characteristics, thus providing key information in the early stages of a project, and guiding data collection and the focus of impact prediction modelling in the later stages. The GARD Guide (2010) recognises the importance of a pre-screening stage (static tests are commonly identified as screening tools; e.g., AMIRA P387A Handbook; Smart et al., 2002), with core logging featuring as part of this. Conceptually, both protocols identify key areas for improving waste characterisation; however, they are limited by the absence of detailed guidelines to perform the recommended techniques. Broadhurst and Petrie (2010) propose the use of ranking and scoring potential environmental risks from solid mine wastes. Whilst detailed waste assessment is afforded, this approach lacks simplicity and therefore has limited widespread application in the pre-feasibility stages of an operation, or for assessing a historic site. Instead, rapid and low-cost methods performable on a large number of samples (i.e., approximating those used in geometallurgical studies; e.g., Alruiz et al., 2009)

must be adopted. These should be organised into a staged approach, which maintains the use of some static tests, as despite their limitations, static tests are routinely used and understood by industry. Test data must be cross-checked with improved mineralogical and textural evaluations, thus providing more data on parameters directly influencing sulphide oxidation. This protocol should guide sample selection for kinetic testing, and ultimately improve waste classification.

1.5 Research aims and thesis framework

1.5.1 Primary objective and research questions

The overarching question motivating this research is "how can waste rock material characterisation be improved using an integrated geochemical-mineralogical and textural ARD classification protocol?" This was not addressed by recent Ph.D theses in this general subject area (e.g.,Weber, 2003; Stewart 2005; Özcelik, 2007; and Servida, 2008). Therefore, the primary objective was to develop a new approach to ore and waste rock characterisation, which systematically integrates geochemical, mineralogical and textural data in order to improve the accuracy of ARD predictions. A detailed understanding of ARD characterisitics of an ore body obtained at the early stages of mine operations can influence decisions on mining, mineral processing and waste disposal so as to reduce the potential for sulphide oxidation. Such an integrated approach must also be adaptable for the classification of waste rock material at abandoned mine sites (Harris, 1997; Feasby and Tremblay, 1995; Strong and Flores, 2008). The general research objectives were:

- To establish a protocol for predictive ARD testing of ores and waste rocks that has the potential to be incorporated into resource block modelling.
- To develop a simple scaled textural ARD evaluation scheme which can be used for deposit-scale ARD domaining.
- To deduce a protocol by which samples are better identified for detailed microtextural sulphide characterisation (i.e., element mapping) and kinetic testing.
- To define the application of geometallurgical tools in ARD predictive studies.

Two study sites were sampled in this research, namely, the historic Croydon lode-gold mines and the operational Ernest Henry iron-oxide copper gold (IOCG) deposit, both located in Queensland, Australia (Figure 1.6). These sites were chosen as the style and mineralogy of the ore-deposits differed, and both sites represented different stages of mine operations. This allowed for the development of a protocol with application both prior to mine operation and post-closure. As ARD is actively being produced at the Croydon mines, research focussed particularly on this site, with results intended to guide future site rehabilitation. The research questions specific for the case study sites were:

1. Which waste rock groups are acid forming at the Croydon gold mines, and how does texture influence acid formation?
2. What are the potentially deleterious elements associated with sulphide minerals identified in the waste rock piles at the Croydon gold mines?

3. Which secondary minerals form in the waste rock piles at the Croydon gold mines, and how do they control the flux of potentially deleterious elements to the downstream environment?
4. How can mineralogical and textural analyses be effectively integrated into column leach testing, and does this improve the understanding of the leachate chemistry?
5. What are the effects of grain size on rate of acid formation and metal leaching for the different acid forming groups identified in waste material from the Croydon gold mines?
6. Which lithologies are acid forming or neutralising at the Ernest Henry IOCG deposit, and how does texture control this behaviour?
7. How can geometallurgical data from the Ernest Henry IOCG operations be best used to define ARD forming or neutralising potential?
8. How can this improved protocol be best used in the pre-feasibility stages of mine operations?

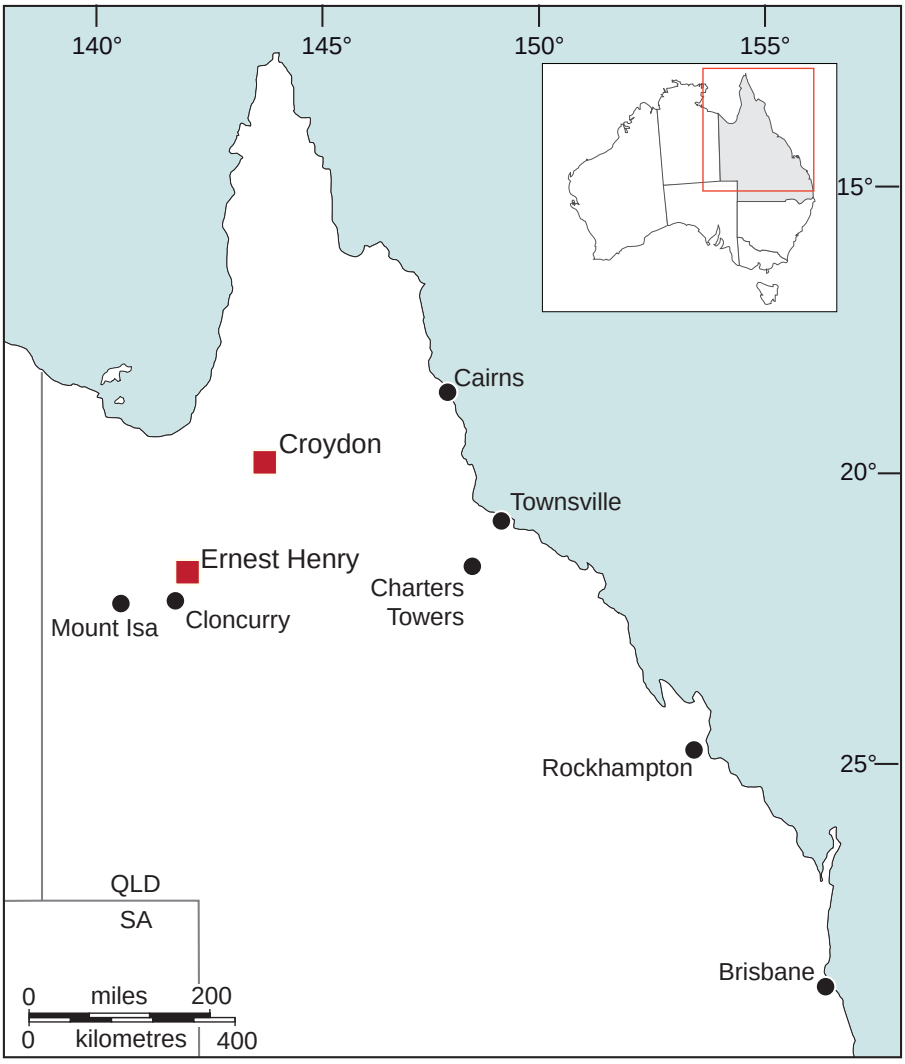

Figure 1.6 Location of the Croydon district and Ernest Henry mines within Australia.

These questions were addressed using a combination of well-established, as well as novel and innovative techniques. Specifically, this research had the unique ability to explore the application of geometallurgical tools such as MLA-SEM and HyLogger (Quigley, 2008) for ARD characterisation. Further opportunity existed to integrate mineral and element maps using MLA-SEM and LA-ICP-MS to examine the distribution of potentially deleterious elements in sulphides. From this, secondary mineral formation and potential leaching pathways as dictated by the associated mineralogy were better understood.

1.5.2 Thesis outline

The following chapters document the Ph.D research. The acid rock drainage index (ARDI) and the geochemistry-mineralogy-texture (GMT) approach are proposed in Chapter 2. The ARDI has been developed to predict acid formation based on intact rock texture. The ARDI evaluates samples by five parameters which influence acid formation. The ARDI forms part of the GMT approach, which is a revised protocol for classifying solid mine waste (i.e., waste rock). The GMT approach consists of three stages and involves parallel use of geochemical, mineralogical and textural analyses. Sample screening is performed at stage-one; routine geochemical tests are performed at stage-two; and advanced geochemical tests and microanalysis are performed at stage-three. Samples from both study sites were used to develop and evaluate the applications and limitations of the ARDI and GMT approach.

A mesotextural classification method for identifying sources of ARD at the historic Croydon-gold mining operations is described in Chapter 3. Through undertaking mesotextural classification, waste rock material with a propensity to form acid was systematically characterised using the GMT approach. This chapter focussed on evaluating the various techniques and classification methods recommended by the GMT approach in Chapter 2, and identified the best tools for use. The acid forming mesotextural groups which posed the greatest environmental risk at Croydon were identified, and subsequently recomended for kinetic testing.

Chapter 4 documents laboratory based column leach kinetic trials performed on four (potentially) acid forming mesotextural groups identified in the waste material obtained from the Croydon gold mining operations. Twelve columns were established, with material from six different samples tested. Two grain sizes (-10mm and -4mm) were used to observe the effects of grain size on pH, metal elution and secondary mineral precipitation. Mineralogical and textural changes were also monitored throughout this experiment, and related to leachate chemistry to identify the controls on sulphide oxidation, and deduce the relative rate of weathering. Laboratory-based results were compared with those obtained from a local geochemical study (in which stream sediment and water quality were assessed), and site rehabilitation strategies were proposed.

To explore the application of geometallurgical techniques for predicting acid formation, data from the Ernest Henry iron-oxide copper gold (IOCG) deposit were obtained and used alongside predictive ARD geochemical and mineralogical data as presented in Chapter 5. Samples from two drill

holes were subjected to GMT analyses, with MLA-SEM, Hylogger, assay and mineral hardness data examined in conjunction. This provided an indication of how best these tools can be integrated into ARD predictive studies. General conclusions are given in Chapter 6, with the research questions revisited. Recommendations for how the GMT approach can be integrated into the mine life cycle are also given. Finally, this thesis outlines areas for further research.

Chapter 2

Proposed methodology for waste rock classification

Chapter 2 is adapted from: Parbhakar-Fox, A.K., Edraki, M., Bradshaw, D. and Walters, S. 2011. Development of a textural index for the prediction of acid rock drainage. Minerals Engineering, v.24 (12), p.1277-1287.

2.1 Introduction

Whilst understanding of sulphide oxidation processes and acid rock drainage (ARD) formation has improved over the past decades (Price, 2009; Lottermoser, 2010; Jamieson, 2011), ARD predictive protocols have not developed as such. It was stated in Chapter 1 that the wheel approach (Morin and Hutt, 1998) and the AMIRA P387A approach (Smart et al., 2002) are the most widely used protocols by which waste rock is classified in terms of ARD formation (e.g., Weber et al., 2005a; Marescotti et al., 2008). However, limitations of both protocols were also described. Therefore, a new, up-to-date approach is required by the mining industry to efficiently identify sources of ARD in order to improve waste rock management. Such an approach should not focus on improving the current geochemical screening tests, but should offer better guidance with regards to test selection and application, as well as providing guidelines for evaluating mineralogy and texture over a range of scales.

Ultimately, the key to improving ARD prediction and waste rock classification is to increase the number of samples analysed so as to account for the geological variability of the ore-deposit. Such an approach has been successfully adopted in other predictive disciplines i.e., geometallurgy whereby samples are obtained at least every 2 metres for analyses (Walters, 2008; Alruiz et al., 2009). Downing and Giroux (1993) provide an example whereby such an approach was adopted for ARD prediction. Their investigation was part of the pre-feasibility study undertaken at the Windy Craggy VMS (Besshi-type) deposit in northwestern British Columbia, Canada. Over 1200 split core samples were subjected to ABA testing with Fe and S assay data for over 1700 samples also used to create a waste rock model consisting of over 100,000 units. However, deposit-wide application of screening geochemical tests in this manner may be considered uneconomical at other mine sites. Therefore, an efficient pre-screening stage (ideally performed in the field) by which an ore deposit or waste rock pile can be classified is required. The GARD Guide (2010) provides a description of what should be included in such a stage. However, it largely revolves around a desk study, and whilst core logging is recommended, no structured guidance

is provided on how to assess acid forming potential. Instead, a pre-screening stage must offer detailed guidance for systematically undertaking mineralogical and textural evaluations in order to address the limitations posed by current techniques. Such an approach must have application at both historic and operational mine sites to ensure consistency when data evaluation is undertaken by both mine operators and regulators.

This research adopts a geochemistry-mineralogy-texture (GMT) approach as a means of improving waste classification (Figure 2.1). This comprises of three stages of tests, within which two require parallel geochemical, mineralogical and textural analyses in order to fully characterise ARD potential and predict metal/metalloid leaching potential. Each stage is performed sequentially. A range of tests have been selected for evaluation in this research. These are described in this chapter, with results presented in Chapters 3 and 5. The most accurate and efficient methods were selected for inclusion in the final GMT approach proposed in Chapter 6. Tests discussed in this chapter were selected based on potential and demonstrated applications in ARD characterisations studies. This approach also proposes the Acid Rock Drainage Index (ARDI), a novel textural evaluation scheme performed on hand-specimen and petrological thin section samples as part of stage-one. After full GMT analyses, waste is adequately classified, with groups classified as acid forming (AF), or extremely acid forming (EAF) recommended for kinetic testing, and a management/rehabilitation plan formulated.

In this research, mine sites in pre-feasibility/feasibility or operational stages are generically referred to as 'operational' and historic or abandoned mines are collectively referred to as 'historic'. As the GMT approach aims to have application at both operational and historic mine sites, some protocol variation is required (e.g., with regards to sample selection) as explained throughout this chapter. With each stage analytical sophistication increases and the number of samples analysed decreases. Stage-one is for pre-screening samples and identifying those required for analysis by routine screening tests which are undertaken at stage-two. Samples with significant acid forming potential are advanced to stage-three whereby controls on sulphide oxidation are identified through detailed characterisation. Thus, as each stage increases, selection of samples for further analyses is determined by mineralogical characteristics. The following sections detail each stage of the GMT approach and provide rationale for the chosen methods/tests.

2.2 Sample selection

Sample selection is the most critical aspect of an investigation aimed at determining the acid-forming potential of mine wastes (Downing, 1999; Price, 2009). Poor sampling techniques and inadequate sample selection can contribute to excessive variance, difficulties in interpretation, and incorrect assessment (Downing, 1999; Morin, 2010). Sampling guidelines are provided in the literature, particularly for operational mines (e.g., Price, 2009; GARD Guide, 2010). This section builds upon these recommendations, and proposes sample selection guidelines for GMT analyses.

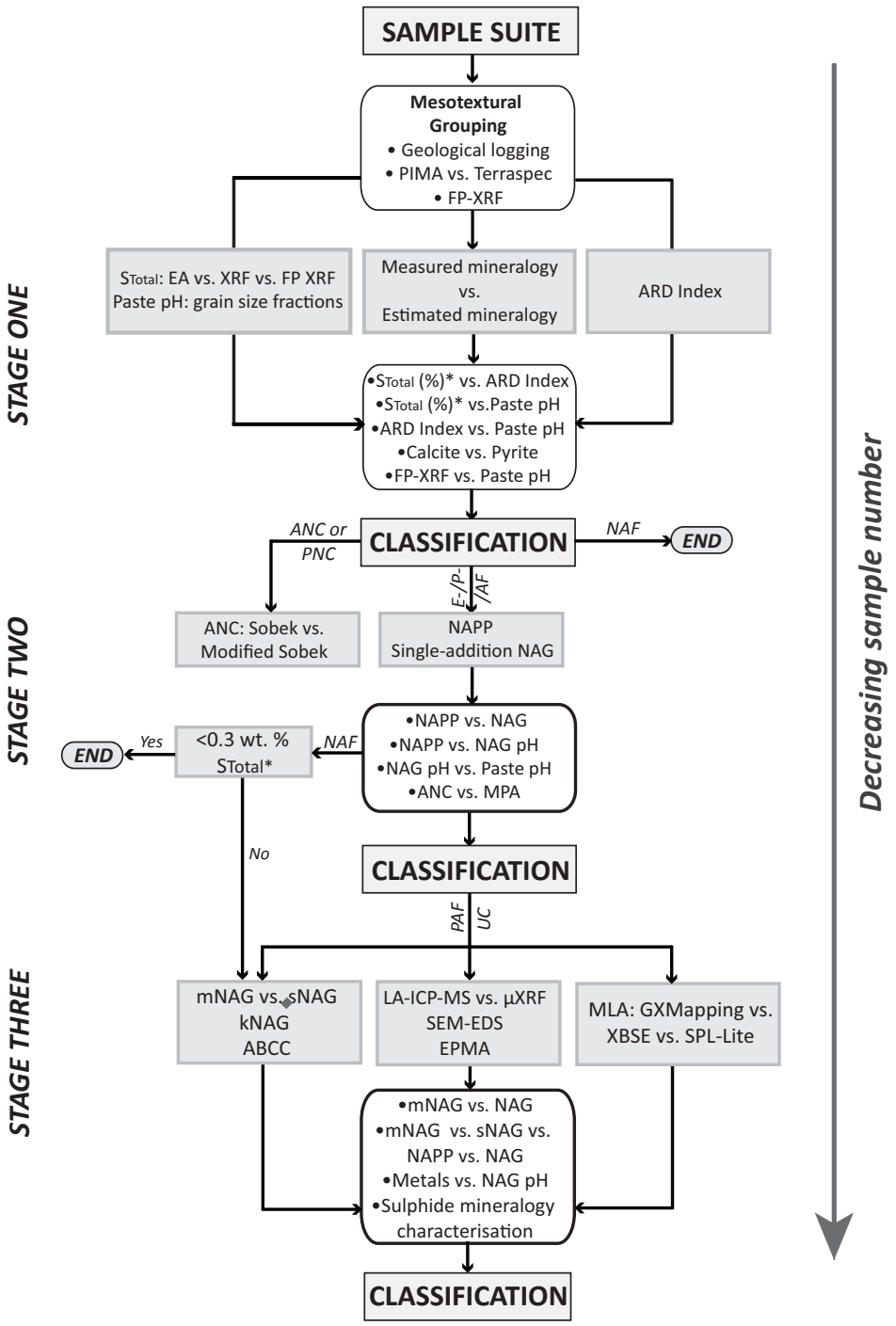

Figure 2.1 Proposed GMT approach with tests/analysis shown in rectangular boxes and evaluations shown in round cornered boxes. Abbreviations: PIMA, portable infrared mineral analyser; EA, elemental microanalysis; (FP) XRF, (field portable) X-ray fluorescence; QXRD, quantitative X-Ray diffractometry; NAPP, net acid producing potential; NAG, net acid generation; MPA, maximum potential acidity; m-, s- and k- NAG, multi-addition-, sequential and kinetic-NAG; LA-ICPMS, laser ablation inductively coupled plasma mass spectrometry; µXRF, micro XRF; SEM-EDS, scanning electron microscopy- energy dispersing spectrometry; EPMA, electron probe microanalysis; MLA, mineral liberation analyser; GXMapping, grain-based X-Ray mapping; XBSE, extended back scattered electron; SPL_Lite, sparse phase liberation_lite; EAF, extremely acid forming; AF, acid forming; PAF, potentially acid forming; PNC, potential neutraising capacity; ANC, acid neutralising capacity. *$S_{Sulphide}$ values are preferred however, S_{Total} values can be used in place.

2.2.1 Operational sites

Samples selected for the GMT approach at a mine in the early stages of operation (e.g., pre-feasibility, feasibility), must be representative of geological, lithological and alteration units in accordance with the GARD Guide (2010). Additionally, samples must be representative of the relative amounts and particle size of each type of material (Downing, 1999). When sampling drill core, Price (2009) recommended that samples should be collected at least 50 m laterally and vertically in order to create a statistically significant waste rock model. Composite samples as used in Hammarstrom et al. (2003), Borden (2003) and Lengke et al. (2010) should be avoided as potentially they could mask geological variability. Downing (1999) reasoned that whilst rigorous sampling can be costly, remediation and reclamation plans developed as a consequence of poor sampling and analysis can become even more expensive, hence the importance of a detailed initial assessment. He argued that costs should not pre-determine the number of samples taken and analysed, but should be dependant on the amount necessary to increase confidence in the data. Therefore, the GMT approach recommends that at least a 5 m linear sampling programme should be employed to obtain samples for stage-one testing. This interval is not fixed and can be changed to a more appropriate value between 2 m to 50 m as determined by site geological personnel. This sampling strategy is independent of lithology, therefore ensuring a greater degree of accuracy rather than compositing samples. Sampling should be undertaken on all drill holes; however, a tighter sampling campaign can be developed for low-grade ore/waste rock/overburden zones. Adopting this approach provides confidence that the geological representivity of the deposit is examined in ARD terms. Additionally, the expected number of samples as published in guidelines given by the Australian Government Department of Industry, Tourism and Resources (2007; Table 2.1) will be approximated.

2.2.2 Historical sites

Theoretically, the most effective sampling campaigns are those based on rock volume per lithology, with recommended sample numbers given in Table 2.2. However, often a limitation is that for historic piles, these values (i.e., rock volume and number of lithologies) are unknown. This limitation manifests in published examples of waste rock characterisation at historic mine sites as relatively low numbers or composited samples are used (e.g., Munroe et al., 1999; Hammarstrom et al., 2003; Harris et al., 2003; Ashley et al., 2004; Akabzaa et al., 2007; Marescotti et al., 2008; Changul et al., 2010). Sampling strategies are not detailed in these examples, with no reference to published guidelines made, suggesting their general absence. However, some guidelines do exist. First, the USEPA (1994) outlined two strategies, one of which (proposed by an unnamed consultancy) stated that 8 to 12 samples should be collected from each significant rock type (whereby a significant rock type is presumed to be 1to 2% of the total mine rock volume). The second strategy recommended that one sample (1.5kg) should be collected per 20,000 t of waste rock, or approximately 50 samples per 1 Mt (USDA Forest Service, 1992). The British Columbia (BC) AMD taskforce (1989) recommend 25 samples as a minimum should be collected from 1 Mt geological units, or 1 sample for every 40,000 t. A limitation of this strategy is that as waste volume increases, the number of samples decreases (i.e., for a unit of 10 Mt the minimum sample number is 250 or one sample for every 125,000 t). Downing (1999) recommended consultation of waste rock curves to deduce the minimum number of samples required with an example developed by SRK (1989) shown

in Figure 2.2. Considering the potential unknowns, the GMT approach recommends a reconnaissance investigation is undertaken prior to sampling to define the number of lithologies present. Based on this, a sampling strategy can be determined, with preference given to those published in Downing (1999) and Price (2009).

Table 2.1 Suggested initial numbers of samples and test work (adapted from Australian Government Department of Industry, Tourism and Resources, 2007 *in* Price, 2009).

Phase	Description
Exploration: prospect testing	At least 3-5 representative samples should be tested for each key lithology/alteration type.
Exploration: resource definition	At least 5-10 representative samples should be tested for each key lithology/alteration type.
Pre-feasibility	Several hundred representative samples of high and low grade ore, waste rock and tailings should be collected for geochemical work, Sufficient samples to populate a block model with reliable distribution of static test data on ore, waste and wall rock. Kinetic tests should be established for at least 1-2 representative samples for each key lithology/alteration type.
Feasibility	Continue to refine block model if necessary and conduct sufficient mineralogical test work to cross check data for key lithologies. If there are insufficient data to assess drainage chemistry and provide a convincing management plan for approval, additional sampling, test work and refinement of block models will be required.

2.2.3 Sample volume

The mass of individual samples collected is generally dictated by the types of tests to be undertaken, and the associated QA/QC protocols. Typically, 500g is sufficient to conduct a comprehensive list of static tests, though 1kg is preferred (Price, 2009). As the GMT approach requires textural evaluations in addition to geochemical and mineralogical tests, 1kg of sample must be obtained as a minimum, with an intact rock slice kept for reference. For material obtained from historical sites, obtaining a sample with the required mass is straightforward. However, at an operational mine drill core is required for other testing (e.g., resource evaluation, geometallurgy, geotechnics), therefore obtaining the required amount may be compromised. In this instance, at least 250g should be obtained for environmental testing (sufficient for stage-one and stage-two GMT tests), and it must be ensured that an intact sample from that interval exists (e.g., MLA polished tile).

Table 2.2 Minimum number of samples collected from each rock/overburden type during initial sampling (Price 2009).

Mass of each separate rock type (tonnes)	Minimum number of samples
<10, 000	3
<100, 000	8
<1,000,000	26
<10,000,000	80

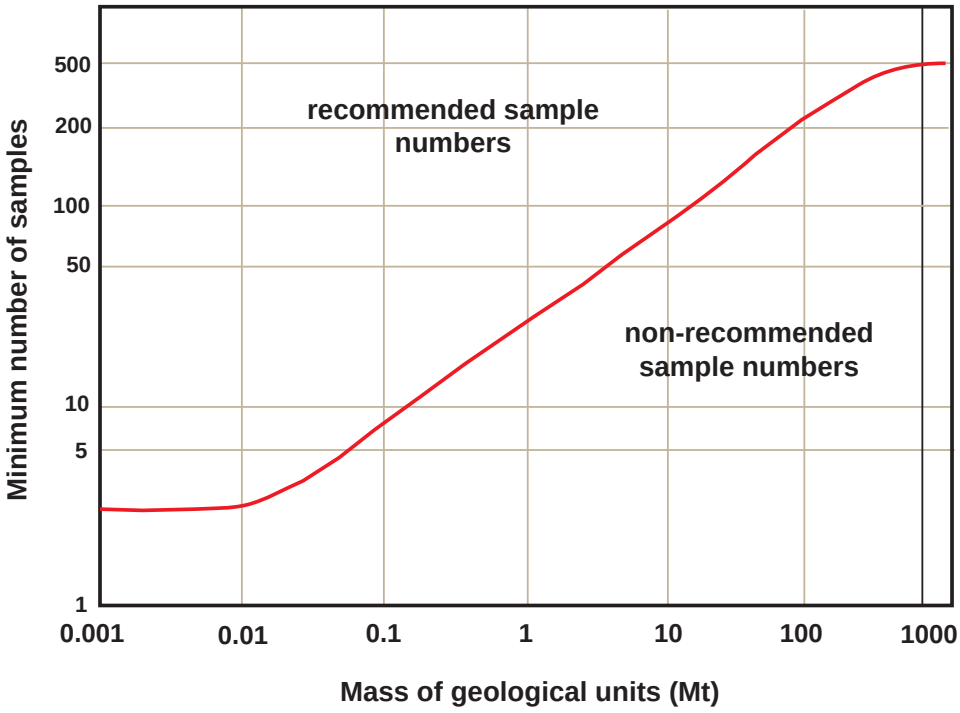

Figure 2.2 Hypothetical curve to determine the number of samples required for ARD prediction/characterisation of a deposit based on mass (modified from SRK, 1989 in Downing, 1999).

2.3 Mesotextural classification

Examples of waste rock characterisation indicate that no formal methods of differentiating between waste rock lithologies are employed (Hammarstrom et al., 2003; Harris et al., 2003; Ashley et al., 2004; Changul et al., 2010; Song and Yanful, 2011). Consequently, waste rock samples identified as sulphidic are not categorised by sulphide type or texture, thus questioning the effectiveness of rehabilitation plans which consider sulphidic material as one entity (Harris et al., 2003; Ashley et al., 2006). Therefore, a mesotextural classification method is proposed whereby all samples are initially grouped as per lithology, mineralogy, texture and element content.

A geological description of each sample is first logged with particular attention given to estimating modal mineralogy, texture and alteration type. Alteration can either increase (e.g., advanced argillic, argillic and phyllic) or decrease (propylitic, carbonate, fine-grained potassic) acid forming capacity as documented in Table 2.3. Table 2.4 shows published neutralising potential (NP) values for minerals commonly observed in waste rock material. Fine-grained pale minerals are common constituents of these alteration assemblages (e.g., kaolinite, dickite, sericite). Such minerals require differentiation as they differ in their NP and susceptibility to weathering (Sverdrup, 1990; Bowell et al., 2000; Dold and Fontbote, 2001).

The application of short-wave infrared (SW-IR) spectroscopy in determining pale, fine-grained alteration minerals has been demonstrated in ore-deposit characterisation studies (e.g., Thompson et al., 1999; Hermann et al., 2001; White et al., 2010). Mineral identification is based on absorption spectra collected from clean, dry, flat, rock surfaces (Gifkins et al., 2005). SW-IR therefore has potential to improve mineral identification of altered waste rock samples, thus aiding mesotextural grouping. Two instruments were selected for testing in this research; a portable infrared mineral analyser (PIMA) (manufactured by Integrated Spectronics, Australia) and a TerraSpec spectroradiometer (manufactured by analytical spectral device (ASD) Inc.) with RS3 software (version 4.0.23). The PIMA measures reflected light in the 1.3 to 2.5 μm region in approximately 600 spectral channels (Kruse, 1994). It is a contact instrument in which the head of the spectrometer is placed in direct contact with the rock (Kruse, 1994). An internal light source is used to illuminate the sample, with the data automatically reduced to reflectance relative to an internal standard (Kruse, 1994). TerraSpec is a compact and field portable precision instrument with a full spectral range (350-2500 nm), a 5 nm spectral resolution, and rapid data collection (1/10th of a second per spectrum).

Field-portable XRF (FP-XRF) analysis has in recent years been used in mine site characterisation studies for determining element concentrations (e.g., Melquiades and Appoloni, 2004; Haffert and Craw, 2010; Higueras et al., 2012). For the purpose of mesotextural classification, FP-XRF analysis is recommended to chemically differentiate between lithologies. Several areas of a clean, flat, dry sample can be analysed with the results averaged. However, to increase accuracy, a homogenised sample should be analysed. It is proposed that powdered pellets as used in conventional XRF analyses (Rollinson, 1993) should be prepared and analysed. In this research, the bench-top Innov-X X50 (30cm x 33cm by 20cm) was used (CODES, UTAS). A standard analysis is based on the emission of X-Rays generated from a 50 kV tube inside the FP-XRF unit (Olympus Corporation, 2012). The sample is placed in front of a window with a shutter, and the chamber locked. When the shutter opens, X-Rays sourced from the tube are absorbed by atoms in the sample, generating fluorescence (Olympus Corporation, 2012). Elements from phosphorus (Z=15) to uranium (Z=92) are analysed. The instrument operates in 'mining' mode (measuring values >1 wt. %), and 'soil' mode (measuring values <1 wt. %). A generic one-step calibration lid was provided by the manufacturer, however, site specific standards can be effectively developed and utilised as demonstrated in Haffert and Craw (2010). Cross-checks of FP-XRF data with XRF must be made on at least 10% of samples per mesotextural group, and additional XRF analyses can be performed at stage-one if deemed necessary.

Following these analyses, grouping of samples displaying similarities in mineralogy, texture and elemental content is possible. By defining and populating groups, the schedule of analysis is improved with all samples subjected to stage-one tests geochemical tests, and at up to 10% of samples from each group subjected to mineralogical and textural characterisation. By grouping samples in this manner, a more organised approach to ARD testing is introduced, which will aid sample selection in later GMT approach stages and will improve waste management strategies.

Table 2.3 The environmental characteristics of various wall-rock alteration types common to hydrothermal mineral deposits (Plumlee, 1999).

Alteration type	Alteration Products	Chemical effects	Physical effects
Acid-sulphate	Vuggy silica (+pyrite), quartz-alunite, kaolinite, ± pyroph-illite, dickite.	Greatly decreases acid-buff-ering capacity of host rocks, and increases acid generating capacity.	Vuggy silica zones, highly permeable. Surrounding clay alteration zones impermeable.
Argillic	Kaolinite, illite, montmoril-lonite, ± pyrite, ± chlorite.	Decreases acid-buffering capacity.	Substantially decreases rock and fracture permeability.
Phyllic	Quartz, sericite, pyrite.	Increases acid-generating capacity.	Slightly decreases rock and fracture permeability.
Potassic	Potassium feldspar, biotite, anhydrite.	Coarse grain size of feldspars decreases rock reactivity.	Shifts permeability to fracture permeability.
Propylitic	Epidote, chlorite, calcite, albite, ± pyrite.	Increases acid-buffering capacity of rock.	Chlorite-rich alteration somewhat decreases fracture permeability.
Silica	Silica, quartz addition to rock and replacement of rock minerals.	Decreases acid-buffering capacity of rock.	Decreases rock permeability, porosity. Increases susceptibil-ity of rocks to fracturing.
Jasperoid	Silica, quartz replacement of carbonate sedimentary rocks.	Greatly decreases acid-buffer-ing capacity.	Can increase porosity, perme-ability of rock; also increases susceptibility of rocks to fracturing.
Greisen	Quartz, muscovite, topaz, flu-orite, cassiterite, magnetite.	Some decrease in acid-buffer-ing capacity, reactivity.	Moderate rock permeability, fracture permeability.
Skarn	Carbonate rocks alter to calc-silicates, magnetite.	Decrease acid-buffering capacity, increase in acid-generating capacity.	May decrease rock perme-ability.
Dolomitization	Alteration of limestones to dolomites.	May decrease acid-buffering capacity.	May decrease or increase rock porosity, permeability.
Carbonatization	Alteration of rock minerals to carbonates.	Substantially increases acid-buffering capacity.	Negligible effect.
Sulphidation	Alteration of Fe-minerals to Fe-sulphides.	Increases acid-generating capacity.	Negligible effect.
Decalcification	Removal of carbonate from rocks, some replacement by silica.	Decreases acid-buffering capacity.	Substantially increases poros-ity, permeability.

At an operational mine, geological logging is routinely undertaken, with drill core lithologically categorised, therefore to some degree, mesotextural classification is routinely performed. Typically, lithological classes are inappropriate for use as several textures of one lithology may be present (i.e., flow-banded rhyolite versus porphyritic rhyolite) and logged as one unit. However, different types of a lithology may contain varying amounts of acid forming minerals and therefore have unique acid

Table 2.4 Selected Sobek neutralising potential (NP) values for common minerals or mineral groups (compiled from Skousen et al., 1997; Jambor et al., 2003; 2006; 2007; Hammarstrom et al., 2003).

Group/mineral	Chemical formula	NP	Reference
Alunogen	$Al_2(SO_4)_3.17H_2O$	0	Hammarstrom et al. (2003)
Amphibole	$Ca_2(Mg,Fe)_4AlSi_7AlO_{22}(OH)_2$	3	Jambor et al. (2002)
Analcime	$Na[AlSi2O_6].H_2O$	11	Jambor et al. (2006)
Apatite	$Ca_5(PO_4)_3(OH,F,Cl)$	8	Jambor et al. (2002)
Biotite	$K(Fe,Mg)_3AlSi_3O_{10}(OH)_2$	>1	Hammarstrom et al. (2003)
Calcite	$CaCO_3$	1000	Jambor et al. (2007)
Chalcopyrite	$CuFeS_2$	0	Hammarstrom et al. (2003)
Chlorite/clinochlore	$(Mg,Fe)_3(Si,Al)_4O_{10}(OH)_8$	6	Jambor et al. (2002)
Cordierite	$(Fe,Mg)_2[Si_5Al_4O_{18}].nH_2O$	4	Jambor et al. (2007)
Dolomite	$CaMg(CO_3)_2$	1086	Jambor et al. (2007)
Epidote	$Ca_2(Al,Fe)_3Si_3O_{12}OH$	1	Jambor et al. (2002)
Garnet/almandine	$Fe_3Al_2Si_3O_{12}$	3	Jambor et al. (2002)
Garnet/grossular	$Ca_3Al_2Si_3O_{12}$	6	Jambor et al. (2002)
Gypsum	$CaSO_4.2H_2O$	1	Hammarstrom et al. (2003)
Hematite	Fe_2O_3	2	Jambor et al. (2002)
Ilmenite	$FeTiO_3$	1	Jambor et al. (2007)
Kaolinite	$Al_4[Si_4O_{10}](OH)_8$	0	Jambor et al. (2002)
K-feldspar	$(K,Na)AlSi_3O_8$	1	Jambor et al. (2000)
Magnetite	Fe_3O_4	2	Jambor et al. (2002)
Muscovite	$KAl_2AlSiO_{10}(OH)_2$	1	Jambor et al. (2000)
Nepheline	$Na_3(Na,K)[Al_4Si_4O_{16}]$	25	Jambor et al. (2006)
Olivine/forsterite	$(Mg,Fe)_2[SiO_4]$	38	Jambor et al. (2002, 2004)
Phlogopite	$KMg_3AlSi_3O_{10}(OH,F)_2$	8	Jambor et al. (2002)
Plagioclase	$NaAlSiO_3O_8$-$CaAl_2Si_2O_8$	1	Jambor et al. (2006, 2007)
Pyrite	FeS_2	0	Hammarstrom et al. (2003)
Pyroxene	$Ca(Fe,Mg)Si2O_6$	5	Jambor et al. (2002)
Pyrrhotite	$Fe_{(1-X)}S$	0	Hammarstrom et al. (2003)
Quartz	SiO_2	0	Jambor et al. (2007)
Serpentine	$Mg_3[Si_2O_5](OH)_4$	32	Jambor et al. (2006, 2007)
Siderite	$FeCO_3$	864	Jambor et al. (2007)
Smectite	$(0.5Ca,Na)_{0.7}(Al,Mg,Fe)_4(Si,Al)_8O_{20}(OH)_4.nH_2O$	8	Jambor et al. (2002)
Sphalerite	ZnS	0	Hammarstrom et al. (2003b)
Talc	$Mg_3Si_4O_{10}(OH)_2$	2	Jambor et al. (2002)
Thomsonite-Ca	$Na_4Ca_8[Al_{20}Si_{20}O_{80}].24H_2O$	13	Jambor et al. (2006)
Titanite	$CaTi[SiO_4](O,OH,F)$	2	Jambor et al. (2007)

Table 2.4 (*continued)*

Group/mineral	Chemical formula	NP	Reference
Tremolite	$Ca_2Mg_5Si_8O_{22}(OH)_2$	>1	Hammarstrom et al. (2003b)
Vermiculite	$(Mg,Fe^{2+},Al)_3(Si,Al)4O_{10}(OH)_2.4H_2O$	>1	Hammarstrom et al. (2003b)

forming characteristics. Therefore, the criteria for defining each lithological unit must be reviewed to determine if it is appropriate directly for mesotextural classification and if not additional parameters must be interpreted. Additionally, FP-XRF analysis must be undertaken on each sample in accordance with the designated sampling interval if they are not already scheduled for full geochemical assay (including elements As, Ba Ce, Cu, La, Nb, Ni, Rb, Sn, Sr, Ta, Th, U, W, Y, Zn and Zr).

2.4. GMT approach: stage-one

Stage-one aims to collect simple ARD data through measurement of sulphur and paste pH, determination of modal mineralogy, and evaluating texture. However, as many methods exist (particularly for sulphur and paste pH measurement), few were selected for review in order to determine the most appropriate for inclusion in the GMT approach. This section provides an overview of these methods, and gives a general introduction to the corresponding analytical instrument used in this research.

2.4.1 Sulphur determination

In ARD characterisation studies determining sulphur and bulk elemental composition (i.e., Al, Ca, Fe, K, Mg, Mn, Na, P, Si, Ti reported as oxides) using XRF is a routine procedure (e.g., Munroe et al., 1999; Dold and Fontbote, 2001; Lapakko, 2002; Hammarstrom et al., 2003; Smuda et al., 2007). However, the time and cost of analyses are relatively high (Price et al., 2009), thus an alternative is sought. Elemental microanalysis (or EA) is a technique to determine S_{Total} (and C_{Total}) values. Its application in waste rock characterisation studies is scarce, though some examples are shown in Denimal et al. (2002), Lei et al. (2005), Hughes et al. (2007) and Hofmann and Schuwirth (2008). Considering results reported by these authors, EA was selected for review as a stage-one test to establish its application as a low-cost method for measuring S_{Total}. This analysis is mandatory for all waste rock samples from historic sites. At an operational mine, if sulphur is routinely assayed at the required GMT approach sample interval, then EA is not required. However, if the routinely assayed interval is greater than that required by the GMT approach, additional EA analysis should be scheduled, with cross-checks made against assayed values.

In this research, a Thermo Finnigan 1112 Series Flash Elemental Analyser (Central Science Laboratory (CSL), UTAS) was selected for use. In a standard analysis 10mg of pulverised sample is placed in a tin capsule and heated to 900°C. Spectra of sulphur, carbon, hydrogen and nitrogen gases (evolved as SO_2, CO_2, H_2O and NO_3) are measured, and converted into wt. % of the sample. Methionine ($C_5H_{11}NO_2S$) and BBOT ($C_{26}H_{26}N_2O_2S$) standards are used, with blanks analysed at random to calculate instrument precision. To cross-check S_{Total} values obtained by EA, XRF and FP-XRF analyses were also performed. A Philips PW1480 X-Ray spectrometer (CODES, UTAS) with a Sc-Mo 3kW side window X-Ray was used following the procedure outlined in Robinson (2003). Corrections for mass

absorption were calculated using Philips X40 software with De Jongh's calibration model and Philips (or CSIRO) alpha coefficients (Danyushevsky et al., 2011). XRF results were also used to cross-check all FP-XRF data collected as part of mesotextural grouping.

2.4.2 Paste pH

Field-based applications of paste pH testing are discussed in Shaw et al. (2000); Weber et al. (2006) and Hughes et al. (2007), indicating its application as a pre-screening test as part of stage-one. It must be performed on all samples (i.e., at both historical and operational sites). Many variations of the paste pH test exist (Table 2.6) which can cause classification discrepancies (e.g., Hammarstrom et al., 2003; Noble et al., 2012). A single method therefore should be selected for use. Based on a review of paste pH techniques and results presented in the literature, the AMIRA P387A paste pH method (Smart et al., 2002) was selected for inclusion in the GMT approach due to its extensive use in recent publications (e.g., Weber et al., 2006; Nugraha et al., 2009; Matthies et al., 2011). Additionally, it is a standard analysis offered by several Australian analytical laboratories (e.g., ALS, 2010). This method recommends that a solid to water ratio of 1:2 (w/w) is used, with the solid left in deionised water for 12-16 hours (or overnight; Smart et al., 2002). As part of GMT approach development, an evaluation of grain size effects on pH was undertaken to determine the accuracy of paste pH testing in the field using non-pulverised samples.

Table 2.5 Examples of common paste pH methods used in the published literature.

Reference	Paste pH method	Procedure
Hammarstrom et al. (2003)	Price et al. (1997) BCRI (White et al., 1999)	10 g splits of <2 mm material. Mine waste is placed in a plastic beaker and 10 mL of distilled water (pH 5.33) is added to make a paste
Weber et al. (2006)	AMIRA P387A Handbook (Smart et al., 2002)	1 part water, 2 parts solid
Hughes et al. (2007)	Sobek et al. (1978)	Small fragments (20 g) of rock were disaggregated in 10 ml distilled water in a 50-ml container, and left for 10 min before measuring pH
Matthies et al. (2011)	AMIRA P387A Handbook (Smart et al., 2002)	Paste pH was determined in triplicate in leachates of 10 g of air-dried tailings and deioinized water (solid: liquid ratio of 1:1) after 15 min reaction
Gurung (2001)	Not stated	Paste pH and EC were measured in 1:1 and 1:5 sample to deionised water ratio respectively

2.4.3 Modal mineralogy

Whilst modal mineralogy is estimated as part of mesotextural classification/geological logging, actual measurement is required to determine the exact sulphide versus carbonate ratio to make an assessment of ARD forming potential (Paktunc, 1999). Typically, XRD is utilised in waste rock characterisation studies (Dold and Fontbote, 2001; Hammarstrom et al., 2003; Marescotti et al. 2008, Moricz et al. 2009, Jamieson et al., 2011). However, this qualitative technique is limited as it only provides an indication of a sample's constituent mineralogy. Despite the high cost per sample (e.g., >$100 per sample, 2011; University of Ballarat, Australia), the proposed GMT approach requires that at least one representative sample per mesotextural group (for an abandoned mine site) is analysed by this method. This is intended to provide a general indication of the mineralogy for the group which the analysed sample represents. For a highly populated mesotextural group, approximately 10% of samples should be analysed. To explore if mineralogy can be accurately estimated using computed methods, the programmes ModAn (Paktunc, 2001), MINSQ (Hermann and Berry, 2002) and A2M (Posch and Kurz, 2007) were selected for review. ModAn estimates mineral quantities or modes by applying Gaussian elimination and multiple linear regression techniques to simulate mass balance equations (Paktunc, 2001). MINSQ is a spreadsheet adaptation of the least squares method (run through Microsoft excel), which iteratively adjusts the proportions of all selected mineral phases to provide a best-fit solution to the whole rock composition data (Hermann and Berry, 2002). A2M evaluates all possible solutions of mineral modes, and returns an estimate on the arithmetic mean of all extreme modes. However, its application to this dataset is limited as it was designed for cases in which the number of minerals is greater than the number of elements/oxides, which is not the case for these samples (Posch and Kurz, 2007).

2.4.4 Acid rock drainage index (ARDI)

The absence of texture in ARD prediction/waste characterisation studies was discussed in section 1.4. It was recognised that a definition of texture in ARD terms must give consideration to a range of parameters which focus on evaluating intrinsic characteristics of acid forming sulphides, and their associated mineralogy. Additionally, adopting a scaled approach is required. Therefore, the acid rock drainage index (ARDI; Figure 2.3) is proposed as a stage-one textural evaluation. The ARDI evaluates acid forming sulphide minerals individually by five key parameters (A-E) on both a meso-scale (3cm x 3cm area of a hand specimen sample) and micro-scale (petrographic thin section). Parameters were specifically chosen based on their direct influence on acid formation (Blowes and Jambor, 1990; Weber et al., 2004; Dold and Fontbote, 2001; Mills et al., 2011). For waste rock pile characterisation, at least one representative sample per mesotextural group is recommended for assessment (Figure 2.4). For an operational mine, the ARDI should be performed on the meso-scale at the same sample interval used for paste pH and EA testing (e.g., every 2m). Micro-scale evaluations should be performed accordingly as dictated by the lithologies encountered, giving due consideration to alteration types, and mineralisation intensity. For example, is the texture is highly variable then microscale evaluations should be performed on a sample representative of a significant change. However, if the lithology is relatively homogeneous, then at least one sample per a nominal distance (i.e. 1 sample in every 50m) should be evaluated.

Stage 1

$Me = [A_{0\text{-}10}+B_{1\text{-}10}+C_{1\text{-}10}+D_{\text{-}5\text{-}10}+E_{\text{-}5\text{-}10}] = X$

$$\frac{\Sigma X}{\text{No. of Me phases}} = \mathbf{X^1}$$

Stage 2

$Mi = [A_{1\text{-}10}+B_{1\text{-}10}+C_{1\text{-}10}+D_{\text{-}5\text{-}10}+E_{\text{-}5\text{-}10}] = Y$

$$\frac{\Sigma Y}{\text{No. of Mi phases}} = \mathbf{Y^1}$$

Stage 3

$$\frac{\mathbf{X^1+Y^1}}{\mathbf{2}} = \textbf{\textit{ARD INDEX}}$$

Me = Meso-scale phase
Mi = Micro-scale phase

A = *Contents* of acid forming phases
B = *Alteration* of acid forming phase
C = *Morphology* of acid forming phase
D = *Content* of neutralising phases
E = *Spatial relationship* between acid forming and neutralising phases

X or **Y** = Total Score (/50)
Σx or **Σy** = Total score for all phases
$\mathbf{X^1}$ = total for Me sample
$\mathbf{Y^1}$ = total for Mi sample

Figure 2.3 The acid rock drainage index (ARDI)

As the ARDI is proposed as part of the pre-screening stage, a ranking system is recommended to efficiently evaluate samples. Previous examples of ranking in petrological evaluations are presented in Blowes and Jambor (1990), Oyen et al. (1998), Moncur et al. (2009), but have been criticised due to their subjective nature (Mills et al., 2011). As the ARDI is intended to be performed manually (i.e., by site-geologists), the subjective nature of ranking can only be minimised by clearly defining each score. Therefore, reference examples must be provided (including photographs, diagrams and/or criteria tables) prior to undertaking ARDI evaluations. Parameters A to C focus on characterising sulphide minerals and are ranked from either 0 or 1(low: not acid forming) to 10 (high: acid forming). Only Fe-sulphides (e.g., pyrite, pyrrhotite, arsenopyrite and chalcopyrite) are assessed by the ARDI as these are the most acid forming sulphides (Hammarstrom et al., 2003; Lottermoser, 2010; Jamieson, 2011). Non-Fe bearing sulphides (i.e., inert) such as galena (PbS) and sphalerite (ZnS) are not directly evaluated, but their presence is considered by Parameters D and E. Assessment by all parameters must be undertaken if acid forming sulphides are identified, or else the ARDI value is void. If sulphide minerals are not identified in a sample it is classified as non-acid forming. Where sulphides are identified, a maximum of twenty Fe-sulphide phases are assessed (by Parameters B to E) if present. Otherwise, the maximum number identified is, and the ARDI values are scaled following the procedure shown in Figure 2.5. A high value indicates acid formation, a low value indicates low or inert acid forming potential, and a negative value indicates an acid neutralising capacity (Table 2.6). Values between 10 and 0 indicate that a sample is either non-acid forming or has a potential neutralising capacity; and must be resolved when cross-checking these values with other data collected in this stage. A brief description of each parameter is given.

2.4.4.1 Parameter A: Sulphide content

The GARD Guide (2010) and Mills et al. (2011) recommend that consideration is given to sulphide contents. Therefore, Parameter A is proposed as a proxy for maximum potential acidity (MPA). Attention is given to Fe-sulphides only, whereas in MPA calculations, S_{Total} or $S_{Sulphide}$ values are used. An estimation of the modal contents (%) of Fe-sulphides within a given area (i.e., *Me*:-scale 3cm x 3cm; *Mi*-scale*:* petrographic thin section) is performed. The higher the Fe-sulphide content, the greater the acid forming

potential. As stated, if no Fe-sulphides are identified (i.e., Parameter A= 0), the sample is classified as NAF and requires no further assessment by the ARDI. However, if the sample contains 100% Fe-sulphides (i.e., Parameter A= 10), then it is classified as extremely acid forming and also requires no further assessment. Such an extreme score (10) indicates a massive-sulphide texture, therefore identifying individual grains for assessment by Parameters B to E would be not be possible. Consideration was given to assessing the size of Fe-sulphides by this parameter; however, difficulty was experienced in determining and measuring the maximum iron sulphide diameter, as well as determining appropriate ranking criteria.

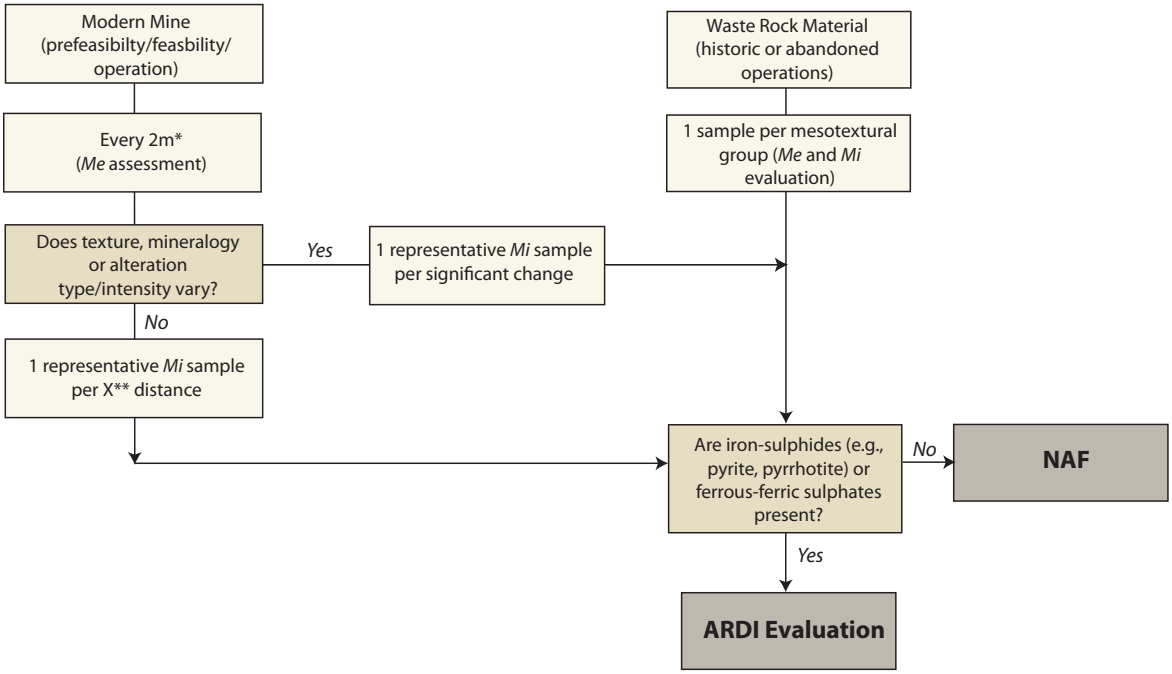

Figure 2.4 Proposed sample selection for ARDI evaluation for both a modern mining operation and a historic/ abandoned operation (*= *Me*-scale evaluations are performed at a minimum on a 2m sampling interval; **= a site-specific nominal distance for *Mi*-scale sampling should be selected based on lithological unit thickness, textural and mineralogical variations observed).

Table 2.6 Classification of acid rock drainage index (ARDI) scores

ARDI Score	Classification
50 to 41	Extremely Acid Forming (EAF)
40 to 31	Acid Forming (AF)
30 to 21	Potentially Acid Forming (PAF)
20 to 11	Non-Acid Forming (NAF)
10 to 0	Non-Acid Forming *or* Potential Neutralising Capacity (PNC)
-1 to -10	Acid Neutralising Capacity (ANC)

Maximum ARDI value	50 for 20 grains 50	=	1000 1000	***recast back in terms of 50 by dividing by 20***

Whereby: 50 (score) x 20 (number of grains evaluated) = 1000
50 (maximum score) x 20 (maximum number of grains) = 1000

Example A:

Me score:	50 for 11 grains 50	=	50 x 11 = 50 x 20	550 → 27.5 1000 50
Mi score:	50 for 7 grains 50	=	50 x 7 = 50 x 20	350 → 17.5 1000 50
Final ARDI value:	27.5 + 17.5 = 45 50 50 100	/2	=	**22.5** **50**

Example B:

Me score:	26 for 17 grains 50	=	26 x17 = 50 x 20	442 → 22.1 1000 50
Mi score:	18 for 16 grains 50	=	18 x 16 = 50 x 20	288 → 14.4 1000 50
Final ARDI value:	22.1 + 14.4 = 36.5 50 50 100	/2	=	**18.25** **50**

Example C:

Me score:	5 50 for 20 grains =		5 x 20 = 50 x 20	100 → 5 1000 50
Mi score:	4 50 for 20 grains=		4 x 20 = 50 x 20	80 → 4 1000 50
Final ARDI value:	5 + 4 = 9 50 50 100	/2	=	**4.5** **50**

Figure 2.5 Scaling of acid rock drainage index (ARDI) evaluations for samples with different number of sulphide grains.

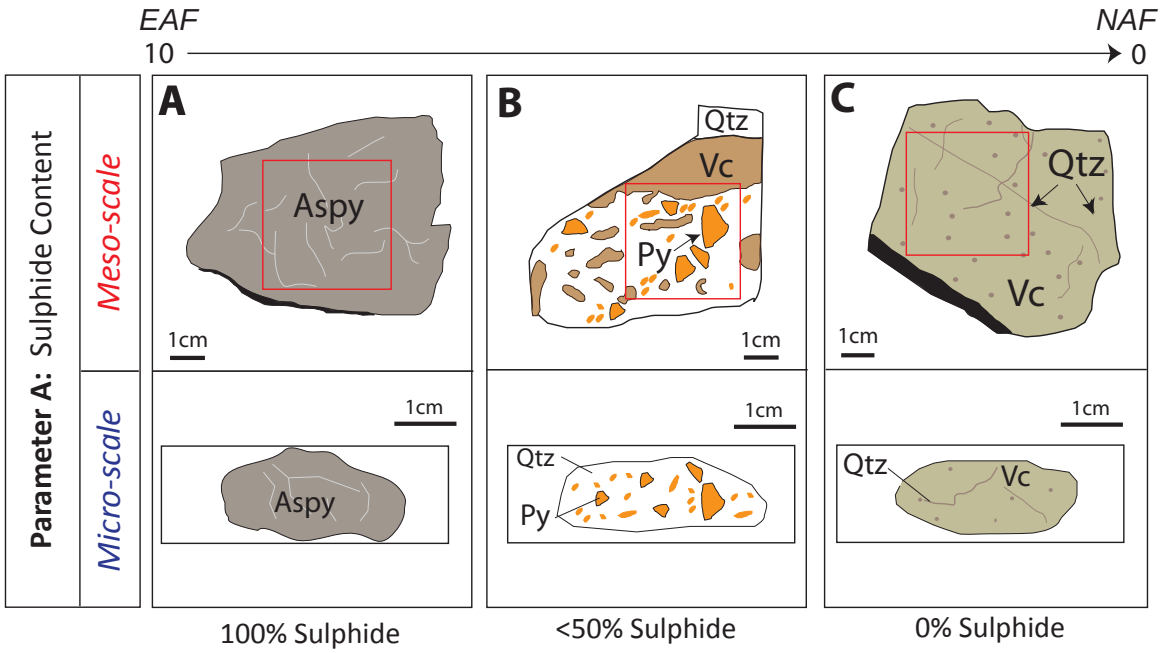

Figure 2.6 Diagramatic examples of ARDI Parameter A evaluations for assessing the content of Fe-sulphides in a sample in a given area: **(A)** 100% arsenopyrite samples scoring 10/10 and no further ARDI evaluation is required; **(B)** 40% pyrite shown scoring 4/10 therefore full ARDI evaluation is required; and **(C)** No iron sulphide grains identified therefore the sample is classified as NAF with no further ARDI evaluation required. Abbreviations: Aspy, arsenopyrite; EAF, extremely acid forming; NAF, non-acid forming; Py, pyrite; Qtz, quartz; Vc, volcanic matrix.

Table 2.7 Acid Rock Drainage Index Parameter A ranking criteria (0 to 10) performed on whole *Me*-scale or *Mi*-scale samples to assess the contents of Fe-sulphide minerals.

Iron sulphide content (%)	ARDI Value
100	10
90	9
80	8
70	7
60	6
50	5
40	4
30	3
20	2
10	1
Contains no sulphides	0

2.4.4.2 Parameter B: Sulphide alteration

Parameter B is adapted from the sulphide alteration index (SAI) of Blowes and Jambor (1990). The SAI was developed as a means of evaluating the degree of weathering of sulphides in the Waite-Amulet tailings impoundment, Canada. A summary of their ranking criteria (also used by Gunsinger et al., 2006), and an alternative SAI proposed by Shaw et al. (1998) are shown in Table 2.8. Pyrrhotite-pyrite and pyrrhotite-pentlandite alteration were respectively evaluated in these indexes. Most recently, Moncur

et al. (2009) revised this index to evaluate pyrite-marcasite-pyrrhotite-chalcopyrite-sphalerite bearing tailings, with each numeric (1 to 10) given a specific criteria. Applications of these SAIs are limited for waste rock material absent of these mineral suites. Additionally, these indexes evaluate thin sections as a whole. Instead, a grain-by-grain approach should be adopted to provide a better insight into the degree of weathering. This forms the objective of Parameter B, with a maximum of 20 grains evaluated. In keeping with the previous parameter (whereby the more potentially acid forming, the higher the score) fresh, unaltered iron-sulphides score 10, partially obliterated/weathered iron-sulphides score 5, and those intensely altered to secondary minerals (e.g., Fe-oxides, ferrous sulphates) are given a low score. Use of a binocular microscope and/or handlens is recommended when evaluating a meso-scale sample. Evaluating Parameter B on a micro-scale is easier than on a meso-scale due to the ability to discern between primary sulphides and their alteration products under reflected light. A limitation of the SAI identified in section 1.3.5.2 was the lack of consideration given to the sulphide mineral associations. This is not addressed here, but by Parameter E. Diagramatic examples of scoring are shown in Figure 2.7 and ranking criteria are shown in Table 2.9.

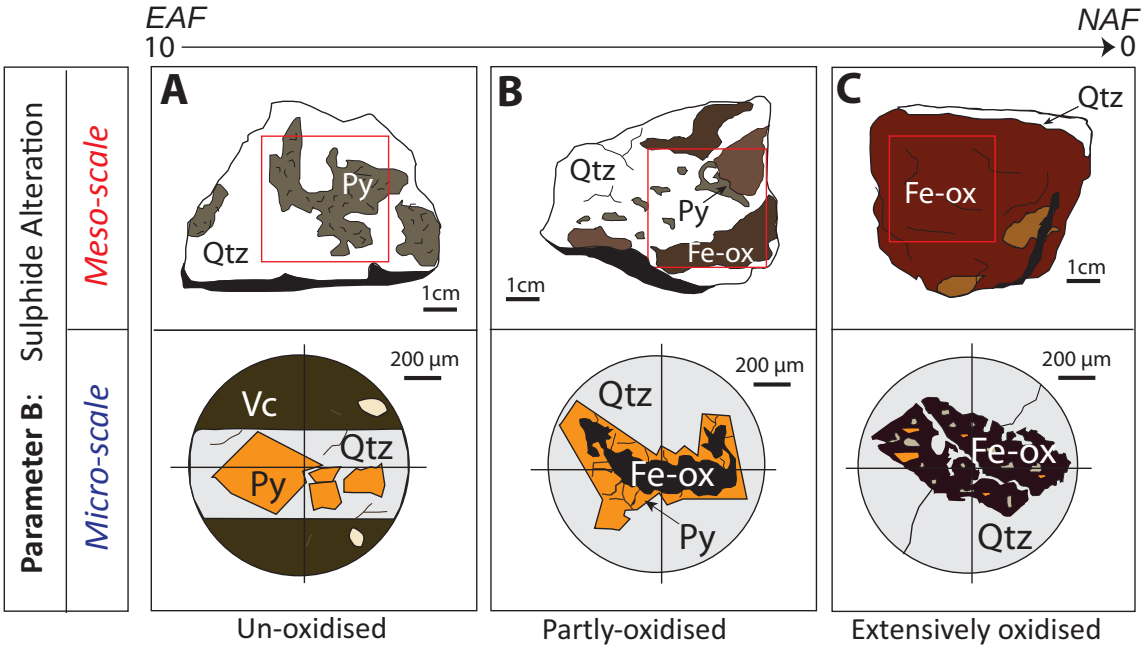

Figure 2.7 Diagramatic examples of ARDI Parameter B evaluations for assessing the degree of weathering alteration of Fe-sulphides: **(A)** Pyrite appears fresh and unweathered scoring 10/10; **(B)** Pyrite is partially weathered scoring 5/10; and **(C)** Pyrite is nearly completely obliterated scoring 1/10. Abbreviations: Aspy, arsenopyrite; EAF, extremely acid forming; Fe-ox, iron hydroxides; NAF, non-acid forming; Py,-pyrite; Qtz, quartz; Vc,volcanic matrix.

2.4.4.3 Parameter C: Sulphide morphology

Morphology is recognised as a significant control on sulphide oxidation (Smith and Beckie, 2003; Weber et al., 2004; Weisner and Weber, 2010), and is therefore evaluated by Parameter C. A different method is proposed when undertaking meso-scale and micro-scale evaluations. The meso-scale evaluation gives consideration to the overall sulphide texture (i.e., the same 3cm x 3cm area assessed by Parameter A). On the meso-scale, a disseminated sulphide texture scores high because the relative surface area available for

Table 2.8 Sulphide Alteration Indexes as used by Blowes & Jambor (1990), Shaw et al. (1998) and Moncur et al. (2009). Additional categories (4-2) were added by Shaw et al. (1998), and further refined by Moncur et al. (2009) to increase classification accuracy.

Jambor & Blowes (1990)		Shaw et al. (1998)		Moncur et al. (2009)	
Numerical Scale	**Degree of alteration of sulphides**	**Numerical Scale**	**Degree of alteration of sulphides**	**Numerical Scale**	**Degree of alteration of sulphides**
10	Pyrrhotite and pyrite obliterated; only traces of sulphide, typically chalcopyrite is present.	10	Pyrrhotite and pentlandite completely obliterated traces of pyrite and chalcopyrite may still be visible.	10	Almost complete oxidation of sulphides; traces of chalcopyrite ±pyrite
9	Similar to 10, but with a few scattered remnant grains of pyrite.	9	Pyrrhotite is absent, but pentlandite with thick alteration rims may be present.	9	Only sparse pyrite and chalcopyrite; no pyrrhotite or sphalerite
8-7	First appearance of trace amounts of pyrrhotite (at scale 8); at scale 7 the vestiges of strongly altered pyrrhotite increases in abundance or degree of preservation.	8-7	Trace amounts of pyrrhotite may be seen as surviving cores in a psuedomorphic replacement; pentlandite is still rimmed.	8	Pyrite and chalcopyrite common, but chalcopyrite proportion higher than normal possibly because of pyrite dissolution; no pyrrhotite or sphalerite
6-2	At scale 6 the pyrrhotite grains have broad alteration rims, but the cores of numerous grains are preserved; gradation to scale 2 is marked by the appearance of narrower alteration rims, and a predominance of unaltered grains.	6-4	Pyrrhotite grains have broad alteration rims (thinning from scale 6 to scale 4), commonly multiphase. Pentlandite grains may have thin rims (at scale 6) or show slightly altered edges (at scale 4).	7	Pyrite and chalcopyrite proportions normal: pyrrhotite absent but sparse sphalerite present
1-0	Only a few grains of pyrrhotite are weakly altered along rims and fractures; >95% of the grains have sharp, fresh margins.	4-2	Rims surrounding pyrrhotite thin as scale grades down to 2, and many grains appear unaltered. Pentlandite appears fresh.	6	Pyrrhotite absent, but sphalerite common
		1-0	Very few grains of pyrrhotite are altered at an index of 1, usually along fractures or discontinuously at grin margins. At scale of 0, all grins are pristine.	5	Pyrrhotite represented by marcasite pseudomorphs

Table 2.8 *Continued.*

Jambor & Blowes (1990)		Shaw et al. (1998)		Moncur et al. (2009)	
Numerical Scale	**Degree of alteration of sulphides**	**Numerical Scale**	**Degree of alteration of sulphides**	**Numerical Scale**	**Degree of alteration of sulphides**
				4	First appearance of pyrrhotite, but only as remnant cores
				3	Cores of pyrrhotite abundant
				2	Well-developed cores of pyrrhotite with narrower alteration rims; replacement by marcasite decreasing, and pseudomorphs are absent
				1	Alteration restricted to narrow rims on pyrrhotite

Table 2.9 Acid Rock Drainage Index Parameter B ranking criteria (1 to 10) performed on individual Fe-sulphide grains for assessing the degree of weathering alteration and fracturing.

Degree of alteration	ARDI Value
0 to 10% fractured and/or altered	10
11 to 20% fractured and/or altered	9
21 to 30% fractured and/or altered	8
31 to 40% fractured and/or altered	7
41 to 50% fractured and/or altered	6
51 to 60% fractured and/or altered	5
61 to 70% fractured and/or altered	4
71 to 80% fractured and/or altered	3
81 to 90% fractured and/or altered	2
91 to 100% fractured and/or altered	1

sulphide oxidation is also high (Fox et al., 1997; Lapakko et al., 2006; Smuda et al. 2007). Therefore, the larger the individual iron-sulphide grains, the lower the assigned score. On the micro-scale, the same iron-sulphide grains assessed by Parameter B are evaluated. Individual grain morphologies are examined, with framboidal grains identified as the most acid forming and euhedral grains scoring much lower as the regular shape offers a smaller surface area for oxidation (Smith and Beckie, 2003; Weber et al., 2004; Weisner and Weber, 2010). Examples of scoring are shown in Figure 2.8 and ranking criteria are shown in Tables 2.10 and 2.11.

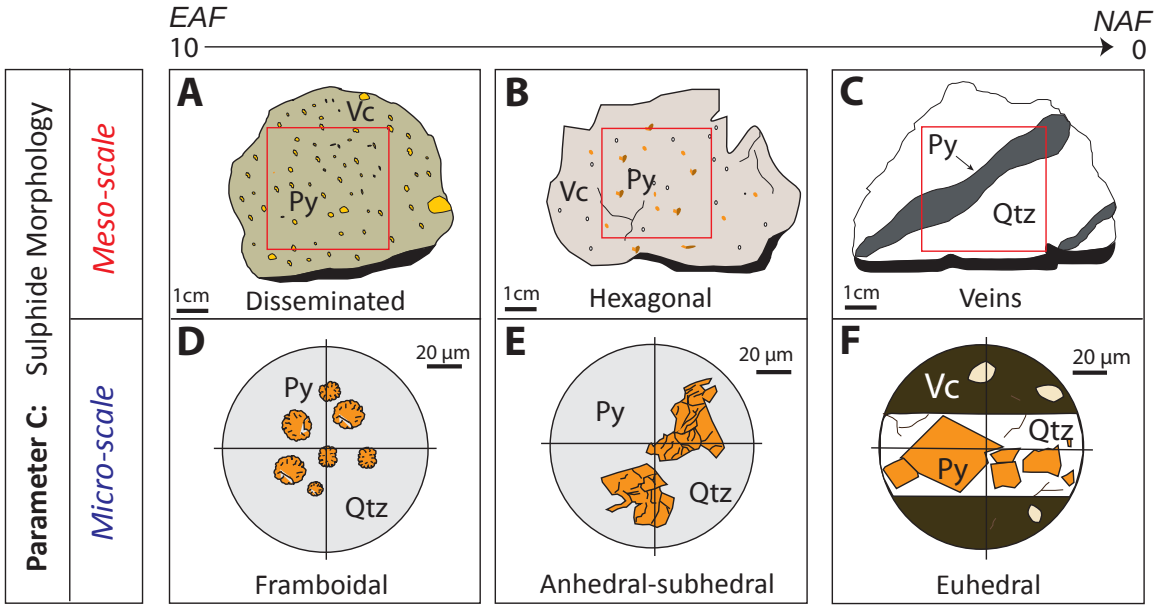

Figure 2.8 Diagramatic examples of ARDI Parameter C evaluations for assessing texture and morphology of Fe-sulphides: **(A)** Disseminated sulphide texture (c.<50%) ranked 8/10; **(B)**Hexagonal pyrite crystals (c.<50%): 6/10; **(C)** Sulphide vein: 2/10; **(D)** Framboidal pyrite in quartz: 10/10; **(E)** Anhedral-subhedral pyrite in quartz: 6/10; **(F)** Unfractured euhedral pyrite in quartz veinlet: 1/10. Abbreviations: Aspy, arsenopyrite; EAF, extremely acid forming; Fe-ox, iron hydroxides; NAF, non-acid forming; Py,pyrite; Qtz, quartz; Vc, volcanic matrix.

Table 2.10 Acid Rock Drainage Index Parameter C meso-scale sample ranking criteria (1 to 10) to assess the sulphide texture of a sample and the relative surface area avaiable for oxidation. Criteria proposed based on observations given in Fox et al. (1997), Plumlee (1999), Smuda et al. (2007) and Lapakko et al. (2006).

Morphology/ hand specimen texture	ARDI Value
Disseminated iron-sulphides covering c. 50 to 100% of the assessed area	10
Disseminated iron-sulphides covering up to 50% of the assessed area	9
Disseminated iron-sulphides covering up to 25% of the assessed area	8
Larger individual iron-sulphide crystals (e.g. hexagonal, pyritohedron) covering c. 50-100% of the assessed area	7
Larger individual iron-sulphide crystals (e.g. hexagonal, pyritohedron) covering up to 50% of the assessed area	6
Larger individual iron-sulphide crystals (e.g. hexagonal, pyritohedron) covering up to 25% of the assessed area	5
Iron sulphide veins (<20mm) covering c. 50-100% of the assessed area	4
Iron sulphide veins (<20mm) covering up to 50% of the assessed area	3
Iron sulphide veins (<20mm) covering up to 25% of the assessed area	2
Massive iron sulphide veins	1

Table 2.11 Acid Rock Drainage Index Parameter C micro-scale sample ranking criteria (1 to 10) for assessing the morphology of individual Fe-sulphide grains. Criteria proposed based on observations given in Smith and Beckie (2003), Weber et al. (2004) and Weisner and Weber (2010).

Morphology	ARDI Value
Framboidal : <20µm	10
Framboidal: >20µm	9
Anhedral and highly fractured	8
Anhedral	7
Subhedral-anhedral	6
Subhedral and highly fractured	5
Subhedral	4
Euhedral-subhedral	3
Euhedral and fractured	2
Euhedral	1

2.4.4.4 Parameter D: Neutraliser contents

Parameter D evaluates the content of neutralising minerals in proximity to acid forming iron-sulphides. Undertaking a general assessment on the meso-scale of the selected 3cm x 3cm area (as done for Parameters A and C) will not give a precise evaluation, as the mineralogy over this area may be highly variable. Therefore, it is proposed that the modal mineralogy of a given area is assessed (i.e., twice the maximum diameter of the Fe-sulphide grains evaluated by Parameter B). At the micro-scale, a 2.5 times magnification should be selected to observe the target iron-sulphide grain and the adjacent field of view examined. If other sulphides are abundant, a high score is given (e.g., 80% surrounded by sulphides scores 8). If neither acid forming nor neutralising minerals are identified, then 0 is given (e.g., pyrite 100% surrounded by quartz). If the area is 100% dominated by primary neutralising minerals (e.g., calcite, dolomite), then -5 is given (Table 2.12). A range (i.e., 0 to 20; 21 to 40% etc…) and not individual values (i.e., 0%, 10%, 20% etc…) are given for primary neutralisers as without staining, carbonates are harder to discern between in both hand-specimen and thin section (Hitzman, 1999). If both acid forming and neutralising minerals surround the iron-sulphide, values are subtracted to give a final score (e.g. 80% sulphide and 20% calcite = 7). Secondary neutralising minerals as identified by Bowell et al. (2000) and Jambor et al. (2002) are scored half that of primary neutralisers (i.e. if 100% dominated by a secondary neutraliser then -2.5 is given). Diagramatic examples of scoring are shown in Figure 2.9.

2.4.4.5 Parameter E- Sulphide mineral associations

Evaluating mineral association is a fundamental parameter which is not routinely assessed (Blowes and Jambor, 1990; Fox et al., 1997; Shaw et al., 2000; Ohlander et al., 2006; Moncur et al., 2009; Jamieson, 2011). However, mineral association can have significant impacts on oxidation rate through sulphide-sulphide galvanic interactions (Kwong et al., 2003; Lottermoser, 2010). If the target iron-sulphide grain is in direct contact with another sulphide (acid or not acid forming), a positive score is assigned, e.g., if

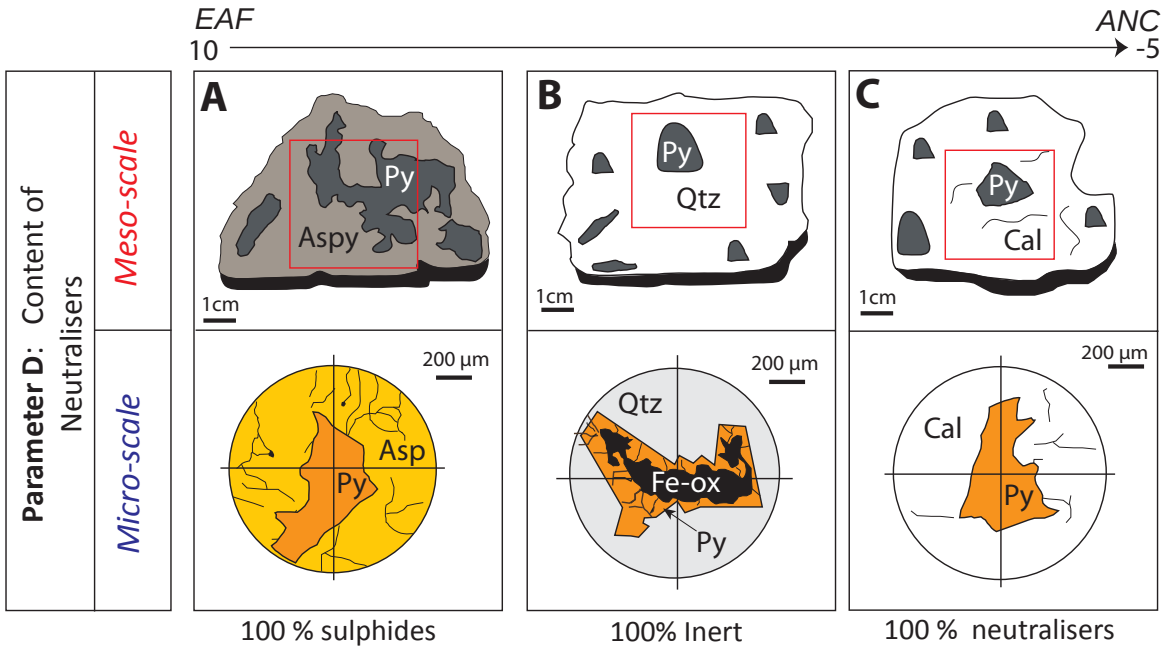

Figure 2.9 Diagramatic examples of ARDI Parameter D evaluations for evaluating the mineralogy surrounding individual Fe-sulphide grains: **(A)** Pyrite surrounded 100% by arsenopyrite: 10/10; **(B)** Pyrite surrounded 100% by quartz: 0/10; **(C)** Pyrite surrounded 100% by calcite: -5/10. Abbreviations: Aspy, arsenopyrite; EAF, extremely acid forming; Fe-ox, iron hydroxides; NAF, non-acid forming; Py,pyrite; Qtz, quartz; Vc, volcanic matrix.

Table 2.12 Acid Rock Drainage Index parameter D scoring criteria (1 to 10) for assessing the neutralising mineral contents adjacent to an Fe-sulphide grain. Primary neutralising minerals are identified as calcite, dolomite, ankerite and magnesite.

Modal mineralogy around acid forming phase	ARDI Score
100% sulphide	10
90% sulphide	9
80% sulphide	8
70% sulphide	7
60% sulphide	6
50% sulphide	5
40% sulphide	4
30% sulphide	3
20% sulphide	2
10% sulphide	1
0% sulphide, 0% primary neutraliser	0
0 to 20% primary neutraliser	-1
21 to 40% primary neutraliser	-2
41 to 60% primary neutraliser	-3
61 to 80% primary neutraliser	-4
81 to 100% primary neutraliser	-5

100% in contact with other sulphides then the maximum score 10 is given. The lower the percentage contact, the lower the score. If the acid forming phase is 100% directly in contact with primary neutralising minerals, then the minimum score of -5 is given. If the acid forming phase is fully bounded by an inert mineral (i.e., quartz) then a value of 0 is given. Diagramatic examples of scoring are shown in Figure 2.10 and ranking criteria are shown in Table 2.13.

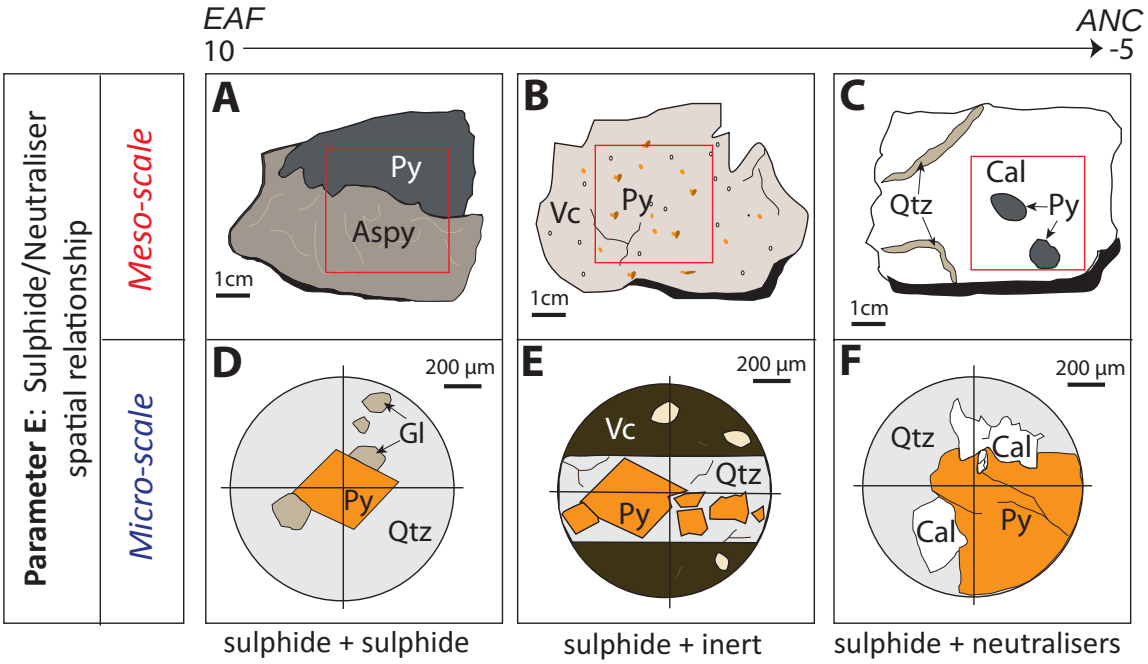

Figure 2.10 Diagramatic examples of ARDI Parameter E evaluations for assessing the mineral associations for individual Fe-sulphide grains: **(A)** Pyrite associated 100% with arsenopyrite: 10/10; **(B)** Pyrite 100% associated with a altered volcanic matrix (e.g., comprising muscovite, potassium feldspar and quatrz): 0/10; **(C)** Pyrite 100% associated with calcite -5/10; **(D)** Pyrite associated 20% with galena; 80% with quartz: 6/10; **(E)** Pyrite associated 100% with quartz 0/10; **(F)** Pyrite associated 20% with calcite; 80% with quartz: -4/10. Abbreviations: Aspy, arsenopyrite; EAF, extremely acid forming; Fe-ox, iron (oxy)hydroxides; NAF, non acid forming; Py, pyrite; Qtz, quartz; Vc, volcanic matrix.

Some ARDI parameters may appear conflicting (e.g., meso-scale evaluation of massive sulphide texture (i.e., >90% sulphide) given high ARDI ranking value by Parameter A, but a lower value by Parameter C). However, conflicts highlight why all parameters are required in conjunction and not isolation, as interpretation by a single parameter alone could produce very different ARDI results. If a finite number of samples selected for indexing have been collected (i.e., when undertaking waste characterisation works at a historic or abandoned mine site), a site-specific index can be easily designed. Additionally, as samples progress through the GMT approach, there is opportunity to re-calibrate the index using geochemical results and mineralogical data (e.g., a sample scoring a high ARDI value will likely have correspondingly high total-sulphur/sulphide and low paste-pH and carbonate values). However, in order to perform this effectively, samples and photographs (with score tables) of Fe-sulphide grains (evaluated on both scales) must be kept. An example of ARD indexing is shown in Figure 2.11.

Table 2.13 Acid Rock Drainage Index parameter E scoring criteria (-5 to 10) for assessing Fe-sulphide mineral associations. Inert minerals are defined as those with NP= 0 (see Table 2.4).

Contents	Value
Sulphide-sulphide boundary 100%: 0 % inert	10
Sulphide-sulphide boundary 80% : 20 % inert	9
Sulphide-sulphide boundary 60% : 40 % inert	8
Sulphide-sulphide boundary 40% : 60 % inert	7
Sulphide-sulphide boundary 20% : 80 % inert	6
Sulphide-sulphide boundary 0%: 100 % inert	5
80% inert (fast weathering); 20 % inert (slow weathering)	4
60% inert (fast weathering); 40 % inert (slow weathering)	3
40% inert (fast weathering); 60 % inert (slow weathering)	2
20% inert (fast weathering); 80 % inert (slow weathering)	1
0% inert (fast weathering); 100 % inert (slow weathering)	0
80% inert ; 20 % primary neutraliser	-1
60% inert ; 40 % primary neutraliser	-2
40% inert ; 60 % primary neutraliser	-3
20% inert; 80 % primary neutraliser	-4
0% inert ; 100 % primary neutraliser	-5

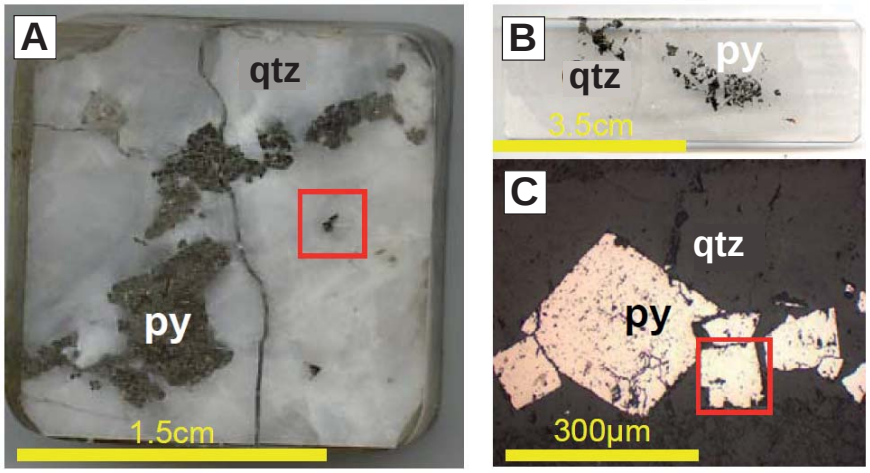

Figure 2.11 Example of an ARDI evaluation of a quartz-pyrite sample. *Me*-scale ARDI = 19/50: NAF (A: 3/10 (for the whole sample area shown in A); B: 10/10 (for highlighted grain shown in A); C: 5/10 (for whole sample shown in A); D: 0/10 (for highlighted grain shown in A); E: 0/10 (for highlighted grain shown in A)); *Mi*-scale ARDI= 29/50: PAF (A: 5/10- (for thin section shown in B); B: 9/10 (for highlighted grain shown in C); C: 1/10 (for highlighted grain shown in C); D: 8/10 (for area shown in C); E: 2/10 (for highlighted grain shown in C)). *Me*-scale ARDI value + *Mi*-scale ARDI value /2 =24/50, this sample is texturally classified as PAF. Abbreviations: py, pyrite; qtz, quartz.

2.4.5 GMT Stage-one classification

Classification of stage-one data follows the principle of cross-checking as recommended in Morin and Hutt (1998). Only through such data comparisons can a well-reasoned classification be assigned, as previous protocols do not consider acid forming potential on a range of scales in the manner that the GMT approach does (e.g., pulverised sample (<75µm) used in paste pH and S_{Total} analyses, intact samples for ARDI evaluation). Whilst some of the classification schemes selected for inclusion in this stage are occasionally used (e.g., paste pH and S_{Total}) the classification fields have been refined. Samples classified as NAF at the end of stage-one require no further analyses by the GMT approach. This ensures that no further efforts (i.e., time and budget) are spent on unnecessary characterisation work (e.g., NAPP/NAG), with only acid forming or neutralising samples focussed upon in stage-two and stage–three.

2.4.5.1 Paste pH versus S_{Total}

Interpretation of data using paste pH versus S_{Total} graphs is a typical part of predictive ARD studies (Morin and Hutt, 1999; Hughes et al., 2007). However, the effectiveness of such a plot is limited by the absence of defined fields by which to classify the data (as with NAPP/NAG plots). Morin and Hutt (1999) addressed this in part, through critiquing ABA criteria for predicting acid potential. Using the international static database (ISD), they evaluated the acid forming potential cut-off values for both paste pH and S_{Total}. The authors reason that using pH 5 as the criterion for defining acidic material is more appropriate than pH 6 which is commonly used set by regulatory agencies. If paste pH alone is being used (e.g., Shaw et al., 2000), then using pH 6 will provide the most conservative identification of acid forming samples and is recommended. However, if paste pH values are used in conjunction with another parameter (in this case S_{Total}), then by using a lower pH cut-off criterion, a better classification of samples can be achieved. Whilst Sobek et al. (1978) stated that acid-toxic samples have a paste pH value of <4, pH 4.5 is the proposed cut-off criterion as it is commonly used in conventional NAPP/NAG geochemical plots (Section 2.4.2). Additionally, using pH 4.5 (and not a higher value such as pH 6) can help to discern between reactive and less-reactive sulphides as listed in Moncur et al. (2009). For example, Hughes et al. (2007) measured paste pH values <3 for pyrite-rich carbonate-poor waste, Schippers et al. (2007) measured pH 3 to 4 for pyrrhotite rich tailings, and higher abrasion pH values are measured for galena (pH 6.70) and bornite (pH 6.56; Noble, 2012).

Typically, samples with S_{Total} concentrations <0.3 wt. % or <0.05 wt. % are classified NAF (Morin and Hutt, 1999; Price, 2009). Based on data from the ISD, Morin and Hutt (1999) argued that neither cut-off criterion is correct, however, only a small percentage (e.g., <5%) of samples were misclassified. Therefore, 0.3 wt. % is the proposed cut-off value used here and in agreement with Price et al. (1997) and the GARD Guide (2009). Using these cut-off criteria as proposed in Figure 2.12, potentially acid forming (PAF) and acid forming (AF) materials can be identified. Therefore, samples with paste pH <4.5 and S_{Total} >0.3 wt. % are classified as AF, with Fe-sulphides expected to dominate the sulphide mineralogy. Samples with paste pH >4.5 and S_{Total} >0.3 wt. % are classified as PAF, and potentially contain less reactive sulphides. Samples with paste pH < 4.5 and S_{Total} <0.3 wt. % are classified as PAF, and are expected to contain almost exclusively Fe-sulphides. Samples with paste pH >4.5 and S_{Total} <0.3 wt. % are classified NAF.

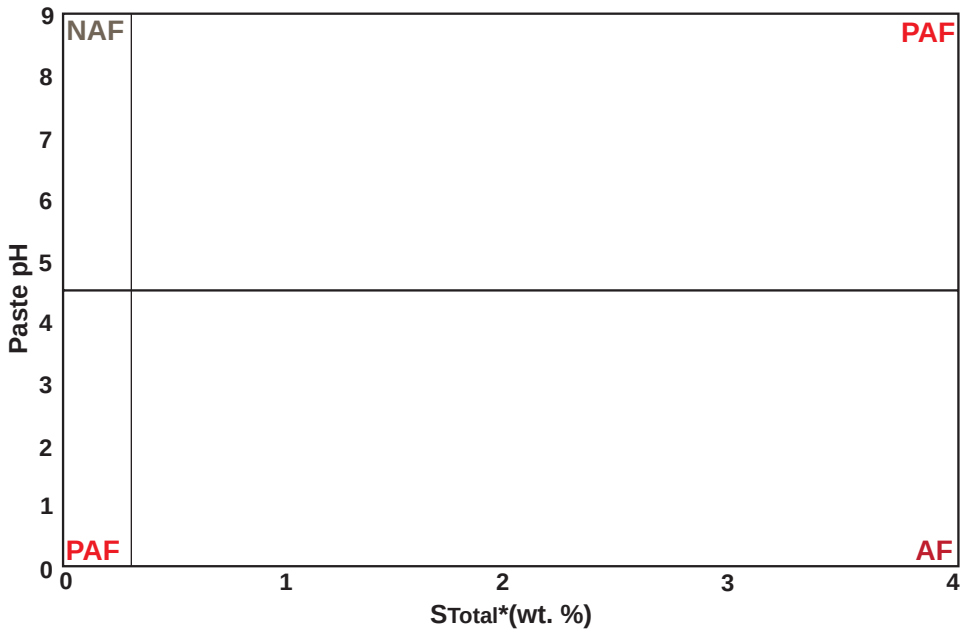

Figure 2.12 Paste pH versus S_{Total} (wt. %) with proposed classification fields shown. Abbreviations: NAF, non-acid forming; PAF; potentially acid forming; AF, acid forming (* indicates that sulphide-sulphur values can be used in place).

2.4.5.2 ARDI versus S_{Total}

ARDI values are recommended for screening against S_{Total} (Figure 2.13). Even if samples have high (i.e., >0.3 wt. %) S_{Total} values, if they have been classified as having ANC by the ARDI (based on a grain-by grain analyses), then overall they remain classified as having ANC. For samples classified as such, it is likely that the majority of S_{Total} comprises non-acid forming sulphur minerals (e.g., gypsum, barite), with carbonates also present. Samples with S_{Total} <0.3 wt. % and ARDI values <20 are considered NAF. Samples with ARDI values >20 are classified as PAF. Samples with S_{Total} >0.3 wt. % and ARDI values >30 are classified as acid forming (i.e., dominated by Fe-sulphides, with a low acid neutralising capacity), and >40 are classified as extremely acid forming (i.e., high Fe-sulphide content and no neutralising capacity). Samples with an ARDI value >40, but an S_{Total} contents of <0.3 wt.% are considered anomalous.These samples must be cross-checked with other stage-one data (e.g., mineralogy) and it is likely that stage-two testing will be required.

2.4.5.3 Paste pH versus ARDI

The final cross-check examines paste pH against ARDI values (Figure 2.14). Again, pH 4.5 is used as the PAF/NAF cut-off criterion, with ARDI classification fields remaining as in Figure 2.13. Like with the previous classification plot (ARDI versus S_{Total}; Figure 2.13), an 'anomalous' field is shown, whereby samples with ARDI values <20 and a paste pH values <4.5 cannot be confidentially classified. Again, samples with ARDI values >20 are PAF. Extremely acid forming samples are defined as those with paste pH values <4.5 and ARDI values >40, and are likely Fe-sulphide dominated with an absence of absence of neutralising minerals.

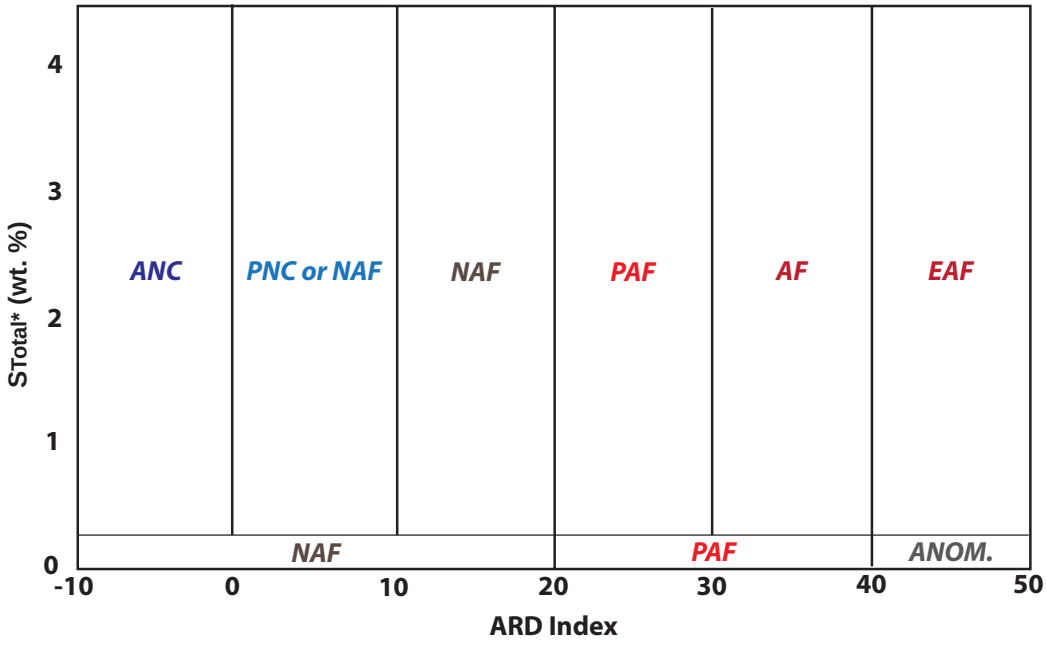

Figure 2.13 Proposed GMT stage-one pre-screening plot of acid rock drainage index (ARDI) values versus S_{Total} (wt. %). Abbreviations: ANC, acid neutralising capacity; PNC, potential neutralising capacity; NAF, non-acid forming; PAF, potentially acid forming; AF, acid forming; EAF, extremely acid forming, Anom., anomalous (* indicates that sulphide -sulphur values can be used in place).

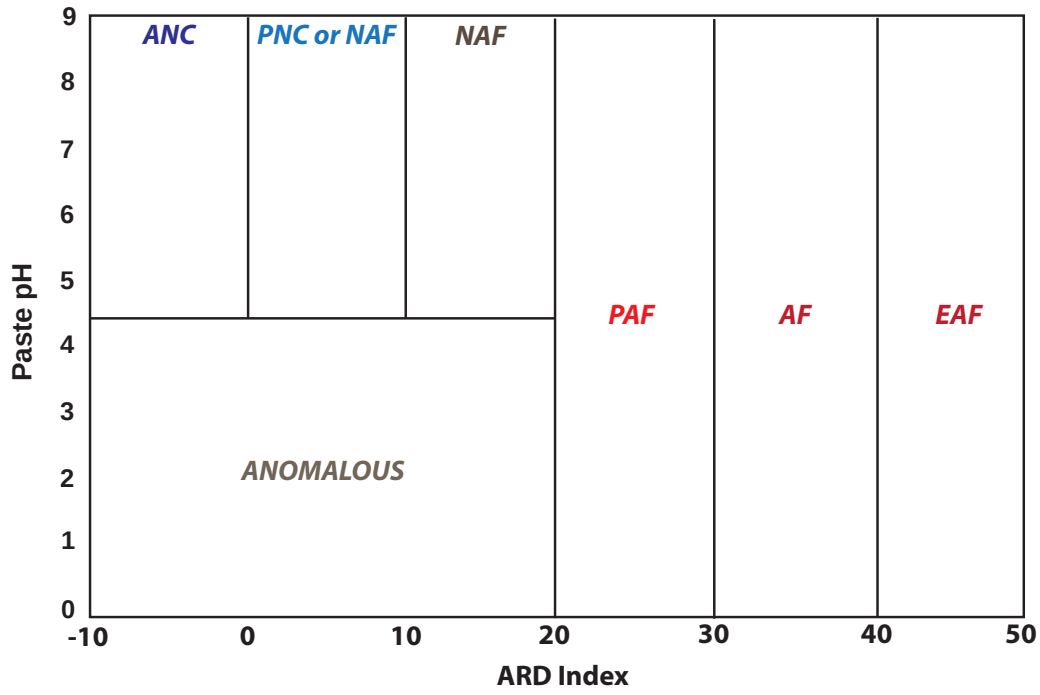

Figure 2.14 Proposed GMT stage-one pre-screening plot of acid rock drainage index (ARDI) values versus paste pH. Abbreviations: ANC, acid neutralising capacity; PNC, potential neutralising capacity; NAF, non-acid forming; PAF, potentially acid forming; AF, acid forming; EAF, extremely acid forming.

Samples with ARDI values >40, but a paste pH value <4.5 are classified as acid forming, as they are probably dominated by iron-sulphides that are less reactive in the paste pH test (i.e., arsenopyrite and chalcopyrite; Noble, 2012). Samples with an ARDI value <0 and a paste pH value <4.5 are most likely to have an acid neutralising capacity.

2.4.5.4 Carbonate versus sulphide

Paktunc (1998) and Craw (2000) inferred that an approximate 3:1 ratio of ANC/MPA is generally required by regulators for any acid produced to be effectively neutralised. Therefore, using a 3:1 ratio of carbonate to sulphide as proxies for ANC and MPA respectively, the acid forming potential can be classified based on mineralogy (Figure 2.15). The use of pyrite or calcite values alone is not recommended (unless the sample contains only these sulphide or carbonate minerals) due to the acid forming nature of other sulphides (e.g., pyrrhotite) and neutralising capacity of other carbonates (e.g., dolomite). Siderite is not recommended for inclusion in the carbonate budget due to its potentially acid forming nature (Skousen et al., 1997). All sulphides (i.e., iron-sulphides and non-iron sulphides) contribute to the sulphide-budget because if the pH declines significantly (e.g., <4.5), oxidation of non-Fe bearing sulphides may occur (via the Fe^{3+} oxidant pathway). Thus, this avoids mis-classification of samples containing non-iron sulphides (e.g., galena and sphalerite) and carbonates present, particularly when considering the stages in the ARD formation diagram shown in Broughton and Robertson (1992). Samples plotting at the origin or directly on the 3:1 line are inert. Carbonate and sulphide values obtained from QXRD or calculated from whole-rock data (i.e., using XRF/FP-XRF data to estimate modal mineralogy) should be plotted in this manner. Alternatively, modal mineralogy estimates undertaken as part of the ARDI or mesotextural grouping can be used, but will only provide less accurate results than by using real quantified data (i.e., from QXRD).

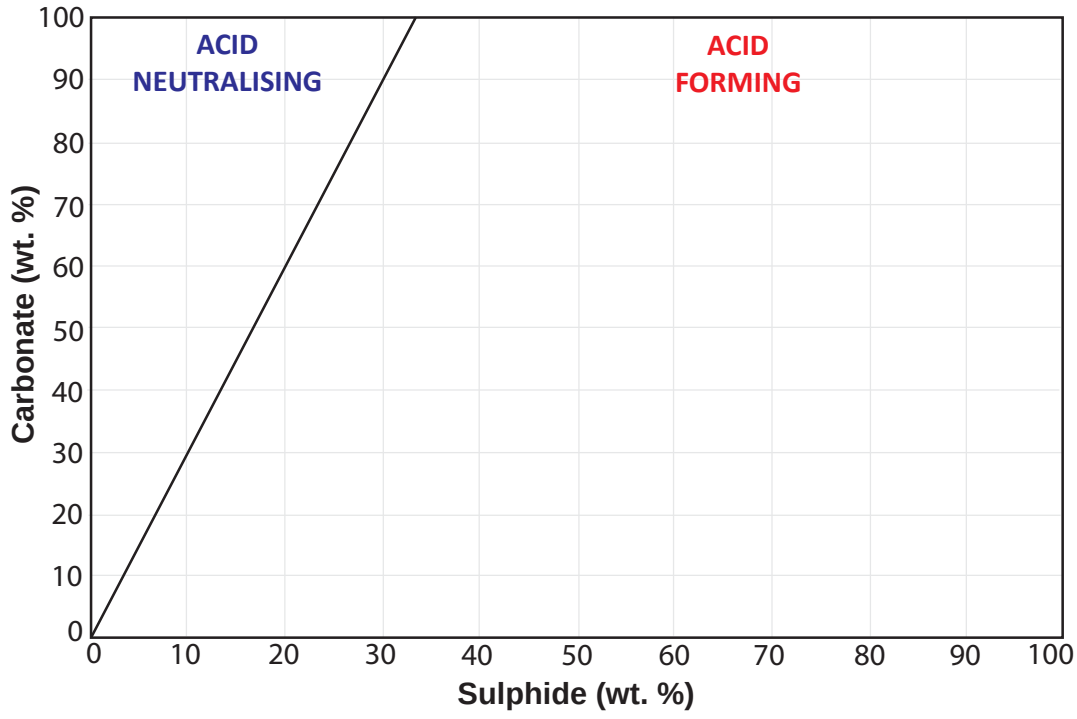

Figure 2.15 GMT stage-one pre-screening plot of carbonate (wt. %) versus sulphide (wt. %). Modified from Paktunc (1998) and Craw (2000).

2.4.5.5 Field portable-XRF versus paste pH

Elemental data collected by field portable-XRF (FP-XRF), XRF or assay (as at operational mines) are considered against paste pH values to construct modified Ficklin plots (Plumlee, 1999; Figures. 2.16 and 2.17).

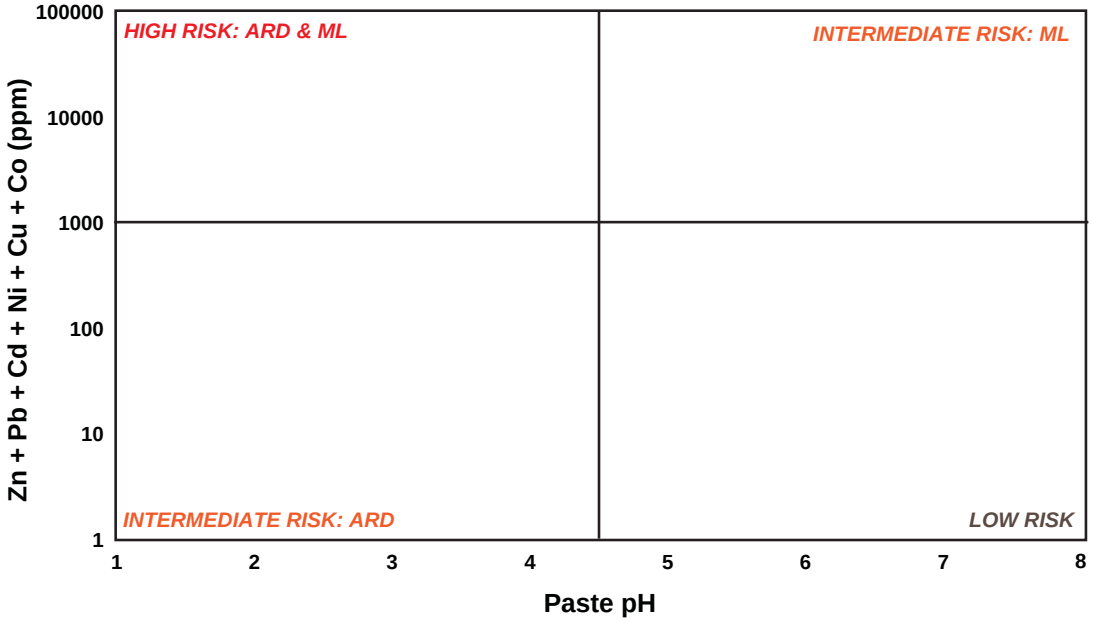

Figure 2.16 Proposed GMT stage-one pre-screening modified Ficklin plot of metal contents versus paste pH. Abbreviations: ARD, acid rock drainage; ML, metal leaching.

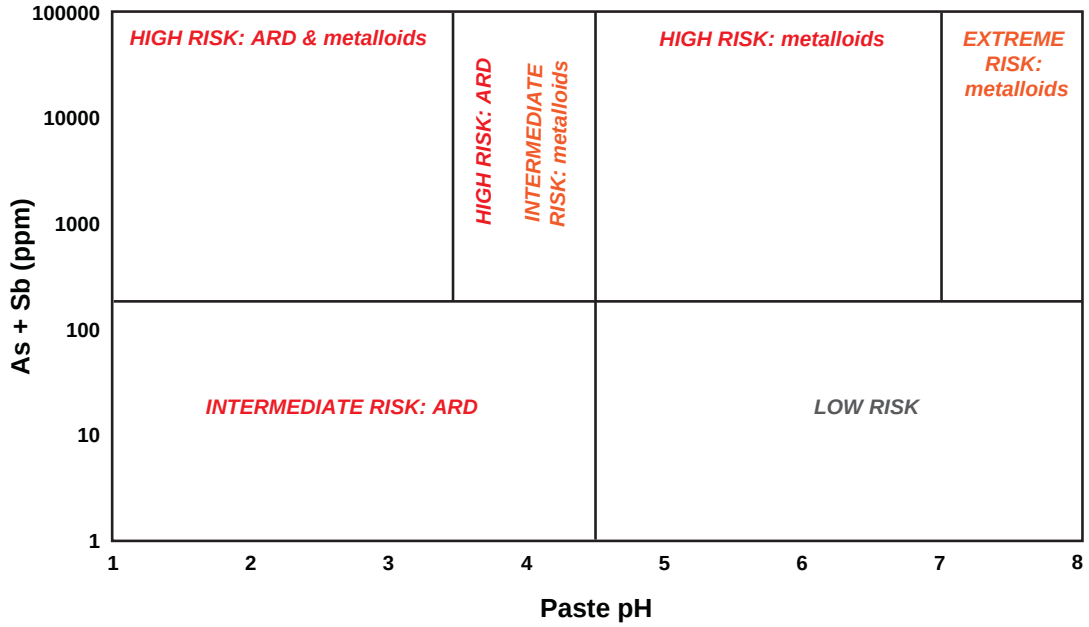

Figure 2.17 Proposed GMT stage-one pre-screening plot of metalloid contents versus paste pH. Abbreviations: ARD, acid rock drainage.

Again, the paste pH cut-off criterion value of 4.5 is used. The metal cut-off criterion shown in Figure 2.17 is proposed based on a review of data presented in Plumlee (1999). The WHO (2006) give drinking water guideline values of 0.01mg/L and 0.02 mg/L for As and Sb respectively. Considering this, concentrations greater than this and with paste pH values <4.5 are considered to have an intermediate

risk. Samples with immediate acidity and very high metal or metalloid contents are classified as high risk (as defined in Broadhurst and Petrie, 2010), which indicates that eventually they may require stage-three testing.

2.4.6 Stage-two sample selection

Table 2.14 summarises how samples are selected for stage-two testing based on stage-one classifications. Sample which are consistently classified as NAF and as low risk in terms of metal/metalloids versus pH do not require any further GMT testing. Samples which are consistently classified as having an acid neutralising capacity (i.e., by the ARDI versus S_{Total}/paste pH and carbonate/sulphide ratio) require stage-two ANC testing only. All other combinations of sample classification indicate a requirement for full stage-two testing.

Table 2.14 GMT stage-one pre-screening classification table with recommendations for further testing indicated. Abbreviations: ANC, acid neutralising capacity; PNC, potential neutralising capacity; NAF, non-acid forming; PAF, potentially acid forming; AF, acid forming; EAF, extremely acid forming; ML, metal leaching; S_{Total}, total sulphur.

Paste pH vs. S_{Total}	ARDI vs. S_{Total}	ARDI vs. paste pH	Carbonate vs. Sulphide	Metals vs. paste pH	Metalloids vs. paste pH	Further Testing
AF	EAF	EAF	Acid forming	High risk: ARD and ML	High risk: ARD and metalloids	Full stage-two testing
PAF	AF	AF		Intermediate risk: ARD	Intermediate risk: ARD	
	PAF	PAF		Intermediate risk: ML	Intermediate risk: metalloids	
	Anomalous	Anomalous				
NAF	NAF	NAF	Inert (or low carbonate contents (i.e., <1 wt. %)	Low Risk	Low Risk	No further testing
NAF	ANC or PNC	ANC or PNC	Acid neutralising	Low Risk	Low Risk	Stage-two ANC testing only

2.5 GMT approach: stage-two

Routine geochemical tests are exclusively used in stage-two of the GMT approach. Both NAPP and NAG tests are recommended for samples identified as PAF, AF and EAF by stage-one. Additionally, XRF/full element assay analyses are also recommended for samples classified as such if these have yet to be performed, unless FP-XRF and XRF values are in very strong agreement (as determined through cross-checking values as part of mesotextural grouping/stage-one). Additional mineralogical analyses can be performed as part of this stage if required (i.e., QXRD on samples containing several sulphides to determine the exact proportion of acid forming sulphides present), however, this is not mandatory and therefore has not been listed in Figure 2.1. A brief explanation of NAPP and NAG test selection rationale is given in this section, followed by an outline of stage-two data classifications.

2.5.1 NAPP and NAG tests

Maximum potential acidity (MPA) calculation requires determination of S_{Total},with values obtained from the most accurate, low cost method identified in stage-one to be used (i.e., either EA, FP-XRF or XRF). As both mine sites used to test the approach are Australian (Section 1.5), the convention of expressing values in kg H_2SO_4/t was applied (Smart et al., 2002). If detailed mineralogy has been undertaken, then the opportunity exists to refine calculation of MPA using sulphide-sulphur values (as this is more accurate) or Fe-sulphide-sulphur values. Stewart (2005) explains how the stoichiometric conversion factor (CF) used in MPA calculations is derived. Essentially, the CF is based on the assumption that all sulphur is present as pyrite, and that all sulphide oxidises to completion according to the pyrite oxidation reaction shown in *equation 1.1*, whereby one mole of FeS_2 produces two moles of H_2SO_4. Stewart (2005) explains that one mole of S (atomic mass 32.1) will produce one mole of H_2SO_4 (molecular mass 98.1). The S_{Total} (wt. %) is multiplied by (98.1/ 32.1) and equals 3.06. This is recast in parts per thousand by multiplying by a factor of 10 to give 30.6. The resulting MPA value is therefore cast in H_2SO_4 in kg/t. Following this method, conversion factors for pyrrhotite, arsenopyrite and chalcopyrite (based on *equations 1.6-1.8*) were calculated and were also 30.6.

Despite arguments presented in Morin and Hutt (2009), it is of importance to select an appropriate method for determining ANC from one of the many existing methods outlined in White et al. (1999), Smart et al. (2002) GARD Guide (2010) and Price (2009). As stated in section 1.3.2, the most widely used methods are the Sobek and Modified Sobek test with examples of their application given in Craw (2000), Weber et al. (2005), Akabzaa et al. (2007) and Stewart et al. (2006). Consequently, both were selected for review, following methods outlined in Smart et al. (2002) and Mills (2011). The Modified Sobek method is recognised as producing a more realistic estimate of ANC because the reaction liquor (2g sample + HCl (aq)) does not require heating (Capanema and Ciminelli, 2003; GARD Guide, 2010). Additionally, the reaction is given longer time to evolve (i.e., 24 hours compared to 2 hours) before back-titration with NaOH. However, Sobek et al. (1978) proposed the heating step of the original Sobek test to accelerate non-carbonate neutralising reactions and therefore include their contribution in the final ANC value (Sherlock et al., 1995; Craw, 2000). Additionally, when considering the number of samples likely required for ARD characterisation at an operational site (Section 2.2), the Sobek test would be more time efficient. An appropriately certified standard reference material is not always identified and recommended for use in published methodologies (e.g., Smart et al., 2002; Price, 2009; Mills 2011). Therefore, the GMT approach recommends the use of KZK-1 (sericitic schist) and NBM-1 (altered feldspar porphyry), which can be obtained from CANMET (Natural Resources, Ottawa). Both reference materials have been used in other ARD studies including Paktunc (2001) and Goodall (2008).

The single-addition NAG test is recommended as part of stage-two as it is the simplest and most established of the six NAG methods (Section 1.3.4). Examples of its application are presented in Hammarstrom et al. (2003); Tran et al. (2003); Stewart et al. (2006); Sapsford et al. (2008) and Broadhurst et al. (2009). The main application of NAG test results here is for screening against paste pH values (as calculated in stage-one) and to provide a value to cross check NAPP data.

2.5.2 GMT Stage-two classification

Traditional NAPP versus NAG pH plots are used to classify samples as PAF, NAF or UC. However, some discrepancy lies in the cut-off criterion to use for NAG pH. For example, Weber et al. (2006) used pH 4, whereas Stewart et al. (2006), Moon et al. (2008) and Broadhurst (2009) favoured the use of pH 4.5. The latter is used here as the cut-off criterion (Figure 2.18). The use of NAG pH versus paste pH values was proposed by Price et al., (1997), however, its application has not been widely demonstrated, despite the fact that it offers an assessment of lag-time to ARD and thus classifies risk. The most recent application of this classification is shown in Weber et al. (2006) where it was used to classify coal mine samples. Therefore, as both NAG and paste pH data are collected through stage-one and stage-two testing, this classification has been modified slightly (to define fields as EAF and AF) and included as part of stage-two (Figure 2.19). It is noteworthy that as more fields are defined, the cut-off criterion used between high risk and medium risk samples is set slightly lower to pH 4, following the value suggested by Sobek et al. (1978).

In a similar manner to carbonate versus sulphide ratio plots (Section 2.4.5.4), ANC and MPA ratio plots are recommended as shown in Figure 2.20. However, they are most effectively used if the MPA has been recalculated in terms of sulphide-sulphur. Otherwise, application of the ANC vs. S_{Total} plot presented in Smart et al. (2002) can be used in their place. To refine estimates of geochemical risk, NAG pH data can be used in place of paste pH when compared against element concentrations (Figures 2.16 and 2.17). These refined geochemical data plots should be compared alongside those produced for paste pH as they provided an indication of the current situation, and NAG pH plots represent an extreme condition whereby all acid forming sulphide has reacted.

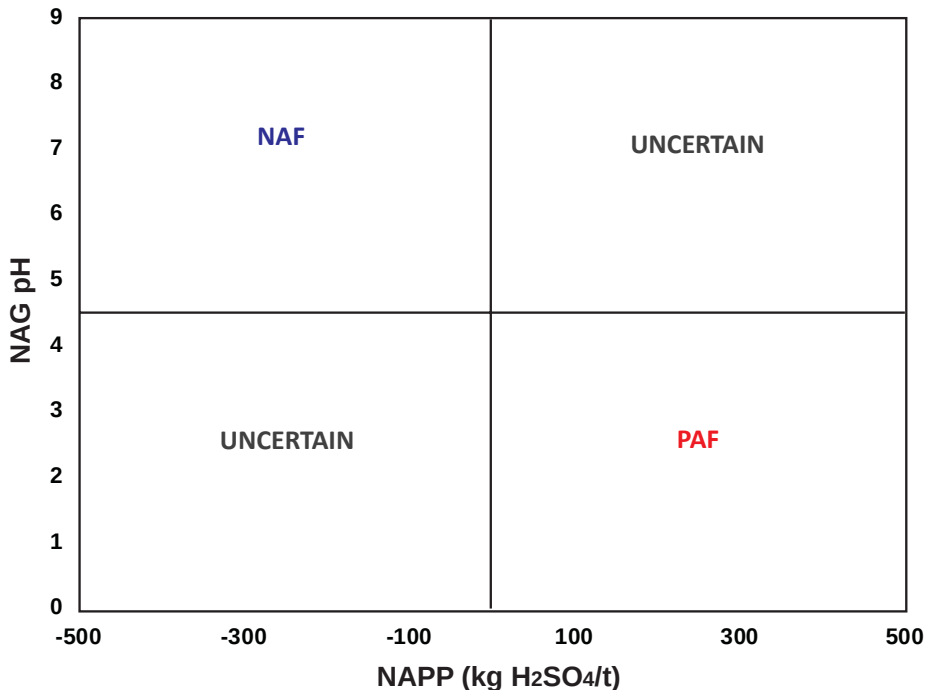

Figure 2.18 GMT stage-two screening plot of NAPP versus NAG pH. Abbreviations: NAF, non-acid forming; PAF, potentially acid forming. Modified after Smart et al. (2002).

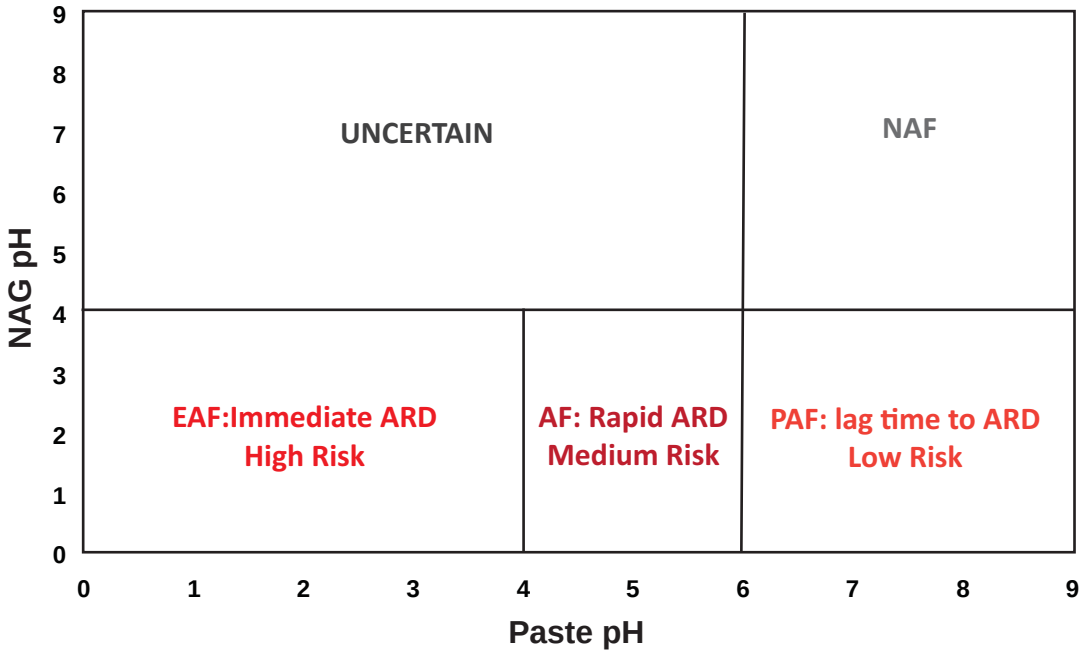

Figure 2.19 GMT stage-two screening plot of NAG pH versus paste pH. Abbreviations: NAF, non-acid forming; PAF, potentially acid forming; AF, acid forming, EAF, extremely acid forming. Modified from Price et al. (1997) and Weber et al. (2006).

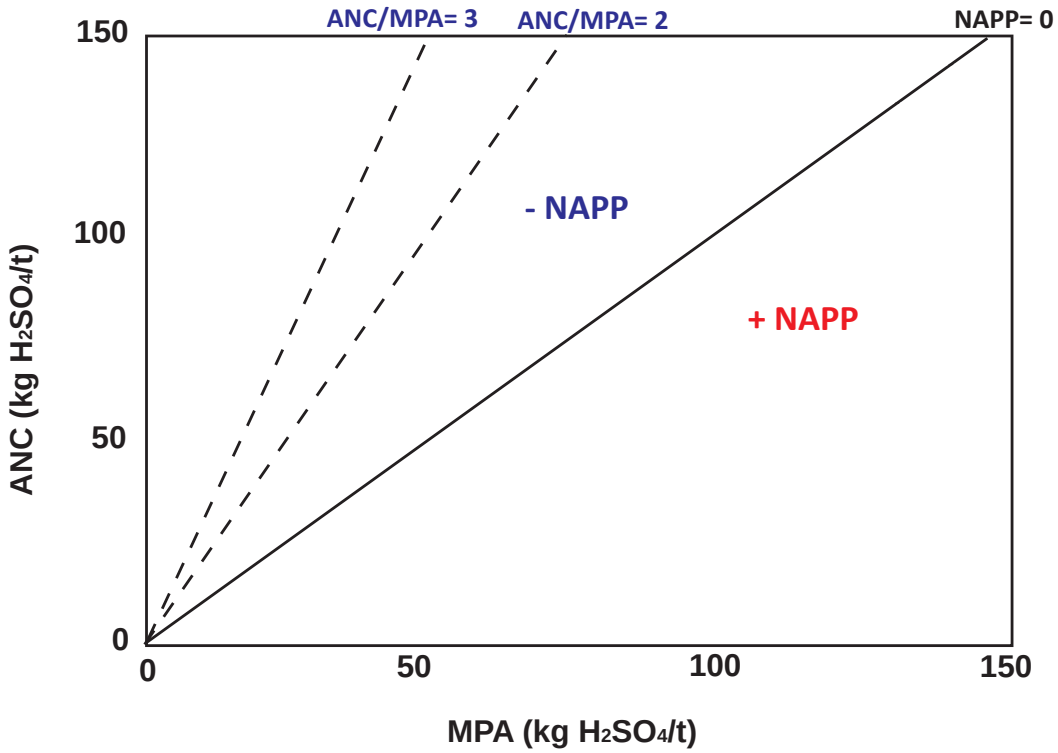

Figure 2.20 GMT stage-two screening plot ANC versus MPA. Abbreviations: ANC, acid neutralising capacity; MPA, maximum potential acidity; NAPP, net acid forming producing potential. Modified from Smart et al. (2002).

2.5.3 Stage-three sample selection

Sample selection for further testing requires careful consideration as stage-three tests are not mandatory. Instead, a select combination of tests is recommended to clarify or further investigate specific questions. In general, samples identified as highly acid forming by stage-one (i.e., consistently AF or EAF), PAF by NAPP vs. NAG pH, and EAF or AF by NAG pH versus paste pH will require further testing. Samples identified with high metal/metalloid concentrations and sulphides are recommended for detailed microanalysis to determine the sulphide mineral chemistry and identify controls on oxidation as outlined in Egiebor and Oni (2007). To observe sulphide microtextures, MLA and SEM analyses should be performed. Advanced NAG testing only is recommended for any ambiguous samples (i.e., conflicting classifications), with QXRD subsequently recommended (if it has not already been performed on these individual samples) if classifications remains inconclusive. Samples with high ANC values are recommended for ABCC testing in order to determine the effective neutralising capacity.

2.6 GMT approach: stage-three

Similar to stage-one of the GMT approach, a combination of geochemical, mineralogical and textural techniques is applied to characterise in detail appropriately selected samples. Unlike stage-one, sophisticated technologies are used, therefore a much smaller number of samples is analysed. This section provides explanation of each selected test or technique (with examples of application) and outlines the how these can be used for ARD prediction/waste classification.

2.6.1 Advanced NAG and ABCC tests

Three NAG tests were selected for inclusion in stage-three, namely the multi-addition NAG (mNAG), sequential NAG (sNAG) and the kinetic NAG (kNAG) tests. The mNAG test procedure involves the stepped addition of H_2O_2 in three increments (100 ml, 100 ml and 50 ml). This allows more time for sulphide oxidation, as incomplete oxidation for samples containing pyritic sulphide >0.7 to 1 wt. % was reported when using the single-addition NAG test due to H_2O_2 decomposition (Stewart, 2005; Chotpantarat, 2010). The sNAG test was also proposed to overcome incomplete oxidation effects, and achieves this through successive single addition NAG tests until the NAG pH >4.5 (Stewart, 2005). The individual NAG acidities are then summed to give total sNAG acidity in kg H_2SO_4/t (Stewart, 2005). The sNAG test is the more favoured of the two methods in published literature, with examples presented in Tran et al. (2003), Weber et al. (2005), Stewart et al. (2006) and Hesketh et al. (2010). Based on a review of the analytical protocols for both tests (Stewart, 2005), the sNAG test is less time efficient as the length of the test and amount of H_2O_2 required is not defined as with mNAG test. No recommendations as to the number of samples selected for analysis (per acid forming mesotextural group or alteration/ lithological class) are given here as this will typically be dictated by the mineralogy of the acid forming samples.

The kNAG test evaluates the lag time to acid formation, and therefore is a valid cross-check to NAGpH vs. paste pH classifications. Essentially the procedure is identical to the single addition NAG test except that the temperature, pH and occasionally EC of the liquor are recorded (Smart et al. 2002;

Stewart, 2005; Chotpantarat, 2010). Smart et al. (2004) and Stewart et al. (2006) presenting a scale up calculation (*equation 2.1*) by which the lag period and oxidation rates in leach columns can be predicted from this data:

Weeks to pH 4 in column = 0.54 × [minutes to pH 4 in kinetic NAG] *(2.1)*

However, Stewart et al. (2006) recommended that in practice, column lag times should be reported in broad terms to reflect the indicative nature of the relationship following Table 2.15.

Table 2.15 Indicative column lags to pH 4 based on kinetic NAG results (from Stewart et al., 2006).

Range of time to pH 4.0 in kNAG (min)	Indicated column lag to pH 4.0
< 5	<1 month
5 to 15	1 to 2 months
15 to 30	2 to 4 months
30 to 50	4 to 6 months
50 to 100	6 to 12 months
100 to 200	1 to 2 years
>200	>2 years

As the kNAG test is the only short-term test commercially available which provides some rate data, it is included in the GMT approach. The application of scaling up calculations on samples containing more than one sulphide mineral will be reviewed (Chapter 4), as Smart et al. (2004) and Stewart et al. (2006) originally proposed this for pyrite-bearing coal samples.

The ABCC test is occasionally regarded as an alternative test to the ANC procedure and intends to provide an indication of the ANC portion available for neutralisation (Miller and Jeffery 1995; Smart et al., 2002; Weber, 2003; Tran et al., 2003; Stewart et al., 2006; Chotpantarat, 2010). The test involves the addition of 100g of water to 2g of a sample and then slow titration with HCl while continuously stirring and monitoring to pH 3 (Smart et al., 2002; Tran et al., 2003). Generally, it is recommended for use when assessing if a sulphidic sample with NAPP <0 and NAG pH= 4.5 has enough readily available carbonate to render it non-acid forming (Smart et al., 2002). ABCC testing is recommended for at least one sample per mesotextural group identified as having (high) ANC, and containing several carbonate minerals (i.e., calcite, dolomite and ankerite).

2.6.2 Microanalytical techniques

Element quantification in stage-one and stage-two has been through bulk analytical procedures (e.g., FP-XRF and XRF). However, in-situ examination of sulphide trace element distribution and sulphide alteration products would allow for a better understanding of each sulphide-bearing mesotextural group. Through understanding these micro-scale processes, better waste rock management/ rehabilitation strategies can be developed, as implied in Jamieson (2011). In-situ element analysis can be undertaken

through several microanalytical techniques which are commonly used in ARD studies (Table 2.15). However, integration of these techniques into ARD predictive protocols is not presented in the literature. This is likely due to the absence of clear guidelines as to when and how to apply these techniques in addition to their relatively high analytical costs. Stage-three addresses this, with the following section selecting the most appropriate techniques when considering time and cost, and provides an overview of standard methodologies.

Table 2.16 Microanalytical techniques used to determine mineral composition in mine waste material, dissolution and other weathering textures, and the residence sites of trace elements (compiled from Diehl et al., 2007 and Jamieson, 2011).

Analytical technique	Application to mine waste mineralogy	Example studies	GMT approach application?
Scanning electron microscopy (SEM)	Mineral species, mineral textures, particle size, cleavage, grain boundaries, surface weathering, deformation structures, microfaults, veins, fractures, semi-quantitative EDS data	Hudson-Edwards et al. (1999), Walker et al. (2005), Weisner and Weber (2010)	Yes
Electron probe microanalysis (EPMA)	Exact residence of minor and trace elements, spatial distribution of minor and trace metals, semi quantitative and quantitative data	Hudson-Edwards and Edwards (2005), Moncur et al. (2009), Walker et al. (2009), Corriveau et al. (2011)	Yes
Transmission electron microscopy (TEM), scanning transmission electron microscopy (STEM)	High-resolution imaging, may include chemical information and electron diffraction	Petrunic et al. (2009)	No
Micro-XRF diffraction using conventional or synchrotron sources (XAS)	Grain scale mineral identification based on crystal structure; application to poorly crystalline materials	Walker et al. (2009), DeSisto et al. (2011)	No
Synchrotron-based X-Ray fluorescence (micro-XRF)	Mineral characterisation based on oxidation state and short-range structure	Foster et al. (1998), Walker et al. (2009), Pérez López et al. (2011), Carbone et al. (2011)	No
Conventional micro-XRF	Minor and trace element semi-quantitative data	Bernaus et al. (2006)	Yes
Laser ablation ICPMS	Minor and trace element quantitative data	Al et al. (2007), Ohlander et al. (2007), Savage et al. (2008)	Yes
Raman spectroscopy	Mineral identification	Das and Hendry (2011)	Yes
Micro- particle induced X-Ray emission (micro-PIXE)	Minor and trace element quantitative data	Cabri et al. (1993), Cabri and Campbell (1998), Jamieson et al., (2005)	No

Techniques selected for review in the GMT approach include LA-ICP-MS and μXRF for element mapping; EMPA and LA-ICPMS for element quantification; and MLA-SEM for examining microtexture. Synchrotron based technologies were avoided by the GMT approach as these specialist techniques cannot be routinely used, and essentially will not provide a significant amount of new data which will impact upon sample classification or indeed the management of a particular mesotextural group.

2.6.2.1 SEM-EDS

Scanning electron microscopy (SEM) is the first microanalytical technique recommended. Previously, application of SEM-EDS was suggested exclusively for samples with sulphide composition abnormalities (Mills, 2011). However, application should not be limited. For example, sulphide minerals often contain micro-inclusions which are not readily identified in optical microscopy studies (e.g., Maslenikov et al. 2009; Thomas et al., 2011). Presence of inclusions causes strain to the crystal structure, diminishing the sulphide's resistance to oxidation (Jambor, 1994; Kwong, 1995; Plumlee, 1999). However, through SEM studies, micro-inclusions are better identified and the relative rate of weathering can be assessed. A broad number of samples from EAF and AF groups should be analysed, particularly those representative of textural variations (i.e., different mineral-associations, sulphide morphologies, sizes, and fracturing). Observations following those listed in Table 2.16 should be made. In this research, a FEI Quanta 600 environmental scanning electron microscope (ESEM; CSL, UTAS) was used, with polished thin sections and laser mounts carbon coated prior to analysis.

2.6.2.2 EPMA

EPMA is the next recommended technique, and should be used to obtain compositional data from distinct oxidation products identified in SEM and optical microscopy studies (i.e., on fewer samples than were analysed by SEM). Identification of these products will enhance the understanding of trace element mobility, as often these act as temporary stores (Lin and Herbert Jr. 1997; Hudson-Edwards and Edwards, 2005; Lottermoser, 2010). These products often form rims and fractures on primary sulphides (e.g., Blowes and Jambor, 1990; Jambor, 2003; Moncur et al., 2009), therefore a small beam size (micron-scale) is required. Quantitative analysis can be hindered as a result of the porous nature of these secondary products (e.g., brown iron oxyhydroxide/ferrihydrite) and admixed impurities, thus results obtained may only be semi-quantitative (Haffert et al., 2010). Analysis should be undertaken on samples representative of each primary sulphide, as these may be required for use an internal standard as part of LA-ICP-MS analysis (see next section). In this research, a Cameca SX100 electron microprobe was used (CSL, UTAS), with polished laser mounts carbon coated prior to analysis.

2.6.2.3 LA-ICP-MS

Following SEM-EDS and EPMA, LA-ICP-MS analysis is recommended for a well chosen sub-set of samples representative of each sulphide mineral (and textural type) identified per acid forming mesotextural group. The main objectives are to determine trace element distribution in primary sulphides in order to understand potential effects on oxidation, and if possible, to deduce secondary mineral trace element contents as lower detection limits are achieved by LA-ICP-MS than EPMA (Koenig, 2008). Applications of spot and line analyses have been demonstrated in previous ARD studies (Ohlander et al., 2007; Savage et al., 2008). Element mapping can be undertaken using EPMA (e.g., Lin and Herbert Jr., 1997; Hudson-Edwards and Edwards, 2005; Diehl et al., 2007), however, this is highly time consuming, and better resolution maps can now be collected using LA-ICP-MS. Examples of LA-ICP-MS element mapping in ARD studies is yet to be published, therefore, the methods used here followed those outlined in Large et al. (2009), Thomas et al. (2011) and Danyushevsky et al. (2011). In this research, a New Wave 213nm solid state laser microprobe coupled either to an Agilent 4500 or an Agilent 7700 quadrupole

ICP-MS was used. Quantification of LA-ICP-MS analyses requires an internal standard as defined by Longerich et al. (1996). Danyushevsky et al. (2011) recommended that for routine cost-effective analysis, the concentration of the internal standard should be easily measurable by other routine micro-analytical techniques such as EPMA, or estimated from stoichiometry. Iron is often chosen as the internal standard for many sulphides (Danyushevsky et al., 2011). Galena and sphalerite were analysed in this research, so stoichiometric Pb and Zn measured by EPMA were used, respectively. During analyses, the calibration standard STDGL2b2 (Danyushevsky et al., 2011) was used, which contains a wide range of chalcophile, siderophile and lithophile elements.

LA-ICP-MS analyses are performed in an atmosphere of pure He. Sulphide element mapping is undertaking by ablating a set of parallel lines arranged in a grid over the sample so the space between lines matched that of the beam (Thomas et al., 2011). In this research, 15, 25 or 30 μm beam sizes were used depending on the size of the target grain. The beam is rastered over the lines at a speed matching the beam size with a nominal 10 Hz repetition rate, thus, every position in the sample is ablated 10 times contributing to five consecutive pixels in the final image, and ablated to a depth of c.5 μm (Thomas et al., 2011). Background levels and drift are measured on the STDGL2b2 standard before and after every image, and if analysis is calculated to exceed 1 hour, then additional standard analyses are performed in the middle of the run. Collection of standard data allows for element map quantification. Image processing involves drift correction, application of a median filter to remove artefacts generated during processing, subtraction of background from filtered counts, and replacement of filtered counts less than background with standard deviation values for that element (Thomas et al., 2011). Images are finally produced for each element, with concentration indicated by a logarithmic colour scale (Thomas et al., 2011). Whilst examples of LA-ICP-MS mapping analyses are presented in Large et al. (2009) and Thomas et al. (2011) for pyrite and pyrrhotite, few examples exist for other sulphide minerals such as arsenopyrite, galena and sphalerite.

2.6.2.4 Micro-XRF

A potential limitation of LA-ICP-MS is the cost per analysis (>$100 per hour; CODES, UTAS); therefore, a lower cost element mapping technique was sought for inclusion in the GMT approach. Conventional μXRF was selected for use as it is a non-destructive, highly accurate technique. Adams et al. (1998) provide a concise overview of μXRF, and attributed its development to the production of relatively simple and cost effective devices for obtaining a small dimension X-Ray beam, i.e., capillary optics. Recent examples of μXRF application are given in Croudace et al. (2006); Rothwell et al. (2006), Katsuta et al. (2007); Coralay and Kadioglu (2008) and Genna et al. (2011), with few studies demonstrated applications in mine waste characterisation (e.g., Bernaus et al., 2006; Hayes et al., 2009). In this research, a Horiba XGT 7000 μXRF was used (CSL, UTAS). This machine uses X-Ray guide tubes (either 100 μm or 10 μm) from which a 10μm high intensity X-Ray beam is irradiated onto the sample. Measurement of elements Na (z=11) to U (z=92) is possible. The analysis probe is set in vacuum, making it possible to analyse the sample at normal atmospheric pressure. A sample on the XY scanning stage can be visually observed via a CCD camera from the same axis as the X-Ray beam. High speed measurements are possible up to 50 times faster than conventional equipment (i.e., EPMA), providing

much greater usability. Fluorescence and transmission X-Rays from the sample are measured during analysis, with this data used to create element maps. Samples require minimal preparation prior to use (i.e., no coatings as with SEM and EPMA are required), and the sample stage can accommodate for a 10cm x 10cm maximum area of analysis. This implies that intact drill-core samples can be analysed at microscale resolution. As no published methods for analysis using this instrument were available, a period of method development was undertaken as part of this research (Appendix 2.2). Several types of sample and various preparation methods were trialled (including optical thin sections, whole and half drill core samples and resin mounted samples). Examples of μXRF analyses performed on laser mount samples only are presented for comparison with LA-ICP-MS data in this research (Chapter 3).

2.6.3 MLA

MLA represents a unique automated method of combining BSE image analysis, X-ray mineral identification and advanced imaging and pattern recognition analysis (Gu, 2003; Fandrich et al., 2007). Applications of MLA in other mining-related disciplines (i.e., applied mineralogy, metallurgical processing) are well established, with examples presented in Bruckard et al. (2010); Chapman et al. (2011); Hunt et al. (2011) and Rizmanoski (2011). Currently, there are no published examples of MLA application in predictive ARD studies. Therefore, MLA is recommended as a stage-three technique, and should be performed on at least one representative sample from each EAF and AF group. Polished laser mounts (as prepared for SEM, EPMA and LA-ICP-MS) or MLA tiles should be analysed. The MLA system used in this research was the FEI Quanta 600 SEM equipped with 2 EDAX ultra thin window Si(Li) energy dispersive X-ray (EDS) detectors (CSL, UTAS).

There are eight basic MLA measurement modes, which vary from a purely BSE-based technique to an almost exclusively X-Ray analysis point counting technique (XMOD; Gu, 2003; Fandrich et al., 2007). The GMT approach recommends the use of sparse phase liberation_Lite (SPL_Lite), extended back scattered electron (XBSE), grain-based X-Ray mapping (GXMAP) and X-ray modal (XMOD) analyses. Prior to analysis, a mineral standard library must be collated for each individual sample suite (i.e., per site) to allow for accurate mineral identification. High quality X-Ray spectra are collected for each mineral identified in the sample suite (Fandrich et al., 2007). During the analysis, spectra for unknown minerals are also collected if specified. After analyses these particles can be selected and identified using EDS, and retrospectively incorporated into the mineral library. SPL_Lite analysis should be performed as standard on every selected EAF and AF sample. This measurement mode works by searching images for particles with BSE grey levels greater than that of the standard, and subsequently maps them (Fandrich et al., 2007). In this research a nickel standard was used. Applications of XBSE and GXMAP analyses to produce mineral maps for whole samples were explored. XBSE operates similar to SPL_Lite, and GXMAP uses X-Ray mapping on phases that cannot be segmented by BSE grey levels alone (Fandrich et al., 2007). The GXMAP technique was of particular use to differentiate between pyrite and magnetite for Ernest Henry samples (Chapter 5). XMOD is based on a point counting method whereby mineral identification is determined by one X-Ray analysis at each counting point (as defined

by the operator; Fandrich et al., 2007). X-Ray spectra are saved for off-line classification, with modal mineralogy information (i.e., percentages) calculated. These data can be used for comparison with QXRD values gathered at stage-one, or to supplement modal mineralogy data per mesotextural group. Off-line data processing is typically performed using MLA Image View software (Gu, 2005), with particles and images classified based on mineralogy. Classified particles and images can be analysed further using Texture Viewer (Nguyen, 2009).

2.6.4 GMT Stage-three classification

Classification of stage-three results first requires comparison of advanced NAG test results with stage-two geochemical test results (i.e., NAPP and NAG). This allows for variation between results to be calculated. It is unlikely that the overall sample classification will change from the previous stages. However, if significant differences are observed between advanced NAG test results and either the single-addition NAG or NAPP tests, additional samples from that particular mesotextural group are recommended for advanced NAG analysis. This is to identify if the error is an anomaly, or representative of a systematic error. Each geochemical test should be plotted against the other, with deviations from the model line (1:1) examined. Additionally, all results should be plotted on a summary graph or comparison table to allow for a direct comparison of data.

Classification of microanalytical data is less defined than when using geochemical and quantitative mineralogical results. A numerical ranking scheme based on observations (similar to that proposed by the ARDI) has not been proposed for BSE images collected during SEM analysis. Instead, the observations made from microanalyses are intended to provide in-depth characterisation of each (potentially) acid forming mesotextural group. However, quantitative element data can be used with NAG pH data (stage-two) to produce highly specific Ficklin style plots (following those shown in Figure 2.16 and 2.17). Additionally, element distribution can be directly correlated with mineralogy through overlying mineral and element maps. Individual elements should be screened against each other to determine relationships using correlation matrices (e.g., Harris et al., 2003; Ashley et al., 2006) thus enhancing the understanding of the potentially deleterious elements sources at a given site. Additionally, these values should be screened against locally determined baseline and guideline values (e.g., ANZECC, 2000; WHO, 2006). This will provide a clear indication of the mesotextural groups posing significant environmental risk at a given site.

2.7 Final GMT classification and implications

Classification results from each stage of the GMT approach should be collated in a summary table as shown in Table 2.17, with three examples given. At the end of each stage, a final classification is assigned per mesotextural group based on the frequency of classifications within that particularly stage. For example, if the majority of classifications are PAF as for sample B (Table 2.17), the group is 'PAF'. Mesotextural groups classified at the end of stage-three as 'EAF: high risk' are prioritised for kinetic testing, however, samples from AF and PAF groups should also be nominated for testing. These groups should be considered by site managers/operators as separate entities when formulating waste rock management/ rehabilitation plans, as they have unique sulphide mineralogy and texture, and therefore specific acid forming characteristics and potential deleterious element issues.

Table 2.17 Example of a GMT Approach summary table

GMT-stage	Classification	Sample A	Sample B	Sample C
Stage-one	ARDI	NAF	PAF	EAF
	S_{Total} vs.ARDI	NAF	PAF	EAF
	S_{Total} vs. paste pH	NAF	PAF	AF
	ARDI vs. paste pH	NAF	PAF	EAF
	Carbonate vs. sulphide	Inert	AF	AF
	FP-XRF vs. paste pH	Low-risk	Intermediate risk- ARD	High risk- ARD, metal leaching and metalloids
	CLASSIFICATION	**NAF**	**PAF**	**EAF**
Stage-two	NAPP vs. NAG pH		PAF	PAF
	NAGpH vs. paste pH		AF- Medium risk	EAF- High risk
	MPA vs. ANC		AF	AF
	XRF vs. NAG pH		Intermediate risk- ARD	High risk- ARD and ML and metalloids
	CLASSIFICATION		**PAF**	**EAF**
Stage-three	mNAG vs. NAG			PAF
	mNAG vs. sNAG			PAF
	sNAG vs. NAG			PAF
	mNAG vs. NAPP			PAF
	sNAG vs. NAPP			PAF
	mNAG vs. sNAG vs. NAG vs. NAPP			PAF
	kNAG			Scale up: 4 weeks
	Elements vs. NAG pH			High risk- ARD and ML and metalloids
	Potential deleterious element issues?			Yes- As, Pb and Zn
	Sulphide microtextures (SEM and MLA results)			3 x pyrite textures identified
	CLASSIFICATION			**EAF: High risk- kinetic testing required**

2.8 Summary

Current methodologies used at the prefeasibility stage of mine operations to characterise waste rock extensively utilise laboratory based geochemical tests (Downing and Giroux, 1993; Morin and Hutt, 1998; Smart et al., 2002; GARD Guide, 2009). Whilst mineralogical analyses are recognised as an integral part of predicting acid formation, they are not effectively used (Diehl et al., 2007). Routine textural analysis is largely absent from sample classification protocols despite the direct control of texture

on acid formation (Plumlee and Nash, 1995; Mills et al., 2011). Therefore, this research proposes an integrated geochemistry-mineralogy-texture (GMT) approach as a protocol for waste rock classification with potential applications at both historic and operational mines sites. This approach aims to use well established routine tests and classification methods, but also explores the application of additional techniques (e.g., μXRF, LA-ICP-MS, MLA-SEM) which have not been widely used in ARD prediction or waste rock classification studies. The GMT approach is arranged in three-stages, with analytical sophistication increasing per stage, and the number of samples analysed decreasing. Samples selected for GMT analyses are arranged into mesotextural groups as defined following routine geological hand-specimen evaluations, FP-XRF analysis and if required mineral identification using SW-IR instrumentation (e.g., PIMA, TerraSpec).

Stage-one is proposed as a pre-screening stage, and comprises of simple, inexpensive tests, some of which can be performed in the field (e.g., paste pH and FP-XRF). A simple evaluation scheme termed the ARD Index (ARDI) is proposed as a stage-one test to evaluate texture. The ARDI assesses acid-forming sulphide minerals individually by five categories A-E, specifically chosen based on the direct influence on acid formation. Parameters A, B and C (ranked from 0 or 1 to 10) evaluates sulphide content, degree of alteration and morphology of the sulphide, with parameters D and E (ranked from -5 to 10) assessing the neutralising mineral content and the mineral associations of sulphides. High scores indicate acid formation, low indicates low or no acid forming potential and negative scores indicate an acid neutralising capacity. Scores from each category are totalled with values 50 to 41 classified as EAF; 40 to 31 as AF; 30 to 21 are PAF; 20 to 11 are non-acid forming NAF; 10 to 0 indicates a sample is either non-acid forming or has a potential neutralising capacity (PNC) and -1 to -10 indicates an acid neutralising capacity. Samples classified as NAF require no further GMT testing. All others are subjected to stage-two with the exception of those classified as having either a PNC or an ANC which require stage-two ANC testing only.

Stage-two uses routine geochemical tests to cross-check stage-one results and determine the actual acid forming or neutralising capacity of samples. Mesotextural groups identified as PAF by stage-two and AF/EAF by stage-one require stage-three testing. A carefully selected sub-set of samples is recommended for advanced NAG tests, and microtextural analyses to characterise microscale controls on acid formation as ultimately these dictate the acid forming nature of a sample (Diehl et al., 2007). Representative samples from mesotextural groups with high ANC values (by stage-two) and several carbonate minerals should be scheduled for ABCC testing to determine the effective ANC. All of these data should be tabulated (e.g., Table 2.17), and from this, samples from EAF/AF mesotextural groups can be selected for kinetic testing if required. Based on GMT testing, improved waste rock management plans can be developed as EAF/AF mesotextural groups are identified as separate entities and have unique sulphide mineralogy and textures and therefore, acid forming characteristics.

The GMT approach is practically evaluated using waste rock samples obtained from the abandoned Croydon mining operations in Chapter 3, and on drill core obtained from the operational Ernest Henry mine in Chapter 5. Applications of FP-XRF, μXRF and LA-ICP-MS are demonstrated in Chapter 3, and alternatives to ABCC tests using geometallurgical tools are shown in Chapter 5.

Chapter 3

Waste rock classification at the historic Croydon mine operations using the GMT approach

3.1 Introduction

Effective management of acid rock drainage (ARD) is a significant reclamation challenge for historic mine sites. At these sites, the exposure of sulphides to water, air and microorganisms, leads to oxidation and produces ARD (Evangelou and Zhang, 1995; Egiebor and Oni, 2007). Under these acidic conditions, liberation of dissolved components including heavy metals (e.g., Cd, Co, Cu, Ni, Pb and Zn) and metalloids (e.g., As, Sb) is promoted (Plumlee, 1999; Ashley et al., 2004). Once metals enter streams, complex pH and redox dependant processes (including transformation, speciation and complexation) influence the transport and fate of metals and determine their concentrations in both surface and subsurface environments (Caruso and Bishop, 2009). Subsequently, aquatic and terrestrial ecosystems downstream of mine works are at risk of significant environmental degradation (Gray, 1997; David, 2003; Hudson-Edwards and Edwards, 2005; Luis et al., 2009).

In Australia, there are many thousands of historic mines which range from isolated minor surface works, to large and complex sites (Franco et al., 2010). Features of these sites can include waste rock piles, tailings storage facilities, mineral processing wastes, and remains of mining infrastructure. Waste rock piles are significant sources of ARD (Harris et al., 2003; Aykol et al., 2003; Ashley et al., 2004; Lottermoser et al., 2005; Mudd, 2005; Smuda et al., 2007; Marescotti et al., 2008; Tarras-Wahlberg and Nguyen, 2008). Therefore, current mining practices dictate that waste rock piles are engineered based on geochemical classifications, with waste rock classes or types defined by acid forming/neutralising characteristics (Tran et al., 2003; Hutchison and Brett, 2006; Andrina et al., 2006; Brown et al., 2009, Smith et al., 2009). However, at historic mine sites, waste rock piles were not constructed in this manner (Lottermoser et al., 1999; Harris et al., 2003; Ashley et al., 2004, Hudson-Edwards and Edwards, 2005), with the costs of remediating associated ARD estimated at AUD$100,000 or more per hectare (Harris, 1997). Current rehabilitation strategies are reactive in nature, adopting a 'blanket approach' whereby techniques such as lime dosing and waste rock capping are commonly applied, with mixed success (Gore et al., 2007; Gasparon et al., 2007; Mudd and Patterson, 2010). Instead, undertaking improved waste material characterisation on an individual site basis may allow for the breakage of source-pathway-receptor chains (Vik et al., 2001), and improve rehabilitation long-term.

This chapter demonstrates the application of the GMT approach for waste material characterisation at the historic Croydon gold mines, north Queensland, Australia. The site geochemistry was examined

through analyses of waste rock and heap leach material, stream sediments and surface waters. The main objectives were: (1) to evaluate the GMT approach in terms of the selected techniques and their recommended application using materials from waste rock and heap leach piles; and (2) to demonstrate that through mesotextural classification, ARD sources can be readily identified and prioritised for remediation as part of an effective long-term rehabilitation plan.

3.2 Croydon mining area

3.2.1 Mining history

The Croydon gold mining district is located approximately 15km northeast of the Croydon township and 400km northeast of Mt. Isa, north Queensland (Figure 3.1). Small-scale historic mining of reef gold was undertaken in the 1880 to 1890s, and modern open pit mines targeted 2.84 Mt of ore (3.4 g/t Au) from 1981 to 1991. The mine workings and waste rock piles have remained undisturbed since 1991. Currently, the Queensland Government Department of Employment, Economic Development and Innovation (DEEDI) is in ownership of this site, with estimated rehabilitation liabilities of AUD $1.8 million for the waste rock piles alone (DME, 2008).

3.2.2 Physiography and climate

Tabletop Creek and Deadhorse Creek drain the Federation/La Perouse and Glencoe sites, respectively (Figure 3.1). Deadhorse Creek is a tributary of Tabletop Creek, with the confluence approximately 10km from the mining operations. Tabletop Creek is in turn a tributary of the Carron River, which flows into the Gulf of Carpentaria. The region has a tropical savannah type climate with an average annual rainfall of 750 mm, much of which falls between December to March. The average annual temperature is 33.8°C, with maximum temperatures experienced during November to January (Bureau of Meteorology, 2011).

Native vegetation differs between the Federation/La Perouse and Glencoe sites. In the vicinity of the Federation/La Perouse waste rock piles, the introduced species Calotrope (*Calotropis procera*) dominates (Cottier, 2011 pers. comm.). Around the waste rock piles at Glencoe, Lancewood (*Acacia shirleyi*) is observed on lateritic duricrusts, in addition to Quinine bush (*Petalostigma banksii*) and Shirley's silver leaf ironbark (*Eucalyptus Shirleyi*; Cottier, 2011 pers. comm.). Soil quality improves along the creeks, with Corymbia species dominating (e.g., Red flowering gum (*Corymbia ficifolia*), Snappy gum (*Eucalyptus brevifolia*), Georgetown box (*Eucalyptus microneura*) and Brown bloodwood (*Corymbia trachyphloia*)). Much of the Croydon district is used for grazing, including the immediate mine area (DME, 2008).

3.2.3 Geology and mineralisation

The geology of the Croydon district is dominated by the Mesoproterozoic rhyolitic Croydon Volcanic Group (CVG) and Esmerelda Supersuite (Figure 3.1). The Croydon lode gold deposits are hosted by the CVG, which is overlain by the clastic Gilbert River Formation. The lodes consist of major quartz, potassium feldspar, muscovite and plagioclase, minor illite, kaolinite, and sulphides (pyrite, arsenopyrite, sphalerite, galena), and traces of pyrrhotite and chalcopyrite (Van Eck and Child, 1990).

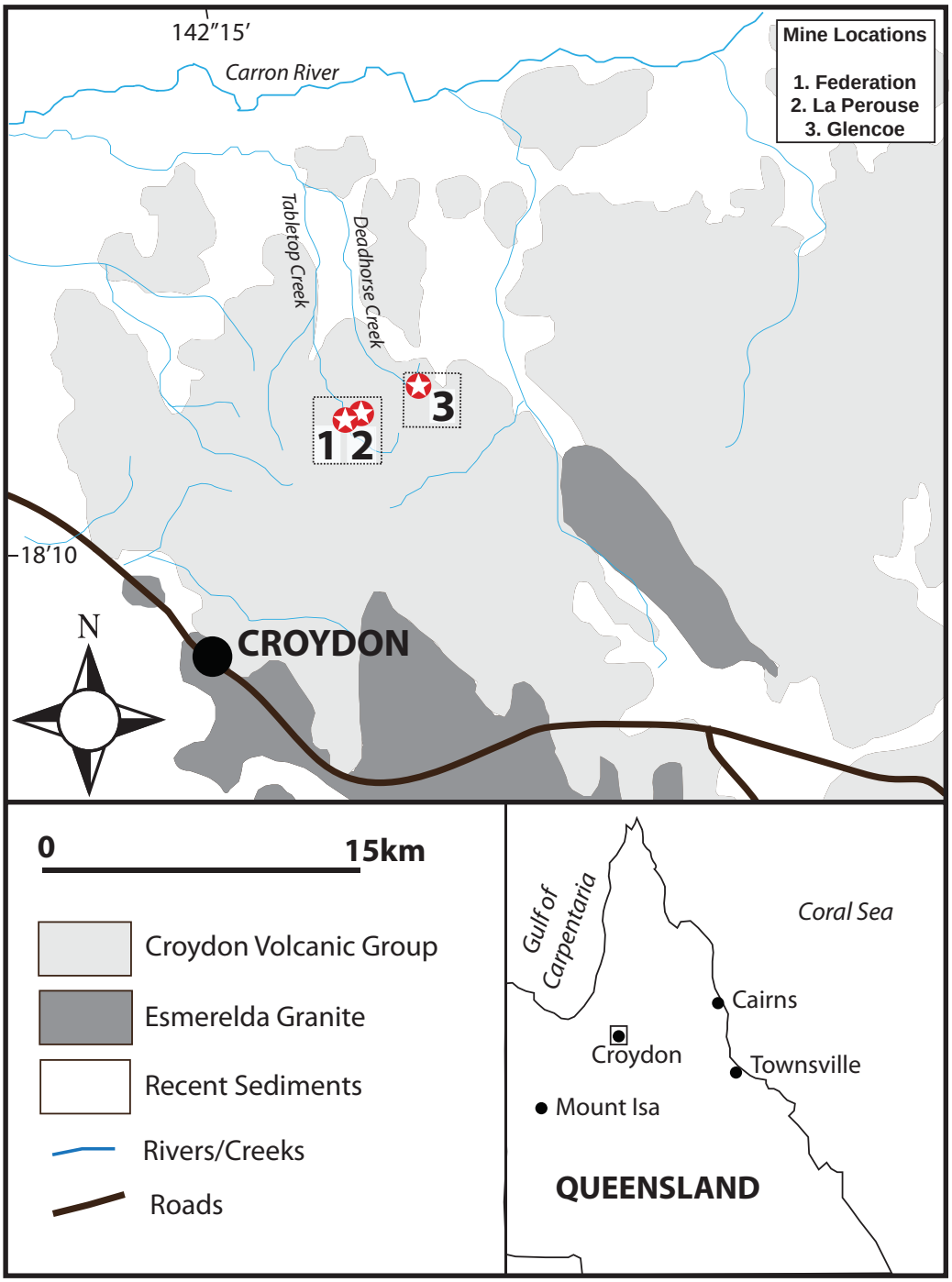

Figure 3.1 Simplified geology of the Croydon area showing locations of abandoned gold mine sites (after Bain et al., 1998).

The CVG has been subjected to varying degrees of hydrothermal alteration, with evidence of silicification, kaolinitisation and sericitisation observed in wall rock adjacent to the quartz veins (Van Eck and Child, 1990). In terms of acid forming potential, the host rocks to mineralisation have little potential for buffering acid produced from sulphide oxidation, as carbonates are notably absent. Effective silicate neutralising minerals (e.g., biotite, chlorite and serpentinite) as defined by Bowell et al. (2000) and Jambor et al. (2002) are also absent.

3.2.4 Site description

The Federation/La Perouse site consists of two pits (Federation: 320 m x 160 m x 35 m; and La Perouse: 270 m x 180 m x 40 m), an underground portal (La Perouse), two waste rock piles (Federation/La Perouse pile: 1.5 million m^3 (Figure 3.2a) and 35,000 m^3), one stockpile (25,000m^3), heap leach pads (55,000m^3; Figure 3.2b), a catch dam (170 m x 65 m; Figure 3.2c), and relict mining infrastructure including crushers and stamp heads. The waste rock piles comprise materials ranging from boulder (>0.5m diameter) through to coarse sand crushings (0.2-1 cm) and abundant fines (<0.2 cm). The entire waste rock piles comprise approximately 70% flow-banded rhyolite, 20% red-stained rhyolites and tuffs, and 10% quartz-sulphide vein material (DME, 2008). Most of this material displays dark to medium brownish-red Fe-staining, with metallic bluish black Mn-stains also observed (Figure 3.2d).

Federation pit captures runoff and seepage from the main Federation/La Perouse waste rock pile. A catch dam was constructed below Federation Pit for the purpose of containing seasonal overflow from the pit lake. However, during the wet season, water overflows from the catch dam into Tabletop Creek (Figure 3.2e). The catch dam is acidic with an average pH of 2.9 (DME, 2008). There is also continual seepage from the waste rock pile directly into Federation and Tabletop Creeks. Operations were smaller at Glencoe with one open pit (330 m x 60 m x 25 m; Figure 3.2f) and a waste rock pile (483,000m^3). Seepage from this waste rock pile enters Deadhorse Creek. Field observations indicate that galena and sphalerite dominate the sulphide mineralogy of this pile.

Acid rock drainage has been established immediately downstream (<2 km) of the mine workings, with elevated concentrations of Cd (max. 80 µg/l) and Zn (max. 8000 µg/l) relative to the local baseline measured within 10 km of the operations. In December 2002, dozens of cattle grazing in the vicinity of Tabletop Creek downstream of the Federation/La Perouse site had died possibly due to Cd poisoning (DME, 2008). Remedial works were undertaken in November 2007 to improve the water quality in Federation pit, through the addition of 140,000 t of lime (CaO) to raise pH. Lime was also sprayed on the pit walls and deposited on the surface of the Federation/La Perouse waste rock pile. Whilst initially pH values rose (pH 11to 12), within two months pH values had declined to pH 3 to 4 (DME, 2008). Therefore, future rehabilitation efforts need to focus on the identification and management of ARD sources rather than the treatment of ARD waters.

3.3 Materials and methods

3.3.1 Sampling and sample preparation

Field work was conducted in May 2008, with over 100 stream sediment, water and mine waste samples collected across the Croydon district (Figure 3.3). Waste rock analyses and results are discussed throughout this chapter, with stream sediment and water samples discussed in Chapter 4. Various estimates of the number of waste rock samples to obtain were calculated (Table 3.1) using strategies discussed in section 2.2.2. Whilst the BC taskforce was the preferred campaign, based on budget and time limitations, the sample numbers recommended by the Mills (1999) method were collected. Hand specimen sized waste rock samples (c.2 kg; n=52) were selected to provide a range of lithologies from four different locations

across the piles. Samples were sawn, with one piece kept for textural studies, and the other jaw crushed to <5 cm (CODES; UTAS). A split was taken, and the remaining material ground in a ring mill to <125 μm for mineralogical and geochemical characterisation.

Heap leach grab samples (n=14) were collected from the surface of the heap leach piles, and consisted of approximately 2 kg of gravel size (average diameter ~1 cm) angular to sub-angular weathered clasts. Half of this material was milled to <125 μm for geochemical and mineralogical analyses. Five samples were selected for detailed mineralogical (XRD) and textural characterisation. Results from these analyses are presented in Appendix 3.1.

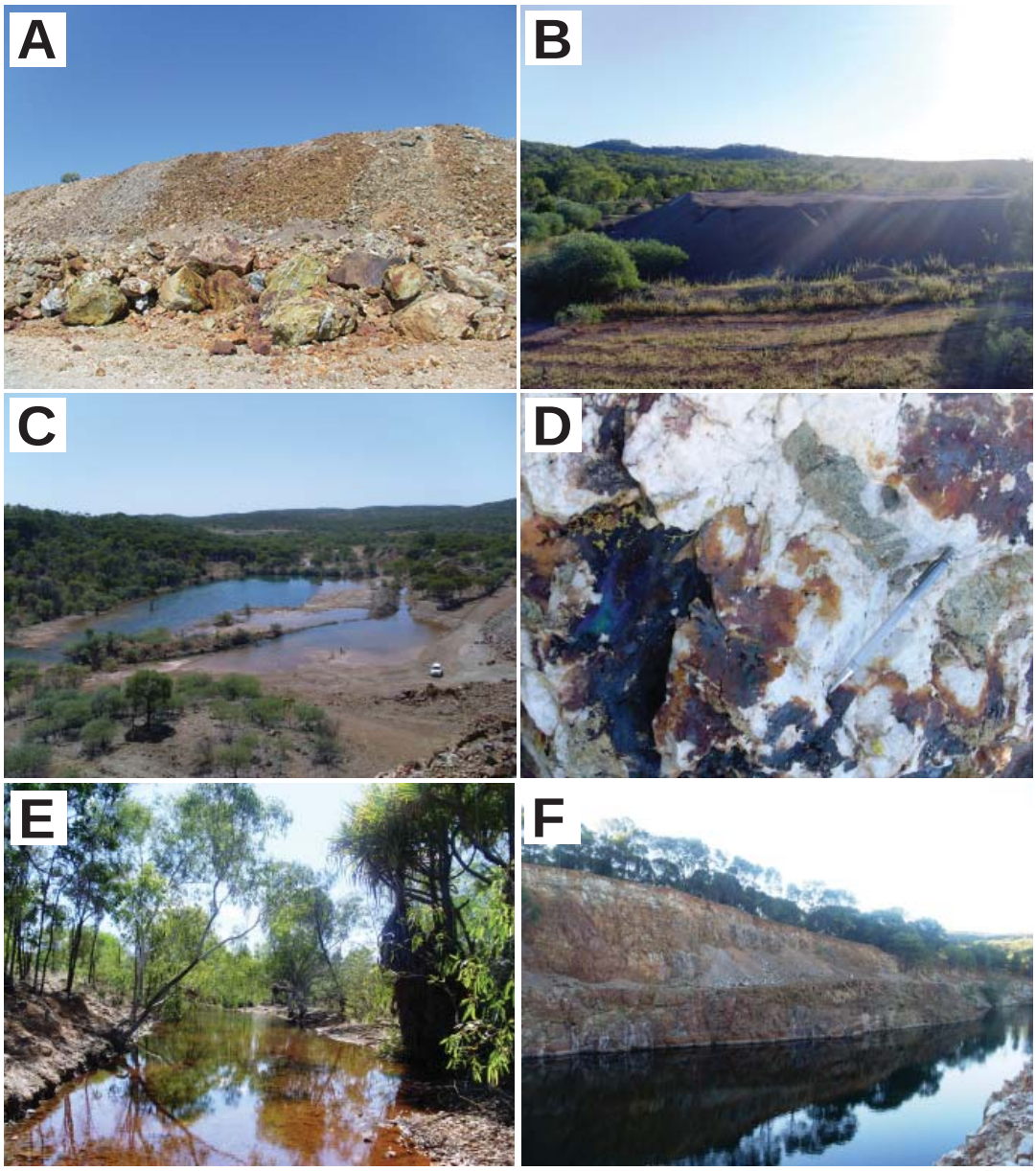

Figure 3.2 Site photographs of the historic Croydon Au-operations: **(A)** Federation/La Perouse waste rock pile (height- 20m); **(B)** Heap leach pads, La Perouse/Federation site; **(C)** Catch dam located adjacent to the Federation pit lake; **(D)** Sulphide mine waste observed in the Federation/ La Perouse waste rock pile with Fe-oxide, and metallic blue-black staining observed; **(E)**Tabletop Creek c.5km downstream of the La Perouse/Federation site; and **(F)** Glencoe pit lake.

Table 3.1 Estimated sample numbers to obtain from each pile based on recommendations suggested in the literature, and actual number obtained.

Pile	Volume (m^3)	USDA (1992)	USEPA (1994)	BC Taskforce	Mills et al. (2011)	Actual number collected
La Perouse & Federation (C2 & C3)	1.5 million m^3	~200	~ 4 min 12 max.	~100	~25	26
Glencoe (CG)	500,000	65	~ 1 min. 12 max.	~33	10	10
Low grade ore (C3)	25,000	~4	~ 1 min. 12 max.	~2	<1	16

3.3.2 Waste rock analyses

3.3.2.1 Mesotextural classification

Previously, only three lithological groups were identified in these waste rock piles (flow-banded rhyolite, red-stained rhyolites and tuffs, and quartz-sulphides; DME, 2008). However, when considering the styles of mineralisation and alteration, it is likely that additional groups exist. Therefore, a mesotextural classification method was developed as a means of identifying the major waste rock lithologies, and measuring their acid forming characteristics. Polished slices were prepared from each waste rock sample to facilitate the identification of primary and alteration minerals and textures, using a handlens and binocular microscope. Lithologies were described, with attention given to the texture (e.g., porphyritic, flow-banded), and estimating the modal mineralogy. As the groundmass of rhyolite samples was fine-grained, short-wave infrared spectroscopy was applied to determine the alteration mineralogy. Both a PIMA and a TerraSpec ASD spectroradiometer were used. Analyses were performed on 1 to 3 areas across the rock surface. Computer assigned mineral identification, using TSG Professional Version 7.01.062 (September 2010), was manually checked against a library of spectra and either accepted, re-interpreted or rejected. Based on the mineralogical and textural differences observed in hand-specimen, samples were categorised into mesotextural groups.

One polished slice from each mesotextural group was evaluated by the Acid Rock Drainage Index (ARDI), whereby textural parameters known to influence acid formation were examined as explained in Chapter 2. Final ARDI values were used alongside static geochemical data to enhance waste classification as proposed in Chapter 2.

3.3.2.2 Geochemical and mineralogical analyses

Geochemical and mineralogical analyses followed stage-one and stage-two of the GMT approach as outlined in Chapter 2. Whilst this recommends that at least one sample per mesotextural group is subjected to whole-rock XRF geochemical analyses, in order to evaluate FP-XRF data, all samples were analysed. The bulk elemental composition (major: Al_2O_3, CaO, Fe_2O_3, K_2O, MgO, MnO, Na_2O, P_2O_5, PbO, SiO_2, TiO_2; trace: Ag, As, Bi, Cd, Cu, Ni, Pb, S, Sb, Zn, Zr) of waste rock samples was assessed by X-ray fluorescence (XRF; Philips PW1480 X-Ray spectrometer; CODES, UTAS). The bulk elemental composition of the same pressed waste rock pellets was analysed by FP-XRF operating in soil mode (As, Ag, Ba, Bi, Ca, Cd, Cl, Cu, Cr, Fe, Hg, I, K, Mo, Mn, Ni, Pb, Rb, S, Sb, Se, Sn, Sr, Ti, U, V, W, Zn,

Zr; Innov-X X50). Three areas were analysed per sample (30 seconds per analysis), with the instrument calibrated using the standard provided by the manufacturer after every 10th analysis. One sample from each mesotextural group were analysed for their mineralogical composition by semi-quantitative XRD (Siemens D501 diffractometer, University of Ballarat, Australia).

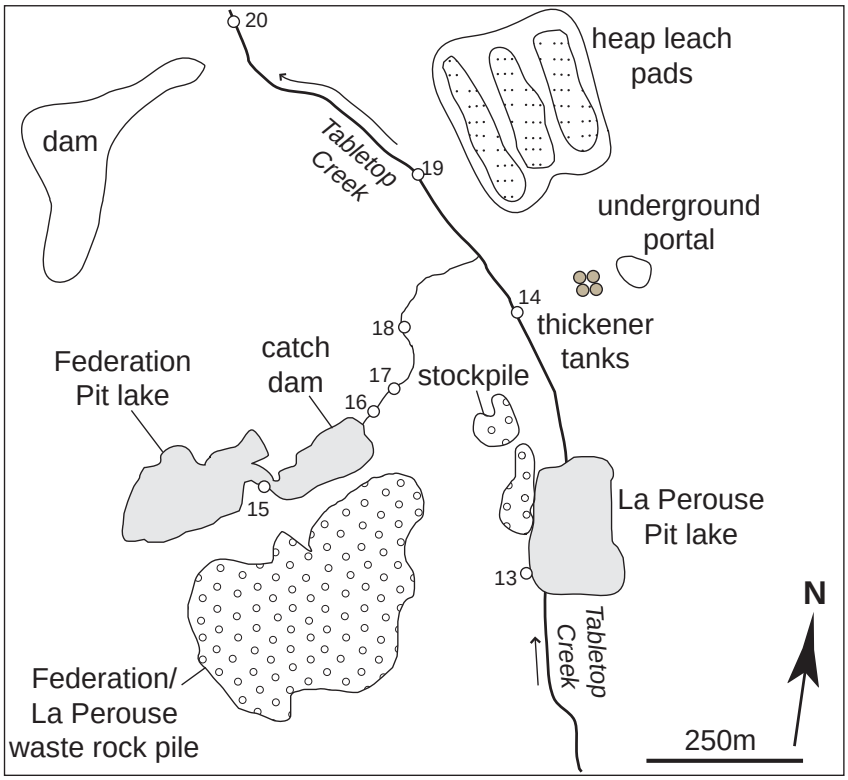

Figure 3.3 Plan view of Federation/La Perouse site showing the location of the waste rock piles and pit lakes. Stream sediment and water locations numbers (13 to 20) are also shown (data from these samples are presented in Chapter 4).

Paste pH tests were performed on all samples following the method given in Smart et al. (2002), whereby uncovered reaction vessels containing 1:2 parts solid (<75 μm size) to water were left to stand overnight (c.14 hours) at a room temperature (c.18 to 21°C). The pH was measured in duplicate, with the anode calibrated to pH 4 and 7 after every sample. Sample blanks (deionised water) were tested before and at the end of each sample batch, and every tenth sample was tested in triplicate. In addition, the pH of coarse and fine crushed samples was measured following the Smart et al. (2002) method (also termed paste pH for consistency). The objective was to identify difference in pH values for different particle sizes in order to determine application of paste pH as a field-based pre-screening test. Approximately 25 g of material was dry sieved (<20 mm) to represent coarse crush material. Another 25 g of material was crushed in a pestle and mortar and sieved (<5 mm) to produce a fine crush size fraction. BET analyses were not (i.e., to measure surface area), as this is not possible to perform in the field. These tests were performed on the C3 and CG sample suites only as the initial site reconnaisance survey indicated they contained the most acid forming samples. Sobek, Modified Sobek and single addition NAG tests were performed on all waste rock samples following procedures given in White et al. (1999) and Smart et al. (2002) (CODES, UTAS; University of Queensland (UQ), Australia). Multi-addition NAG and sequential NAG tests were performed on select samples following methods given in Stewart (2004; CODES, UTAS). Eight sulphide-bearing samples were sent to ALS, Brisbane for kinetic NAG testing.

3.3.3 Sulphide analyses

Samples from mesotextural groups C (porphyritic rhyolite with sulphide bearing quartz veinlets), E (flow-banded rhyolite containing disseminated sulphide), G (semi-massive sulphide containing quartz-galena-sphalerite), H (massive sulphide containing quartz-arsenopyrite-pyrite) and J (massive sulphide containing quartz-pyrite) were selected for microtextural analysis (FEI Quanta 600 environmental scanning electron microscope (ESEM); CSL, UTAS). In this analysis, the relationship between primary sulphides and secondary minerals (e.g., scorodite, anglesite, rhomboclase as identified by XRD), were examined. Additionally, inhomogeneties, which may influence trace element distribution (e.g., compositional zoning or mineral inclusions), were observed.

The cadmium and iron concentrations in sphalerite grains (n=4) from mesotextural group G were measured using electron probe microanalysis (EPMA; Cameca SX100 electron microprobe, CSL, UTAS; 20 keV accelerating voltage, 15 nA beam current and a 2 μm beam diameter). Element mapping analysis was performed on these samples using micro-XRF (μXRF; Horiba XGT 7000, CSL, UTAS; 50 keV accelerating voltage, 1 mA beam current, 100μm XGT, 10 μm beam diameter). Measurement of beamlines K and L allowed for detection of elements with atomic numbers between 11 and 92, with detection limits varying according to the element and sample matrix. The μXRF maps contained 256 x 256 pixels (with a 40 μm pixel width). Additionally, element mapping and trace element quantification were performed on samples from groups G, H and J (n=10) using laser ablation inductively coupled mass spectrometry (LA-ICP-MS; Agilent HP4500 Quadripole ICPMS, UTAS, Australia; 15, 20 or 30 μm spot size, 10 Hz, frequency 5 or 10).

Following on from ARDI evaluations, polished tiles (3cm x 3cm) from groups A, C, E, G, H and J were subject to XBSE mineral mapping to examine sulphide mineral associations (FEI Quanta 600 mineral liberation analyser scanning electron microscope (MLA-SEM), CSL, UTAS). Additional laser mounts from groups G and J were analysed using the sparse-phase liberation (SPL_Lite) technique as described in Gu (2003) and Fandrich et al. (2007). Data were processed in MLA Image View to produce classified images for each sample based on a site-specific mineral library. Classified images were interpreted using Texture Viewer (Nguyen, 2009).

3.3.4 Quality Assurance/Quality Control

The quality assurance/quality control (QA/QC) programme focussed on assessing the reliability of analyses using replicate samples, cross-laboratory checks and reference standards to calculate analytical precision and accuracy. Certified reference materials KZK-1 and NBM-1 were analysed during Sobek and modified Sobek tests to determine analytical precision, with the relative standard deviation from certified values calculated as <5 % (Appendix 3.2). To determine accuracy, at least two duplicate samples were analysed in each run of static tests (paste pH, Sobek, modified Sobek, NAG and advanced NAG tests), with selected samples sent for external analyses at a NATA accredited laboratory (Australian Laboratory Services, Brisbane). The relative standard deviation between these data was also <5 %.

3.4 Results

3.4.1 Waste rock mesotextural groups

Ten mesotextural groups were identified (A to J), with one representative sample from each group shown in Figure 3.4. Group A is a mid-grey muscovite altered porphyritic rhyolite dominated by quartz phenocrysts (Figure 3.4a). Several generations of quartz veins (some of which display iron oxide staining) are observed, however only the larger quartz veins (>2 cm diameter) contain disseminated pyrite. The matrix is dominated by fine-grained quartz and muscovite. Group B is a grey-white flow-banded rhyolite-tuff containing both quartz and muscovite altered potassium feldspar phenocrysts. Additionally, fiamme and graphite clots are observed (Figure 3.4b). Group C is a light-grey porphyritic rhyolite, but differs to group A in colour, degree of weathering, and contains fewer quartz veins. Disseminated pyrite was observed within the sub-cm diameter quartz veinlets (Figure 3.4c). Group D is an intensely weathered grey-white flow-banded rhyolite with quartz veinlets cross-cutting the primary fabric. Alteration of potassium feldspar phenocrysts is frequently observed (Figure 3.4d). Group E is yellow-grey and porphyritic, but also has a weak flow-banded fabric. Both quartz and muscovite altered phenocrysts are observed, and disseminated pyrite is identified in the fine-grained quartz-potassium feldspar-muscovite groundmass (Figure 3.4e). Group F displays a porphyritic texture, and contains abundant potassium feldspar in the groundmass as indicated by the overall pink coloration (Figure 3.4f). Phenocrysts are dominated by rounded to sub-rounded quartz. Waste rock containing quartz-sphalerite-galena and minor pyrite is classified as group G. Galena and sphalerite are present as individual minerals and intergrown, with some weathered sulphides also observed (Figure 3.4g). Massive arsenopyrite-pyrite-quartz is identified as group H. Arsenopyrite is highly fractured, however, the fracture-fill secondary mineral is not readily identifiable by routine microscopy (Figure 3.4h). Group I is blue-grey, intensely weathered silicified porphyritic rhyolite with fractured quartz and altered potassium feldspar phenocrysts (Figure 3.4i). Semi-massive quartz-pyrite constitutes group J. Pyrite is observed in a variety of forms including larger euhedral grains, inclusion rich grains and small aggregate grains (Figure 3.4j).

Starred areas shown on Figure 3.4 were subjected to PIMA and TerraSpec analyses to determine alteration mineralogy. Muscovite is confirmed as the dominant alteration mineral in all rhyolite groups (as indicated in Figure 3.4). Comparisons of PIMA and TerraSpec results were undertaken, with examples from groups A and D shown in Figure 3.5. Spectra collected by Terra Spec (Figure 3.5b and d) were better defined (i.e., less noise) and show better agreement with the reference spectra. Results from PIMA showed greater deviation from the reference spectra for group A (Figure 3.5a), and were aspectral from group D (Figure 3.5b). Based on these results, the TerraSpec is the preferred instrument. Additionally, TerraSpec is not restricted to analysis of pale-coloured minerals like PIMA and can detect a greater range of minerals including iron-oxyhydroxides.

3.4.2 Stage-one results

3.4.2.1 Geochemical characterisation

Waste rock materials were chemically and mineralogically similar within each group, with summary statistics of major and trace element contents shown in Table 3.2. Quartz dominated in all groups (55.6

to 86.9 wt. %) except in group H, where Fe_2O_3 dominated (36 wt. %). Concentrations of CaO and MnO (not shown) were below 0.2 wt. % in all groups. Low concentrations (<8.6 wt. %) of K_2O were also measured. In order to deduce the degree of alteration per group, the feldspar-biotite model ((2Ca + Na + K)/Zr vs Al/Zr) of Downing and Madeisky (1997) was constructed (Figure 3.6). Group I was the least altered, as it plotted above the unaltered feldspar line. All other groups were altered, and plotted below the model line which infers no significant buffering potential. The model indicates that groups G, H and J have undergone extreme acid leaching with several samples plotting along the X-axis (Downing and Madeisky, 1997). Vuggy quartz-sulphide textures were observed in waste rock material providing field evidence for such leaching.

Major (i.e., >1 wt. % or 10,000 ppm) mean concentrations of As were present in mesotextural groups H and J only, with minor mean concentrations (i.e. >100 ppm) detected in groups A, B, C, D and F (Table 3.2). All groups except I contained minor mean concentrations of Pb. Mesotextural groups E, G, H, I, and J contained minor mean Zn concentrations. Mean concentrations of Bi, Cu, Cd, Ni and Sb were below <100 ppm for all groups. Concentrations of As, Cd, Cu, Pb and Zn (ppm) were plotted against sulphur (wt. %) per mesotextural group (Figure 3.7) to indicate the mineralogical sources of these elements. Mesotextural groups A-F and I contained low concentrations of As, Cd, Cu, Pb, S and Zn. Arsenic and S show strong positive correlation in groups J and H (Figure 3.7a). Cadmium, and Zn are greatest in group G and broadly correlation with S concentration (Figure 3.7b and 3.7e). However, Zn concentrations were relatively low (i.e., <1000 ppm) for the majority of samples in groups H and J (Figure 3.7e). Copper directly correlates with S in groups G, H and J (Figure 3.7c). Lead measured the highest (i.e., >10,000 ppm) in samples from groups G and J (Figure 3.7d). Based on these relationships, sulphides are considered the likely primary sources of these elements in these groups.

3.4.2.2 XRF versus FP-XRF

Comparisons of element concentrations (As, Cd, Cu, Pb, Sb and Zn) measured by XRF and FP-XRF are shown in Figure 3.8. The majority of groups plot on the model line for As (Figure 3.8a). However, significant deviation is seen for five samples (groups B, C, E and F), with significantly lower FP-XRF values measured. Despite this, strong correlation (R^2=0.98) was observed. These anomalies originate from samples with differing mineralogy (i.e., not from the same group), this is unlikely to be the control on the measurement error. Additionally, this error is not observed for other elements (Figure 3.8b-f), thus these anomalies likely represent an instrumental, not an operator error. As low Cd values were measured by both techniques, an evaluation of the correlation between the two datasets is limited (Figure 3.8b). Some deviation from the model line was observed for Cd bearing samples from groups J and H, but overall for the whole data set showed strong correlation (R^2=0.99). Correlation for copper concentrations for the whole data set was also strong (R^2=0.96; Figure 3.8c). However, like with Cd, some deviation was observed for sulphide bearing samples from groups G, H and J. This deviation is non systematic i.e., one technique did not consistently return a greater or lower value than the other. The strongest correlation was observed for Pb (Figure 3.8d) with R^2=0.99 for all groups. The majority of samples contained low Sb (Figure 3.8e). However, where detected, XRF values were generally greater than FP-XRF, (R^2=0.94). Strong correlation was also observed for Zn (R^2=0.99; Figure 3.8f), with only slight deviation from the

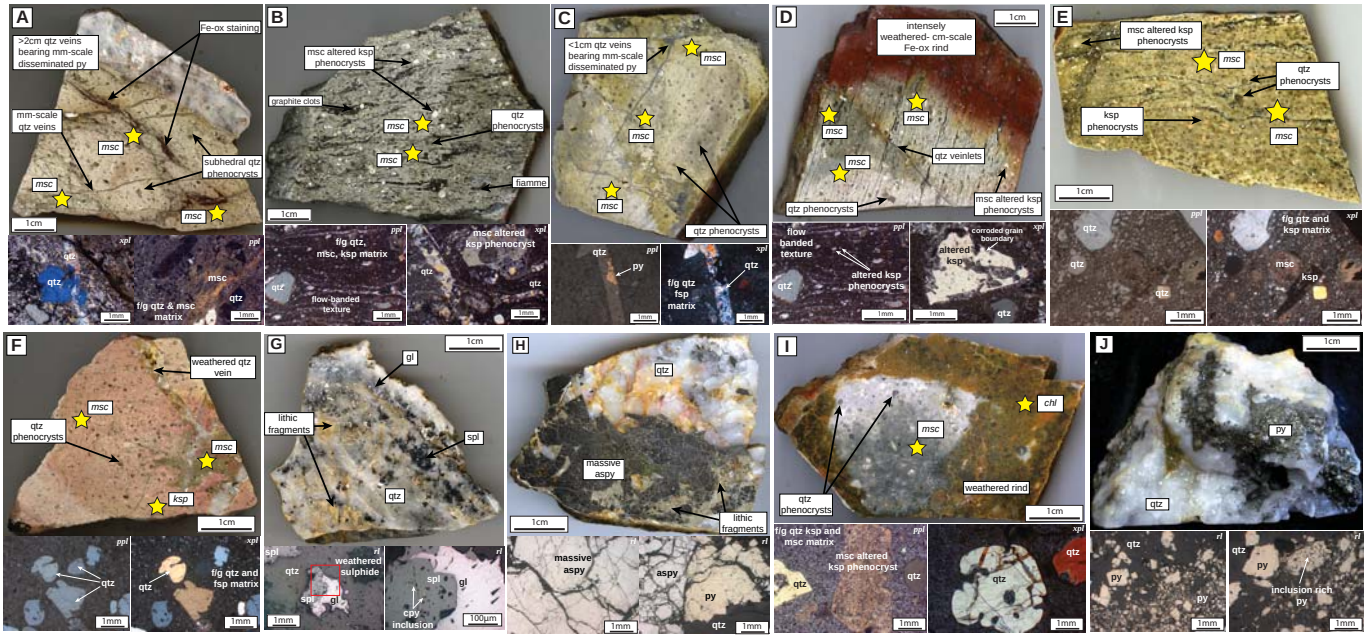

Figure 3.4 Representative mesotextures (A-J) of the ten main lithologies observed at the Federation/La Perouse and Glencoe waste rock piles: **(A)** Porphyritic rhyolite with pyrite bearing quartz veins; **(B)** Flow-banded rhyolite with quartz and muscovite phenocrysts and graphite clots; **(C)** Porphyritic rhyolite with pyrite bearing quartz veinlets; **(D)** Intensely weathered flow-banded rhyolite; **(E)** Porphyritic rhyolite with a weak flow-banded fabric and disseminated pyrite in the groundmass; **(F)** Porphyritic rhyolite with quartz phenocrysts; **(G)** Quartz- galena-sphalerite with minor pyrite; **(H)** Massive arsenopyrite-pyrite-quartz; **(I)** Intensely weathered porphyritic rhyolite; and **(J)** Quartz-pyrite. Abbreviations: aspy, arsenopyrite; Fe-ox, iron oxide; gl, galena; ksp, potassium feldspar; msc, muscovite; py, pyrite; qtz, quartz; spl, sphalerite; f/g, fine-grained; ppl, plane polarised light; rl, reflected light; xpl, cross polarised light. Yellow stars indicate PIMA and TerraSpec analysed areas.

THIS PAGE IS INTENTIONALLY BLANK

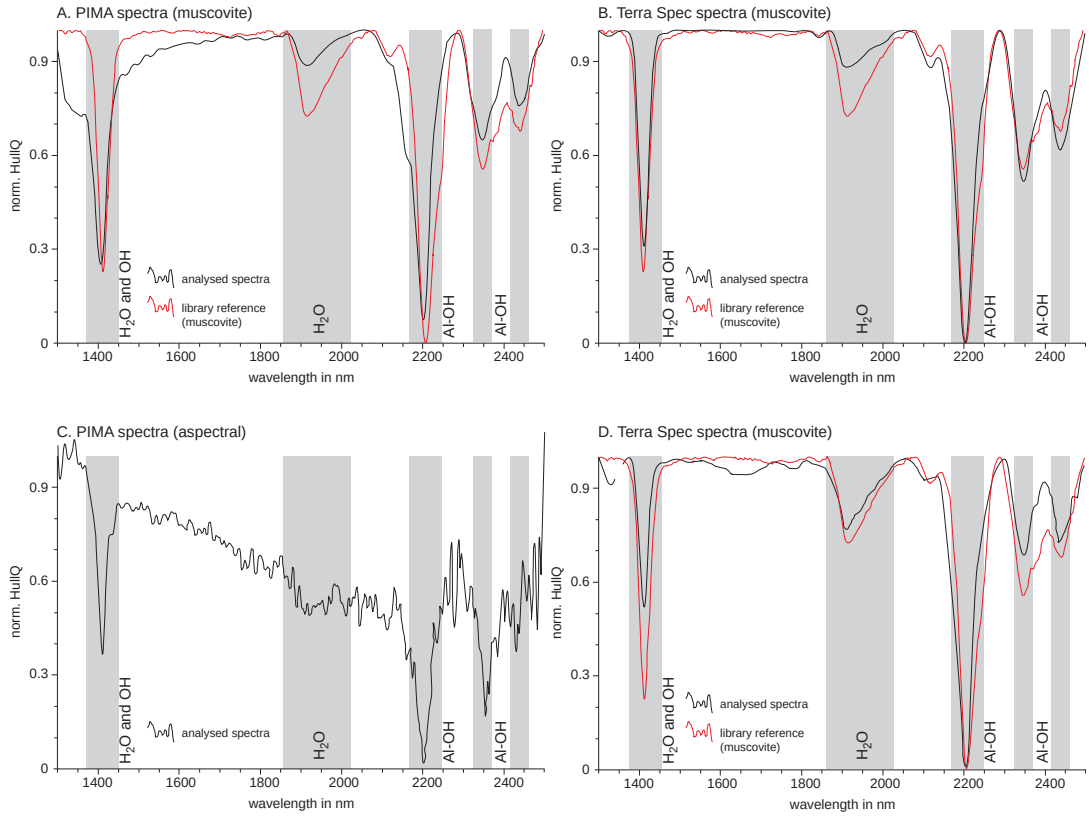

Figure 3.5 Example of alteration mineral identification in Croyon waste rock samples: **(A)** Group A analysed on a PIMA with muscovite identified; **(B)** Group A analysed on a TerraSpec with muscovite identified confidentally; **(C)** Group D analysed on a PIMA with an aspectral result; and **(D)** group D analysed on a TerraSpec with muscovite identified confidentally.

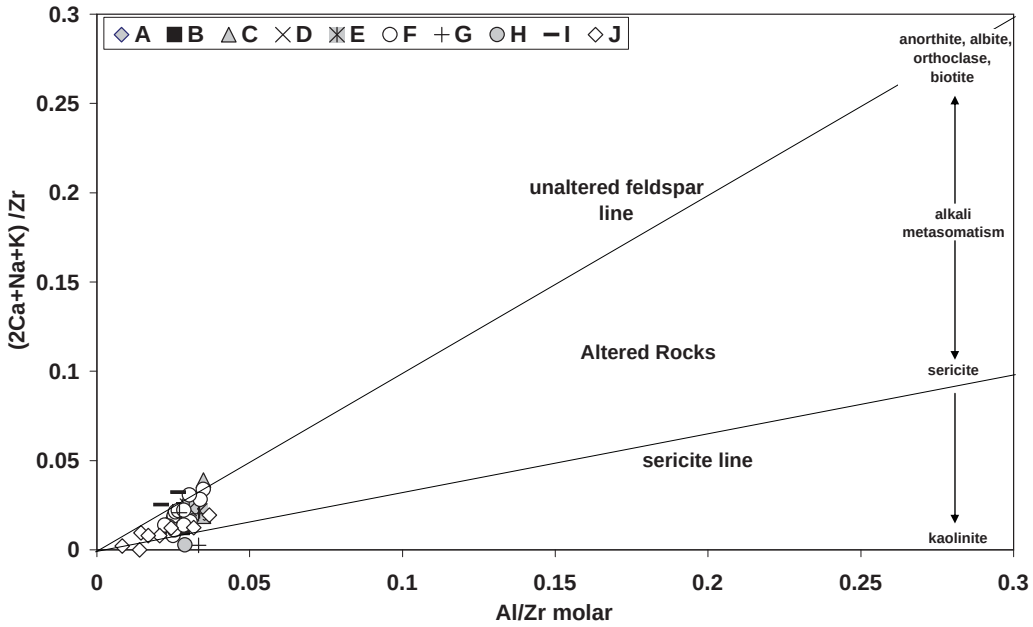

Figure 3.6 Croydon waste rock alteration type classification using the feldspar-biotite model of Downing and Madeisky (1997). Samples are shown in mesotextural groups (groups A to J; n= 52).

Table 3.2 Major and trace element chemistry of the the Croydon waste rock samples, grouped according to mesotextures A to J. Values for major elements (SiO_2 to S) are given in wt. % and trace elements (Ag to Zn) are given in ppm. Abbreviations: BDL, below detection limit.

Group		SiO_2	TiO_2	Al_2O_3	Fe_2O_3	MgO	CaO	Na_2O	K_2O	S	Ag	As	Bi	Cd	Cu	Ni	Pb	Sb	Zn
A	Max.	79.6	0.3	13.1	2.3	0.2	BDL	0.1	4.5	0.3	6	939	BDL	BDL	70	3	3000	13	56
	Min.	76.9	0.2	11.4	1.8	0.2	BDL	0.1	3.5	0	0	200	BDL	BDL	12	2	584	2	31
	Median	78.3	0.25	12.3	2.1	0.2	BDL	0.1	4	0.2	3	570	BDL	BDL	41	3	1792	8	44
	Mean	78.3	0.25	12.3	2.1	0.2	BDL	0.1	4	0.2	3	570	BDL	BDL	41	3	1792	8	44
B	Max.	80.3	0.3	13.2	6.1	0.2	BDL	0.1	6.2	0.1	BDL	1548	BDL	2	64	4	443	9	28
	Min.	76.7	0.2	7.7	0.7	0.1	BDL	0.1	2.2	0.1	BDL	11	BDL	2	11	3	105	3	25
	Median	77.2	0.3	12.9	1.3	0.1	BDL	0.1	5.8	0.1	BDL	15	BDL	2	15	4	161	6	27
	Mean	77.9	0.2	11.7	2.3	0.1	BDL	0.1	5	0.1	BDL	397	BDL	2	26	4	217.5	6	27
C	Max.	85	0.3	15.2	2.1	0.2	BDL	0.1	8.6	0.8	4	2100	15	4	18	5	1509	13	216
	Min.	71.4	0.1	8.3	1	0.1	BDL	0.1	2.8	0.1	4	5	15	1	3	2	77	2	15
	Median	78.1	0.3	12.2	1.3	0.2	BDL	0.1	5.6	0.2	4	70	15	2	7	4	397	3	77
	Mean	77.9	0.2	12.3	1.4	0.2	BDL	0.1	5.4	0.3	4	257	15	2	9	4	603	4	84
D	Max.	76.6	0.3	12.1	4.7	0.1	BDL	0.1	6.3	BDL	BDL	235	BDL	1	31	4	501	2	40
	Min.	76.3	0.2	11.7	2.4	0.1	BDL	0.1	3.8	BDL	BDL	22	BDL	1	18	2	471	2	22
	Median	76.5	0.25	11.9	3.6	0.1	BDL	0.1	5.05	BDL	BDL	128	BDL	1	25	3	486	2	31
	Mean	76.5	0.2	11.9	3.5	0.1	BDL	0.1	5	BDL	BDL	128.5	BDL	1	25	3	486	2	31
E	Max.	78.4	0.3	13.7	2	0.2	BDL	0.1	6.1	0.5	BDL	21	BDL	2	20	5	658	5	212
	Min.	76.3	0.2	12.1	1.4	0.2	BDL	0.1	4.9	0.3	BDL	7	BDL	2	6	3	74	3	31
	Median	76.6	0.2	13.1	1.6	0.2	BDL	0.1	5.5	0.4	BDL	14	BDL	2	13	5	103	4	114
	Mean	76.6	0.2	13.3	1.6	0.2	BDL	0.1	5.5	0.4	BDL	15	BDL	2	13	4.4	212	4	102

Group		SiO_2	TiO_2	Al_2O_3	Fe_2O_3	MgO	CaO	Na_2O	K_2O	S	Ag	As	Bi	Cd	Cu	Ni	Pb	Sb	Zn
F	Max.	80.4	0.3	14.5	1.8	0.3	0.1	0.2	6.5	0.2	3	600	5	1	48	4	999	189	66
	Min.	74.9	0.2	11.2	0.5	0.1	0.1	0.1	2.9	0.1	3	11	5	1	3	2	37	2	16
	Median	77.1	0.3	13.3	1.1	0.1	0.1	0.1	5.4	0.2	3	29	5	1	9	2	181	3	24
	Mean	77.4	0.3	13	1.1	0.1	0.1	0.1	5.1	0.1	3	129	5	1	13	3	254	20	29
G	Max.	85.2	0.3	13.1	27	0.2	BDL	0.2	6.4	3.2	35	628	21	144	105	13	33700	92	36300
	Min.	69.7	0.3	0.2	1.4	0.1	BDL	0.1	0.5	0.4	35	108	21	2	40	3	104	6	270
	Median	74.3	0.3	1.7	2.2	0.2	BDL	0.2	3.5	1.1	35	526	21	12	54	4	6200	24	609
	Mean	76.4	0.3	5	10.2	0.1	BDL	0.2	3.4	1.6	35	421	21	53	66	7	13335	41	12393
H		21.4	BDL	0.5	36	BDL	BDL	BDL	BDL	14.5	N/A	260500	N/A	BDL	387	20	408	45	795
I	Max.	75.3	0.3	13	3	0.3	0.2	2.2	5.8	BDL	BDL	79	BDL	1	27	9	82	3	407
	Min.	73.7	0.3	12.3	2.8	0.1	0.1	1.4	5.6	BDL	BDL	7	BDL	1	11	8	43	3	224
	Median	74.5	0.3	12.7	2.9	0.2	0.2	1.8	5.7	BDL	BDL	43	BDL	1	19	9	63	3	316
	Mean	74.5	0.3	12.7	2.9	0.2	0.2	1.8	5.7	BDL	BDL	43	BDL	1	19	9	63	3	316
J	Max.	86.9	0.1	3.9	21.6	BDL	BDL	BDL	1.4	17.4	117	107200	141	46	805	46	33800	202	16800
	Min.	55.6	0.1	0.1	4.9	BDL	BDL	BDL	0	3.8	5	73	2	2	33	3	320	3	10
	Median	76.8	0.1	0.5	10.7	BDL	BDL	BDL	0.3	8.2	29.5	1500	4	2	71	10	1022	15	109
	Mean	74.7	0.1	1.2	13	BDL	BDL	BDL	0.5	9.8	40	16890	27	16	174	14	6301	35	2398

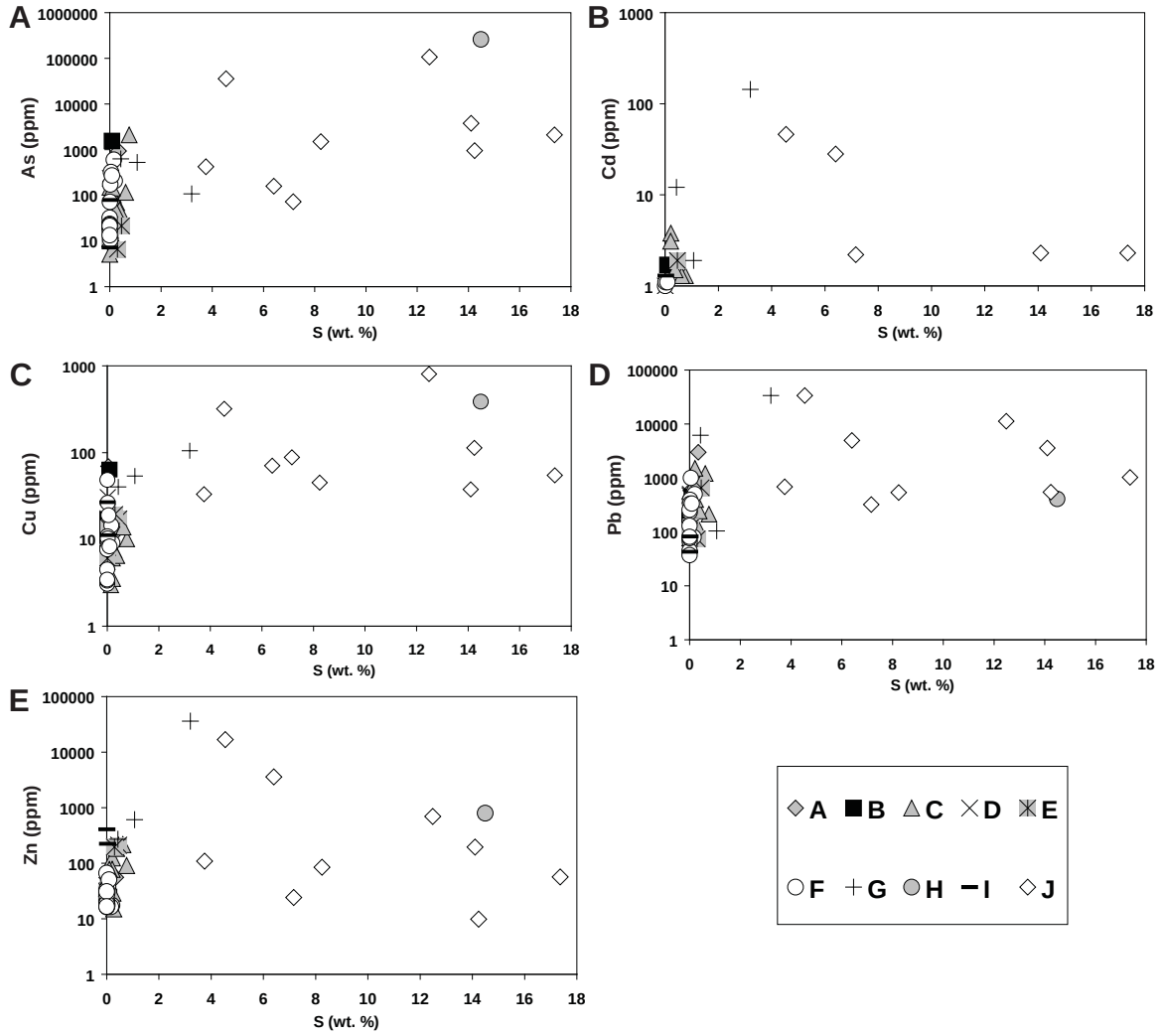

Figure 3.7 Concentations in ppm of As **(A)**, Cd **(B)**, Cu **(C)**, Pb **(D)**; and Zn **(E)** plotted against S contents (wt. %) as measured by XRF for Croydon waste rock samples as grouped by mesotexture (A to J; n=52).

model line observed for two group J samples which contained the greatest Zn concentrations, with FP-XRF returning higher values. These results indicate that FP-XRF is an appropriate screening technique for obtaining concentrations of common potentially deleterious elements (i.e., As, Cu, Pb and Zn) in altered rhyolite and quartz-sulphide lithologies.

3.4.2.3 S_{Total} measurement

Measurement of S_{Total} was performed on all samples using three different techniques (XRF, FP-XRF and EA) with results shown in Figure 3.9. S_{Total} values measured by FP-XRF consistently returned the highest results, particularly for mesotextural groups G, H and J. Data returned by FP-XRF is therefore considered to have overestimated $S_{Total.}$ Both XRF and EA are well established techniques which utilise appropriate standards. Consequently, measurements made by XRF and EA showed very strong correlation (R^2= 0.99). Based on XRF and EA data only, the highest S_{Total} values were measured in groups H and J, followed by G. One sample in group A contained high S_{Total} (3.7 wt. %), due to containment of disseminated pyrite in quartz veins. The remainder of samples have low (<0.7 wt. %) S_{Total} contents. Based on this, EA has demonstrated its application as a low-cost method to measure S_{Total} and calculate MPA, as for

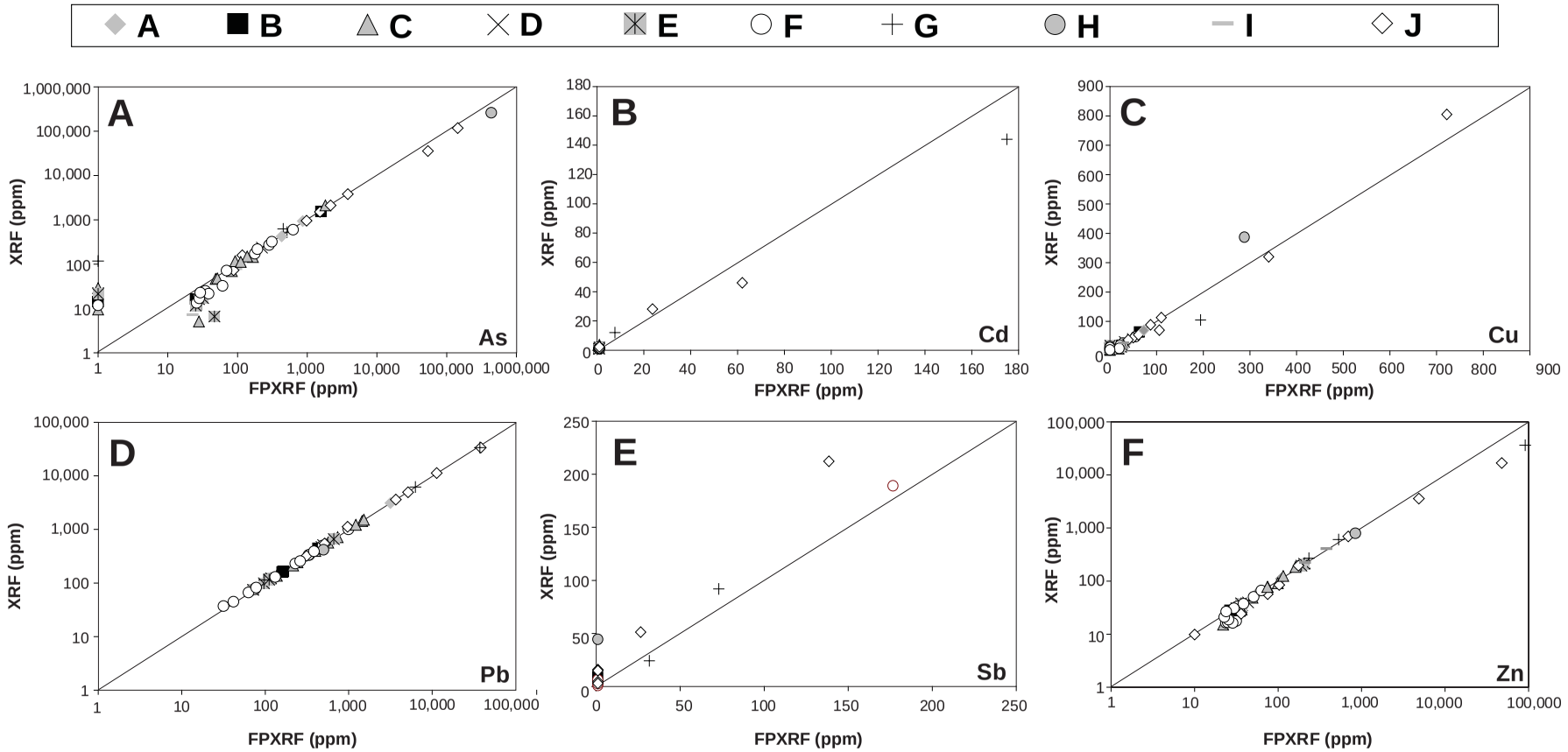

Figure 3.8 Concentrations (ppm) of selected elements: As **(A)**; Cd **(B)**; Cu **(C)**; Pb **(D)**; Sb **(E)**; and Zn **(F)** measured in Croydon waste rock samples as grouped by mesotexture (A to J) by Field Portable XRF (FP-XRF) and XRF techniques.

different lithologies, results closely approximate those of XRF. FP-XRF should only be utilised to provide an indication of relative sulphur contents, and not to obtain values from which to classify waste rock at stage-one, or to calculate MPA.

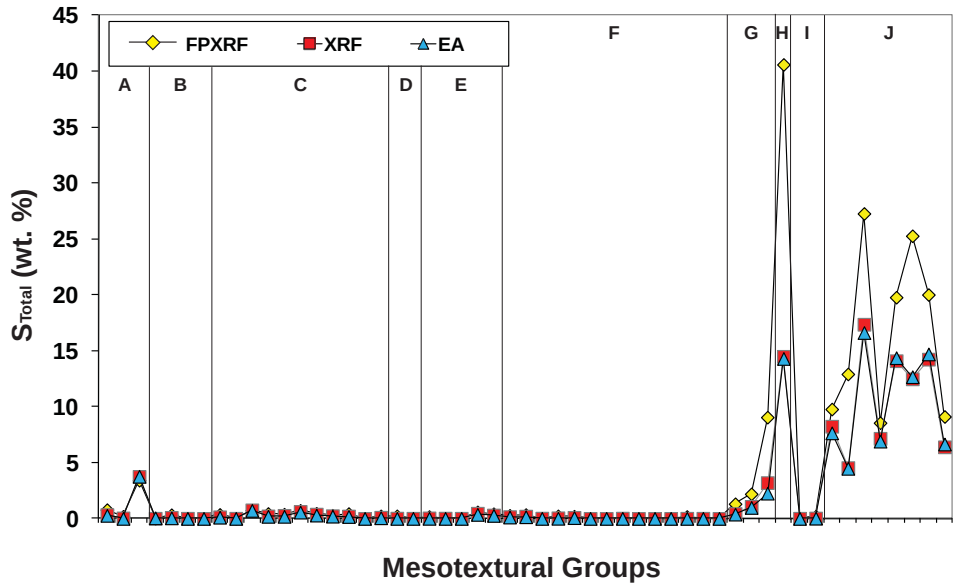

Figure 3.9 Comparison of S_{Total} concentrations measured for Croydon waste rock samples as grouped by mesotexture (A to J; n=52) by three different techniques. Abbreviations: FP-XRF, field portable X-Ray fluorescence; XRF, X-Ray fluorescence; EA, elemental microanalysis.

3.4.2.4 Paste pH

Paste pH and EC values for all samples (<75 µm size fraction) are shown in Figure 3.10 following the classification shown in Price et al. (1997). These values indicate that the majority of mesotextural group J samples and one group G are currently acid forming with high dissolved metal contents. A paste pH value of 5.05 was measured for the group H sample, which is higher than several from group J with similar S_{Total} contents.This correlates with the high arsenopyrite contents in group H, confirming that arsenopyrite is less reactive than pyrite in the paste pH test. The remainder of samples returned paste pH values pH >4, and therefore are classified as not currently acid forming. Generally paste pH values for mesotextural groups, which do not contain pyrite, cluster (i.e., groups D, I, F). A spread is seen for pyrite bearing groups; even those with minor pyrite quantities i.e., group C.

Results from the <20 mm and <5 mm grain size fraction paste pH tests are shown with <75 µm values in Table 3.3. Results from the <75 µm fraction consistently returned the highest pH values, followed generally by <20 mm and <5 mm fractions. Inspite of this, the majority of samples are classified the same by all tests with the exception of four (CG1W1, CG1W3, CG1W8 and C3W6). Based on S_{Total} values of 0.3 wt. % for sample CG1W1 (group E) and 0.09 wt. % for sample CG1W3 (group F), these are likely not currently acid forming, thus the <5 mm values underestimate pH. Sample CG1W8 (group H) and C3W6 (group J) are classified as currently acid forming by both the <20 mm and <5 mm tests but not by the <75 µm fraction test. Such results contradict the expected outcome in which the pulverised samples would return the lowest values as all sulphide minerals are fully liberated (Lapakko et al., 2006).

Table 3.3 Paste pH values performed on <75 µm, fine crush (c.5 mm) and coarse crush (c.20 mm) for selected Croydon waste rock material (Sample suites C3WX and CG1WX) with classifications following Price el al. (1997) given.

Group	Sample	<75 µm (pulverised)		<5 mm (fine crush)		<20 mm (coarse crush)	
		pH value	Classification	pH value	Classification	pH value	Classification
C	CG1W7	6.9	NAF	4.22	NAF	4.15	NAF
E	CG1W4	6.49	NAF	4.71	NAF	5.74	NAF
E	CG1W1	4.74	NAF	3.69	AF	3.94	AF
F	CG1W10	7.86	NAF	4.74	NAF	5.11	NAF
F	C3W1	7.61	NAF	4.32	NAF	4.28	NAF
F	C3W2	7.56	NAF	4.15	NAF	4.79	NAF
F	CG1W3	7.57	NAF	3.82	AF	5.58	NAF
F	CG1W5	7.81	NAF	4.64	NAF	5.59	NAF
F	CG1W6	7.37	NAF	4.34	NAF	5.64	NAF
G	CG1W2	5.38	NAF	4.62	NAF	4.47	NAF
G	C3W4	3.24	AF	2.62	AF	3.01	AF
H	CG1W8	5.05	NAF	3.77	AF	3.99	AF
I	CG1W9	6.81	NAF	4.24	NAF	5.16	NAF
J	C3W3	3.74	AF	2.72	AF	2.63	AF
J	C3W6	4.45	NAF	2.92	AF	3.51	AF
Control		*5.11*		*5.22*		*5.15*	

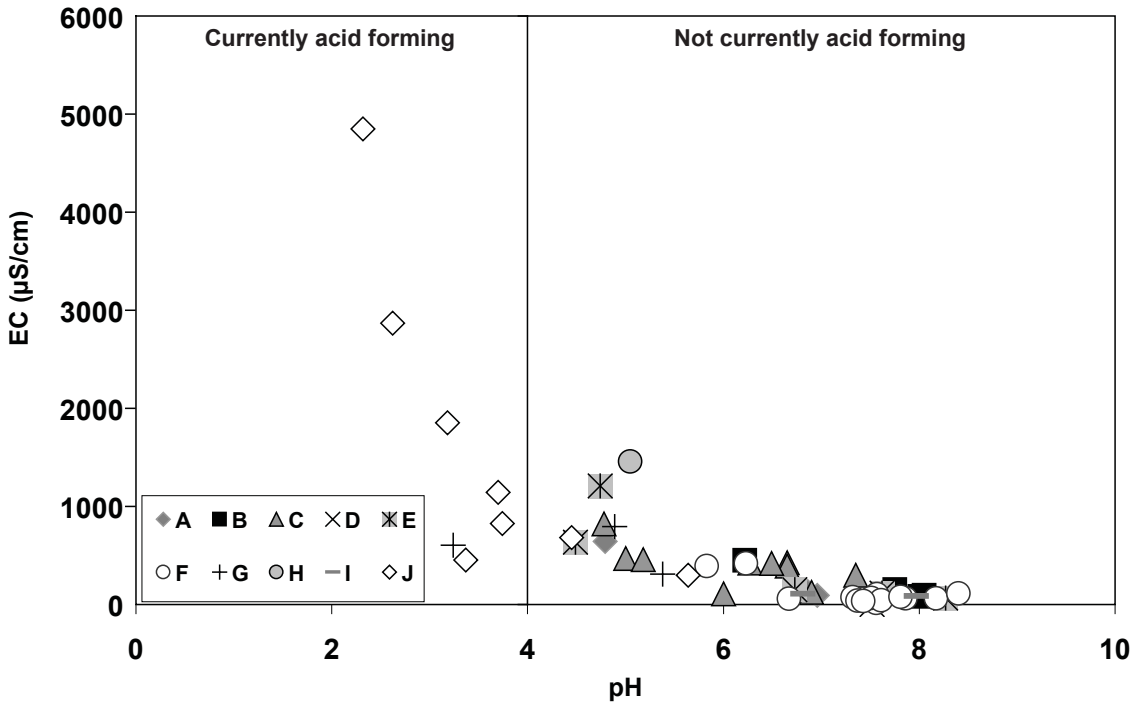

Figure 3.10 Classification of current acidity using paste pH values (from the <75µm grain size tests) and EC (µS/cm) measurements for Croydon waste rock samples as grouped by mesotexture (A to J; n=52).

Samples with S_{Total} values below detection limit (i.e., group F) return lower pH values in the <20 mm and <5 mm tests.Their classification remains overall unaffected, when pH 4 is used as the cut-off criterion. If pH 6 has instead been used as recommended by Lapakko and Anston (2003), then materials from both coarse and fine crush tests would be classified as acid forming which is incorrect. The decreases in pH relative to the control samples indicate a non-sulphide source of protons. This group was iron-oxide stained (red) on the outer surface, thus indicating a potential source. Protons most likely originate from precipitation of Fe^{3+} hydroxides as shown by *equation 3.1* (Lottermoser, 2010).

$$2Fe^{3+} + 6H_2O \rightarrow 2Fe(OH)_3 + 6H^+ \qquad (3.1)$$

These results suggest that during <75 µm fraction tests, interactions between H^+ ions (released from sulphide oxidation, *equation 1.1*), and other pulverised minerals (e.g., potassium feldspar and muscovite) occur following reactions presented in Table 3.4. This causes a rise in pH relative to coarse and fine crush tests, with similar results reported in Shaw et al. (2000). Reaction kinetics are temperature dependent and as sulphide oxidation is exothermic (Lottermoser, 2010) the greater the reactive sulphide surface area, the higher the reaction temperature potentially encouraging these H^+ ion consumption reactions.

Table 3.4 Common silicate mineral neutralisation reactions contributing to the overall neutralising potential (Bowell et al., 2000).

Biotite Dissolution
$KMg_{1.5}Fe_{1.5}AlSi_3O_{10}(OH)_2(s)+7H^++0.5H_2O \rightarrow K^++1.5Mg^{2+}+1.5Fe^{2+}+H_4SiO_4 + 0.5Al_2Si_2O_5(OH)_4(s)$
Anorthite Dissolution
$CaAl_2Si_2O_8(s) +2H+ +H_2O \rightarrow Ca^{2+} + 5Al_2Si_2O_5(OH)_4(s)$
Muscovite Dissolution
$KAl(AlSi_3O_{10})(OH)_2(s) +H^+ +1.5H_2O \rightarrow K^+ +1.5Al_2Si_2O_5(OH)_4(s)$
Albite Dissolution
$NaAlSi_3O_8(s) + H^+ +4.5H_2O \rightarrow Na^+ + 2H_4SiO_4 + 0.5Al_2Si_2O_5(OH)_4(s)$
Potassium Feldspar Dissolution
$KAlSiO_8(s)+ H^+ + 4.5H_2O \rightarrow K^+ +2H_4SiO_4 + 0.5Al_2Si_2O_5(OH)_4(s)$

The <20 mm fraction, returning lower pH values than the <75 µm fraction can be simply explained by the surface area available for buffering reactions being significantly lower in the larger grain size fraction. However, proton release and buffering appears more complicated in the <5 mm fraction. For samples from groups G, H and J, the sulphide surface area has increased in the <5 mm fraction relative to <20 mm tests allowing for a greater quantity of protons to be released. However, buffering of pH through reaction with minerals listed in Table 3.4 is not occurring as efficiently as in the <75 µm tests (and reactions are less exothermic), thus the net effect is the measurement of a relatively lower pH value. Additionally, there may be a coupled effect of Fe-hydroxide precipitation. Overall, results indicate paste

pH tests should not be performed on pulverised samples alone, but on a range of size fractions. This is also recommended in Shaw et al. (2000). Initially in the field the <20 mm fraction could be used, and then in the (field) laboratory, <5 mm and <75 µm size fractions could be prepared, tested and data from all tests critiqued in a similar manner to that shown here, with results compared with sample mineralogy.

3.4.2.5 Waste rock mineralogy

The mineralogy of one representative sample from each mesotextural group (as measured by QXRD) is summarised in Table 3.5. Rhyolite mesotextural groups were dominated by quartz, muscovite, potassium feldspar and kaolinite. Secondary iron-sulphates szomolnokite ($FeSO_4.H_2O$) and rhomboclase ($HFe(SO_4)2.4(H_2O)$) were detected by QXRD analysis between 0.4 to 2.1 wt. % (all groups) and 0.4 to 3.7 wt. % (groups B to J), respectively. Both minerals are pyrite weathering products (Jambor, 2000). Scorodite ($FeAsO_4.2H_2O$) was identified by QXRD analysis in groups A to C, E, G and H with contents ranging from 0.4 to 0.9 wt. %. Harvey et al. (2006) and Murciego et al. (2009) identified scorodite as an early weathering product of arsenopyrite. Anglesite ($PbSO_4$) was identified in mesotextural groups A to F and I to J ranging from 0.4 to 1.1 wt. % and is an early alteration product of galena (Diehl et al., 2008; Lottermoser, 2010). Goethite ($\alpha FeO(OH)$) and jarosite ($KFe^{3+}{}_3(OH)_6(SO_4)_2$) were not detected in the sulphide-bearing mesotextural groups (C, E, G, J & H).

As not all samples were subjected to QXRD (due to the high cost per sample), estimates of the normative mineralogy (as defined in Neuendorf et al., 2005) were deduced using computer programmes ModAn (Paktunc, 2001), MINSQ (Hermann and Berry, 2002) and A2M (Posch and Kurz, 2007; Section 2.4.3). Only estimated mineralogy calculated by ModAn and MINSQ were compared with QXRD values (Figure 3.11), as A2M generated erroneous data. Limitations were encountered when using both programmes. For example, neither programme contains secondary sulphate minerals (e.g., scorodite and anglesite) in their original mineral databases, nor was it clear how to input these minerals. For most mesotextural groups this is acceptable as the secondary sulphate contents was low. However, in the case of the group G (Figure 3.11), 1.6 wt. % szomolnokite was measured, and is not accounted for by computed methods. In MINSQ, values for the sum of the residuals squared (residual SSQ) are calculated, and provide an indication of the accuracy of the results. Hermann and Berry (2002) stated that residual SSQ values <0.5 are acceptable. For this dataset, residual SSQ values ranged from 0.3 to 11.5. Lower residual SSQ values were calculated for altered rhyolite groups, with higher SSQ values calculated for sulphide-bearing mesotextural groups. Better approximations were achieved using ModAn, particularly for groups B-E. However, a significant limitation of ModAn is its assumption that all S reported in the whole rock analyses is tied to pyrite, which is not the case for mesotextural groups G and H. Paktunc (2001) acknowledges this, and states that an updated version of the programme would be made available specifically for sulphide rich samples; however, this is not yet publically available. Considering this, MINSQ has a better application for sulphidic samples (i.e., waste rock), as it ties S to both sulphides (e.g., chalcopyrite, pyrite, galena) and common sulphates (e.g., gypsum, barite).

Table 3.5 Mineralogy of Croydon waste rock samples as measured for one sample from each mesotextural group by quantitative X-Ray diffractometry (Major: >1 wt. %; Minor: 0.4 to 1 wt. %; detection limit: 0.3 wt%).

Mesotextural Group	Gangue minerals	Primary sulphides	Secondary sulphates and (hydro)oxides
A	**Major**	**Minor**	**Minor**
	quartz	pyrite	szomolnokite
	muscovite	chalcopyrite	anglesite
	kaolinite	galena	scorodite
	Minor		
	fluorite		
B	**Major**	**Minor**	**Major**
	quartz	arsenopyrite,	goethite
	muscovite	pyrite	**Minor**
	kaolinite	galena	anglesite
			szomolnokite
			gypsum
			rhomboclase
			scorodite
C	**Major**	**Major**	**Minor**
	potassium feldspar	pyrite	anglesite
	quartz	Minor	gypsum
	muscovite	arsenopyrite	szomolnokite
	Minor	chalcopyrite	rhomboclase
	fluorite	galena	
D	**Major**	**Minor**	**Minor**
	quartz	pyrite	szomolnokite
	potassium feldspar	galena	anglesite
	muscovite		rhomboclase
	kaolinite		
	Minor		
	fluorite		
	chlorite		
E	**Major**	**Minor**	**Minor**
	quartz	pyrite	anglesite
	potassium feldspar	chalcopyrite	szomolnokite
	muscovite	galena	scorodite
	Minor		rhomboclase
	fluorite		
	chlorite		

Table 3.5 Mineralogy of Croydon waste rock samples (Cont.)

Mesotextural Group	Gangue minerals	Primary sulphides	Secondary sulphates and (hydro)oxides
F	**Major**	**Minor**	**Minor**
	quartz	galena	szomolnokite
	potassium feldspar	pyrite	anglesite
	muscovite		rhomboclase
	Minor		
	fluorite		
	chlorite		
G	**Major**	**Major**	**Major**
	quartz	sphalerite	szomolnokite
	muscovite	galena	anglesite
	Minor	**Minor**	**Minor**
	albite	chalcopyrite	gypsum
	K-feldspar		scorodite
	kaolinite		rhomboclase
H	**Major**	**Major**	**Minor**
	quartz	arsenopyrite	scorodite
	apatite	pyrite	szomolnokite
			hematite
			anglesite
			rhomboclase
I	**Major**	**Minor**	**Minor**
	quartz	pyrite	szomolnokite
	microcline	galena	anglesite
	albite	chalcopyrite	rhomboclase
	muscovite		
	chlorite		
	Minor		
	fluorite		
	kaolinite		
J	**Major**	**Major**	**Major**
	quartz	pyrite	rhomboclase
	Minor	**Minor**	szomolnokite
	fluorite	galena	anglesite
	muscovite		**Minor**
	magnetite		gypsum

In terms of using the estimated normative mineralogy to classify samples based on the carbonate: sulphide ratio (as recommended by the GMT approach), the overall classification of these samples remains unchanged by these different methods, with the majority plotting as inert (i.e., at the graph origin) or as acid forming. However, agreement between classifications assigned from computed methods based on carbonate:sulphide ratio only arose due to the low-negligible carbonate contents of these samples, and does not reflect the accuracy of the computer programmes. Despite the inaccuracies between computed data and QXRD values, these results suggest that with refinement, such computed methods could be able to estimate mineralogy of mine waste samples accurately. If this could be done so using accurate element data collected from FP-XRF, this would significantly improve the understanding of sample mineralogy for a relatively low-cost. But currently, measurement by QXRD is recommended for at least one sample per mesotextural group, with the same carbonate:sulphide ratio classification subequently assigned to all samples within each group. Classifications are best cross-checked against hand-specimen estimations of modal mineralogy made during mesotextural grouping, Based on this classification, samples from group G, J and H are clearly acid forming, with the remainder plotting around the graph origin (i.e., inert or non-acid forming; Figure 3.12).

3.4.2.6 ARDI values

Final ARDI evaluation results are shown in Table 3.6. As no primary neutralising minerals are present, the 10 to 0 ARDI field (Table 2.6) is considered as NAF. Groups D and I were classified as NAF (0/50) as they do not contain any visible sulphides or primary neutralising minerals (and S_{Total} values measured by XRF and EA were below detection limit). Groups B and F were also classified as NAF, with traces of disseminated subhedral pyrite grains identified in the rhyolite groundmass. Group A contained minor pyrite (euhedral, showing very little weathering) in quartz veins so overall was classified as NAF. Group C also contained euhedral pyrite grains in quartz veins but returned a higher value than group A as more veins were pyrite bearing (Figure 3.13a). Group E was classified as PAF as subhedral pyrite was contained in the volcanic groundmass (Figure 3.13b). These grains had intensely weathered cores, with the original grain boundary remaining well defined, and secondary phases were not consistently observed on grain rims. Group G was classified as PAF because galena and sphalerite dominated the sulphide mineralogy and are not evaluated by the ARDI. Groups H and J were classified as EAF as both were massive/semi-massive sulphide textures predominately associated with quartz (Figure 3.13c). In group H, massive arsenopyrite was highly fractured presenting some difficulty in defining individual grains for ARDI evaluation (Figure 3.13d). Therefore, each fractured portion was considered an individual grain and evaluated. In group J, pyrite grain size varied, with grains generally euhedral, demonstrating some fracturing and a moderate degree of weathering.

3.4.2.7 Stage-one classification

Pre-screening classification results as per stage-one of the GMT approach are shown in Figure 3.14 to Figure 3.19. Classifications varied when the different grainsizes (<20 mm, <5 mm and <75 μm) were plotted against S_{Total} for select samples (Figure 3.14). Paste pH values from the <5 mm tests classified samples from groups F and I as potentially acid forming, when both contain very low S_{Total} (<0.07 wt. %). Therefore, these are not recommended for use in stage-one classification.

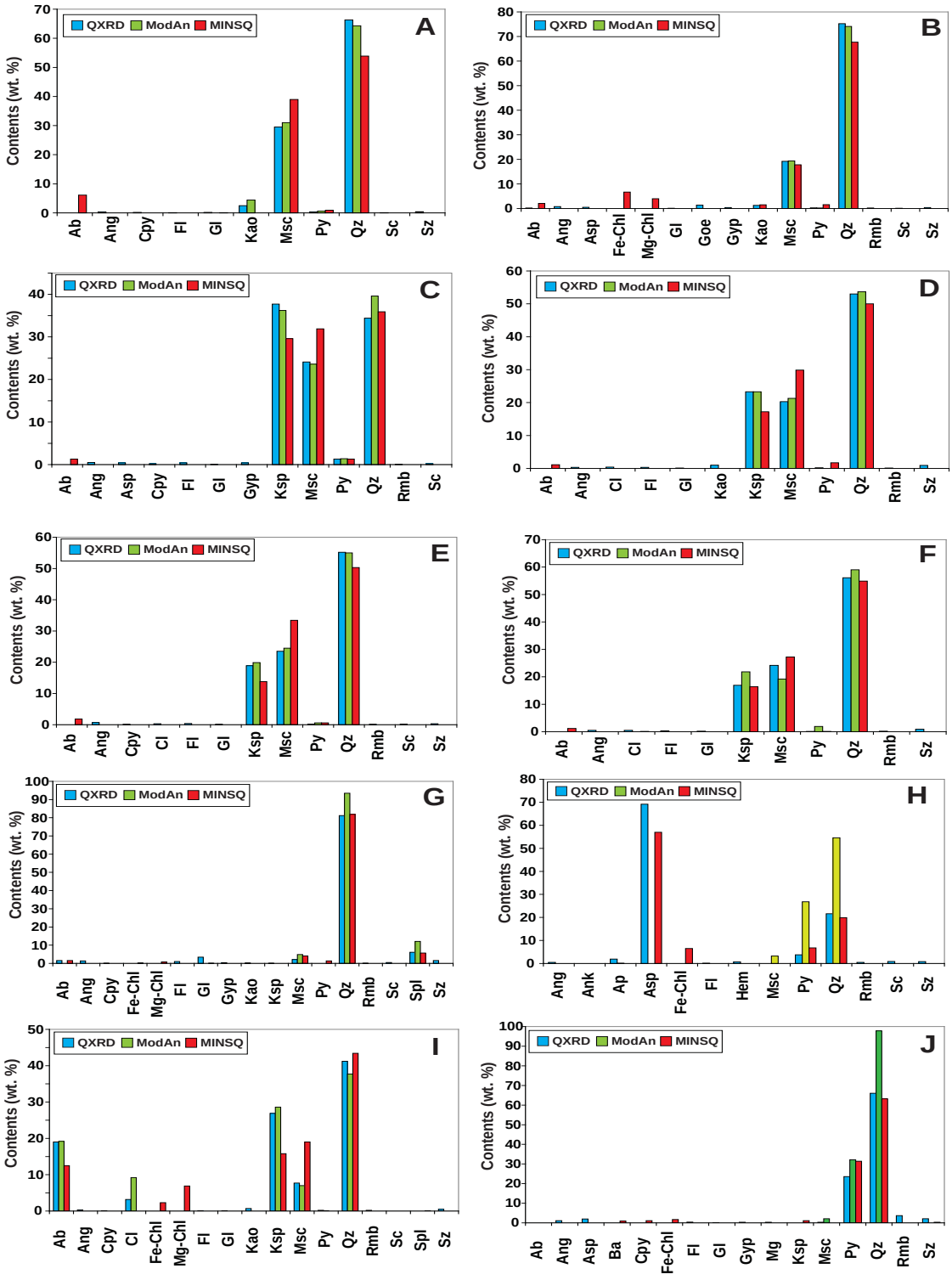

Figure 3.11 Comparison of Croydon waste rock mineralogy (one per mesotextural groups A to J) as measured by QXRD and estimated by ModAn (Paktunc, 2001) and MINSQ (Hermann and Berry, 2002). Abbreviations: Ab, albite; Ank, ankerite; Ang, anglesite; Ap; apatite; Asp, arsenopyrite; Ba, barite; Cl, chlorite; Cpy, chalcopyrite; Fe-chl, iron rich chlorite; Fl, fluorite; Gl, galena; Goe, goethite; Gyp, gypsum; Kao, kaolinite; Ksp, potassium feldspar; Msc, muscovite; Py, pyrite; Qz, quartz; Rmb, rhomboclase; Sc, scorodite; Sz, szomolnokite.

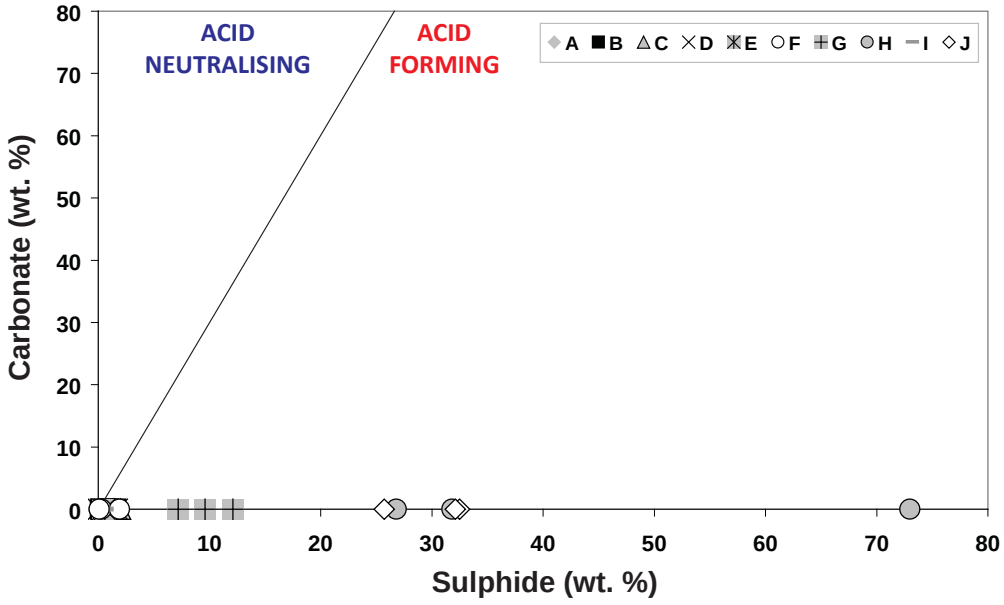

Figure 3.12 Acid forming potential classification of Croydon waste rock samples (one per mesotextural group A to J) based on carbonate and sulphide values (wt. %) as determined by quantiative X-Ray diffractometry.

Table 3.6 Acid rock drainage index (ARDI) values and classifications for Croydon waste rock mesotextural groups A to J. ARDI values calculated for one representative sample per group. Abbreviations: NAF, non-acid forming; PAF, potentially acid forming; EAF, extremely acid forming.

Group	Final ARDI value (/50)	Classification
A	8	NAF
B	3	NAF
C	16	NAF
D	0	NAF
E	21	PAF
F	8	NAF
G	22	PAF
H	41	EAF
I	0	NAF
J	43	EAF

Whilst <20 mm values return lower paste pH than the <75 µm fraction, classifications were generally similar demonstrating its potential field based application. However, as the <75 µm size fraction is recommended originally by Smart et al. (2002), these values only are used further in stage-one. The majority of samples from groups A, B, D, E, F, and I were classified as NAF by paste pH (<75 µm) versus S_{Total} (measured by EA; Figure 3.15). Group G samples were classified as PAF or AF, group H as PAF, and group J was dominantly AF. Classifications by S_{Total} and paste pH (<75 µm) versus ARDI values (Figure 3.16 and Figure 3.17, respectively) indicate that groups J and H are EAF, groups E and G are PAF, and all others are NAF. These classifications are in agreement with sample mineralogy.

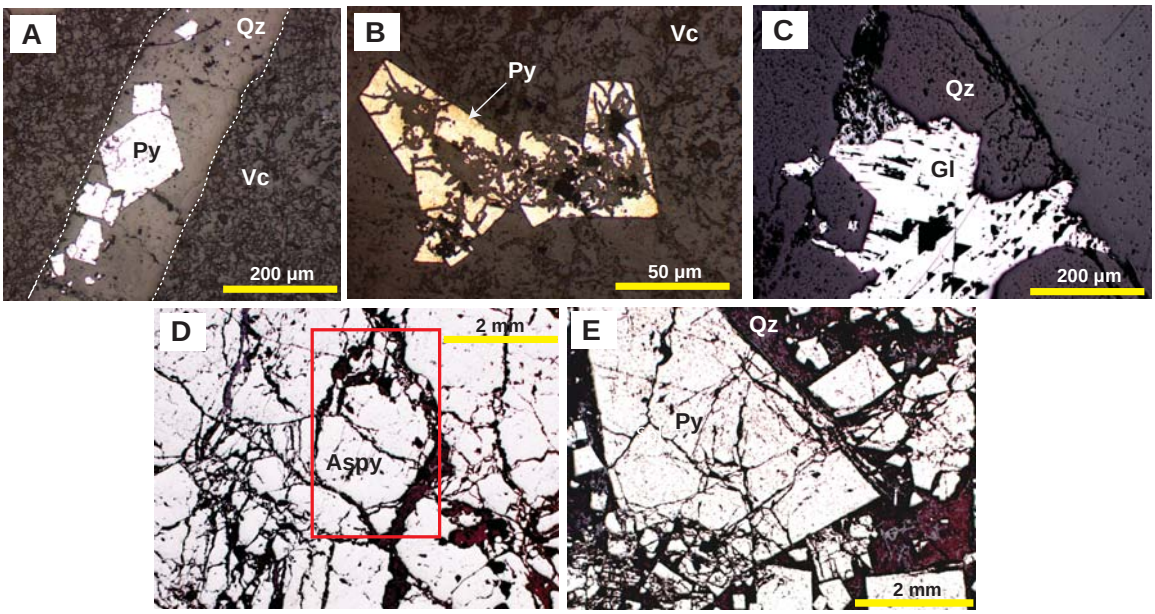

Figure 3.13 Reflected light photomicrographs of sulphide textures observed in Croydon waste rock: **(A)** Euhedral pyrite contained in quartz veins; **(B)** Intensely weathered subhedral pyrite contained within a volcanic (quartz-muscovite) groundmass; **(C)** Quartz-associated subhedral galena; (**D**) Massive, intensely fractured arsenopyrite (with the red square depicting an area considered as a 'grain' for ARDI evaluation); **(E)** Semi-massive quartz-associated euhedral pyrite grains with some fracturing. Abbreviations; Aspy, arsenopyrite; Gl, galena; Py, pyrite; Qtz, quartz; Vc, volcanic groundmass.

Metal (Cd, Co, Cu, Ni, Pb and Zn) and metalloid (Au and Sb) contents (as determined by FP-XRF) were plotted against paste pH (<75 µm) values to provide an indication of the risk posed to the drainage chemistry by each mesotextural group (Figure 3.18 and Figure 3.19). Group J samples were consistently classified as high risk, with ARD likely and high metal and metalloid contents. Group G samples were overall classified as high to intermediate risk with high metal contents reported due to the presence of galena and sphalerite in this group (Figure 3.18). Group H was classified as intermediate risk as the measured paste pH was higher than the pH 4.5 cut-off criterion. However, group H contained the greatest amount of As than any other group (as expected when considering mineralogy). Some samples from groups A and C were classified as intermediate risk with potential for metal leaching, and B and F for metalloids. This indicates that whilst relatively minor amounts of pyrite were identified in these samples, the pyrite is likely trace element rich. The remainder of samples were classified as low risk.

A stage-one classification summary is provided in Table 3.7. Groups A, B, D, F, and I are not required for further GMT testing as essentially, these are considered as 'inert' samples with no acid forming or neutralising potential. Groups C and E are required for further testing as there are conflicts with their classification (i.e., both PAF and NAF samples exist within the groups). Additionally, these groups are pyritic, and potentially represent minor ARD sources. Groups G, H and J are consistently identified as PAF or AF or EAF, and must be further tested. Despite these recommendations, all samples were subjected to stage-two tests in order to fully evaluate stage-one classifications and the GMT approach.

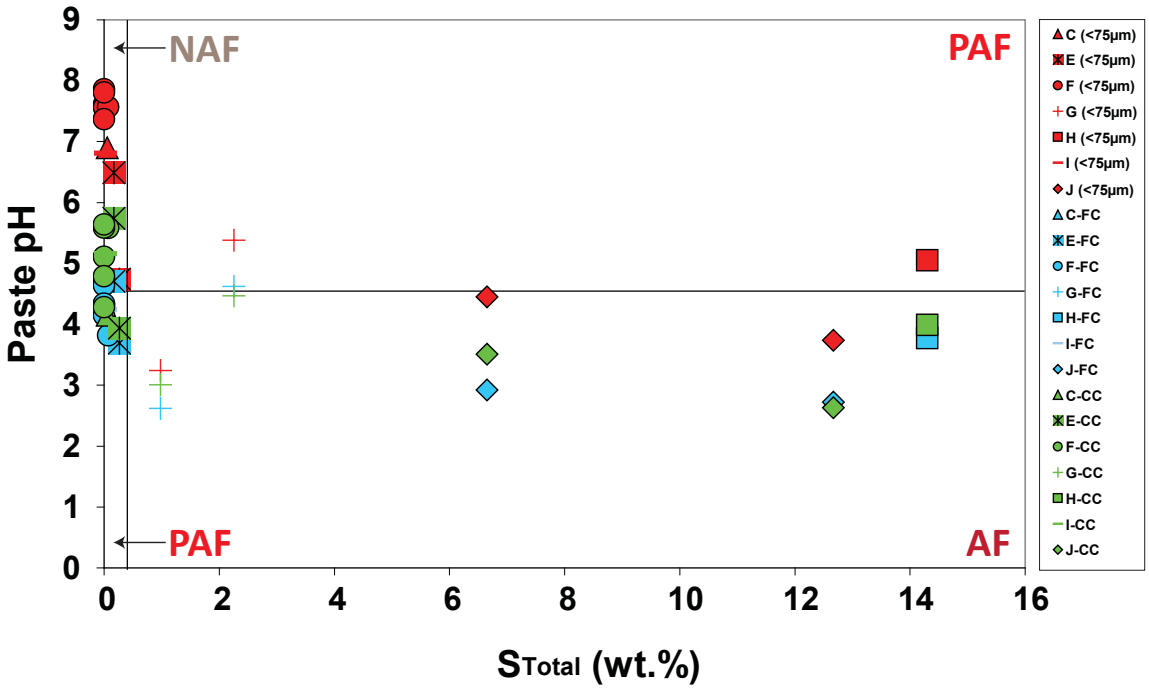

Figure 3.14 Paste pH values measured for three grain size fractions (<75 µm; <5 mm or FC; <20 mm or CC) shown against S_{Total} values (as measured by elemental microanalysis) for selected Croydon waste rock samples (n=15). Abbreviations: AF, acid forming; CC, coarse crush; FC, fine crush; NAF, non-acid forming; PAF, potentially acid forming.

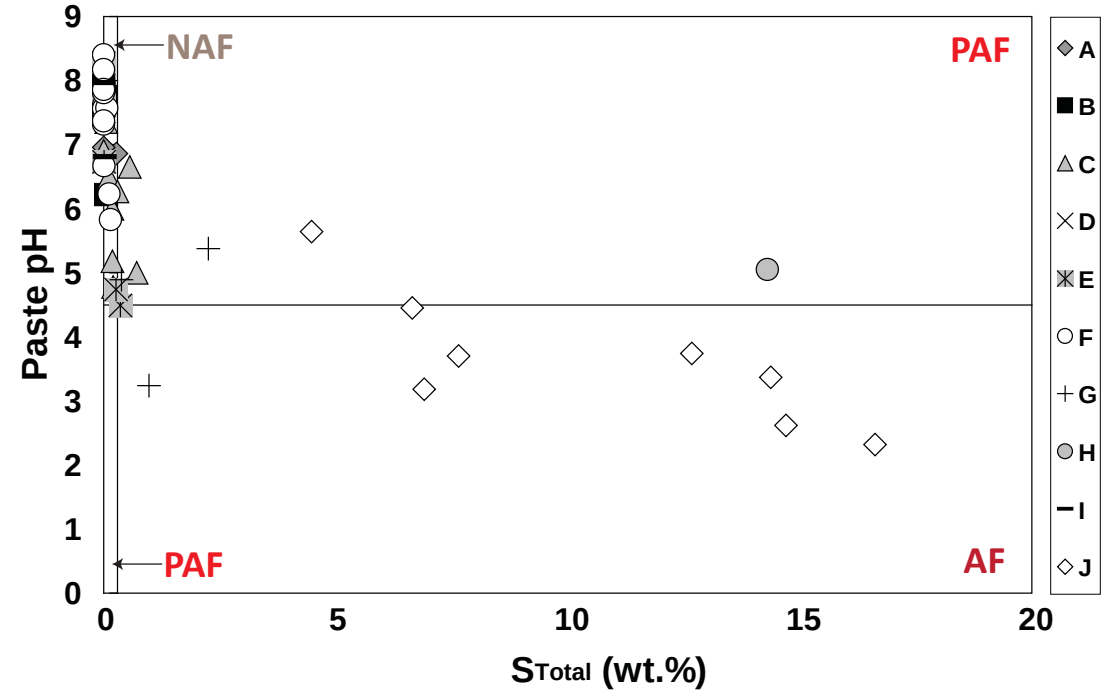

Figure 3.15 Classification of Croydon waste rock samples from mesotextural groups A to J (n=52) using paste pH values (<75 µm grain size fraction) plotted against S_{Total} values (as measured by elemental microanalysis). Abbreviations: AF, acid forming; NAF, non-acid forming; PAF, potentially acid forming.

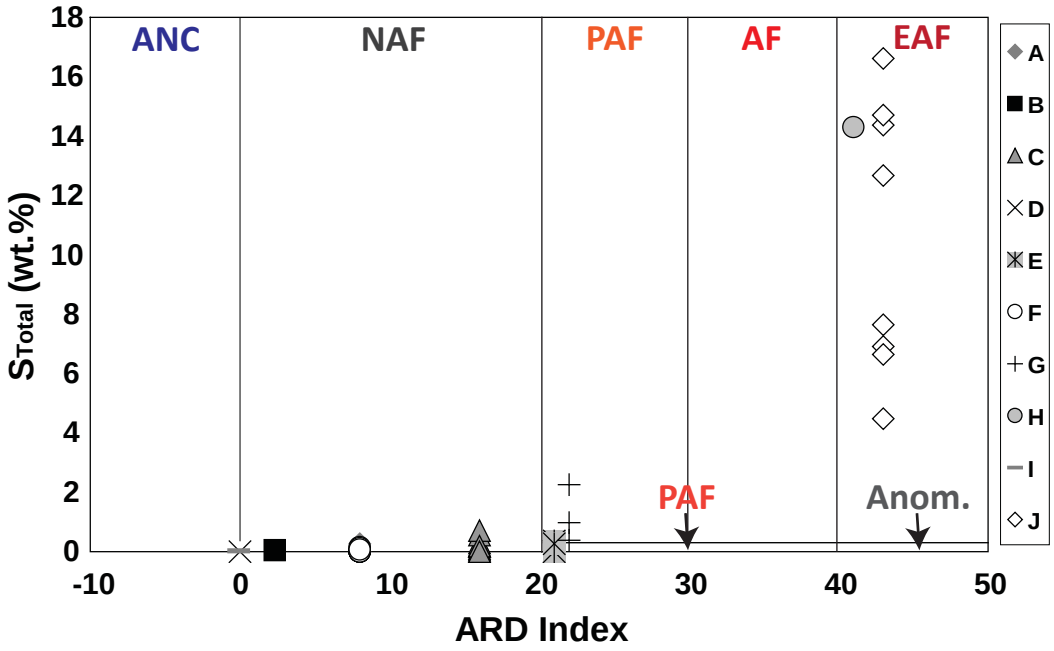

Figure 3.16 Classification of Croydon waste rock samples from mesotextural groups Ato J (n=52) using S_{Total} (as measured by elemental microanalysis) shown against acid rock drainage index (ARDI) values. Abbreviations: AF, acid forming; ANC, acid neutralising capacity; Anom., anomalous; EAF, extremely acid forming; NAF, non-acid forming; PAF, potentially acid forming.

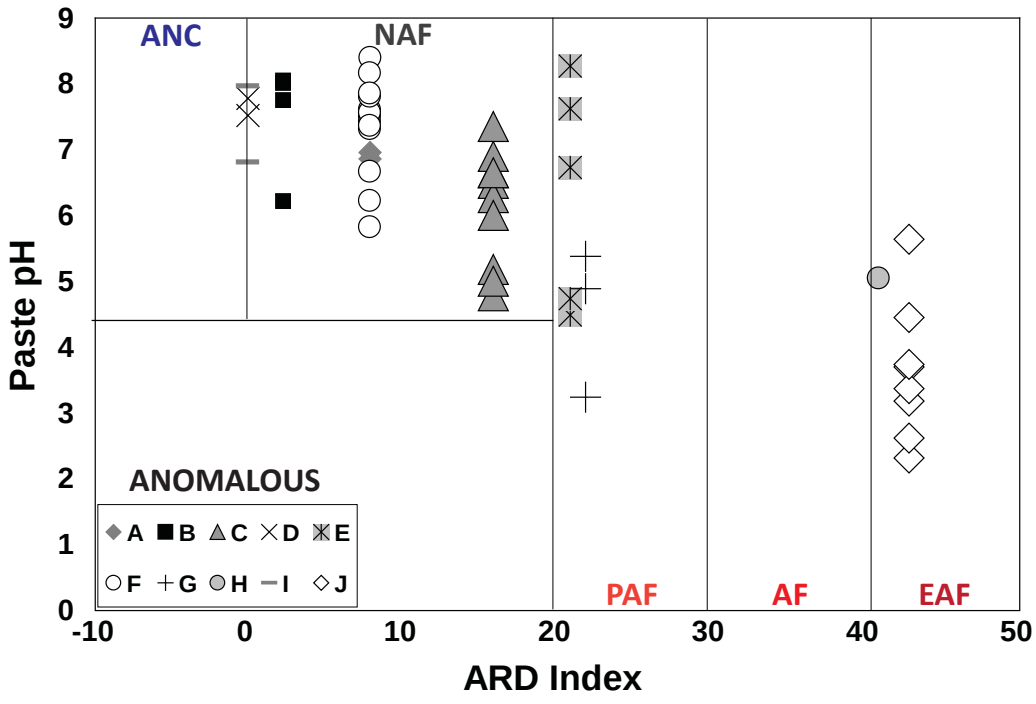

Figure 3.17 Classification of Croydon waste rock samples from mesotextural groups A to J (n=52) using paste pH (<75 µm grain size fraction) versus Acid Rock Drainage Index (ARDI) values. Abbreviations: AF, acid forming; ANC, acid neutralising capacity; EAF, extremely acid forming; NAF, non-acid forming; PAF, potentially acid forming.

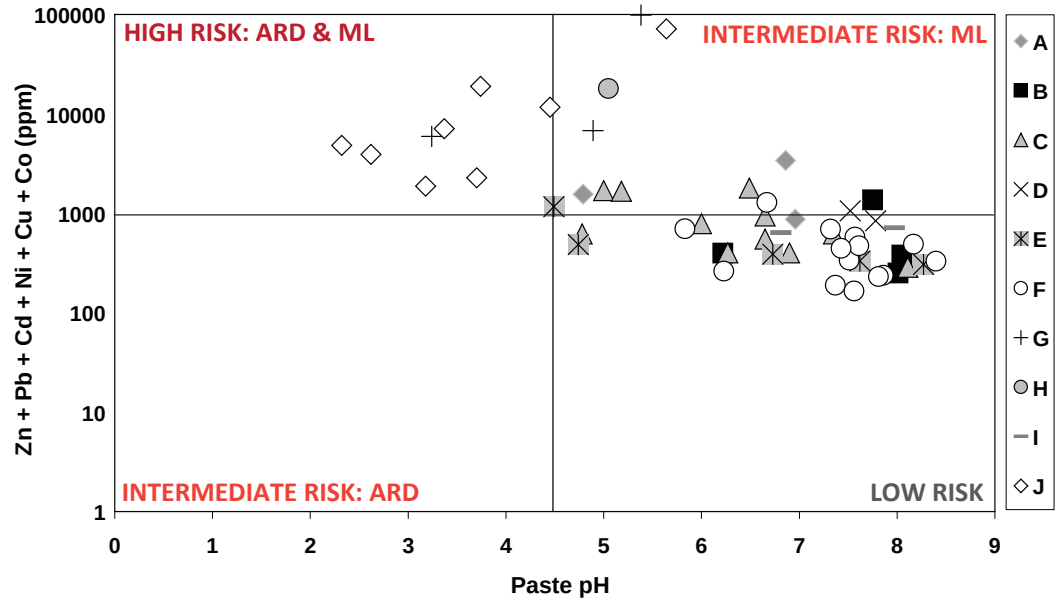

Figure 3.18 Risk classification of Croydon waste rock samples from mesotextural groups A to J (n=52) based on metal contents (measured by FP-XRF) versus paste pH. Abbreviations: ARD, acid rock drainage; ML: metal leaching.

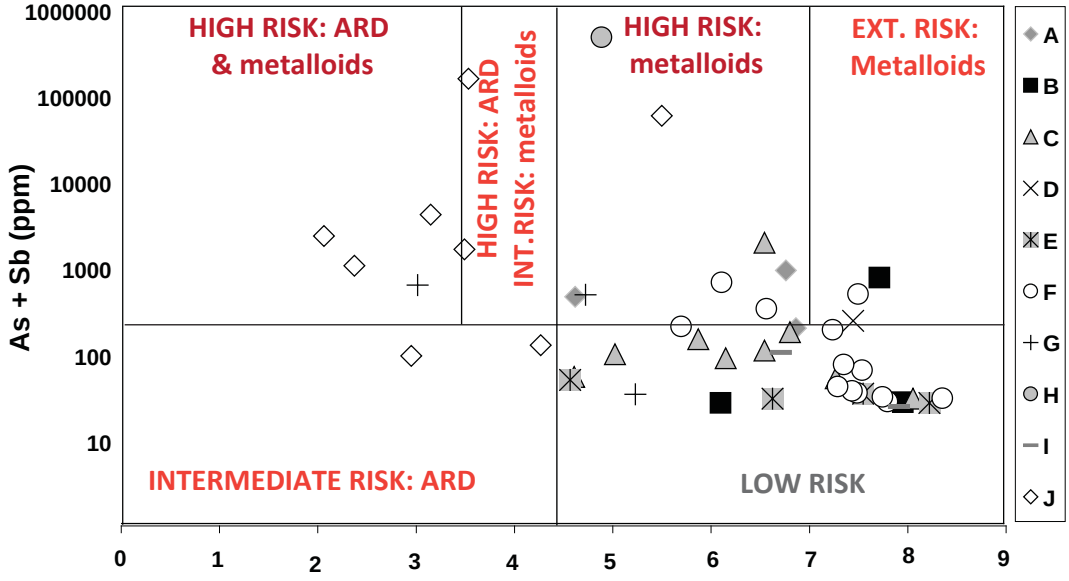

Figure 3.19 Risk classification of Croydon waste rock samples from mesotextural groups A to J (n=52) based on metalloid (As and Sb) contents (measured by FP-XRF) versus paste pH. Abbreviations: ARD, acid rock drainage.

3.4.3 Stage-two results

3.4.3.1 Static geochemical tests

A summary of static geochemical results are shown in Table 3.8. MPA was calculated directly from S_{Total} as $S_{Sulphate}$ contents were very low for these samples as indicated by QXRD and hand specimen observations. Furthermore, as QXRD was not undertaken on all samples, it was considered inappropriate to use $S_{Sulphide}$ based on Fe-sulphide content for only some samples. Groups G, H and J returned relatively

Table 3.7 Stage-one classification summary table for Croydon waste rock samples as grouped by mesotexture (groups A-J; n=52). Abbreviations: NAF, non-acid forming; PAF, potentially acid forming; AF, acid forming; EAF, extremely acid forming; Int, intermediate; ML, metal leaching; ARD, acid rock drainage.

Group	Paste pH vs. S_{Total}	ARDI vs. S_{Total}	ARDI vs. paste pH	Carbonate vs. Sulphide	Metals vs. paste pH	Metalloids vs. paste pH	Summary classification	Stage-two testing required?
A	NAF	NAF	NAF	AF	Int. (ML) to low risk	Low risk	NAF	No
B	NAF	NAF	NAF	NAF	Int. to low risk	Int. to low risk	NAF	No
C	NAF/PAF	NAF	NAF	AF	Int. to low risk	Int. to low risk	NAF/PAF	Yes
D	NAF	NAF	NAF	AF	Low risk	Low risk	NAF	No
E	NAF/PAF	PAF	PAF	AF	Int. to low risk	Low risk	PAF	Yes
F	NAF	NAF	NAF	NAF	Int. to low risk	Low risk	NAF	No
G	PAF	PAF	PAF	AF	High to int. risk	Int. (ARD) to low risk	PAF	Yes
H	PAF	EAF	EAF	AF	Int. risk	Int. (ML) risk	AF	Yes
I	NAF	NAF	NAF	AF	Low risk	Low risk	NAF	No
J	PAF/AF	EAF	EAF	AF	High to int. risk	High to int. risk	EAF	Yes

high MPA values ranging from 37 to 431 kg H_2SO_4/t as was expected based on their S_{Total} values. ANC values were calculated using both Sobek and Modified Sobek methods with a comparison of results shown in Figure 3.20. Modified Sobek results infer that there is significant neutralising capacity offered by these samples, particularly in groups D, E and G. However, cross-checking with published NP values of the constituent minerals (Table 2.5) and ARD characteristics of rhyolites (Plumlee, 1999) indicated that these results are erroneous. This contradicts observations made by Capanema and Ciminelli (2003) and the GARD Guide (2009) which state that the Modified Sobek method is of greater accuracy. To further cross check ANC values, calculations to determine ANC based on whole rock data shown in Lawrence and Scheske (1997) were performed. These values showed poor correlation against Sobek (R^2= 0.1) and Modified Sobek (R^2= 0.02) results. Paktunc (1998a) described the limitations of this method, and proposed an alternative method by which to calculate NP mineralogically (Paktunc, 1998b). Results calculated were more aligned to Sobek values. Based on this, values obtained by the Sobek method were used in NAPP calculations. Average NAPP values were relatively low for all groups (-2 to 5 kg H_2SO_4/t) with the exception of groups G, H and J for which values >20 kg H_2SO_4/t were calculated, identifying these as PAF (Skousen et al., 2002).

Typically, NAPP and NAG values are not compared directly despite static test methods requiring calculation of NAG values to pH 4.5 and pH 7.0 (Smart et al., 2002). Therefore, NAPP and NAG values to pH 7.0 are compared in Figure 3.21. For groups B, C, D, E, F and I results plot on the model 1:1 line. Groups A, J and one sample from group G return greater NAPP values, and the group H sample returns a greater NAG value. Based on the mineralogy, MPA overestimates are likely for group G. However, it is also possible that NAG values are underestimated in the single-addition test as a result of H_2O_2 denaturing (Stewart, 2004). This conflict indicates that stage-three advanced geochemical testing is likely required for groups H and J.

NAPP values were plotted against NAG pH (Figure 3.22) and indicated groups H and J have significant acid forming potential, whilst groups C, E and G have a weak potential for acid formation. The majority of samples are NAF confirming stage-one classifications. Comparison of NAG pH and paste pH values (Figure 3.23) confirms risk classifications assigned in Figures 3.17 and 3.18, with group J posing a high ARD risk, and the majority of group G, H, C and E classified as medium/intermediate risk.

3.4.3.2 Stage-two classification

A classification summary for this stage is shown in Table 3.9, and confirmed that groups G, H and J are the most acid forming thus requiring stage-three testing. Advanced geochemical testing for these groups was mandatory on at least one sample per group to cross-check single addition NAG values. Additionally, microanalyses were required to determine the composition of the major sulphides and their textural relationship with secondary minerals identified by QXRD. Classification discrepancies arose for groups C and E, therefore one sample from each was recommended for further geochemical testing, and quantitative sulphide elemental analysis. No samples are required for ABCC testing, as there is an absence of carbonate minerals in these samples. Classifications are in agreement with those given at the end of stage-one (Table 3.7), indicating its accuracy as a pre-screening stage.

Table 3.8 Static test geochemical data for Croydon waste rock samples from mesotextural groups A to J (n= 52), with average values for each group shown (*= kg H_2SO_4/t).

Group	Maximum Potential Acidity*	Sobek ANC*	Net Acid Producing Potential*	NAG pH	No. of samples
A	4	5	-1	5.20	2
B	1	1	0	5.32	4
C	8	0	8	3.54	10
D	0	4	-4	4.89	2
E	4	2	2	4.53	5
F	1	4	-3	5.24	13
G	37	0	37	2.69	3
H	438	-2	440	1.46	1
I	0	4	-4	5.73	2
J	299	-3	302	1.73	10

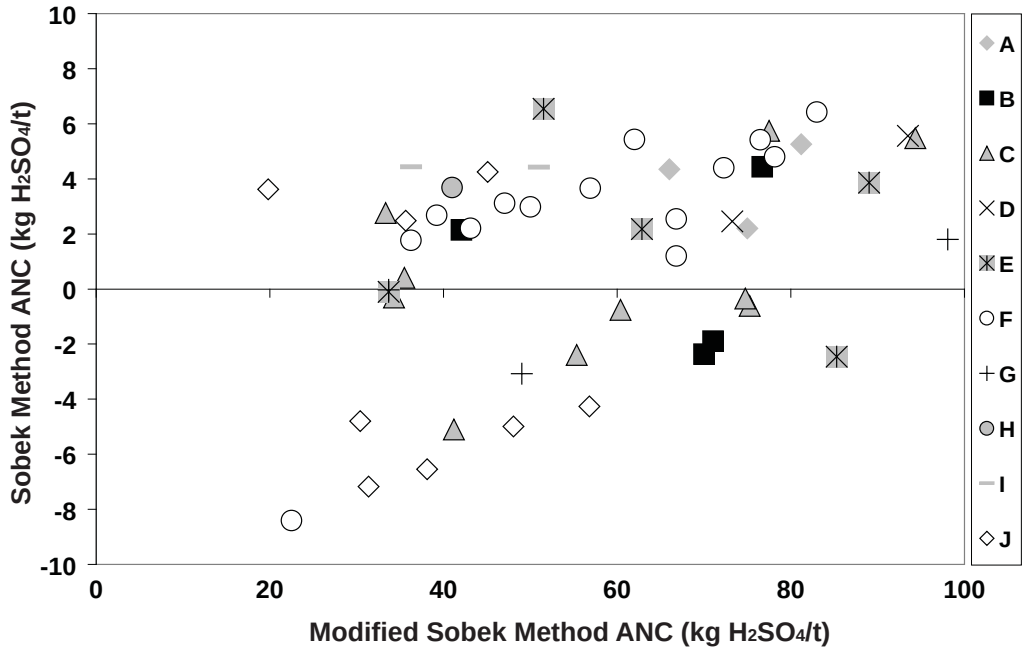

Figure 3.20 Sobek ANC values shown against Modified Sobek ANC values (kg $H_2SO4/_t$) for Croydon waste rock samples from mesotextural groups A to J (n=52).

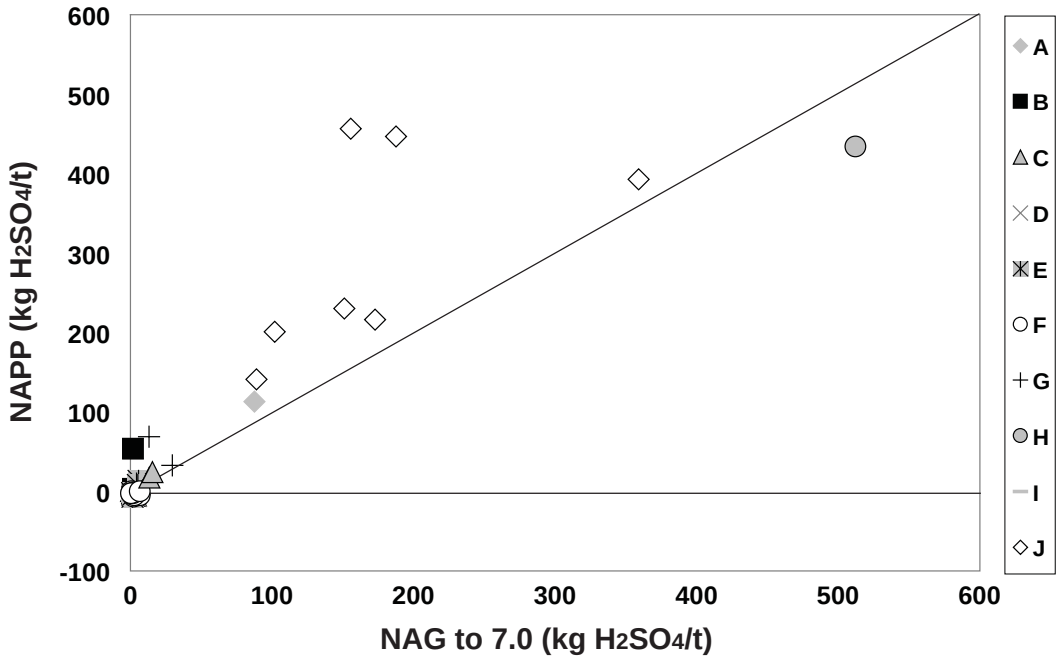

Figure 3.21 NAPP values shown against NAG pH values to 7.0 (kg H_2SO_4/t) for Croydon waste rock samples from mesotextural groups A to J (n=52).

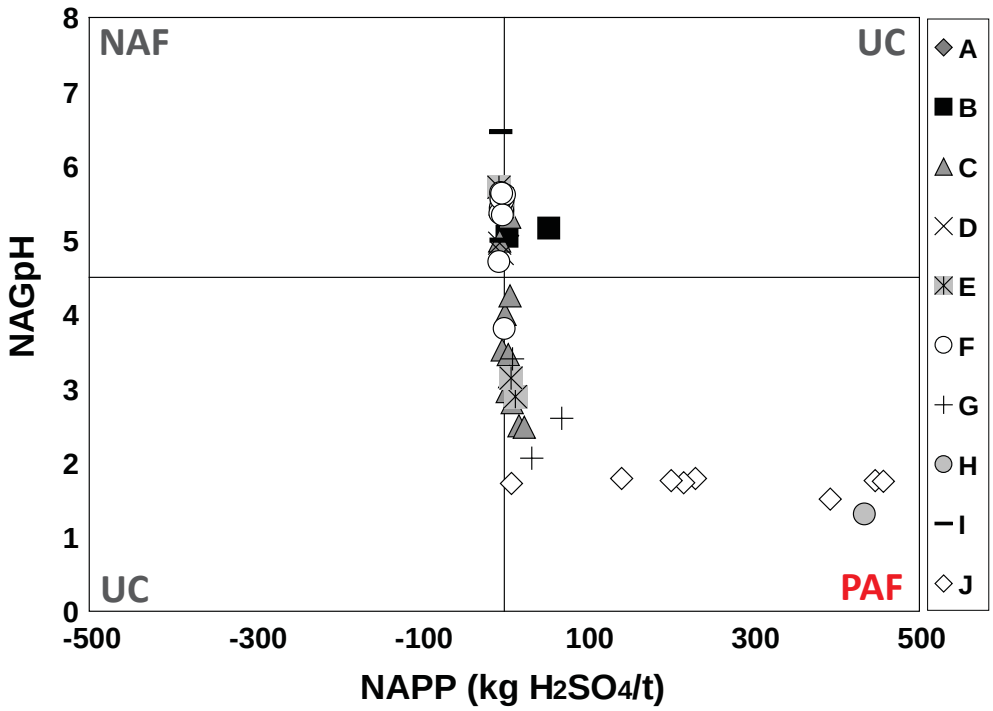

Figure 3.22 Classification of ARD potential for Croydon waste rock samples as grouped by mesotexture (A to J; n=52) based on NAPP and NAG pH values. Abbreviations: PAF, potentially acid forming; NAF, non-acid forming; UC, uncertain.

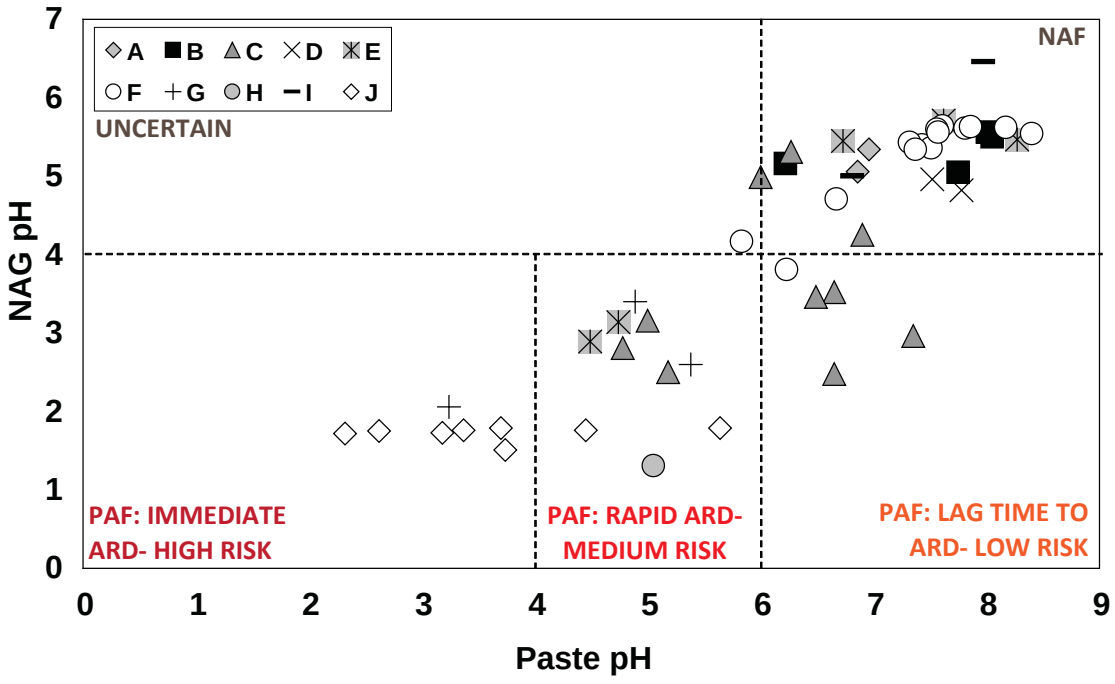

Figure 3.23 Classification of ARD potential for Croydon waste rock samples as grouped by mesotexture (A to J; n=52) based on paste pH and NAG pH values. Abbreviations: PAF, potentially acid forming; NAF, non-acid forming; UC, uncertain.

Table 3.9 Stage-two classification summary table for Croydon waste rock samples as grouped by mesotexture (groups A to J; n=52). Abbreviations: AF, acid forming; ANC, acid neutralising capacity; ARD, acid rock drainage; EAF, extremely acid forming; HR, high risk; LR, low risk; ML, metal leaching; MPA, maximum potential acidity; MR, medium risk; NAF, non-acid forming; PAF, potentially acid forming.

Group	NAPP vs. NAG pH	NAG pH vs. Paste pH	ANC vs. MPA	Summary classification	Stage-one agreement?	Stage-three testing?
A	NAF	NAF	PAF	NAF	Yes	No
B	NAF & UC	NAF	PAF	NAF	Yes	No
C	NAF & PAF	NAF & PAF (LR & MR)	PAF	PAF	Yes	Ye s (low priority)
D	NAF	NAF	NAF	NAF	Yes	No
E	NAF & PAF	NAF & PAF (MR)	PAF	PAF	Yes	Ye s (low priority)
F	NAF	NAF	PAF	NAF	Yes	No
G	PAF	PAF (LR & MR)	PAF	AF	Yes	Ye s (high priority)
H	PAF	PAF (MR)	PAF	EAF	Yes	Ye s (high priority)
I	NAF	NAF	NAF	NAF	No	No
J	PAF	PAF (MR & HR)	PAF	EAF	Yes	Ye s (high priority)

3.4.4 Stage three results

3.4.4.1 Advanced NAG tests

Sequential NAG (sNAG) tests were performed on one sample each from groups A, C, E, G, H and J. Final NAG pH values at each stage are shown in Figure 3.24, with a general trend of increasing pH observed for each sample. This indicates that sulphide oxidation is occurring uninterrupted in the absence of strong acid buffering reactions (Stewart, 2005). The amount of reactive sulphide decreases with each stage as it becomes oxidised, resulting in less acid release and higher pH with successive stages (Stewart, 2005). The group H sample took the most number of stages to achieve a NAG pH 4.5 as anticipated considering its high S_{Total} (Table 3.10). This was followed by group E which was unexpected considering its relatively low S_{Total} (Table 3.10). Next were groups A and J, followed by both groups C and G which required three stages only. These results indicate a temperature influence on oxidation rate, which is particularly illustrated by a comparison of group A,C, E and J samples. On H_2O_2 addition, the liquor boils for samples containing high S_{Total} (Figure 3.25) thus accelerating sulphide oxidation (Lottermoser, 2010). However, for samples with lower S_{Total} (i.e., group E) temperature has limited effect on reaction kinetics as the reaction liquor was not seen to effervesce (Figure 3.25). Therefore, a greater number of stages than expected are required to achieve NAG pH ≥4.5. This effect appears not to be realised if very low S_{Total} contents are measured (i.e., <0.2 wt. %; group C), with the number of stages to achieve NAG pH ≥4.5 controlled by sulphur content alone.

A general rate of sulphide reactivity only is implied by these results as different S_{Total} values have been used in each test. Sphalerite and galena bearing samples oxidise the quickest as the least number of stages was required to achieve NAG pH ≥4.5. This was followed by pyrite and subsequently arsenopyrite. These are in agreement with Keith and Vaughan (2000) and Moncur et al. (2009).

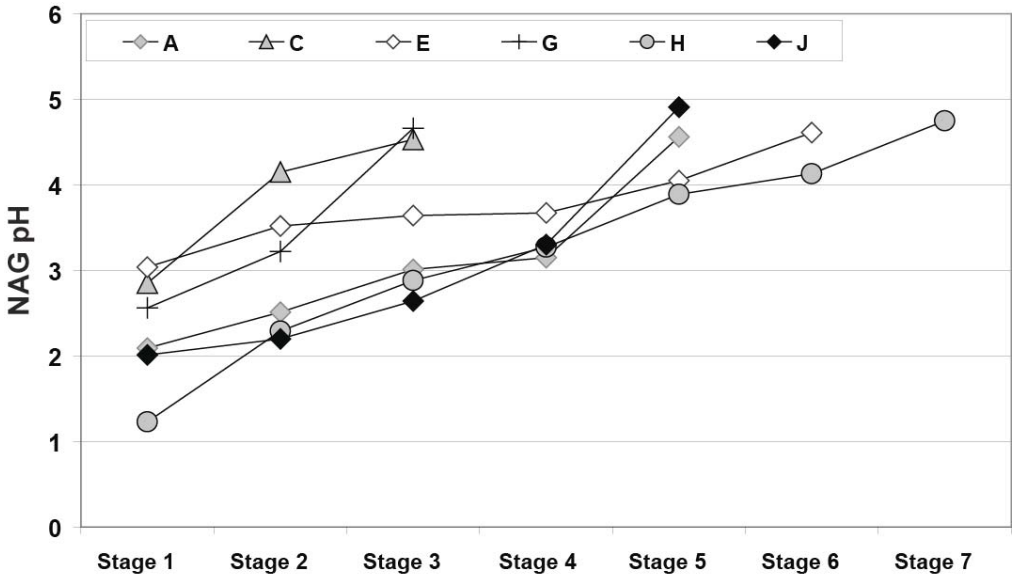

Figure 3.24 Final pH after each sequential NAG stage for samples from Croydon waste rock mesotextural groups A, C, E, F, G, H and J.

Table 3.10 Number of stages until pH 4.5 was achieved in the sNAG test compared against S_{Total} values for one sample each from Croydon waste rock mesotextural groups A, C, E, G, H and J.

Group	Number of stages til pH ≥4.5	S_{Total} (wt. %)
A	5	3.75
C	3	0.14
E	6	0.46
G	3	3.20
H	7	14.50
J	5	8.24

Comparison of sNAG values with single addition NAG results showed that greater acidity is returned from the prior test (Figure 3.26). Highly sulphidic samples from group H and J (Table 3.10) showed the greatest deviation from the model (1:1) line with the sNAG test returning values 47 and 30 kg H_2SO_4/t respectively. This is, however, within the acceptable 20% error margin for samples with >1 wt. % proposed in Stewart (2005). Comparison of mNAG values against single addition NAG is shown in Figure 3.27. Deviation from the 1:1 line was non-systematic even within mesotextural groups, with three group J samples plotting above, and one below. Similar observations were made in Stewart (2005) for coal mine waste samples. Two samples with >1wt. % S_{Total} exceeded the acceptable 20% error margin

(Stewart, 2005). However, no differences were observed when mNAG values were used instead of NAG values in the NAG versus paste pH classification, with pyrite rich samples from group J consistently identified as high risk (Figure 3.28).

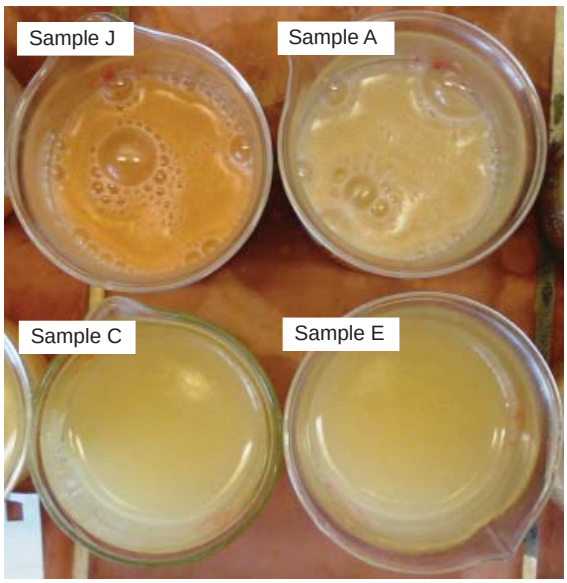

Figure 3.25 Sequential NAG pH reaction liquors at stage 1. Sample J and A only effervesced, indicating a temperature increase, and therefore, an influence on sulphide oxidation reaction kinetics.

A comparison of acidity values calculated for single addition NAG, sNAG, mNAG, and NAPP tests is shown in Figure 3.29. No test method consistently measured the most/least acidity; however, some general observations can be made. Firstly, the single addition NAG test generally returned the lowest results, which for group J (quartz-pyrite) is significant when compared against NAPP and sNAG values. This indicates that pyrite-rich mine wastes should routinely be subjected to advanced NAG tests (i.e., bypassing single addition NAG). Considering that the majority of S_{Total} from this group is from $S_{Sulphide}$ (pyrite), the NAPP values cannot be presumed to have overestimated acidity. Therefore, sNAG appears the more accurate advanced NAG test, as these values most closely approximated NAPP.

Whilst mNAG and sNAG both return greater quantities of acidity than single addition NAG and NAPP, the difference between them was 13 kg H_2SO_4/t. For the group H sample, the sNAG test took seven stages to reach completion using 1.75 litres H_2O_2. The mNAG test used 250ml H_2O_2 and took less time to achieve a result which was within the 20% accepted error margin for samples containing S_{Total} >1 wt. % (Stewart, 2005). Additionally, the high result for groups C and E were measured by the sNAG test, which would classify them both as PAF, but by all other methods the analysed samples were identified as NAF. Potentially, this implies sNAG is overaggressive for samples with low S_{Total} values; for these samples, single-addition NAG values most closely approximated NAPP. Thus, for sulphide-rich, carbonate-poor samples with low S_{Total} (i.e., <0.3 wt. %), the single addition NAG test is appropriate for use. For samples containing S_{Total} >0.3 to 3 wt. % the mNAG test should instead be routinely performed. It should also be performed on samples dominated by sulphides other than pyrite (i.e., arsenopyrite, galena, and sphalerite). If results deviate greatly from NAPP (due to an overestimation

based on the MPA calculation assumption), then single addition NAG can be performed to cross-check mNAG values. For samples containing >3 wt. % pyrite, the sNAG test should be undertaken, as the mNAG test underestimated acidity relative to NAPP.

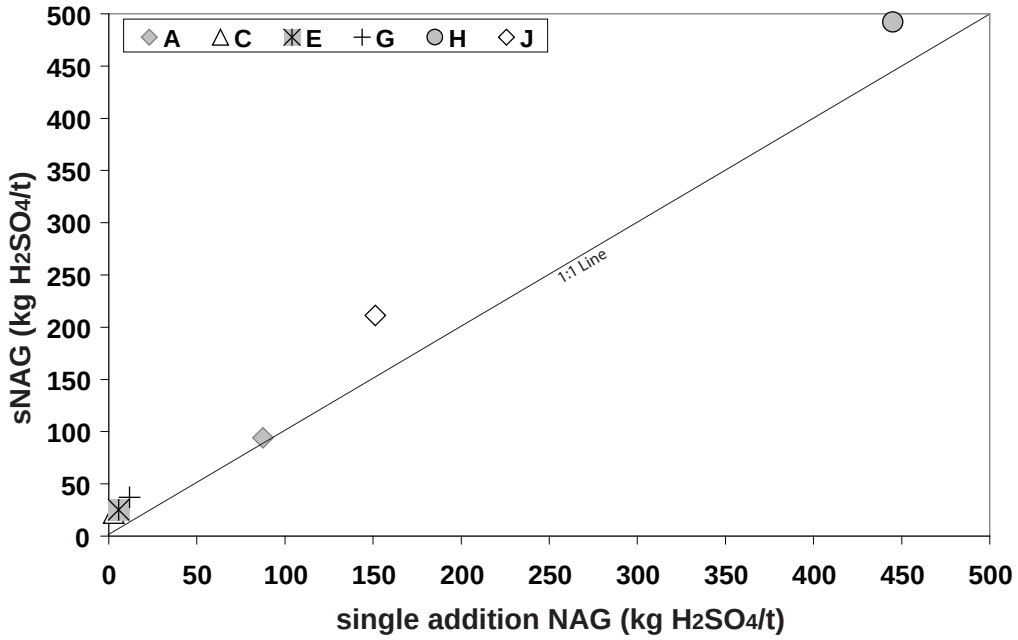

Figure 3.26 Sequential NAG acidity versus single addition NAG acidity to pH 7.0 for samples from Croydon waste rock mesotextural groups A, C, E, F, G, H and J.

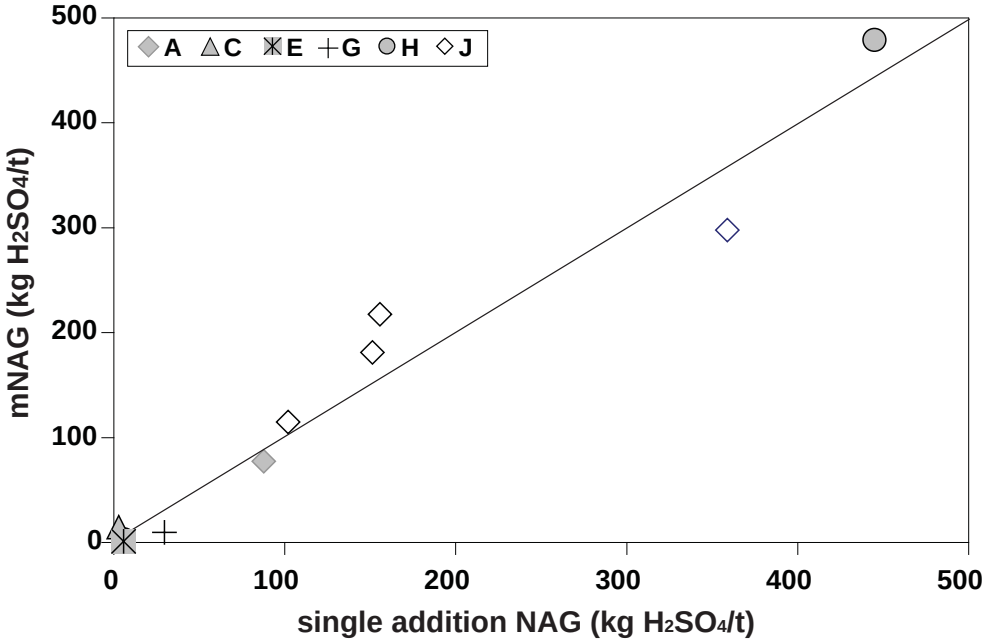

Figure 3.27 Multi-addition NAG acidity versus single addition NAG acidity to pH 7.0 for samples from Croydon waste rock mesotextural groups A, C, E, G, H and J.

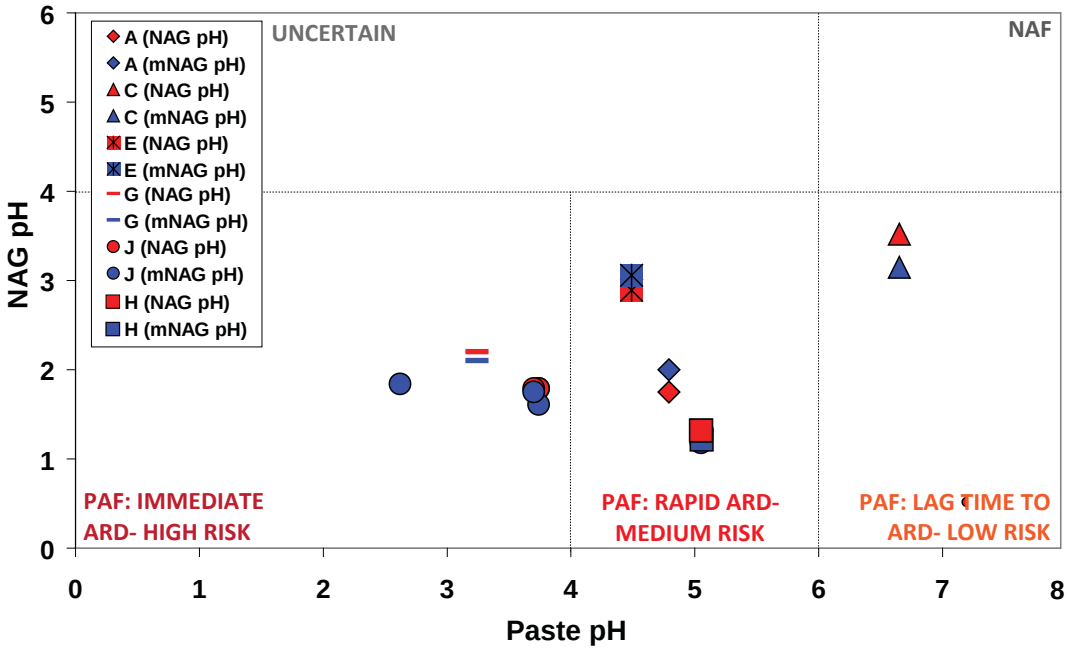

Figure 3.28 Risk classification comparisons of multi-addition NAG pH and single addition NAG pH values shown against paste pH for samples from Croydon mesotextural groups A, C, E, G, H and I.

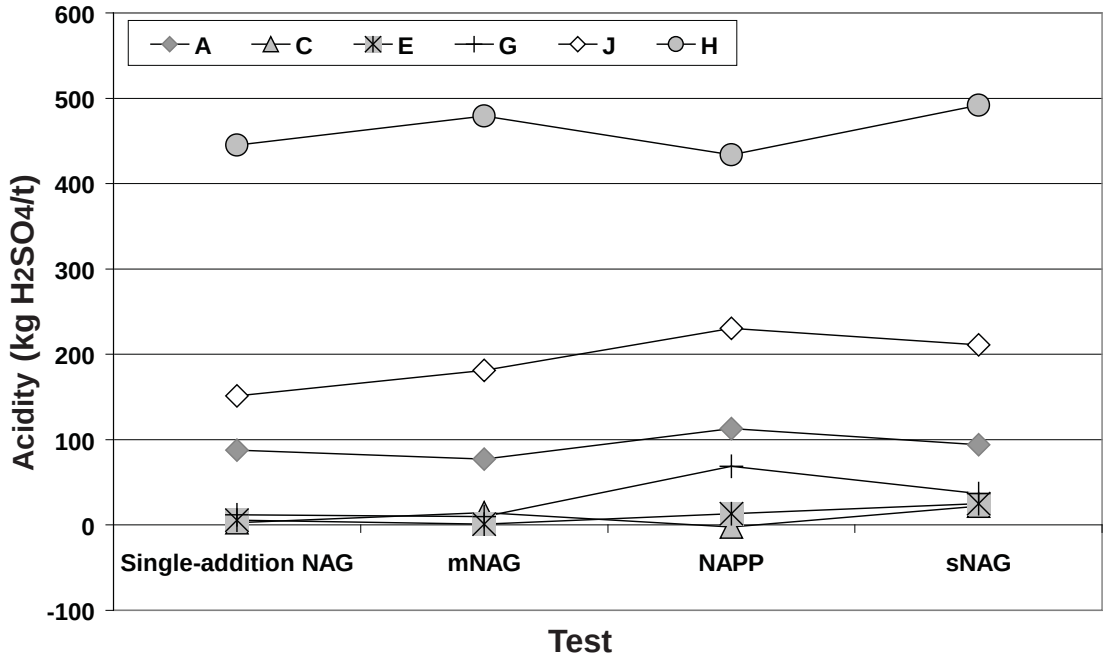

Figure 3.29 Acidity values measured by different testing methods: single addition NAG, sequential NAG, multi-addition NAG and NAPP (values in kg H_2SO_4/t).

Kinetic NAG tests were performed on eight samples from group C, G, H and J (Figure 3.30). The minor pyrite bearing sample (group C) consistently remained above pH 4.0 to test completion (Figure 3.30a). However, the pH declines through the duration of the test, indicating slow pyrite oxidation. By the scale-up table proposed by Stewart et al. (2006), ARD conditions would not be established in a column leach test containing this waste material for at least two years. Two different results were obtained from galena-sphalerite-pyrite samples (group G), with a steady pH decline observed in Figure 3.30b (pH 4.0 at 50 minutes), and a rapid decline in Figure 3.30c (pH 4.0 at 5 minutes). The pH of the sample shown in Figure 3.30c continued to decline; however, for the sample shown in Figure 3.30b, it remained around pH 4.0 for the duration of the test. Differences are attributed to mineralogical variations, with the sample shown in Figure 3.30c containing more galena and pyrite than that tested in Figure 3.30b. The scale-up method proposed by Stewart et al. (2006) cannot be applied to this group as it contained a high proportion of mixed sulphides (Stewart, 2005). Pyritic (group J) samples achieved pH 4.0 between 5 to 17 mins (and remained pH <4 for the test duration), and therefore are predicted to take between 1 to 4 months for ARD conditions to be established in column leach tests (Stewart et al., 2006). The arsenopyrite sample (group H) achieved pH 4.0 after ~5 minutes (Figure 3.30h), and sustained the lowest pH (1 to 2) values to test completion out of all the groups. The temperature profile showed a different curve to the characteristic curve for pyritic samples as described in Stewart (2005; Figure 3.30d-g), with a maximum temperature of ~32°C measured compared to >50°C for pyrite-bearing samples. This indicates that arsenopyrite is less reactive than pyrite in the NAG test. The lower sustained pH conditions reflect that the group H sample used had a higher sulphide content (60.3 wt.% arsenopyrite) than the group J samples (max. 5.2 wt.% pyrite).

3.4.4.2 Textural and chemical analysis of sulphide bearing groups

A combination of microanalyses (MLA, SEM, EPMA, LA-ICPMS and μXRF) were performed on samples from groups A, C, E, G, H and J to: (1) examine sulphide mineral-associations (and cross-check assumptions made by the ARDI); (2) observe sulphide weathering products (as identified by QXRD) and; (3) quantify trace elements in sulphides and measure their distribution. Results of these analyses are given in the following sections.

• *Group A*

The MLA XBSE function measured <1 wt. % pyrite in the Group A MLA-tile, with the mineralogy dominated by quartz (59 wt. %) followed by muscovite (19 wt. %; Figure 3.31a). In this mesotextural group, pyrite was identified in quartz veins only (Figure 3.4). However, XBSE analysis also identified <100μm disseminated pyrite in the groundmass (Figure 3.31c). Quartz-associated pyrite has undergone weathering as a consequence of fluid migration via micro-fractures (Figure 3.31b), with secondary sulphates precipitated. Muscovite-quartz-associated pyrite has also extensively weathered, with more secondary sulphate phases identified in the groundmass than primary pyrite grains. These observations indicate that the ARDI classification of this sample as NAF is valid, as based on the modal content of pyrite in this sample, <1kg H_2SO_4/t would be produced.

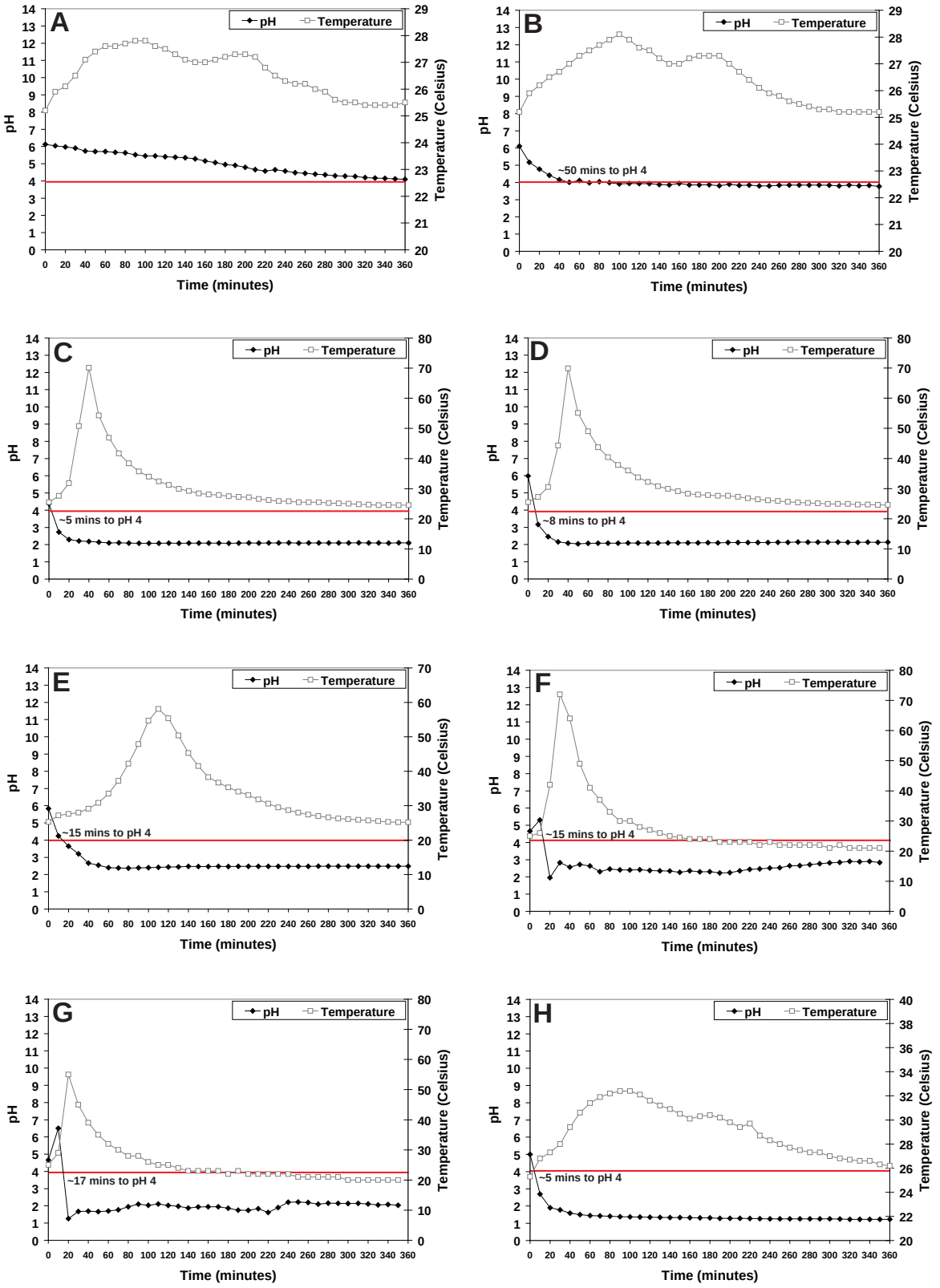

Figure 3.30 Kinetic NAG results for Croydon waste rock samples: **(A)** Group C; **(B)** and **(C)** Group G; **(D)** to **(G)** Group J; and **(H)** Group H.

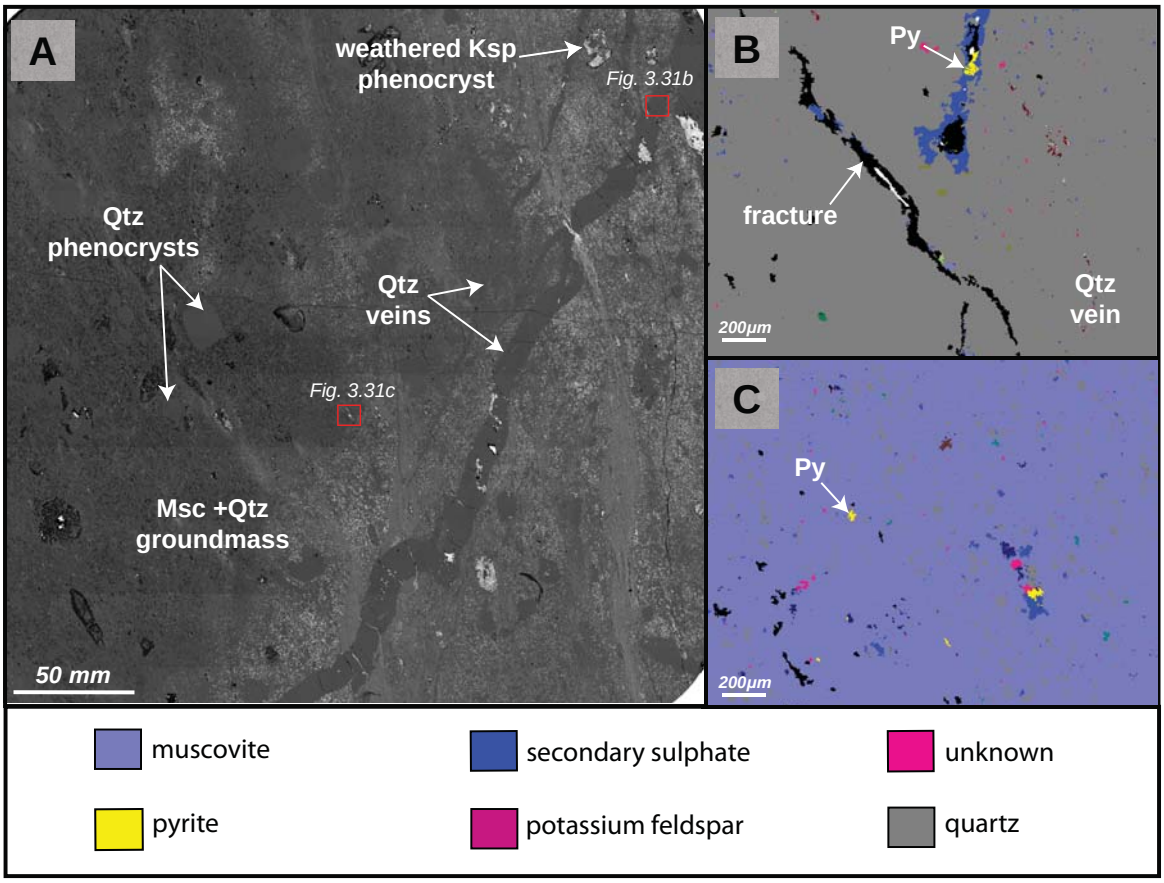

Figure 3.31 MLA tile (3cm x 3xm) analysis of material from Croydon waste rock mesotextural group A (porphyritic rhyolite): **(A)** Back scattered electron image of the MLA tile; **(B)** XBSE mineral map from a section in a quartz vein containing pyrite with an extensive secondary sulphate rim; **(C)** XBSE mineral map of a portion of the muscovite dominated groundmass with disseminated pyrite sparsely distributed. Abbreviations: Ksp, potassium feldspar; Msc, muscovite; Py, pyrite; Qtz, quartz.

• *Group C*

MLA XBSE analyses indicated that sulphides (<1 wt. %) were present in both the groundmass and quartz veinlets in group C (Figure 3.32). In general, muscovite-quartz associated pyrite was less weathered than in group A, with fewer secondary phases identified. Larger muscovite-quartz associated pyrite grains were euhedral, whereas smaller anhedral grains appeared more weathered (Figure 3.32b). Galena micro-inclusions were occassionally observed in the weathered portion of muscovite-quartz associated pyrite grains. Arsenopyrite, which had not been identified during mesotextural classification, was located in quartz veins (Figure 3.32c) and the groundmass. SEM analyses showed that muscovite-quartz associated arsenopyrite grains were rimmed with scorodite, with original euhedral grain boundaries preserved (Figure 3.33a). Galena microinclusions were observed in the weathered portion of muscovite-quartz associated pyrite grains (Figure 3.33b).

LA-ICP-MS element mapping was undertaken on a quartz-associated pyrite grain where a distinct weathering product was observed to rim the primary grain (Figure 3.34a). The BSE image (Figure 3.34b) shows the upper weathered portion to contain galena, with some micro-inclusions also seen in the main body of the grain. SPL_Lite mineral mapping (Figure 3.34c) identified three secondary mineral phases in the weathered portion, two secondary sulphates (here termed Ss1 and Ss2) and a hydrous ferric oxide

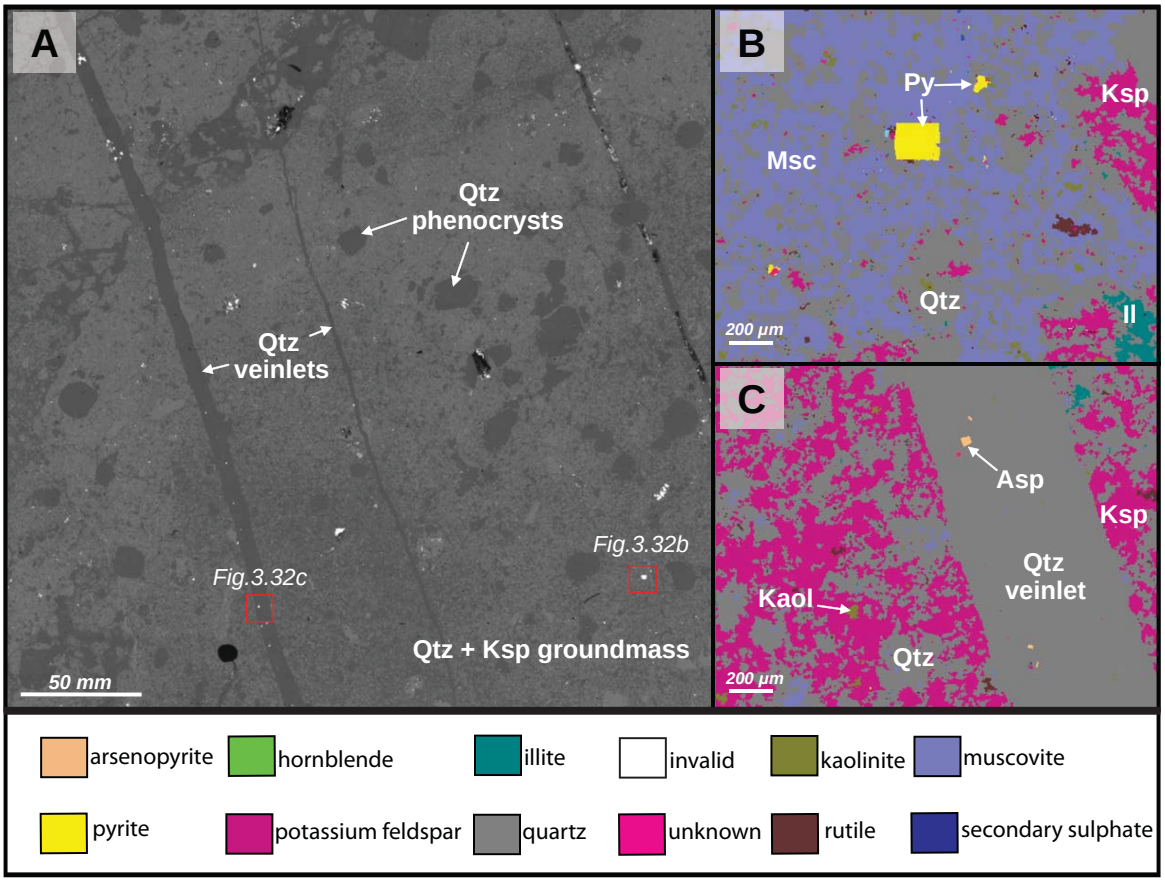

Figure 3.32 MLA tile (3cm x 3xm) analysis of material from Croydon waste rock mesotextural group C (porphyritic rhyolite): **(A)** Back scattered electron image of MLA tile; **(B)** XBSE mineral map of pyrite in the fine-grained muscovite-quartz groundmass; **(C)** XBSE mineral map of arsenopyrite in a quartz vein. Abbreviations: Asp, arsenopyrite; Il, illite; Kaol, kaolinite; Ksp, potassium feldspar; Msc, muscovite; Qtz, quartz.

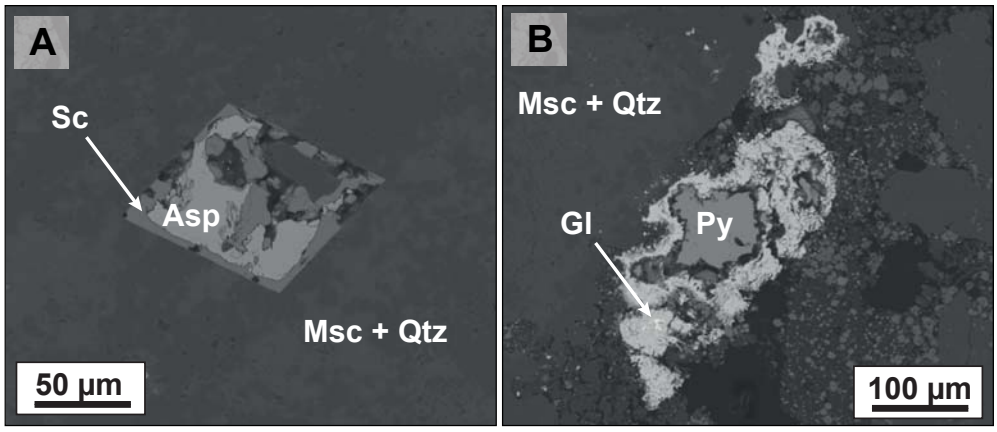

Figure 3.33 Back scattered electron images of sulphides from Croydon waste rock mesotextural group C: **(A)** Muscovite-quartz associated arsenopyrite with a well developed scorodite rim; **(B)** Muscovite-quartz associated weathered pyrite with galena microinclusions identified in the weathered portion. Abbreviations: Aspy, arsenopyrite; Gl, galena; Msc, muscovite; Py, pyrite; Qtz, quartz; Sc, scorodite.

(HFO). Qualitative element maps (left-hand images) and element maps overlain on mineral maps (right-hand images) are shown in Figures 3.34d to 3.34k. The grain core is dominated by As and Au, and secondary sulphate phases by Co and Ni. Hotspots of Pb, Ag, Zn and Sb are located both within the grain, and in the upper weathered portion.

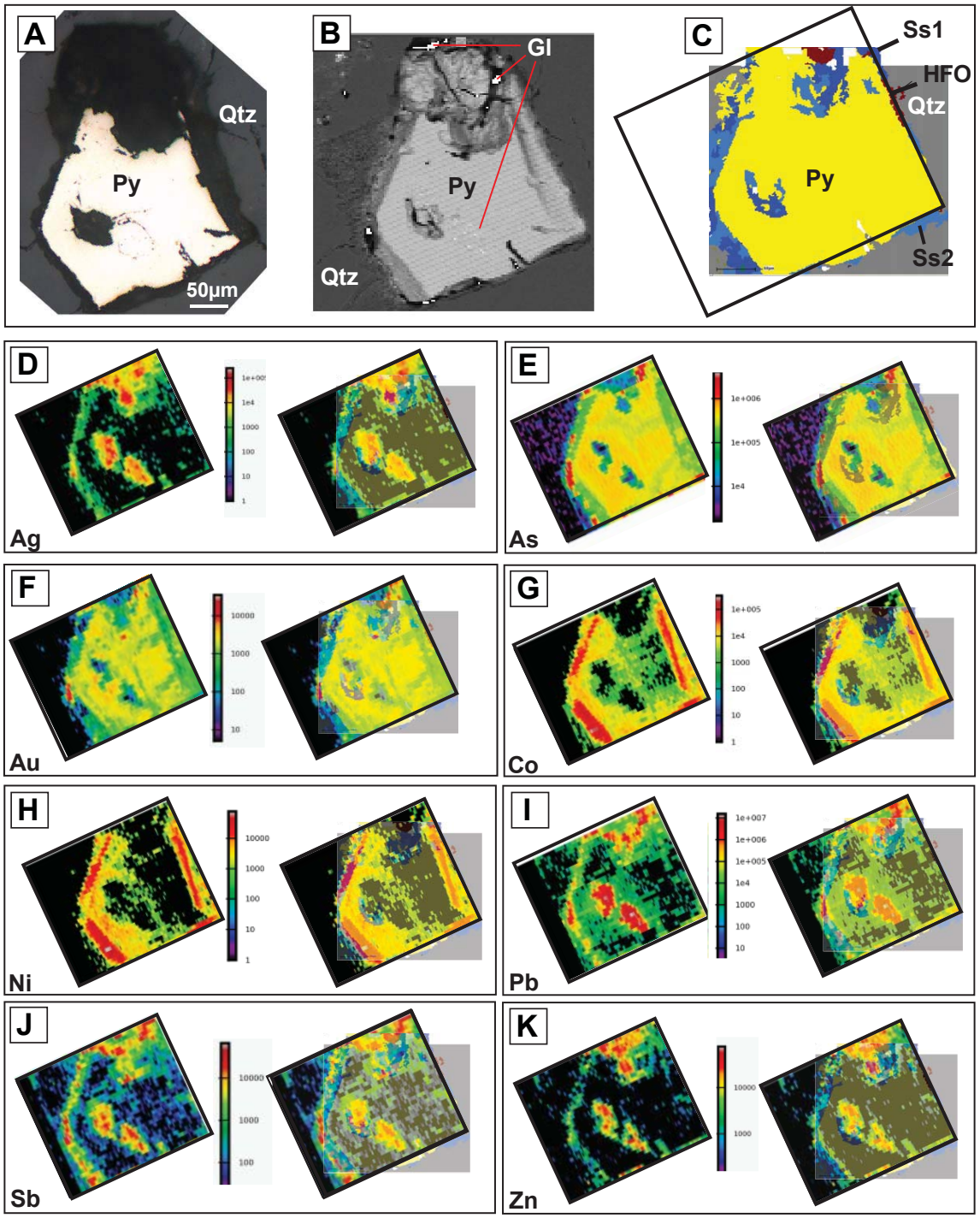

Figure 3.34 MLA SPL_Lite mineral maps and LA-ICP-MS element maps of a quartz-associated pyrite grain from Croydon waste rock mesotextural group C: **(A)** Reflected light image; **(B)** BSE image of the grain shown in A; **(C)** Classified MLA mineral map; **(D to K)** Selected element maps shown to the left, and the element map overlain on the mineral map to the right. Abbreviations: Gl, galena; HFO, hydrous ferric oxide; Py, pyrite; Qtz, quartz; Ss1, secondary sulphate phase 1; Ss2, secondary sulphate phase 2.

The element distribution suggests three generations of pyrite growth, with early stage fluids being Pb-rich, causing precipitation of galena microinclusions, fluids were then depleted in Pb during the intermediate stage, and then finally were Pb-rich, with larger galena inclusions developed. Pyrite core weathering is occurring due to the presence of galena micro-inclusions causing strain on the pyrite lattice (cf. Lottermoser, 2010), with weathering textures as shown in Figure 3.13b formed. Oxidation

of the outer grain boundary has occurred due to the presence of galena inclusions, however, these are larger so an extensive weathering zone has developed around the grain. QXRD identified anglesite, which is depicted in Figure 3.34c as secondary sulphate phase 1 (Ss-1) as suggested by the distribution of Pb. Szomolnokite mixtures can have a significant capacity to retain Zn as shown in Buckby et al. (2003) where a szmolnokite/halotrichite/copiapite sample obtained from the Rio Tinto mining district contained 179,000 ppm Zn. Given the relative enrichment of Zn in secondary-sulphate phase-2 (Ss-2), this is inferred to be either szomolnokite and/or rhomboclase.

• *Group E*

MLA XBSE analyses indicated that Group E also had a low pyrite content (<1 wt. %), the majority of which is located within the muscovite-potassium feldspar-quartz groundmass (Figure 3.35). In general, pyrite grains were subhedral-anhedral. Muscovite-associated pyrite (Figure 3.35b) appeared more susceptible to weathering than potassium feldspar-associated pyrite (Figure 3.35c). Additionally, larger muscovite-associated pyrite grains (<200 µm) appeared more weathered than smaller grains, with their grain boundaries more serrated and secondary sulphate replacement products extensively developed as rims (Figure 3.36).

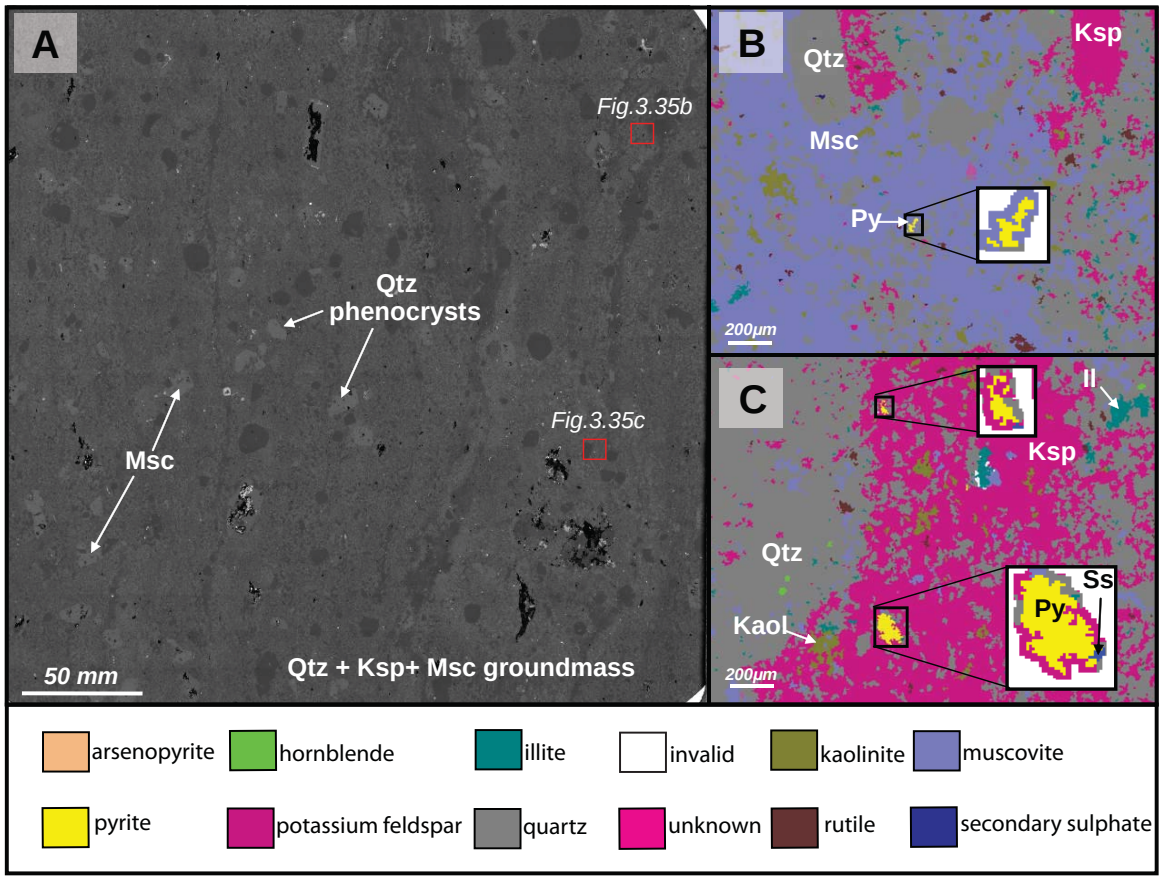

Figure 3.35 MLA tile (3cm x 3xm) analysis of material from Croydon waste rock mesotextural group E (porphyritic-flow banded rhyolite): **(A)** Back scattered electron image of MLA tile; **(B)** XBSE mineral map of muscovite-associated pyrite; **(C)** XBSE mineral map of potassium feldspar- and quartz-associated pyrite. Abbreviations: il, illite; Kaol, kaolinite; Ksp, potassium feldspar; Msc, muscovite; Py, pyrite; Qtz, quartz; Ss, secondary sulphate.

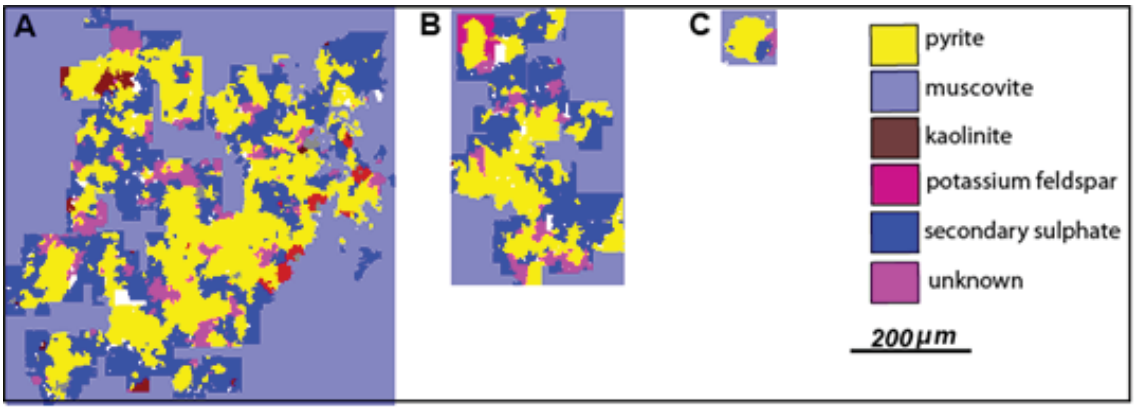

Figure 3.36 Classified XBSE mineral maps of muscovite-associated pyrite grains from Croydon waste rock mesotextural group E, indicating stronger weathering of larger pyrite grains.

• *Group G*

MLA XBSE mineral mapping confirmed that sphalerite and galena were associated with each other and with quartz in group G (Figure 3.37a). Larger sphalerite grains (>500 µm) appeared more weathered than smaller grains (<100 µm; Figure 3.37b and c). Larger quartz-associated sphalerite grains contained pyrite intercalated within fractures (Figure 3.37b) with secondary sulphates forming from its weathering. Quartz-associated galena appeared unweathered over a range of grain sizes (i.e., <100 µm: Figure 3.37d; >200 µm: Figure 3.37e). When sphalerite and galena are intergrown, both appear more weathered with serrated grain boundaries observed and secondary sulphates (including anglesite) developed (Figures 3.37f and 3.37g).

Secondary electron images of galena grains revealed the presence of two galena microtextures (Figures 3.38a to 3.38c). The first shows differential alteration within a galena grain (Figures 3.38a and 3.38b). A well-developed reaction front is observed, with dull-grey, fine-grained porous anglesite forming as a secondary product in the lower portion of the grain, and the upper portion of the grain unweathered. Similar observations are shown in Diehl et al. (2008), who stated that at the reaction interface, metals are likely to enter solution. Galena is much less weathered in the second microtexture, but is anhedral with a serrated grain boundary. This indicates early stages of weathering (i.e., acid-etching of the grain boundary), with anglesite yet to develop. Within group G, preferentially oxidation of sphalerite with galena inclusions was observed (Figure 3.38e). Coarse-grained sphalerite appears fractured; however, no secondary products were observed (Figure 3.38f).

Sphalerite composition is variable as a result of cation substitution within the ZnS structure with Fe the most common element to substitute followed by Cd and Mn (Stanton et al., 2008). Substitution of such cations affects oxidation rate as discussed with high Fe contents (i.e., >6 wt. %) increasing dissolution rate (Weisner et al., 2004; Stanton et al., 2006). Sphalerite in group G is iron rich, containing on average 8.4 wt. % Fe and 0.19 wt. % Cd (n=4). The bulk chemical composition was calculated as $(Zn_{0.85}, Fe_{0.15})S$. Therefore, these grains are likely to be relatively susceptible to weathering (compared to trace element poor sphalerite). Element mapping and spot analyses were undertaken to examine Fe

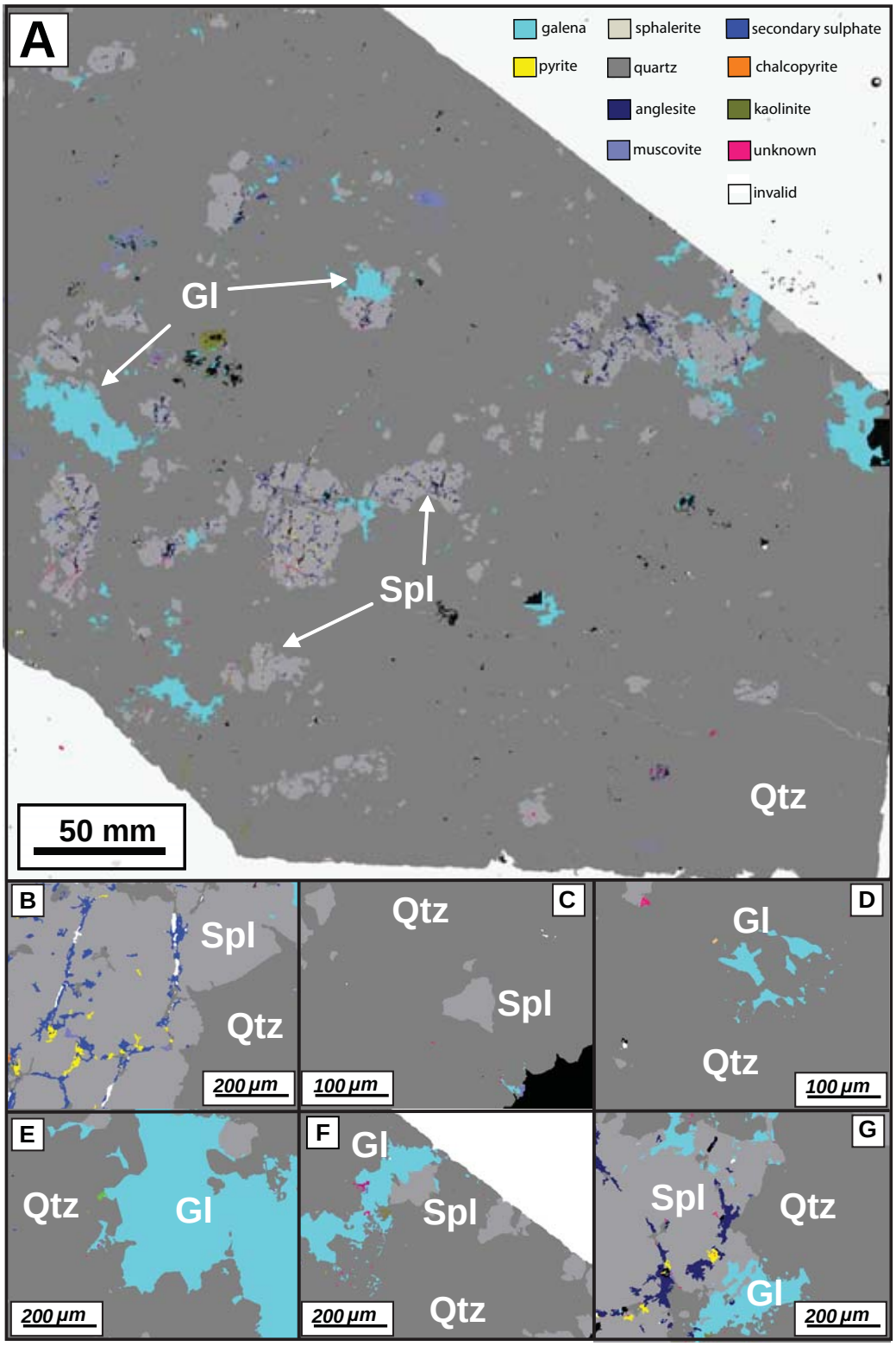

Figure 3.37 MLA tile (3cm x 3xm) analysis of material from Croydon waste rock mesotextural group G (semi-massive quartz-sulphide): **(A)** Classified XBSE mineral map image of the whole MLA tile; **(B)** Quartz-associated sphalerite with intercalated pyrite weathering to secondary sulphate; **(C)** Unweathered <100 µm quartz-associated sphalerite; **(D)** Unweathered <100 µm quartz-associated galena; **(E)** Unweathered >200 µm quartz-associated galena; **(F and G)** Intergrown galena and sphalerite with anglesite precipitating within sphalerite fractures. Abbreviations: Gl, galena; Qtz, quartz; Spl, sphalerite.

and trace element distribution. A comparative example of element maps collected using LA-ICP-MS and μXRF for a sphalerite grain with galena inclusions is shown in Figure 3.39. Major elements Zn, S and Pb were detected by μXRF, and indicated that the grains are homogenous (Figure 3.39a) which was confirmed by LA-ICP-MS (Figure 3.39b). While Cd was not detected by μXRF (Figure 3.39a), it was detected by LA-ICP-MS (Figure 3.39b) and measured in spot analyses shown in Figure 3.39c (0.16-0.19 wt. %). Additionally, μXRF failed to identify Pb micro-inclusions which are distinct in LA-ICP-MS maps (Figure 3.39b). As a consequence of its inability to map trace elements, μXRF was not used further.

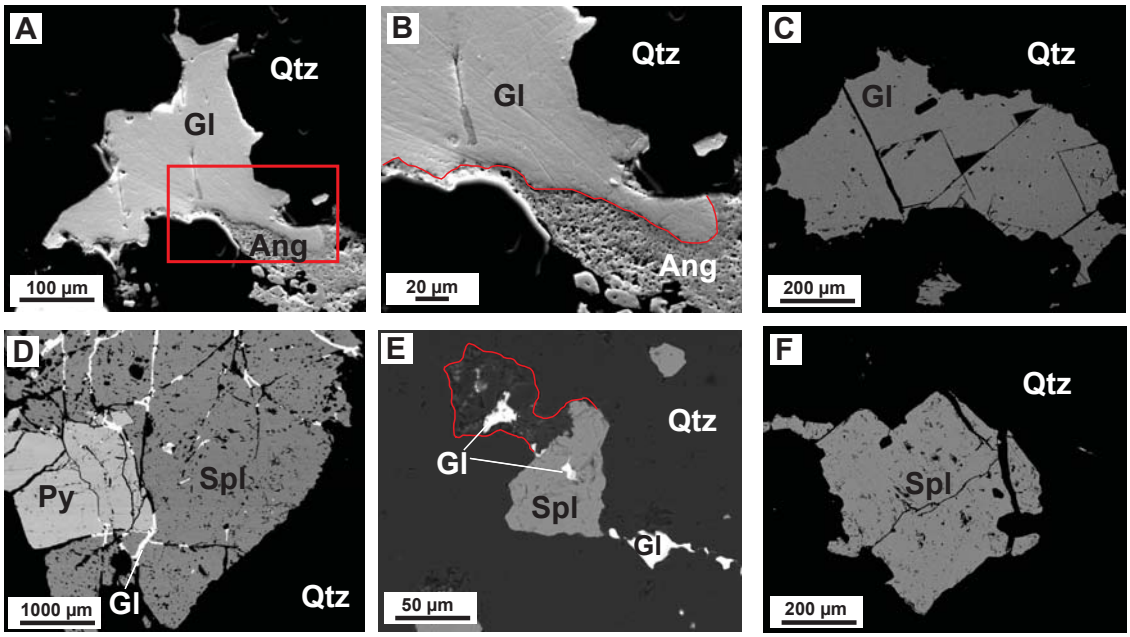

Figure 3.38 Back scattered electron (BSE) and secondary electron (SE) images of galena in waste rock samples from mesotextural group G (semi-massive quartz-sulphide): **(A)** SE Image of galena weathering to porous anglesite; **(B)** Close-up of the altered reaction interface between galena and anglesite; **(C)** Acid-etched grain boundary of a larger galena grain with secondary products yet to develop; **(D)** Sphalerite with galena fracture-fill and chalcopyrite micro-inclusions; **(E)** Finer-grained weathered sphalerite grains (skeletal grain outlined) intergrown with galena; **(F)** Coarser-grained unweathered sphalerite. Abbreviations: Ang, anglesite; Gl, galena, Py, pyrite; Qtz, quartz, Spl, sphalerite.

Additional sphalerite element maps were collected with examples shown in Figure 3.40a and 3.40b. Distribution of Fe and Cd remained relatively homogeneous with both pervasively distributed across the grain. This implies that Fe and Cd are in solid solution, as is typical for these elements (Cook et al., 2009). The measured concentration (by EPMA) of Fe and Cd was greater in sphalerite grains <2000 μm (Figure 3.41). The mapped distribution of Cu (Figure 3.40a and 3.40b) indicates its present as sub-5 μm blebs characteristic of chalcopyrite disease, whereby blebs are typically excreted along crystallographic axis or twin boundaries (Barton and Bethke, 1987; Cook et al., 2009). Otherwise, the measured Cu concentration was generally low (0.02 wt. %). Lead distribution is explained by the presence of galena veins cross-cutting sphalerite (Figures 3.38d and 3.40b). These veins have partially weathered, leaving localised patches of anglesite. A slight decrease in Zn concentration at the grain boundary was observed, which provides evidence for the dissolution of sphalerite to form a Zn-deficient layer (Weisner et al., 2004; Cook et al., 2009).

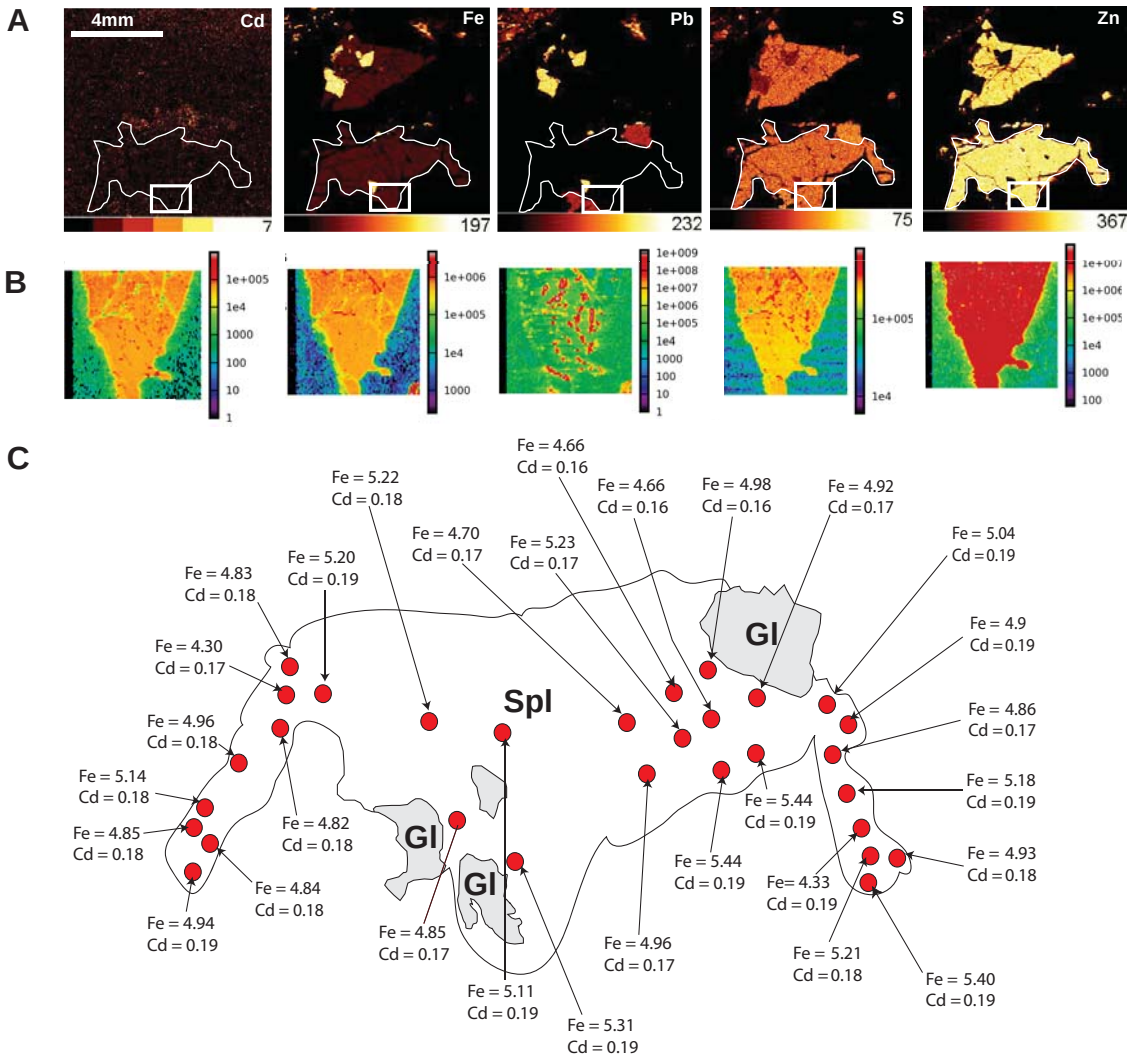

Figure 3.39 Element (Cd, Fe, Pb, S, Zn) distribution in a sphalerite grain (with galena intergrowths) from Croydon waste rock mesotextural group G: **(A)** Qualitative element maps collected by micro-XRF; **(B)** Qualitative element maps collected by LA-ICP-MS (for the area shown in a white box in Figure 3.39a); **(C)** LA-ICP-MS measured Fe and Cd concentrations (n=29) for the grain outlined in Figure 3.39a (Zn measured by EPMA was used as the internal standard).

Galena from group G was also subjected to element mapping with an example shown in Figure 3.40c. Trace element zoning was not observed in the unweathered grain (right-hand portion of the image), which is consistent with observations made by Bethke and Barton (1971) for lead sulphides associated with igneous activity or heated after formation (i.e., orogenic areas). Galena appears relatively enriched in Bi (average: 0.18 wt. %) and Sb (average: 0.05 wt. %), with the weathered portion of the grain (to the left) relatively enriched in As and Fe with similar distributions reported by Diehl et al. (2008). Zinc distribution indicates the presence of sphalerite inclusions in the weathered portion. Where galena and sphalerite are intergrown, oxidation likely progressed at a greater rate as a result of galvanic interactions with sphalerite preferentially weathering as a result of its lower rest potential (-0.24 V) relative to galena (0.28 V; Kwong et al., 2003; Lottermoser, 2010).

Diehl et al. (2007) stated that trace-element rich galena (particularly Ag) is more susceptible to weathering. Trace elements commonly identified in galena include Ag, Bi, Cu, Cd, Fe, Zn, Ni and Sn (Blackburn and Schwendeman, 1977; Foord and Shawe, 1989; Shaefer et al., 2004). These elements were measured in several galena grains using LA-ICP-MS (n= 61).

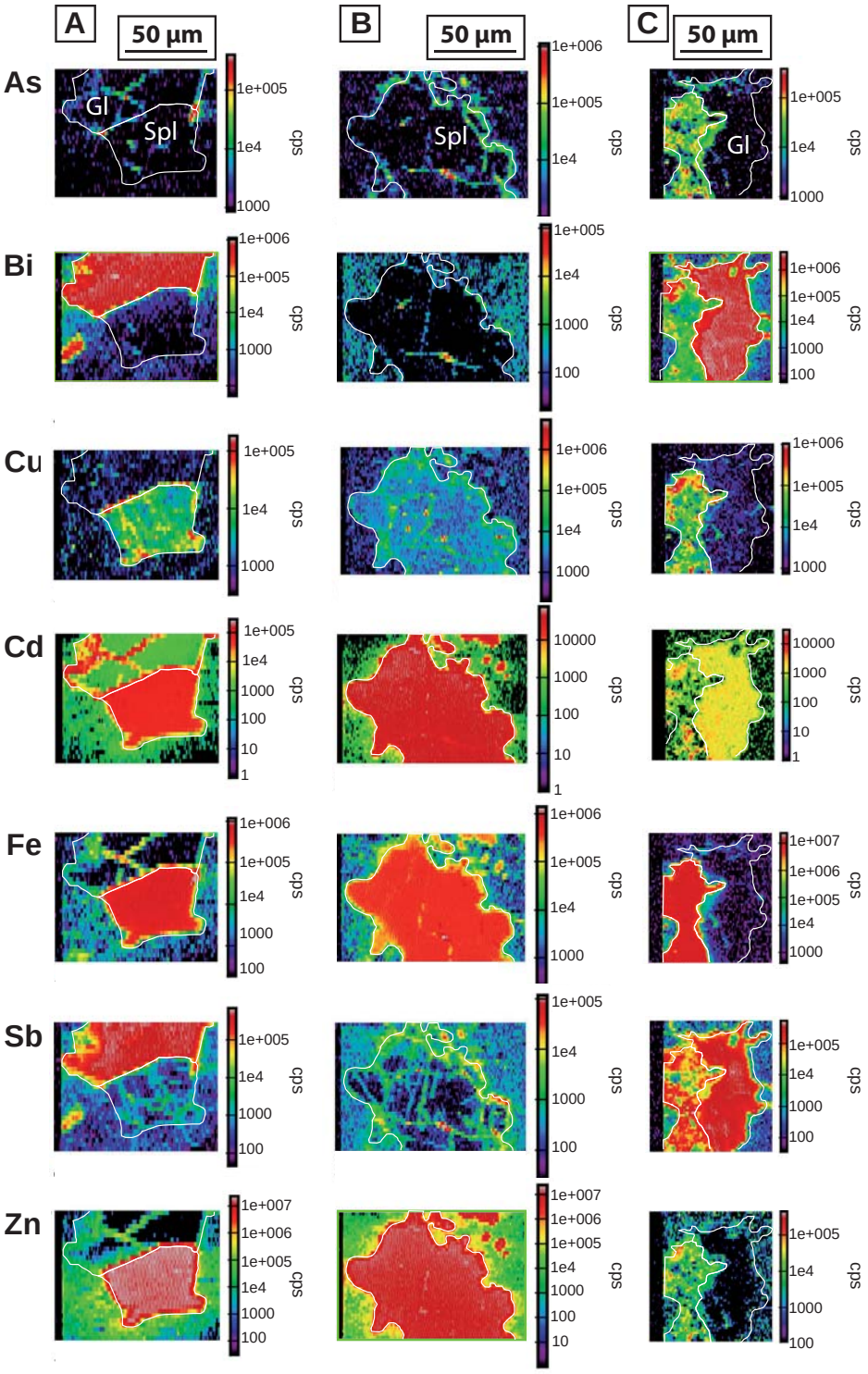

Figure 3.40 Qualitative element maps of Croydon waste material from mesotextural group G: **(A)** Quartz-associated intergrown galena (upper portion) and sphalerite (lower portion); **(B)** Quartz-associated sphalerite and **(C)** Quartz-associated galena (red spots depict LA-ICP-MS spot analyses locations; 47µm spot size, 10 Hz). Abbreviations: Gl, galena; Spl, sphalerite.

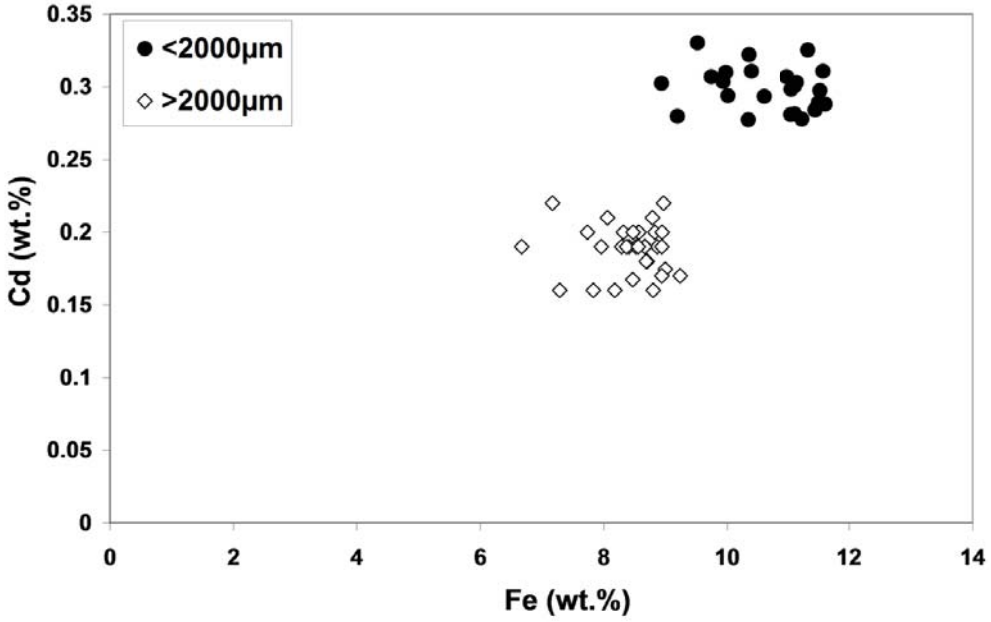

Figure 3.41 Cd and Fe contents in sphalerite from Croydon waste rock mesotextural group G as measured by EPMA (2µm beam size, 20KeV, 15nA; n=58). Data for two different grain sizes are shown.

Both larger (>200 µm) and smaller (<200 µm) grains were analysed and results are summarised in Table 3.11. Significantly higher maximum concentrations of Ag, As, Bi, Cd, and Cu were measured in larger grains, with similar concentrations of Sb measured in both grain sizes. However, mean values were similar for both grain sizes. Thus, galena in group G is considered trace-element rich, and therefore susceptible to weathering (cf. Diehl et al., 2007). Smaller galena grains appeared relatively more weathered (Figures 3.38b and 3.38c), which indicates that grain size is the dominant control on galena oxidation.

Table 3.11 Element concentrations (ppm) in unweathered galena from Croydon waste rock mesotextural group G as measured by LA-ICP-MS spot analysis (spot size: 50 µm; frequency: 5 Hz; energy: 60 %; n= 61). The value for stoichiometric Pb in galena was obtained from www.webmineral.com and was used as the internal standard).

Large galena (>200 µm; n=56)								
	Ag	**As**	**Bi**	**Cd**	**Cu**	**Fe**	**Sb**	**Zn**
Max.	1367	184	1508	80	171	184	1026	51
Min.	504	BDL	340	4	BDL	1	218	BDL
Median	827	4	430	17	9	14	847	1
Mean	840	13	483	19	16	26	790	3
Small galena (<200 µm; n=5)								
Max.	850	3	436	16	6	7	1006	1
Min.	749	1	391	8	3	2	763	BDL
Median	802	2	433	13	3	4	991	-
Mean	806	2	425	12	4	4	943	-

• *Group H*

Mesotextural group H displayed a massive arsenopyrite-pyrite-quartz texture with scorodite extensively precipitated at the interface of these minerals, and within fractures (Figure 3.42a). Pyrite appears relatively unweathered when encapsulated in scorodite, with euhedral grains well preserved (Figures 3.42b and 3.42c). When intergrown with arsenopyrite, quartz-associated pyrite is weathered to a greater degree (Figure 3.42d). Scorodite is relatively thick within arsenopyrite, with a dendritic texture observed (Figure 3.42e). Smaller quartz-associated arsenopyrite grains (<200 μm) appear unfractured and unweathered (Figure 3.42f). Galena was observed on the boundary of an arsenopyrite grain (Figure 3.42g). Back scattered electron images show scorodite rims have precipitated on finer-grained arsenopyrite in addition to kankite ($FeAsO_4.3.5(H_2O)$; Figure 3.43a). Scorodite was observed in a variety of microtextures when associated with pyrite (Figure 3.43b) with scorodite 'ribbons' and scorodite spherules (cf. Murciego et al., 2009; DeSisto et al., 2010) observed in fractures, and outside the grain as a mass. Galena micro-inclusions remain a common feature within pyrite, with massive arsenopyrite relatively more fractured than pyrite (Figure 3.43c). Scorodite is observed as a layer of uniform thickness forming parallel to pyrite and/or arsenopyrite (Figures 3.43d and 3.43e). Figure 3.43d shows that adjacent to this layer are amorphous phases rich in As, Cu, Fe and Pb. These represent weathered scorodite, with Cu and Pb likely from sourced chalcopyrite micro-inclusions in pyrite and galena (Murciego et al., 2009). Scorodite is more crystalline adjacent to arsenopyrite than pyrite (Figure 4.43e). Pyrite adjacent to scorodite appears to weaken (with a lighter BSE colour shown) indicating the growth direction of scorodite is away from arsenopyrite. Where scorodite precipitates within arsenopyrite (Figure 4.43f), it does so as a mass, consequently placing strain upon arsenopyrite and causing extensive fracturing.

Lottermoser (2010) stated that minor and trace element substitution does not occur in arsenopyrite as with other sulphides such as galena. Electron microprobe spot analyses of both larger (<200 μm) and smaller (<200 μm) arsenopyrite grains returned concentrations of Cd, Cu, Co, Ni, Pb, Sb and Zn below detection limit. However, qualitative element mapping of unweathered arsenopyrite revealed that Co and Ni concentrate within the main body of the grain (Figure 4.44). In smaller arsenopyrite grains, oscillatory zoning of these elements was observed. Where Co and Ni concentrate fractures are not observed, indicating these elements increase resistance to oxidation as was reported for pyrite by Kwong (1993). Some galena microinclusions are identified in Figure 4.44b, and likely cause the fracturing (seen in the photomicrograph) around this hotspot. Concentrations of Cd, Pb and Zn are relatively high in grain fractures and rims compared to arsenopyrite and quartz, indicating adsorption of these elements to scorodite.

• *Group J*

Pyrite was observed as both grains and very fine (<100 μm) veinlets in group J (Figure 3.45a). Larger euhedral-subhedral pyrite grains appeared slightly more weathered than smaller grains, with serrated grain boundaries displayed; however, secondary products have yet to develop (Figure 3.45b, 3.45c and 3.45d). Pyrite was occasionally intergrown with galena and demonstrated anhedral morphology (Figure 3.45e).

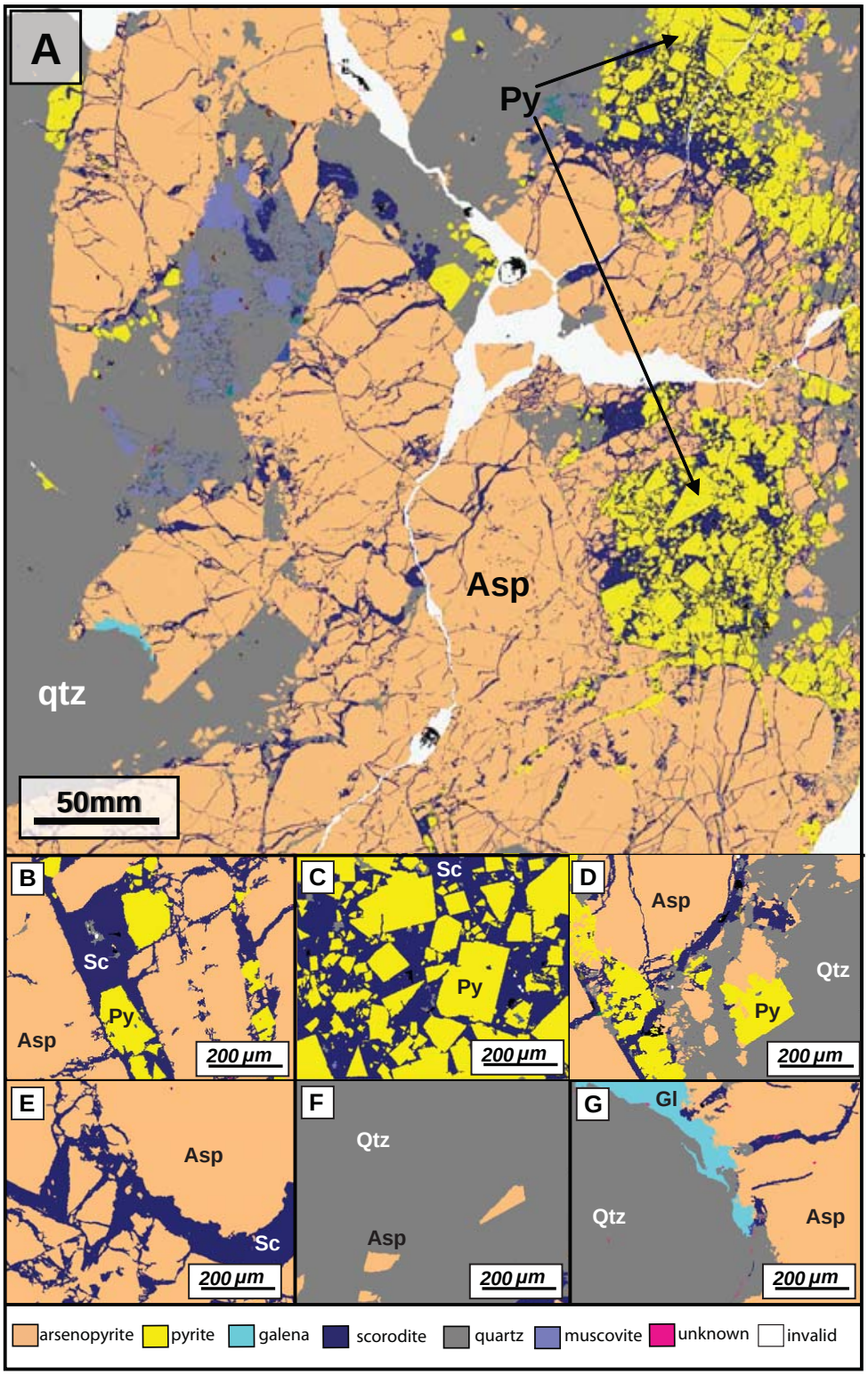

Figure 4.42 MLA tile (3cm x 3xm) analysis of material from Croydon waste rock mesotextural group H (massive arsenopyrite-pyrite-quartz): **(A)** Classified XBSE mineral image of the whole MLA tile; **(B)** Pyrite encapsulated in scorodite within arsenopyrite fractures; **(C)** Pyrite encapsulated within scorodite; **(D)** Arsenopyrite-pyrite intergrowths in quartz; **(E)** Arsenopyrite with thick scorodite precipitated in fractures; **(F)** Quartz-associated arsenopyrite; **(G)** Galena on the rim of massive arsenopyrite. Abbreviatons: Asp, arsenopyrite; Gl, galena; Py, pyrite; Qtz, quartz; Sc, scorodite.

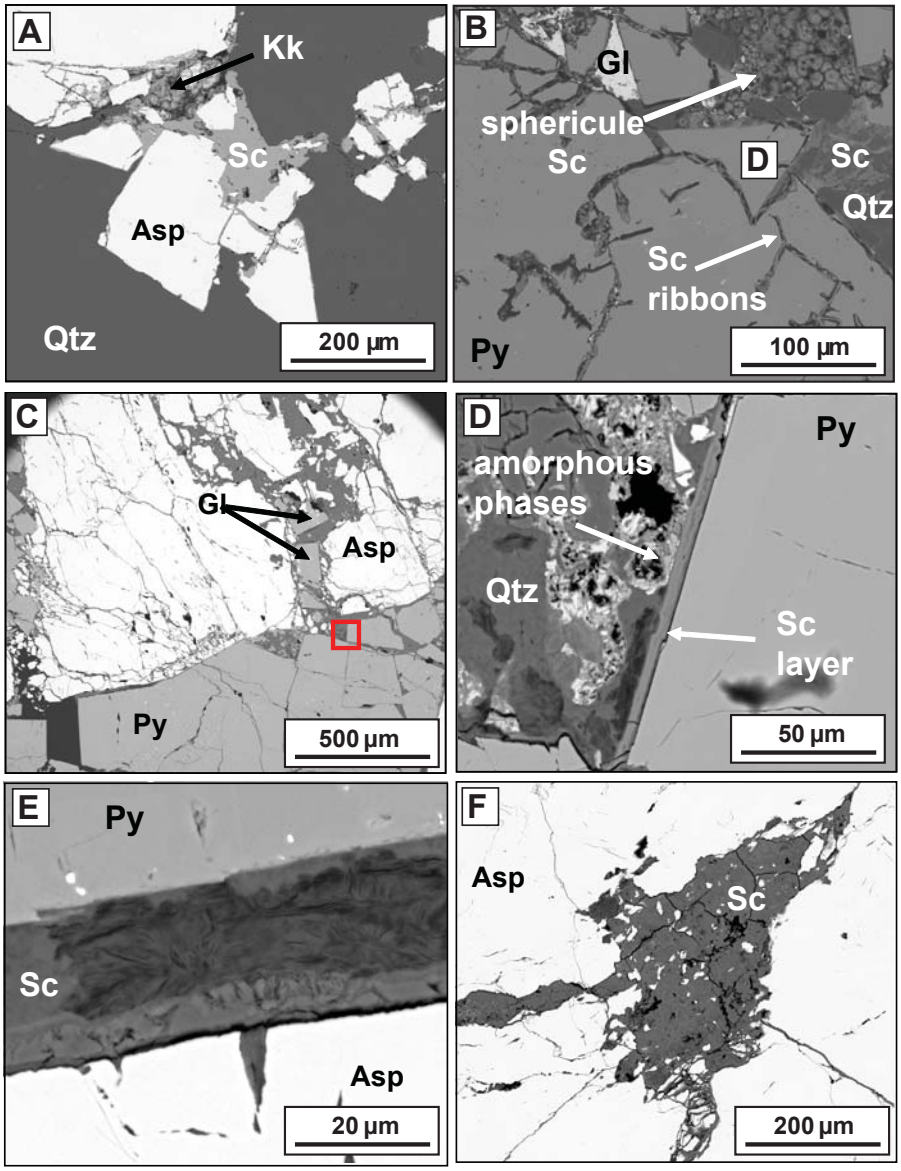

Figure 3.43 Back scattered electron images of arsenopyrite microtextures identified in Croydon waste rock mesotextural group H: **(A)** Scorodite and kankite rimming arsenopyrite; **(B)** Scorodite microtextures (ribbons, spherules and masses) identified in pyrite; **(C)** Massive arsenopyrite and pyrite; **(D)** Poorly crystalline phases identified adjacent to a scorodite layer; **(E)** Internal texture of scorodite rimming both arsenopyrite and pyrite; and **(F)** Scorodite precipitated within massive arsenopyrite. Abbreviations: Asp, arsenopyrite; Gl, galena; Kk, kankite; Py, pyrite; Qtz, quartz; Sc, scorodite.

Pyrite veins in quartz (Figure 3.45f) and the muscovite-quartz groundmass (Figure 3.45g) have weathered along grain boundaries with secondary sulphates formed. Pyrite within the volcanic groundmass (Figure 3.45g) appears more weathered than grains encapsulated in quartz. Back scattered images of quartz-associated pyrite are presented in Figure 3.46. Larger grains are more susceptible to fracturing than smaller grains (Figures 3.46a and Figure 3.46b). The presence of galena micro-inclusions does not directly cause fracturing in isolation, as several are observed in the unfractured grain shown in Figure 3.46a. Instead larger pyrite grains likely have structural defects (i.e., imperfect or distorted lattice) leading to physical stress (Lottermoser, 2010). Complex weathering is shown in Figure 3.46c whereby a poorly crystalline secondary aggregate had precipitated within a

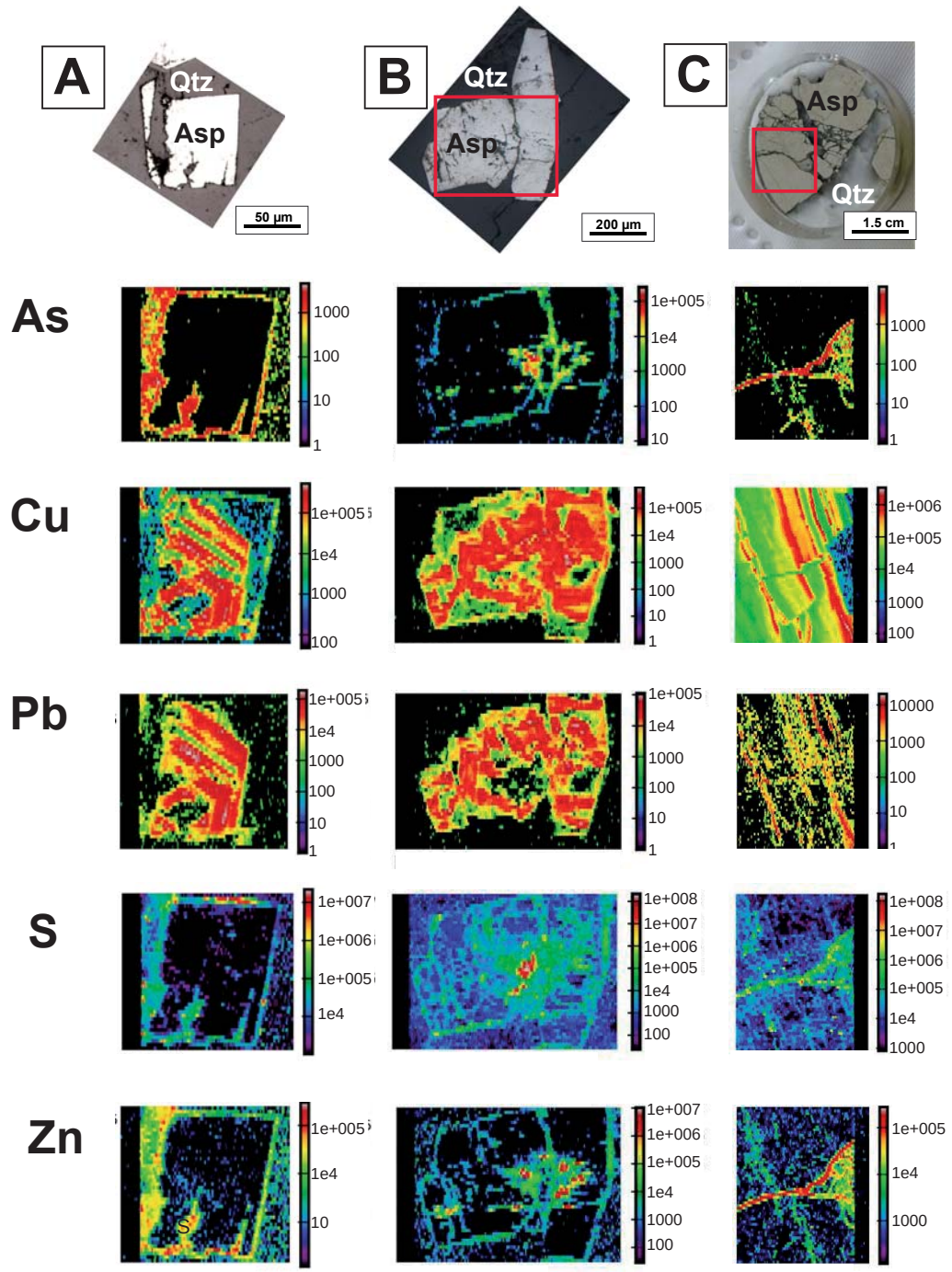

Figure 3.44 LA-ICP-MS qualitative element maps of Croydon waste rock material from mesotextural group H: **(A)** Quartz-associated arsenopyrite grain (<100 µm); **(B)** Quartz-associated arsenopyrite grain (>200µm); and **(C)** Quartz-associated massive arsenopyrite (red boxes depict LA-ICP-MS mapped areas (47µm spot size, 10 Hz)). Abbreviations: Asp, arsenopyrite; Qtz, quartz.

euhedral crystal, with relict pyrite and galena observed within the grain. Additionally, alteration of pyrite to hohmannite ($Fe_2(SO_4)_2(OH)_2.7H_2O$), a low temperature secondary precipitate in oxidised iron sulphide deposits (Scordari, 1978), was indicated by SEM-EDS (Figure 3.46d). An unweathered pyrite grain was observed adjacent to it, indicating chemical differences (i.e., trace elements) between pyrite grains for such differential weathering to have occurred.

Trace elements commonly identified in pyrite include Ag, As, Au, Bi, Cd, Co, Ga, Ge, Hg, In, Mo, Ni, Pb, Sb, Se, Sn, Ti, Tl and V (Lottermoser, 2010). Element distribution maps for both unweathered and weathered pyrite grains (n=7) were produced for group J considering these elements, however, element maps for As, Cu, Pb, S and Zn only are shown in Figure 3.47. Co and Ni were not detected in significant quantities (Appendix 3.3). Element maps of relatively small (<200 μm) pyrite grains with differing degrees of fracturing are shown in Figures 3.47a to 3.47c. The pyrite cores are Pb- and Zn-rich, and additionally contain Cu. Arsenic rims these cores with highest concentrations measured when in contact with the core, and decreasing to the grain rim, suggesting that the core was once As-rich. Arsenic in pyrite decreases resistance to oxidation (cf. Plumlee, 1999; Blanchard et al., 2007), here this has caused accelerated weathering of these cores, which was further enhanced by galena microinclusions (<10 μm diameter) straining the lattice (as indicated as Pb hotspots in Figure 3.46a to 3.46c). Sulphur maps for these grains show a uniform distribution (Figure 3.47a to 3.47c), suggesting that fractures are infilled with secondary sulphates, and not HFO. The quantitative maps shown in Figure 3.47d show some similarities to the previous examples, with three distinct Zn high, As-low areas identified. Lead and As appear to concentrate in the weathered portion to the left of the grain, where S decreases slightly indicating secondary sulphate formation. Element maps presented in Figure 3.47e show the deficiency of As and S in the main portion of the weathered brown phase to the right of the pyrite grain. However, there are localised high patches. This zone is relatively Pb and Fe-rich (Appendix 3.3), indicating this may be a HFO phase. Element maps for extensively fractured larger (>500 μm) grains are shown in Figures 3.47f and 3.47g. No significant compositional zoning was observed in Figure 3.47f; however, Pb distribution indicates widespread intercalation of galena micro-inclusions with further evidence provided by the distribution of Ag and Bi (Appendix 3.3). Arsenic concentrates in fractures with localised Pb-hotspots indicating micro-inclusions of galena are again present (Figure 3.47g). The Zn hotspot towards the bottom right portion suggests that this grain once had a core similar to those observed in Figures 3.47a to 3.47c.

3.4.4.3 Stage-three classification

Advanced geochemical testing results did not change the classification assigned at the end of stage-two (Table 3.12). Of the two advanced geochemical tests, preference is given to the mNAG test for routine use (i.e., to replace NAG testing) when undertaking future geochemical testing at Croydon, or indeed for any waste rock sample >0.3% $S_{sulphide}$. Group H was identified by kNAG tests to be the most acid forming, with pH <2 recorded after 5 minutes, followed by group J. Whilst group G contained on average less pyrite than groups H and J, it is considered high risk because pyrite is intergrown with galena and sphalerite, thus encouraging leaching of base metals Cd, Pb and Zn. Based on full GMT analyses, groups G, H and J were identified as requiring column leach testing, with results presented in Chapter 4.

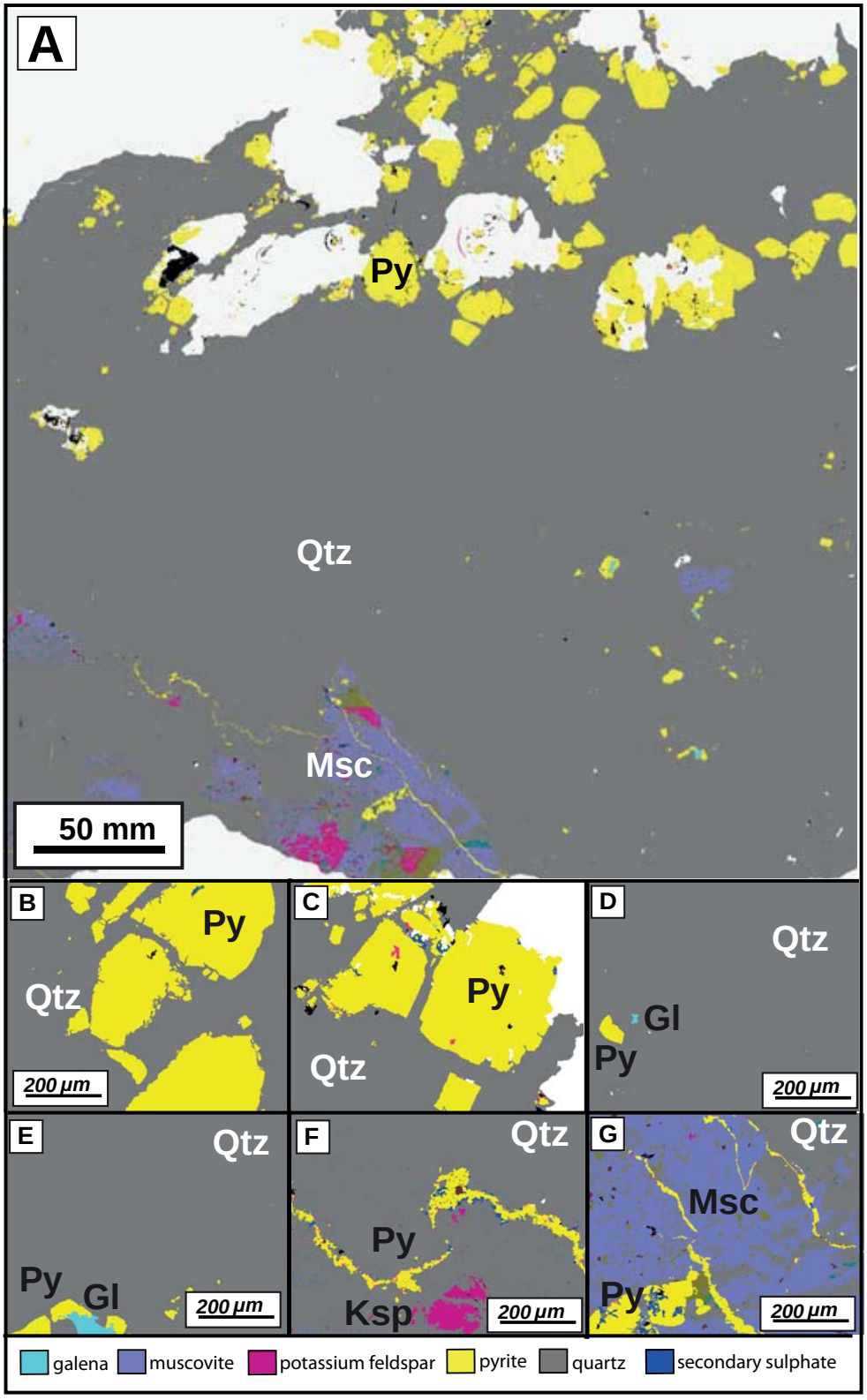

Figure 3.45 MLA tile (3cm x 3xm) analysis of material from Croydon waste rock mesotextural group J (massive pyrite-quartz): **(A)** Whole tile classified image; **(B** and **C)** >200 µm pyrite encapsulated in quartz with slightly serrated grain boundaries; **(D)** <100 µm pyrite in quartz; **(E)** Pyrite-galena intergrowths in quartz; **(F)** Weathered pyrite vein in quartz; **(G)** Muscovite-quartz associated weathered pyrite grain and pyrite veins. Abbreviations: Gl, galena; Msc, muscovite; Ksp, potassium feldspar; Py, pyrite; Qtz, quartz.

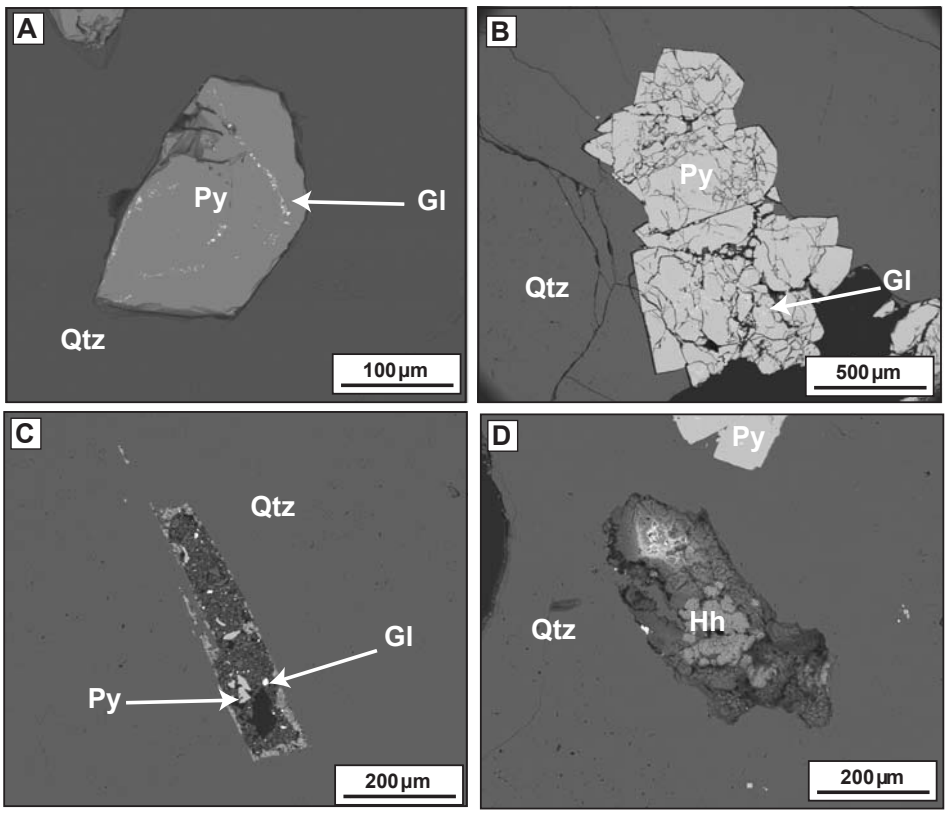

Figure 3.46 Back scattered electron images of quartz-associated pyrite from Croydon waste rock mesotextural group J: **(A)** Unweathered pyrite with galena microinclusions; **(B)** Highly fractured pyrite with galena microinclusions; **(C)** Secondary aggregate replacing pyrite with remnants in the core; **(D)** Pyrite replacement to hohmannite with unweathered pyrite towards the top of the image. Abbreviations: Gl, galena; Hh, hohmannite; Py, pyrite; qtz, Quartz.

Table 3.12 Stage-three GMT approach classification of Croydon waste rock sulphide-bearing mesotextural groups A, C, E, G, H and J.

Group	Stage-two Classification	sNAG	mNAG	kNAG	Potential for metal leaching ?	Final GMT Approach cassification	Risk classification	Column leach testing required?
A	NAF	PAF	PAF	-	No	NAF	Low	No
C	PAF	PAF	NAF	NAF	No	PAF	Low	No
E	PAF	PAF	NAF	-	No	PAF	Low	No
G	AF	PAF	PAF	AF	Yes: Cd, Pb, Zn	PAF	High	Yes
H	EAF	High PAF	High PAF	AF	Yes: As	EAF	High	Yes
J	EAF	High PAF	High PAF	AF	Yes: As, Pb, Zn	EAF	High	Yes

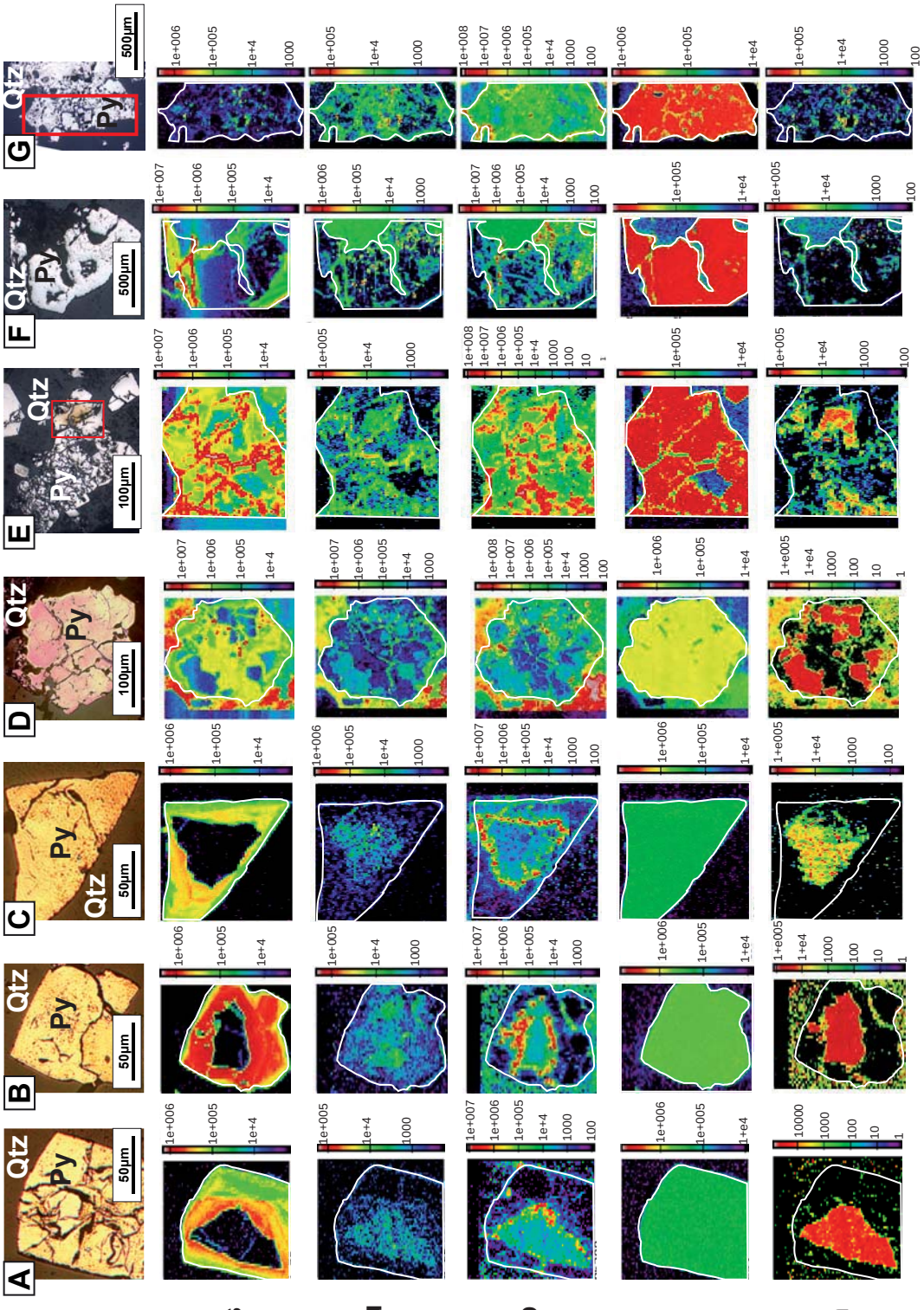

Figure 3.47 LA-ICP-MS element maps of pyrite grains from Croydon waste rock mesotextural group J: (**A** to **C**) Quartz-associated pyrite grains; (**D**) Fractured quartz-associated pyrite grain (>200µm); (**E**) Quartz-associated pyrite with a well developed secondary phase; (**F** and **G**) Extensively weathered >500µm quartz-associated pyrite (red boxes depict LA-ICP-MS mapped areas; parameters for each analysis are given in Appendix 3.3). Abbreviations: Py, pyrite; Qtz, quartz.

3.5 Discussion

3.5.1 Acid forming groups and metal/metalloid sources

Detailed microtextural and chemical studies of the main sulphide-bearing groups (A, C, E, G, H and J) revealed a diversity minerals and, in conjunction with geochemical data indicated the current ARD and metal/metalloid sources. Groups A (muscovite-altered porphyritic rhyolite with minor disseminated pyrite in quartz veins), C (porphyritic rhyolite with disseminated pyrite in quartz veinlets) and E (porphyritic rhyolite with disseminated pyrite in the groundmass) show that groundmass-associated sulphides are more susceptible to weathering than quartz-associated sulphides. Smuda et al. (2007) made similar observations at the Excelsior waste rock dump, Cerro de Pasco, Peru. These authors concluded that fine-grained disseminated pyrite in a volcanic groundmass oxidised much faster than massive pyrite from the ore body due to the high porosity. Element mapping indicated that pyrite in group C is As-rich increasing its susceptibility to oxidation relative to pure pyrite (cf. Plumlee, 1999; Blanchard et al., 2007). Considering this, a significant contribution to the net-ARD was likely made by waste rocks assigned to groups A, C and E. These groups are now classified as either PAF or NAF (as indicated by geochemical test results) with only a small quantity (<1 wt. %) of weathered sulphides remaining.

Paste pH experiments indicate that group G rocks (quartz-galena-sphalerite-minor pyrite) are weakly acid forming (Figure 3.10) with the ARDI classifying them as PAF materials (Table 3.6). Cadmium is primarily sourced from finer-grained sphalerite (<200 μm), which is undergoing oxidation at a greater rate than coarser-grained sphalerite (>200 μm) as a function of surface area, higher Fe-content and presence of galena inclusions (cf. Weisner et al., 2004; Stanton, 2005; Moncur et al., 2009; Lottermoser, 2010). Zinc is also primarily sourced from sphalerite. Neither Zn nor Cd is retained surficially on sphalerite as inferred by element maps (Figure 3.40b), indicating that on oxidation, metal deficient surface layers have formed (cf. Buckley et al., 1989). Chalcopyrite was not detected as a major sulphide mineral in any mesotextural group. However, it was observed in sphalerite as micro-inclusions and is therefore a source of Cu source in the Croydon waste rock piles, however, only low concentrations were measured (average: 0.02 wt.%). Presence of these micro-inclusions causes sphalerite lattice destabilisation, particularly in larger grained sphalerite and enhancing oxidation (cf. Urbano et al., 2007, Lottermoser, 2010).

Galena in group G is rich in Ag, Bi and Sb increasing its potential for weathering and Pb release (cf. Savage et al., 2000; Diehl et al., 2003; Diehl et al., 2007). Similar average trace element contents were measured for coarser-grained (>200 μm) and finer-grained (<200 μm) galena (Table 3.11), yet the latter appeared more weathered with anglesite developing (Figure 3.38; Table 3.5). This indicates that grain size is the dominant control on the galena oxidation rate which is in accordance with Liu et al. (2008). Diehl et al. (2008) stated that anglesite does not function as a protective barrier against fluid infiltration because it is porous and fine-grained. However, Moncur et al. (2009) stated that anglesite rims slow oxidation progress. From these analyses, more evidence supporting Diehl et al. (2008) was observed.

Waste rocks belonging to mesotextural group H (arsenopyrite-pyrite-quartz) were classified as extremely acid forming by geochemical tests and the ARDI, with kNAG tests indicating a long-term

elution of ARD. Massive, highly fractured arsenopyrite dominated (Figure 3.42a), and is in early stages of weathering, with scorodite and kankite the dominant (post-mining) secondary minerals. Scorodite behaves as a protective weathering barrier under acidic conditions as its dissolution is slow (10^{-9} to 10^{-10} mol m^2 sec^{-1}; Harvey et al., 2006). Kankite precipitation and dissolution follows that of scorodite (Haffert et al., 2010). Scorodite precipitates within arsenopyrite fractures and on grain boundaries as confined laminated layers of uniform thickness parallel to grain boundaries (Figures 3.42 and 3.43a). Where scorodite growth is unconfined (e.g., in proximity to pyrite), a greater diversity of microtextures is observed, including spherules (Murciego et al., 2009, DeSisto et al., 2010) and ribbons. Paste pH results indicate that to an extent, scorodite and kankite are retarding acid formation, as Craw et al. (2003) summarised that even at submicron-scale, these minerals offer protection. The arsenopyrite trace element content indicated relative enrichment of Co and Ni over a range of grain sizes (Figure 3.44). It is postulated that these elements increase the resistance to oxidation as is the case for pyrite (cf. Kwong, 1993) when compared to fracture distribution. Therefore, whilst this group has the highest metalloid content, it may not be the primary As source.

Waste rocks from mesotextural group J (quartz-pyrite) were consistently classified the most acid forming group at Croydon by all geochemical methods and the ARDI, with kNAG indicating relatively rapid acid formation (i.e., within one month of atmospheric exposure). In general, larger pyrite grains were more weathered as a result of extensive fracturing. Group J samples had the highest total concentration of metals (Cd, Cu, Ni, Pb and Zn). Pyrite cores are As-rich, which increases susceptibility to oxidation as do galena micro-inclusions which were commonly identified (cf. Jambor, 1994; Kwong, 1995; Plumlee, 1999; Lottermoser, 2010). Pyrite grains are subsequently fractured, within which HFO have precipitated and adsorbed elements released on pyrite oxidation, particularly As (Foster et al., 1998). In addition, szomolnokite and rhomoboclase have precipitated and also represent a transient store of trace elements (Buckby et al., 2003; Lottermoser, 2010). These minerals are highly soluble under the pH range (3.0 to 4.7) measured in paste pH tests (cf. Harris et al., 2003). Therefore, they are identified as a significant source of As, Cd, Cu, Pb and Zn. Diversity in the degree of weathering was observed with some grains completely replaced to minerals such as hohmannite. However, this likely reflects chemical heterogeneity of the ore forming fluids with respect to trace elements (with these containing more As, and galena) as it is common for lode-Au deposits (Kruezer, 2006; Thomas et al., 2011).

3.5.2 ARDI Application

To evaluate the application of the ARDI, results were screened against the geochemical data most commonly used to classify ARD forming potential. ARDI was first compared against MPA (Figure 3.48) and successfully identified groups J and H as the most acid forming. Results in Figure 3.23 show these samples as high-risk with ARD formation immediate. Therefore, classifying samples with an ARDI value >40 as extremely acid forming is considered appropriate. Groups containing lesser amounts of pyrite (i.e., C, E) are PAF only. This is because the ARDI considered the amount, type and mineral association of the acid forming sulphides present and not just the total amount of sulphur/sulphide present as MPA does. ARDI values were compared with ANC (Figure 3.49), with sample classifications considered accurate

when cross-checking against mineralogy (i.e., no samples falling in the ANC field). Figure 3.50 shows the majority of samples to have plotted in the ANC/NAF field. If the classification was based on NAPP alone, many samples would be considered potentially acid forming as they have values >20kg H_2SO_4/t. However, plotting these data against the ARDI has allowed for more accurate classification, as many of these samples have been classified as ANC/NAF by other GMT classifications. Figure 3.51 shows the ARDI compared to NAG/mNAG values, with samples given the same classifications as in the previous graphs.

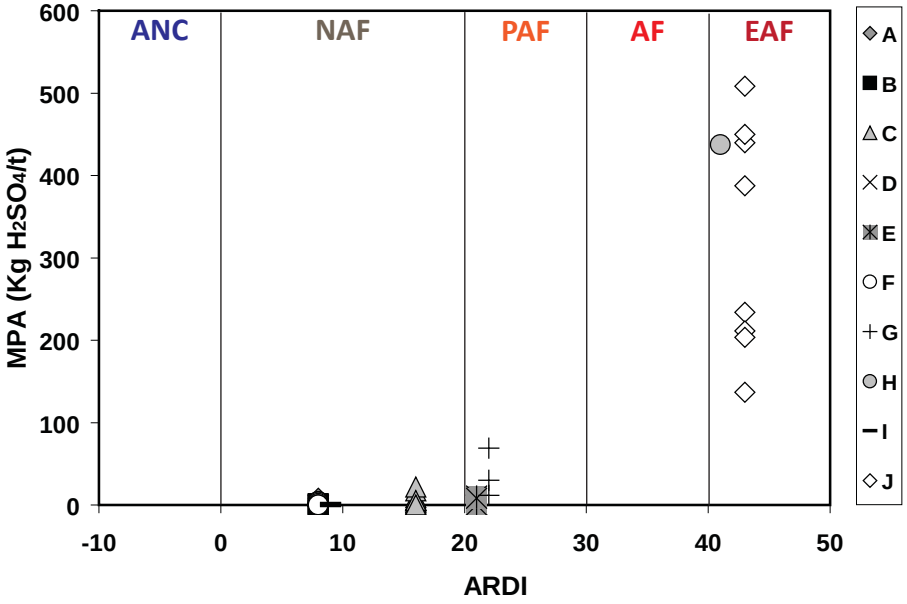

Figure 3.48 Maximum potential acidity (MPA) values in kg H_2SO_4/t shown against ARDI values for Croydon waste rock samples as grouped by mesotexture (A to J; n=52) Abbreviations: AF, acid forming; ANC, acid neutralising capacity; EAF, extremely acid forming; NAF, non-acid forming; PAF, potentially acid forming.

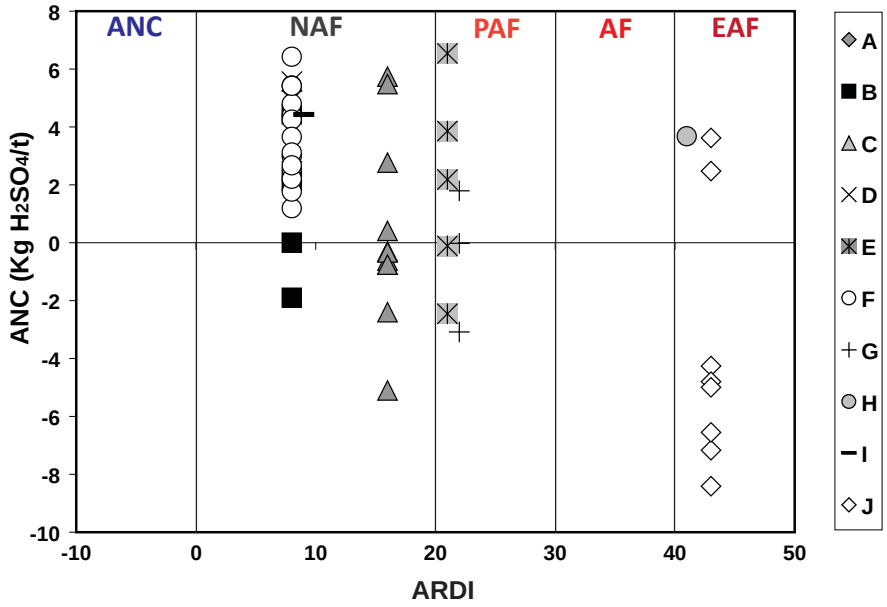

Figure 3.49 Acid neutralising capacity (ANC) values in kg H_2SO_4/t shown against ARDI values for Croydon waste rock samples as grouped by mesotexture (A to J; n=52). Abbreviations: AF, acid forming; ANC, acid neutralising capacity; EAF, extremely acid forming; NAF, non-acid forming; PAF, potentially acid forming.

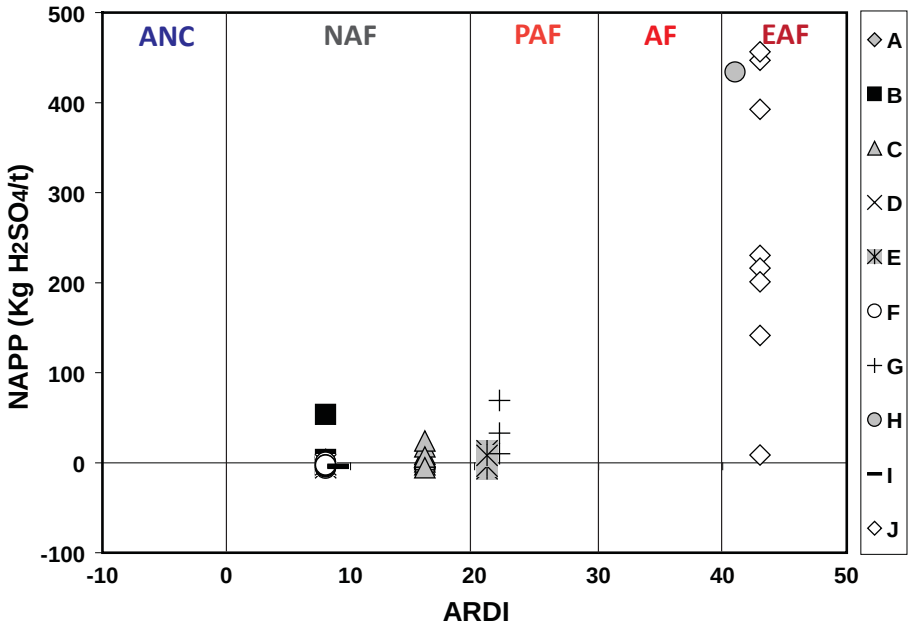

Figure 3.50 Net acid producing potential (NAPP) values in kg H_2SO_4/t shown against ARDI values for Croydon waste rock samples as grouped by mesotexture (A to J; n=52). Abbreviations: AF, acid forming; ANC, acid neutralising capacity; EAF, extremely acid forming; NAF, non-acid forming; PAF, potentially acid forming.

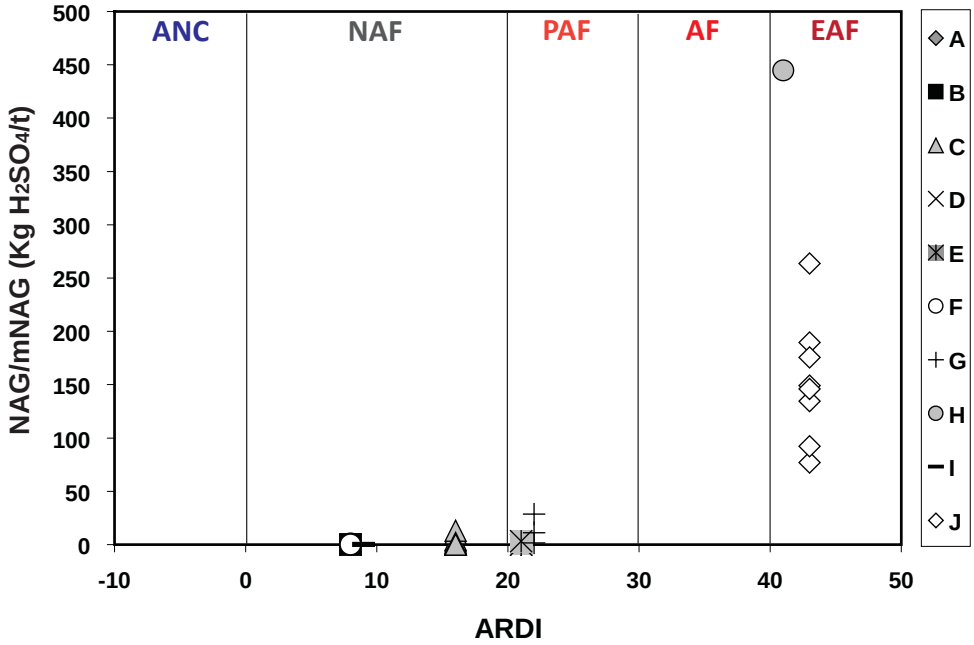

Figure 3.51 Comparison of net acid generation (NAG) and multi-addition NAG (mNAG) values in kg H_2SO_4/t shown against ARDI values for Croydon waste rock samples as grouped by mesotexture (A to J; n=52). Abbreviations: AF, acid forming; ANC, acid neutralising capacity; EAF, extremely acid forming; NAF, non-acid forming; PAF, potentially acid forming.

These comparisons provide evidence that the ARDI is an accurate pre-screening tool, and that through evaluating acid forming potential over a range of scales (i.e., geochemical analysis performed on <125 µm material and evaluation of intact rock textures), an improved understanding of the acid forming potential is achieved. These results also demonstrate that assessing at least one sample by the ARDI (on both a meso-scale and micro-scale) and applying this result to all samples in a group does not lead to misclassification.

3.5.3 Effectiveness of the GMT Approach

Mesotexturally grouping waste rock samples at the start of the investigation by supplementing traditional geological logging with FP-XRF and SWIR data (using a TerraSpec instrument: Figure 3.5), allows for a more organised approach to classification. Geochemical results obtained from stages-one to stage-three tests indicated that mesotextural grouping performed at Croydon was accurate, with similar geochemical, mineralogical and ARD characteristics measured within each group.

Mineralogy of waste rock must be established at the start of a classification programme, and not to merely help resolve classifications of ambiguous samples as is stated in Smart et al. (2002). Therefore, stage-one requires measurement of the bulk mineralogy of at least one sample per group. However, this is a limitation, as a better understanding would be ascertained if each sample was measured, but due to high-costs associated with QXRD, this may not be feasible, particularly if sampling methodologies proposed by the USDA (1992) or the BC Taskforce (Table 3.1) were adhered to. Whilst estimates of modal mineralogy were calculated using computer software based on whole-rock data, a range of sulphide values were obtained which did not match measured QXRD results (Figure 3.11). In the case of Croydon which has a relatively simple mineralogy (i.e., absence of carbonates), the overall sample classification would not alter. Yet, the waste rock classification at other lode-Au mines with a more diverse mineralogy (e.g., Mother Lode, California, US: Savage et al., 2000; Macraes Mine, New Zealand: Craw et al., 2003), this could lead to significant misclassifications. Thus, there is a requirement for improved computer software to precisely calculate mineralogy using bulk geochemical data. Results from stage-one indicated that bulk geochemical data for all samples can be accurately obtained using FP-XRF and not XRF (Figure 3.8). However, S_{Total} values measured by FP-XRF were occasionally erroneous. As an alternative, EA was proven as an accurate lower cost technique to obtain S_{Total} when values are compared against XRF (Figure 3.9). Paste pH tests showed that different values are obtained depending on the grain size used in the test. Shaw et al. (2000) stated that non-pulverised samples should be used to give more a realistic of acidity, as pulverising samples liberates neutralising minerals (particularly secondary neutralisers), resulting in overestimated paste pH values. Results presented in Table 3.3 supported this, therefore, paste pH tests should be performed on at least two grain size fractions (i.e., <20 mm and <75 μm) to provide a range of values.

It is necessary to incorporate routine geochemical tests into this approach, as is done so by stage-two. It is recommended that the Sobek test is performed on all tests, and only systematic cross-checks made with another method (e.g., Modified Sobek) and mineralogy. Classification of NAG pH values plotted against paste pH data following Price et al. (1997; Figure 3.23) is not routinely undertaken, despite these data often having already been collected. However, such a classification provides with reasonable accuracy the lag-time to acid formation (as a comparison with kNAG tests indicated for these samples), thus this type of classification should be more extensively utilised.

At stage-three, detailed mineralogical and textural analyses provided a general indication of the dominant mineral associations, thus supporting ARDI evaluations. However, a limitation of the MLA was its ability to classify fine-grained material, for example, producing a classified image of porphyritic

and flow-banded rhyolite proved inaccurate, thus only BSE images for whole tiles have been shown for minor-sulphide bearing textural groups (A, C and E). Additionally, MLA-analysis were unable to resolve the mineralogy of fine-grained secondary phases, which had to be classified manually by cross referencing the classified image with the low-quality BSE image and touching up the image frame-by-frame. On completion, the XBSE file was too large to process, thus additional SPL_Lite analyses had to be undertaken. Based on this, the most appropriate use of MLA is targeted SPL_Lite mapping of sulphides, with XBSE images accumulated over the sample area. This will indicate the presence of mineralogical features requiring detailed SEM-EDS analysis. The Horiba-XGT7000 Micro-XRF proved inadequate for element mapping (Figure 3.39) as the detection limits were not low enough to detect trace elements. However, if this technology is optimised (i.e., replacement of the detector), then there is potential for its application at stage-one as a pre-screening tool. Mesotextural samples could then be mapped to quickly identify the intact elemental distribution, and select areas for detailed microanalyses by LA-ICP-MS and EPMA.

A summary of GMT classifications assigned throughout each of the stages is given in Table 3.13. Final classifications are in agreement with pre-screening stage-one classifications for sulphide bearing groups A, E, G, H and J, and for non-acid forming groups B, D, F and I. At the end of stage-one, group C was indicated as NAF/PAF, and was resolved as PAF by stages-two and -three. This indicates the potential application of stage-one to rapidly, and cost effectively characterise historic sites such as this rather than undertaking an intense geochemical testing program as suggested in Smart et al. (2002). Furthermore, as additional fields (e.g., AF, EAF) are given when classifying stage-one data (Figure 3.16 and 3.17), more detailed ARD characterisation is afforded earlier on, as routinely used methods (e.g., NAPP versus NAG pH) only classify samples as PAF, NAF and UC.

3.6 Summary

- Waste rock samples (n=52) were collected from the abandoned Croydon mine operations (north Queensland, Australia) and used to test the GMT approach to provide an accurate sample classification in terms of acid forming potential.
- Mesotextural grouping of samples prior to GMT analyses using geological logging techniques, FP-XRF and SW-IR analyses (using a TerrSpec) identified ten major groups A to J, which comprised of hydrothermally altered rhyolites and massive/semi-massive sulphides.
- Stage-one pre-screening classifications identified group J (pyrite-quartz) as extemely acid forming, and group H (arsenopyrite-pyrite-quartz) as acid forming. Groups C (porphyritic rhyolite with disseminated pyrite in quartz veinlets), E (porphyritic rhyolite with disseminated pyrite in the groundmass) and G (quartz-galena-sphalerite-minor pyrite) were classified as PAF, and all other groups were NAF.
- Stage-two screening classifications were in agreement with stage-one, with groups J and H consistently identified as the most acid forming (and high risk), with the lag-time to ARD formation identified as rapid for group J.
- Detailed mineralogical and textural evaluations performed at stage-three assigned classifications in agreement with the previous stages, and recommended groups G, H and J for kinetic testing.

Table 3.13 Summary of GMT approach classifications of waste rock material from Croydon as grouped by mesotexture (A to J; n=52). Abbreviations: AF, acid forming; ANC, acid neutralising capacity; ARD, acid rock drainage; Int, intermediate; NAF, non-acid forming; ML, metal leaching; MPA, maximum potential acidity; PAF, potentially acid forming; UC, uncertain).

	GROUP	A	B	C	D	E	F	G	H	I	J
Stage One	ARDI	NAF	NAF	NAF	NAF	PAF	NAF	PAF	EAF	NAF	EAF
	S_{Total} vs. ARDI	NAF	NAF	NAF/ PAF	NAF	NAF/ PAF	NAF	PAF	PAF	NAF	PAF/AF
	S_{Total} vs. paste pH	NAF	NAF	NAF	NAF	PAF	NAF	PAF	EAF	NAF	EAF
	ARDI vs. paste pH	NAF	NAF	NAF	NAF	PAF	NAF	PAF	EAF	NAF	EAF
	Carbonate vs. sulphide	AF	NAF	AF	AF	AF	NAF	AF	AF	AF	AF
	Metals vs. paste pH	Int. to low risk	Int. to low risk	Int. to low risk	Low risk	Int. to low risk	Int. to low risk	High to int. risk	Int. risk	Low risk	High to int. risk
	Metalloids vs. paste pH	Low risk	Int. to low risk	Int. to low risk	Low risk	Low risk	Low risk	Int. (ARD) to low risk	Int. (ML) risk	Low risk	High to int. risk
	Classification	*NAF*	*NAF*	*NAF/ PAF*	*NAF*	*PAF*	*NAF*	*PAF*	*AF*	*NAF*	*EAF*
Stage Two	NAPP vs. NAG pH	NAF	NAF & UC	NAF & PAF	NAF	NAF & PAF	NAF	PAF	PAF	NAF	PAF
	NAG pH vs. paste pH	NAF	NAF	NAF & PAF	PAF	NAF & PAF	NAF	PAF	PAF	NAF	PAF
	MPA vs. ANC	PAF	PAF	PAF	NAF	PAF	PAF	PAF	PAF	NAF	PAF
	Classification	***NAF***	***NAF***	***PAF***	***NAF***	***PAF***	***NAF***	***AF***	***EAF***	***NAF***	***EAF***
Stage Three	sNAG	PAF	-	PAF	-	PAF	-	PAF	High-PAF	-	High-PAF
	mNAG	PAF	-	NAF	-	NAF	-	PAF	High-PAF	-	High-PAF
	kNAG	-	-	NAF	-	-	-	AF	AF	-	AF
	Metal leaching issues?	No	-	No	-	No	-	Cd, Pb, Zn	As	-	As, Pb, Zn
	Classification	*PAF*	*NAF*	*PAF*	*NAF*	*PAF*	*NAF*	*PAF (High risk)*	*EAF (High risk)*	*NAF*	*EAF (High risk)*
	Column leach testing required?	**No**	**No**	**No**	**No**	**No**	**No**	**Yes**	**Yes**	**No**	**Yes**

Chapter 4

Mineralogical and chemical evolution of sulphidic mine wastes (Croydon gold mines, Australia) upon kinetic testing

4.1 Introduction

Waste rock piles are dynamic, heterogeneous systems, with the primary mineralogy and drainage chemistry ever changing as a function of several factors including climate (Harris et al., 2003; Smuda et al., 2007; Lottermoser, 2010; Nordstrom, 2009; Jamieson, 2011) and hydrology (Tran et al., 2003; Sracek et al., 2004; Lottermoser, 2010). Laboratory-based kinetic tests give consideration to this by subjecting waste rock to dissolution with the leachate chemistry evaluated, as a means of predicting drainage chemistry in the field (Lapakko et al., 2006). As with static tests, many kinetic testing protocols exist with column-leach and humidity cell test methods favoured as summarised in Chapter 1 (Section 1.3.7). However, a significant limitation of these protocols is that routine mineralogical analysis is not recommended, despite the fact that relationships between mineralogy, texture, microstructural features (i.e., fractures) and trace element deportment are critical in influencing leachate chemistry (Diehl et al., 2007). Some examples exist in the literature whereby kinetic test samples have been subjected to XRD, SEM, and EPMA analyses (e.g., Weber et al., 2004; Lapakko et al., 2006; Miller et al., 2010). However, such analyses were infrequently performed (i.e., at either the beginning or halfway through an experiment). This implies that changes in leachate chemistry and mineralogy are not directly correlated in these tests, and as a consequence, the microscale processes controlling acid formation and metal leaching are not fully understood. A potential reason for the absence of routine mineralogical analyses from kinetic testing protocols may relate to the relatively short time-scale that tests are performed over, with some protocols stating that tests can be concluded as early as 20 weeks (White et al., 1999). Therefore, it may be reasoned that the mineralogy is unlikely to undergo significant changes and is subsequently not evaluated. However, as described in previous chapters, processes of sulphide oxidation are complex and can be significantly influenced by parameters such as the presence of micro-inclusions, or the content of specific trace elements. Thus, tracking temporal changes relating to these parameters will result in a better understanding of leachate chemistry ultimately improving the understanding of sulphide oxidation processes and subsequently the quality of waste rock management plans and site rehabilitation strategies.

Another limitation of kinetic testing is that typically, only one grain size is recommended for use, and often this value is inconsistent between different protocols. For example, four humidity cell test methods were summarised in Lapakko (2003) with recommended grain sizes ranging from <6.3 mm to <10 cm, and the AMIRA P387A handbook recommends using a -4mm size fraction (Smart et al., 2002). Stromberg and Banwart (1999) demonstrated that 80% of the reactivity in waste rock occurs in

particles <250 µm. Thus, using the afore mentioned size fractions is appropriate as they will include some quantity of the high surface area fines. However, a study was undertaken by Lapakko et al. (2006) which kinetically tested six grain sizes (<0.053 mm to 6.35-19 mm) from three lithologies (norite, mudstone and breccia). They reported that pH decreased with decreasing grain size for the norite, the opposite for the mudstone, and no clear trend for the breccia. Therefore, their study indicates that the relationship between leachate pH and grain size cannot be assumed, and therefore, a range of particle sizes should be subjected to kinetic testing.

This chapter aims to provide recommendations for improving kinetic testing through demonstrating the benefits of integrating mineralogical analyses and testing different grain sizes, using samples obtained from the historic Croydon waste rock piles. Waste materials from mesotextural groups E (porphyritic rhyolite: quartz-potassium feldspar-muscovite with disseminated pyrite), G (semi-massive sulphide: quartz-sphalerite-galena-pyrite), H (massive sulphide: arsenopyrite-pyrite-quartz) and J (massive sulphide: quartz-pyrite) were selected for use following the recommendations of the GMT approach (Chapter 3). The specific objectives were to: 1) explore the applications of mineralogical analyses (e.g., QXRD, SEM, LA-ICP-MS) systematically undertaken during kinetic testing; 2) evaluate the effect of grain size on leachate chemistry; 3) relate laboratory observations to stream sediment and surface water chemistry measured around the Croydon district; and 4) recommend rehabilitation strategies appropriate for this particular site.

4.2 Materials and methods

4.2.1 Waste-rock selection

Waste rock samples (n=20; c.3-5kg) representative of sulphidic material were collected from the Croydon waste rock piles by DEEDI (February and April 2010). This material had been oxidising in these piles for at least 19 years (i.e., since mine closure in 1991). Samples were shipped to CODES, UTAS, and upon receipt, were sawn in two, with the smaller piece mesotexturally classified by the method described in Section 2.3, with laser-mount samples also prepared. From this suite, six samples were selected for kinetic testing (Figure 4.1). Three samples were selected from group J (sample 3, 6 and 19), as this was classified by the GMT approach as high risk/extremely acid forming (EAF). Some textural variation was observed between these samples. Sample 3 contained <10 mm pyrite grains present in clusters, whereas in samples 6 and 19, pyrite was dominantly present in dendritic veins. One sample from group H (sample 18) was selected as it was also classified as high risk/ EAF by the GMT approach. One sample from group G was also chosen as it was classified as potentially acid forming (PAF) by the GMT approach, and contained the highest quantities of sphalerite and galena (i.e., potential sources of Cd, Pb and Zn). Finally, one sample from group E (sample 15) was selected as disseminated pyrite was observed in the muscovite-altered rhyolite groundmass, allowing for textural effects of mineral association on pH to be examined.

4.2.2 Kinetic test selection and experimental design

Column leach testing was chosen in preference to humidity cell tests (as described in USEPA, 2003) as these more accurately approximate the climatic conditions experienced at Croydon (Section 3.2.2).

Specifically, the AMIRA P387A free draining column leach procedure was selected (Smart et al., 2002). This methodology is the most commonly used in Australia both in research (e.g., Stewart, 2005; Miller et al. 2010; Munksgaard and Lottermoser, 2011), and by industry as it is offered by many laboratories including ALS (2010). This procedure allows flexibility in the experimental design and therefore was modified with respect to grain size, sample mass and frequency of leachate collection. Two grain sizes were selected: (1) a -4 mm fraction (as recommended by the procedure); and (2) a coarser -10 mm fraction. The -10 mm fraction was selected as sulphides were anticipated to be well encapsulated in quartz or rhyolite relative to the -4 mm fraction. Each sample was jaw crushed and sieved with approximately 1kg of each grain size fraction prepared as column feed (JKMRC, University of Queensland).

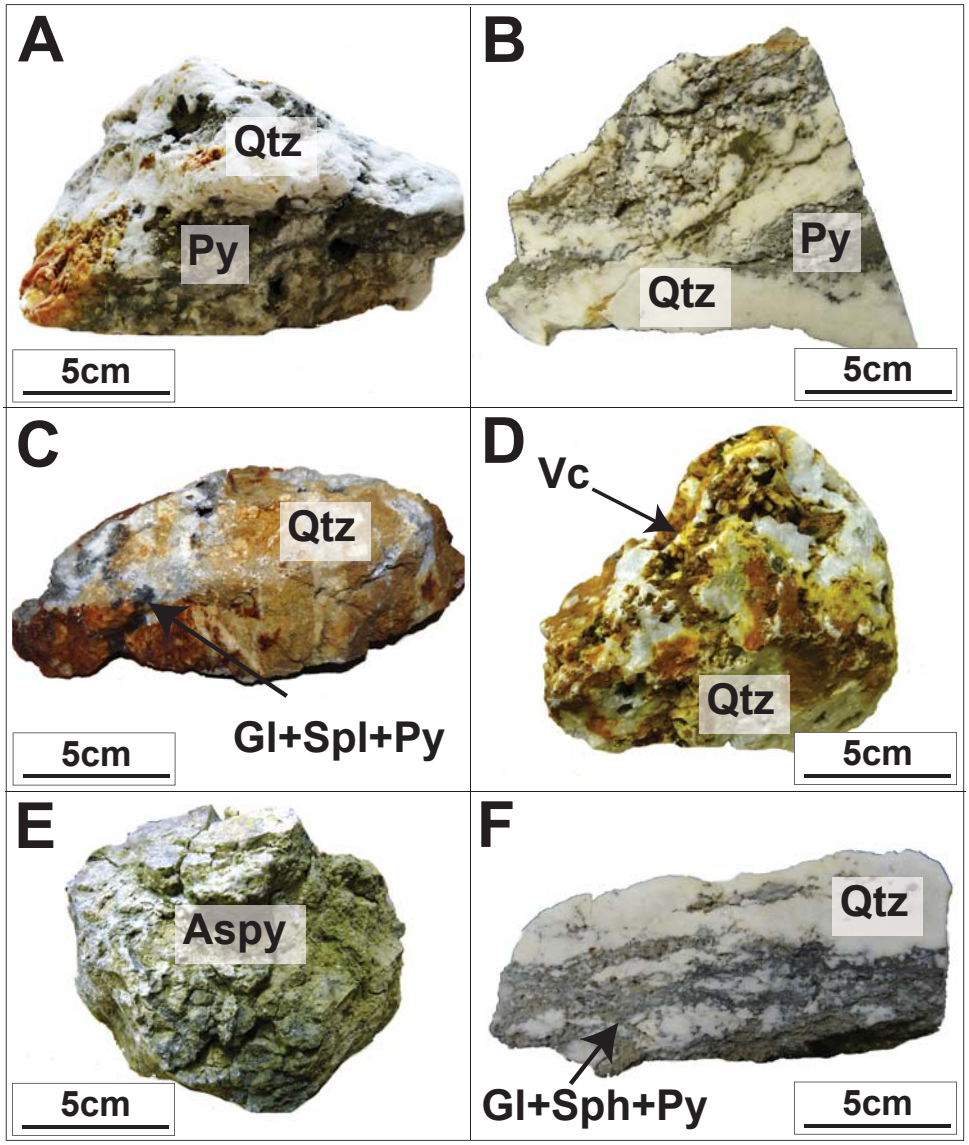

Figure 4.1 Croydon waste rock samples selected for kinetic testing: **(A)** Sample 3, semi-massive quartz-pyrite representative of mesotextural group J; **(B)** Sample 6, quartz-pyrite representative of mesotextural group J; **(C)** Sample 14, coarse sphalerite intercalated with massive quartz, representative of group G; **(D)** Sample 15, porphyritic rhyolite fragments in massive quartz, with pyrite present in both quartz veinlets and the rhyolite groundmass, representative of group E; **(E)** Sample 18, massive arsenopyrite, representative of mesotexture H; **(F)** Sample 19, semi-massive quartz-pyrite representative of group J. Abbreviations: Aspy, arsenopyrite; Gl, galena; Py, pyrite; Qtz, quartz; Spl, sphalerite; Vc, volcanics/rhyolite.

Twelve column leach tests were established in October 2010 (CODES, UTAS) with the -4 mm fraction fed into six columns, and the -10 mm into the remaining six (Figure 4.2). Heat lamps with 150 W bulbs are recommended to maintain surface temperatures of 30 to 35°C (Smart et al., 2002). However, as the maximum temperatures exceed this at Croydon (Section 3.3.2), 275 W bulbs were used, with surface temperatures maintained at 35 to 40°C. Lamps were switched on for ten hours per day for days one to five, and were switched off on days six and seven. The test solution used was deionised water (DI). This was applied to the surface of columns on day five; approximately three hours after heat lamps were switched off. The volume of test solution added varied as the procedure recommends to fill until the surface of material in each funnel is saturated (Smart et al., 2002). On average, approximately 500 ml was added to columns containing coarse (-10 mm) material, and 200ml to fine (-4 mm). Leachate drained into 1 litre collection vessels and was collected weekly on day seven. Clean collection vessels were then placed at the base of the Buchner funnels, and the weekly cycle repeated. These tests were conducted for thirty weeks as recommended by Smart et al. (2002).

To confirm acid forming potential prior to testing, 100 g of each sample (n=6) was subjected to elemental microanalysis (for S_{Total}), NAPP and single addition NAG testing (ALS, Brisbane, Australia). Additionally, these samples were assayed to determine the element contents (ALS, Brisbane, Australia). To measure the bulk mineralogy, additional samples (n=6) from the -4 mm column were analysed by QXRD (University of Ballarat, Australia). Corresponding -10 mm column samples (n=6) were analysed using SEM-EDS and MLA (SPL-Lite function, with Ni used as the standard) to evaluate sulphide microtextures and mineral associations (FEI Quanta 600; CSL, UTAS).

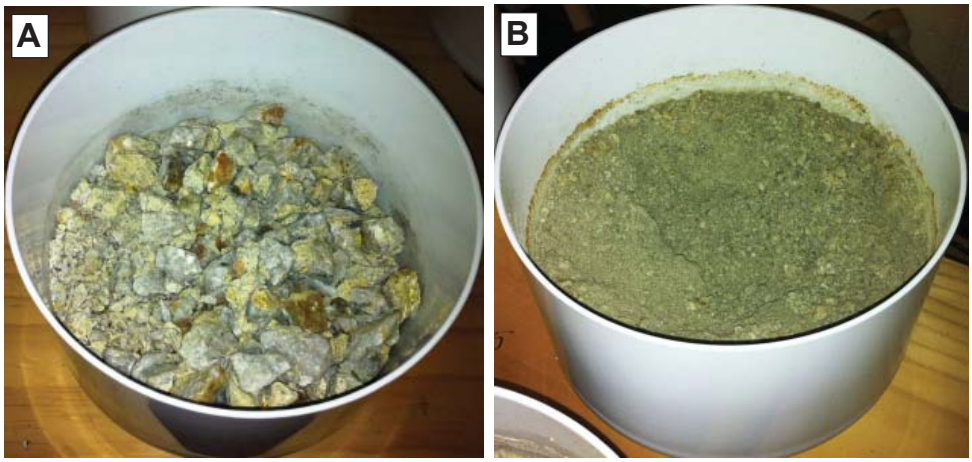

Figure 4.2 Column feed in Buchner funnels as used in column leach testing with an example from mesotextural group E (sample 15) shown : **(A)** -10mm fraction and **(B)** -4mm fraction.

4.2.3 First flush experiments

Prior to kinetic testing, first flush experiments were performed to establish the effect of secondary mineral dissolution on drainage chemistry. The pre-oxidised samples (n=12) were loaded into Buchner funnels with DI water subsequently added to each until the surface of materials was fully saturated. The pH and electrical conductivity (EC) of leachates were measured after 24 hours and selected trace elements (Ag, Al, As, Ba, Be, Cd, Co, Cr, Cu, Fe, Mn, Ni, Pb, Sb, Se, Zn) were determined using ICP-MS techniques (Agilent 4500 ICP-MS; CODES, UTAS). Detection limits for these elements are given in Appendix 4.1.

4.2.4 Leachate chemistry

Leachate pH was measured weekly (Eutech Instruments 510 pH meter). The pH probe was calibrated to pH 4 and 7 using standard buffer solutions (Merck Ltd.) after each sample measurement. Sample blanks (DI water) were tested before and at the end of each sample batch. The EC was also measured weekly, with the anode calibrated prior to use with a 0.01 M KCl solution. For element assays (Ag, Al, As, Ba, Be, Cd, Co, Cr, Cu, Fe, Mn, Ni, Pb, Sb, Se, Zn), a 10 g split of leachate was filtered (0.45 µm) and preserved (acidified to pH 2) prior to ICP-MS analysis (Agilent 4500 ICP-MS; CODES, UTAS). Leachate from weeks 1 to 4, 6, 8, 10, 12, 14, 16, 18, 20, 22, 24, 26, 28 and 30 were analysed. Sulphate measurements were also performed on these samples (ALS, Brisbane, Australia).

4.2.5 Column mineralogy

A grab sample (c.10 g) was obtained from the surface of each -4 mm column every five weeks (week 0 to 30) for QXRD analysis (University of Ballarat, Australia) in order to provide a general indication of mineralogical changes in the column. This sample was collected on day 5 of each weekly cycle (i.e., prior to the addition of the DI water test solution), to allow for any secondary efflorescent minerals formed as a result of pore-water evaporation to be identified.

At least one particle from the -10 mm column was also obtained every five weeks (also on day 5 of each weekly cycle), and used in SEM (CSL, UTAS) and LA-ICP-MS (New Wave UP-213 Laser; CODES, UTAS) studies. This was undertaken in order to examine the degree of sulphide weathering, and changes in trace element chemistry over time. Preparation of the laser mount presented some difficulties as the surface of the -10 mm particle was irregular, and thus care was taken when polishing surfaces so as to not dislodge any weathering products. A limitation of this sampling method was that the same -10 mm particle was not analysed every five weeks, which would have allowed for temporal mineralogical changes to be better observed. However, taking a sample in this manner would require its preparation (i.e., carbon coating) and analyses during time that the sample should have been in the column. Alternatively, laser mount samples could have been prepared and characterised at the start and then placed in the column, with one taken every five weeks. However, freshly exposing sulphides mounted in resin may have induced non-representative mineralogical changes. Similar sampling approaches to that used here (i.e., removal of samples at given time intervals) were previously adopted by Weisner and Weber (2010) and Miller et al. (2010). Results from mineralogical analyses performed on the -4 mm and -10 mm grain size fractions were used concurrently to better understand processes occurring in each column.

4.2.6 Stream sediments and surface waters

Surface water samples (n=29) were collected directly from Tabletop and Deadhorse Creeks, and at their confluence (Figure 4.3). These were collected to compare the water quality eluting from the Federation/ La Perouse and Glencoe sites. Additionally, samples were obtained from the surfaces of Federation (35 m depth), La Perouse (40 m depth) and Glencoe (25 m depth) pit lakes. Water samples were collected for analysis of major cations and anions (unfiltered) and trace metals (0.45 µm filtered) with samples preserved using 10% HNO_3. Conductivity and pH were measured in the field.

Stream sediment samples (n=39) were collected upstream and downstream of the Federation/ La Perouse site, representing background and 'mine-impacted' materials. Samples were taken at, and downstream of, Glencoe only. Sediment samples were collected from the middle of streams at a depth of 0 to 10 cm. Samples were dry sieved (using a stainless steel sieve) to <63 µm, with both the whole and the fine fraction (<63 µm) analysed for geochemical comparison. For water and sediment analyses, sampling equipment and HDPE sample bottles were cleaned prior to sampling by soaking them in HNO_3 (trace metal grade) and rinsing in DI water.

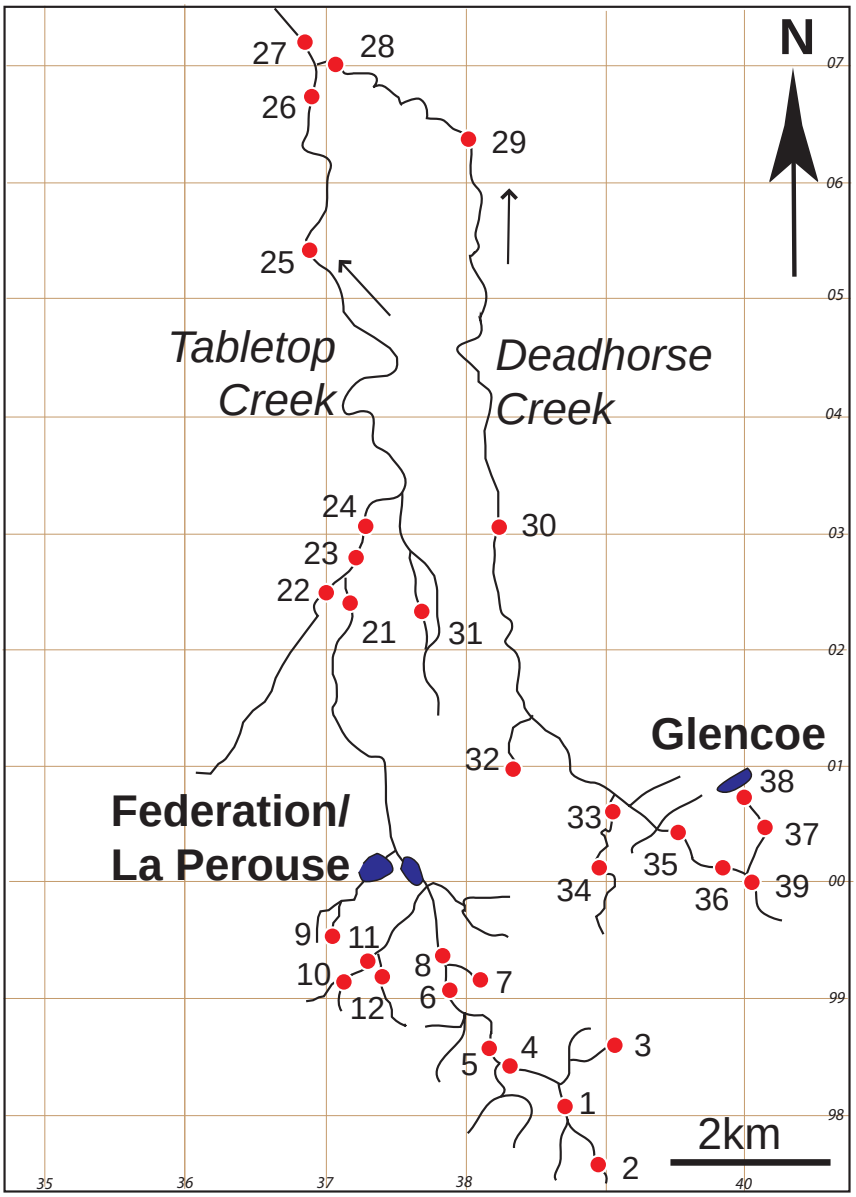

Figure 4.3 Plan view of stream sediment and water sample locations (and numbers) obtained both upstream and downstream of the Federation/ La Perouse and Glencoe operations, Croydon.

Selected sediments were analysed for their mineral composition by XRD powder diffraction (Bruker D8 Advance X-Ray diffractometer; UQ, Brisbane). A six-step sequential extraction analysis was also performed (CMLR, UQ, Australia) on Fe-rich stream sediments (collected at the Federation/ La Perouse site) to determine the solid speciation of selected metals. The analytical procedure of Dold

(2003a) was followed, which differentiated between water soluble, ion exchangeable, Fe^{3+} oxyhydroxide, Fe^{3+} oxide, organic/ sulphide and residual fractions. An additional step was added to include Mn oxides (20 mL 0.1 M NH_2OH-HCl; pH 2; shake 2 hrs).

Both the whole sediment and the fine-grained (<63 μm) sediment fraction were partially digested in hot aqua regia. The resulting extractants and the water samples collected from around the Croydon district were analysed for selected trace elements (Ag, Al, As, Ba, Be, Cd, Co, Cr, Cu, Fe, Mn, Ni, Pb, Sb, Se, Zn) using ICP-MS techniques (UQ, Australia). During ICP-MS analysis, two reference standards were used, a multi-element calibration standard-2A (Agilent Technologies) and an arsenic reference standard (Eawag aquatic research, Swiss Federal Institute of Aquatic Science and Technology). Both were analysed before and at the end of each sample run in addition to two blank samples. The relative standard deviation for these data was less than 10% (Appendix 4.2).

4.3 Waste rocks

4.3.1 Initial sample characterisation

4.3.1.1 Geochemical classification

Prior to kinetic testing, measurements of S_{Total}, NAPP and NAG were undertaken to confirm the acid forming potential of these samples (Table 4.1). Classification of samples on a NAPP/NAG pH plot confirmed that all samples are PAF (Figure 4.4). The group H sample was the most acid forming. Samples from groups J and G were also acid forming, with values from Group J varying as a function of S_{Total} contents. Group E was the le Preparation of the laser mount presented some difficulties as the surface of the -10 mm particle was irregular, and thus care was taken when polishing surfaces so as to not dislodge any weathering products. ast acid forming, which is in agreement with the GMT classification of this group (Table 3.12).

Table 4.1 Net acid producing potential (NAPP), net acid generation (NAG), acid neutralising capacity (ANC) and total sulphur (wt. %) values for Croydon waste rock samples selected for kinetic testing (*= kg H_2SO_4/t).

	Mesotextural Group					
	C	G	H	J	J	J
Sample ID	15	14	18	3	6	19
NAPP*	11.8	20.8	426	134	60	98.8
NAG pH	3.3	3.4	1.6	2.2	2.6	2.4
NAG (to pH 4.5)*	6.6	6.8	357	88.7	31.6	64.9
NAG (to pH 7.0)*	4.2	9.5	531	95.5	37.3	74.2
ANC*	<0.5	<0.5	<0.5	<0.5	<0.5	<0.5
Total Sulphur	0.39	0.68	13.9	4.4	1.96	3.28

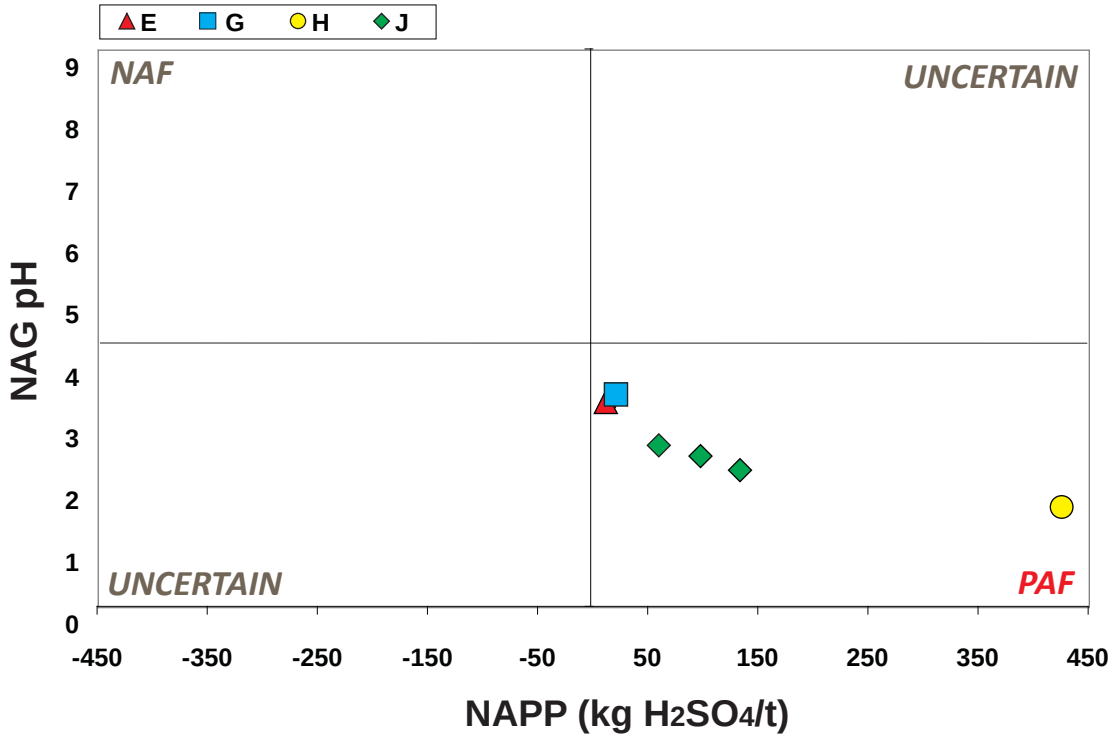

Figure 4.4 Initial geochemical classification of Croydon waste rock samples using NAPP (kg H_2SO_4/t) versus NAG pH for groups E, G, H and J selected for kinetic testing (n=6). Abbreviations: NAF, non-acid forming; PAF, potentially acid forming.

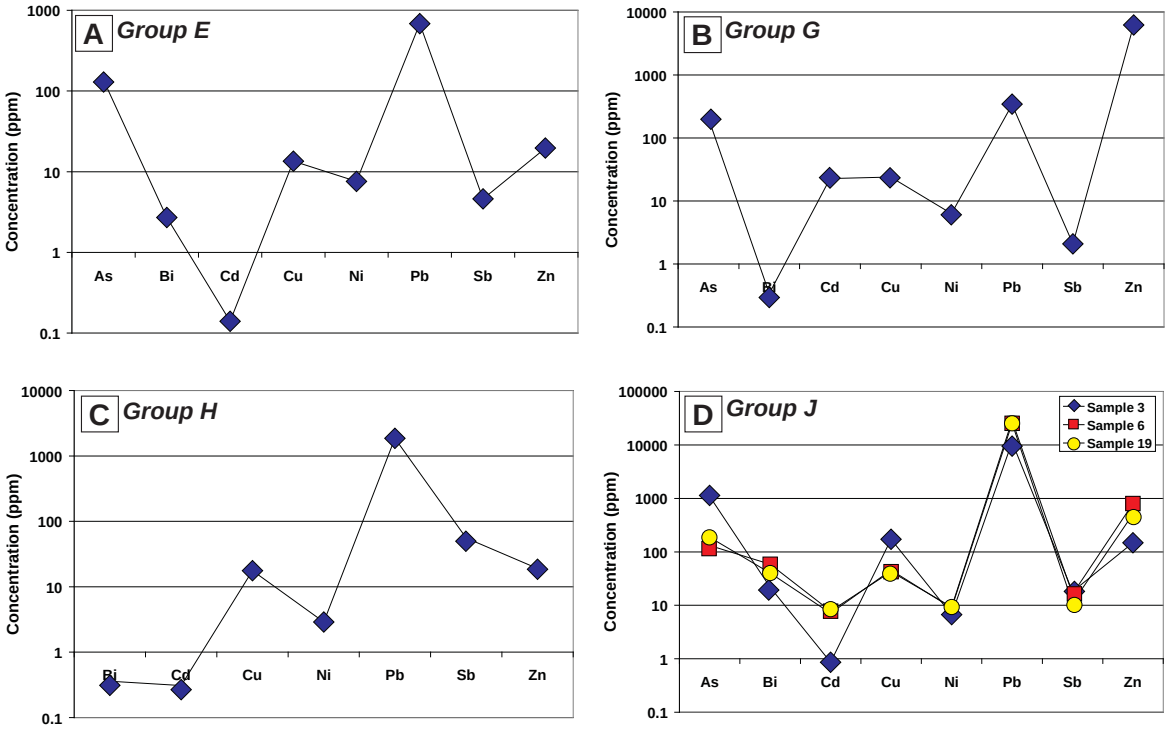

Figure 4.5 Total element concentrations (ppm) measured in Croydon mesotextural groups prior to kinetic testing: **(A)** Group E; **(B)** Group G; **(C)** Group H; and **(D)** Group J.

4.3.1.2 Total element geochemistry

The total element contents of each sample is given in Appendix 4.3, with concentrations of As, Bi, Cd, Cu, Ni, Pb, Sb and Zn shown in Figure 4.5. Only As and Pb were >100 ppm in group E (Figure 4.5a). Group G contained the highest Zn (>1000 ppm; Figure 4.5b). Whilst group H contained high Pb (>1000 ppm; Figure 4.5c) the highest Pb concentrations were measured in group J (>10,000 ppm; Figure 4.5d). Similar quantities of Cd were measured in groups G and J (>10 ppm; Figures 4.5b and 4.5d), however, both retained this in different mineralogical forms as described in the previous chapter (Section 3.4.4.2).

4.3.1.3 Mineralogy

The modal mineralogy of these samples is shown in Table 4.2. All groups except H are dominated by quartz and muscovite. Group E contained <2.1 wt. % pyrite and galena, and traces of secondary minerals rhomboclase, anglesite and scorodite. MLA (SPL-Lite) analysis confirmed the dominance (>90%) of quartz-associated pyrite grains in group E. Two pyrite types dominated: (i) fine-grained (<100 µm diameter), euhedral unweathered pyrite (Figure 4.6a), and (ii) coarser-grained (>150 µm diameter) subhedral-anhedral pyrite, with fractures and intergrowths/micro-inclusions of chalcopyrite and galena

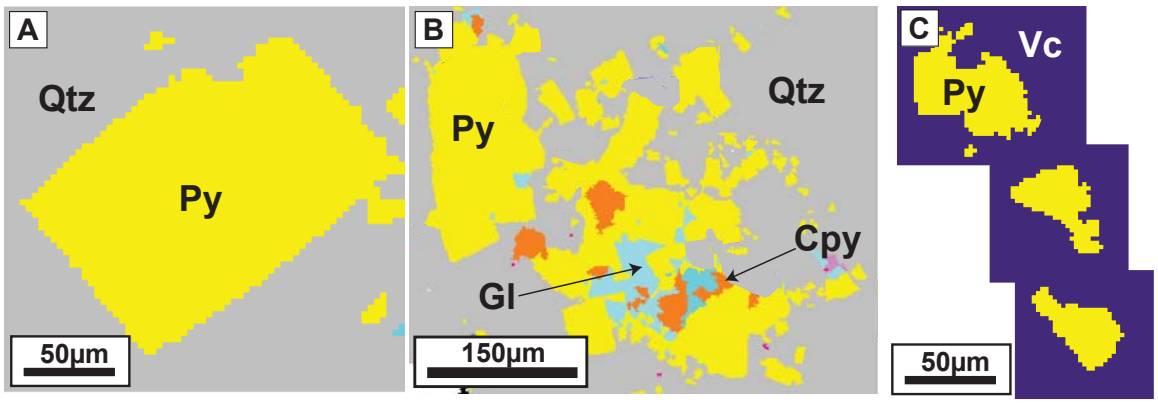

Figure 4.6 Classified mineral maps (MLA-SPL_lite) of the three pyrite types observed within waste material from Croydon representative of mesotextural group E: **(A)** Fine-grained euhedral pyrite in quartz; **(B)** Coarser-grained anhedral pyrite containing galena and chalcopyrite inclusions; and **(C)** Fine-grained subhedral-anhedral pyrite in the rhyolite muscovite-altered groundmass. Abbreviations: Cpy, chalcopyrite; Gl, galena; Py, pyrite; Qtz, quartz; Vc, muscovite-altered rhyolite groundmass.

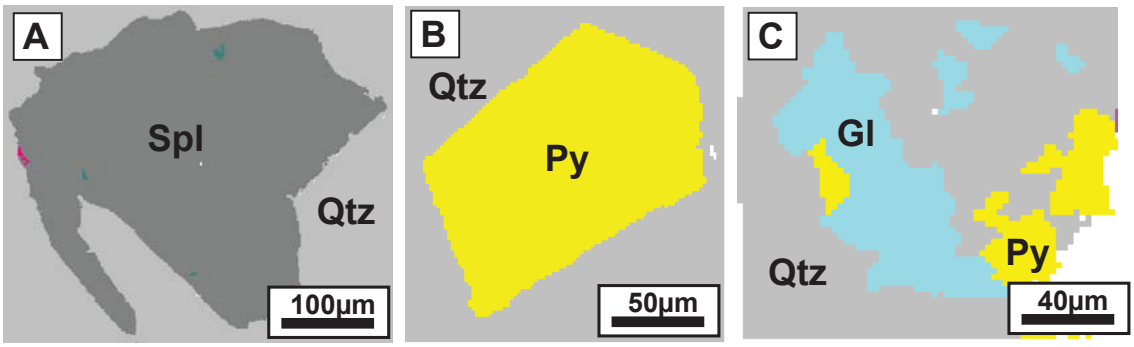

Figure 4.7 Classified mineral maps (MLA-SPL_lite) of the three dominate sulphides observed within waste material from Croydon representative of mesotextural group G: **(A)** Coarser-grained anhedral sphalerite in quartz; **(B)** Fine-grained euhedral pyrite in quartz; and **(C)** Fine-grained anhedral galena intergrown with pyrite in quartz. Abbreviations: Gl, galena; Py, pyrite; Qtz, quartz; Spl, sphalerite.

(Figure 4.6b). In addition, <10% of fine-grained (<100 μm diameter) pyrite grains were subhedral-anhedral and associated with the rhyolite groundmass (i.e., quartz, muscovite and potassium feldspar; Figure 4.6c).

Group G was dominated by sphalerite, pyrite and, galena. Sphalerite was the coarsest of the three sulphides (>100 μm) and did not appear weathered (Figure 4.7a). Pyrite was either euhedral and quartz-associated (Figure 4.7b), or present as small intergrowths associated with fine-grained galena (Figure 4.7c). Similar quantities of anglesite and galena were measured, indicating that some galena oxidation had already occurred (Table 4.2).

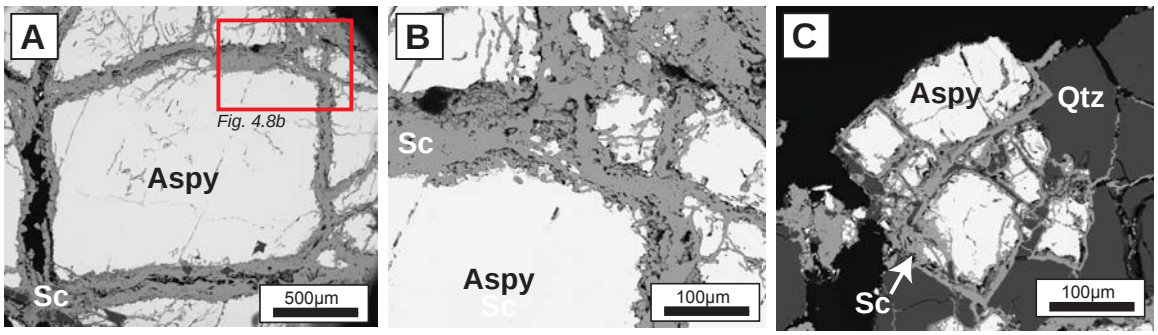

Figure 4.8 Back scattered electron images collected from waste material representative of Croydon mesotextural group H: **(A)** Massive arsenopyrite with scorodite precipitated extensively in fractures; **(B)** Scorodite mass comprised of spherules and acicular grains; **(C)** Finer-grained arsenopyrite with a scorodite rim, with scorodite also precipitated in quartz fractures. Abbreviations: Aspy, arsenopyrite; Sc, scorodite; Qtz, quartz.

Group H was dominated by arsenopyrite, scorodite and quartz, with only minor quantities of other sulphides and their alteration minerals measured (Table 4.2). Back scattered electron images showed extensive precipitation of scorodite along fractures in arsenopyrite (Figure 4.8a). When examined at higher magnification scorodite appeared present to be comprised of both spherules (as observed in Haffert and Craw, 2010) and acicular/fibrous grains (Figure 4.8b). Scorodite was also present as rims on smaller arsenopyrite grains (Figure 4.8c).

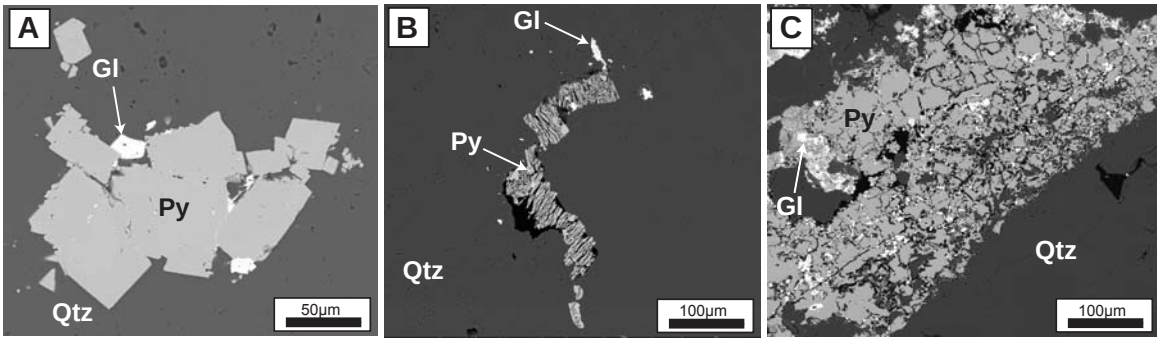

Figure 4.9 Back scattered electron images collected from waste material representative of Croydon mesotextural group J: **(A)** Sample 3 contained relatively unweathered pyrite grains, with occasional galena intergrowths; **(B)** Sample 6 contained strongly weathered anhedral pyrite with galena micro-inclusions; **(C)** Sample 19 dominated by fractured pyrite masses with galena micro-inclusions. Abbreviations: Gl, galena; Py, pyrite; Qtz, quartz.

Pyrite content in Group J varied (2.5 wt. % to 5.2 wt. %) with significant contents of galena also measured (1.6 wt. % to 2.4 wt. %; Table 4.2). Whilst the mineral associations were similar between samples in this group (i.e., sulphide-quartz or sulphide-sulphide), the degree of weathering and micro-textures varied as shown in Figure 4.9. Sample 3 contained euhedral-subhedral unweathered pyrite with some galena intergrowths, and demonstrated the closest resemblance to mesotextural group J samples described in the previous chapter (Figure 4.9a). Individual pyrite grains appeared more weathered in sample 6 with irregular morphologies (i.e. lathes) observed (Figure 4.9b). A similar degree of weathering was observed in sample 19, with large pyrite masses appearing highly fractured, and galena micro-inclusions and intergrowths observed (Figure 4.9c).

Table 4.2 Quantitative modal mineralogy (wt. %) as measured by QXRD, of Croydon waste rock samples selected for kinetic testing. Secondary minerals refer to those formed as a consequence of sulphide oxidation (BDL: below detection limit).

Sample ID	15	14	18	3	6	19
Group	E	G	H	J		
Non sulphides						
Albite	1.2	1.3	1.3	1.1	1.5	1.2
Illite	*BDL*	0.8	*BDL*	*BDL*	*BDL*	*BDL*
Kaolinite	*BDL*	3	*BDL*	*BDL*	*BDL*	0.8
Muscovite	5.8	13.8	*BDL*	6	11.4	7
Quartz	89.8	78.8	21.5	84.9	81.6	82.3
Sulphides						
Arsenopyrite	*BDL*	*BDL*	62.3	*BDL*	*BDL*	0.4
Galena	0.4	*BDL*	0.3	1.6	1.3	2.4
Pyrite	2.1	0.6	*BDL*	5.2	2.5	3
Pyrrhotite	*BDL*	*BDL*	*BDL*	0.3	0.3	*BDL*
Secondary minerals						
Anglesite	*BDL*	0.5	0.3	*BDL*	0.9	2.1
Alunite	*BDL*	0.4	*BDL*	*BDL*	*BDL*	*BDL*
Jarosite	BDL	BDL	BDL	BDL	BDL	BDL
Rhomboclase	*BDL*	0.3	*BDL*	0.6	0.3	0.4
Scorodite	*BDL*	*BDL*	11.8	*BDL*	*BDL*	*BDL*

4.3.1.4 First-flush leachate chemistry

First-flush leachate pH and EC values are shown in Figure 4.10. All group J samples were classified as acid forming, with pH values between 3 and 3.4 measured. Lower pH and higher EC values were measured from the -4 mm grain size fraction of sample 6 and 19 . Sample 3 returned the lowest average pH, corresponding to the relatively high pyrite contents (Table 4.2). Both Group H samples were acid forming, with a small pH difference (0.1 pH units) recorded between the two grain sizes. Groups E and G were classified as currently non-acid forming corresponding with their relatively low pyrite and secondary mineral contents

(Table 4.2). Following the same trend as the previously described samples, the group E -4 mm grain size fraction returned a lower pH value than the -10 mm. However, for group G the -10 mm grain size fraction returned a lower pH. This sample contained the greatest quantity of muscovite (Table 4.2). Thus, any net-neutralisation offered by muscovite (Table 3.4) was likely to be realised in the -4 mm sample as a function of grain size thus accounting for the higher leachate pH value relative to the coarser -10 mm fraction.

Element concentrations in first-flush leachate are shown in Figure 4.11. Despite the low quantities of soluble secondary minerals (Table 4.2), relatively high element concentrations were measured when

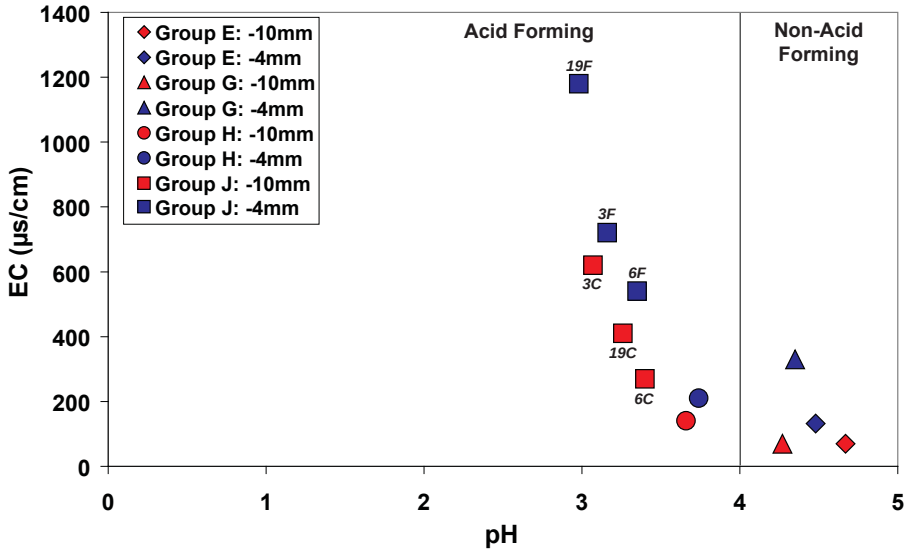

Figure 4.10 First-flush leachate pH and EC values measured from material representative of Croydon waste-rock mesotextural groups E, G, H and J (F refers to the fine (-4 mm) grain size fraction, and C to the coarse (-10 mm) grain size fraction).

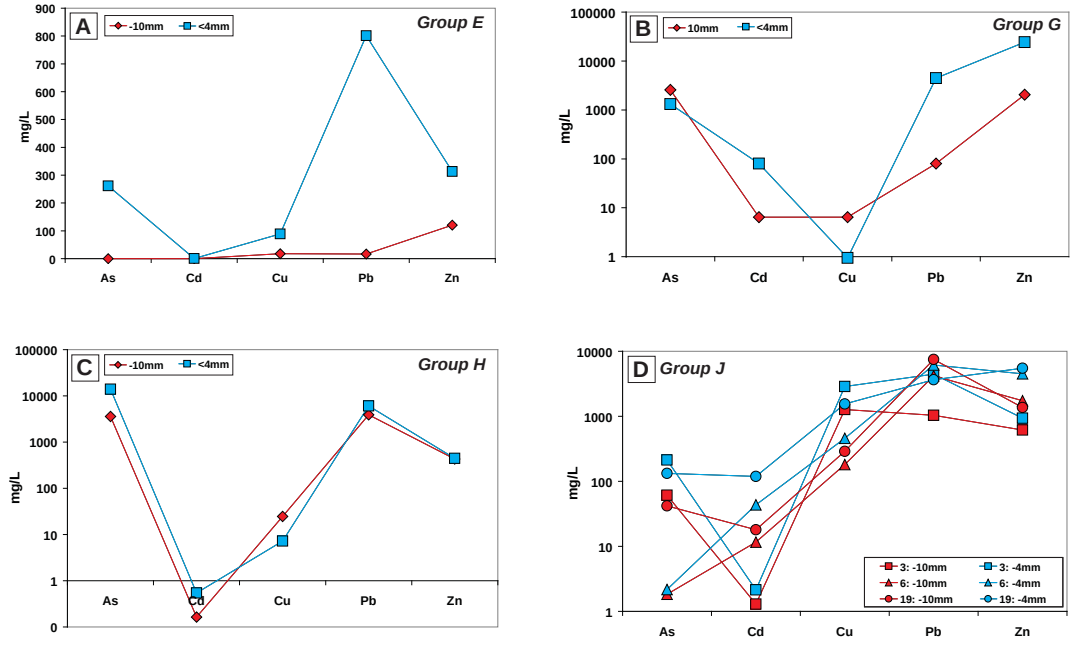

Figure 4.11 First flush leachate chemistry (As, Cd, Cu, Pb and Zn) for Croydon waste-rock mesotextural groups E, G, H and J: **(A)** Group E; **(B)** Group G; **(C)** Group H; and **(D)** Group J. Values from both the -10 mm and -4 mm grain size fractions are shown.

In group H relatively similar element concentrations were measured between the two grain size fractions, with higher As, Cd, Pb and Zn measured in the -4mm fraction (Figure 4.11c). The highest As concentrations were measured (~1 wt. %) corresponding to the high arsenopyrite and scorodite contents (Table 4.2). High concentrations of Pb were measured from both grain sizes, but the quantity of Pb-bearing minerals (i.e., galena and anglesite; Table 4.2) identified in this sample appeared too low to account for such values. Therefore, it was postulated that an alternative Pb source must be present. Element mapping of scorodite revealed that it contained between 100-1000 ppm Pb, indicating this may be a significant source of this element (Figure 4.12). To the author's knowledge such Pb concentrations in scorodite have not been extensively documented.

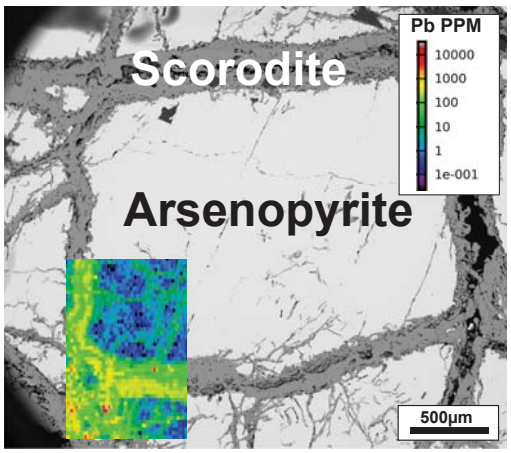

Figure 4.12 Quantified LA-ICP-MS lead distribution map (ppm) of massive arsenopyrite with scorodite in waste rock material representative of Croydon mesotextural group H. (LA-ICP-MS parameters: spot size: 22 µm, 10 Hz frequency, 50% energy).

For group J, the -4 mm fraction consistently measured the highest values for each element, with the exception of Pb in sample 19. Group 3 contained the highest As (-4 mm: ~210 mg/L), followed by group 19 (-4 mm: ~130 mg/L) and the lowest was in sample 6 (-10 mm: ~2 mg/L). These values correlate to pyrite content (Table 4.2), and indicate that on weathering, As is liberated from pyrite (Table 4.2; Figure 4.9). Primary sources of Cd (i.e., sphalerite) were not detected in this group. However, Cd concentrations ~120 mg/L were measured from the -4mm fraction of sample 19. Therefore, secondary minerals present in this group are likely Cd-bearing, with Irwin et al. (1997) and Tauson et al. (2004) identifying anglesite as a source. High concentrations of Cu were measured in leachate from samples 3 (-4 mm: ~2900 mg/L) and 19 (-4 mm: ~1500 mg/L), and correlates to both the presence of Cu in pyrite, and minor chalcopyrite as identified in SEM and MLA studies. Lead concentrations directly correlated with galena and anglesite contents with both measured the highest in sample 19 (Table 4.2). Zinc is likely sourced from pyrite and its alteration products rhomboclase and anglesite (cf. Buckby et al., 2003; Giere et al., 2003; Nordstrom, 2004).

4.3.1.5 Summary

- Geochemical characterisation of samples selected for kinetic testing from mesotextural groups E, G, H and J confirmed all as acid forming in accordance with final GMT approach classifications (Table 3.12).
- SEM and MLA-studies demonstrated the heterogeneity of sulphides within each group. Three pyrite

types were identified in group E: (i) fine-grained euhedral quartz-associated pyrite; (ii) coarse-grained subhedral-anhedral quartz-associated pyrite; and (iii) fine-grained, subhedral-anhedral, muscovite-potassium feldspar-quartz-associated pyrite. Sphalerite, pyrite and galena were all identified in group G. Arsenopyrite and scorodite dominated group H. Element mapping of scorodite indicated that it contained high Pb. In group J, the degree of pyrite weathering and presence of galena intergrowths differed between the samples, with sample 3 the least weathered, and sample 6 the most.

- Total element contents reported high As (>10,000 ppm) in group H relating to arsenopyrite and scorodite contents (62.3 wt. % and 11.8 wt. % respectively). High Pb (>10,000 ppm) and As (100-1000 ppm) were measured in group J indicating that pyrite is As-rich, and QXRD confirming the presence of >1 wt. % galena in this group. Group G contained the highest Cd and Zn relating to the presence of sphalerite in this group.
- First-flush pH and EC values indicated that only group H and J were currently acid forming, despite relatively high contents of pyrite in group E (Table 4.2). However, lower pH values were not consistently measured for the -4 mm fraction, indicating a potential contribution to neutralising potential by silicate minerals (i.e., muscovite, albite) when the surface area is increased, particularly for group G.
- In general, first-flush metal contents (As, Cd, Cu, Pb and Zn) were highest from the -4 mm grain size fraction leachates. Extremely high As values (~1 wt. %) were measured from group H, the highest Pb (1000-10,000 ppm) from group J, and the highest Cd (100 mg/L) from group G. These values are in agreement with the measured modal mineralogy and total element contents of these samples.

4.3.2 Mesotextural group E

4.3.2.1 Mineralogical observations

The modal mineralogy of the -4 mm sample (measured from weeks 5 to 30) is shown in Table 4.3. The contents of non-sulphide minerals were unchanged over the experiment with quartz dominating (93.3 to 95.2 wt. %). Pyrite generally decreased from week 5 to 30, and rhomboclase increased, providing an indication that weathering had occurred over time. Galena content was relatively unchanged, however, anglesite slightly increased from week 15 onwards.

Back scattered electron images of sulphide grains from the -10 mm column are shown in Figure 4.13. At week 5, fine-grained, euhedral, quartz-associated pyrite (type i) was unweathered (Figure 4.13a). Comparatively, coarse-grained, quartz-associated pyrite (type ii) was more weathered, with hydrous ferric oxide (HFO) cement developed (Figure 4.13b). This cement rimmed pyrite grains (Figure 4.13c), potentially limiting internal weathering. The HFO cement was also observed in week 10 (Figure 4.13d and 4.13e), where it had developed in deep mechanically-induced fractures (likely formed as a consequence of sample preparation). Fine-grained, rhyolite groundmass-associated pyrite (type iii) appeared strongly weathered by week 15, with embayed grain boundaries and no secondary rims having developed (Figure 4.13f). At week 20, coarse-grained, quartz-associated pyrite (type ii) demonstrated a highly complex internal texture with galena inclusions, a serrated grain boundary and no HFO cements observed (Figure 4.13g). At higher magnification, pyrite appeared to have developed a porous texture (Figure 4.13h), a

feature which was more distinctly observed at week 25 (Figure 4.13i). Alteration of galena to anglesite was also recognised at this time (Figure 4.13g). By week 30, fine-grained quartz-associated pyrite (type i) had started to undergo weathering, with fracturing observed (Figure 4.13k). By week 30, coarse-grained quartz-associated pyrite (type ii) was strongly weathered, with a secondary mineral aggregate developed (Figure 4.13l).

Table 4.3 Quantitative modal mineralogy (wt. %) as measured by QXRD at weeks 5, 10, 15, 20, 25 and 30 of samples obtained from the -4 mm grain size fraction of Croydon waste rock mesotextural group E. Secondary minerals refer to those formed as a consequence of sulphide oxidation (BDL: below detection limit i.e., <0.3 wt.%).

Week	5	10	15	20	25	30
Non-sulphides						
Albite	0.8	0.7	1.3	1.1	1.4	0.5
Illite	*BDL*	*BDL*	0.5	0.3	*BDL*	0.5
Kaolinite	*BDL*	0.6	0.4	1.2	0.5	0.4
Muscovite	1.6	2.3	0.8	0.6	1.2	0.9
Quartz	94.1	93.3	94.2	94.3	95.2	94.6
Sulphides						
Arsenopyrite	*BDL*	*BDL*	0.2	*BDL*	*BDL*	0.3
Galena	0.3	0.3	0.3	0.5	0.5	0.3
Pyrite	1.9	1.3	1.0	0.6	0.5	0.6
Secondary minerals						
Alunite	0.6	0.5	*BDL*	BDL	BDL	BDL
Anglesite	*BDL*	*BDL*	0.6	0.5	0.3	0.7
Orpiment	*BDL*	*BDL*	0.4	0.3	*BDL*	*BDL*
Rhomboclase	BDL	BDL	*BDL*	*BDL*	*BDL*	0.8
Scorodite	*BDL*	0.5	*BDL*	*BDL*	*BDL*	*BDL*
Sulphur	*BDL*	0.3	*BDL*	0.3	*BDL*	0.4

4.3.2.2 Leachate chemistry

Leachate pH values remained above pH 4 from both the -10 mm and -4 mm columns until week 8 (Figure 4.14). Values then remained below pH 4 from the -4 mm fraction until week 30. A similar trend was observed from the -10 mm column, with pH values consistently higher than the -4 mm column by <0.6 pH units. Leachate EC from the -10 mm fraction was high at week 1 (90 µS/cm), but rapidly dropped, with a final value of ~30 µS/cm measured at week 30 (Figure 4.14). Electrical conductivity values measured from the -4 mm leachate fluctuated more than the -10 mm, with a maximum of ~80 µS/cm measured around week 4. Cumulative mass release of sulphate is shown in Figure 4.15. Whilst less leachate was evolved from the -4 mm column, the rate of sulphate release was higher (~11.4 mg/L^{-1}) than from the -10 mm column (4 mg/L^{-1}), implying a faster rate of sulphide oxidation.

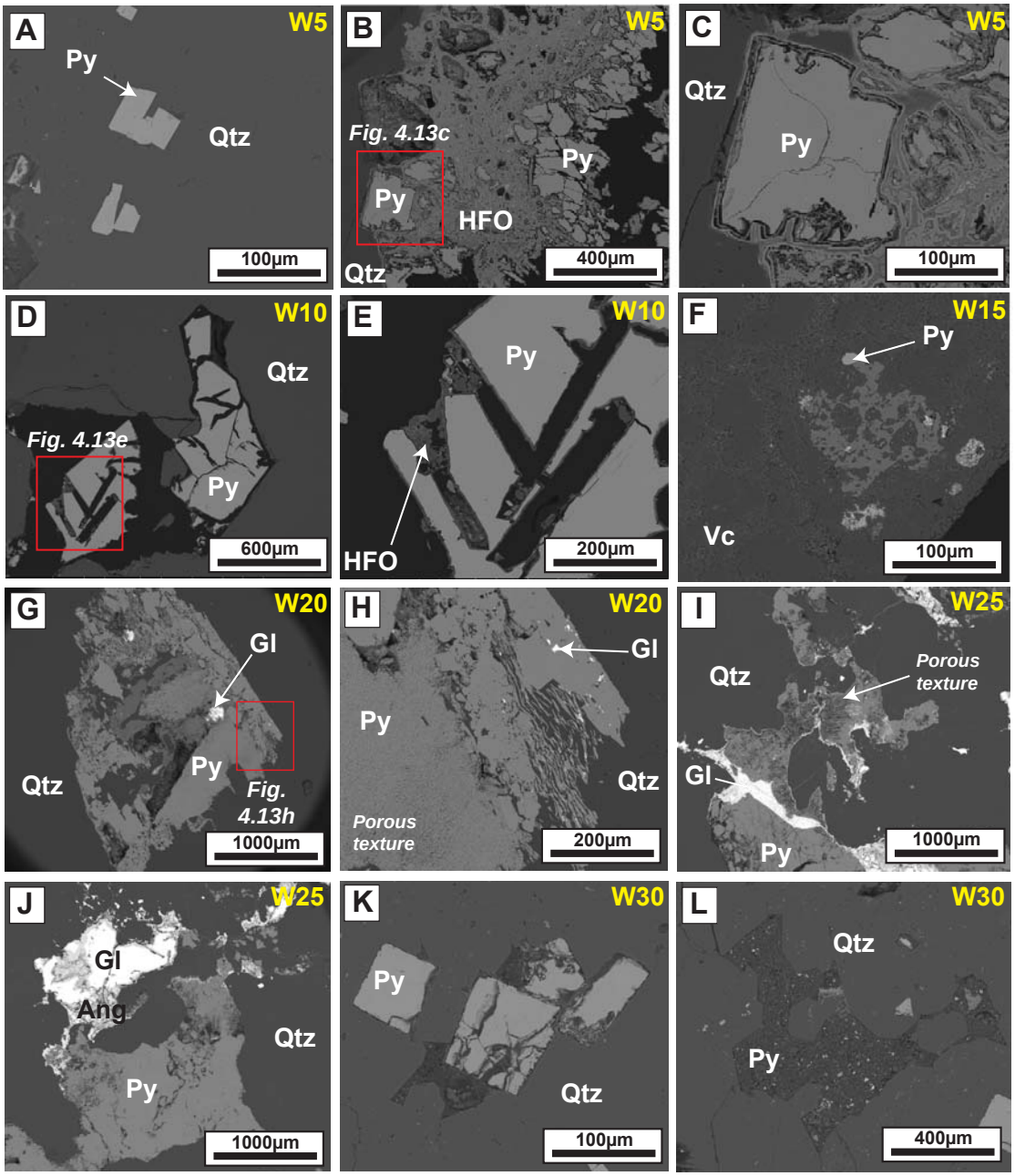

Figure 4.13 Back scattered electron images of Croydon mesotextural group E particles obtained from the -10 mm column at weeks 5, 10, 15, 20, 25 and 30: **(A)** Unweathered fine-grained quartz-associated pyrite; **(B)** Extensive formation of HFO cement around pyrite; **(C)** Pyrite grain contains few fractures, indicating armouring from oxidation by HFO cement; **(D)** and **(E)** HFO precipitation in mechanically induced pyrite fractures; **(F)** Fine-grained groundmass-associated pyrite strongly weathered; **(G)**, **(H)** and **(I)** Coarse-grained quartz-associated pyrite complexly weathered, with an absence of HFO coating, and a porous texture developing within pyrite; **(J)** Galena replacement by anglesite; **(K)** Fine-grained quartz-associated pyrite is fractured, with some secondary minerals developing on the rim; **(L)** Strongly weathered coarse-grained quartz-associated pyrite pseudomorphically replaced by a pyrite aggregate. Abbreviations: Ang, anglesite; HFO, hydrous ferric oxides; Gl, galena; Py, pyrite; Qtz, quartz: Vc, volcanic (muscovite-altered rhyolite) groundmass, W, week.

Cumulative mass release of As, Fe, Pb and Zn in leachate measured over the 30 weeks is shown in Figure 4.16. Very low cumulative mass releases of all elements were measured from both grain size fractions when compared to first-flush values (Figure 4.16). Greater quantities of As, Fe and Pb were leached from the -4 mm column. The rate of As release was relatively constant from the -10 mm fraction,

however, for the -4 mm column it increased from 0.02 to 1.38 mg/L^{-1} at week 28. A similar trend was observed for Fe, with a relatively constant leach rate from the -10 mm column (0.29 mg/L^{-1}), but an initially slow rate from the -4 mm column (0.19 mg/L^{-1}), which subsequently increased (2.9 mg/L^{-1}). Lead showed the inverse, with a relatively constant release rate calculated from the -4 mm column (0.28 mg/L^{-1}), but an initially fast release rate from the -10 mm column (0.4 mg/L^{-1}) which soon dropped to 0.03 mg/L^{-1}. A greater quantity of zinc was leached from the -10 mm column, with a relatively constant release rate (0.1 mg/L^{-1}) measured up until week 20.

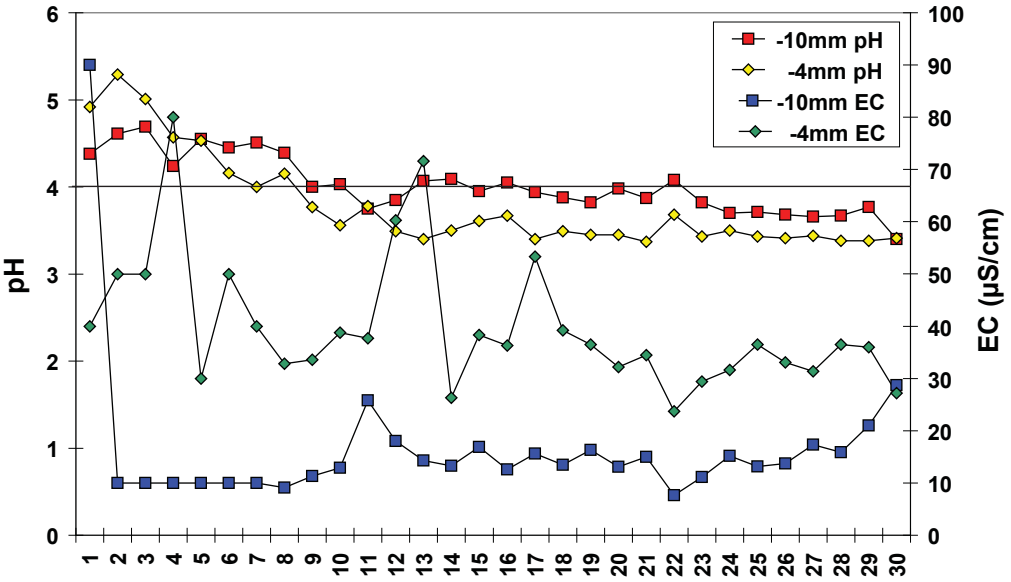

Figure 4.14 Leachate pH and EC values measured weekly (1 to 30) from kinetic test columns containing -10 mm and -4 mm grain size fractions of Croydon waste rock mesotextural group E.

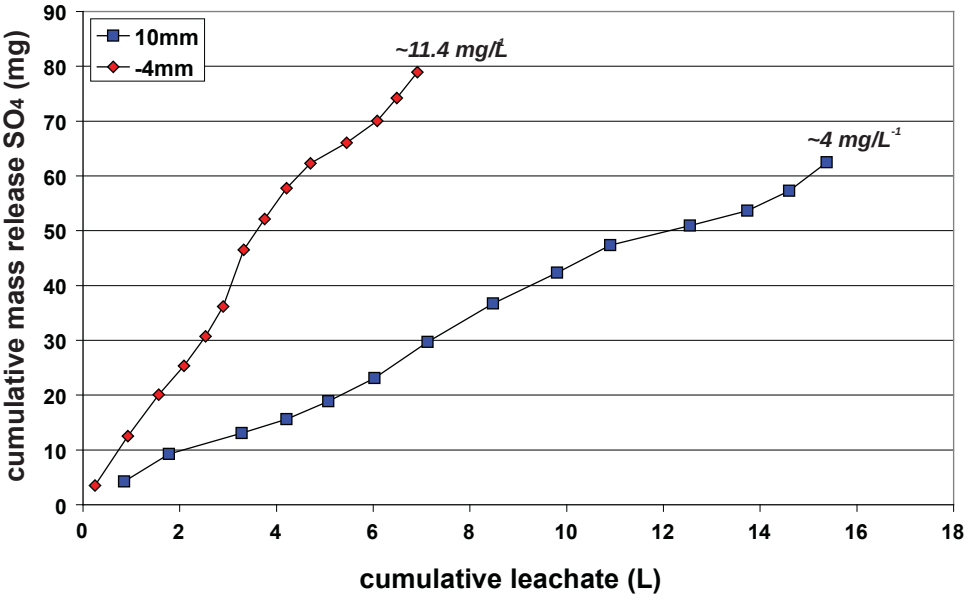

Figure 4.15 Cumulative mass release of sulphate shown against cumulative leachate volume (litres) from kinetic test columns containing -10 mm and -4 mm grain size fractions of Croydon waste rock mesotextural group E.

4.3.2.3 Trace element chemistry

To determine the content and distribution of trace elements (As, Cu, Co, Fe, Mn, Ni, Pb and Zn) in pyrite, quantitative element mapping (ppm) of representative grains from the -10 mm fraction at weeks 10, 20 and 30 was undertaken using LA-ICP-MS. Coarse-grained subhedral-anhedral pyrite (type ii) was focussed on as BSE images suggested that this type underwent the most weathering during the experiment. At week 10, As appeared zoned in the body of the pyrite grain (Figure 4.17a). Copper, Pb and Zn were located in fractures, and therefore in secondary HFO. Cobalt and Ni concentrations were <10 ppm in both pyrite and its secondary products. At week 20, the porous microtexture observed in the BSE image of pyrite was depicted by the speckled distribution of Fe and As (Figure 4.17b). Lead was distributed across the grain as micro-inclusions, particularly in the regions demonstrating the porous microtexture. Lead does not co-exist with As in these areas. Cobalt and Ni are elevated in regions where pyrite appears unweathered providing evidence for Kwong's (1993) statement that where pyrite is enriched in these elements, resistance to oxidation is increased. A complexly weathered grain (representative of type ii) was mapped at week 30 (Figure 4.17c). The primary pyrite grain was intergrown with secondary HFO, as indicated by the distribution of Fe. Arsenic, Cu, and Pb appear to be pervasively distributed. Areas of relatively high Co and Ni (10 to 100 ppm) correlated to zones of less weathered pyrite. Manganese and Zn were low in both pyrite and its alteration products.

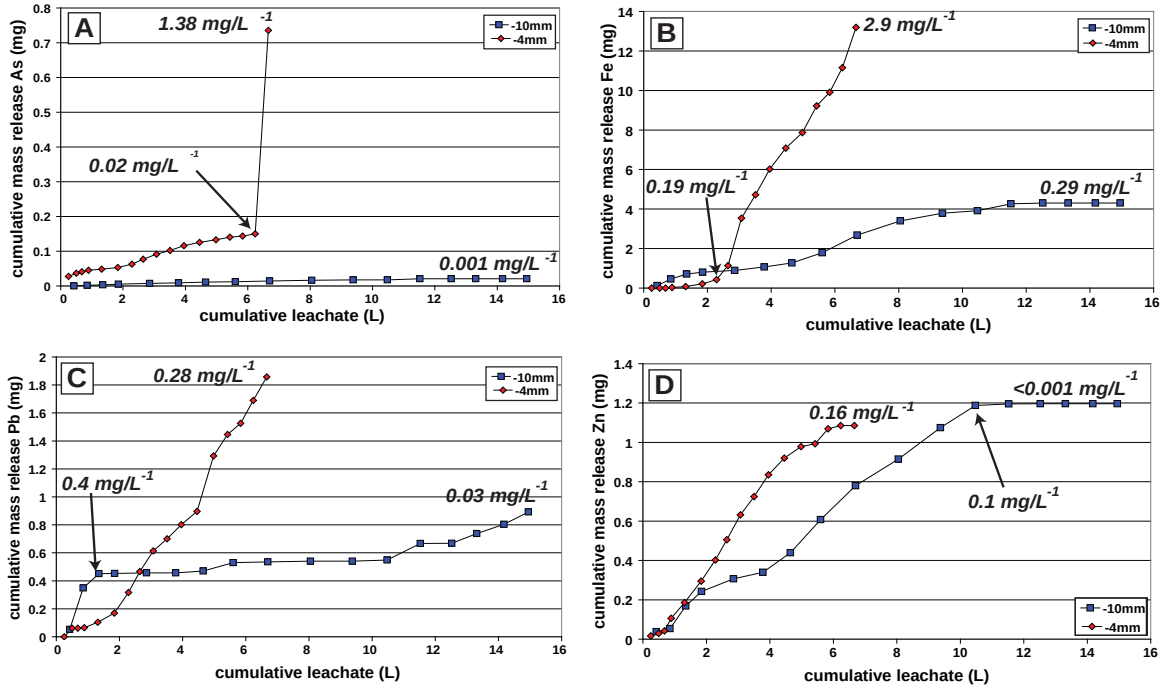

Figure 4.16 Cumulative mass release of trace elements versus cumulative leachate volume (litres) from kinetic test columns (-10 mm and -4 mm fractions) containing Croydon waste rock material representative of mesotextural group E: As **(A)**; Fe **(B)**; Pb **(C)**; and Zn **(D)**.

Several grains from fine-grained pyrite (type i) were also mapped using LA-ICP-MS at week 30 for comparison (Figure 4.17d). Clear zonation of As was observed, with deficient cores grading out into an enriched zone, with the concentration rapidly declining to the grain boundary, and is similar to that shown in Figure 3.46. Cobalt was present within the grain, with maximum concentrations adjacent to high arsenic zones. Nickel and Cu were pervasively dispersed across the grains, with high Cu areas

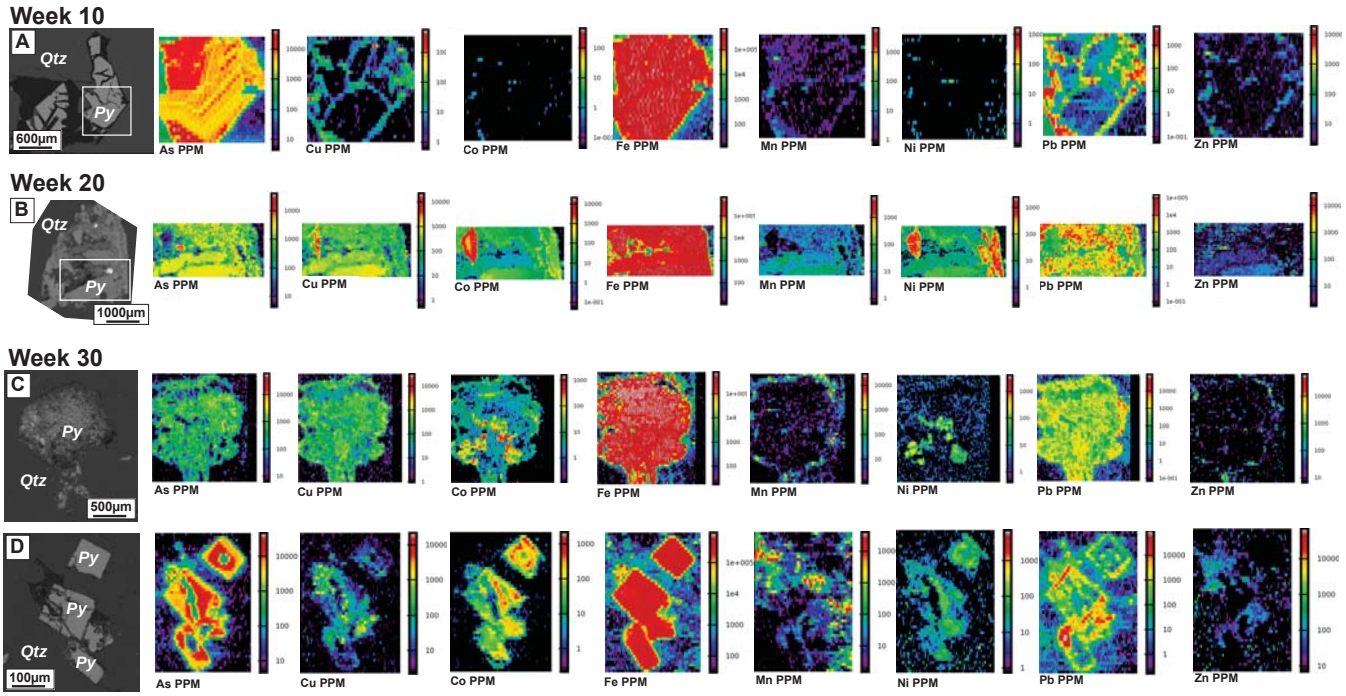

Figure 4.17 Quantified LA-ICP-MS element distribution maps (ppm) of pyrite grains (from Croydon waste rock material representative of mesotextural group E) obtained from the -10mm kinetic test column: **(A)** Coarse-grained quartz-associated pyrite (type ii) at week 10; **(B)** Coarse-grained quartz-associated pyrite (type ii) at week 20; **(C)** Coarse-grained quartz-associated pyrite (type ii) at week 30; and **(D)** Fine-grained quartz-associated pyrite (type i) at week 30. NB. Element maps shown in full in Appendix 4.4, with mapping parameters given. Abbreviations: Py, pyrite; Qtz, quartz.

THIS PAGE IS INTENTIONALLY BLANK

corresponding with weathered pyrite. Lead concentrated exclusively in weathered pyrite. Comparison of these maps with those collected at for coarse-grained pyrite (type ii; Figure 4.17a-c) confirmed that both have similar trace element signatures, with As dominating, and elevated Co and Ni in localised areas. The coarse-grained pyrite (type ii) contained more galena micro-inclusions as depicted by the element map than fine-grained pyrite (type i), indicating that this is a more significant control on oxidation than trace element content.

4.3.2.4 Summary

- Of the three pyrite types identified in group E, coarse-grained quartz associated pyrite (type ii) underwent the most weathering, with hydrous ferric oxides (HFO) formed. Whilst fine-grained groundmass associated pyrite (type iii) was strongly weathered from the start of the experiment, BSE images indicated that additional weathering had occurred. Fine-grained quartz-associated pyrite (type i) was the least weathered, with a small degree of fracturing and HFO developing by week 30. Thus, the contribution of each sulphide type to the net-acidity is likely in the order: type ii> type iii> type i.
- Leachate pH values remained above pH 4 from both the -10 mm and -4 mm grain size fractions until week 8, when the pH generally declined to <4 until week 30. The -4 mm column was slightly more acid forming than the -10 mm column.
- The cumulative mass-release of elements leached during the experiment were considerably lower relative to first-flush values from both grain sizes, despite the high contents of As, Pb (as micro-inclusions) and occasionally Co and Ni in the primary pyrite grains. This can be attributed in part to the small quantity (<1 wt. %) of soluble secondary minerals (rhomboclase and anglesite) precipitated during these experiments.

4.3.3 Mesotextural group G

4.3.3.1 Mineralogical observations

The modal mineralogy (measured from week 5 to 30) for the -4 mm sample is shown in Table 4.4. Overall, quartz dominated (79.4 to 85.4 wt. %). Muscovite content declined from 8.2 wt. % to 2.6 wt. %, whilst the kaolinite content increased implying that muscovite weathering may have occurred (cf. Murphy and Gilkes, 2010). Albite and illite contents remain relatively constant for the duration of the experiment.

Sphalerite dominated the sulphide mineralogy of the -4 mm column, with its content generally decreasing over time (from 4.7 wt. % at week 5, to 1.7 wt. % at week 30), suggesting oxidation had occurred. Edwards et al. (2000) identified native sulphur as a sphalerite oxidation product, and here its concentration increased over time (from BDL to 1.2 wt. %). Evidence for oxidation in the -10 mm column was observed in SEM studies (Figure 4.18). At week 5, quartz-associated sphalerite appeared relatively unfractured (Figure 4.18a). In the week 10 sample, fractures were observed in grains (Figure 4.18d), and when observed under higher magnification, sphalerite appeared porous in proximity to them, with a 'cornflake' texture formed across the grain (Figure 4.18e). Whilst some material was observed in these fractures, identification of these minerals was not possible using EDS given their amorphous

nature. Galena veins were observed in sphalerite (Figure 4.18f), the presence of which likely increased the weathering rate of sphalerite (cf. Abraitis et al., 2004). By week 20, the porous pattern and cornflake texture had further developed (Figure 4.18h), and by week 30, sphalerite grain boundaries appeared serrated (Figure 4.18l).

An overall decrease in pyrite contents was indicated in the -4 mm column (1.6 wt. % to 1.2 wt. %), and a minor increase in rhomboclase and jarosite was observed over time, suggesting the occurrence of oxidation (Table 4.4). BSE images showed that at week 5, sphalerite-quartz associated pyrite was hardly fractured (Figure 4.18a), however, by week 15 fractures were abundant, with secondary phases (likely HFO developed as a result of jarosite weathering) developed (Figure 4.18g). The degree of pyrite fracturing had increased by weeks 25 and 30 (Figures 4.18i, 4.18k and 4.18l). Galena micro-inclusions were observed in proximity to fractures (Figure 4.18l).

Table 4.4 Quantitative modal mineralogy (wt. %) measured at weeks 5, 10, 15, 20, 25 and 30 of samples obtained from the -4 mm grain size fraction of Croydon waste rock mesotextural group G. Secondary minerals refer to those formed as a consequence of sulphide oxidation (*BDL*: below detection limit, i.e., <0.3 wt. %).

Week	5	10	15	20	25	30
Non sulphides						
Albite	1.7	1.5	3	2.2	1.1	1.2
Illite	0.7	0.6	1.6	1.9	1.5	1.8
Kaolinite	1.4	1.5	*BDL*	*BDL*	2	2.2
Microcline	BDL	BDL	BDL	*BDL*	0.4	*BDL*
Muscovite	8.2	8	5	5.5	1.7	2.6
Quartz	79.4	79.5	81.6	79.9	85	84.4
Sulphides						
Arsenopyrite	0.7	0.5	0.4	0.5	0.6	0.9
Galena	0.4	0.3	0.3	0.3	*BDL*	0.4
Pyrite	1.6	1.3	0.8	1.3	1	1.2
Pyrrhotite	*BDL*	*BDL*	0.3	0.3	*BDL*	*BDL*
Sphalerite	4.6	4.9	4	4.2	2	1.7
Secondary minerals						
Alunite	0.4	1	0.5	0.3	*BDL*	*BDL*
Anglesite	0.3	*BDL*	0.4	0.5	1	0.4
Jarosite	0.3	*BDL*	0.5	0.9	0.9	1.3
Orpiment	*BDL*	*BDL*	0.3	0.5	0.4	*BDL*
Rhomboclase	*BDL*	*BDL*	0.4	*BDL*	0.5	0.6
Scorodite	*BDL*	0.3	*BDL*	0.4	0.4	*BDL*
Sulphur	*BDL*	*BDL*	0.7	1.1	1.1	1.2

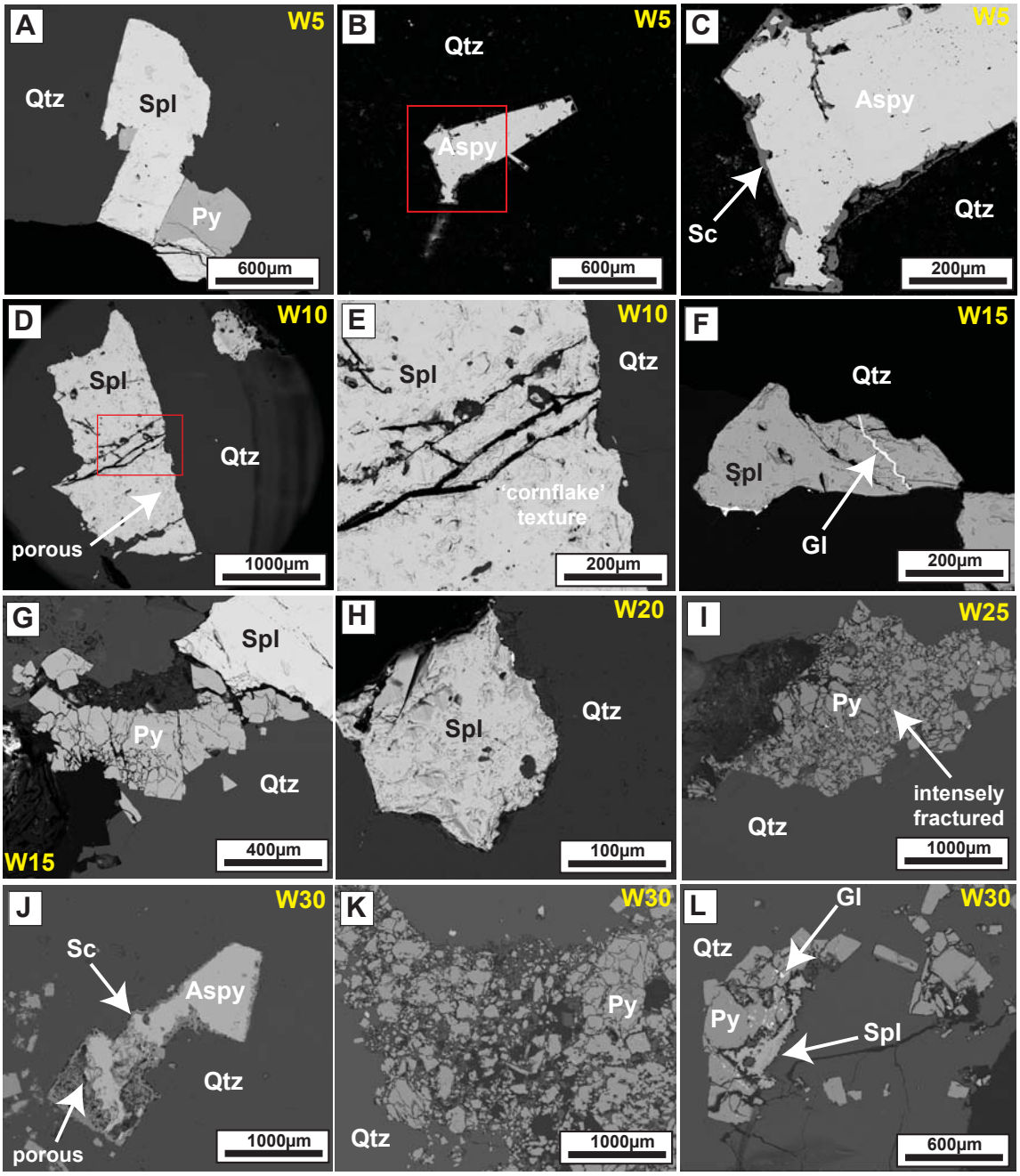

Figure 4.18 Back scattered electron images of Croydon mesotextural group G particles obtained from the -10 mm column at weeks 5, 10, 15, 20, 25 and 30: **(A)** Intergrown unweathered pyrite-sphalerite in quartz; **(B)** and **(C)** Arsenopyrite rimmed by scorodite; **(D)** and **(E)** Fractures developed in sphalerite, with sphalerite appearing 'porous in proximity to the fractures, and an overall cornflake texture demonstrated; **(F)** Galena veins seen in mildly weathered sphalerite; **(G)** Highly fractured pyrite, with the adjacent sphalerite grain also fractured in proximity to the sulphide-grain contact; **(H)** Further development of the sphalerite cornflake weathering texture; **(I)** Extensively fractured pyrite; **(J)** Scorodite rim persisting on arsenopyrite, with an internal porous texture; **(K)** Strongly weathered massive pyrite; **(L)** Relict sphalerite intergrown with galena-bearing pyrite. Abbreviations: Aspy, arsenopyrite; Gl, galena; Py, pyrite; Qtz, quartz: Sc, scorodite; Spl, sphalerite; W, week.

Arsenopyrite contents were relatively similar over the experiment (0.5 to 0.9 wt. %), however, the presence of orpiment (As_2S_3) indicated that some direct oxidation had occurred (Craw et al., 2003). Scorodite was consistently identified by QXRD, and formed rims around arsenopyrite grains (e.g., Figure 4.18b and 4.18c). Scorodite rims on arsenopyrite had thickened by week 30 (Figure 4.18j), with

scorodite having developed a porous internal texture, suggesting some alteration to an amorphous ferric arsenate phase may have occurred (cf. Harvey et al., 2006; Murciego et al., 2011).

The small variation in galena contents over time indicated that its oxidation progressed slowly, if at all, with anglesite not identified in BSE studies. Low quantities of pyrrhotite were occasionally detected i.e., weeks 15 and 20 (~0.3 wt. %). As this material is pre-oxidised (c.20 years atmospheric exposure), pyrrhotite is likely to have preferentially undergone weathering in accordance with the sulphide alteration index (SAI), with only traces now remaining, and pyrite and sphalerite dominating (Blowes and Jambor, 1990; Gunsinger et al., 2006; Moncur et al., 2009).

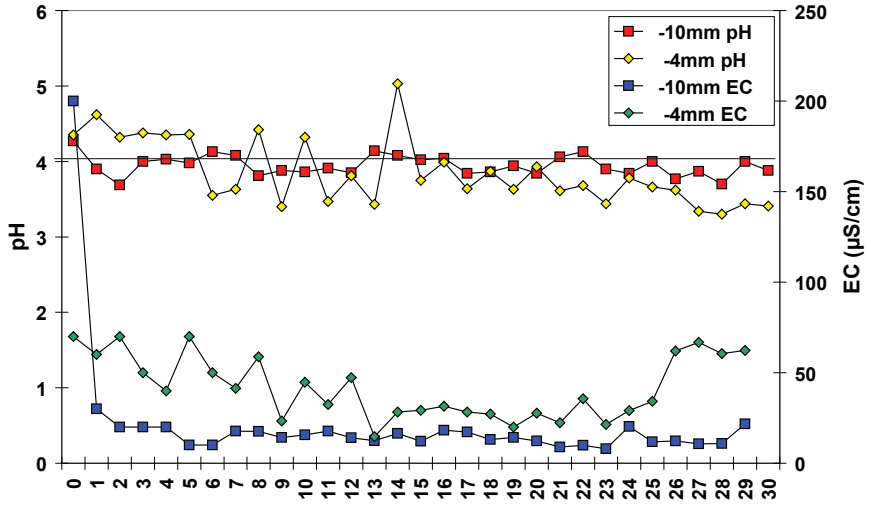

Figure 4.19 Leachate pH and EC values measured weekly (0-30) from kinetic test columns containing -10 mm and -4 mm grain size fractions of Croydon waste rock mesotextural group G.

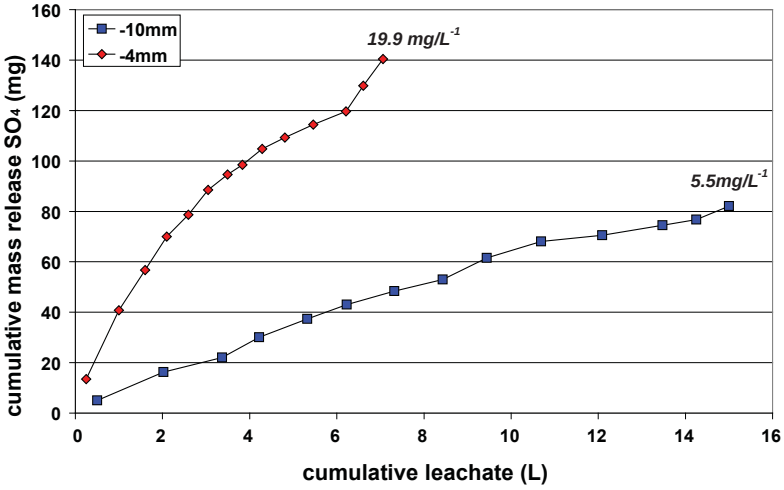

Figure 4.20 Cumulative mass release of sulphate shown against cumulative leachate volume (litres) from kinetic test columns containing -10 mm and -4 mm grain size fractions of Croydon waste rock mesotextural group G.

4.3.3.2 Leachate chemistry

ARD conditions (pH <4) were established in the -10 mm column from week 2 onwards (Figure 4.19). However, the leachate pH from this column oscillated throughout the experiment (pH range: 3.7 to 4.3). ARD conditions were established later (week 7) in the -4 mm column, with low pH conditions

more persistent, however a greater range was measured overall (pH 3.4 to 5). Leaching out of any acid forming mineral in this sample is not suggested by this data (i.e., rapid and sustained change in values), which is in agreement with mineralogical observations. The high EC value initially measured from the -10 mm column leachate (200 µS/cm) indicates that the first-flush experiment (performed at week 0) did not completely dissolve all soluble minerals. However, from week 3 onwards, EC values were low (<30 µS/cm) for the -10 mm column leachate, with values slightly higher for the -4 mm column leachate from week 2 onwards. Potentially, this indicates more rapid formation of soluble secondary minerals in the -4 mm column.

Cumulative mass release of As, Cd, Fe, Mn, Pb and Zn in leachate collected from mesotextural group G is shown in Figure 4.21. Overall, relatively low concentrations of all elements relative to first-flush values were measured (Figure 4.11b). Cumulative mass release of As and Fe was consistently higher from the -10 mm fraction, with other elements higher in the leachate from the -4 mm fraction column. The decrease in mass release of As from week 10 onwards from both grain size fractions (Figure 4.21a) potentially relates to the progressive formation of scorodite as an arsenopyrite replacement product (Figure 4.18c and 4.18j). Cadmium release rate from sphalerite in the -10 mm fraction was steady and extremely low (~ 0.008 mg/L^{-1}; Figure 4.21b).

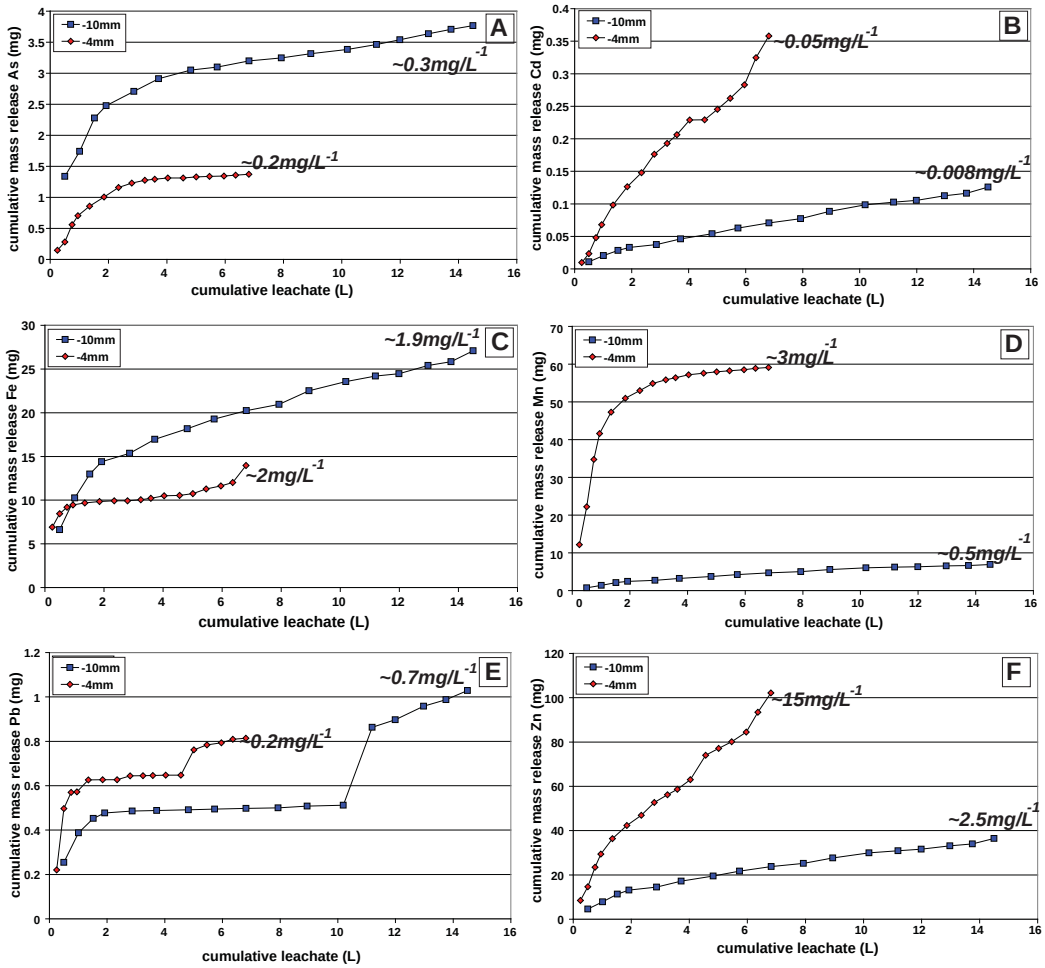

Figure 4.21 Cumulative mass release of As **(A)**; Fe **(B)**; Pb **(C)**; and Zn **(D)** from mesotextural group G shown against cumulative leachate volume (litres). Data for both grain sizes fractions (-10 mm and -4 mm) are shown.

Steady release rates were also calculated for other elements sourced from sphalerite in the -10mm fraction including Mn (~0.5 mg/L^{-1}; Figure 4.21d) and Zn (~ 2.5 mg/L^{-1}; Figure 4.21f) . Overall, a faster rate of sphalerite (and pyrite) oxidation was likely to have occurred in the -4 mm column (as inferred by pH and sulphate data). Nordstrom and Alpers (1999) inferred Cd and Zn uptake by rhomboclase through measurement of the element content of waters from the Richmond mine. Jarosite also has the ability to uptake Cd and Zn (Pappu et al., 2006; Hudson-Edwards and Wright, 2011). As these minerals were identified in the -4 mm fraction (Table 4.4), their dissolution is likely to have contributed to the overall Cd and Zn contents, in addition to sphalerite.

Lead showed a pulsed cumulative mass-release pattern for both columns (Figure 4.21e), however, a higher quantity and faster release rate were calculated for the -4 mm column. Final cumulative values were low from both columns (<0.7 mg/L^{-1}), reflecting low galena contents. If anglesite was present in trace quantities, it is likely to have formed at a similar rate to galena oxidation, thus limiting Pb concentration in solution.

4.3.3.3 Minor/trace element chemistry

Quantified LA-ICP-MS element maps (ppm) for selected sphalerite/pyrite grains from the -10 mm fraction column were produced to evaluate trace element contents in the primary sulphides, and their weathering products. Sphalerite grains were mapped at weeks 0, 10 and 20 (As, Cd, Cu, Fe, In, Mn and Pb) and pyrite at weeks 25 and 30 only (As, Cu, Co, Ni, Pb and Zn). Results from both sulphides are discussed separately in this section.

The sphalerite-pyrite grain mapped at week 0 (Figure 4.22a) showed homogenous Cd distribution, indicating a slow rate of crystal growth (Di Benedetto et al., 2005). Whilst Fe and Mn were present pervasively across this grain, concentrations increased with distance from the pyrite grain. Di Benedetto et al. (2005) and Cook et al. (2009) report that typically, Zn and Mn demonstrate an antithetic relationship; however, this was not observed here. Maximum In concentrations were <100 ppm, which is relatively low compared to ranges presented in Cook et al. (2009). Thallium was consistently low (<1 ppm), and is therefore not shown. Arsenic was distributed only along fractures, however, As hotspots (~12,000 ppm) indicated the presence of arsenopyrite inclusions, with examples of these also reported in Lynch and Mendel (1995), Simmons and Brown (1997), and Schwarz-Schampera and Herzig (2002). Chalcopyrite micro-inclusions ('chalcopyrite disease'; Barton and Bathke, 1987) were also present in sphalerite as indicated by Cu hotspots. Micro-inclusions appear to have aligned parallel to the long-axis grain boundary. Fracturing related to the presence of either type of sulphide inclusion was not seen. Lead was dominantly located in the pyrite grain as micro-inclusions. Overall, both sulphide grains appears relatively unweathered which is in accordance with leachate chemistry (i.e., low concentrations of elements measured).

No significant elemental distribution or concentration changes were observed at week 10 (Figure 4.22b). Arsenic and Pb concentrated in proximity to the main grain fracture, suggesting that the presence of micro-inclusions had promoted fracturing and oxidation. Iron, In and Mn were more homogeneously

distributed than in week 0, reflecting a compositional difference between the analysed grains (i.e., a more pervasive element distribution in relatively coarser grains), and not a change induced by this experiment.

At week 20, fewer micro-inclusions of As and Pb were observed (Figure 4.22c), however, an unweathered galena rim was observed around the grain shown. Chalcopyrite inclusions appeared more pervasively distributed, and generally in proximity to the major grain fractures. Lower Mn concentrations (<100 ppm) were measured compared to previous weeks, however, Cd, Fe and In were consistent. Overall, relatively little change in the element distribution was measured over time, with no distinct secondary products identified. This confirms that at a -10 mm grain size, sphalerite oxidation proceeded slowly despite the relatively high content of Cd and Fe which have been reported to increase oxidation rate (Weisner et al., 2003).

Element distribution in pyrite grains from weeks 25 and 30 were similar with heterogeneous element distribution observed in both (Figures 4.23a and 4.23b). Generally, Co and Ni concentrated in pyrite, with Zn showing an antithetic relationship to these elements. Arsenic concentrations in these pyrite grains exceeded those measured in group E, and the range quoted for arsenian pyrite (c.10. wt% e.g., Abraitis et al., 2004; Blanchard et al., 2007). This may suggest the presence of pervasively distributed sub-microscopic arsenopyrite inclusions. As with pyrite grains examined from group E, Pb micro-inclusions were present, and identified in proximity to fractures. Localised hotspots of Cu were observed in pyrite, with similar concentrations reported in Radcliffe and McSween (1969). Compared to the small portion of pyrite mapped at week 0 (Figure 4.22a), pyrite oxidation appears to have proceeded rapidly over the 30 weeks compared to sphalerite. However, where both sphalerite and pyrite are intergrown, galvanic interactions take place with the prior preferentially weathered (Abraitis et al., 2004; Hita et al., 2006).

4.3.3.4 Summary

- Grain size exerts a significant control on sphalerite oxidation in this mesotextural group. Sphalerite oxidation occurred at a greater rate in the -4 mm column, with higher cumulative mass release of Zn and SO_4. Additionally, modal mineralogy measurements indicated a decrease in sphalerite and an increase in its oxidation products (i.e., sulphur) from weeks 5 to 30. Whilst there was some textural indication of oxidation having occurred in the -10 mm column, it was not significant in terms of impacting leachate chemistry, with low cumulative mass release rates (<2.5 mg/L^{-1}) of elements calculated. The distribution of Cd, Fe and In in sphalerite from the -10 mm fraction column remained relatively unchanged from weeks 0 to 20, with only a decrease in Mn inferred by quantified element maps.
- ARD conditions were measured at week 6 in the -4 mm column and week 1 in the -10 mm column, however this was not sustained in the latter. Low pH values (i.e., pH <4) measured are attributed to pyrite oxidation, with textural evidence implying that pyrite weathered at a greater rate than sphalerite, contradicting Keith and Vaughan (2000) and Moncur et al. (2009).
- Compositionally, pyrite is highly heterogeneous, with zones of high As, Cu, Co, Ni and Zn identified.

The presence of micro-inclusions (i.e., galena and arsenopyrite) in pyrite exhibited the greatest control on oxidation rate. After the initiation of fracturing, secondary minerals likely developed and caused more fracturing as crystal lattices were wedged apart (cf. Abraitis et al., 2004). HFO eventually formed in fractures, with Ni and Co co-precipitated or adsorbed to HFO phases (Moncur et al., 2009). Incorporation of As increases pyrite oxidation rate (Blanchard et al., 2007), on weathering, As has been leached from the primary grains, and fixed in HFO (Morin and Calas, 2007).

- Higher quantities of Zn were measured in these leachates compared to mesotextural group E, confirming that mesotextural group G is a significant Zn source in the Croydon waste rock piles, posing a risk to the downstream creek systems.

4.3.4 Mesotextural group H

4.3.4.1 Mineralogical observations

The mineralogy of the -4 mm fraction column was significantly different to the previous samples, with arsenopyrite dominating, followed by quartz and scorodite (Table 4.5). Albite, illite and muscovite were present in minor to trace quantities, as were pyrrhotite and sphalerite. Generally, the modal abundance of arsenopyrite measured in the -4 mm fraction column decreased from week 5 to 30 (64.6 wt. % to 53.8 wt. %), whilst scorodite increased (11 wt. % to 19.8 wt. %), suggesting that arsenopyrite is directly oxidising under acid conditions to scorodite in accordance with Dove and Rimstidt (1985) and Zhu and Merkel (2001). In weeks 25 and 30, sulphur was identified and was reported by McGuire et al. (2001) as another product of arsenopyrite oxidation.

Back scattered electron images indicated that arsenopyrite oxidation also occurred in the -10 mm column (Figure 4.24). At week 5, scorodite formed a distinct rim around both fine- and coarse-grained arsenopyrite (Figure 4.24a). Some scorodite was also observed along grain fractures. Pyrite intergrown with arsenopyrite also contained arsenopyrite inclusions and had developed a fine scorodite rim (Figure 4.24b and 4.24c). By week 10, the development of scorodite was no longer restricted to fractures, and had grown across the main body of arsenopyrite grains, with a linear pattern demonstrated (Figure 4.24d). Continued scorodite growth was seen at week 15, with the linear patterns across grains less evident and instead thicker, dendritic patterns observed (Figure 4.24e). Where scorodite had extensively precipitated, it comprised of acicular/fibrous grains (Figure 4.24f). At week 20, pyrite fragments appeared cemented within scorodite (Figure 4.24g). In addition to acicular grains, scorodite spherules were also observed (Figure 4.24h). Massive arsenopyrite appeared strongly weathered by week 25 (Figure 4.24i). When observed at higher magnification, scorodite appears more crystalline than in previous weeks (Figure 4.24j). At week 30, massive scorodite appeared to start weathering, with a slightly diffuse appearance adopted (Figure 4.24k). This suggests development of Fe-As phases, as similarly reported by Murceigo et al. (2009). At week 30, fine-grained arsenopyrite appeared relatively unchanged since week 5 (Figure 4.24l), which provides evidence that massive arsenopyrite weathered at a greater rate than finer-grained arsenopyrite.

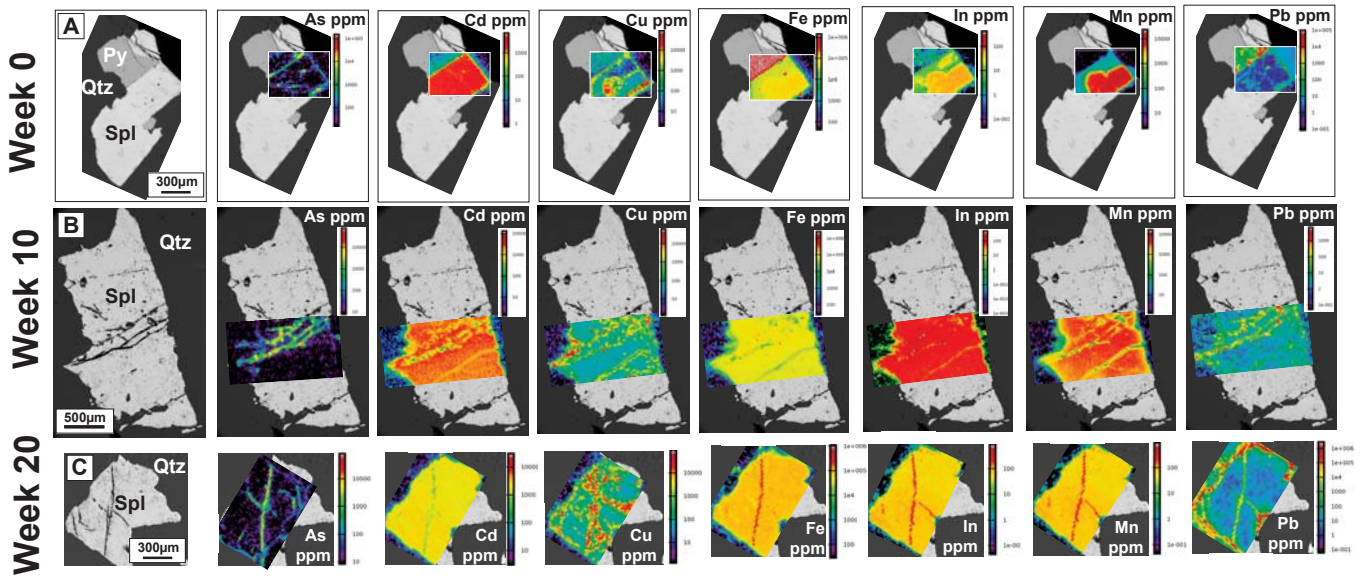

Figure 4.22 Quantified LA-ICP-MS element distribution maps (ppm) of sphalerite grains (from Croydon waste-rock mesotextural group G), obtained from the -10 mm kinetic test column: **(A)** Sphalerite-pyrite grain, relatively unweathered collected at week 0; **(B)** Sphalerite grain collected at week 10 showing early stages of weathering with fractures developed; **(C)** Sphalerite grain taken at week 20 still showing only early stages of weathering. Abbreviations: Py, pyrite; Qtz, quartz; Spl, sphalerite. NB. Element maps shown in full in Appendix 4.5, with mapping parameters there given.

THIS PAGE IS INTENTIONALLY BLANK

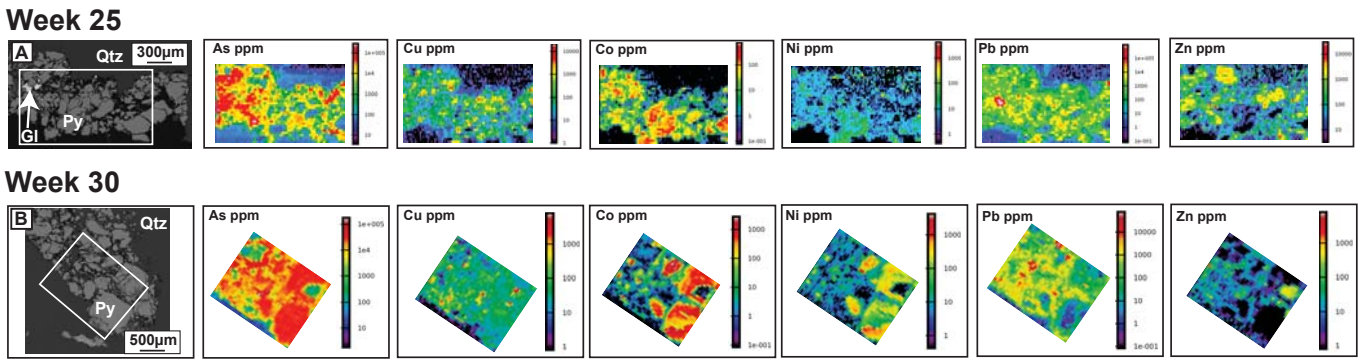

Figure 4.23 Quantified LA-ICP-MS element distribution maps (ppm) of pyrite grains (from Croydon waste-rock mesotextural group G), obtained from the -10 mm kinetic test column: **(A)** Strongly weathered pyrite grain collected at week 25; **(B)** Strongly weathered pyrite grain collected at week 30. Abbreviations: Py, pyrite; Qtz, quartz, Spl, sphalerite. NB. Element maps shown in full in Appendix 4.5, with mapping parameters there given.

THIS PAGE IS INTENTIONALLY BLANK

Similar observations of strongly altered arsenopyrite and formation of distinct scorodite cements were documented by Recio-Vazquez et al. (2011) and Murceigo et al. (2011). Flemming et al. (2005) summarised that the stability of ferric arsenate relates to the degree of crystallinity, with amorphous phases having a higher solubility than crystalline scorodite. Considering this, scorodite from this mesotextural group is likely to have a low solubility under the oxidising conditions experienced in this experiment as it appeared crystalline (cf. Drahota and Filippi, 2009). Dove and Rimstidt (1985) and Krause and Ettel (1988) reported that the low solubility of scorodite limits As concentration in ARD environments, thus the type of scorodite observed in this mesotextural group would be a desired secondary alteration phase in accordance with Pichler et al. (2001) and Haffert and Craw (2009).

Table 4.5 Quantitative modal mineralogy (wt. %) as measured by QXRD at weeks 5, 10, 15, 20, 25 and 30 of samples obtained from the -4mm grain size fraction of Croydon waste rock mesotextural group H. Secondary minerals refer to those formed as a consequence of sulphide oxidation (*BDL*: below detection limit i.e., <0.3 wt. %).

Week	5	10	15	20	25	30
Non-sulphides						
Albite	0.4	0.7	2	2.3	1.6	1.3
Illite	*BDL*	1.4	1.1	0.3	*BDL*	*BDL*
Muscovite	BDL	BDL	BDL	BDL	BDL	BDL
Quartz	21.5	20	24.4	23.2	21.5	20.4
Sulphides						
Arsenopyrite	64.6	63.8	58.9	57.1	50.5	53.8
Pyrite	*BDL*	1	1.4	*BDL*	*BDL*	0.3
Pyrrhotite	0.5	0.4	*BDL*	0.5	*BDL*	*BDL*
Sphalerite	0.6	*BDL*	*BDL*	*BDL*	0.3	*BDL*
Secondary minerals						
Alunite	1	0.6	0.8	0.7	0.3	0.6
Anglesite	*BDL*	0.3	*BDL*	*BDL*	0.5	0.3
Orpiment	*BDL*	*BDL*	0.4	*BDL*	2	1.8
Rhomboclase	*BDL*	*BDL*	*BDL*	0.4	*BDL*	*BDL*
Scorodite	11	11.6	10.8	15.3	19.4	19.8
Sulphur	*BDL*	*BDL*	*BDL*	*BDL*	3.4	1.7

4.3.4.2 Leachate chemistry

The leachate pH remained below pH 4 in both the -10 mm and -4 mm for the duration of the experiment (Figure 4.25). Values were relatively similar between both grain sizes for the first three weeks however, at week 4 there was a pH increase in the -10 mm leachate, but a continued decrease in the -4 mm leachate. From week 8 to 22 onwards, a near identical pH trend was measured for both columns, with values pH <3 occasionally recorded for the -4 mm column. At week 29, the pH declined to its lowest value (pH 2.6) in the -4 mm column. Overall, EC values were higher for the -4 mm fraction, with the highest value recorded at the start (730 µS/cm) which subsequently decreased values until around week 29. Electrical conductivity values were <115 µS/cm in -10 mm column leachate from week 2 onwards.

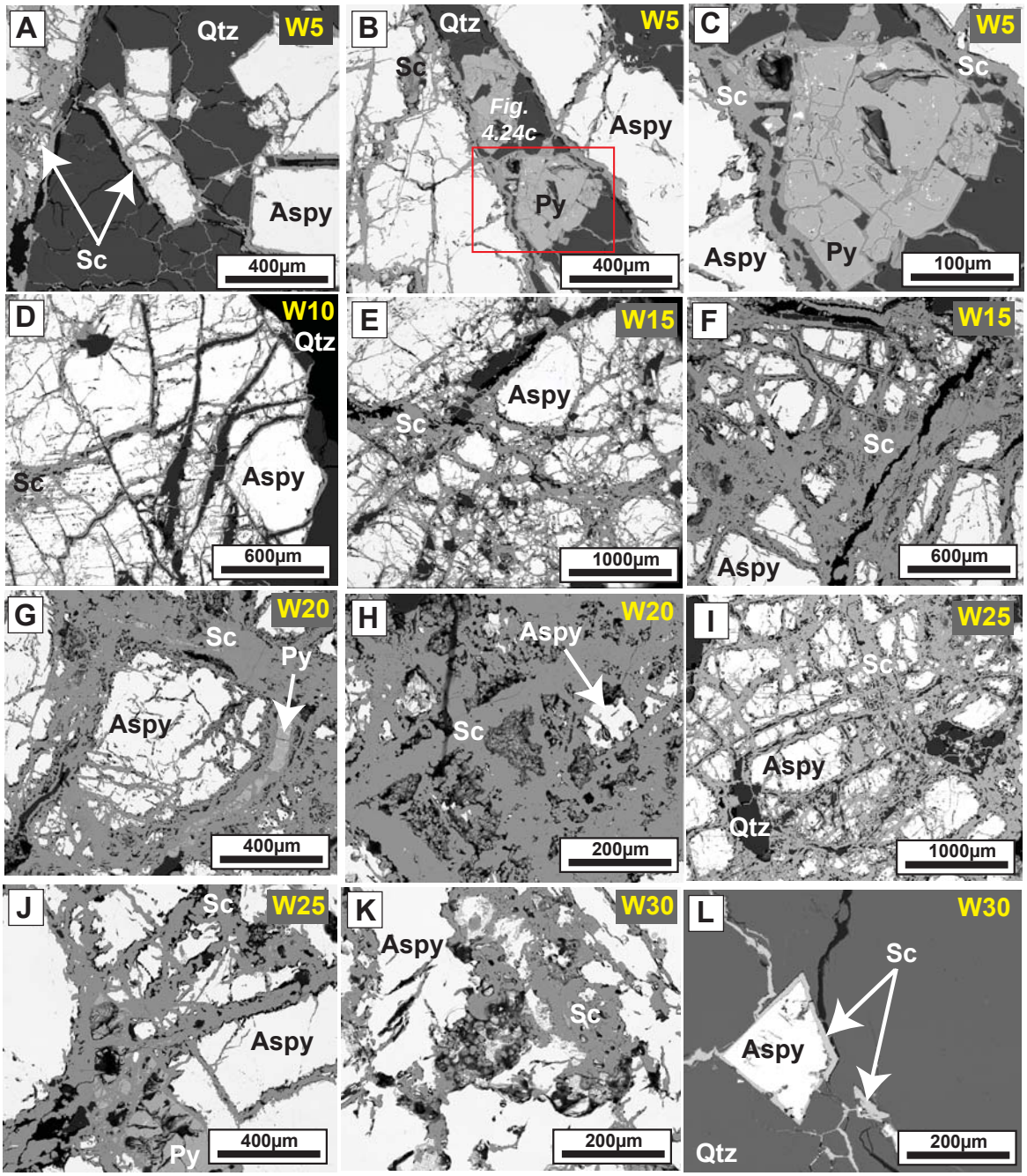

Figure 4.24 Back scattered electron images of particles obtained from the -10 mm grain size fraction of Croydon mesotextural group H: **(A)** Fine-grained arsenopyrite in quartz with a scorodite rim; **(B)** and **(C)** Pyrite intergrown between massive arsenopyrite with scorodite rims formed between the sulphides; **(D)** Linear growth patterns of scorodite in massive arsenopyrite; **(E)** Strongly altered massive arsenopyrite; **(F)** Scorodite mass comprised of acicular/fibrous grains; **(G)** Pyrite encapsulated in scorodite; **(H)** Strongly weathered arsenopyrite in a crystalline scorodite mass comprised of acicular/fibrous grains and spherules; **(I)** Strongly weathered massive arsenopyrite extensively replaced to scorodite; **(J)** Highly fragmented pyrite encapsulated in scorodite; **(K)** Scorodite weathering with a diffuse grain boundary observed; **(L)** Fine-grained arsenopyrite in quartz with a scorodite rim. Abbreviations: Aspy, arsenopyrite; Gl, galena; Py, pyrite; Qtz, quartz; Sc, scorodite; Spl, sphalerite, W, week.

Cumulative mass release of sulphate from both columns is shown in Figure 4.26. Final values from both grain size fractions are greater than those measured for groups E and G. This is because scorodite formation produces sulphate (*equation 4.1*: Dove and Rimstidt, 1985). Additionally, this reaction explains why low pH values were measured throughout the experiment.

$$FeAsS\ (arsenopyrite) + 14Fe^{3+} + 10H_2O \rightarrow 14Fe^{2+} + SO_4 + FeSO_4.2H_2O\ (scorodite) + 16H^+ \qquad (4.1)$$

Whilst approximately 50% less leachate passed through the -4mm column, the final cumulative mass and rate of SO_4 release was greater (~58 mg/L^{-1}), indicating faster oxidation in the -4 mm column. No significant gradient changes were identified on the graph for either column (with the exception of at week 24 in the -10 mm column when too much test solution was added resulting in sulphate dilution), suggesting a steady rate of oxidation.

Cumulative mass release of As was high from both columns (Figure 4.27a) compared to the other mesotextural groups, with release rates of 11.4 mg/L^{-1} and 3 mg/L^{-1} calculated for the -4 mm and -10 mm columns respectively. Iron was also consistently high in leachate (Figure 4.27b) and is a product of scorodite formation as indicated by *equation 4.1*. Lead was measured in both leachates (Figure 4.27c) and was released at a constant rate from the -4 mm column, but showed an increase in release from week 22 onwards from the -10 mm column. Some Zn was also measured (Figure 4.27d), but in general the concentrations were low, with similar final cumulative mass release values measured from both columns, despite differences in cumulative leachate volumes. Cumulative mass release of Co, Cu and Ni were <1 mg over the experiment, and therefore are not shown.

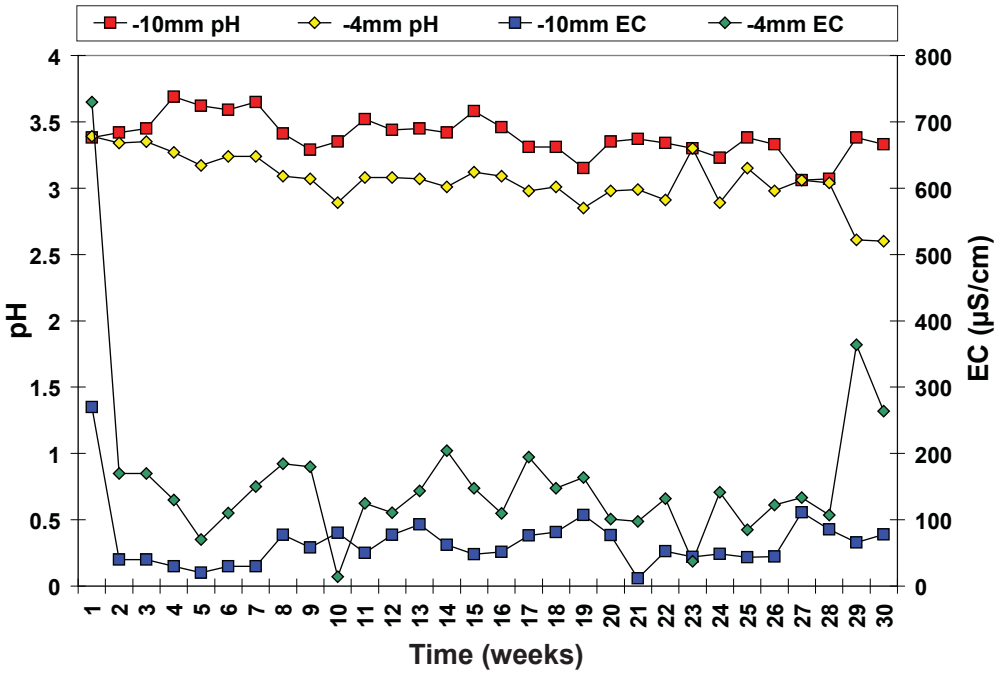

Figure 4.25 Leachate pH and EC values measured weekly (1 to 30) from kinetic test columns containing -10 mm and -4 mm grain size fractions of Croydon waste rock mesotextural group H.

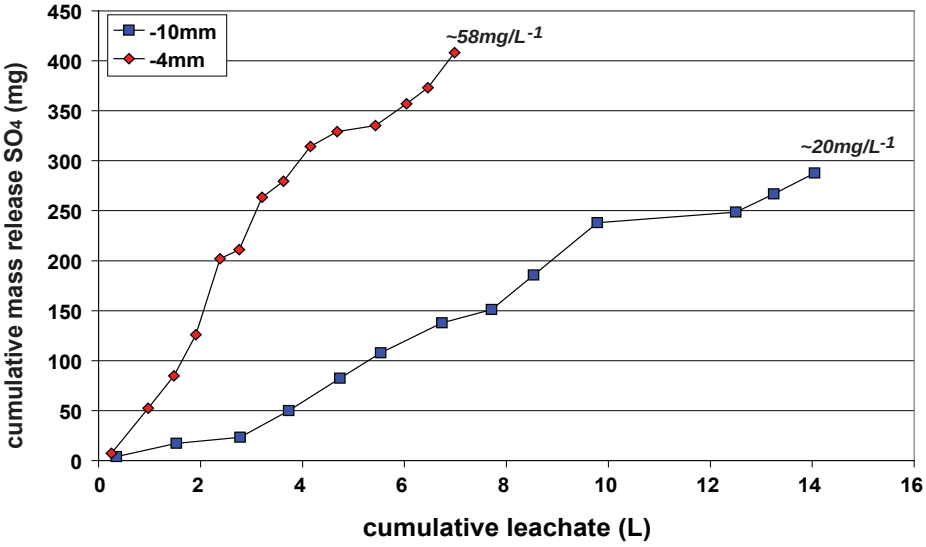

Figure 4.26 Cumulative mass release of sulphate from mesotextural group H shown against cumulative leachate volume (litres). Data for both grain sizes fractions (-10 mm and -4 mm) are shown.

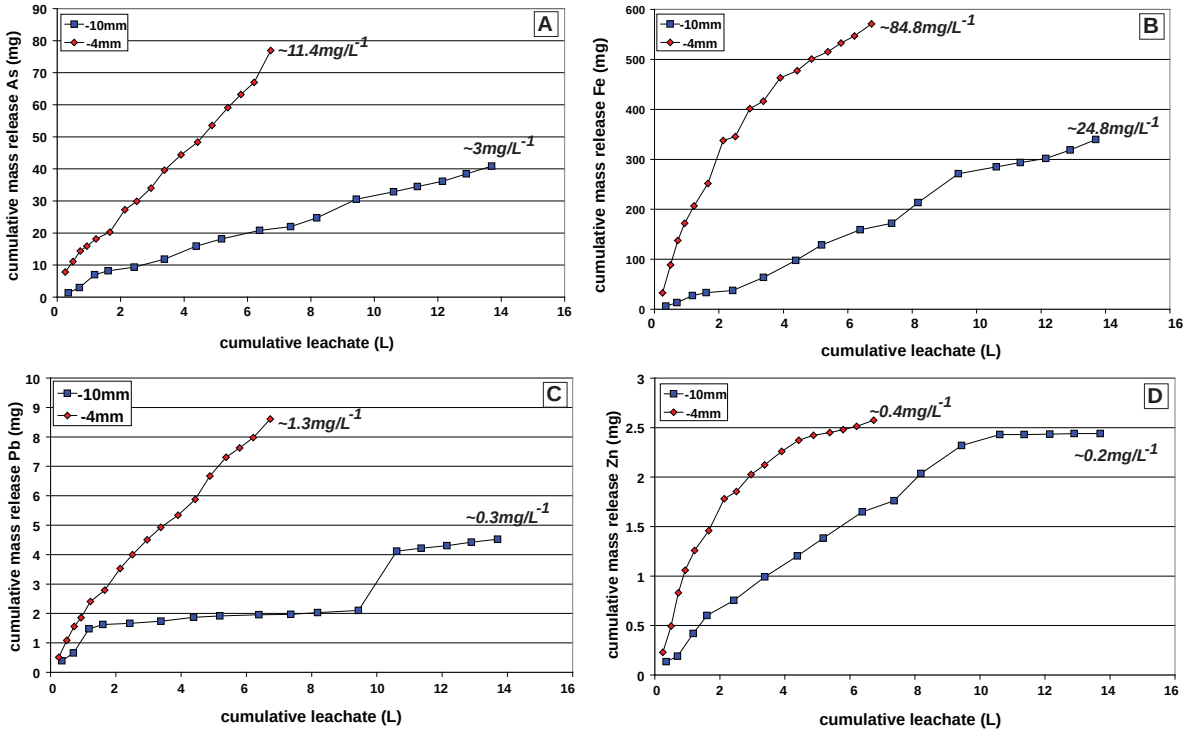

Figure 4.27 Cumulative mass release of trace elements from mesotextural group H shown against cumulative leachate volume (litres) from grain size fractions -10 mm and -4 mm: As **(A)**; Fe **(B)**; Pb **(C)**; and Zn **(D)**.

4.3.4.3 Trace element chemistry

Quantitative LA-ICP-MS spot analyses (ppm) performed on arsenopyrite (week 0, 15 and 30) showed that the trace element contents are low, with no systematic trend of decreasing element content over time. Only Sb was identified at >100 ppm levels (Table 4.6) which is typical for mesothermal gold deposits, with Sb likely present in solid solution (Craw, 2002; Craw et al., 2004).

Table 4.6 Element concentrations (ppm) in arsenopyrite from Croydon waste rock mesotextural group H (week 0, 15 and 30) as measured by LA-ICP-MS spot analysis (spot size: 50 µm; frequency: 10 Hz; energy: 50%). NB. stoichiometric Fe in arsenopyrite was used as the value for the internal standard (*BDL*: below detection limit).

	Co	Cu	Ni	Pb	Sb	Zn
Week 0 (n=11)						
Max.	27	23	5	75	200	71
Min.	*BDL*	*BDL*	*BDL*	*BDL*	100	*BDL*
Mean	10	4	1	13	142	10
Median	3	1	1	7	133	*BDL*
Week 15 (n=15)						
Max.	29	20	3	68	146	13
Min.	*BDL*	*BDL*	*BDL*	0	70	*BDL*
Mean	5	4	1	19	97	3
Median	2	1	*BDL*	8	94	*BDL*
Week 30 (n=16)						
Max.	62	32	10	91	276	18
Min.	1	*BDL*	*BDL*	1	98	*BDL*
Mean	21	3	2	11	145	2
Median	15	1	1	6	135	*BDL*

Quantified element maps (ppm) were collected for select grains from week 5, 10, 15, 20, 25 and 30 as shown in Figure 4.28. Previous observations suggested that the presence of both Co and Ni may retard arsenopyrite oxidation (Section 3.4.4.2). Sampson and Phillips (2001) showed that the oxidation of an arsenopyritic-gold concentrate with a mixed culture of *Acidithiobacillus ferrooxidans* and *Leptospirillum ferrooxidans* was significantly inhibited by the addition of Ni, Co and Cu (40-80 mM). Some evidence is provided here that Co alone may have this effect, as less weathered areas contained Co (10-100 ppm) in concentric bands.

The element content of scorodite was measured by EPMA at weeks 0, 10, 20 and 30 (Appendix 4.6). The Fe:As ratio ranged between 0.74 to 0.82, with slightly higher concentrations of Fe and As measured in later weeks. Copper, Pb and Zn were observed in scorodite rims and fractures throughout the experiment (Figure 4.28). Copper and Zn incorporation in scorodite within these concentration ranges (<1000 ppm) is not uncommon as reported in Monhemius and Swash (1999), Fujita et al. (2008) and Gomez et al. (2011). Singhania et al. (2006) stated that in the presence of both Cu and

Zn, scorodite stability is not measurably affected. A decrease in Cu concentration over time is indicated at weeks 25 and 30 (Figure 4.28e and 4.28f) and Zn at week 30 (Figure 4.28f) when compared to the previous weeks. Pb shows a continued presence in scorodite (particularly up to week 20) but at much lower concentrations (<100 ppm). LA-ICP-MS spot analyses indicated a systematic decrease in Co, Cu, Zn and Pb in scorodite over time (Figure 4.29; Table 4.7). However, this was not reflected in the leachate chemistry, as no consistent increase in the mass release of these elements was observed (Figure 4.27). Therefore, redistribution of these elements to another secondary phase is likely occurring with amorphous ferric arsenate phases potential candidates (i.e., some massive arsenopyrite and scorodite has weathered to such Fe-arsenates by week 30; Figure 4.24k).

Table 4.7 Element concentrations (ppm) in scorodite from Croydon waste rock mesotextural group H (week 0, 15 and 30) as measured by LA-ICP-MS spot analysis (spot size: 35 µm; frequency: 10 Hz; energy: 50%). NB. stoichiometric Fe in arsenopyrite was used as the value for the internal standard. (*BDL*: below detection limit).

	Co	Cu	Ni	Pb	Sb	Zn
Week 0 (n= 12)						
Max.	8	66	1	601	115	143
Min.	*BDL*	1	*BDL*	4	57	2
Mean	3	31	*BDL*	141	93	77
Median	2	32	*BDL*	114	94	73
Week 15 (n= 15)						
Max.	7	47	*BDL*	182	104	80
Min.	1	9	*BDL*	22	43	12
Mean	3	26	*BDL*	78	69	38
Median	2	26	*BDL*	70	72	26
Week 30 (n= 8)						
Max.	2	49	11	363	189	332
Min.	*BDL*	*BDL*	*BDL*	*BDL*	*BDL*	2
Mean	1	13	2	66	51	62
Median	1	7	1	4	15	10

4.3.4.4 Summary

- Whilst both columns produced acidic leachate from week 1 onwards, the -4 mm fraction was more acid forming than the -10 mm fraction.
- Weathering of arsenopyrite to scorodite was observed in BSE images and indicated through measurements of modal mineralogy. As time progressed in the experiment, amorphous Fe-As phases and fine-grained ferric arsenates were identified, with the latter two representing potential sinks for trace elements liberated during weathering.
- Crystalline scorodite as observed in BSE images has low solubility under acid, oxidising conditions (Drahota and Fillippi, 2009). Comparison of As measured in leachate with pH values confirmed this, with the solubility value of ~3 mg/L at pH 3.4 to 3.7 calculated for the -10 mm grain size, and ~13 mg/L at pH 2.6 to 3.4 for the -4 mm grain size.

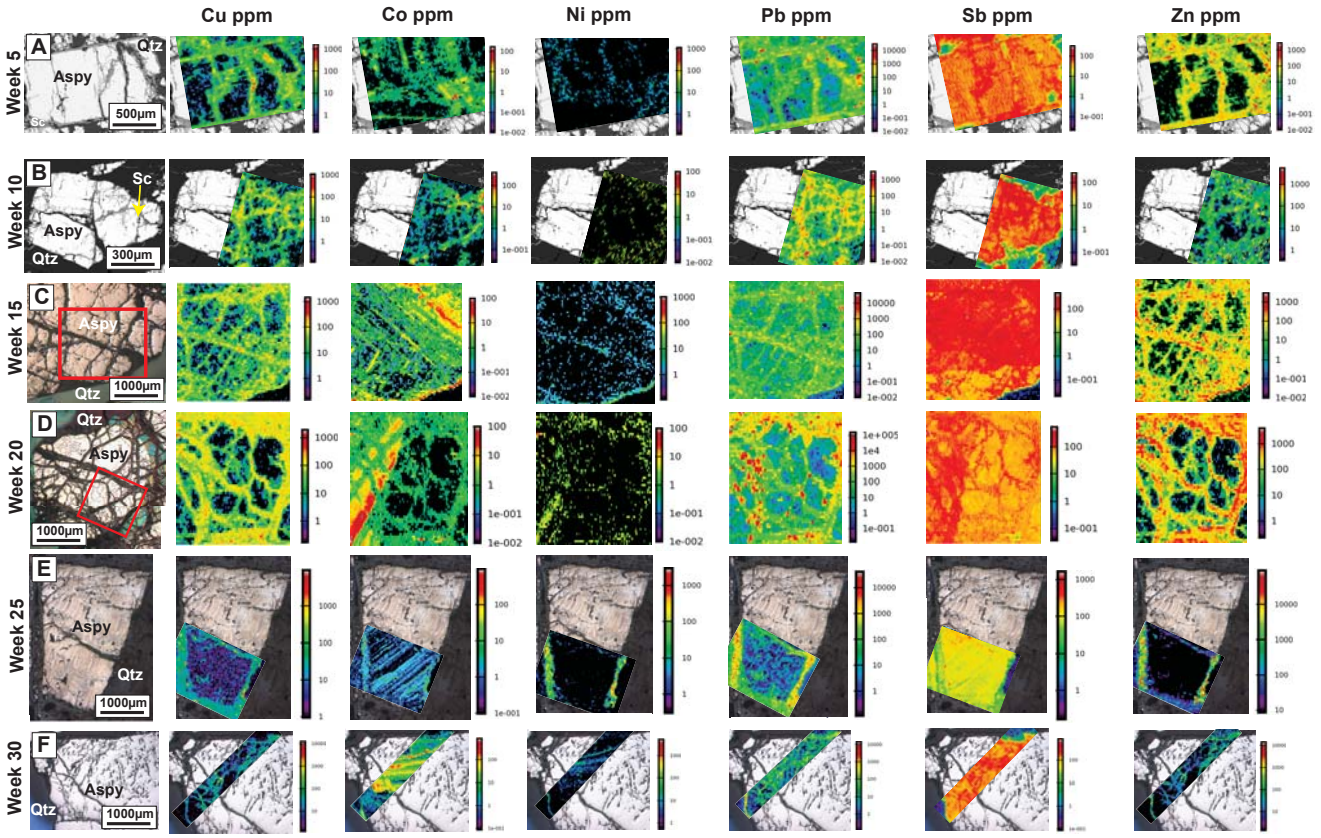

Figure 4.28 Quantified LA-ICP-MS element distribution maps (ppm) of arsenopyrite grains (from Croydon waste-rock mesotextural group H), obtained from the -10 mm kinetic test column: **(A)** Week 5; **(B)** Week 10; **(C)** Week 15; **(D)** Week 20; **(E)** Week 25; **(F)** Week 30. Abbreviations: Aspy, arsenopyrite; Qtz, quartz, Sc, scorodite. NB. Element maps shown in full in Appendix 4.6, with mapping parameters there given.

THIS PAGE IS INTENTIONALLY BLANK

- Trace element content of arsenopyrite was characteristically low, with only Sb measured (~90-200 ppm). Cobalt was identified in a banded pattern in less fractured portions of arsenopyrite grains, indicating that its presence, even at low concentrations, may increase resistance to weathering.
- Trace elements identified in scorodite included Cu, Sb, Pb and Zn. Whilst Sb is sourced from arsenopyrite, the other elements are not (i.e., these elements originated from the weathering of sulphides present in other mesotextural groups (i.e., C, G and J) present in the heterogeneous waste rock piles). Lead is likely to be weakly adsorbed to scorodite, as its concentration decreased over time in this experiment.

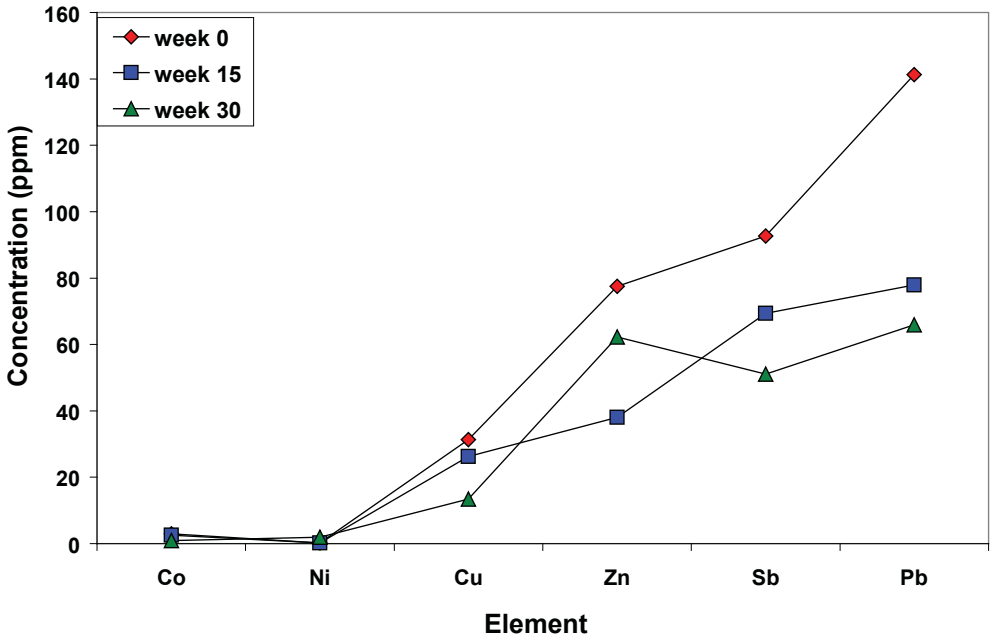

Figure 4.29 Element concentrations (Co, Ni, Cu, Zn, Sb and Zn) measured in scorodite at weeks 0, 15 and 30 analysis (spot size: 35 μm; frequency: 10 Hz; energy: 50%).

4.3.5 Mesotextural group J

4.3.5.1 Mineralogical observations

Quartz consistently dominated the mineralogy of the -4mm fraction for group J samples (3, 6 and 19; Table 4.8), and low (<2 wt. %) contents of kaolinite, muscovite and albite were measured in each column (Appendix 4.7). For sample 3, pyrite contents decreased from 11.2 to 8.8 wt. % and galena from 3.2 to 0.8 wt. % over the thirty weeks. In sample 6, galena dominated (1.9 to 2.9 wt. %), with less pyrite measured relative to the other group J samples, however, a general decrease in its content was measured over time. Sample 19 also contained relatively high galena (1.6 to 2.1 wt. %), but the sulphide mineralogy was dominated by pyrite (3.2 to 4.1 wt. %). No systematic decrease of pyrite was observed over time in sample 19; however, a small decrease of galena was measured. Minor (<1 wt. %) arsenopyrite, sphalerite and pyrrhotite were identified in these samples (Appendix 4.7). Secondary minerals in all -4 mm columns were dominated by anglesite and rhomboclase, with the content of these minerals increasing over time. Rhomboclase, jarosite and alunite have likely formed from pyrite weathering (Jambor et al., 2000), and anglesite from galena (Diehl et al., 2008) as previously discussed. A net-decrease in anglesite was observed in the -4 mm fraction of sample 6, indicating that it too underwent weathering. Scorodite and sulphur are identified as weathering products of the minor sulphides present in these samples.

Table 4.8 Quantitative modal mineralogy (QXRD; wt. %) of samples 3, 6 and 19 from Croydon waste rock mesotextural group J (-4mm fraction), measured at weeks 5, 10, 15, 20, 25 and 30. Post-mining minerals refer to those formed as a consequence of sulphide oxidation. Results are shown in full in Appendix 4.8. (*BDL*: below detection limit i.e., <0.3 wt. %).

Mineral	Sample	5	10	15	20	25	30
Quartz	3	81.2	83.7	85.5	84	84	86.5
	6	86.4	83.7	89.5	90	89.2	90.5
	19	88.4	86.4	86.4	89.2	91.4	89.8
Galena	3	3.2	3.1	1.6	1.9	1	0.8
	6	2.3	2.9	2	1.9	1.9	2.2
	19	2.1	1.7	1.8	1.6	1.6	1.6
Pyrite	3	11.2	9.5	8.6	9.4	9.5	8.8
	6	2.3	2.1	1.4	1.5	1	1
	19	3.2	3.6	4.1	3.3	3.6	3.6
Alunite	3	*BDL*	*BDL*	*BDL*	*BDL*	*BDL*	*BDL*
	6	0.6	0.3	0.4	*BDL*	*BDL*	*BDL*
	19	0.5	0.6	0.3	*BDL*	*BDL*	0.3
Anglesite	3	0.5	0.8	0.4	0.9	0.5	0.9
	6	2.8	3.9	1.4	1.3	1.6	1
	19	2	3.4	2.1	2	1.1	1.7
Jarosite	3	0.5	*BDL*	*BDL*	0.5	*BDL*	*BDL*
	6	*BDL*	0.6	BDL	*BDL*	*BDL*	*BDL*
	19	*BDL*	*BDL*	*BDL*	*BDL*	*BDL*	*BDL*
Rhomboclase	3	*BDL*	*BDL*	*BDL*	0.3	0.7	0.8
	6	*BDL*	0.3	0.7	*BDL*	*BDL*	0.8
	19	*BDL*	*BDL*	*BDL*	*BDL*	*BDL*	0.3
Scorodite	3	*BDL*	*BDL*	*BDL*	*BDL*	*BDL*	*BDL*
	6	0.2	0.5	0.7	*BDL*	*BDL*	*BDL*
	19	0.2	0.5	*BDL*	0.2	*BDL*	*BDL*
Sulphur	3	*BDL*	*BDL*	0.5	0.3	0.3	0.5
	6	0.5	0.9	1.3	1.2	0.8	0.3
	19	1.4	2	0.6	1.1	0.5	0.4

Back scattered electron images of particles obtained from the -10 mm fraction of sample 3 are shown in Figure 4.30. At week 5, <200 μm diameter quartz-associated euhedral pyrite grains appear less weathered relative to subhedral-anhedral grains (Figure 4.30a and 4.30b). By week 10, >200 μm diameter subhedral quartz-associated pyrite grains, containing abundant galena micro-inclusions, appear to develop an internal pitted texture (Figure 4.30c). By comparison, fine-grained (<100 μm diameter) quartz-associated euhedral pyrite grains appeared less weathered (Figure 4.30d). Extensive fracturing was observed in pyrite grains by week 15, with galena (observed on the grain rim) weathered to porous anglesite (Figures 4.30e and 4.30f). The degree of fracturing generally increased in the following weeks in

both euhedral (Figure 4.30g) and subhedral-anhedral pyrite grains (Figure 4.30h). However at week 30, <100 µm diameter quartz-associated euhedral pyrite grains (with some galena micro-inclusions) appear unweathered. These observations indicate that in this column, larger pyrite grains are more susceptible to weathering than smaller grains. Additionally, subhedral/anhedral grains are weathering faster than euhedral, providing evidence to support ARDI ranking of grain morphology (Section 2.4.4.3).

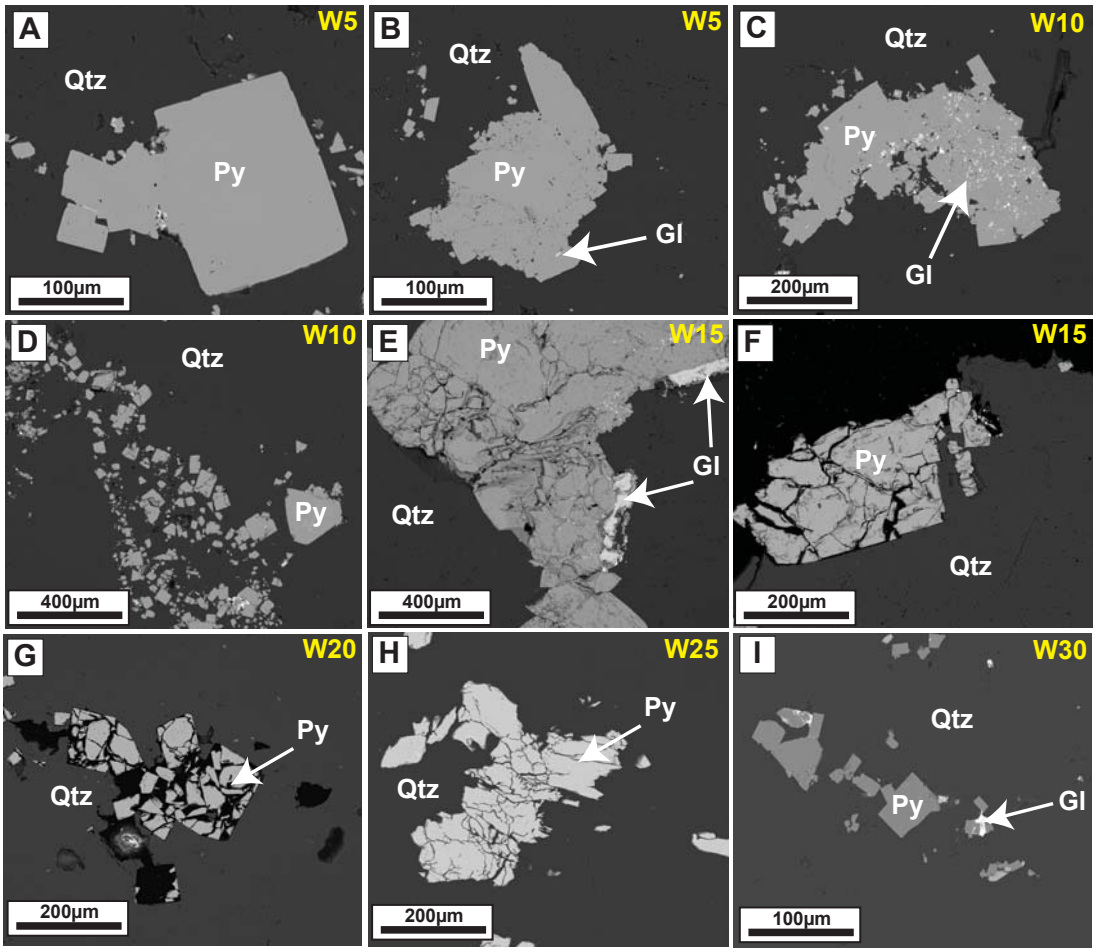

Figure 4.30 Back scattered electron images of particles obtained from the -10 mm fraction of sample 3 (Croydon waste rock mesotextural group J): **(A)** Finer-grained euhedral quartz-associated pyrite, relatively unweathered; **(B)** Finer-grained subhedral-anhedral quartz-associated pyrite, comparatively more weathered; **(C)** Coarser-grained anhedral quartz-associated pyrite with galena micro-inclusions and a pitted texture developing; **(D)** Fine-grained quartz-associated pyrite appears relatively unweathered; **(E)** Coarser-grained pyrite appears extensively fractured, with galena weathering to anglesite; **(F)**, **(G)** and **(H)** Subhedral quartz-associated pyrite (various sizes) demonstrating fracturing; **(I)** Fine-grained quartz-associated pyrite appears unweathered. Abbreviations: Gl, galena; Py, pyrite; Qtz, quartz; W, week.

BSE images collected from particles obtained from the -10 mm fraction of sample 6 (weeks 5 to 30) showed pyrite present as veins (in quartz), which was distinctly different to sample 3 (Figure 4.31). At week 5, quartz-associated vein galena appears partially weathered to anglesite (Figure 4.31a), whilst coarser vein galena material is less weathered (Figure 4.31b). By week 10, quartz-associated pyrite was moderately weathered with fracturing seen throughout (Figure 4.31c). Extensive weathering of vein galena was observed by week 20 with platy anglesite formed (Figure 4.31d). Extensive weathering of galena was implied at week 25, with pyrite and galena intergrown, and fine-grained anglesite extensively

formed (Figure 4.31e). This was expected when considering the electrochemical properties of these two sulphides, specifically their rest-potential values (cf. Payant et al., 2011). At week 30, coarser-grained pyrite with galena micro-inclusions had become fractured (Figure 4.31h), with microcrystalline replacement of pyrite to HFO. In general, finer galena-pyrite veins appeared to weather the fastest, with anglesite forming rapidly. This is followed by coarser galena-pyrite veins, where anglesite developed around week 20. Pyrite oxidised more slowly, with fine-grained pyrite intergrown with galena weathered first. Larger pyrite grains (~1000 µm diameter) started to weather by week 30, with microcrystalline aggregates of HFO replacing pyrite.

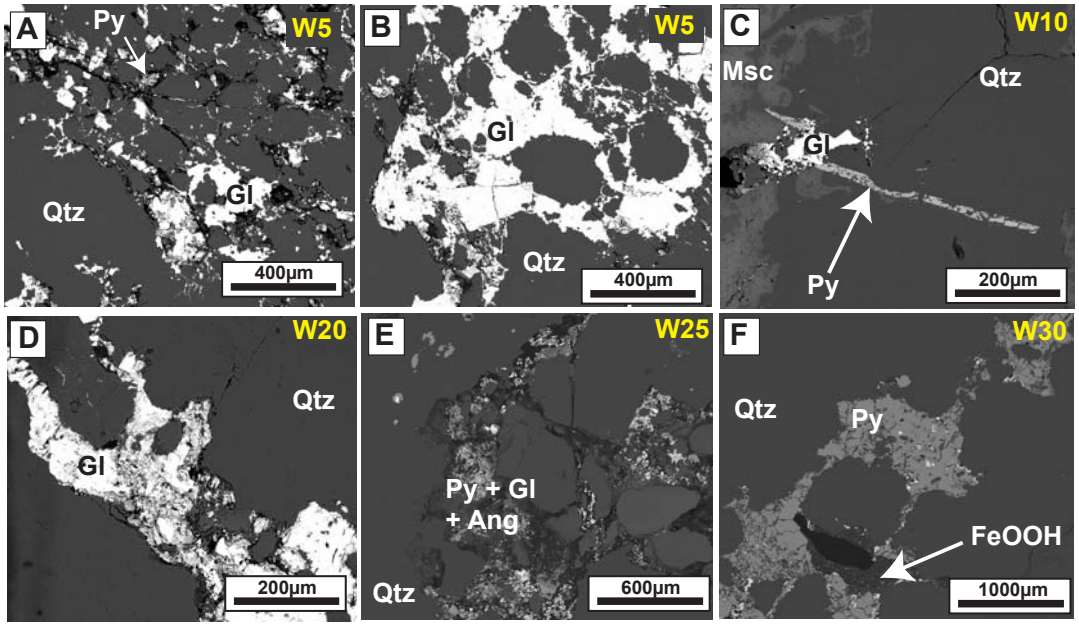

Figure 4.31 Back scattered electron images of particles obtained from the -10mm fraction of sample 6 (Croydon waste rock mesotextural group J): **(A)** Fine galena-pyrite veins in quartz, with galena weathered to anglesite; **(B)** Coarse galena vein material appearing relatively less weathered than in (A); **(C)** Moderately weathered quartz-associated acicular pyrite; **(D)** Coarse-grained galena weathered to platy anglesite: **(E)** Replacement of pyrite-galena vein material to anglesite; **(F)** Coarse-grained pyrite weathered to HFO. Abbreviations: Ang, anglesite; Gl, galena; Msc, muscovite; Py, pyrite; Qtz, quartz; W, week.

Back scattered electron images obtained from the -10 mm fraction of sample 19 showed that pyrite and galena are coarser-grained relative to other group J samples (Figure 4.32). At week 5, pyrite already appeared moderately weathered, with intense fracturing observed within grains (Figure 4.32a). Galena was identified along pyrite grain boundaries; however, alteration to anglesite was not observed. At week 10, evidence for progressive pyrite oxidation is shown (Figure 4.32b). Weathering of massive galena to anglesite was observed at week 15, with a box-work texture displayed (Figure 4.32c). Weathering of pyrite continued, with secondary platy minerals having pseudomorphically replaced quartz-associated subhedral grains by week 20 (Figure 4.32d). By week 25, coarse-grained anhedral pyrite appeared strongly weathered, with a fibrous internal texture developed. Galena present along pyrite grain boundaries had started to weather to anglesite (Figure 4.32e). By week 30, pyrite grains had weathered to microcrystalline aggregates (Figure 4.32f).

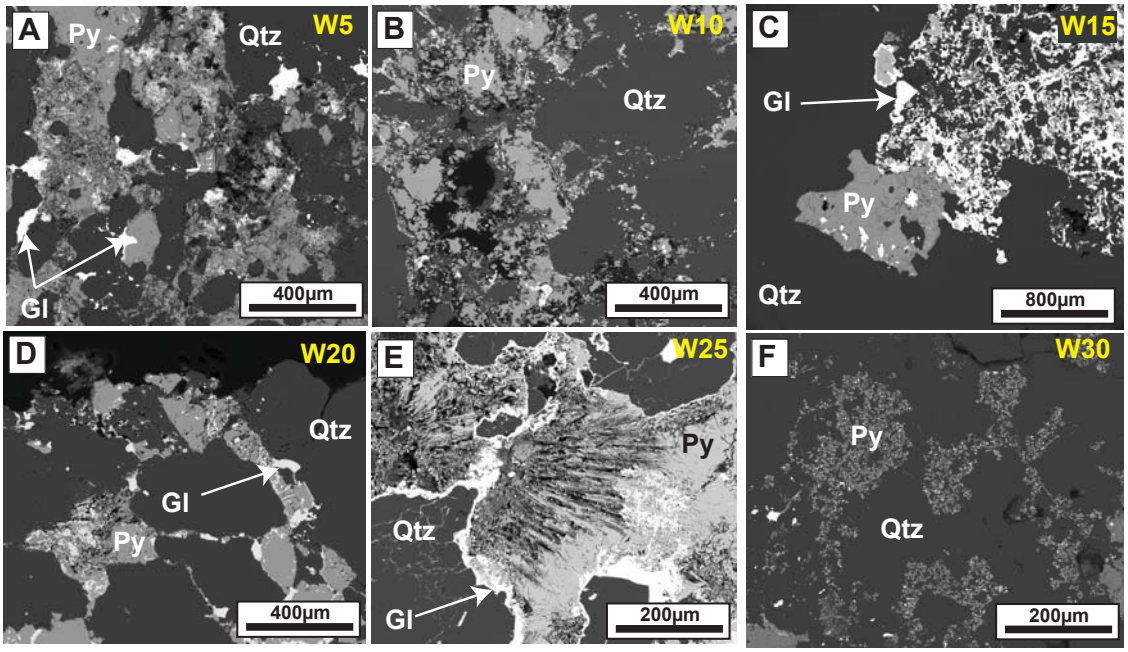

Figure 4.32 Back scattered electron images of particles obtained from the -10 mm fraction of sample 19 (Croydon waste rock mesotextural group J): **(A)** Coarse-grained weathered pyrite intergrown with galena, porous texture observed; **(B)** Fractured coarse-grained pyrite; **(C)** Massive galena forming a boxwork weathering texture; **(D)** Pyrite replaced by secondary platy HFO minerals, with continued development of the porous texture; **(E)** Strongly-weathered massive pyrite with a highly porous internal texture demonstrated; **(F)** Extensive replacement of pyrite to microcrystalline aggregate. Abbreviations: Gl, galena; Py, pyrite; Qtz, quartz; W, week.

4.3.5.2 Leachate chemistry

Leachate pH values for all mesotextural group J samples are shown in Figure 4.33, with similarities between the samples observed. Low pH conditions (i.e., pH<4) were measured from the -10 mm fraction of sample 3 from weeks 1 to 8, with pH subsequently increasing over time. However, pH values decreased over time from the -4 mm fraction of sample 3, with pH <4 measured from week 26 onwards. This indicates that armouring secondary phases (i.e., HFO) were slow to form in pyrite micro-fractures (these had formed in the -10 mm column), thus allowing pyrite oxidation to occur in the first eight weeks of the experiment (Figure 4.30).

Overall, leachate pH values were lower from the -4 mm fraction than the -10 mm for sample 6. The initially low pH (weeks 1 and 2) measured from the -10 mm fraction potentially correlates with dissolution of secondary efflorescent minerals formed before the start of the experiment which were not removed during first-flush experiments (cf. Mills et al., 2011). Subsequently, ARD conditions were not measured in leachate from either grain size fraction until week 28. This pH trend was expected based on the mineralogical observations, as galena has been preferentially weathered relative to pyrite in accordance with Moncur et al. (2009) and Payant et al. (2011). Thus, lower pH conditions were not measured as galena oxidation is not an acid producing reaction under the conditions experienced in this experiment (cf. Dold, 2006; Lottermoser, 2010).

Leachate pH values from both sample 19 grain size fractions were the lowest of all group J samples, with both relatively similar throughout the experiment (Figure 4.33). Therefore, grain size appears to have less pH control in this sample relative to the other samples. For the first 13 weeks, leachate pH values were consistently pH ≤4 for both grain size fractions. At week 14, a small increase was measured from both (pH>4) and persisted in the -10 mm fraction until week 19, and then dropped once again to pH<4 where it remained until week 30. The leachate pH from the -4 mm fraction increased again to pH>4 by week 24, but subsequently dropped again to pH values 3.5 to 4.

Leachate EC values were initially high from all columns (Figure 4.34), but this likely corresponded to dissolution of soluble secondary efflorescent minerals not removed during the first-flush experiments as previously stated. Values subsequently dropped to below 100 μS/cm for all columns for the duration of the experiments, implying low contents of dissolved metals in all leachates.

Higher cumulative quantities and mass release rates of SO_4 were measured from the -4 mm columns relative to -10 mm for mesotextural group J (Figure 4.35). This indicated that oxidation occurred faster in the finer grain size fraction. The greatest rates for both fractions were measured from sample 3 which corresponds to its higher pyrite content.

Cumulative mass release of Fe, Mn, Pb and Zn only for group J samples are shown in Figure 4.36, as the cumulative mass at week 30 for other measured elements (e.g., As, Cd Co, Cu, Ni) was <1 mg. Iron was present in the greatest quantities (Figure 4.36a), with the highest values leached from sample 19. This is in accordance with mineralogical observations of the most extreme pyrite weathering in this group. The lowest cumulative mass release of Fe was from the -4 mm grain size fractions of samples 3 and 6. A similar observation was made with regards to mass release of Mn for these columns (Figure 4.36b). Presumably, these elements are being retained in secondary Fe-sulphate and HFO phases formed on pyrite oxidation. The highest cumulative mass release of Pb was from sample 19 (Figure 4.36c) and correlates directly to the relatively high degree of galena weathering observed in this sample. Mass release of Zn was low (Figure 4.36d), indicating its low content in pyrite.

4.3.5.3 Trace element chemistry

Leachate chemistry data indicated a low concentration of potentially deleterious elements, hence few element maps were collected (Figure 4.37). Euhedral-subhedral pyrite grains from sample 3 were examined, with the grain selected at week 0 showing no weathering; however, by week 30 grains had intensely mottled. A portion of a larger weathered pyrite grain from sample 6 was also mapped. This sample was specifically chosen as towards the end of the experiment, leachate chemistry data indicated lower pH values, and a slight increase in the mass release of elements.

The pyrite grains from sample 3 at week 0 have an As-rich core (>1000 ppm) which is surrounded by banded Co and Ni (>100 ppm; Figure 4.37a). Copper was distributed in pyrite grain-rims only, with higher concentrations measured at week 30 (>1000 ppm). This suggests that dissolution of minor chalcopyrite (Figure 4.6b) occurred over the 30 weeks, with Cu co-precipitated or adsorbed by secondary

minerals (e.g., HFO), and not eluted in the leachate. Lead was distinctly present as galena micro-inclusions. However, more micro-inclusions were observed at week 0 than 30, suggesting weathering to anglesite and leaching of Pb, which broadly correlates with leachate data (Figure 4.36c). Element mapping confirmed low contents of Zn in pyrite at both weeks (not shown). The geochemical signature of the sample 6 pyrite grain differed to sample 3 potentially explaining the small differences in leachate chemistry. Overall, this sample has lower As, no banded distribution of Co and Ni, Cu located within the grain and not as a rim, and a higher concentration of Pb within the grain (Figure 4.37c).

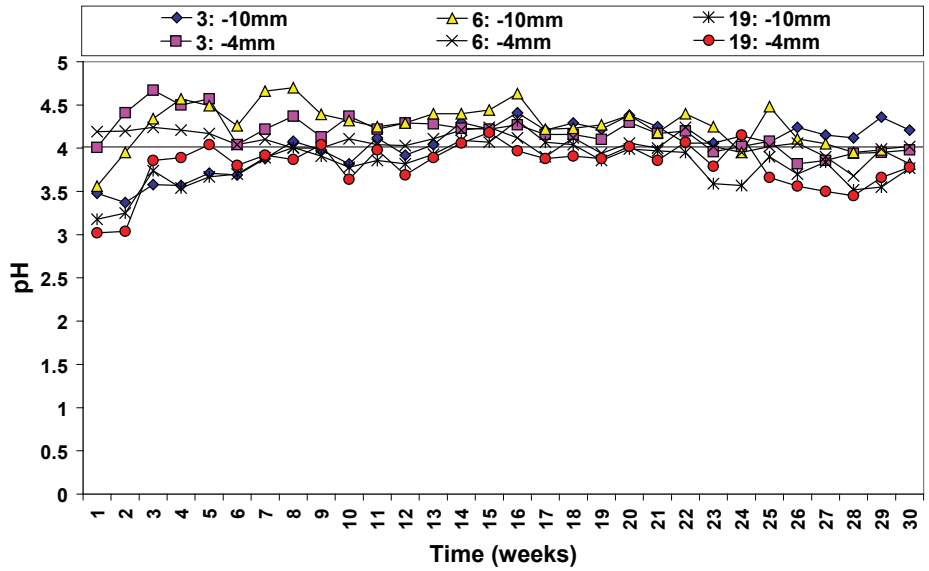

Figure 4.33 Leachate pH values measured weekly (weeks 1 to 30) from kinetic test columns containing -10 mm and -4 mm grain size material from Croydon waste rock mesotextural group J samples 3, 6 and 19.

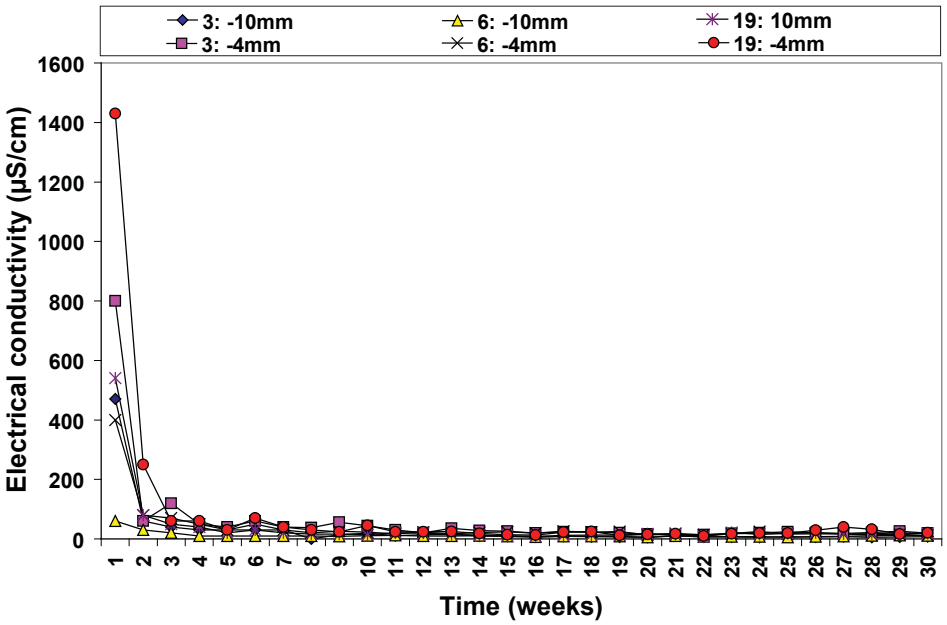

Figure 4.34 Leachate EC values measured weekly (weeks 1 to 30) from kinetic test columns containing -10 mm and -4 mm grain size material from Croydon waste rock mesotextural group J samples 3, 6 and 19.

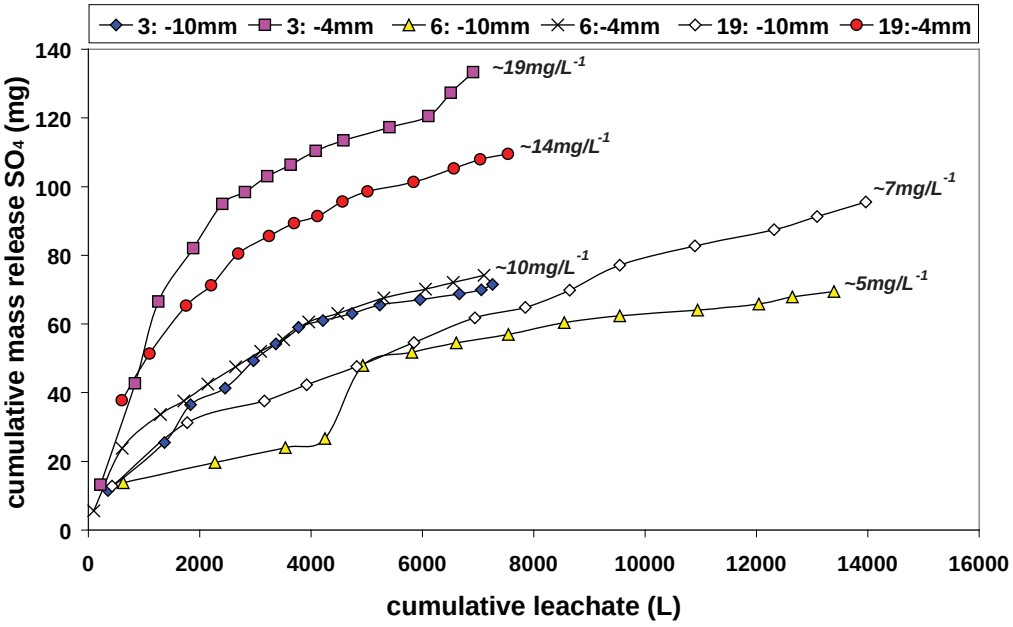

Figure 4.35 Cumulative mass release of sulphate from samples 3, 6 and 19 from mesotextural group J, shown against cumulative leachate volume (litres). Data for both grain sizes fractions (-10 mm and -4 mm) are shown.

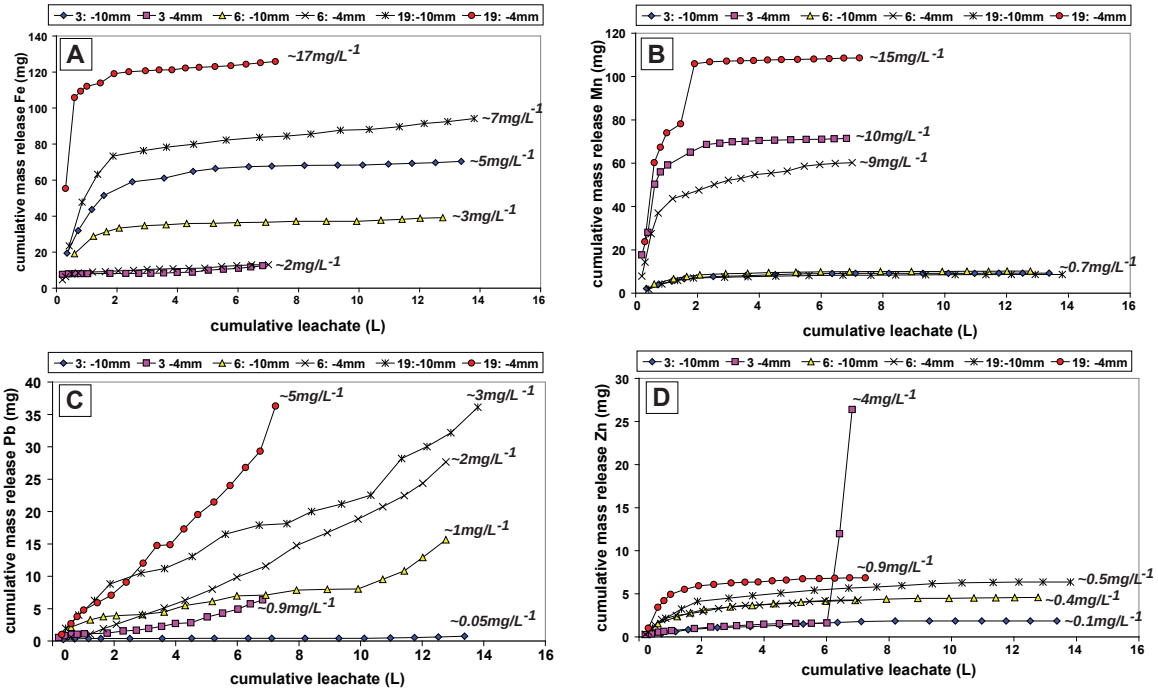

Figure 4.36 Cumulative mass release of trace elements from mesotextural group J samples 3, 6 and 19 shown against cumulative leachate volume (litres), including data for both grain sizes fractions (-10 mm and -4 mm): As **(A)**; Fe **(B)**; Pb **(C)**; and Zn **(D)**.

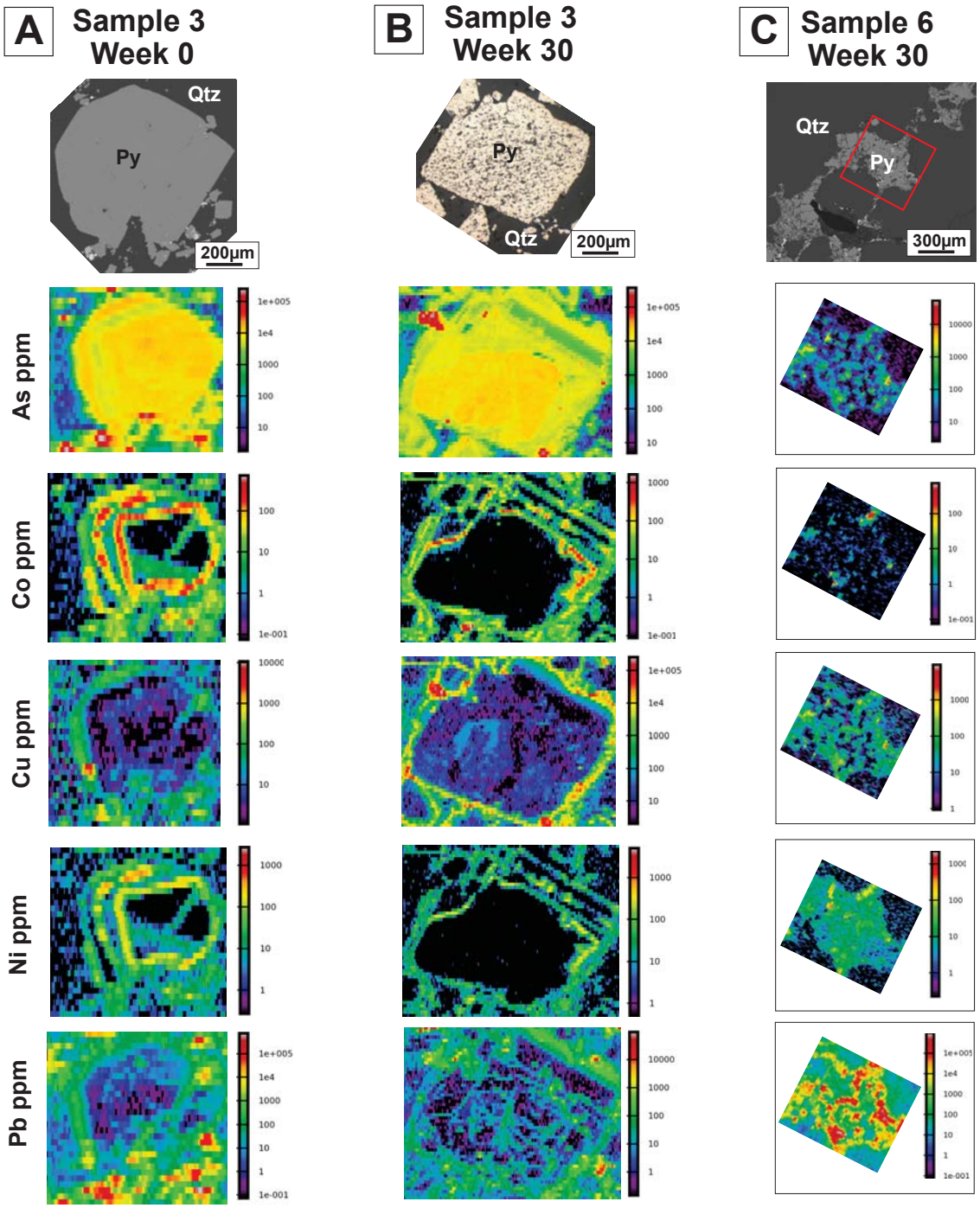

Figure 4.37 Quantified LA-ICP-MS element distribution maps (ppm) of pyrite grains from Croydon waste rock mesotextural group J, obtained from the -10 mm grain size fraction: **(A)** Sample 3 at week 0; **(B)** Sample 3 at week 30; and **(C)** Sample 6 at week 30. NB. All element maps from each grain and analytical parameters are shown in Appendix 4.7. Abbreviations: Py, pyrite, Qtz, quartz.

4.3.5.4 Summary

- Sample 19 was the most acid forming of the three mesotextural group J samples. Consequently, the highest concentrations of Fe, Mn and Pb were measured in leachate from this sample, with higher values measured from the -4 mm grain size fraction.
- In sample 3, pyrite contents decreased from week 5 to 30 in the -4mm fraction, implying oxidation had occurred. BSE images from the -10 mm fraction identified two types of quartz-associated pyrite: (i) fine-grained (<200 μm) and (ii) coarse-grained (>200 μm). Observations indicated that coarser grains weathered at a greater rate.
- Element mapping of pyrite grains obtained from the -10 mm fraction of sample 3 indicated the presence of galena micro-inclusions, and additionally revealed that these grains contain As which increases oxidation rate (cf. Lehner et al., 2007; Lehner and Savage, 2008; Qiong-Li et al., 2011). However, low concentrations of As, Cu and Pb were measured in the leachate from both grain sizes, implying their retention in secondary sulphate and HFO phases.
- Despite the high pyrite content, chemical measurements indicated that ARD conditions were not sustained in either sample 3 grain size fraction, and may relate to the fact that pyrite is well encapsulated in quartz.
- In sample 6, ARD was not established consistently until after week 25 for both grain size fractions. BSE images indicated that fine vein-galena weathered at the greatest rate of the sulphides identified in this sample, followed by coarse vein-galena, and pyrite.
- Anglesite formed from galena weathering in both sample 6 and 19, but itself underwent weathering as time progressed, with a platy to honeycomb microtexture observed. Small quantities of lead were also released as a consequence of both galena and anglesite weathering.
- The galvanic interactions between pyrite and galena were more distinct in sample 19 as a consequence of the increased surface area between the two minerals (due to the higher net-content, and the intergrown relationship demonstrated; cf. Payant et al., 2011).

4.3.6 Geochemical characterisation at the conclusion of kinetic trials

Routine static tests (NAPP, NAG, ANC, S_{Total}) were performed at week 30 on samples obtained from each of the -4 mm columns (ALS, Brisbane). A geochemical plot of NAPP versus NAG pH shows that the sample classifications are unchanged since the start of the experiment, with all samples classified as PAF (Figure 4.38). Group H remained the most acid forming of all samples. Group E was also identified as the least acid forming, with its NAPP value having decreased relative to the start of the experiment.

4.4 Stream sediments and surface waters

Results from stream sediment and surface water sampling undertaken around the Croydon mines, are presented in the following section. These results are shown here to identify to what extent the release of leachate (and waste erosion) from the Federation/La Perouse and Glencoe waste rock piles impacts on the chemistry of the creeks downstream of the operations.

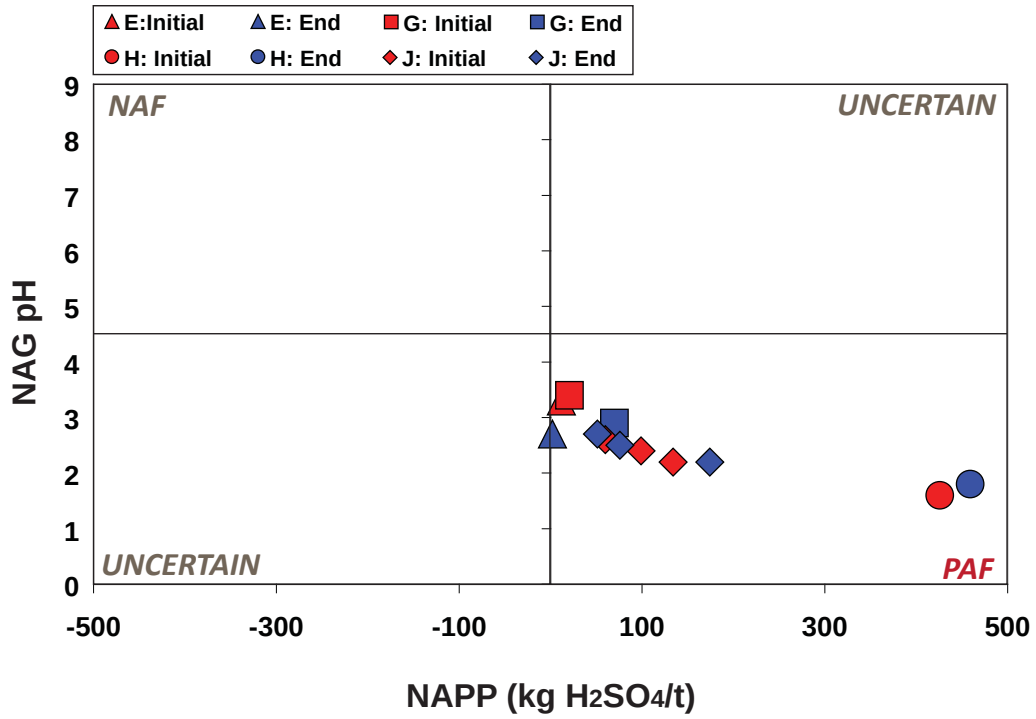

Figure 4.38 Geochemical classification of Croydon waste rock samples using NAPP (kg H_2SO_4/t) versus NAG pH for groups E, G, H and J shown at the start and the end of kinetic testing (n=12). Abbreviations: NAF, non-acid forming; PAF, potentially acid forming.

4.4.1 Stream sediments

The upstream (local baseline), on site, and downstream concentrations of select metals and metalloids in both the whole and fine (<63 µm) fractions are shown in Figure 4.39. The background (upstream of the mine operations) samples generally contained low concentrations of As (<20 mg/kg), Cd (<1.5 mg/kg), Cu (<65 mg/kg), Pb (<50 mg/kg) and Zn (<200 mg/kg), and are within the lower level of ANZECC (2000) Interim Sediment Quality Guidelines (ISQG). Occasionally, few background samples contained elevated As, Cu, Pb and Sb relative to ISQG levels (Figure 4.39a and 4.39c to 4.39e), but such element enrichment is likely geogenic i.e., due to the mobilisation of metals and metalloids from sulphide bearing lodes and mineralised rocks into the local catchment.

At the Federation/La Perouse site, elevated concentrations of As (whole and <63 µm), Cd (<63µm), Cu (<63 µm), Pb (<63 µm) and Sb (whole and <63 µm) relative to ISQG levels were measured. Only As (whole and <63 µm) was elevated relative to the ISQG upper-level at the Glencoe site. In Tabletop Creek downstream of Federation/La Perouse, As remained elevated (relative to ISQG upper-level) in the <63 µm fraction to approximately 7.7km (Figure 4.39a). Arsenic (<63 µm) concentrations broadly correlated with Fe (R^2= 0.73), and sequential extraction results showed As presence in Fe (III) oxide and hydroxide fractions (54.2%; Appendix 4.2).

Cadmium (both fractions) was below the ISQG upper-level downstream of the Federation/La Perouse site. However, in the <63 µm fraction of Cd, concentrations fluctuated around the ISQG lower-level until the confluence. Maximum concentrations of Cd (<63 µm) and Zn (<63 µm), exceeding the

ISQG upper-levels, were measured in Deadhorse Creek ~0.95 km downstream of the Glencoe site. By 1.3 km, these concentrations had dropped, but rose again at 4.3 km (Figure 4.39b and 4.39f). Copper concentrations fluctuated to the confluence (10.06 km; Figure 4.39c). Lead also fluctuated to 7.7 km, after which it was below the ISQG upper-level (Figure 4.39d). At the confluence of Tabletop and Deadhorse Creeks concentrations for As, Cu, Cd, Pb and Zn were below ISQG upper-levels. Monitoring (since 1998) of Tabletop Creek below the confluence (~17 and 30 km downstream of the Federation/La Perouse site) reported concentrations below ISQG for lower-levels As, Cu, Cd, Pb and Zn (DME, 2008).

4.4.2 Surface waters

The pH values measured across the Croydon district are shown against concentrations of As, Cd, Cu, Pb and Zn in Figure 4.40 (NB. Sb is not shown as values were below detection limit). In Tabletop Creek upstream of the Federation/La Perouse site the pH range was 6.4 to 8.6, and low concentrations of As (<6.1 µg/L) Cd (<2 µg/L), Cu (<3 µg/L), Pb (<1.1 µg/L) and Zn (<9 µg/L) were measured. At the Federation/La Perouse site, pH values decreased to a minimum of 3.7. Maximum concentrations of As (9.6 µg/L), Cd (83.6 µg/L) and Pb (58.5 µg/L) were measured, and are elevated relative to upstream/ background and ANZECC drinking water guideline (DWG) values (2000). Maximum concentrations of Cu (534 µg/L) and Zn (2018 µg/L) were elevated relative to background values only. Downstream, pH values generally increased with a maximum of pH 7.6 recorded (~3.5 km), and concentrations of Cd, Cu, Pb and Zn decreased. Arsenic concentrations did not follow the same trend, with a maximum of 12.5 µg/L measured ~4.3 km downstream of the Federation/ La Perouse site.

At Glencoe, pH values were between 4.31 and 6.29. Elevated concentrations of As (20.4 µg/L), Cd (53 µg/L), Pb (14 µg/L) and Zn (7715 µg/L) relative to ANZECC (2000) DWG values were also measured. In Deadhorse Creek ~1.1km downstream of the site, pH 3.95 was measured, but by ~1.7 km this increased to pH 10.95. High dissolved Fe (2125 µg/L) was also measured at this location. At the confluence of Tabletop and Deadhorse Creeks, a near-neutral pH of 6.7 was measured, with only Cu (13 µg/L) and Zn (137 µg/L) elevated relative to upstream concentrations, but not compared to ANZECC (2000) DWG values.

Element concentrations and pH values for Federation, La Perouse and Glencoe pit lakes are given in Table 4.9. Federation pit was the most acidic (pH 3.9) whilst La Perouse and Glencoe were only mildly acidic with measured values of pH 6.1 and 6.3, respectively. These values are similar to previous monitoring data collected by the DEEDI since 1998 (DME, 2008). The Federation Pit lake contained the highest concentrations of Cd (83.6 µg/L), Cu (989.6 µg/L), Ni (65.6 µg/L), Pb (71.3 µg/L) and Zn (1918 µg/L), and the highest As concentration was measured at Glencoe (20.4 µg/L). Elevated concentrations relative to ANZECC (2000) DWG values were detected for As (Glencoe) and Pb (Federation). Overall, La Perouse and Glencoe pit lakes have better water quality than Federation. Since the construction of the catch dam, water quality in Federation pit has deteriorated as in the dry season, water quality in the catch dam worsens due to evapo-concentration of solutes, and in the wet season the water bodies become linked (Cottier, 2011, pers. comm.).

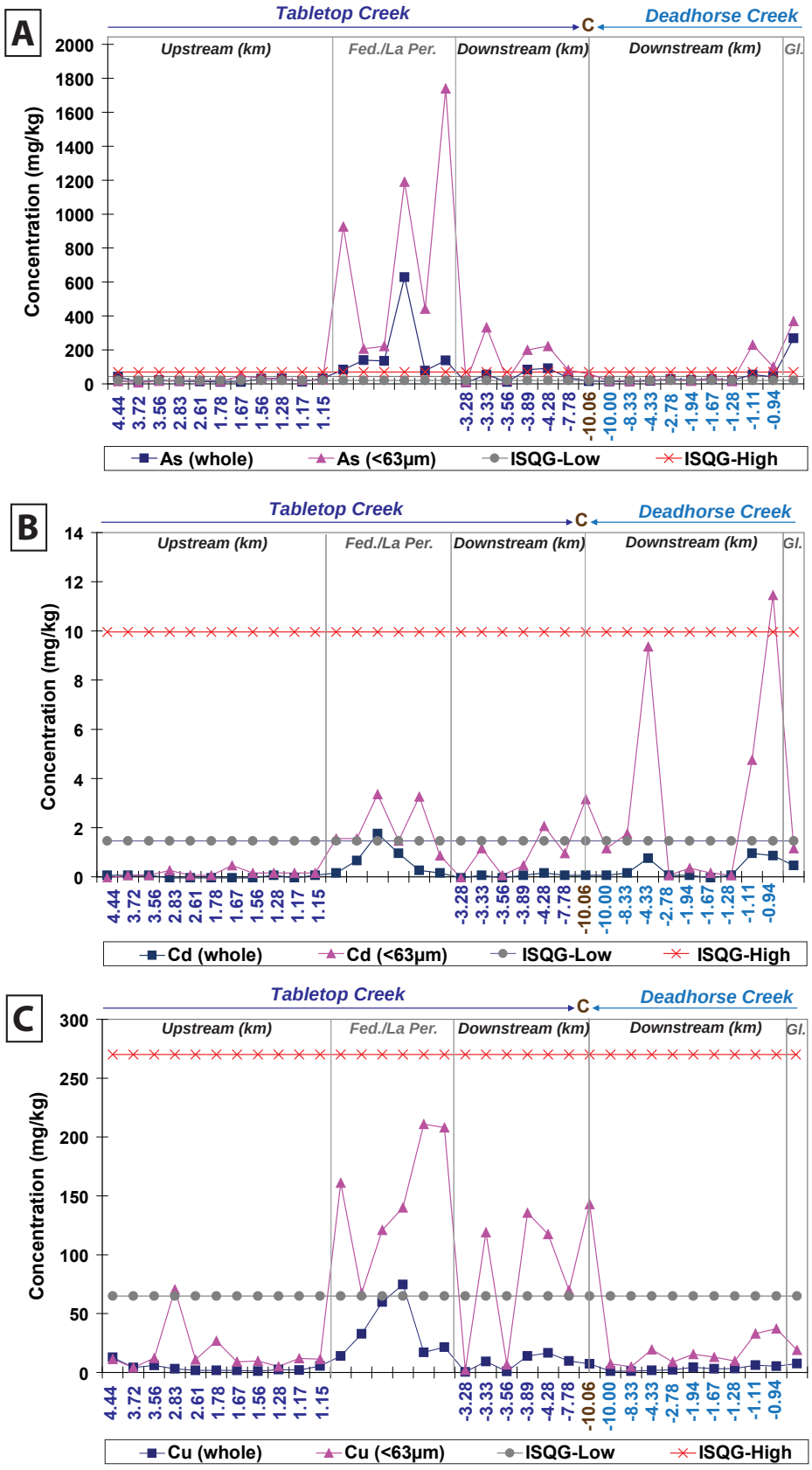

Figure 4.39 Trace element content (mg/kg) in stream sediments (total and <63 µm fraction) around the Croydon district compared to ANZECC (2000) ISQG-high and ISQG-low values: (**A**) As; (**B**) Cd; (**C**) Cu. Abbreviations: Gl, Glencoe; C, confluence of Deadhorse and Tabletop Creeks.

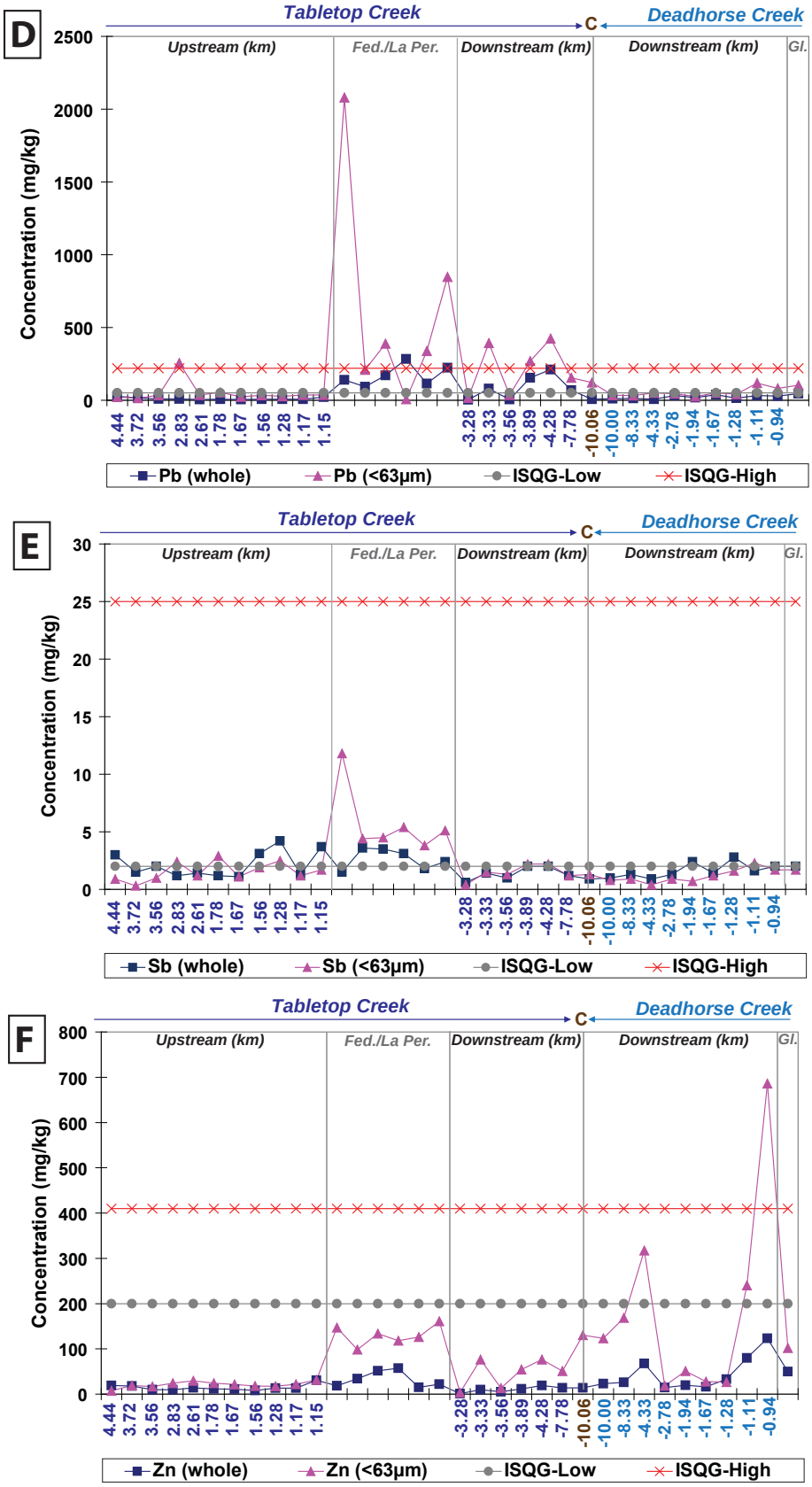

Figure 4.39 (*Continued):* Trace element content (mg/kg) in stream sediments (total and <63 µm fraction) around the Croydon district compared to ANZECC (2000) ISQG-high and ISQG–low values: (**D**) Pb; (**E**) Sb; (**F**) Zn. Abbreviations: Gl, Glencoe; C, confluence of Deadhorse and Tabletop Creeks.

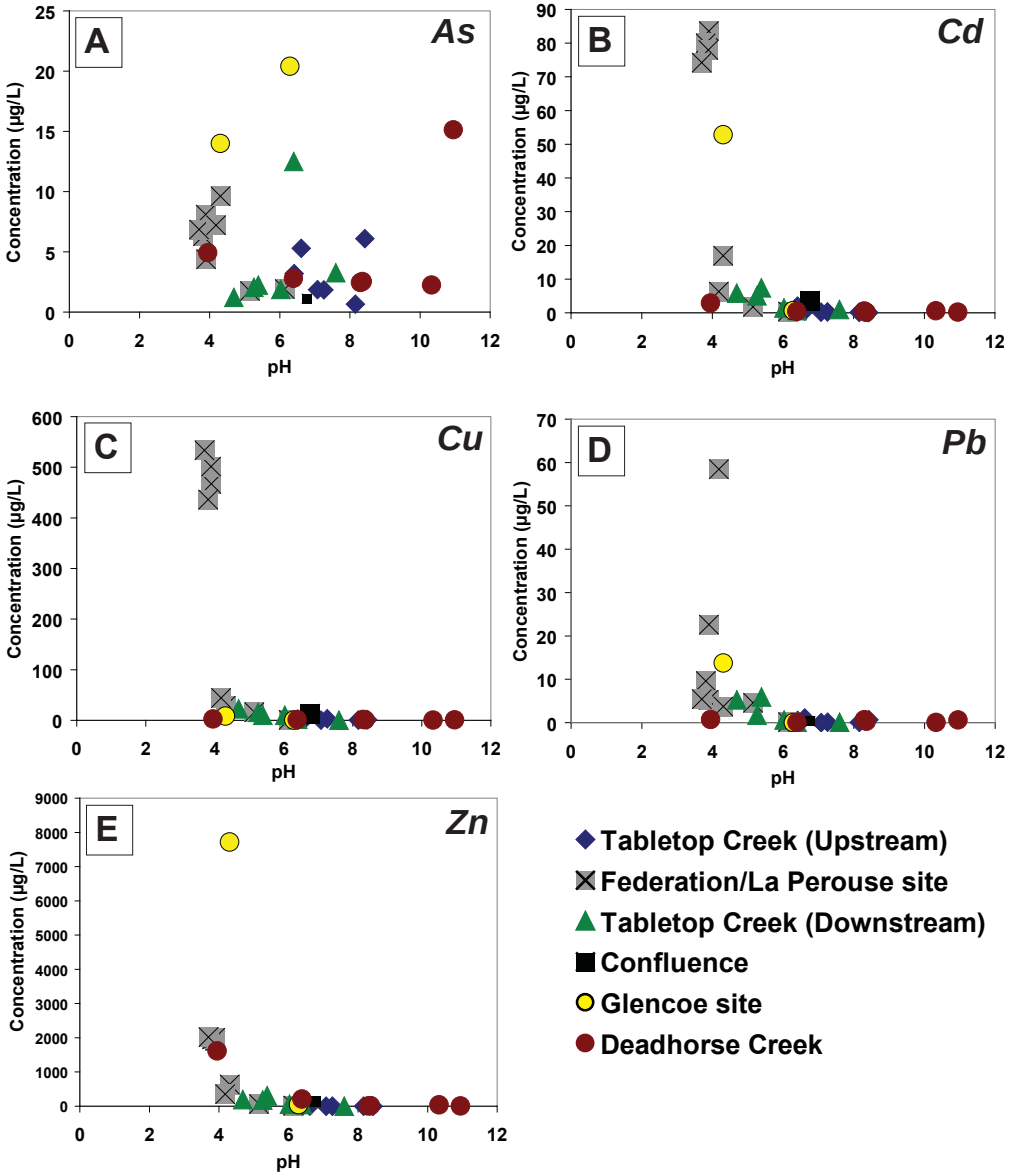

Figure 4.40 Trace element concentration versus pH in surface water samples from around the Croyon district: As **(A);** Cd **(B);** Cu **(C);** Pb **(D)**; and Zn **(E)**.

Table 4.9 Element concentrations (µg/L) and pH values measured in Federation, La Perouse and Glencoe pit water samples (obtained from the surface). Drinking water guidlines (DWG) published by ANZECC (2000) are shown for comparison.

	Federation	La Perouse	Glencoe	DWG
pH	3.9	6.1	6.3	6.5 to 8.5
Al	17680	25	11	-
Ag	1	1	1	100
As	4	2	20	7
Cd	84	*BDL*	1	2
Co	2	*BDL*	*BDL*	-
Cr	4	6	6	50
Cu	990	2	1	2000

Table 4.9 (*Continued*)

	Federation	La Perouse	Glencoe	DWG
Fe	44	105	56	-
Mn	609	53	77	-
Ni	66	3	4	-
Pb	71	*BDL*	*BDL*	20
Rb	14	7	10	-
Se	11	*BDL*	1	10
Sr	44	6	3	-
Ti	743	10	20	-
Tl	*BDL*	*BDL*	*BDL*	-
U	39	*BDL*	*BDL*	10
V	2	3	3	-
Zn	1918	17	43	3000

4.5 Discussion

4.5.1 Mineralogical controls on sulphide weathering

Fundamentally, drainage chemistry is controlled by both the primary and secondary mineralogy. Element content and residence of trace and minor metals in sulphides have an impact upon weathering behaviour (Hammarstrom and Smith, 2002). Upon release, evaporation concentrates mobile elements and acidity, promoting the formation of highly water-soluble secondary minerals or efflorescent salts with high concentrations of metals (Jambor et al., 2000; Nordstrom, 2011). Through systematically sampling and analyses of both the -4 mm and -10 mm columns, both of these parameters were evaluated, and an understanding of the mineralogical processes occurring during kinetic testing was gained.

Initial characterisation of each sample indicated that each mesotextural group contained high quantities of potentially deleterious elements (e.g., As, Cu, Pb and Zn; Figures 4.5, 4.17, 4.22, 4.28 and 4.37). However, such high concentrations were not measured in cumulative column leachates (Figures 4.16, 4.21, 4.27 and 4.36), with even less measured in surface waters downstream of mining operations (Figure 4.40). However, routine microtextural observations and measurements of bulk-mineralogy indicated that some weathering had occurred. Individual sulphides and metal release pathways are described in the following section.

4.5.1.1 Pyrite

Pyrite in groups E, G and J underwent weathering as suggested by the measured (QXRD) net decrease in its contents, SEM observations, and the constant mass release of sulphate. Differential rates of oxidation were observed with (i) coarser grains (>200 μm), (ii) those with irregular morphologies (i.e. anhedral), or (iii) those containing galena micro-inclusions weathering faster. The higher degree of weathering observed in coarser pyrite grains (e.g., Figure 4.13) is potentially a consequence of the topological effect as defined in Ghorbani et al. (2011). This refers to leaching (and weathering) being governed by the

way in which mineral grains are distributed within single rock particles, with grains either liberated and exposed, or encapsulated inside particles (e.g., Figure 1.5). Effects of irregular pyrite morphologies and the presence of micro-inclusions increasing oxidation rates have been documented in Kalinnikov et al. (2001), Lottermoser (2010) and Weisner and Weber (2010). BSE images and element maps provided evidence to suggest that fractures had developed in proximity to galena micro-inclusions (e.g., Figures 4.13 and 4.31). Additionally, the presence of such micro-inclusions caused pyrite to form an internal porous texture (Figure 4.32). BSE observations suggest that HFO, under the influence of temperature, abundant molecular oxygen, and pH >3, are rapidly forming fine armouring layers in fractures and on pyrite grain surfaces (cf. Blowes and Jambor, 1990; Lottermoser, 2010; Smart et al. 2010; Volrath, 2012). This explains why the high degree of fracturing observed in later weeks does not directly correlate with pH values.

Abraitis et al. (2004) stated that secondary iron-sulphates precipitate in fractures, and subsequently cause more fracturing as they wedge the crystal lattice apart. Minor quantities of rhomboclase were occasionally mesaured in -4 mm columns (Tables 4.3, 4.4, 4.8) suggesting that some fracturing in pyrite was potentially induced by this process, thus increasing the rate of oxidation, however, the net effect is likely to be relatively minor.

Microtextural observations of sample 6 and 19 showed that pyrite was complexly intergrown with galena, particularly in the latter sample. Pyrite is galvanically protected by galena (Payant et al., 2011). As oxidative dissolution of galena is not acid forming (Dold, 2006; Lottermoser, 2010), the pH values from these column are not as low (3.5 to 4.5) as expected based on the bulk-pyrite content. Similar observations were made by Kwong and Fergusson (1997), who reported that galvanic processes significantly controlled ARD at the Keno Hill mining district, where near-neutral values were measured despite the presence of highly reactive pyrite in waste rock piles.

Lehner et al. (2007) and Lehner and Savage (2008) showed that pyrite containing As, Co or Ni impurities oxidise slightly faster than pyrite with low impurity concentrations at pH 2. This contradicts Kwong (1993) who indicated that the presence of Co and Ni increases the resistance to oxidation. These authors all stated that pyrite containing high As is more reactive than Ni or Co which relates to its p-type conductivity, with these observations recently confirmed by Qiong-Li et al. (2011). There was limited evidence to suggest that the presence of these elements had increased oxidation rate. Pyrite grains either have an As-rich core (e.g., Figures 4.17a; 4.37), which decreases to the rim, or an As deficient core, with a concentric zone of high As which then graded out towards the rim (e.g., Figure 4.17d). Generally, where there were areas of high Co and Ni, less fracturing was observed (e.g., Figure 4.23) thus providing more evidence to support Kwong (1993). Lehner and Savage (2008), however, stated that whilst oxidation rates differ with impurities in pyrite, these differences are probably too small to warrant explicit consideration in environmental modelling applications. Thus, it is unclear what overall impact the trace element distribution observed here will have on the rate of ARD formation, relative to pure sulphides contained in similar mesotextural groups.

Whilst several microscale controls on pyrite oxidation have been identified (e.g., presence of micro-inclusions, trace element distribution, mineral association), the quantities of potentially deleterious elements measured in leachate were low from pyrite-dominated groups E and J (sample 3, 6, 15 and 19). This is attributed to the substantial control of HFO on element release (Das and Henry, 2010). Moncur et al. (2009) showed that dissolved Cd, Co, Ni and Zn are commonly attenuated by early-forming HFO, followed by Cu and Pb (e.g., Figure 4.17a). Garcia-Sanchez et al. (2002) similarly reported HFO affinity for As. However, as the crystallinity of HFO increases, their sorptive capacity for these elements decreases, potentially resulting in a later flux in the concentration of these elements in leachate. These observations suggest that group E and J are in early-maturing stages of weathering in the updated mine waste paragenesis proposed by Moncur et al. (2009). This is supported further by the presence of minor pyrrhotite (<1 wt. %) and the identification of both rhomboclase, and occasionally jarosite. As HFO matures, Zn and Ni become more mobile, which likely explains the sudden increase in Zn release observed in sample 19 (Figure 4.36). Providing conditions remain around pH 4 (as was measured), As will be immobilised in HFO (Garcia-Sanchez et al., 2002).

4.5.1.2 Arsenopyrite

Group H was dominated by arsenopyrite, and was the most acid forming of all the mesotextural groups. Arsenopyrite weathering was much less complicated than that for pyrite. Its oxidation followed *equation 4.1*, with iron, sulphate, scorodite and H^+ identifed as the reaction products (Figures 4.25-4.27), the contents of which increased over time, indicating progressive oxidation. Massive arsenopyrite appeared more fractured and subsequently weathered than finer grains (Figure 4.24), suggesting that the topological effect is also significant in controlling oxidation in this group (Ghorbani et al., 2011). Trace element contents in primary arsenopyrite were low, with only Sb consistently identified in accordance with Craw et al. (2003), Craw et al. (2004) and Lottermoser (2010). However, 10-100 ppm Co and Ni were measured in arsenopyrite, with a banded distribution observed (Figure 4.28). Where these were present, fractures were absent. Whilst this could be coincidental, it is postulated that these elements may be increasing resistivity to oxidation through toxicity effects experienced by iron oxidising bacteria as indicated by Sampson and Philips (2001).

Trace elements measured in scorodite included Cu and Zn which have previously been identified in this mineral (Monhemius and Swash, 1999; Fuijita et al., 2006; Gomez et al., 2011). In addition, Pb was also measured (Figure 4.27). These elements are sourced from other mesotextural groups, which have been transported as a result of fluid percolation through the waste rock pile. The mechanism of Pb incorporation into scorodite is not known. Concentrations of Cu, Zn and Pb in scorodite over time decreased. However, the concentration of Cu and Zn did not increase in the leachate, suggesting their redistribution to scorodite weathering phases towards the end of the experiment (i.e., Figure 4.24k). These weathering products are likely to be amorphous ferric arsenates (cf. Murceigo et al., 2011).

4.5.1.3 Galena and sphalerite

The weathering of galena (dominantly observed in sample 6 and 19 of mesotextural group J) was relatively uncomplicated and was likely encouraged by galvanic interactions with pyrite (cf. Payant et al., 2011),

with anglesite forming. Anglesite dominantly exhibited a porous, non-crystalline microtexture similar to that described in Diehl et al. (2006), indicating that it did not serve as an armouring layer to galena in the manner described in Heidel and Tichomirowa (2011). Instead, it likely behaved as a discrete source of aqueous Pb^{2+} (cf. Diehl et al., 2006). Anglesite appeared to succumb to weathering in later weeks (e.g., Figure 4.31), explaining why a small increase in the Pb release rate was observed for galena-rich samples (Figure 4.36).

Sphalerite generally showed the most resistance to weathering of all sulphides, with no oxidation products directly observed, and only inferred by the identification of sulphur in the bulk mineralogy (cf. Edwards et al., 2000; Diehl et al., 2006). No weathering textures were observed. Instead an increasing amount of fracturing was observed, in addition to the formation of a 'cornflake' texture across the body of these grains (Figure 4.18). Considering the relatively high content of Cd in these grains (Figure 4.22), higher release rates of Cd were anticipated in the leachate, but instead was <0.05 mg/L^{-1} (Figure 4.21). This is likely a function of the pH conditions, as Stanton et al. (2008) demonstrated that Cd release rate from sphalerite increases linearly with lower pH. This explains why slightly increased rates of Cd release were observed towards the end of the experiment in the -4 mm column, as the pH dropped to ~3.4. Stanton (2005) compared the leach chemistry from fine- and coarse-grained sphalerite at both pH 2 and 4. They reported that fine-grained, high-Fe sphalerite (12.1 wt. %) leached at pH 2 to 3 (25°C) produces dissolved Fe and Zn concentrations approaching 50 and 180 mg/L, respectively, within one week of reaction. Release rates of Zn and Cd from mesotextural group G (Figure 4.21) were far below values reported by Stanton (2005), indicating that under the pH conditions measured in the column, sphalerite is relatively stable, and is therefore anticipated to be in the waste rock enviroment if pH conditions remains similar to those measured in the field (i.e., pH~3.7).

4.5.2 Grain size effects on leachate chemistry

Lower pH values and higher dissolved metal contents were consistently measured from finer-grain size fractions (-4 mm) for sample 15 (mesotextural group E), sample 18 (mesotextural group H) and sample 6 (mesotextural group J). In sample 14 (mesotextural group G), no trend was observed between grain size and pH. This is explained by the increased contribution to neutralisation from silicate minerals as a result of the increased surface area, an effect which was also observed in Lapakko et al. (2006). This effect is more pronounced in this column, as the highest quantities of muscovite and albite were measured.

Similar pH values were measured for both grain sizes from sample 19 (mesotextural group J) for the duration of the experiment. Potentially this indicates that pyrite-galena surface areas in contact were broadly similar in both columns, with preferential galvanic oxidation of galena experienced. Higher pH values were measured from the -4 mm column up to week 15 in sample 3, then became similar to the -10 mm column until week 26 after which time pH values became lower than the -10 mm column. These results suggest that if this experiment had evolved for longer than the 30 weeks, the -4 mm column would likely have been the more acid forming.

4.5.3 Metal and arsenic dispersion at Croydon

Many metals (e.g., Cd, Cu, Fe, Pb and Zn) are soluble under the pH conditions of ARD fluids (Plumlee, 1999; Ashley et al., 2004). At Croydon, surface water downstream of both mine sites is generally classified as acid-low metal to neutral-low metal (Figure 4.41). Arsenic concentrations obtained around the Croydon district were compared against the Krause and Ettel (1998) solubility curve (Figure 4.42). This showed that scorodite precipitation potentially limits As at Croydon, as is commonly reported for similar sites (e.g., Krause and Ettel, 1988; Vink, 1996; Ashley and Lottermoser, 1999; Smedley and Kinniburgh, 2002; Borba et al., 2003; and Haffert et al., 2010). Thus, under the pH range measured from waste rock pile leachate at both sites (shown in Figure 4.42 as lines B and C), maximum concentrations of 1 mg/L dissolved As are possible in mine water (Figure 4.42). The lowest pH value measured during the column leach testing (-4 mm fraction; week 30) is also shown (Figure 4.42; line A), and indicated that maximum dissolved As concentrations of ~10 mg/L are possible. This value closely approximated that measured at week 30 (9.9 mg/L), confirming the dominant control of scorodite on dissolved As in these mine waters.

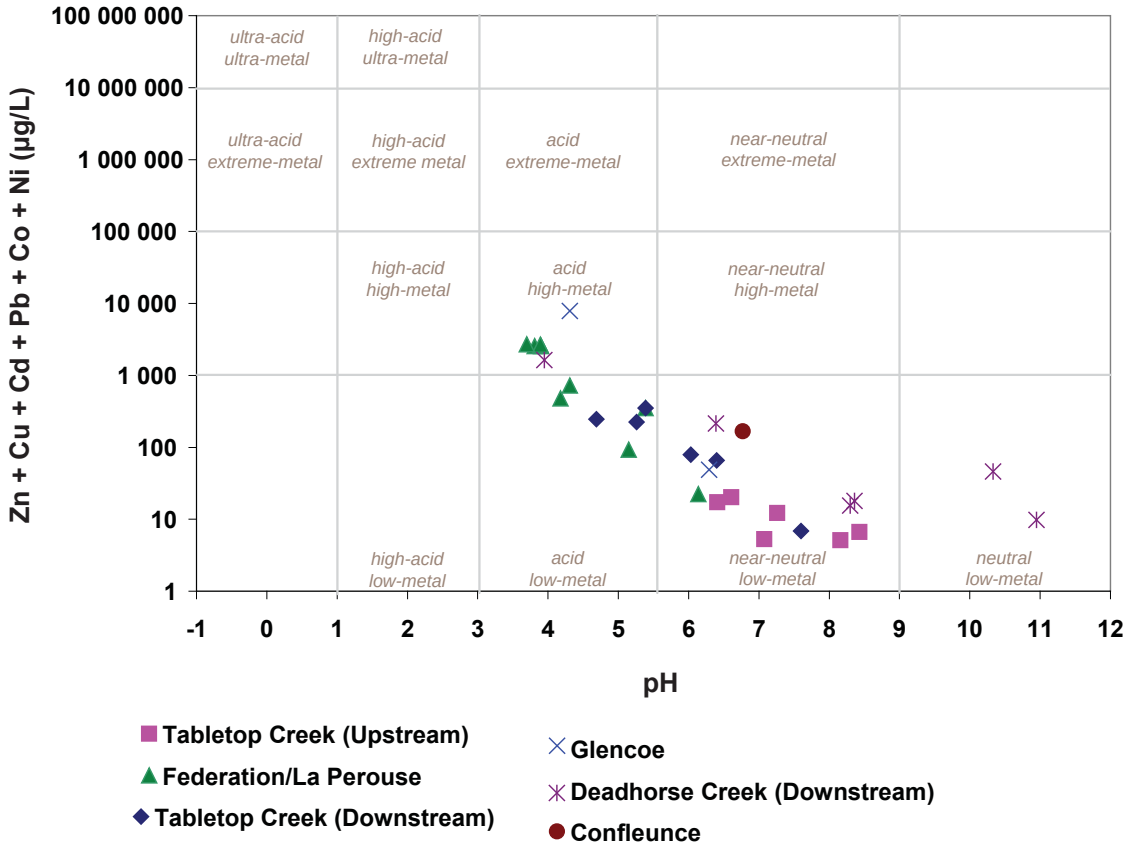

Figure 4.41 Geochemical classification plot (Ficklin diagram) for surface waters in the Croydon district based on the sum of dissolved metals (Cd, Co, Cu, Ni, Pb, and Zn) and pH. Modified after Ficklin et al. (1992) and Plumlee et al. (1999).

As pH values increased above 4.5 downstream of both the Federation/La Perouse and Glencoe sites, concentrations of these elements declined. Around pH 4.5 to 5 As and Pb have likely sorbed onto Fe-bearing precipitates, with sequential extraction results (Appendix 4.2) indicating concentration of

these elements to this fraction (cf. Ashley et al., 2004; Hudson-Edwards and Edwards, 2005; Lottermoser, 2010). Concentrations of Cu, Cd and Zn declined downstream, with Cu sorbed onto Fe-bearing precipitates around neutral pH (Hudson-Edwards and Edwards, 2005). Cadmium and Zn concentrations correlate with Mn (Figure 4.43) indicating coprecipitation of these elements with manganese oxides. At the confluence 10 km downstream of both sites, neutral pH was measured, with metal (Cd, Cu, Pb and Zn) concentrations similar to upstream values and below guideline values recommended by government authorities (e.g., ANZECC, 2000), indicating effective attenuation. However, at Croydon seasonal fluxes of metals may occur as a function of low flow conditions (low pH) or heavy rainfall events (high pH) causing desorption of elements (cf. Harris et al., 2003; Ashley et al., 2004; Nordstrom, 2009).

Generally water quality is similar in both creeks. Elevated Cd and Zn concentrations measured in Deadhorse Creek provide an indication that material representative of mesotextural group G dominates in the Glencoe waste rock pile. The death of livestock around the Croydon district was attributed to Cd-poisoning. However, these results suggest that Cd concentrations are relatively low from 1 km downstream of Glencoe. As the Croydon mine sites are currently designated grazing land, a more likely cause of death is through consumption of the plant Calotrope observed around the Croydon mines (cf. Lottermoser, 2011).

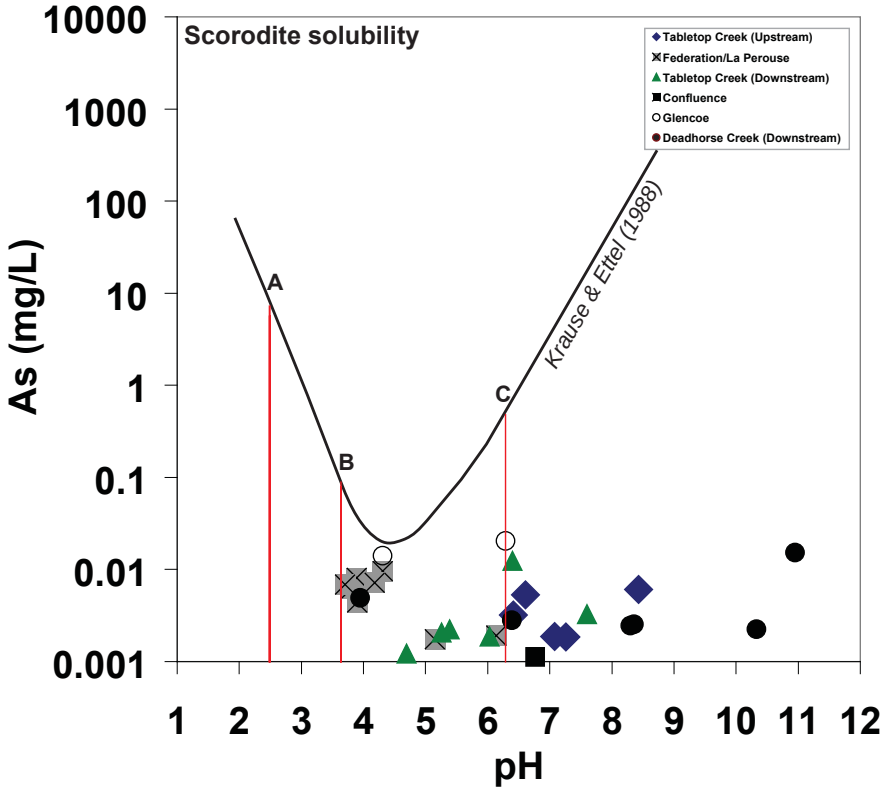

Figure 4.42 Compositions of surface water around the Croydon district on a dissolved As versus solution pH diagram. The scorodite solubility curve is from Krause & Ettel (1988). A indicates the lowest pH value measured in kinetic testing of mesotextural group H (arsenopyrite-pyrite-quartz); and B and C indicate the pH range of waste rock pile leachate meaured in the field.

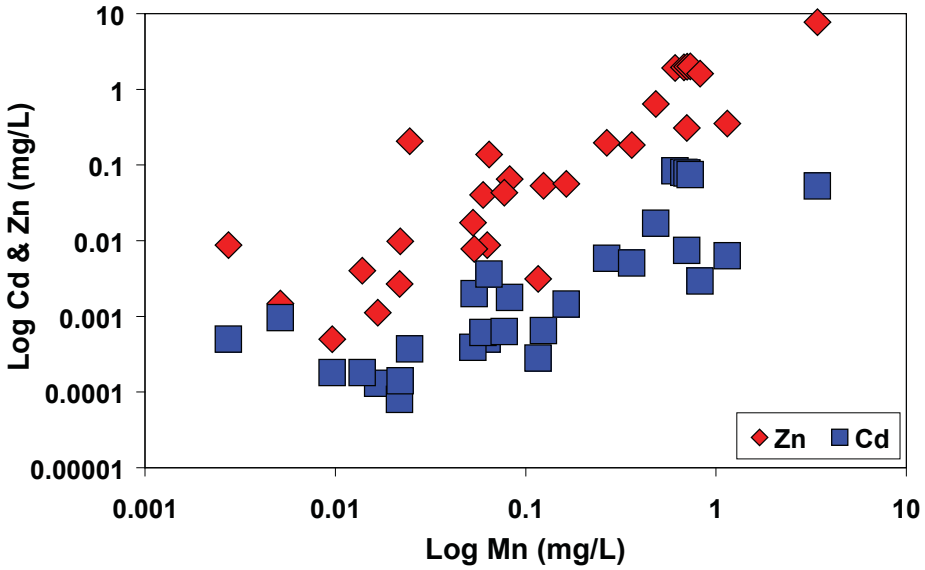

Figure 4.43 Dissolved Cd and Zn relative to Mn in surface waters in the Croydon district.

4.5.4 Implications of kinetic trials for site rehabilitation

Historic metalliferous mine sites often require rehabilitation. However, limited capital and excessive costs associated with planning and remediation works means that comprehensive site rehabilitation is rarely achievable. At historic mine sites, rehabilitation is driven primarily by impacts on soil and water quality e.g., Alvarez and Ridolfi (1999) and Mudd and Patterson (2010). If water quality data alone is used to assess the requirement for rehabilitation at Croydon, the site would not be prioritised under Queensland's Abandoned Mine Lands Program (AMLP). Kinetic trials indicated that sulphidic mine wastes are in early-maturing weathering stages by the general mine waste paragenesis proposed by Moncur et al. (2009). First-flush data indicated that there would be significant elution of metals and As after a heavy rainfall event (Figure 4.5; cf. Harris et al., 2003). Thus, both Croydon sites are considered as long-term contamination sources posing significant environmental risk to the downstream environment.

Previous rehabilitation strategies at the site focused on raising pH in pit lakes with very limited success (Cottier, 2010, pers. comm). A more effective long-term strategy should focus on the relocation of ARD sources into newly constructed capped impoundments, with waste rock pile material domained into the ten mesotextural groups identified. Material representative of mesotexutural group H is a the dominant source of As, with its concentration in dissolved waters controlled by scorodite. However, there evidence of scorodite weathering was observed, indicating a potential increase in dissolved As in waste pile leachates. Material representative of mesotextural group G contains significant quantities of Cd (and Zn) which is homogenously distributed in sphalerite grains, thus is a long-term source of these elements. Whilst relatively low metal and As concentrations were measured from mesotextural group J in kinetic trials (eluting at a relatively slow rates), it is identified a significant contamination source due to its high pyrite contents (i.e., generating low pH conditions). Thus, mesotextural groups G, H and J should be treated as individual entities and managed separately, as co-disposal has potential to increase

the environmental risk posed, through geochemical interactions. Such waste segregation practices are described in the GARD guide (2010). For example, sphalerite leaching is enhanced at low pH (2 to 4; Stanton et al., 2008), and leachate pH evolved from group H was well below 4 (Figure 4.25). Therefore, co-disposal may enhance sphalerite oxidation, releasing increased amounts of dissolved Cd and Zn.

Neutralisation strategies must be implemented in the impoundments containing material representative of mesotextural groups G and J (and E, which can be co-disposed with J) waste in order to raise pH and reduce heavy metal and metalloid mobility (cf. Ashley et al., 2004). Alternatives to lime should be sought given the limited success previously experienced (DME, 2008). As scorodite has extensively precipitated in mesotextural group H (Figure 4.24), the pH in the repository containing it should be maintained in a range where it is relatively insoluble. Bluteau and Demopoulous (2007) reported low solubility rates (0.35 mg/L^{-1}) of As at pH 5, with its dissolution from pH 5 to 9 similarly low. However, Krause and Ettel (1988) reported that ~90 mg/L^{-1} As was leached from scorodite at pH 5. Drahota and Fillippi (2009) proposed that reasons for these differences may be linked to the degree of scorodite crystallinity used, with two types of scorodite texture observed in here (spherules, and acicular grains). Therefore, prior to recommending the geochemical conditions at which this material representative of this mesotextural group should be maintained at, further work is required to elucidate the crystallinity and stability of scorodite in this mesotextural group.

4.6 Summary

- Following the GMT approach classification of Croydon mine waste, material representative of mesotextural groups G (sphalerite-galena-pyrite-quartz), H (arsenopyrite-pyrite-quartz), J (quartz-pyrite) and E (porphyritic rhyolite with disseminated pyrite) were selected for kinetic testing.
- Two grain sizes were used as column feed (-10 mm and -4 mm) to examine the control of grain size on leachate chemistry. Twelve free-draining column leach samples were kinetically leached for thirty weeks following the AMIRA P387A Handbook (Smart et al., 2002).
- Material representative of mesotextural group H was the most acid forming, with pH values below 4 from the start of the column leach tests. Lower pH and high release rates of elements were measured from the -4 mm column, showing a clear grain size control for this group. Highest dissolved As was measured in leachate from this group.
- Material representative of mesotextural group G also showed a similar relationship between pH and grain size, with the -4 mm overall more acid forming. The highest dissolved Zn was measured in leachate from this group.
- Several pyrite microtextures were identified in material representative of mesotextural groups E and J, and pH values were not sustained below pH 4 as with other mesotextural groups (i.e., H). However, the -4 mm grain size fraction overall returned lower pH values, and higher dissolved metal and As concentrations.
- Elevated Cd, Pb and Zn relative to ANZECC ISQG (2000) were measured within 10 km downstream of the site operations, indicating that these sources of contaminants are impacting the local environment.
- Based on results of these kinetic trials, segregation of waste rock materials into mesotexural groups (G, H and J/E) is recommended for more effective site rehabilitation.

Chapter 5

Applications of geometallurgical data for predicting ARD: Examples from the Ernest Henry IOCG deposit, Queensland

5.1 Introduction

The emerging discipline of geometallurgy focuses upon integrating geology, geostatistics and metallurgy. Consequently, geometallurgy is becoming increasingly recognised as a discrete and high-value activity that reflects an ongoing commercial trend towards more effective mine site integration and optimisation (Walters and Kojovic, 2006; Walters, 2008; Jackson et al., 2011; Keeney et al., 2011; Dunham et al., 2011; Montoya et al., 2011). The fundamental aim of geometallurgy is to provide constrained inputs that reflect inherent geological variability and its impact on metallurgical performance. This requires quantification of ore deposits in terms of machine-based process parameters such as hardness, comminution energy, size reduction, liberation potential and product recovery (Walters, 2008). These parameters are used to populate deposit-scale block models typically through the application of geostatistics (Walters, 2008; Jackson et al., 2011; Dunham et al., 2011). Incorporation of geometallurgical parameters into resource modeling supplements traditional geology and grade-based attributes, enabling a more holistic approach to economic optimisation of mineral production (Ashley and Callow, 2000; Williams and Richardson, 2004; Dunham and Vann, 2007; David, 2007 *in* Walters, 2008).

Geometallurgy integrates data from a wide range of existing activities including process mineralogy, mine geology, metallurgy, process control, resource modeling and geostatistics which contribute to the 'ore body knowledge' or 'ore characterisation' (Walters, 2008). The most significant Australian research project to date which has focused on developing an integrated geometallurgical approach was the four-year AMIRA P843 GeM^{III} project (Geometallurgical Mapping and Mine Modeling), which commenced in 2005. This project was a collaborative research effort between CODES, University of Tasmania and the Julius Kruttschnitt Mineral Research Centre (JKMRC), University of Queensland. The project aims were to deliver fundamental knowledge, tools and methods to define mineralogy, element deportment and texture in geometallurgical terms at a range of scales, which could then be linked to mineral processing performance and efficiency. Outcomes were improved indices of processing performance that could be embedded in resource block models to define processing domains to be targeted in mine planning and optimisation (Walters, 2008).

Despite the collection of a vast range of data for geometallurgical modeling, no published examples exist of it being utilised for environmental characterisation. However, the sampling strategies utilised as part of geometallurgical campaigns i.e., 2m sampling (e.g., Alruiz et al., 2009; Leichliter et al., 2011)

represent an appropriate sampling interval for deposit-scale ARD domaining as discussed in Chapter 2 (section 2.2.1). Additionally, there is significant potential to utilise data collected for geometallurgical studies for ARD prediction, thus adding value to these data sets. Considering this, the aim of this chapter is to identify links between the GMT approach and existing geometallurgical data at an operational mine site. A sample set was obtained from the Ernest Henry iron-oxide copper gold (IOCG) deposit for this study, as this site has been geometallurgically characterised in detail as part of the AMIRA P843 GeM project. Additionally, the mineralogy of this site was significantly different to the Croydon Au-mines, with a higher content of neutralising minerals and no known reports of ARD. Thus, selection of samples from this site allowed for the GMT approach to be critically evaluated.

5.2 Site description

5.2.1 Location and mine history

The Ernest Henry (EH) mine is located ~40 km northeast of Cloncurry in northern Queensland, Australia and is the largest of a diverse group of iron-oxide copper gold (IOCG) deposits in the Cloncurry district in the eastern part of the Mount Isa inlier (Figure 5.1 and Figure 5.2; Ryan, 1998; Marks et al., 2006; Hunt and Clifford, 2008). Ernest Henry is the second largest IOCG deposit in Australia after Olympic Dam. Detailed project feasibility work commenced in 1992, with the final feasibility work completed in 1995 (Tredinnick and Tuesley, 2000). The design and construction of the project infrastructure occurred over a two year time frame (Tredinnick and Tuesley, 2000). The total capital commitments for establishing the new venture were $420 million, of which, $315 million was associated with on-site capital programs (Tredinnick and Tuesley, 2000).

The mine was designed to have a life of 15 years, with more than 50 Mt of rock mined per year from a large open pit (Figure 5.3), of which ~10 Mt was ore containing 1.1% Cu and 0.55 g/t Au (Tredinnick and Tuesley, 2000). Open pit operations commenced in 1997, with the orebody mined on 16m benches by conventional load and haul methods using large-scale mining equipment (Collier and Bryant, 2003). Ore processing through the concentrators yields Cu/Au concentrate (Tredinnick and Tuesley, 2000). This concentrate is sold to Mt Isa Mines Pty. Ltd., where it was further processed through the copper smelter at Mt. Isa and the copper refinery at Townsville (Tredinnick and Tuesley, 2000).

Underground mining commenced in 2011, extending the life of the mine to 2024 (Quigley, 2012). Ernest Henry's ore reserve estimate in mid-2010 was 88 Mt at 1% Cu, 0.5 g/t Au and 23% magnetite (Xstrata Copper, 2011). Concentrate produced in 2010 consisted of approximately 75,000 t s of Cu, and 91,000 ounces of Au, with traditional grinding and flotation methods used for recovering both (Quigley, 2012). Magnetite is also liberated from this process, thus a new magnetite extraction plant recovering iron ore from the concentrator tailings was constructed, and will produce 1.2 Mt magnetite concentrate per year (Quigley, 2012).

5.2.2 Climate and physical environment

The climatic setting of Ernest Henry is similar to that of Croydon (Section 3.3.2), with two distinct seasons controlled by the monsoon. The wet season is experienced from December to March, with the

average annual rainfall ~500 mm (Bureau of Meteorology, 2012). The dry season experiences milder temperatures, low to nil rainfall, and strong south easterly-winds (Tredinnick and Tuesley, 2000).

The mine is located on flat black soil plains with the vegetation dominated by Mitchell grass and Flinders grass (Tredinnick and Tuesley, 2000). Since the mid-1860s, the predominant land use in this area has been cattle grazing (Tredinnick and Tuesley, 2000). The main drainage line is the Cloncurry River, ~9 km west of the mining operation. The Cloncurry River drains into the Gulf of Carpentaria 300 km to the north (Tredinnick and Tuesley, 2000). The mine site is located over a sub-basin of the Great Artesian Basin aquifer.

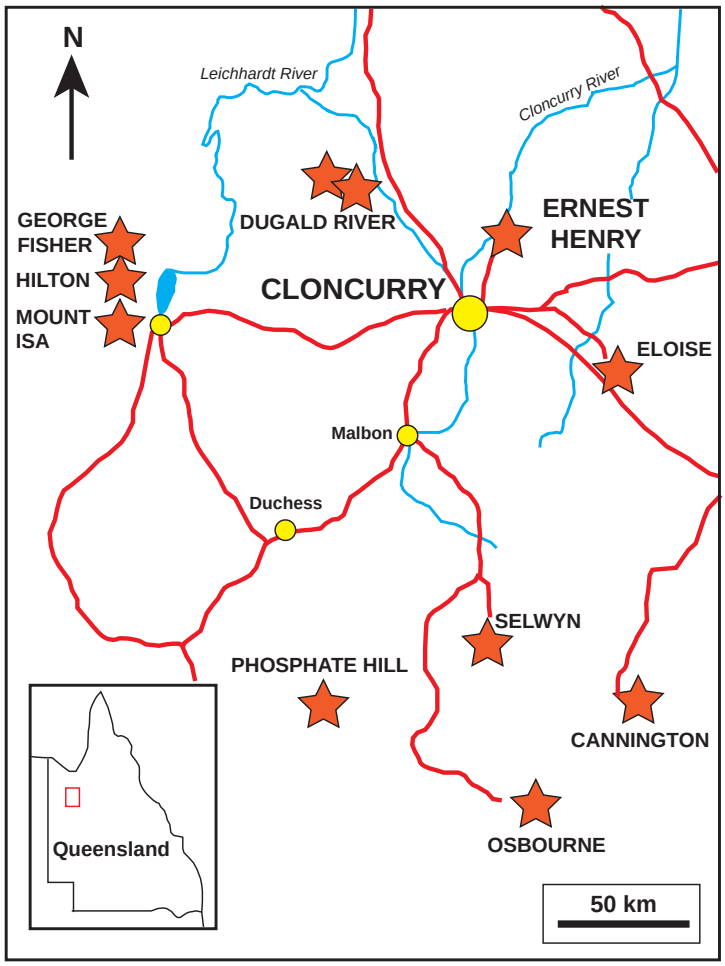

Figure 5.1 Loaction of Ernest Henry within the Cloncurry/Mount Isa district in northern Queensland. Modified from Tredinnick and Tuesley (2000).

5.2.3 Geology and mineralisation

The Ernest Henry deposit is hosted by ~1740 Ma (Proterozoic) plagioclase-phyric meta-andesitic volcanic rocks (identified as having low to moderate neutralising potential following the classification by Plumlee, 1999). These are locally intercalated with siliciclastic calc-silicate-rich (scapolite-bearing) and graphitic metasedimentary rocks and ~1660 Ma metadiorites, which are collectively known as Cover Sequence 2

(Ryan, 1998; Mark et al., 2006). Host rocks have been affected by Na-Ca alteration, characterised by hematite-bearing albite, disseminated biotite-magnetite alteration, and garnet-potassium feldspar-biotite alteration (Ryan, 1998; Mark et al., 2006; Hunt and Clifford, 2008).

The orebody location is structurally controlled, and occurs within volcanic rocks that were brecciated during reverse fault movement along bounding shear zones (Mark et al., 2000). Breccia infill is composed of a magnetite-carbonate-sulphide assemblage that also contains biotite, potassium feldspar, hematite, garnet, barite, fluorite and quartz (Ryan, 1998; Mark et al., 2000; Hunt and Clifford, 2008). Emplacement of mineralisation was approximately coeval with emplacement of the Williams and Naraku batholiths ~1540 to 1500 Ma (Blake et al., 1990; Mark et al., 2000, 2006; Williams et al., 2005; Hunt and Clifford, 2008). This event is associated with extensive potassium feldspar-hematite alteration (Ryan, 1998; Mark et al., 2000, 2006; Hunt and Clifford, 2008). Post-ore alteration is dominated by carbonate (Hunt and Clifford, 2008).

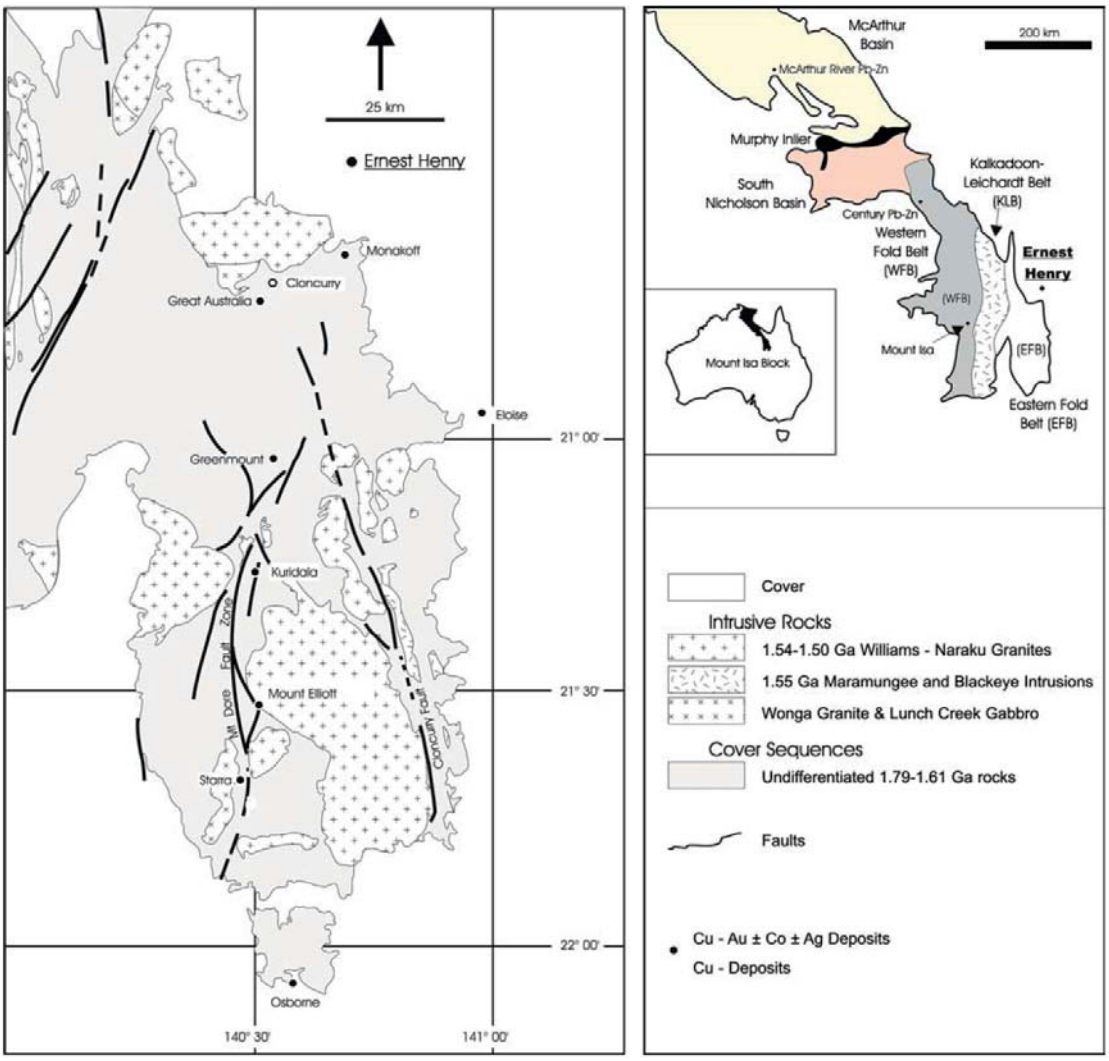

Figure 5.2 The geology and mineral deposits of the Cloncurry district compiled from published AGSO maps and modified from Williams (1998) in Mark et al. (2006)

Primary and supergene mineralised zones were present prior to mining (Hunt and Clifford, 2008). Chalcopyrite and pyrite dominate the primary zone, and chalcocite, hematite, calcite and siderite are abundant in the supergene zone (Hunt and Clifford, 2008). Copper and gold concentrations strongly correlate in the primary zone. Anomalous amounts of As, Ba, Co, F, Mo, REE and U are associated with copper mineralisation in both zones (Ryan, 1998; Mark et al., 2000, 2006; Hunt and Clifford, 2008). Mineralisation is hosted in a pipe-like complex breccia between two shear zones, with breccia textures indicating the presence of several ore shoots within it (Hunt and Clifford, 2008). Low grade ore occurs on the margin of the breccia pipe in the potassium feldspar-altered crackle breccia (Hunt and Clifford, 2008). There are two dominant types of chalcopyrite mineralisation within the main area of brecciation: 1) widespread fine-grained disseminated chalcopyrite and 2) coarser-grained chalcopyrite associated with quartz-carbonate veins (Hunt and Clifford, 2008).

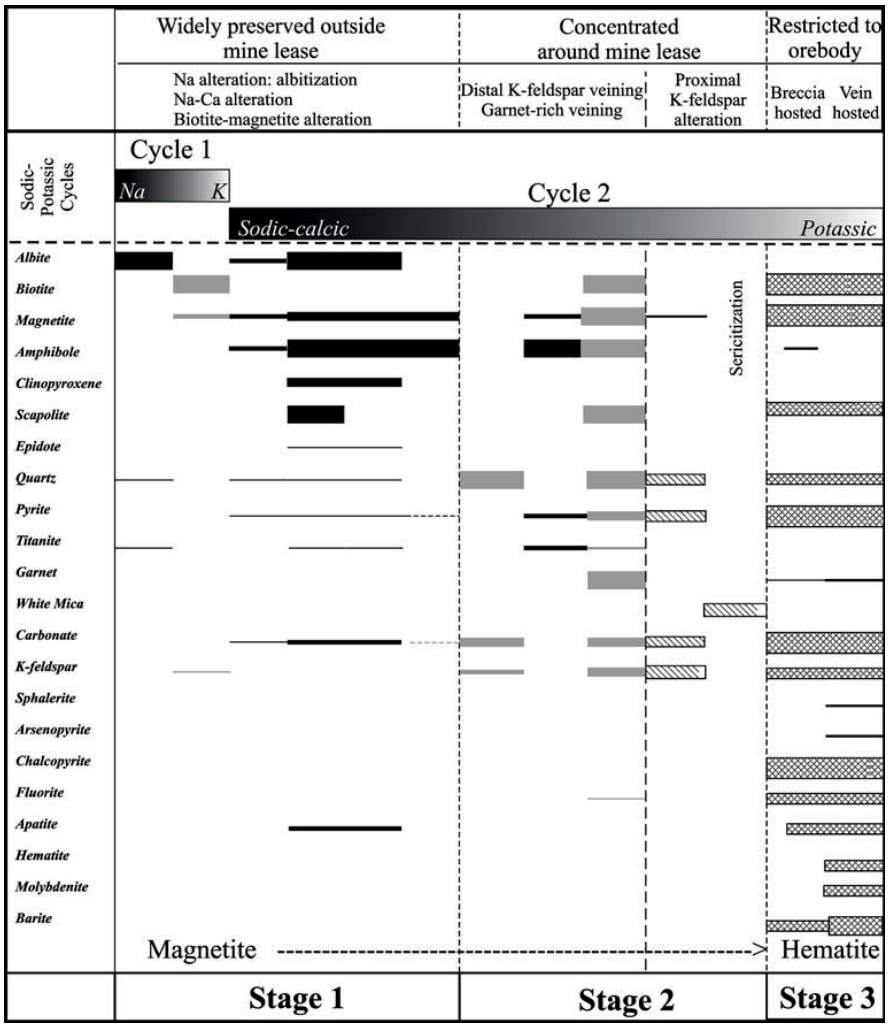

Figure 5.3 Paragenetic sequence and spatial distribution of pre- and syn- ore hydrothermal alteration in Ernest Henry term lease. The width of individual lines refers to the relative abundance of a mineral formed during a particular stage. Stippled lines represent trace mineral abundances. Black fill denotes relatively sodium rich pre-ore mineral assemblages. Grey fill denotes potassium rich mineral assemblages deposited prior to ore-related potassium feldspar alteration (from Mark et al., 2006).

Hydrothermal alteration at EH is divided into three main phases (Figures 5.3 and 5.4; Mark et al., 2006); Stage 1: hydrothermal associations produced during the early stages of hydrothermal evolution e.g., albitisation and Na-Ca alteration; Stage 2: hydrothermal associations chemically linked but occurring prior to Cu-Au mineralisation; and Stage 3: hydrothermal associations temporally, spatially and chemically linked to the ore. Structurally-controlled pervasive albitisation and Na-Ca alteration formed along with localised breccia-hosted alteration along NE trending fluid conduits (Mark et al., 2006). Pre-ore potassic alteration associated with Ba, Fe and Mn enrichment formed along NE-trending footwall fluid conduits and the shear zones bounding the deposit (Mark et al., 2006). Dilation induced hydrothermal brecciation and Cu-Au mineralisation formed locally, with weak sulphide mineralisation also formed along some conduits other than those that host the main orebody (Mark et al., 2006).

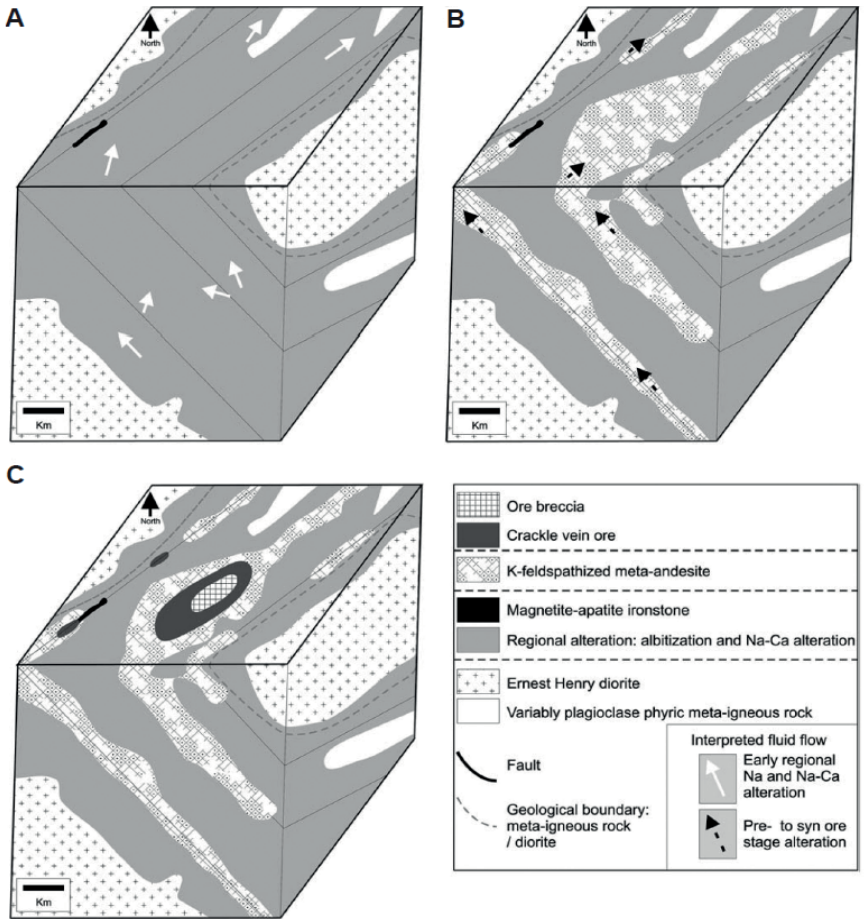

Figure 5.4 Interpretation of the spatial and temporal evolution of the Ernest Henry hydrothermal system: **(A)** Early sodic-calcic alteration; **(B)** Pre-ore potassic alteration; **(C)** Local brecciation and Cu-Au mineralisation. From Mark et al. (2006).

5.2.4 Previous ARD characterisation

Acid rock drainage characterisation and management strategies at Ernest Henry were outlined in Tredinnick and Tuesley (2000). They stated that 700 Mt of waste rock would be mined, with 50 Mt/y of waste rock placed in terraced dumps with a height of 70 m and covering approximately 8 km^2. Static testwork to develop the initial ARD model (Phase 1) was undertaken on 96 waste rock samples,

with net acid producing potential (NAPP) values and acid neutralising capacity (ANC) to maximum potential acidity (MPA) ratios used to determine the cut-off limits. The main lithology identified as acid forming was the Mesozoic pyritic black shale unit (66 Mt) which overlies the Proterozoic volcanics (i.e., the orebody host). The Proterozoic volcanics were subjected to kinetic column leach tests (n=11) with leachate from all samples remaining alkaline (pH >7.6) after 27 months. Analysis of the rate of sulphate generation indicated that lag-time to acid-formation was in the order of hundreds of years. Based on static and kinetic testing, Tredinnick and Tuesley (2000) stated that a cut-off value of -20 kg H_2SO_4/t was appropriate to differentiate between PAF and NAF samples. Initial ARD modelling showed that 51% of the waste rock was non-acid forming.

A second phase of ARD testwork was undertaken during the first year of operations in order to develop the life of mine environmental budget (Tredinnick and Tuesley, 2000). This was to identify if non-acid run-of-mine waste rock could be used for forming and decommissioning the waste rock dump and tailings storage facility. A 3D waste rock block model was formulated based on NAPP, NAG, paste pH and EC values. To develop this model, approximately 4000 m of existing core was split and assayed, and an additional 3000 m was drilled at a total cost of AUD $243,000 (Tredinnick and Tuesley, 2000). The model indicated that there was 88.2% non-acid forming waste rock, 5.2% potentially acid forming waste rock and 6.6% acid waste rock (Tredinnick and Tuesley, 2000).

A third phase of ARD investigations was undertaken during the first two years of mining (1997to 1999), whereby an understanding of the spatial distribution of ARD characteristics related to lithology and structure was ascertained. The ARD block model for the Proterozoic waste rock was reinterpreted into 5 ARD classes which are shown in Table 5.1.

Table 5.1 ARD classes and spatial distribution of waste rock at Ernest Henry (Tredinnick and Tuesley, 2000)

ARD class	Cut offs	Mt	% volume of total	Distribution
High sulphur, potentially acid forming	Sulphur >0.6 wt.% NAPP>-20kg H_2SO_4/t	79	14	Ore body
Low sulphur, potentially acid forming	Sulphur <0.6 wt.% NAPP>-20kg H_2SO_4/t	101	18	Hanging wall ore body margins
High sulphur, non-acid forming	Sulphur >0.6 wt.% NAPP< -20kg H_2SO_4/t	57	10	Footwall
Low sulphur, non-acid forming	Sulphur <0.6 wt.% NAPP< -20kg H_2SO_4/t	271	47	Intermediate distance into hanging walls
Acid-consuming (no sulphides)	-	64	11	Pit limits hanging wall

The ARD control strategy for waste rock adopted a three-fold approach comprising: 1) selective placement of material within the waste rock pile; 2) surface water management; and 3) leachate collection (Tredinnick and Tuesley, 2000). Acid forming material (including pyritic black shales) were placed in discrete cells within the pile, surrounded by NAF material and eventually capped with a minimum

of 0.5m Tertiary clays (Tredinnick and Tuesley, 2000). These clays were compacted by the movement of run of mine trucks, with the clay acting as a means of reducing water flux through the black shale (Tredinnick and Tuesley, 2000). To date, this has proved a successful management strategy, with relatively few reported incidences of contaminated waters discharging from the waste rock pile documented. The most recent incident was reported in 2010, where elevated sulphate levels were measured 20 km north of the site (http://www.derm.qld.gov.au).

Comparison of the waste rock block model against waste rock grade control results showed good agreement more distant from the ore body. However, due to structural, alteration and lithological complexities close to the margins of the ore body, additional ARD characterisation was required (Tredinnick and Tuesley, 2000). Therefore, only Proterozoic volcanic samples were used in this chapter.

5.3 Materials and methods

5.3.1 GMT characterisation

A limited number of offcuts (<10 cm x 10 cm) from Ernest Henry drill holes EH 633 and EH 635 (n=30; Table 5.2) were obtained from the AMIRA P843 GeM project with permission from Professor Steve Walters. Access to the GeM Ernest Henry geometallurgical database was allowed. These drill holes were chosen as they were the most recently drilled (i.e., assumed to be the least weathered) and demonstrated a variety of sulphide textures due to the proximity of the holes to the ore body (Figure 5.5). Additionally, these drill holes had been subjected to the most geometallurgical characterisation. After mesotextural evaluation, samples were selected for GMT characterisation if they were considered as representative of a major lithology, alteration style or texture. Samples were sawn in two, with one piece (~3cm x 3cm) kept for intact mineralogical and textural evaluation, and the other jaw-crushed and milled to <75 µm for geochemical analyses. The primary aim of GMT classification of these samples was to obtain predictive ARD data for comparison against the geometallurgical database.

Paste and rinse pH tests were performed (n=20; CODES, UTAS) on both pulverised (< 75µm) and intact off cut samples (>2 cm^2) following the method outlined in the AMIRA P387A Handbook (Smart et al., 2002). Intact off cuts were weighed, deionised water added (in a 2:1 water: solid ratio), and samples left standing for 24 hours prior to measurement. A Eutech Instruments 510 pH meter was used following the methods outlined in Section 3.3.2.2 and Section 4.2.4. Sulphur values were obtained using a Thermo Finnigan EA 1112 Series Flash Elemental Analyser (EA; CSL, UTAS) following the procedure outlined in Section 2.4.1 and Section 3.3.2.2. Samples were identified as containing high barite and were therefore scheduled for $S_{Sulphate}$ analysis to determine $S_{Sulphide}$ (ALS, Brisbane, Australia). Meso-scale ARDI evaluations only were performed on all samples, as it was stated in Section 3.5.1 that these values alone provided a sufficient evaluation of ARD forming potential. Additionally, this allowed for an understanding of how best to integrate the ARDI into routine drill core logging practices.

Quantitative X-Ray diffraction (QXRD) of 9 samples was undertaken at the University of Ballarat (Australia) following the method described in Section 3.3.2.2. As this material had been assayed as part of the AMIRA P843 GeM project, no FP-XRF analyses were undertaken on this material. Based on stage-

one classification, 16 samples were selected for further GMT characterisation with ANC (Sobek) and the single-addition NAG tests performed (ALS, Brisbane, Australia).

Table 5.2 Samples from drill holes EH 633 and EH 635 used in this study, together with the original lithological code (based on lithology, alteration and texture) assigned at Ernest Henry by Xstrata.

Hole ID	Depth (m)	Lithological code	Description
EH 633	879	AMV2	Altered Mosaic Mafic Volcanics - matrix supported breccia with moderate to strong digestion of clasts
	941		
	965		
	975	FV2	Mosaic Felsic Volcanics - matrix supported breccia with moderate to strong digestion of clasts
	1009		
	1131	FV1	Fractured Felsic Volcanics - brittle fracturing, clast supported, can be an overprinting alteration
	1147	AMV	Altered Mafic Volcanics, generally phenocryst poor, very fine to fine grained, variably amygdaloidal, massive to banded volcanic rock.
	1159		
	1165	FV	Felsic Volcanics - not fractured, veined or brecciated
EH 635	831	IV2	Intermediate volcanics-matrix supported breccia
	841		
	851	AMV1	Altered Fractured Mafic Volcanics - brittle fracturing, clast supported, can be an overprinting alteration
	855		
	879	AMV2	Altered Mosaic Mafic Volcanics - matrix supported breccia with moderate to strong digestion of clasts
	923	FV2	Mosaic Felsic Volcanics - matrix supported breccia with moderate to strong digestion of clasts
	939		
	947		
	949		
	953		
	957		
	961		
	969		
	979	FV3	Lithon Felsic Volcanics - generally matrix supported with aligned clasts
	993		
	1001	FV2	Mosaic Felsic Volcanics - matrix supported breccia with moderate to strong digestion of clasts
	1011		
	1015	FV3	Lithon Felsic Volcanics - generally matrix supported with aligned clasts
	1019		
	1027		
	1099	IV2	Intermediate volcanics-matrix supported breccia

As stage-three tests are not mandatory (Section 2.6.4), only geochemical and textural analyses were performed on selected samples. Multi-addition NAG tests (n=16; CODES, UTAS) and kinetic-NAG tests (n=4; ALS, Brisbane, Australia) were undertaken. Considering the relatively high and diverse carbonate contents of these samples, acid buffering characterisation curve (ABCC) tests were also performed (n=6; ALS, Brisbane) to calculate the effective neutralising potential.

Polished MLA tiles (n=5) were prepared and analysed by MLA using XMOD and GXMap techniques (CSL, UTAS). The GXMap technique uses back-scattered electron (BSE) images to define phase boundaries and X-ray spectra to identify the mineralogy of each phase as described in Section 2.6.3. An X-Ray trigger was used to overcome difficulties in differentiating between magnetite and pyrite. The target minerals mapped included magnetite, pyrite, and several gangue phases including calcite. Nickel was used as the standard in these analyses. 200 frames were mapped per sample with a frame resolution of 512 x 400 pixels. Given the variation in content of the target minerals and the grain size, the analysis time varied from 8-22 hours per sample. Images were processed in MLA Image View and Texture Viewer.

5.3.2 Geometallurgical techniques

5.3.2.1 Sample selection

Seven holes were chosen from the Ernest Henry deposit for sampling by the AMIRA P843 GeM project (Table 5.3; Figure 5.5). Drill holes and sampling intervals were chosen with the help of site personnel in order to provide samples from all parts of the known ore body (Hunt and Clifford, 2008). This included mineralisation in the open pit and underground areas of the deposit.

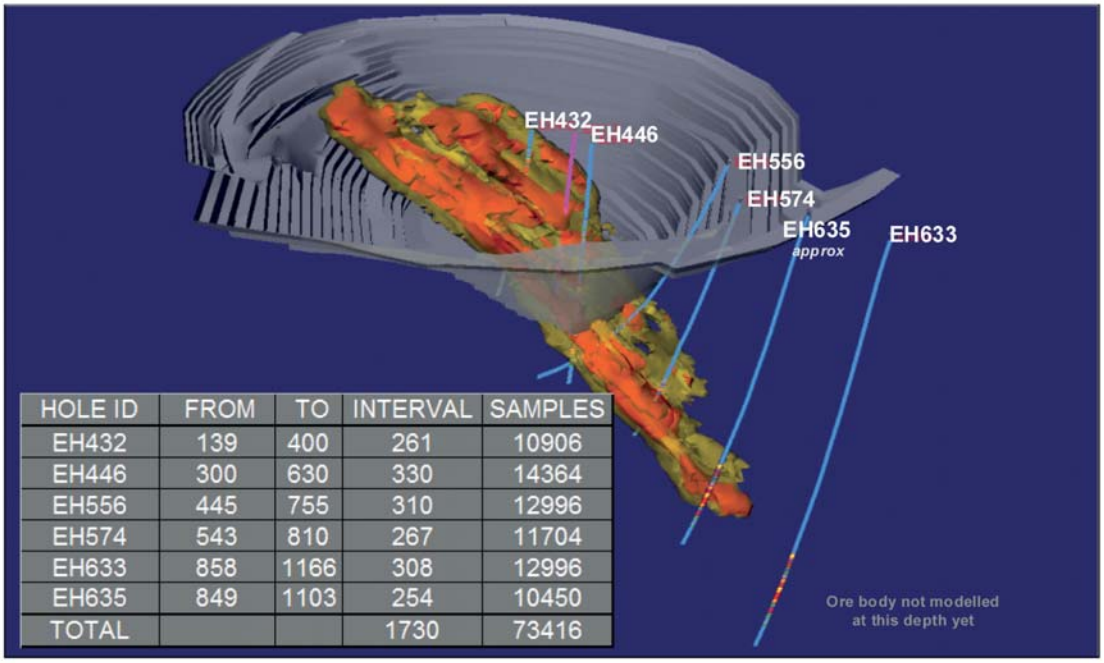

HOLE ID	FROM	TO	INTERVAL	SAMPLES
EH432	139	400	261	10906
EH446	300	630	330	14364
EH556	445	755	310	12996
EH574	543	810	267	11704
EH633	858	1166	308	12996
EH635	849	1103	254	10450
TOTAL			1730	73416

Figure 5.5 Location of sampled drill holes EH 633 and EH 635 relative to the Ernest Henry ore body (Quigley, 2008).

Table 5.3 List of drill core intervals sampled by the AMIRA P843GeM project at the Ernest Henry deposit (Hunt and Clifford, 2008). Abbreviations: SWIR, Short Wave Infrared; NIR, Near-Infrared; TIR, Thermal Infrared; VNIR, Visible Near-Infared.

Drill hole ID	From(m)	To (m)	Description
EH 512	209	483	Drill core used in comminution development work.
EH 432	150	390	Geophysical characterisation, hardness testing.
EH 446	300	620	Hylogger SWIR and NIR spectral analysis, image analysis and comminution work.
EH 556	450	750	
EH 574	550	810	
EH 633	860	1180	
EH 635	810	1100	Geophysical characterisation, hardness testing, Hylogger SWIR, NIR and TIR spectral analysis, image analysis and comminution work.

5.3.2.2 SWIR/VNIR/TIR measurements

The Australia-developed HyLoggingTM systems (Figure 5.6) are automated platforms to rapidly and systematically collect infrared spectroscopic reflectance data at dense sample spacing from drill core, chips or powders (Huntington et al., 2006; Quigley, 2012). Consitituent mineralogy is determined based on the principles of reflectance spectroscopy (Lyon, 1962; Farmer, 1974; Hunt 1977; Clark, 1999 *in* Quigley, 2012). Mineral spectroscopy involves the capture of reflected, scattered or emitted light from a sample with the variable light intensities recorded across hundreds of narrow contiguous wavelength channels by a spectrometer's detector (Quigley, 2012). Each measurement generates a spectral response curve (spectrum) displaying relative absorption and reflection features (troughs and peaks) at specific diagnostic wavelengths (Huntington et al., 2006; Quigley, 2012). This technique is responsive to the chemical composition and crystal structure of a mineral (Quigley, 2012). Thus, mineral identification is made possible based on the resulting 'spectral fingerprint' or 'signature' observed in the spectral response curve (Huntington et al., 2006; Quigley, 2012). A select suite of minerals can be identified based on their diagnostic spectral absorption features (Table 5.4) displayed in the Visible to Near-Infrared (VNIR, 350-1000 nm), Short-Wave Infrared (SWIR, 1000-2500 nm) and the Thermal Infrared (TIR, 5000-14,000 nm) region of the electromagnetic spectrum (Quigley, 2012).

Continuous down-hole mineral information is achieved with Hylogging, improving confidence when modelling by providing a data dense 3D representation of the bulk rock and its inherent geological variability (Quigley, 2012). HyLogging has several advantages over other mineral identification techniques (e.g., XRD and automated SEM instruments including MLA and QEMSCAN) through its rapidity (up to 1000m of core per day), its low cost per sample, and its non-contact, non destructive approach (Huntington et al., 2006; Quigley, 2012). Considering this, there is a potential application of Hylogger data in the GMT approach.

Table 5.4 Examples of minerals able to be identified from the VNIR, SWIR and TIR reflectance spectroscopy. NB. Some minerals are able to be identified from more than one wavelength region, with carbonate shown twice (Quigley, 2012). Abbreviations are listed in Table 5.3.

Wavelength region	Mineral group	Mineral species examples
VNIR (350 – 1000 nm)	Iron Oxide	hematite and goethite
SWIR (1000 – 2500 nm)	Al-hydroxyl minerals	paragonite, muscovite, phengite, illite, pyrophyllite, kaolinite, halloysite, dickite, gibbsite and smectite varieties
	Sulphates	alunite, jarosite and gypsum
	Fe-hydroxyl minerals	saponite and nontronite
	Mg-hydroxyl minerals	chlorites (Mg/Fe), biotite, phlogopite, antigorite, tremolite, actinolite, talc, hornblende and brucite
	Carbonate	calcite, dolomite, magnesite, ankerite and siderite
TIR (5000 – 14000 nm)	Quartz	silica
	Feldspar	plagioclase (e.g., albite) and K-feldspars (e.g., orthoclase)
	Olivine	fayalite and fosterite
	Garnet	almadine and spessatine
	Pyroxene	clinopyroxenes and orthopyroxenes
	Carbonate	calcite, dolomite, magnesite, ankerite and siderite

In November 2006, 1730 m of core from six drill holes (Table 5.3) was scanned on-site with the (VNIR-SWIR) HyChips HyLogging system (Figure 5.6; Quigley, 2008). Sample preparation was minimal, and involved dusting or washing down drill core to remove dust, mud and drillers grease if present (Quigley, 2012). Approximately 73,000 hyperspectral reflectance measurements were collected over five days, with the data acquisition rate c.10 minutes for a seven section core tray using a 25mm sample spacing interval (Quigley, 2012). Measurements were captured from a 10mm x 10 mm field-of-view along the middle of the core, and continuous imagery across the full width of the core was synchronously acquired and subsequently used to create labelled core trays (Quigley, 2012). Iron oxides, carbonate and Al-, Fe- and Mg-hydroxyl-bearing mineral information was extracted to create objective, consistent and systematic mineral logs (Quigley, 2012). One drill hole was also scanned with the prototype TIR-Hylogger in May 2007 (CSIRO North Ryde laboratory, Sydney) to identify additional anhydrous silicate minerals e.g., quartz and feldspars (Quigley, 2012). Approximately ~62,000 measurements were collected from the ~230 m of drillcore scanned at 4mm spacing with a 10 mm x 14 mm field-of-view, and an acquisition time of ~5 minutes for a 7 section core tray (Quigley, 2012). Hyperspectral data analysis and mineral interpretation were carried out in version V7.1.0.016 of The Spectral Geologist (Quigley,

2012). HyLogging derived mineralogy was intended for comparison with MLA-SEM results (EH 635) to validate the mineral interpretation and assess the potential for quantifying spectro-mineralogical results (Quigley, 2012).

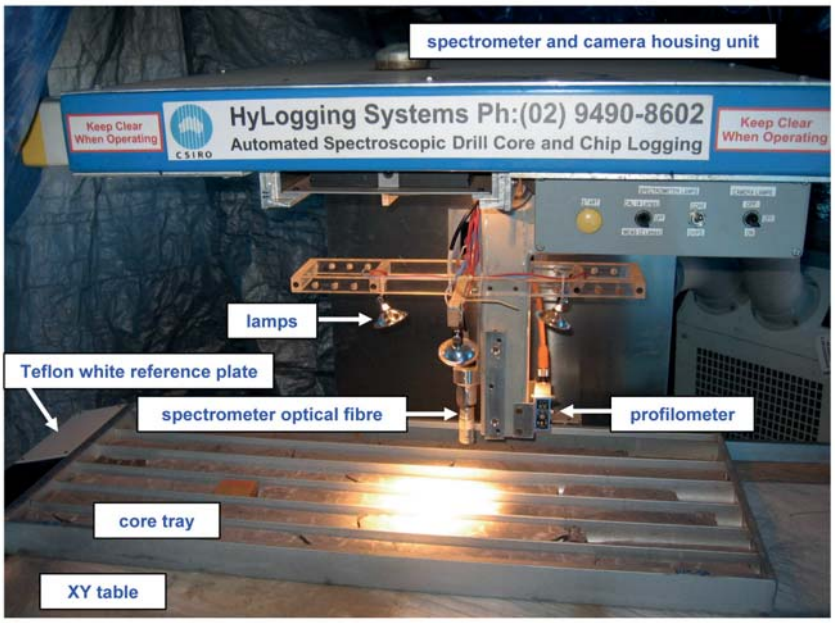

Figure 5.6 HyChips 6.2 hardware components. Image and labels from Quigley, (2012).

5.3.2.3 Petrophysical logging

In metalliferous mining, borehole logging is rarely performed when compared to its application at oil fields and coal mines due to logistical constraints, as explained in Vatandoost and Fullagar (2008). As an alternative, automated petrophysical drill core logging is now being undertaken in geometallurgy. Petrophysical contrasts can be used to discriminated ore from waste, e.g., magnetic susceptibility has long since been used as a direct grade indicator at magnetic mines (Vatandoost et al., 2008b). Petrophysical parameters including natural gamma-rays and conductivity have also been used for this purpose, with costs of grinding, processing waste and volume of tailings ultimately reduced. Vatandoost et al. (2008b) summarised that characterisation of rock masses is best achieved by an integrated approach whereby multiple measurements of petrophysical parameters are selected.

Considering this, a GEOTEK multi-sensor petrophysical core logger was utilised in the AMIRA P843 GeM project. This is a portable, bench-scale laboratory device which allows for simultaneous measurements of density, P-wave velocity, P-wave amplitude and magnetic susceptibility to be made on drill core (Vatandoost and Fullagar, 2008). In addition, high-resolution images (40 µm pixel) are collected using two camera systems at 45° inclination. The resulting images are occasionally subjected to automated classification of modal mineralogy, allowing for assessment of ore textural types (Vatandoost and Fullagar, 2008). Thus, data generated by a GEOTEK logger has the potential for use to undertake mesoscale ARDI evaluations more efficiently using classified modal mineralogical maps of drill core. At Ernest Henry, petrophysical measurements of the drill holes listed in Table 5.3 were recorded on a total of c.1700 m of NQ half core, with measurements taken at 9 cm intervals (Vatandoost et al., 2008b). After data reduction and processing, averages of the petrophysical parameters were computed over 2 m assay intervals.

5.3.2.4 Mineral hardness

An understanding of the susceptibility of a lithology to weathering is required to understand how rapidly potentially acid forming minerals will become exposed in a waste rock pile. This is qualitatively evaluated by the ARDI through parameter E (Table 2.13), however, it is not directly measured. Therefore, the application of EQUOtip is here explored. EQUOtip is a rebound hardness tester used in the AMIRA P843 GeM project as a routine non-destructive core-based measurement technique (Appendix 5.1; Keeney, 2008). Measurements can be performed directly on site and in any orientation. The EQUOtip unit consists of an impact device and a control/logging box (Figure 5.7). The impact device comprises a 3 mm diameter spherical tungsten carbide test tip that is spring mounted in an impact body (Keeney, 2008). During a hardness test, the test tip impacts under spring force against the test surface with an impact energy of approximately 11Nmm and then rebounds. Impact and rebound velocities are measured in a contactless manner when the test tip is located 1mm from the test surface (Keeney, 2008). The measurement is obtained by a permanent magnet built into the impact body which passes through a wire coil (Keeney, 2008). The measurement takes a few seconds to record (Keeney, 2008). The Leeb (Ls) hardness value (0 to 1000) is automatically calculated, and is the quotient of the rebound velocity over the impelled velocity multiplied by 1000 (Keeney, 2008). The impact body rebounds faster from harder test samples than it does from softer ones, resulting in a greater value. Typically, EQUOtip data is used as a domaining tool for orebody characterisation and for geometallurgical matrix modelling where the absolute values are used in regression models (Keeney, 2008).

At Ernest Henry, EQUOtip data was collected on-site for the drill holes listed in Table 5.3 with an average hardness value (Ls) for each 2 m interval calculated from measurements taken at 2.5 cm intervals (Keeney, 2008). Data was compared with uniaxial compressive strength (UCS) values, as these are most commonly used by industry to determine rock hardness (Keeney, 2008). The down hole profiles of EQUOtip results had a 5% smoothing applied to the curve to minimise the variability in the profiles (Keeney, 2008).

5.3.2.5 Automated microscopy

Quantifying textural and mineralogical relationships in rocks that affect processing performance is a critical aspect of geometallurgy. Berry and McMahon (2008) summarised that automated mineral recognition had largely been applied to opaque minerals (e.g., sulphides, magnetite), with little attempt made to recognise individual gangue phases (cf. Lane et al., 2008). However, for the purpose of ARD domaining, it is essential for the gangue mineralogy to be well defined. Considering this, the AMIRA P843 GeM project sought to improve automated optical microscopy by using both MLA-SEM and a Leica DM6000 optical microscope.

MLA-SEM analysis (FEI Quanta 600; CSL, UTAS) was performed on 368 samples obtained from the drill holes identified in Table 5.3. The primary motivation of this analysis was to determine Au deportment and examine the liberation potential of chalcopyrite. These samples were cut into 3cm x 3 cm blocks/tiles. It was acknowledged that these tiles are not wholly representative of a particular interval (e.g., 2 m assay interval), but they allowed for a database of intact textural attributes (e.g., chalcopyrite

distribution and association) to be populated (Kamenetsky, 2008). These samples were analysed using the X-ray modal (XMOD) and Sparse Phase Liberation-Lite (SPL-Lite) functions (conditions: 25 kV, accelerating voltage; 40 nA, beam current; 6.4 μs, amp time; spot size, 6-7 units) with Ni used as the brightness/contrast standard (Kamenetsky, 2008).

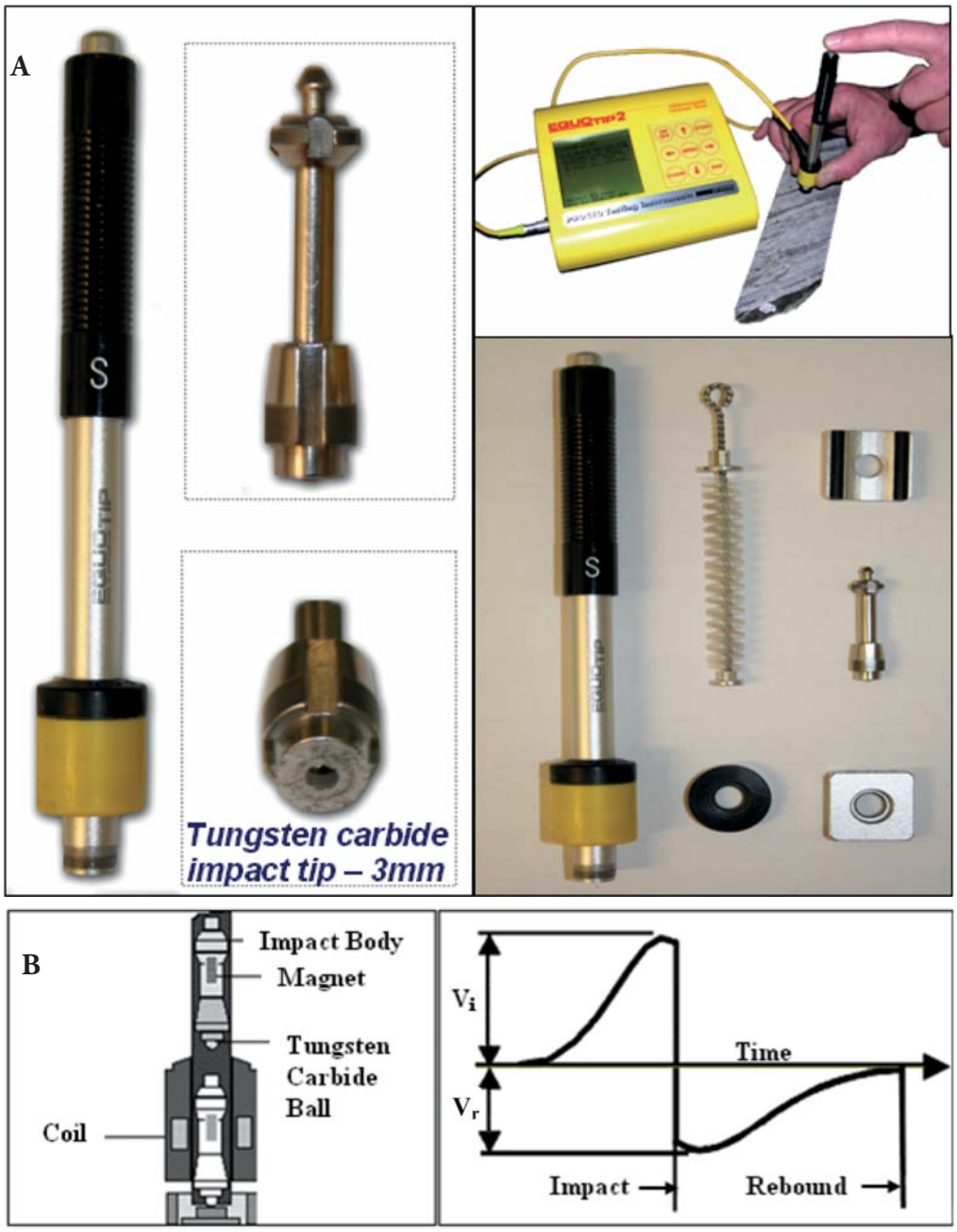

Figure 5.7 EQUOtip Impact Device used in the AMIRA P843 GeM Project at Ernest Henry, and accessories for the EQUOtip head unit: (**A)** Cross section of EQUOtip impact device. (**B)** Voltage signal generated by movement of the impact body (from Keeney, 2008).

The Leica DM6000 microscope (CODES, UTAS) has a high precision stage (<1 micron error in reproducibility) allowing for direct tiling of frames and therefore was used to analyse several hundred samples from the same EH drill holes (Berry and McMahon, 2008). This system utilised a Leica DFC420C 5Mpixel camera which has long exposure times (~10 minutes) allowing for collection of high-quality reflected, cross-polarised and fluorescence images (Berry and McMahon, 2008). Each pixel is approximately 4.73 μm in size, thus the smallest object recognised was 10 μm across (Berry and McMahon, 2008). Such resolution is appropriate for Mi-scale ARDI evaluation, however, Berry and McMahon (2008) stated that some difficulties are encountered when determining grain shapes of particles <50 μm diameter. Image analysis was performed using Definiens Developer V7 (Berry and McMahon, 2008).

5.4 Results

This section first presents GMT classification results from the EH 633 and EH 635 off cut sample set. Next, these results are considered alongside geometallurgical datasets collected by the AMIRA P843 GeM project, to explore how these data can be used for predicting ARD formation.

5.4.1 Mesotextural groups

As samples had been previously grouped by site personnel (based primarily on lithology, with some consideration also given to the alteration style and texture), this system was adhered to in this study however, samples were assigned new group names for clarity (Table 5.5).

A representative sample from each group used in this study is shown in Figure 5.8. Group EH-1 is a matrix supported breccia (Figure 5.8a). Potassium feldspar clasts are hosted in a magnetite-calcite-quartz matrix which contains fine-grained disseminated pyrite and chalcopyrite. These sulphides are dominantly associated with magnetite. This group has been subjected to weak potassic alteration. Group EH-2 has a fine-grained potassium feldspar and magnetite matrix (Figure 5.8b). No clasts are observed, with only few calcite veins present. Some disseminated chalcopyrite and pyrite are present in the matrix in addition to amygdaloids. Group EH-3 comprises of felsic volcanics which have been subjected to strong potassic alteration (Figure 5.8c). Calcite dominates with some magnetite clasts observed, and fine-intermediate grained pyrite and chalcopyrite disseminated in the potassically altered matrix. Group EH-4 is a breccia showing diverse texture with two distinct zones observed (Figure 5.8d). Fine-grained disseminated pyrite and chalcopyrite in a magnetite matrix is seen in one zone, and a similar matrix but with additional calcite and potassium feldspar clasts in the other. Based on these observations, it is anticipated that this group will likely show the most geochemical diversity when subjected to GMT testing depending on which textural zone dominates the analysed samples. Group EH-5 is a crackle-breccia with a calcite matrix, and contained potassium feldspar altered clasts, along the base of which relatively coarse-grained chalcopyrite and pyrite were observed (Figure 5.8e). Two distinct zones were also observed in group EH-6, a breccia with coarse-grained intergrown pyrite-chalcopyrite in a calcite-quartz matrix observed in one zone, and fine-grained disseminated pyrite and chalcopyrite in a magnetite-potassium feldspar altered matrix in the other (Figure 5.8f). As with group EH-4, variable GMT results are anticipated from this group.

Group EH-7 is texturally similar to group EH-1, however, it contains less calcite and a much higher proportion of sulphides which are coarser-grained (Figure 5.8g). In several of these groups (e.g., EH-1, EH-4 and EH-7), pyrite and chalcopyrite are observed in a magnetite matrix. The acid forming potential of magnetite was discussed recently in Moncur et al. (2009), with its oxidation shown in *equation 5.1*.

$$Fe^{2+}Fe^{3+}{}_2O_4 + 0.25O_2 + 4.5H_2O \rightarrow 3Fe(OH)_3 \qquad (5.1)$$

These authors describe that magnetite may be acid forming through the oxidation of Fe^{2+} and hydrolysis of Fe^{3+} (*equations 1.3* and *1.5*), however, it is considered to have a high resistance to oxidation. Therefore, it is here considered in a similar manner to non-Fe sulphides (i.e., not acid forming).

Table 5.5 Group names of lithologies sampled in drill holes EH 633 and EH 635.

EH group name	New name assigned in this study	Sampled in this study?
IV2	EH-1	Yes
AMV	EH-2	Yes
FV	EH-3	Yes
FV2	EH-4	Yes
FV3	EH-5	Yes
FV3/FV2	EH-6	Yes
AMV2	EH-7	Yes
AMV1	EH-8	No
FV1	EH-9	No
VN	EH-10	No
MV	EH-11	No
IV	EH-12	No
IV1	EH-13	No

5.4.2 GMT approach: stage-one

5.4.2.1 Mineralogy

The modal mineralogy of one representative sample per group is shown in Figure 5.9. Calcite and potassium feldspar dominated in groups EH-1 and EH-3, with chalcopyrite dominating the sulphide mineralogy (Figure 5.9a and 5.9c). Potassium feldspar dominated in EH-2, followed by quartz and calcite, with higher chalcopyrite contents measured relative to pyrite (Figure 5.9b). Based on mineralogy, these groups are expected to be non-acid forming, instead offering significant neutralising potential. Group EH-4 has a distinctively different mineralogy to the previous groups, and was dominated by magnetite followed by potassium feldspar and barite (Figure 5.9d). This group contains more sulphides relative to carbonates, so is anticipated to be acid forming. Group EH-5 is likely strongly neutralising, as it contained ~73 wt. % calcite (Figure 5.9e). Similar to group EH-4, EH-6 was dominated by magnetite, which was closely followed by quartz and potassium feldspar (Figure 5.9f). Potassium feldspar also dominated in group EH-7, followed by magnetite, with pyrite the dominate sulphide (Figure 5.9g). The carbonate:sulphide ratio for these samples is shown in Figure 5.10 with groups EH-4, EH-6 and EH-7 classified as acid forming.

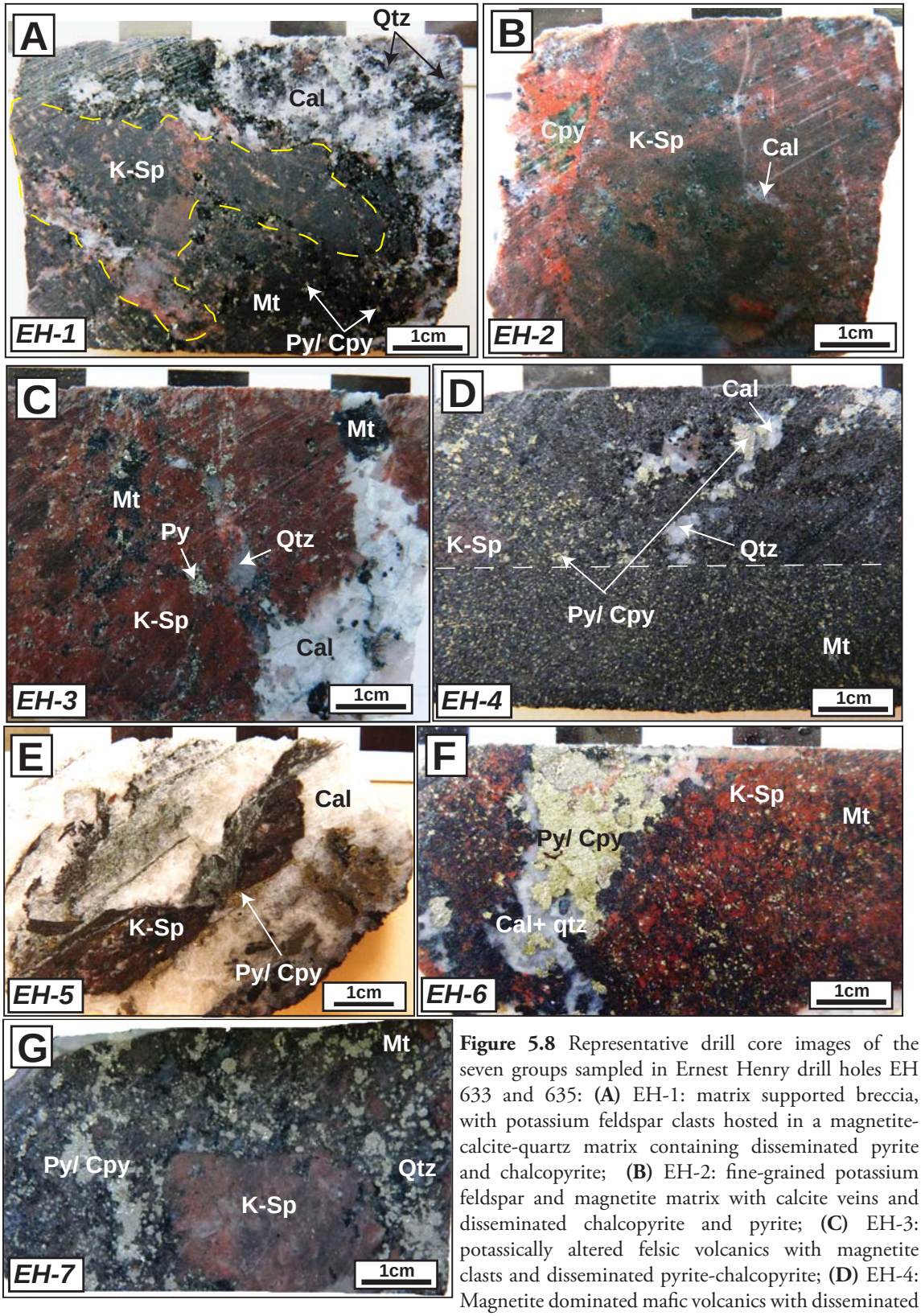

Figure 5.8 Representative drill core images of the seven groups sampled in Ernest Henry drill holes EH 633 and 635: **(A)** EH-1: matrix supported breccia, with potassium feldspar clasts hosted in a magnetite-calcite-quartz matrix containing disseminated pyrite and chalcopyrite; **(B)** EH-2: fine-grained potassium feldspar and magnetite matrix with calcite veins and disseminated chalcopyrite and pyrite; **(C)** EH-3: potassically altered felsic volcanics with magnetite clasts and disseminated pyrite-chalcopyrite; **(D)** EH-4: Magnetite dominated mafic volcanics with disseminated pyrite and chalcopyrite and occasional calcite and potassium feldspar clots; **(E)** EH-5: Crackle-breccia, calcite dominated matrix with potassium feldspar altered clasts and coarse clast-aligned chalcopyrite-pyrite clots; **(F)** EH-6: Potassium feldspar-magnetite dominated volcanics with coarse pyrite and chalcopyrite in carbonate veins; **(G)** EH-7: matrix supported breccia, with potassium feldspar clasts hosted in a magnetite-calcite-quartz matrix containing coarse pyrite and chalcopyrite. Abbreviations: Cal, calcite; Cpy, chalcopyrite; K-Sp, K-feldspar; Mt, magnetite; Py, pyrite; Qtz, quartz.

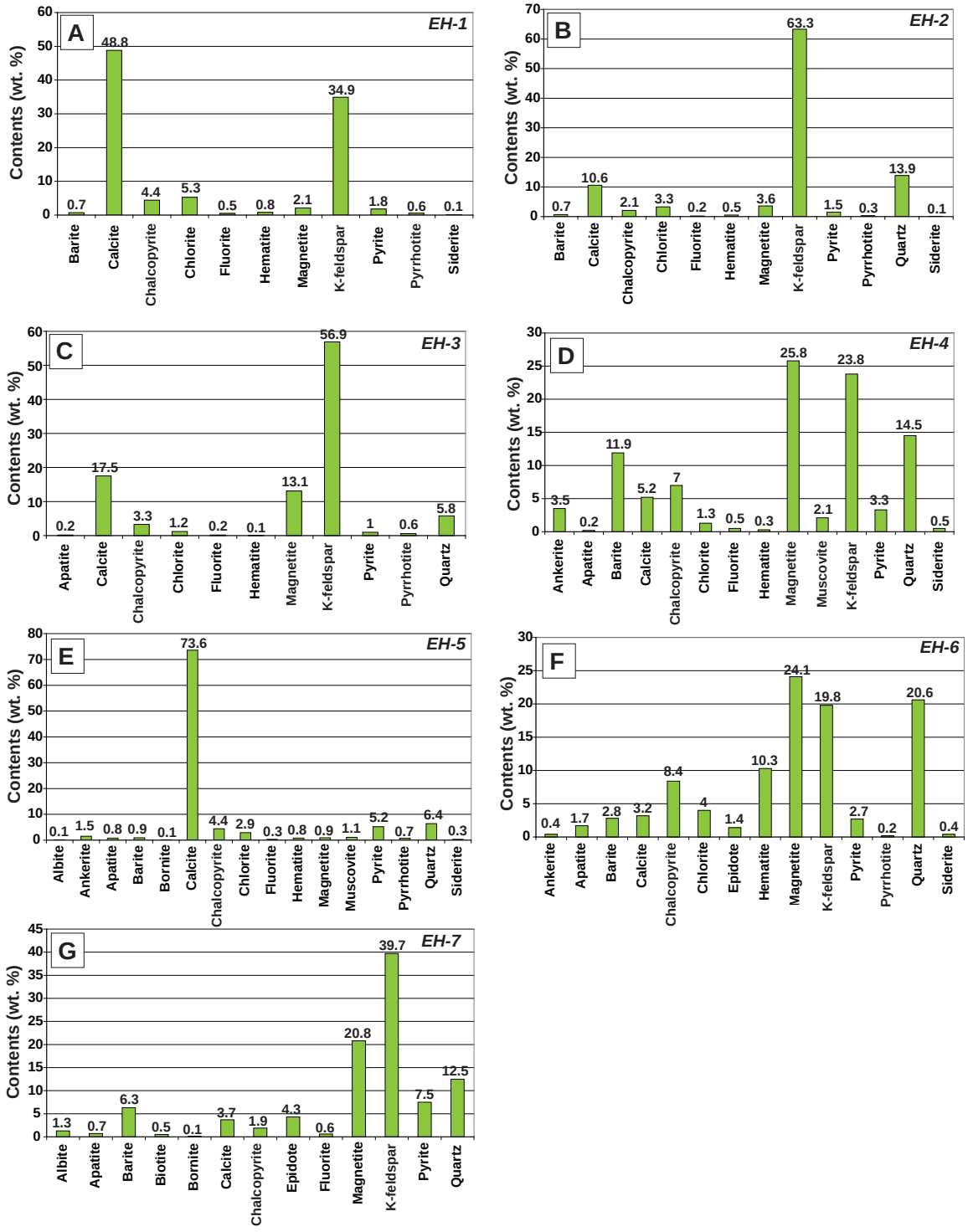

Figure 5.9 Quantitative modal mineralogy of one sample from each Ernest Henry group (A to G corresponding to groups EH-1 to EH-7, respectively) identified in EH 633 and EH 635 as determined using Quantitative X-Ray diffractometry (QXRD).

5.4.2.2 Geochemical characterisation

Values from paste pH and rinse pH testing on samples from EH 633 and EH 635 are presented in Figures 5.11. For each sample, the paste pH value was greater by at least one pH unit relative to the rinse pH measured from the intact sample (> 2 cm^2). This is due to the reduction in particle size (i.e., from an intact piece to <75 µm) increasing the surface area of primary neutralising minerals, thus increasing their reactivity (Weber et al., 2006). For EH 633, the overall pH ranges were pH 5.9 to 6.6 for intact samples and pH 7.5 to 8.5 for pulverised samples. For EH 635, the ranges were similar, with pH 6.6 to 7.1 measured for intact samples, and pH 7.1 to 8.2 for the pulverised fraction. Overall, these ranges suggest that all samples are currently weakly-moderately neutralising. For groups EH-4 and EH-6, this contradicts the mineralogical classification shown in Figure 5.10.

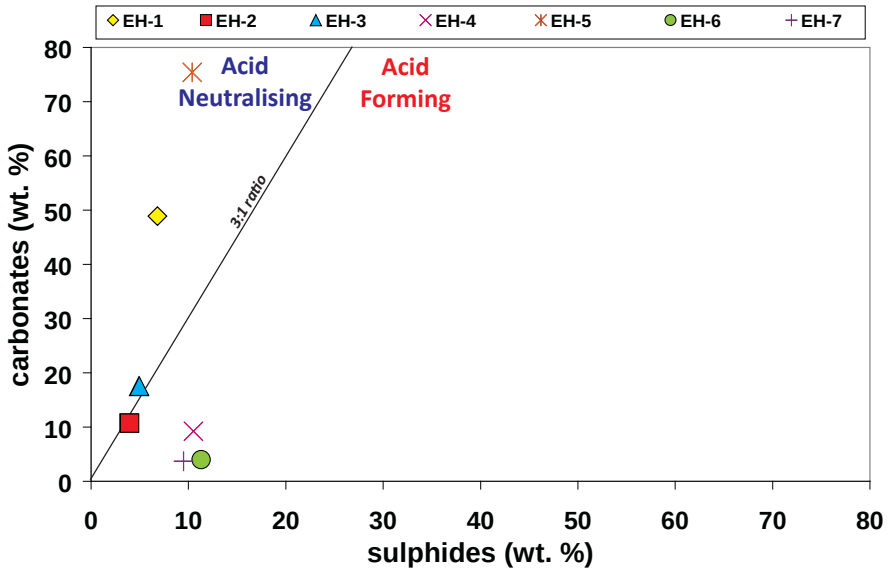

Figure 5.10 Acid forming potential classification based on carbonate: and sulphide values (wt. %) for one sample from each Ernest Henry group (EH-1 to EH-7) identified in drill holes EH 633 and EH 635 as determined by Quantitative X-Ray diffractometry..

As some barite was identified in these samples, $S_{Sulphide}$ was calculated and used instead of S_{Total}. These values were plotted against paste pH values as shown in Figure 5.12. No systematic trends relating to lithology, mineralogy or alteration style were observed. By this classification, all samples with the exception of three are classified as PAF.

Based on the relatively high calcite content of these samples, it was decided that the 0 to 10 ARDI field should be assigned as indicating a potential neutralising capacity (PNC). Average ARDI values for each group are shown in Table 5.6. ARDI values for groups EH-1, EH-2, EH-3 and EH-5 were below 10 therefore classifying these having PNC. This indicated that despite containing both pyrite and chalcopyrite they were either in direct mineralogical association with, or in proximity to calcite, thus a classification of PAF was not assigned. A broader range of ARDI values was calculated for samples in groups EH-4, EH-6 and EH-7, with one from each group identified as acid forming (AF; ARDI= >30/50). Such a range was anticipated for EH-4 and EH-6 following the identification of textural variation within these groups (as shown in Figure 5.8).

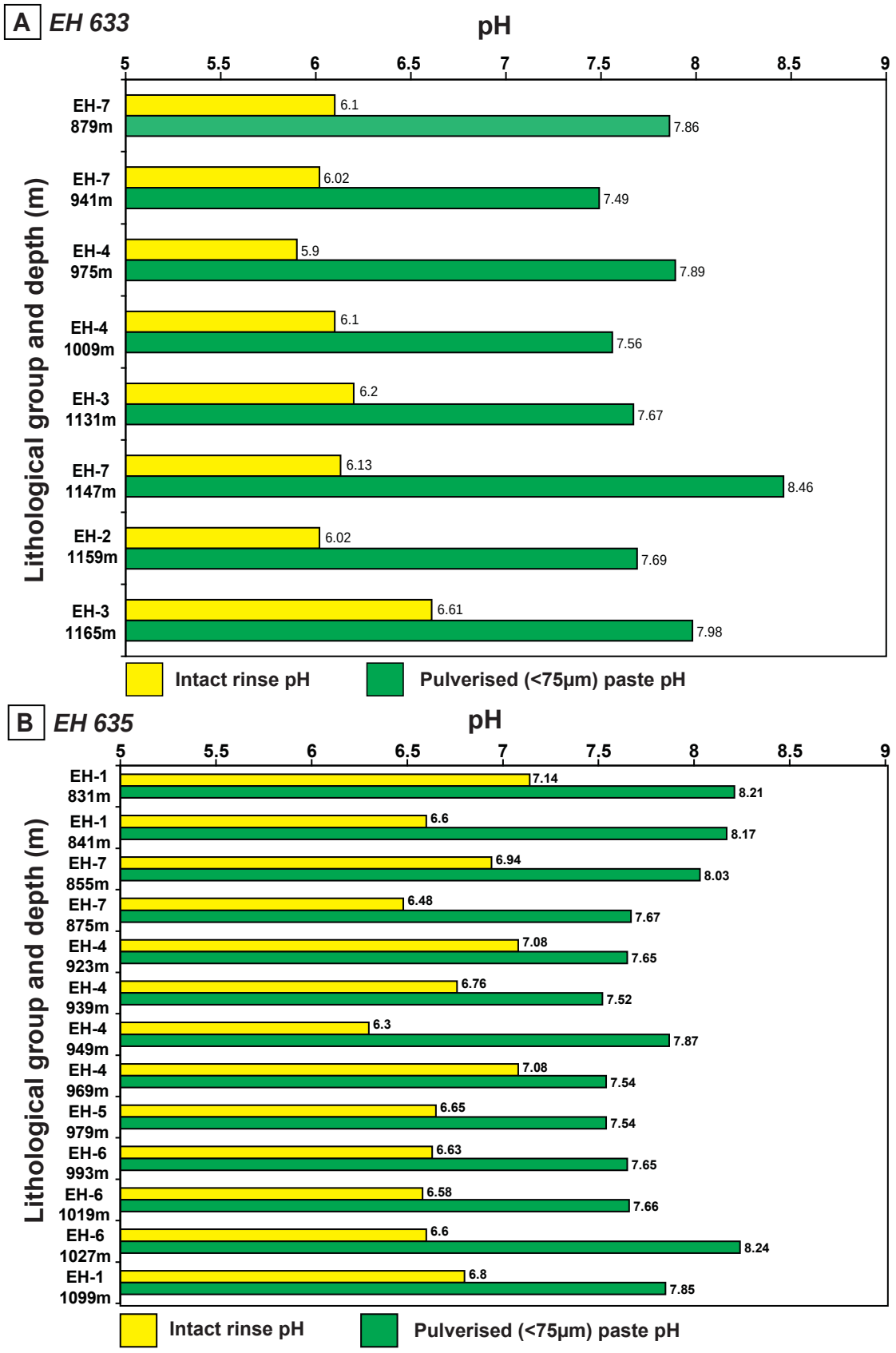

Figure 5.11 Pulverised (<75 µm) paste pH and intact (>2 cm^2) rinse pH values for Ernest Henry drill holes: **(A)** EH 633; and **(B)** EH 635.

Table 5.6 Acid rock drainage index (ARDI) values and classifications for Ernest Henry drill core samples (EH 633 and EH 635) as grouped primarily by lithology (EH-1 to EH-7). ARDI values were calculated for each sample, with an average value for each group shown. Abbreviations: NAF, non-acid forming; PNC, potential neutralising capacity, NAF.

Group	Average ARDI Value (/50)	Classification
EH-1	3	PNC
EH-2	9	PNC
EH-3	6	PNC
EH-4	11	NAF
EH-5	8	PNC
EH-6	15	NAF
EH-7	16	NAF

Cross-checks were made between paste pH, $S_{Sulphide}$ and ARDI values. Paste pH plotted against ARDI values showed all samples from groups EH-1, EH-2, EH-3 and EH-5 as having a PNC (Figure 5.12). Despite relatively high paste pH values, one sample each from EH-4, EH-6 and EH-7 was identified as AF as a result of their high ARDI values. Similar classifications were returned when comparing $S_{Sulphide}$ against ARDI values (Figure 5.13). If paste pH and $S_{Sulphide}$ values are plotted against each other, then the majority of samples are classified as PAF (Figure 5.14). This conflicts with the classifications assigned in Figures 5.12 and 5.13. The paste pH test appears to be strongly influenced by the reactivity of the carbonates, as discussed in Weber et al. (2006). Thus, these results classify samples as either NAF or having a PNC (Figure 5.12 and 5.13). Despite this, the $S_{Sulphide}$ content for the majority of samples is greater than the cut-off criterion (>0.3 wt. %) explaining the assigned PAF classifications. These results prove the need for a third discriminator to critique classifications made using these conventional data ($S_{Sulphide}$ and paste pH). By evaluating texture through using the ARDI a reasonable critique of acid forming potential is given thus identifying it as the required discriminator.

Concentrations of metals (Cd, Co, Ni, Pb and Zn) and metalloids (As, Sb) plotted against paste pH values are shown in Figures 5.15 and 5.16, respectively. The majority of samples contained >1000 ppm metals reflecting the presence of chalcopyrite (i.e., source of Cu; ~5,600- 183,000 ppm). Additionally, Co was high (~250-625 ppm) and was sourced from pyrite. Base metal (i.e., Cd, Pb, Zn) contents were low, reflecting the general absence of galena and sphalerite. Samples from group EH-2 were identified as the lowest risk, correlating to the low sulphide contents of this group. All other samples pose an intermediate risk. The majority of samples were considered low risk in terms of metalloid contents, with several from EH-1 and EH-4 falling in the extreme risk field, largely as a conservative criterion (based on WHO, 2006 driking water guideline values) has been used.

5.4.2.3 Stage-one classification

A summary of stage-one classifications is presented in Table 5.7. No group returned a consistent stage-one classification. The main conflict arose from the paste pH versus $S_{Sulphide}$ classification identifying the majority of groups as PAF, whilst other pre-screening methods contradicted this.

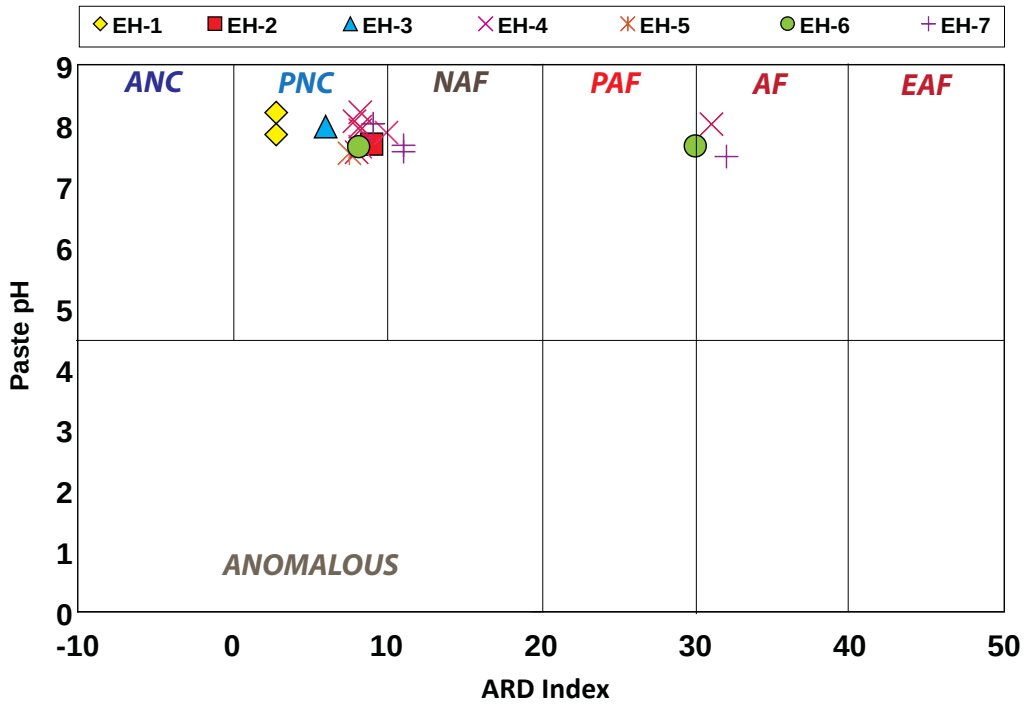

Figure 5.12 Acid rock drainage index (ARDI) versus paste pH values for samples obtained from Ernest Henry drill holes EH 633 and EH 635 (shown in groups: EH-1 to EH-7). Abbreviations: ANC, acid neutralising capacity; AF, acid forming; EAF, extremely acid forming; NAF, non-acid forming; PAF, potentially acid forming.

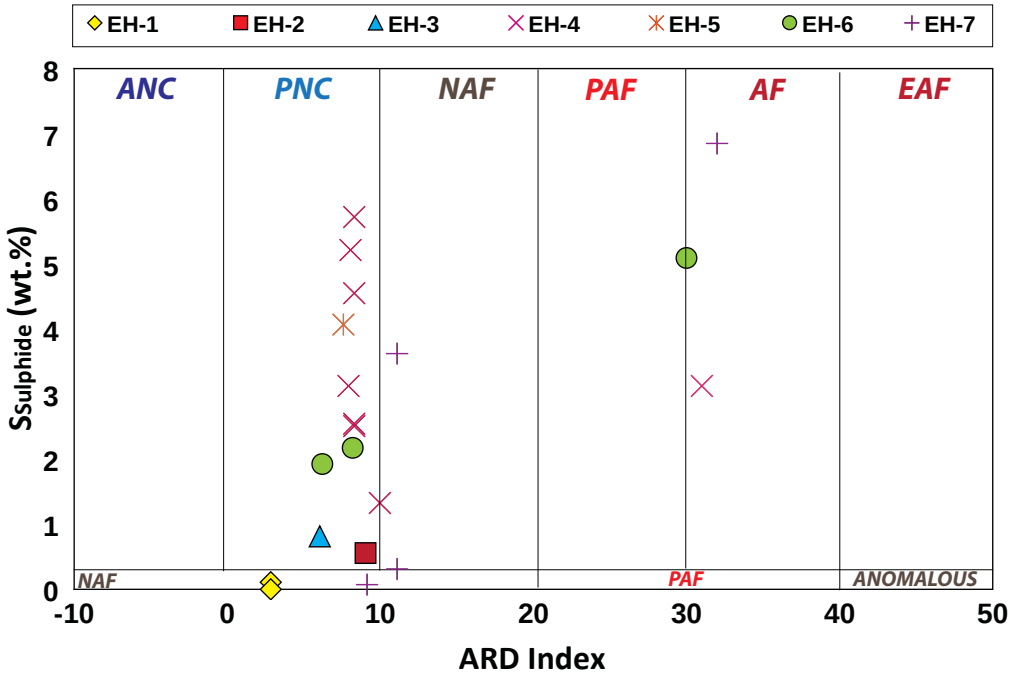

Figure 5.13 Acid rock drainage index (ARDI) versus $S_{Sulphide}$ (wt. %) values for samples obtained from Ernest Henry drill holes EH 633 and EH 635 (shown in groups: EH-1 to EH-7). Abbreviations: ANC, acid neutralising capacity; AF, acid forming; EAF, extremely acid forming; NAF, non-acid forming; PAF, potentially acid forming.

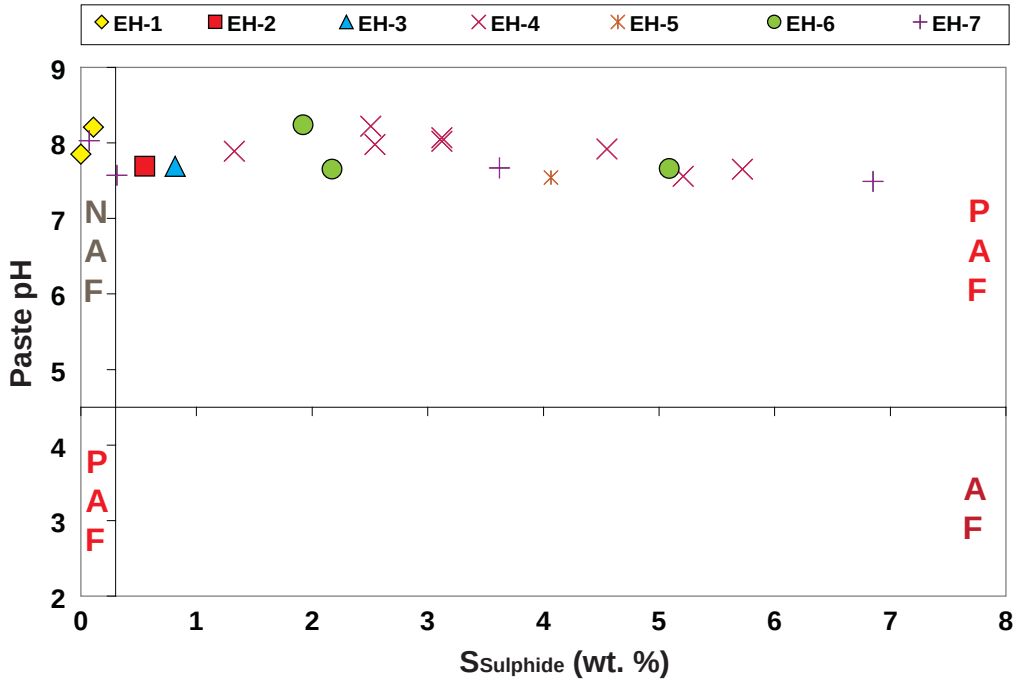

Figure 5.14 Paste pH versus $S_{Sulphide}$ (wt. %) values for samples obtained from Ernest Henry drill holes EH 633 and EH 635 (shown in groups: EH-1 to EH-7). Abbreviations: AF, acid forming; NAF, non-acid forming; PAF, potentially acid forming.

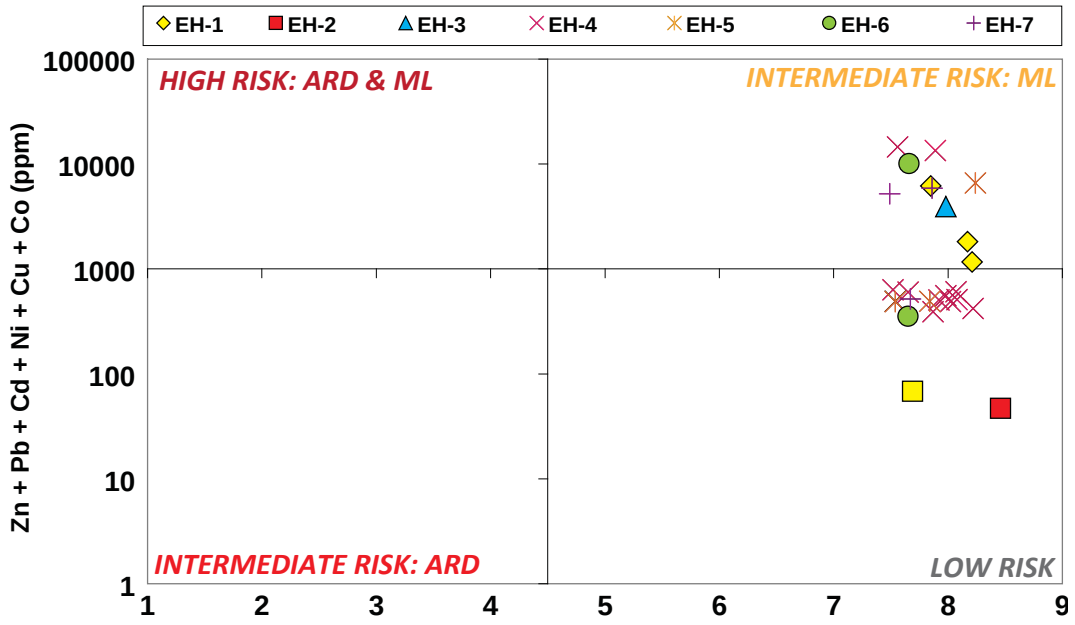

Figure 5.15 Metal contents versus paste pH values for samples obtained from Ernest Henry drill holes EH 633 and EH 635 (shown in groups: EH-1 to EH-7). Abbreviations: ARD, acid rock drainage; ML, metal leaching.

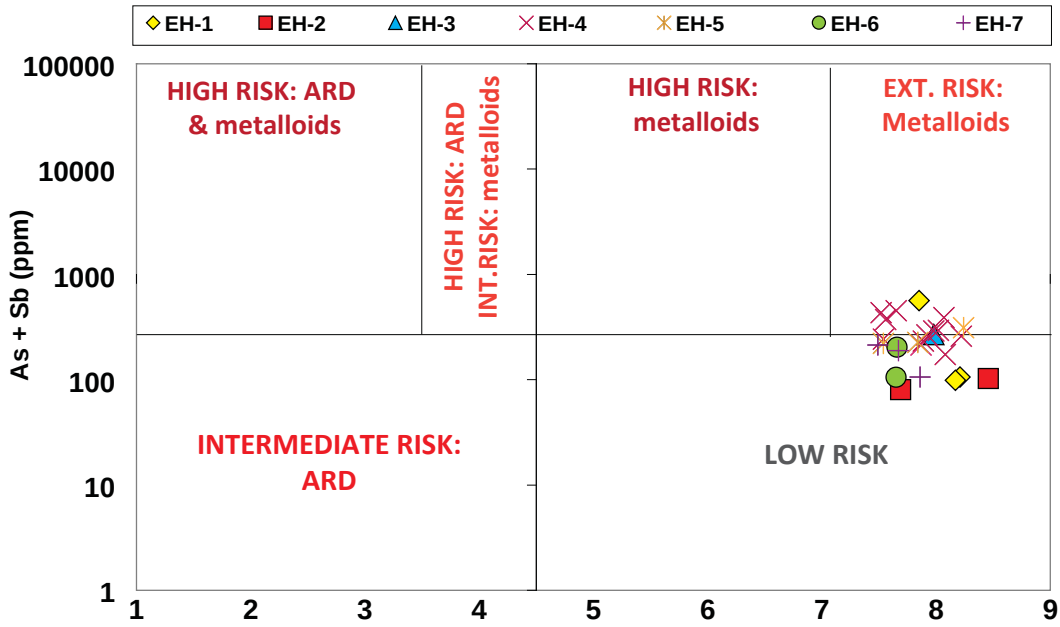

Figure 5.16 Metalloid contents versus paste pH values for samples obtained from Ernest Henry drill holes EH 633 and EH 635 (shown in groups: EH-1 to EH-7). Abbreviations: ARD, acid rock drainage.

This is reasoned by the fact that using $S_{Sulphide}$ as an ARD assessment parameter is highly conservative, and is used most efficiently to discriminate NAF/inert samples. Overall, groups EH-1, EH-2, EH-3 and EH-5 were classified as PNC, however, calcite values indicated that groups EH-1 and EH-5 are more likely to have significant ANC. Additionally, conflicting classifications (i.e., PAF, NAF and PNC) arose for groups EH-4, EH-6 and EH-7, which was anticipated following evaluation of their intact textures. These results indicated that stage-two testing was required for all groups.

5.4.3 GMT approach: stage-two

5.4.3.1 Static geochemical tests

A comparison of ANC versus MPA values (Figure 5.17) indicated that the majority of samples in group EH-4 had higher MPA than ANC values, and were therefore PAF (with positive NAPP values calculated). Groups EH-1 and EH-5 had significant neutralising capacity. NAPP values were next plotted against NAG pH (Figure 5.18) which allowed for one sample from groups EH-4, EH-6 and EH-7 to be identified as PAF, and several from these groups as uncertain. All other groups were NAF. A comparison of NAPP against NAG values showed the same three samples as PAF, with NAG values between 24-74 kg H_2SO_4/t measured (Figure 5.19). Whilst these samples are PAF, a comparison of NAG pH and paste pH values indicated these are low-risk samples with a lag-time to acid generation predicted (Figure 5.20).

5.4.3.2 Stage-two classification

A classification summary for this stage is shown in Table 5.8, and confirmed that groups EH-1 and EH-5 are likely to have significant neutralising capacity. Based on this, samples underwent stage-three ABCC testing, with an assessment of the modal mineralogy having indicated the presence of several carbonates (i.e., calcite, ankerite, siderite). Therefore, it was necessary to determine the effective ANC. Classification discrepancies were again identified for groups EH-4, EH-6 and EH-7, with samples identified as UC, NAF and PAF.

Table 5.7 Stage-one classification summary table for Ernest Henry drill core samples from EH 633 and EH 635 shown in groups EH-1to EH-7 (n=30). Abbreviations: ANC, acid neutralising capacity; Int, intermediate; NAF, non-acid forming; PAF, potentially acid forming.

Group	Paste pH vs. $S_{Sulphide}$	ARDI vs. $S_{Sulphide}$	ARDI vs. paste pH	Carbonate vs. Sulphide	Metals vs. paste pH	Metalloids vs. paste pH	Stage-one classification	Stage-two testing required?
EH-1	NAF	PNC	PNC	NAF	Int. risk	Low and extreme risk	PNC	Yes
EH-2	PAF	PNC	PNC	NAF	Low risk	Low risk	PNC	Yes
EH-3	PAF	PNC	PNC	NAF	Int. risk	Low risk	PNC	Yes
EH-4	PAF	PNC &AF	PNC & AF	PAF	Int. risk	Low and extreme risk	AF & NAF	Yes
EH-5	PAF	PNC	PNC	NAF	Int. risk	Low risk	PNC	Yes
EH-6	PAF	PNC &AF	PNC & AF	PAF	Int. risk	Low risk	PAF & NAF	Yes
EH-7	PAF & NAF	PNC, NAF & AF	NAF & AF	PAF	Int. risk	Low risk	AF & NAF	Yes

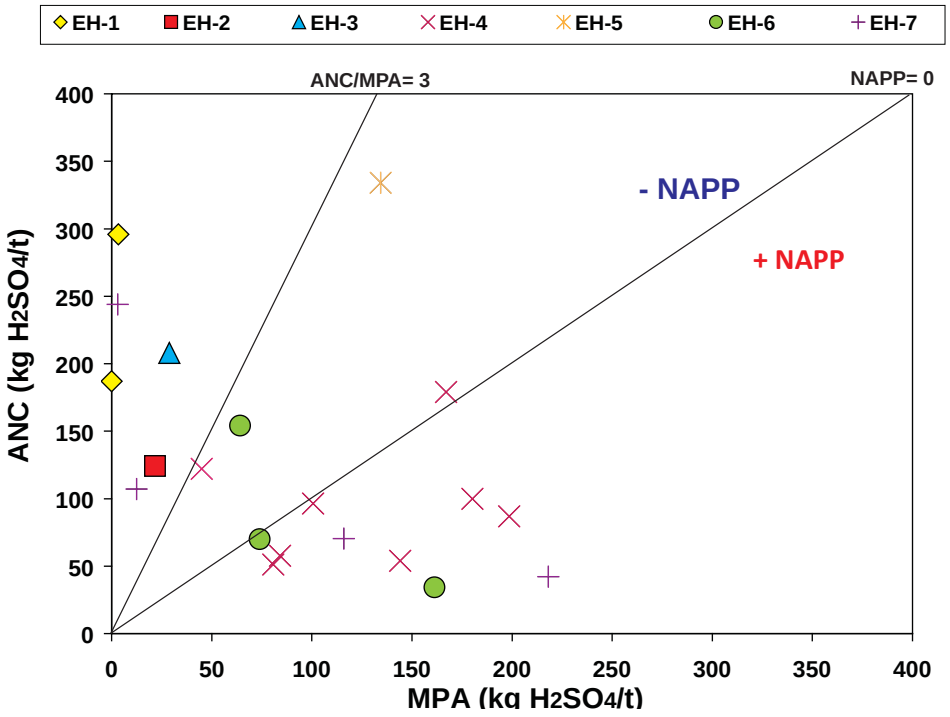

Figure 5.17 Classification of ARD potential based on ANC versus MPA for samples obtained from Ernest Henry drill holes EH 633 and EH 635 (shown in groups: EH-1 to EH-7). Abbreviations: ANC, acid neutralising capacity; MPA, maximum potential acidity; NAPP, net acid producing potential.

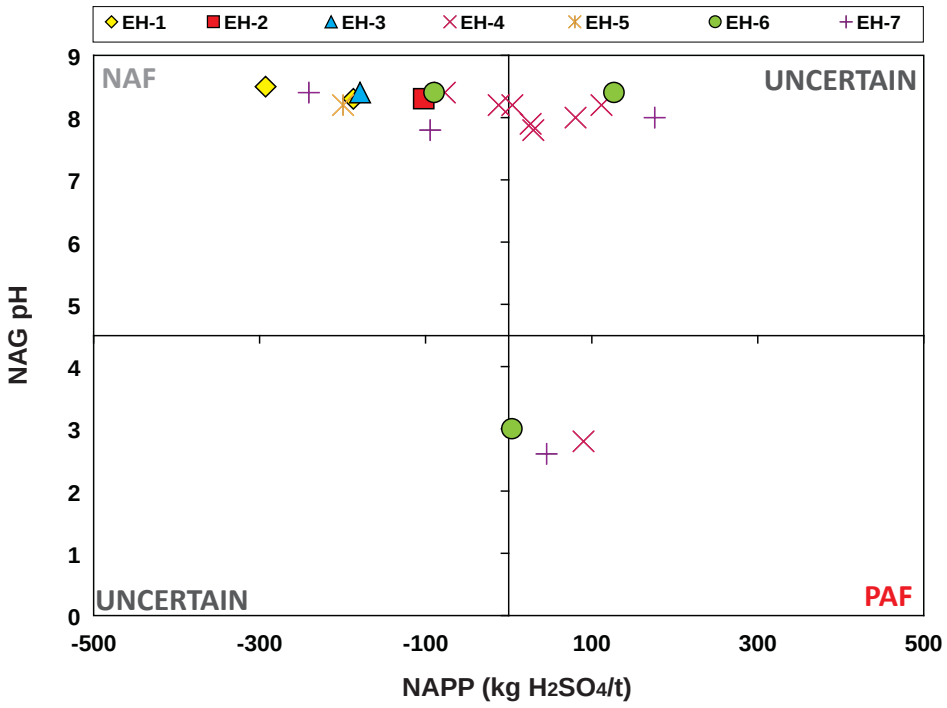

Figure 5.18 Classification of ARD potential for samples obtained from Ernest Henry drill holes EH 633 and EH 635 (shown in groups: EH-1 to EH-7) based on NAPP and NAG pH values. Abbreviations: PAF, potentially acid forming; NAF, non-acid forming; UC, uncertain.

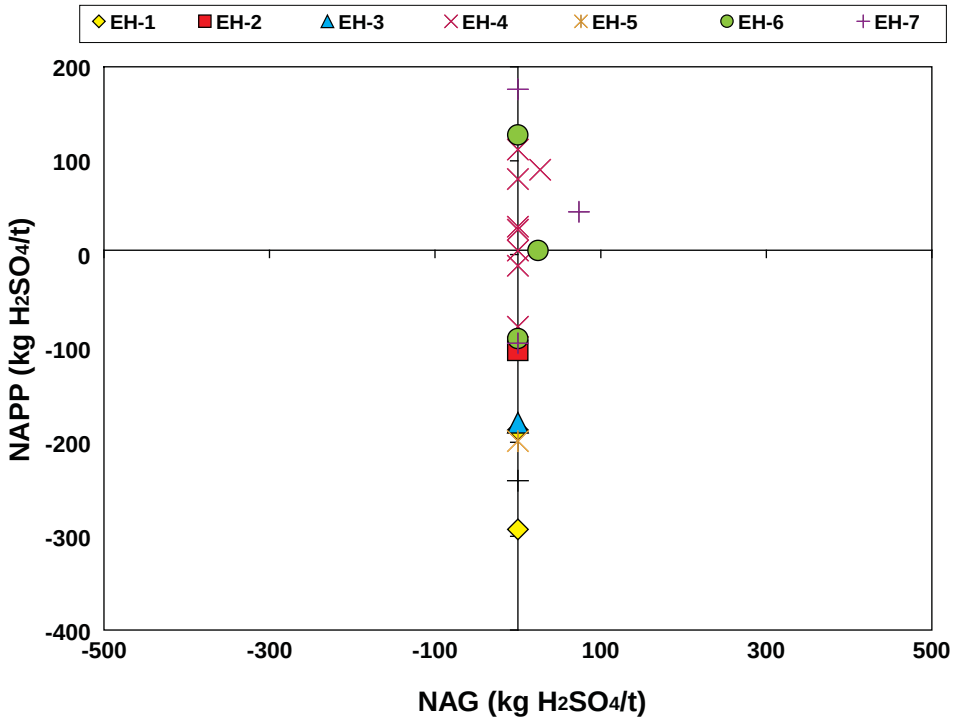

Figure 5.19 NAPP versus NAG pH (to 7.0) values (kg H_2SO_4/t) for samples obtained from Ernest Henry drill holes EH 633 and EH 635 (shown in groups: EH-1 to EH-7).

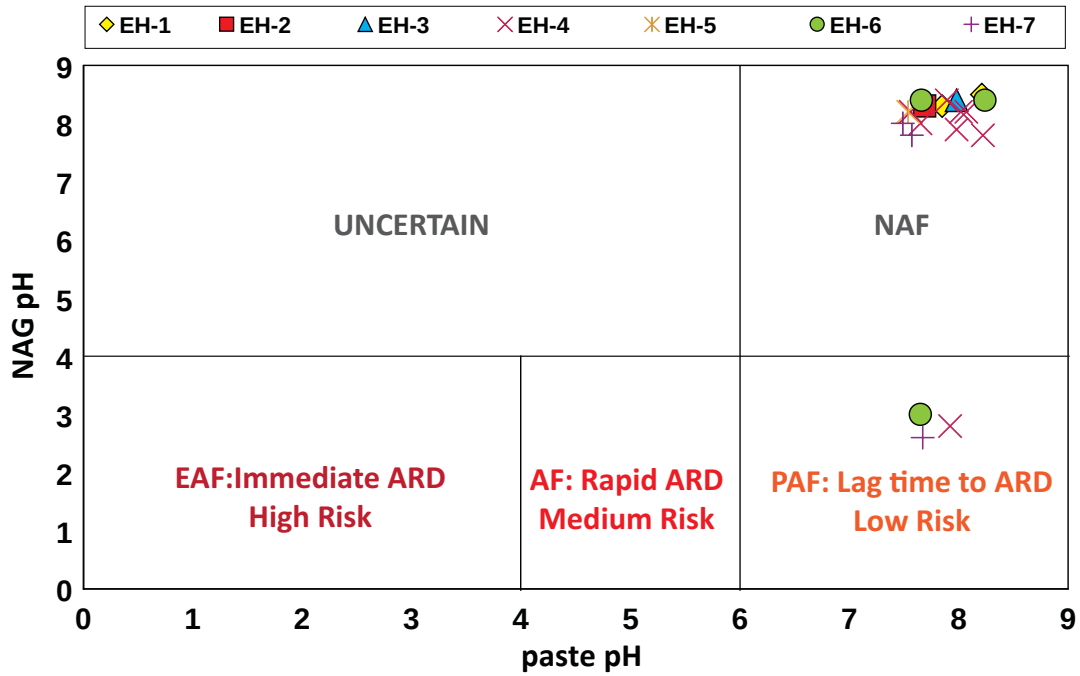

Figure 5.20 Classification of lag-time to ARD formation and risk classification based on paste pH and NAG pH values obtained from Ernest Henry drill holes EH 633 and EH 635 (shown in groups: EH-1 to EH-7). Abbreviations: AF, acid forming; EAF, extremely acid forming; NAF, non-acid forming; PAF, potentially acid forming.

Table 5.8 Stage-two classification summary table for samples obtained from Ernest Henry drill holes EH 633 and EH 635 (shown in groups: EH-1 to EH-7; n=16). Abbreviations: NAF, non-acid forming; PAF, potentially acid forming; ANC, acid neutralising capacity; UC, uncertain.

Group	NAPP vs. NAG pH	NAG pH vs. Paste pH	ANC vs. MPA	Summary	Stage-one agreement?	Stage-three testing?
EH-1	NAF	NAF	ANC	ANC	Yes	Yes: ANC
EH-2	NAF	NAF	NAF	NAF	Yes	No
EH-3	NAF	NAF	NAF	NAF	Yes	No
EH-4	NAF, UC & PAF	NAF & PAF	NAF & PAF	NAF & PAF	Yes	Yes: NAG tests
EH-5	NAF	NAF	ANC	ANC	Yes	Yes: ANC
EH-6	NAF, UC & PAF	NAF & PAF	NAF & PAF	NAF & PAF	Yes	Yes: NAG tests
EH-7	NAF, UC & PAF	NAF & PAF	NAF & PAF	NAF & PAF	Yes	Yes: NAG tests

This implies that the sample grouping system developed by the mine operator and used here is not appropriate for undertaking the GMT approach. This is a direct result of the significant variation in mineralogy and texture on a very fine scale (i.e., cm), as indicated particularly by groups EH-4 and EH-6. Despite the errors introduced by using the established grouping system, samples from EH-4, EH-6

and EH-7 underwent stage-three advanced NAG geochemical testing to more accurately determine maximum acid forming potential. Groups EH-1 and EH-5 were further characterised using ABCC tests to define the effective ANC. As the metal/metalloid contents were relatively low for these samples (with the exception of Cu in chalcopyrite, and Co in pyrite), no LA-ICP-MS element mapping was undertaken.

5.4.4 GMT approach: stage-three

5.4.4.1 Advanced NAG testing

The mNAG test was proven accurate and the most efficient in terms of cost and time from all the available NAG tests in Section 3.4.4.1. Thus, mNAG tests were performed on samples from all groups (n=16) except EH-1. In this study, mNAG pH values were generally lower than single addition NAG values, except for three outlier samples from EH-4, EH-6 and EH-7 which returned very similar results for both tests (Figure 5.21). These results suggest that overall, the single addition NAG test underestimated acid forming capacity by <1.5pH units. Despite this, using mNAG pH values instead of NAG pH does not alter the classifications of these samples. As mNAG pH values >7 were measured, the amount of acidity potentially formed could only be calculated for the three outliers, with results compared to NAG and NAPP values (Table 5.9). No consistent trend was observed, with the mNAG test returning the highest value for EH-6, the single addition NAG test for EH-7, and NAPP for EH-4. Based on the small sample set, it was not possible to identify which method was the least accurate. Given the range of values calculated by these methods, net-acidity from highly acid forming samples at this site should be based on an average value of these tests.

Table 5.9 Single addition NAG, multi-addition NAG and NAPP values (kg H_2SO_4/t) calcuated for three EH drill core off cut samples (from drill hole EH 635).

Sample ID	NAG	mNAG	NAPP
EH-4	27	74	25
EH-6	85	40	-3
EH-7	52	48	51

Kinetic NAG test results from two group EH-4 samples and one sample each from groups EH-6 and EH-7 are presented in Figure 5.22. The pH values remained above 7 for the duration of the test, indicating a lag-time to acid formation. The temperature profile from samples shown in Figure 5.23b and 5.23d indicated that sulphide oxidation was occurring, but the generated acidity had likely been directly buffered by calcite. Once all the calcite has been consumed, these will be net acid forming. The EH-6 sample is the least acid forming, with a low maximum temperature measured (33°C), and the measured pH remaining constant.

5.4.4.2 Acid buffering characterisation curve (ABCC) testing

As samples from each group were identified as having acid neutralising capacity, ABCC tests were undertaken on one sample from each group (with the exception of group EH-3 due to limited sample material; Figure 5.23). These curves were compared against the standard curves presented in Stewart et

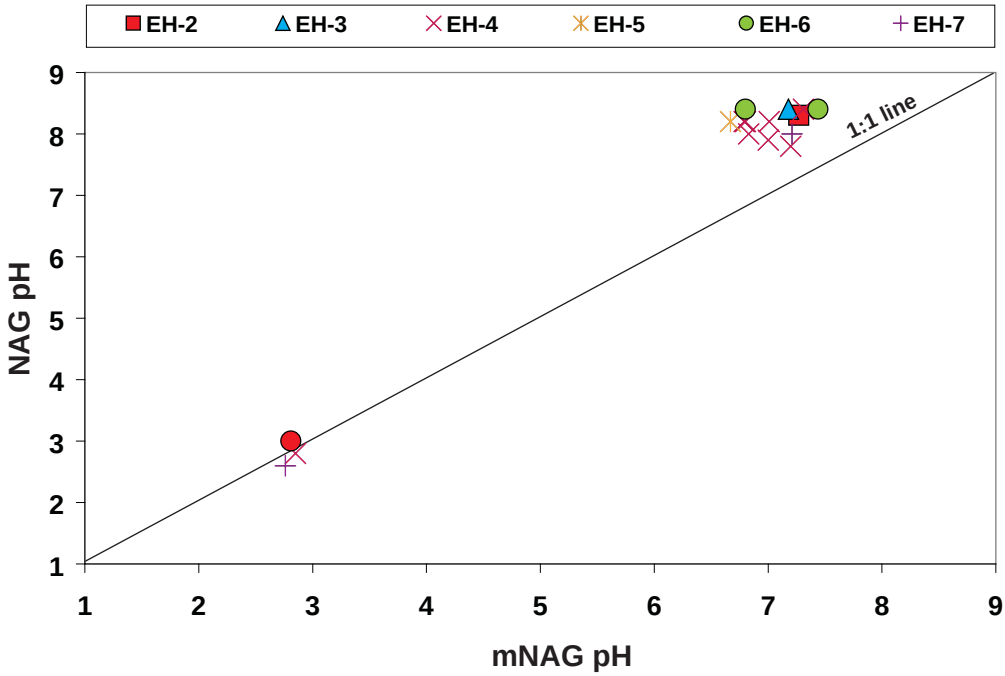

Figure 5.21 Comparison of single addition NAG pH values against multiple addition NAG pH values for samples obtained from Ernest Henry drill holes EH 633 and EH 635 (shown in groups: EH-2 to EH-7).

al. (2006). This test confirmed that EH-1 and EH-5 are the most effective neutralisers (Figure 5.23a and 5.23d), with neutralising capacities greater than those calculated by the Sobek ANC method (~350 kg H_2SO_4/t and 680 kg H_2SO_4/t respectively). A comparison of these curves against the published standards (Stewart et al., 2006) suggested that ANC largely originates from calcite, and possibly (ferroan) dolomite too as the curves gently decline over a lower pH range than as shown for calcite. Dolomite was not identified in samples analysed by QXRD and may not have been effectively differentiated from calcite during initial mesotextural evaluations (as only cold HCl was used to identify carbonates). Despite this, dolomite is an effective neutraliser (Jambor et al., 2002; Stewart et al., 2006), so both groups should be considered effective neutralisers.

The Sobek ANC values calculated for groups EH-2 and EH-4 were in agreement with ABCC results with the pH values dropping to 4 around the Sobek ANC values (Figure 5.23b and 5.23c). Again the shape of the curves were similar to that for calcite (Stewart et al., 2006), but over a slightly lower range (much like that seen for groups EH-1 and EH-5), suggesting once again the presence and contribution of relatively minor (ferroan) dolomite. Overall these groups offer effective neutralisation. ANC was overestimated by the Sobek ANC method in EH-6 and EH-7 (i.e., pH 4 was measured before reaching Sobek ANC values; Figure 5.23e and 5.23f). Whilst the EH-6 curve closely resembled calcite, overall is considered to be the least effective neutraliser of the groups analysed. The carbonates in group EH-7 appear to also be dominated by calcite, indicating that overall, the Sobek values accurately estimate neutralising potential.

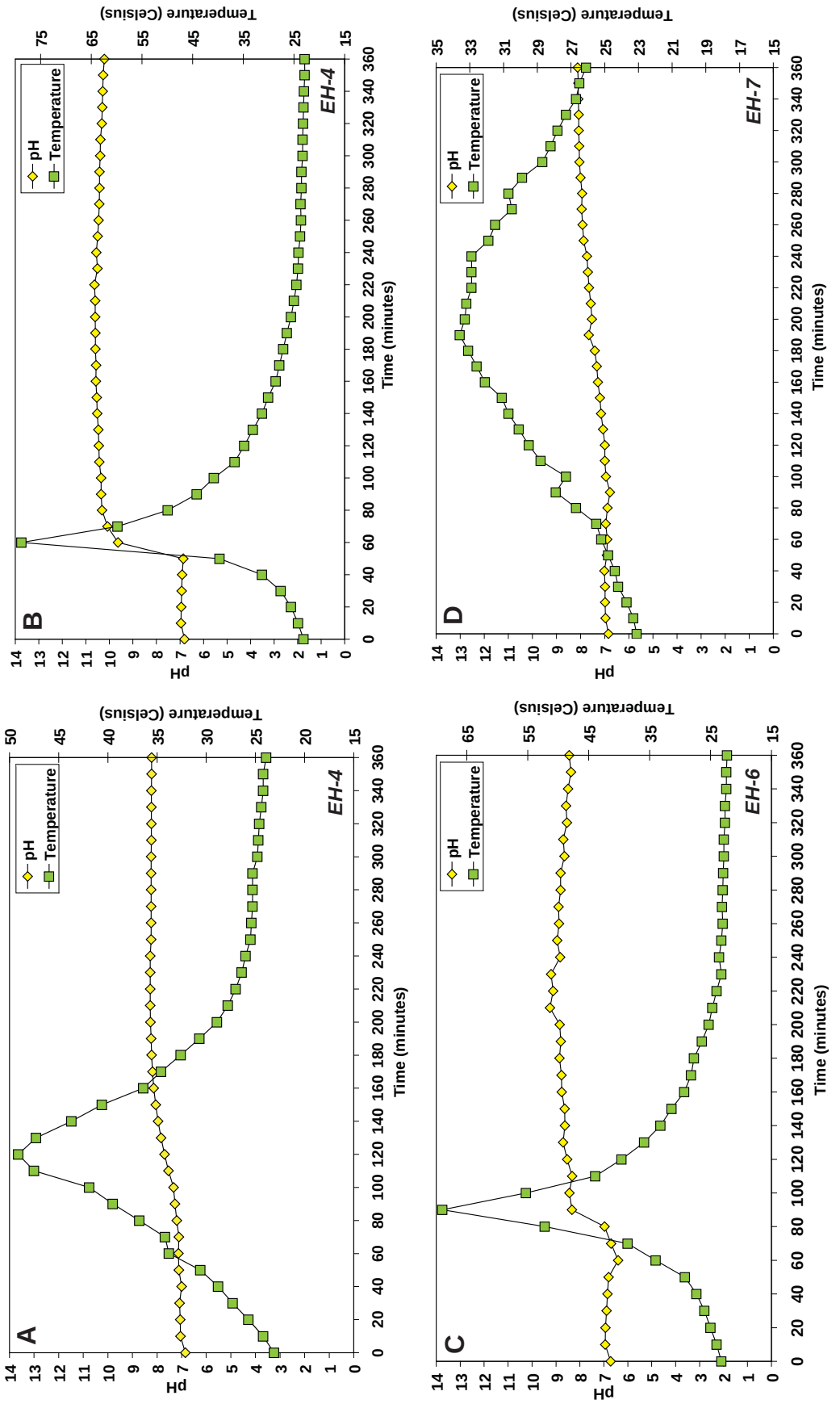

Figure 5.22 Kinetic NAG results for Ernest Henry samples: **(A)** and **(B)** Group EH-4; **(C)** Group EH-6; **(D)** EH-7.

Overall, these results confirm that NAPP values based on Sobek ANC values at stage-two are likely accurate for all groups except EH-6, EH-7 and EH-3 (as these were not tested). NAPP values for groups EH-6 and EH-7 should have been higher, and may have altered the classification of some uncertain samples to PAF. Siderite was identified in minor quantities (<1 wt. %) in several groups (Figure 5.9), however, siderite was not detected in these curves, with the presence of (ferroan) dolomite inferred instead. Thus, the carbonate mineralogy of these samples is more complicated than as inferred by mesotextural evaluations and QXRD results. Therefore, at a deposit such as Ernest Henry, the carbonate mineralogy must be better understood in order to critique geochemical results and refine ARD assessments. Comparison to ABCC values is complicated and costly; therefore an alternative method should be sought.

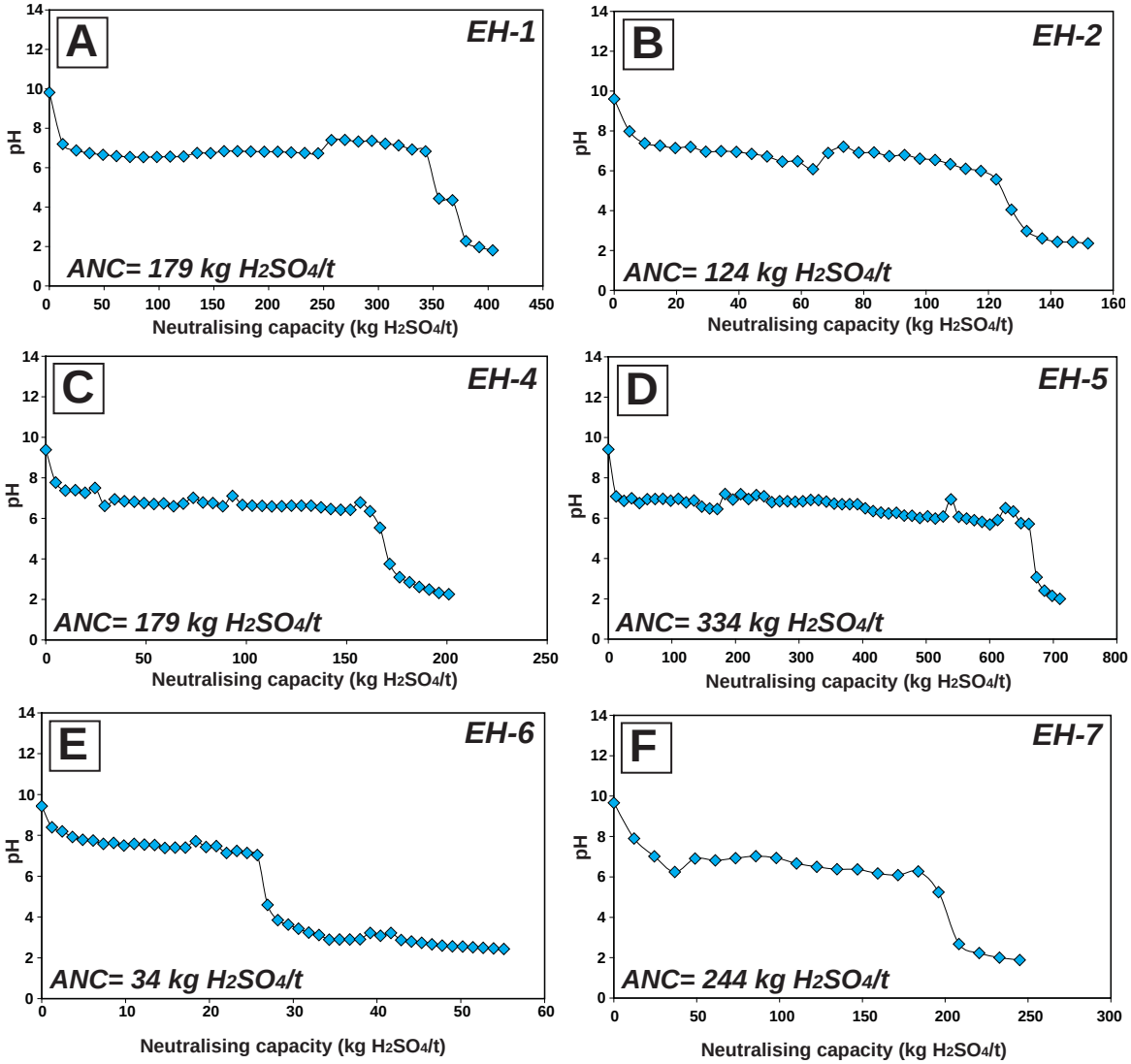

Figure 5.23 Kinetic NAG results for Ernest Henry samples: **(A)** EH-1; **(B)** EH-2; **(C)** EH-4; **(D)** EH-5; **(E)** EH-6; and **(F)** EH-7.

5.4.4.3 Mineralogical and textural analyses

Textural analyses of samples using MLA were undertaken on samples from groups EH-1, EH-3, EH-4, EH-5 and EH-7. The aims were to measure the intact modal mineralogy for comparison with QXRD values, and to evaluate the potential of establishing ARDI values on images generated by the MLA using the GXMAP technique (described in Section 2.6.3).

A greater suite of minerals was identified by the XMOD analysis than QXRD as indicated in Figure 5.24. Agreement between both methods was strong (i.e., within 10%) for groups EH-1, EH-3 and EH-5. In group EH-2, potassium feldspar values were quite different (Figure 5.24b), however, hyalophane $(K,Ba)[Al(Si,Al)Si_2O_8]$ contents of 48 wt. % were reported by XMOD. It is likely that QXRD has identified hyalophane as potassium feldspar (due to the similarity of the spectra), thus by summing both values, the same result as XMOD (63 wt. %) was calculated. In group EH-4, pyrite contents varied significantly between both methods, showing that within just one sample from this group there is high mineralogical variability (Figure 5.24d). Thus, the spread of classifications (i.e., NAF, UC and PAF) assigned to this group at stage-one and stage-two are explained. Both methods confirmed that magnetite, potassium feldspar and quartz dominated the mineralogy of EH-6; however, the relative proportions of these minerals varied (Figure 5.24f), and XMOD reported higher pyrite contents than QXRD. Similarly, for EH-7, the proportions of magnetite, potassium feldspar and quartz varied between both methods, but overall these minerals dominated, with the measured contents of sulphides in closer agreement (Figure 5.24g).

The carbonate: sulphide ratio calculated from XMOD values is shown alongside values calculated by QXRD in Figure 5.25. The overall classifications based on mineralogy for all groups except EH-2 remained unchanged. Less chalcopyrite was measured by QXRD for this group, however, geochemical static testing for other samples within this group indicated it as NAF. Therefore, the XMOD value is considered a slight overestimation. Overall, such a comparison indicates that XMOD values can be used to determine carbonate:sulphide ratios, and assign mineralogical classifications of acid forming potential.

ARDI values were calculated from classified MLA images with evaluations performed on the first twenty sulphide grains identified in each analysed tile. Performing the ARDI in this manner was less subjective than undertaking the *Me*-scale assessment at stage-one. This is because the mineralogy of each frame is classified (i.e., better depicted) and the modal mineralogy calculated thus improving the accuracy of ranking for each parameter.

MLA analysis confirmed that calcite and potassium feldspar dominate the intact mineralogy of the group EH-1 (Figure 5.26). Chalcopyrite and traces of pyrite were identified in this sample, with subhedral chalcopyrite both chlorite- and calcite-associated (Figure 5.26c). Chlorite has a NP value of 6 (Table 2.4), and therefore is considered a very weak neutraliser. Pyrite was dominantly potassium feldspar associated, thus returning slightly higher ARDI values (NP= 1; Table 2.4 and Figure 5.26d). An average ARDI value of 9/50 was calculated indicating this sample has a PNC which, whilst slightly greater than the stage-one *Me*-scale evaluation, is in agreement with the assigned classification.

Group EH-3 contained more potassium feldspar and coarser-grained subhedral-euhedral pyrite than group EH-1, but less chalcopyrite (Figure 5.27). Pyrite was dominantly associated with potassium feldspar and magnetite and as a consequence, the final calculated *Mi*-scale value was 11/20, classifying the sample as NAF. This was greater than the *Me*-scale value whereby it was classified as PNC. Therefore, textural evaluation indicated a greater acid forming potential than as suggested by mineralogical and chemical analyses.

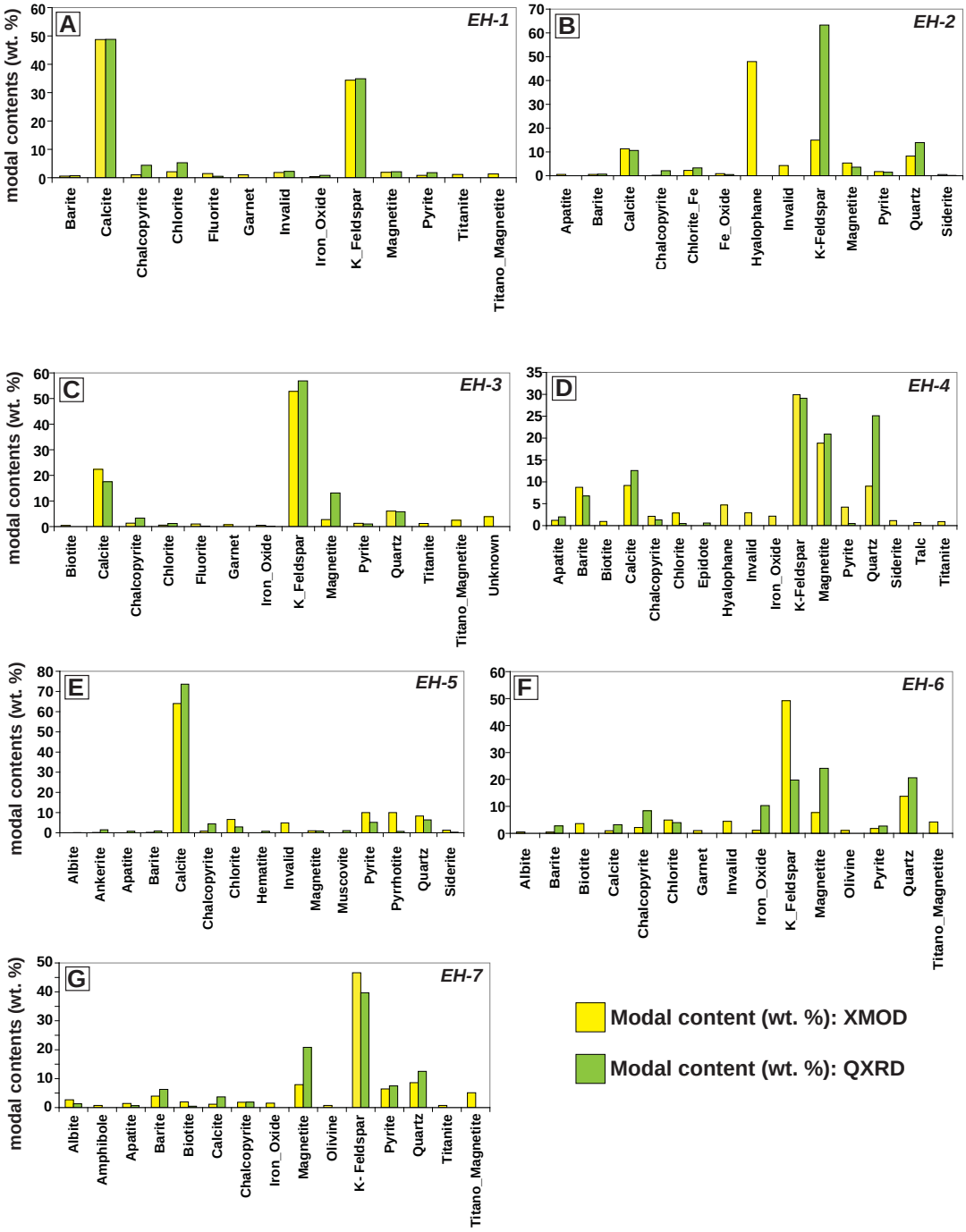

Figure 5.24 Ernest Henry mineralogy (one per group EH-1 to EH-7) as measured by QXRD and MLA-XMOD.

Group EH-4 was dominated by quartz, with a fine-grained potassium feldspar-magnetite and calcite matrix (Figure 5.28a and 5.28b). Relatively coarse chalcopyrite grains and veins were observed along with minor pyrite. Chalcopyrite mineral associations were diverse, whilst pyrite was dominantly chalcopyrite- and quartz-associated. Higher scores for parameter E were given due to the association of pyrite with chalcopyrite (e.g., Figure 5.28d), thus an ARDI value of 16/50 was calculated. Whilst this value is higher than that assigned at stage-one (*Me*-scale value: 11/50), both stage-one and stage-three classify this sample as NAF.

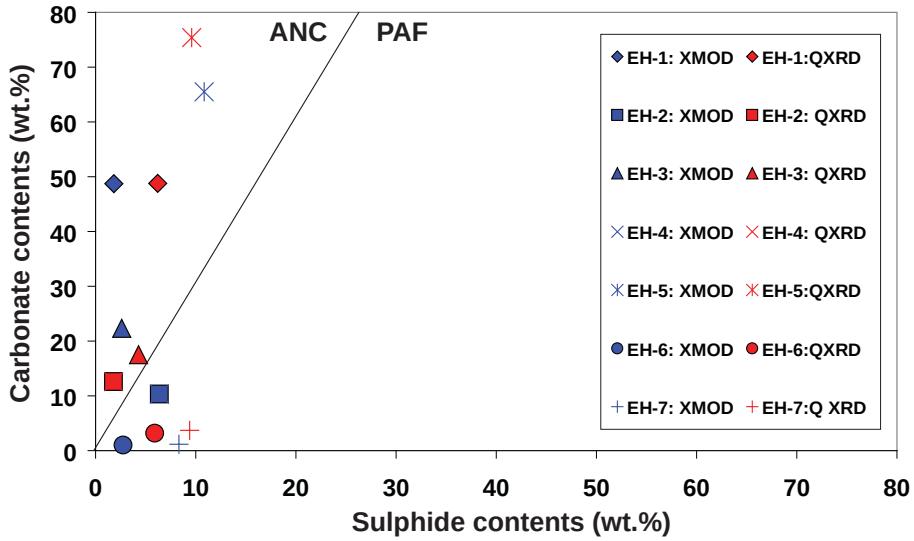

Figure 5.25 Carbonate and sulphide values measured by QXRD and XMOD for one sample from each Ernest Henry group identified in drill holes EH 633 and EH 635.

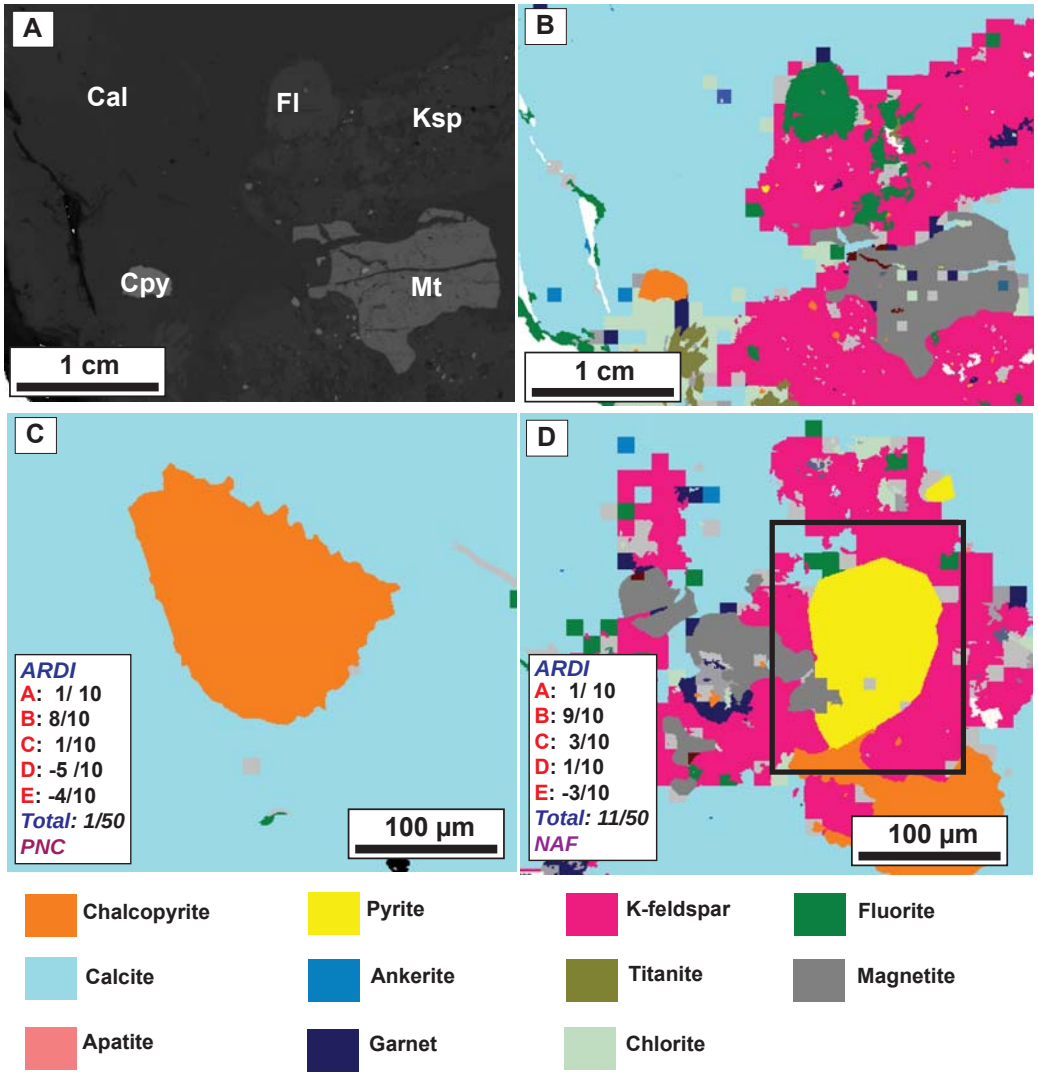

Figure 5.26 MLA textural analysis of Ernest Henry group EH-1: **(A)** BSE image of MLA tile; **(B)** Classified GXMap image of MLA tile; **(C)** Chalcopyrite grain in a calcite matrix (with ARDI value shown); and **(D)** Pyrite-chalcopyrite in a potassium feldspar-calcite matrix (with ARDI value shown for the highlighted grain). Abbreviations: Cal, calcite; Cpy, chalcopyrite; Ksp, potassium feldspar; Mt, magnetite.

Group EH-6 was dominated by potassium feldspar and quartz, with subhedral-anhedral chalcopyrite and minor pyrite identified. A lower quantity of calcite was observed in this sample than the previous groups (Figure 5.29a and 5.29b). Chalcopyrite was dominantly potassium feldspar-associated (Figure 5.29c), however, it was occasionally intergrown with pyrite (Figure 5.29d). Whilst several PAF grains were identified, the ARDI evaluation returned a value of 17/50 classifying this sample as NAF, which was in agreement with *Me*-scale evaluations.

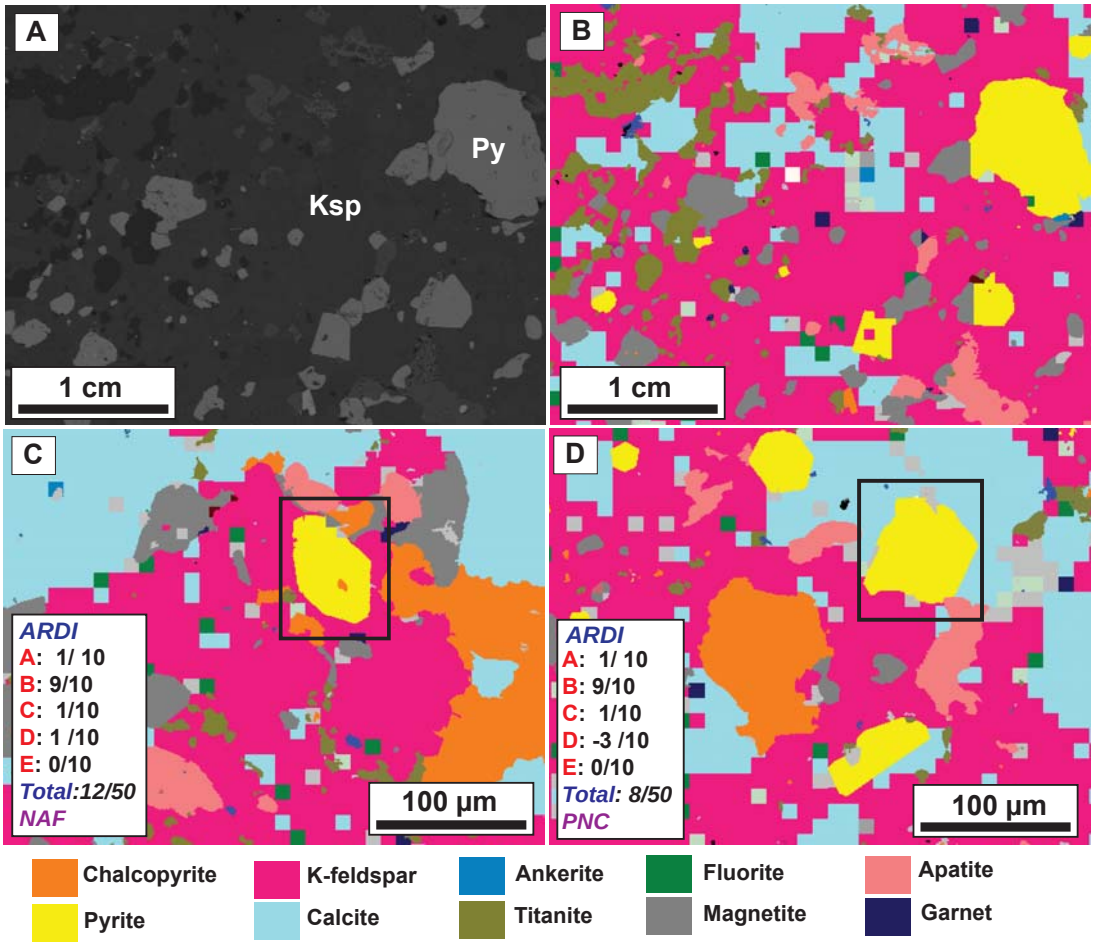

Figure 5.27 MLA textural analysis of Ernest Henry group EH-3: **(A)** BSE image of MLA tile; **(B)** Classified GXMap image of MLA tile; **(C)** Pyrite located in a matrix dominated by potassium feldspar, calcite and magnetite, with chalcopyrite also identified (with ARDI value shown for highlighted grain); and **(D)** Pyrite in a similar matrix (with ARDI value shown for the highlighted grain). Abbreviations: Ksp, potassium feldspar; Py, pyrite.

Group EH-7 was recognised as the most acid forming, with a higher proportion of pyrite observed in the MLA-tile (Figure 5.30a and 5.30b). This sample also contained garnet, which was not previously observed. Jambor et al. (2002) calculated that almandine ($Fe_3Al_2Si_3O_{12}$) has a NP of 3, whereas grossular ($Ca_3Al_2Si_3O_{12}$) has a NP of 6. Almandine was identified in this sample, thus garnet in this samples was considered as a very weak neutraliser. Pyrite demonstrated anhedral morphologies, and was often intergrown with chalcopyrite, thus an overall *Me*-scale value of 20/50 was calculated, classifying this sample as PAF.

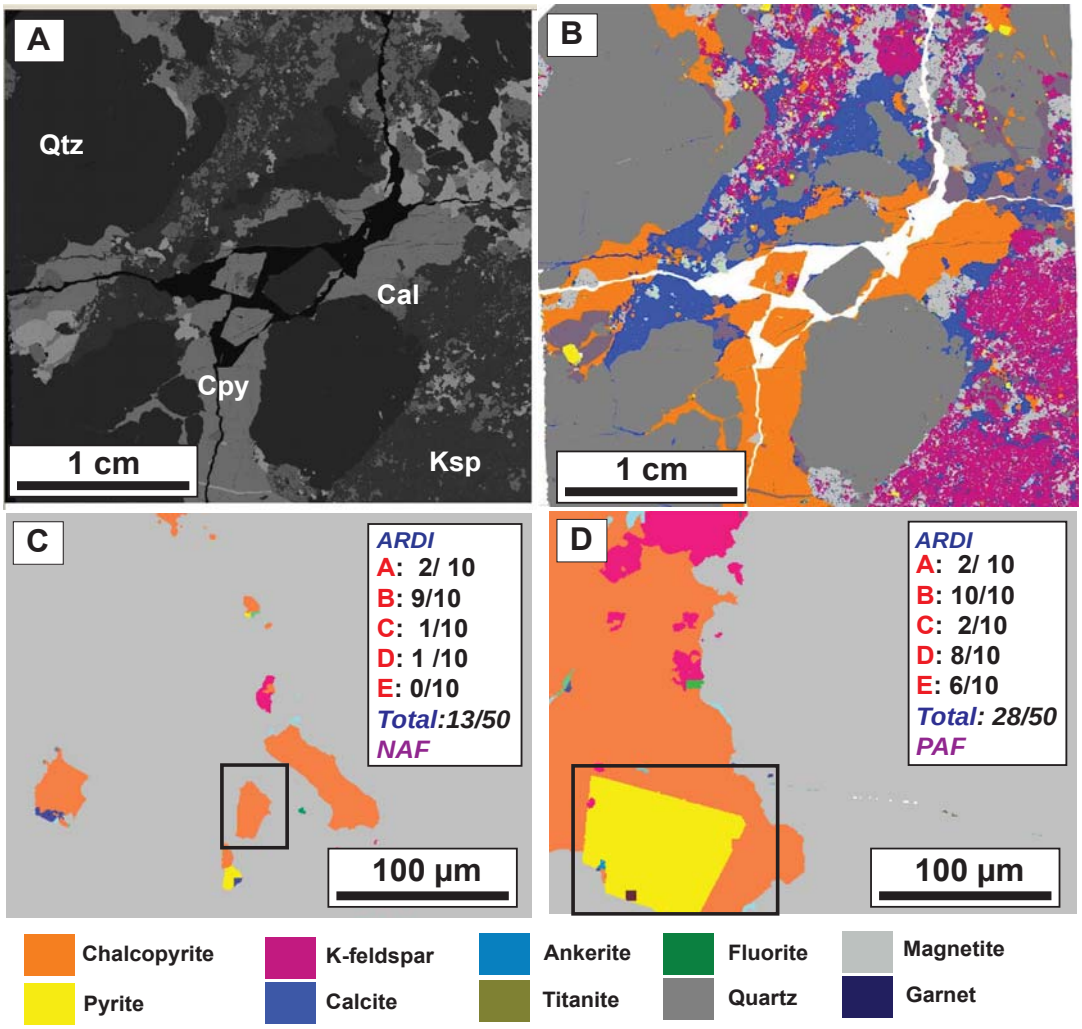

Figure 5.28 MLA textural analysis of Ernest Henry group EH-4: **(A)** BSE image of MLA tile; **(B)** Classified GXMap image of MLA tile; **(C)** Chalcopyrite located in a magnetite matrix (with ARDI value shown for highlighted grain); and **(D)** Pyrite directly associated with chalcopyrite and magnetite (with ARDI value shown for the highlighted grain). Abbreviations: Cal, calcite; Cpy, chalcopyrite; Ksp, potassium feldspar; Qtz, quartz.

5.4.4.4 Stage-three classification

Multi-addition NAG testing results did not change the geochemical classification assigned at the end of stage-two (Table 5.10), with acidity produced through the accelerated oxidation of chalcopyrite, and pyrite directly buffered by calcite. However, lower mNAG pH values (<1.5 pH units) were returned, providing additional evidence that single addition NAG testing is only effective on samples containing <0.3 wt. % S_{Total} or $S_{Sulphide}$. Kinetic NAG tests performed on samples from groups EH-4, EH-6 and EH-7 indicated they were NAF. ABCC testing showed that group EH-1, EH-2, EH-4, EH-5 and EH-7 had an effective neutralising capacity. However, in group EH-2, EH-4 and EH-7, the net acid neutralising capacity was likely to be utilised due to the contents of acid forming sulphides. Therefore, only groups EH-1 and EH-5 are regarded as actually having significant acid neutralising capacity. Modal mineralogy values calculated by XMOD showed good agreement with QXRD measurements. ARDI values calculated through examination of MLA GXMap images returned values which were slightly greater than those reported by *Me*-scale evaluations undertaken at stage-one. However, the overall classifications remained

unchanged, and indicated that group EH-7 was the most acid forming. Based on these classifications, a final classification was assigned, with group EH-4, EH-6 and EH-7 reported as potentially acid forming (Table 5.10). KNAG tests indicated a significant lag-time to ARD formation, thus these are regarded as low-risk groups.

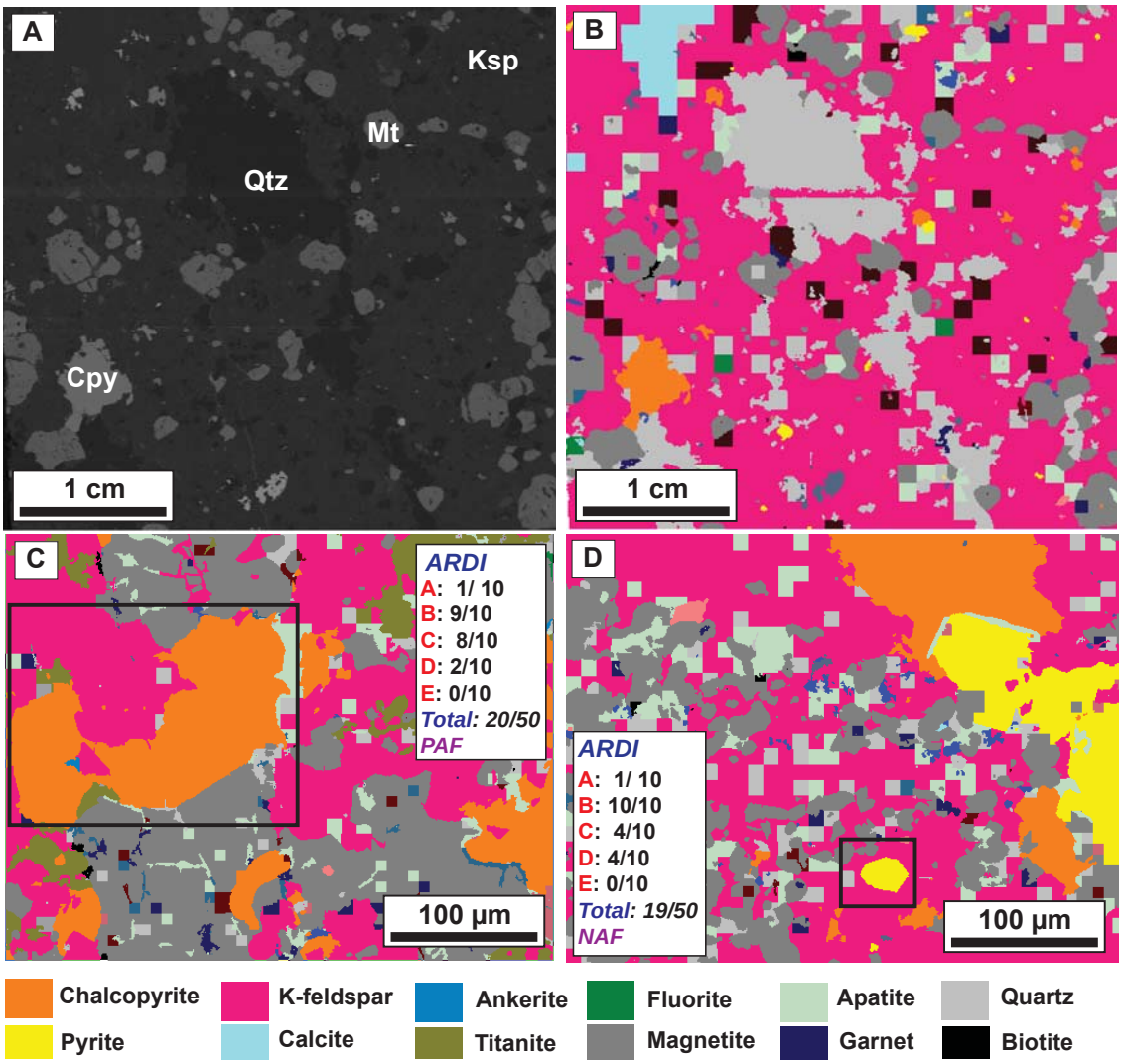

Figure 5.29 MLA textural analysis of Ernest Henry group EH-6: **(A)** BSE image of MLA tile; **(B)** Classified GXMap image of MLA tile; **(C)** Anhedral chalcopyrite located in a potassium feldspar-magnetite dominated matrix (with ARDI value shown for highlighted grain); and **(D)** Pyrite associated with potassium feldspar (with ARDI value shown for the highlighted grain).

5.4.5 Comparison of geometallurgical data with GMT classification

GMT classification results were considered against the Ernest Henry geometallurgical dataset (collected by the AMIRA P843 GeM project) to explore how such data can be used to identify ARD forming potential in these drill holes. The motivation for comparing these datasets was to understand when geometallurgical data can be effectively utilised to make ARD predictions. First, the effectiveness of grouping samples by lithology for ARD characterisation was evaluated, with the potential for instead using geometallurgical groups explored. Next, the accuracy of using MLA-XMOD data for calculating

downhole carbonate:sulphide ratios (i.e., data required at stage-one of the GMT approach) was assessed. Better evaluation of ANC values using relative carbonate data from a HyLogger was subsequently undertaken, so as to replace the requirement for ABCC tests performed at stage-three of the GMT approach. Carbonate data generated by the HyLogger was also used alongside sulphur assay values to explore the possibility of domaining NAPP, with data compared against GMT classifications. Finally, the application of EQUOtip data (also used alongside sulphur assay values) to domain mineral hardness as a first pass means of indicating the lag-time to acid formation was tested, with classifications compared with NAG pH versus paste pH values plotted at stage-two of the GMT approach.

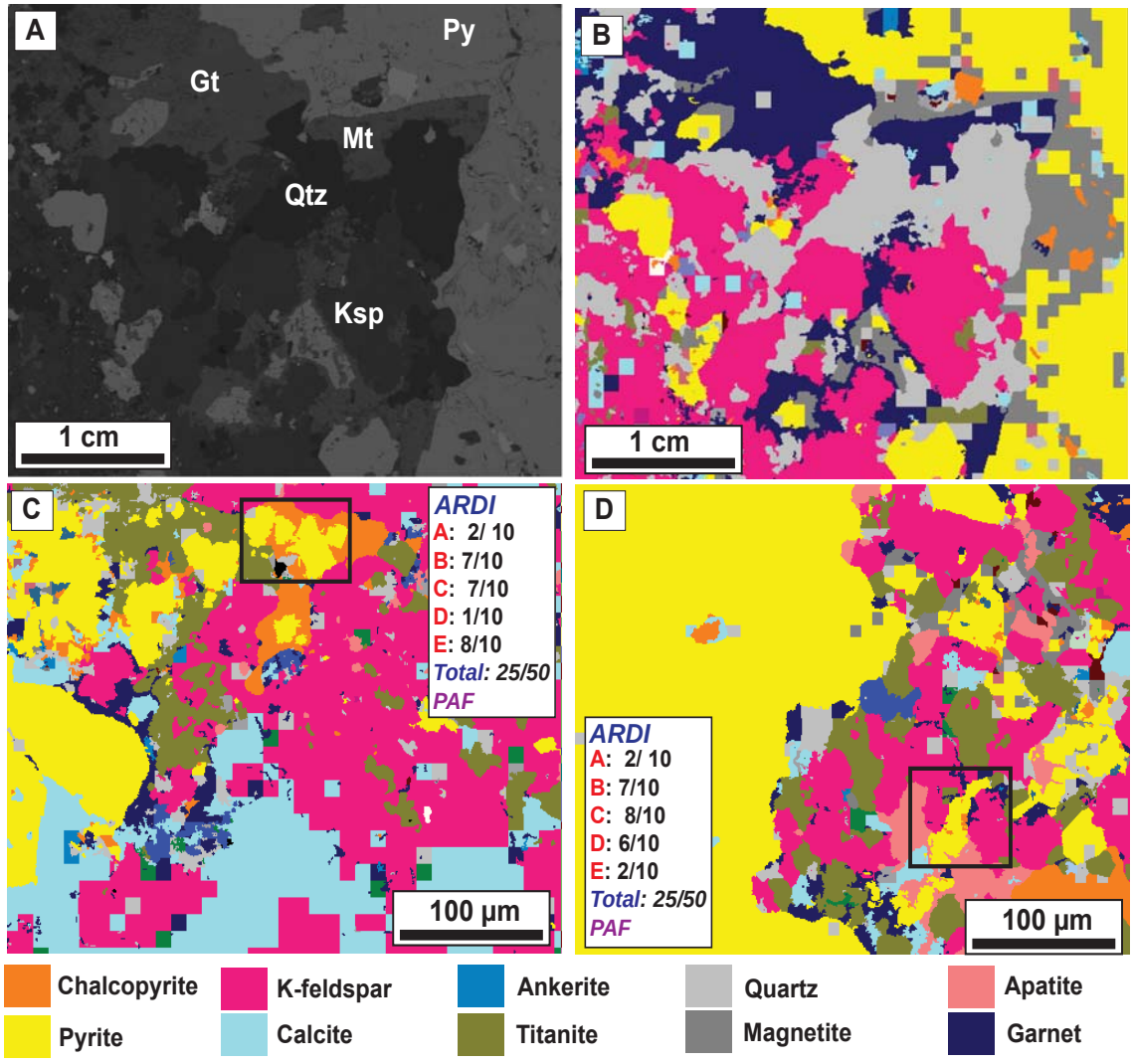

Figure 5.30 MLA textural analysis of Ernest Henry group EH-7: **(A)** BSE image of MLA tile; **(B)** Classified GXMap image of MLA tile; **(C)** Pyrite-chalcopyrite intergrowths located in a matrix dominated by potassium feldspar and calcite (with ARDI value shown for highlighted grain); and **(D)** Anhedral pyrite in a dominantly sulphide-potassium feldspar matrix (with ARDI value shown for the highlighted grain). Abbreviations: Gt, garnet; Ksp, potassium feldspar; Mt, magnetite; Py, pyrite.

Table 5.10 Stage-three classification summary table for Ernest Henry drill core samples from EH 633 and EH 635 shown in groups EH-1to EH-7. Abbreviations: NAF, non-acid forming; PAF, potentially acid forming; ANC, acid neutralising capacity.

Group	Stage-two Classification	Multi-addition NAG	Kinetic NAG	ABCC testing	MLA ARDI classification	Final GMT approach classification	Column leach testing required?
EH-1	ANC	-	-	High & effective ANC	PNC	ANC	No
EH-2	NAF	NAF	-	Effective ANC	-	NAF	No
EH-3	NAF	NAF	-	-	NAF	NAF	No
EH-4	NAF & PAF	NAF & PAF	NAF	Effective ANC	NAF	PAF	Yes
EH-5	ANC	NAF	-	High & effective ANC	-	ANC	No
EH-6	NAF & PAF	NAF & PAF	NAF	NAF	NAF	PAF	Yes
EH-7	NAF & PAF	NAF & PAF	NAF	Effective ANC	PAF	PAF	Yes

5.4.5.1 Mesotextural grouping

The GMT approach was undertaken using the sample (lithological) grouping system developed on site during logging. However, these results consistently indicated that acid forming and neutralising samples were not adequately discriminated, particularly for groups EH-4 and EH-7. This suggests that whilst it was stated in the geological logs obtained from the AMIRA P843 GeM database that the grouping system gave consideration to alteration and texture, evidentially it was not done so effectively. Indeed, at operational mine sites it is common practice to obtain samples for ARD testing from groups defined by lithology e.g., Cadia Valley Operations, NSW, Australia (Mesh Environmental Inc., 2009) and Lake Cowal, NSW, Australia (Geo-Environmental Management Pty Ltd., 2008). Thus, if the GMT approach was applied at these sites based on geological logging alone, results would not be as effective than if adequate mesotextural grouping (as performed at Croydon) had been undertaken. Bonnici (2012) also identified this as a limitation for mineral processing, as mineral liberation characteristics are often related to textural and not geological groupings. Thus, Bonnici (2012) proposed a new textural classification to aid mineral processing at Ernest Henry, with reference images and liberation characteristics assessed as shown in Figure 5.31. Where possible, samples used in the GMT approach have been reconsidered in terms of Bonnici's (2012) classification, and the acid forming potential commented upon (Table 5.11).

Classification of group EH-5 proved difficult using Bonnici's (2012) scheme. This particular group would be considered BF2 (i.e., carbonate dominated), however, it did not resemble the representative image (Figure 5.31b) shown for this group. In the AMIRA P843 project, a total of 1455 meso-scale

images were texturally grouped by Bonnici's (2012) classification from the six nominated EH drill holes. Textural groups BF3 and MF3 dominated (65%) with both classified as PAF (Table 5.12). NAF textural groups comprised 17% only (Table 5.12).

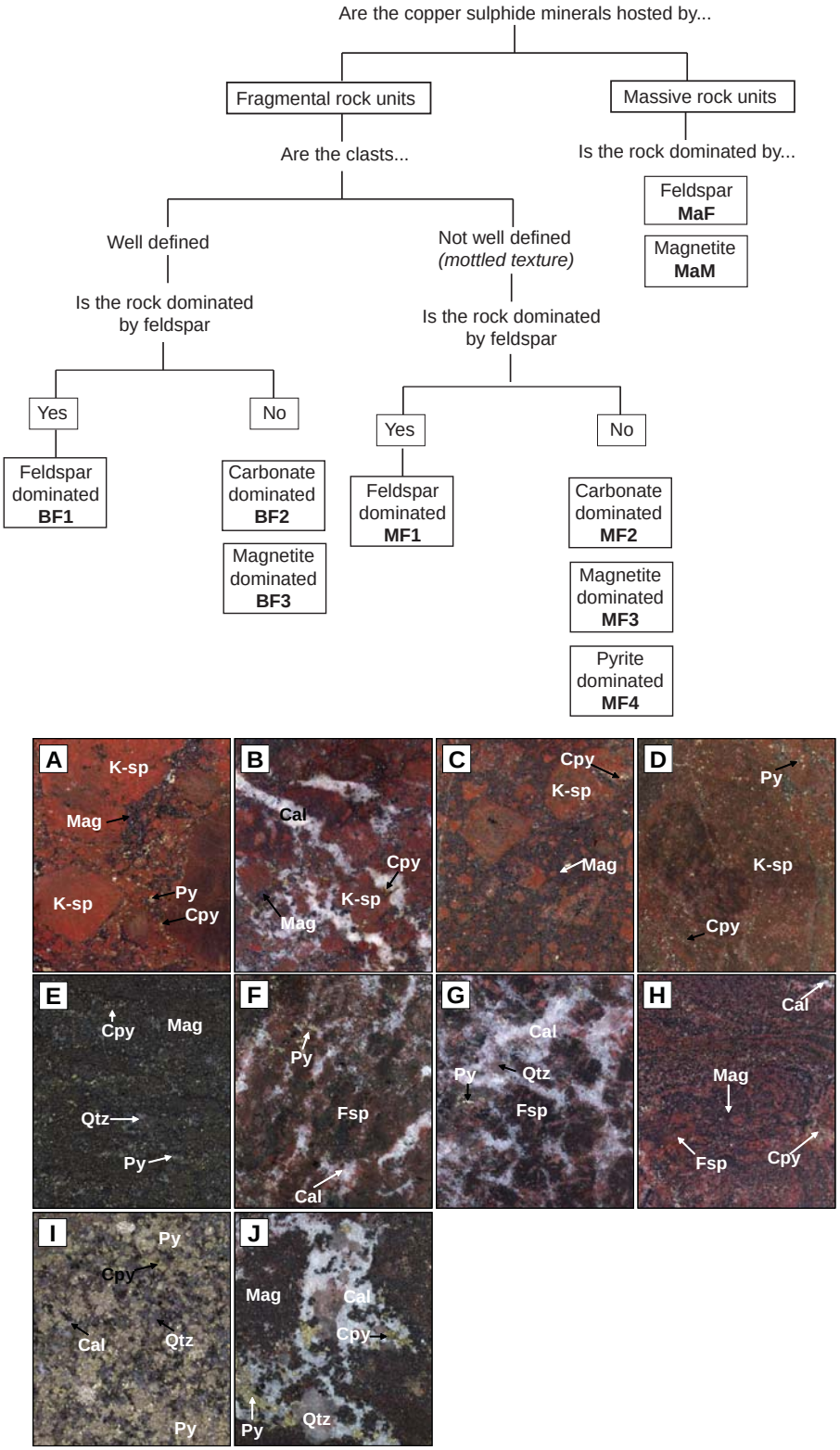

Figure 5.31 Mesotextural decision tree and examples of meso-scale texture classes for Ernest Henry proposed by Bonnici (2012): **(A)** BF1; **(B)** BF2; **(C)** BF3; **(D)** MF1; **(E)** MF2; **(F)** MF3; **(G)** MF4; **(H)** MaF; **(I)** MaM; **(J)** clotted chalcopyrite. Abbreviations: Cal, calcite; Cpy, chalcopyrite; Fsp, feldspar; K-sp, potassium feldspar; Mag, magnetite; Py, pyrite; Qtz, quartz.

Table 5.11 Meso-scale textural classes for Ernest Henry and their descriptions proposed by Bonnici (2012). Potential acid forming characteristics based on GMT classification of similar samples are given. Abbreviations: AF, acid forming; NAF, non-acid forming; PAF, potentially acid forming.

Textural class	Description	Acid forming/neutralising characteristics
BF1	Fragmental unit with well defined feldspar clasts. Rock is predominantly feldspar.	Textural similarity to group EH-2 Disseminated pyrite and chalcopyrite in a dominantly feldspar matrix: *PAF*
BF2	Fragmental unit with well defined feldspar clasts. Matrix dominated by carbonate minerals and minor quartz.	Textural similarity to group EH-3 Minor disseminated chalcopyrite in association with calcite: *NAF*
BF3	Fragmental unit with well defined feldspar clasts. Matrix dominated by magnetite.	Disseminated chalcopyrite and pyrite identified in association with magnetite and feldspar: *PAF*
MF1	Fragmental unit with clast edges not defined clearly giving the rock a mottled appearance. Rock is predominantly feldspar.	Disseminated pyrite and chalcopyrite identified in a dominantly feldspar matrix: *PAF*
MF2	Fragmental unit with clast edges not defined clearly giving the rock a mottled appearance. Matrix is dominated by carbonate and minor quartz.	Textural similarity to group EH-4 Minor disseminated chalcopyrite identified and in association with calcite: *NAF*
MF3	Fragmental unit with clast edges not defined clearly giving the rock a mottled appearance. Matrix is dominated by magnetite.	Textural similarity to group EH-1 Disseminated chalcopyrite and pyrite identified in association with magnetite and feldspar: *PAF*
MF4	Fragmental unit with clast edges not defined clearly giving the rock a mottled appearance. Matrix is dominated by pyrite.	Disseminated pyrite and chalcopyrite identified in association with calcite: *NAF*
MaF	Massive unit dominated by feldspar minerals.	Disseminated pyrite and chalcopyrite identified in a dominantly feldspar matrix: *PAF*
MaM	Massive unit dominated by magnetite.	Textural similarity to group EH-7 Disseminated pyrite and chalcopyrite identified in a dominantly magnetite matrix: *AF*

Table 5.11 *Continued*

Textural class	Description	Acid forming/neutralising characteristics
D	Fine-grained to coarse-grained disseminated chalcopyrite. Typically occurs with disseminated pyrite.	Sulphides dominate the modal mineralogy: *AF*
C	Coarse aggregates (clots) of chalcopyrite with magnetite-calcite-quartz-pyrite phenocrysts. Typically occurs in the matrix of fragmental units.	Textural similarity to group EH-6, located in an EH-4 unit: *AF*

Table 5.12 Meso-scale textural classes for Ernest Henry as defined by Bonnici (2012) with the population per class shown. Based on a comparison with final GMT results calculated in this study, ARD classifications have been assigned.

Textural class	Number of images	Population (%)	ARD classification
MaF	145	10	PAF
MaM	60	4	AF
BF1, MF1	37	2	PAF
BF2, MF2	251	17	NAF
BF3, MF3	951	65	PAF
MF4	11	1	NAF

5.4.5.2 Mineralogical domaining using MLA data

The application of MLA-XMOD data to calculate carbonate:sulphide ratios was explored in Section 5.4.4.3, with results compared against QXRD values, and strong agreement between the two data sets indicated. This suggests that, where such geometallurgical data have already been collected as part of pre-feasibility studies (as is the case for several operations studied in the AMIRA P843 GeM project), a modal mineralogy database exists and must be utilised in ARD predictive studies. These data can be used at stage-one of the GMT approach, rather than scheduling a small sample set for QXRD analyses. Carbonate:sulphide values measured by XMOD for drill holes EH 633 and EH 635 are shown in Figures 5.32 and 5.33.

By the carbonate:sulphide ratio, groups EH-7 and EH-4 can be classified as acid forming in EH 633. Group EH-8 (altered mosaic mafic volcanics comprising: magnetite-potassium feldspar-carbonate-pyrite-chalcopyrite; not sampled by the GMT approach) was identified as acid neutralising. Whilst groups EH-2 and EH-3 contained carbonate material, it was not in a 3:1 ratio with sulphides and therefore was classified as acid forming. Zones of acid forming and neutralising potential did not correlate as well with groups in drill hole EH 635. However, groups EH-4 and EH-7 in the upper half of the drill hole were acid forming, and EH-1 acid neutralising. Towards the contacts between the groups, the characteristics change. For example at around 973m depth, EH-4 appears to have a neutralising zone, but this is in proximity to the contact with EH-5 (classified by the GMT approach as a neutraliser). This behaviour is repeated again at 1009 m depth.

5.4.5.3 NAPP domaining using Thermal Infrared (TIR) and assay data

A limitation of the Sobek ANC test is the determination of the carbonate species present and their constituent amounts (White et al., 1999). Whilst ABCC tests were designed in-part to overcome this, they are relatively difficult to interpret (i.e., results are compared against standard curves). A much simpler manner of domaining carbonates may exist through the interpretation of TIR data. As stated in Section 5.2.3.2, HyLogger data were collected as part of the AMIRA P843 project for drill holes EH 633 and EH 635 and its application in ARD prediction is explored here.

TIR mineral characterisation identified three carbonate bearing populations: 1) abundant calcite (~6580nm); 2) moderate ankerite/siderite (~6530nm); and 3) minor dolomite (~6490nm; Quigley, 2012). These results were consistent with the carbonate identification made from SW-IR analysis; however, greater abundances were reported using TIR (Quigley, 2012). Thus, where high calcite zones were identified, ANC can be considered as effective. Relationships between HyLogger data (carbonate intensity values) with Sobek ANC and paste pH values were explored to identify if these values can be predicted from HyLogger data. Correlation between Sobek ANC values and carbonate intensity was weak (Figure 5.34), with downhole ANC values calculated (using the equation shown in Figure 5.34) returning inaccurate values. Paste pH values showed even less correlation with carbonate intensity values (Figure 5.35), with paste pH values calculated (using the equation shown in Figure 5.35) for samples in both drill holes considered incorrect (i.e., all were assigned a value of pH 7.8). Fundamentally, this type of correlation is limited by the size of the data set, thus with more Sobek ANC and paste pH measurements, a better relationship could be defined. Additionally, to improve Sobek ANC and paste pH estimates made from HyLogger data, mathematical relationships should be defined per group, and not for the whole data.

Despite the qualitative nature of TIR data, relative carbonate intensity was compared against sulphur assay data, as a first pass means of identifying acid forming/neutralising zones (Figures 5.36 and 5.37). Zones were compared against final GMT classifications. Acid forming zones were defined by >0.3 wt. % S_{Total} contents, and low calcite + dolomite abundance. This criterion successfully identified regions containing EH-7 and EH-4 as acid forming in both drill holes, and was in agreement with GMT classifications. Group EH-2 and EH-3 were considered as NAF by the GMT approach; however, this first-pass screening considered them PAF. Additionally, group EH-5 was classified as a highly effective neutraliser by the GMT approach, but is shown here as PAF (Figure 5.37). Groups EH-8 to 12 were not tested by the GMT approach (due to an absence of sample material). However, this assessment indicates these may have a significant neutralising capacity.

Thus. this study shows there is potential to predict and domain NAPP using the HyLogger/ sulphur assay method. Samples from each zone domained by this method as PAF or having an ANC could be specifically obtained for GMT sampling (i.e., as an alternative to advancing samples through the GMT approach based on mesotexture). However, if such an approach is adopted, then it must be cross checked at least against lithology and alteration styles as a means of guiding GMT sampling. As in the case of EH 635 (Figure 5.37), groups EH-4 and EH-7 would not have been differentiated between 866m and 1104m depth, and samples from groups EH-5 and EH-6 may not have been identified.

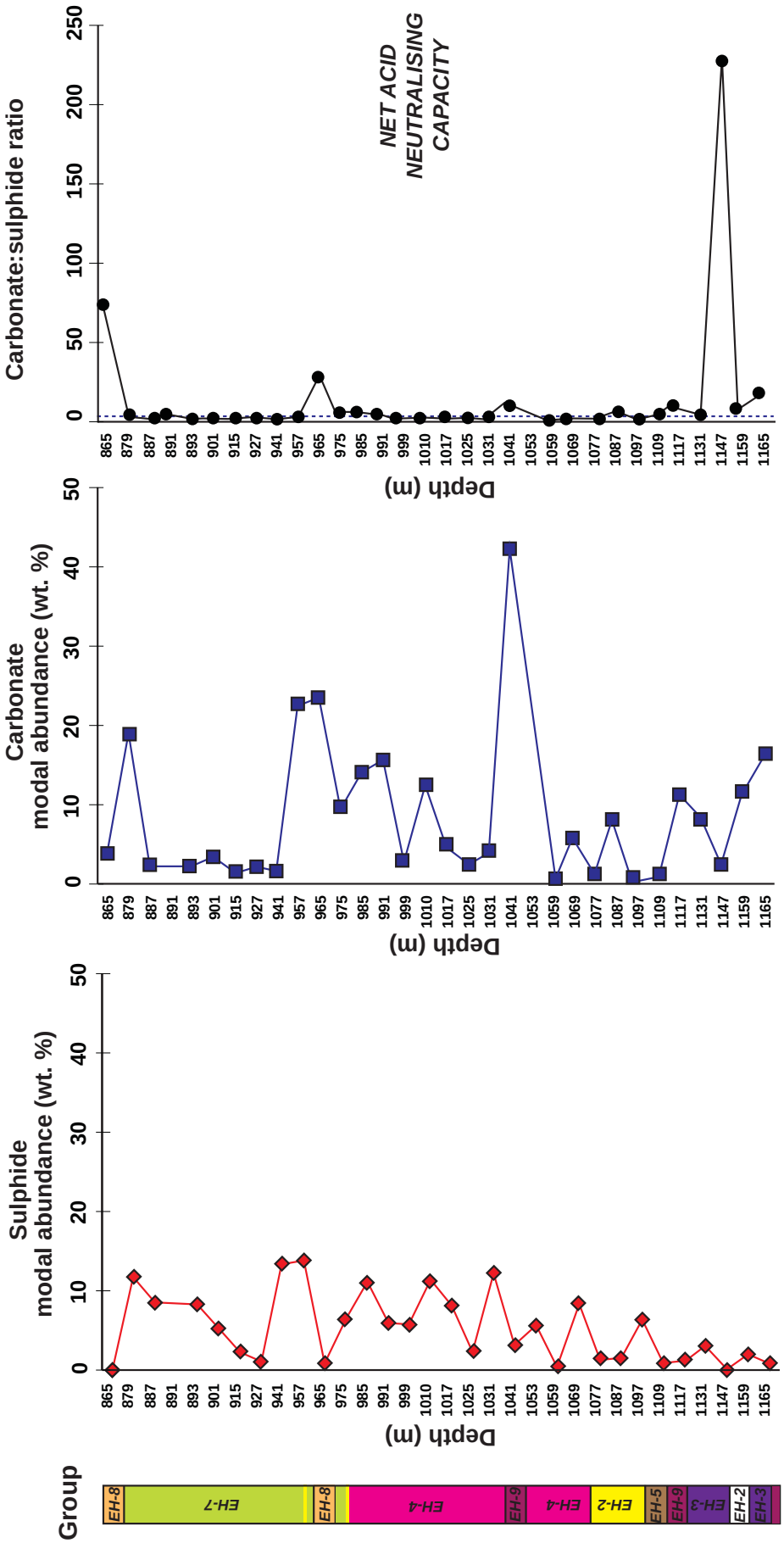

Figure 5.32 Downhole carbonate and sulphide values for EH 633 (865m-1165m) as measured by MLA-XMOD with the carbonate:sulphide ratio shown. The net acid neiutralising capacity field is shown ro the right of the purple dashed line.

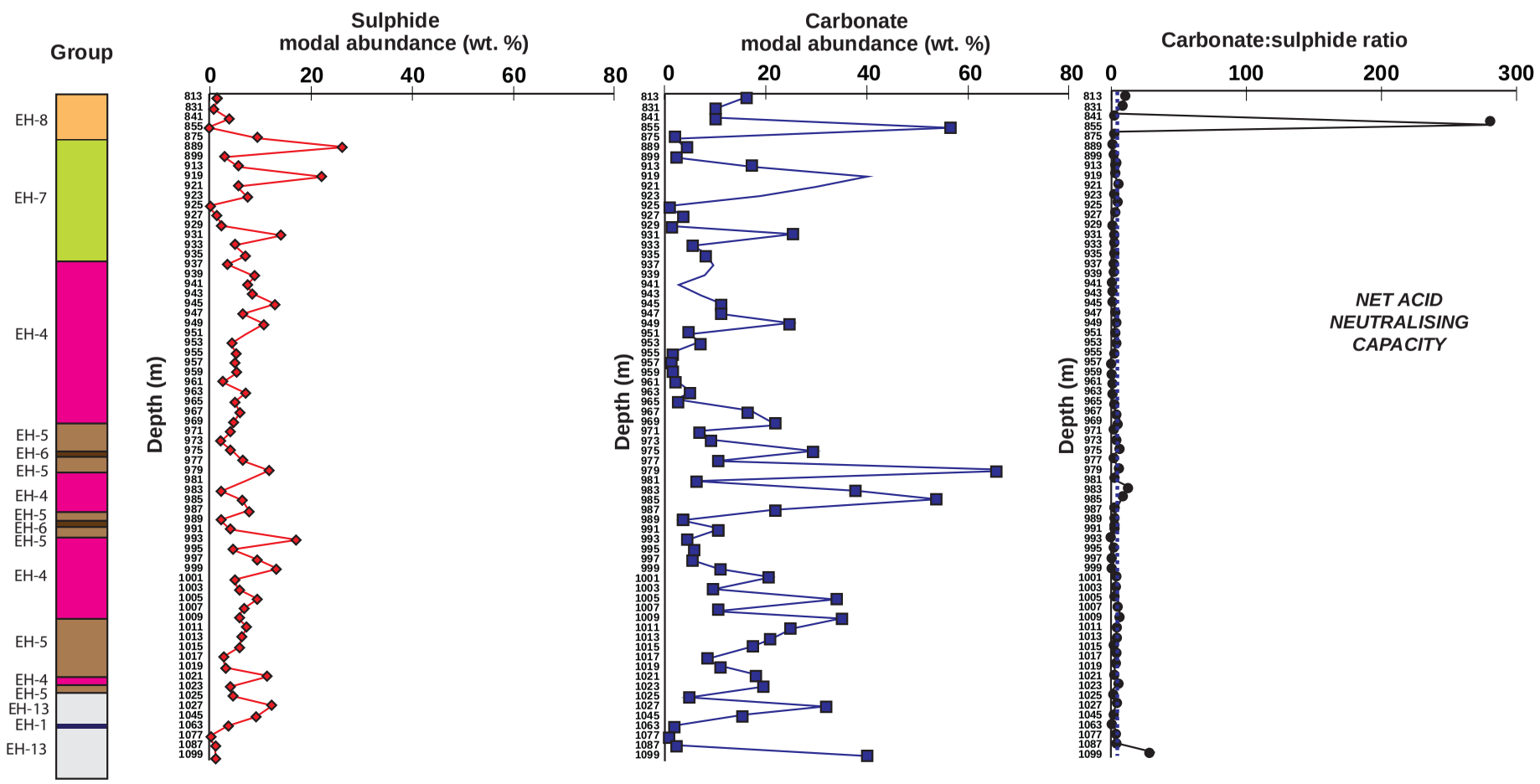

Figure 5.33 Downhole carbonate and sulphide values for EH 635 (813m-1099m) as measured by MLA-XMOD with the carbonate:sulphide ratio shown. The net acid neiutralising capacity field is shown ro the right of the purple dashed line.

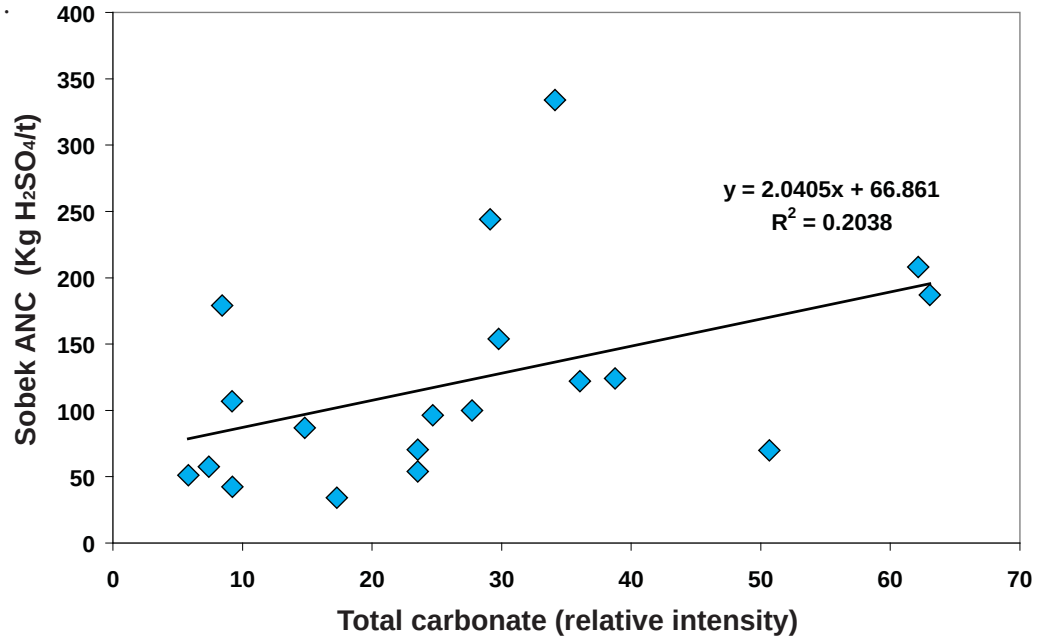

Figure 5.34 Correlation plot of Sobek ANC (kg H_2SO_4/t) versus Hylogger total carbonate (relative intensity) values for samples from Ernest Henry drill holes EH 633 and EH 635 (n=20).

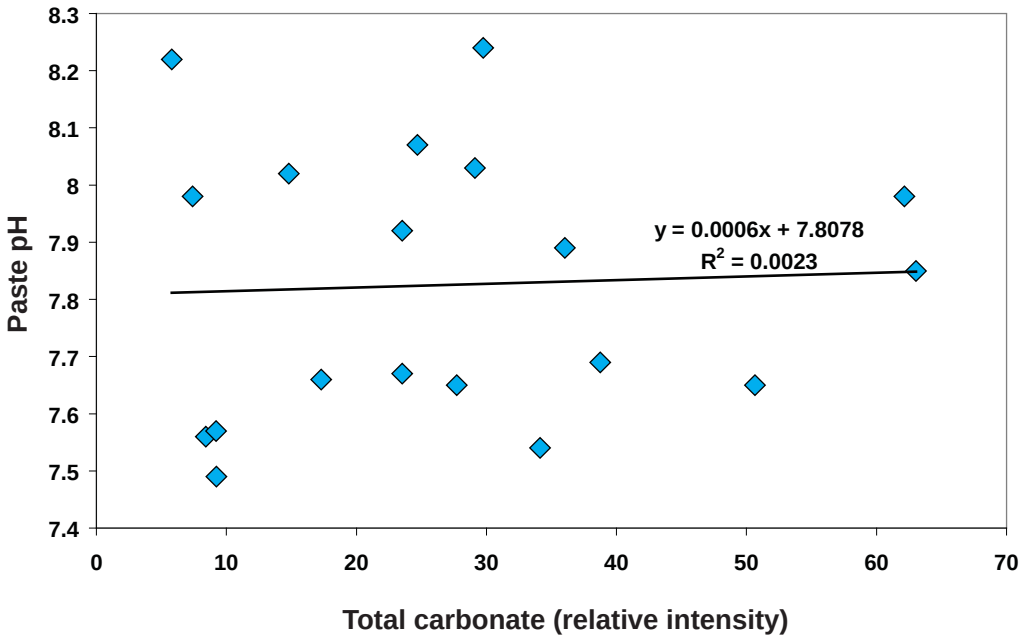

Figure 5.35 Correlation plot of paste pH versus Hylogger total carbonate (relative intensity) values for samples from Ernest Henry drill holes EH 633 and EH 635 (n=20).

5.4.5.4 Predicting weathering rate

Keeney (2008) reported a range of 570 Ls to 800 Ls for EQUOtip values measured from the Ernest Henry drill holes tested. Keeney (2008) stated that EH 633 had a reasonably constant profile (~700 Ls) between 950 and 1100m, which was bound on either side by regions of harder rock (~750 Ls). Keeney

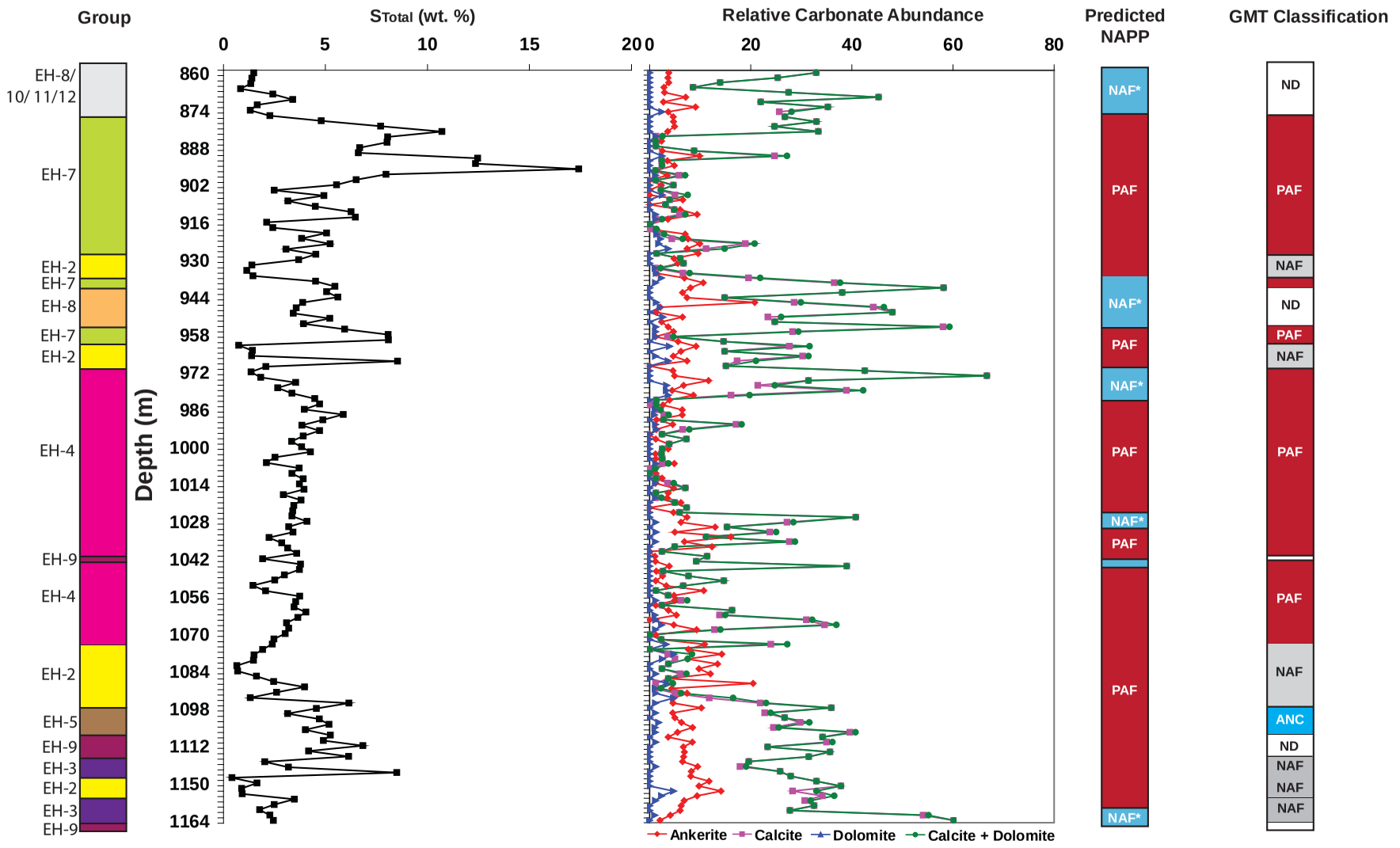

Figure 5.36 Domaining of NAPP in Ernest Henry drill hole EH 633 based on S_{Total} values (obtained from assay) and relative carbonate abundance (measured using HyLogger by Quigley, 2008). Red indicates the potential for acid formation, blue indicates an acid neutralising capacity and grey indicates non-acid forming characteristics. Abbreviations: ANC, acid neutralising capacity; NAF, non-acid forming, NAF*, non-acid forming, but with a likely neutralising capacity; ND, no data; PAF, potentially acid forming.

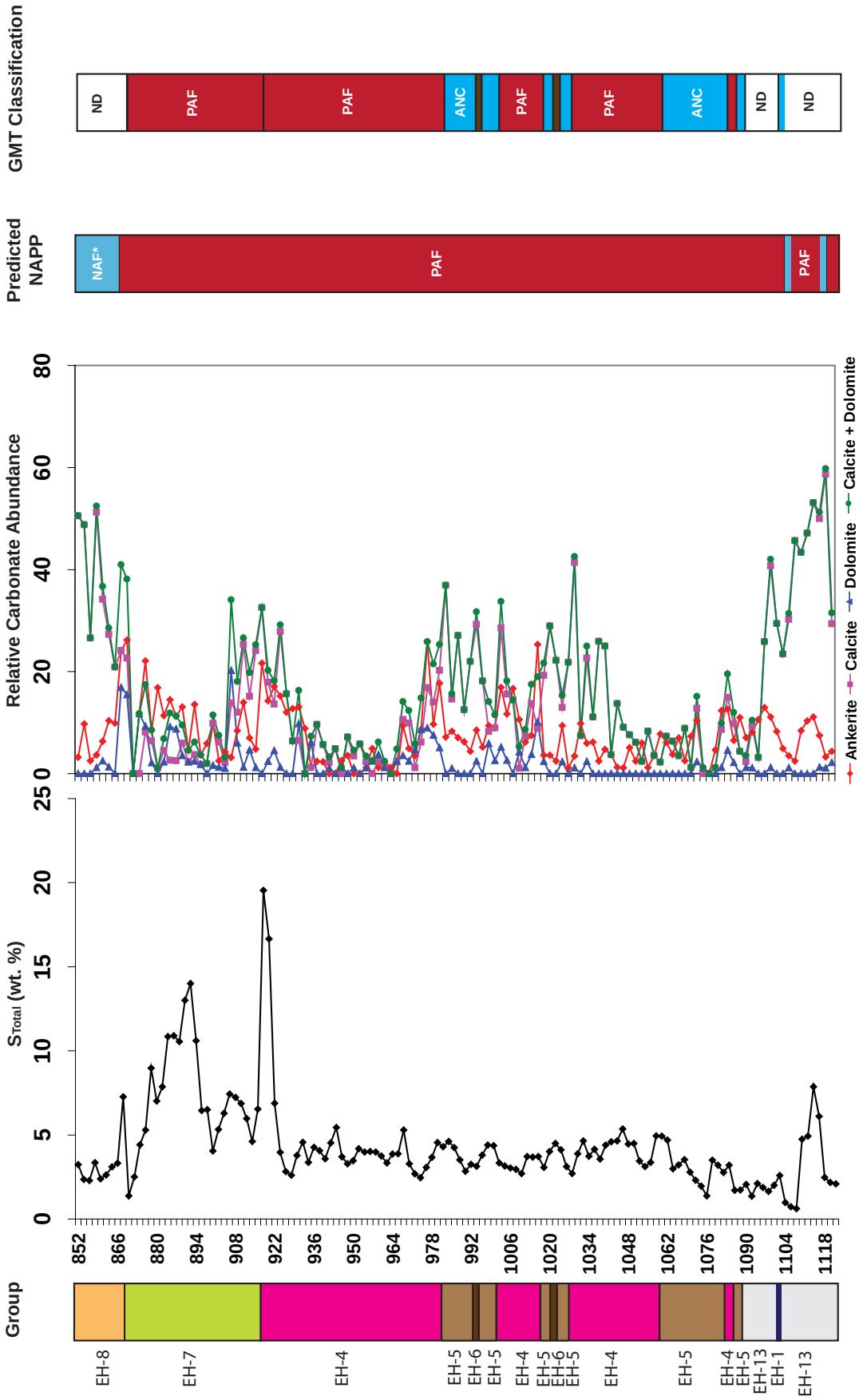

Figure 5.37 Domaining of NAPP in Ernest Henry drill hole EH 635 based on S_{Total} values (obtained from assay) and relative carbonate abundance (measured using HyLogger by Quigley, 2008). Red indicates the potential for acid formation, blue indicates an acid neutralising capacity and grey indicates non-acid forming characteristics. Abbreviations: ANC, acid neutralising capacity; NAF, non-acid forming, NAF*, non-acid forming, but with a likely neutralising capacity; ND, no data; PAF, potentially acid forming.

(2008) also stated that EH 635 showed a general increase in hardness with depth between 875 m and 1050 m, with rocks at a depth of 1050 m the hardest material consistently observed in the Ernest Henry deposit. Keeney (2008) undertook a stochastic trend analysis (STA) on these data in order to identify regions of homogeneity in terms of hardness. Based on the STA, seven hardness categories were defined as shown in Table 5.13. EQUOtip data have been considered here as a indicator for likely weathering behaviour. For example, samples classified by EQUOtip as very soft are considered to weather at a fast rate, whereas samples which are classified as very hard are predicted to weather slowly. Interpretation of data in this manner is purely qualitative. Additionally, no consideration is given to grain size and the presence of fractures, with the latter influencing weathering rate by acting as conduits for oxygen and water (Plumlee, 1999). Despite these limitations, EQUOtip values were considered against lithology and sulphur assay values in order to assess the potential for, and lag time to acid formation (Figures 5.38 and 5.39). These values were compared against GMT stage-two NAG pH versus paste pH classifications.

The predicted lag time to ARD for EH 633 based on EQUOtip and assay data varied between NAF (i.e., hard zone with relatively low S_{Total}) and AF (rapid rate of ARD formation, medium risk) as shown in Figure 5.39. More variation was observed for EH 635, particularly from 860 m to 1020 m with NAF, PAF and AF zones identified (Figure 5.40). In general, these classifications were more conservative than those assigned by NAG pH versus paste pH, with the most common conflict the classification of a zone as PAF rather than NAF (i.e., EH 633, ~970 m; Figure 5.39). However, in EH 635 a NAF zone was identified from ~1030 m to ~1075 m by this classification, but by the NAG pH versus paste pH classification, ~1030 m to ~1060 m was identified as PAF (Figure 5.39). Thus, this hardness/assay classification is unlikely to be used as an accurate indication of lag-time to acid formation. Instead it can be used to provide a general indication of weathering rate prior to NAG pH, paste pH or kinetic NAG geochemical data being reported.

Table 5.13 Table of EQUOtip hardness categories with average values shown (Ls- leebs). From Keeney (2008).

EQUOtip hardness classification	Mean (Ls)	Predicted weathering rate
Very hard	793	Very slow
Hard	763	
Medium hard	737	
Medium	716	
Medium soft	695	
Soft	648	
Very soft	596	Very fast

The most significant limitation of the hardness/assay method is that no direct consideration of the mineralogy and texture is given. Thus, a more accurate method of interpreting weathering rate would be based on the content of individual mineral components in a sample as determined by QXRD or XMOD. The relative reactivities of several major rock forming minerals at pH 5 are shown in Table 5.14. Using these values, a modal mineralogy weathering index (MMWI) is proposed as shown in *equation 5.2*.

MMWI= [Modal content (wt. %) x relative reactvity at pH 5] for each identified mineral *(5.2)*

In this analysis, the modal content (in wt. %) of each non-acid forming mineral is multiplied by the relative reactivity value shown in Table 5.14. Each value is summed, with a maximum value of 100 possible. For example, a sample containing 100% calcite which has a relative reactivity of 1 will be given a value of 100/100; and a sample containing 100% quartz with a relative reactivity of 0.004 is given a value of 0.4/100. The criteria are shown in Table 5.15. Comparison of this value against the ARDI gives consideration to texture (as required), with a final classification proposed in Figure 5.40, with data from this study shown (i.e., ARDI *Me*-scale group average values and QXRD data).

By using this approach EH-5 and EH-1 are identified as having a PNC with a fast weathering rate, and group EH-4, EH-6 and EH-7 as NAF with a slow-intermediate weathering rate. Potentially, this method is a better way of domaining the lag-time to ARD formation rather than comparing EQUOtip values with sulphur assay data. Furthermore, modal mineralogy estimates can be made by MLA-XMOD increasing the potential number of samples screened in this manner. However, the absence of a large, statistically valid repository of corresponding ARDI values could be a potential limitation, and therefore must be addressed to effectively develop the MMWI further.

Table 5.14 Relative reactivities of minerals as pH 5 (after Sverdrup (1990) and Kwong (1993), from Lawrence and Scheske (1997) and Plumlee (1999).

Mineral group	Typical minerals	Relative reactivity at pH 5
Dissolving	calcite, aragonite, dolomite, magnesite, brucite	1.00
Fast weathering	anorthite, nephaline, forsterite, olivine, garnet, jadeite, leucite, spodumene, diopside, wollastonite	0.40
Intermediate weathering	sorosilicates (epidote, zoisite), pyroxenes (enstatite, hypersthene, augite, hedenbergite), amphiboles (hornblende, glaucophane, tremolite, actinolite), phyllosilicates (serpentinite, chrysotile, talc, chlorite, biotite), magnetite, hematite	0.02
Slow weathering	plagioclase feldspars (albite, oligoclase, labradorite), clays (vermiculite, montmorillonite), barite	0.01
Very slow weathering	potassium feldspars, muscovite	0.01
Inert	quartz, rutile, zircon	0.004

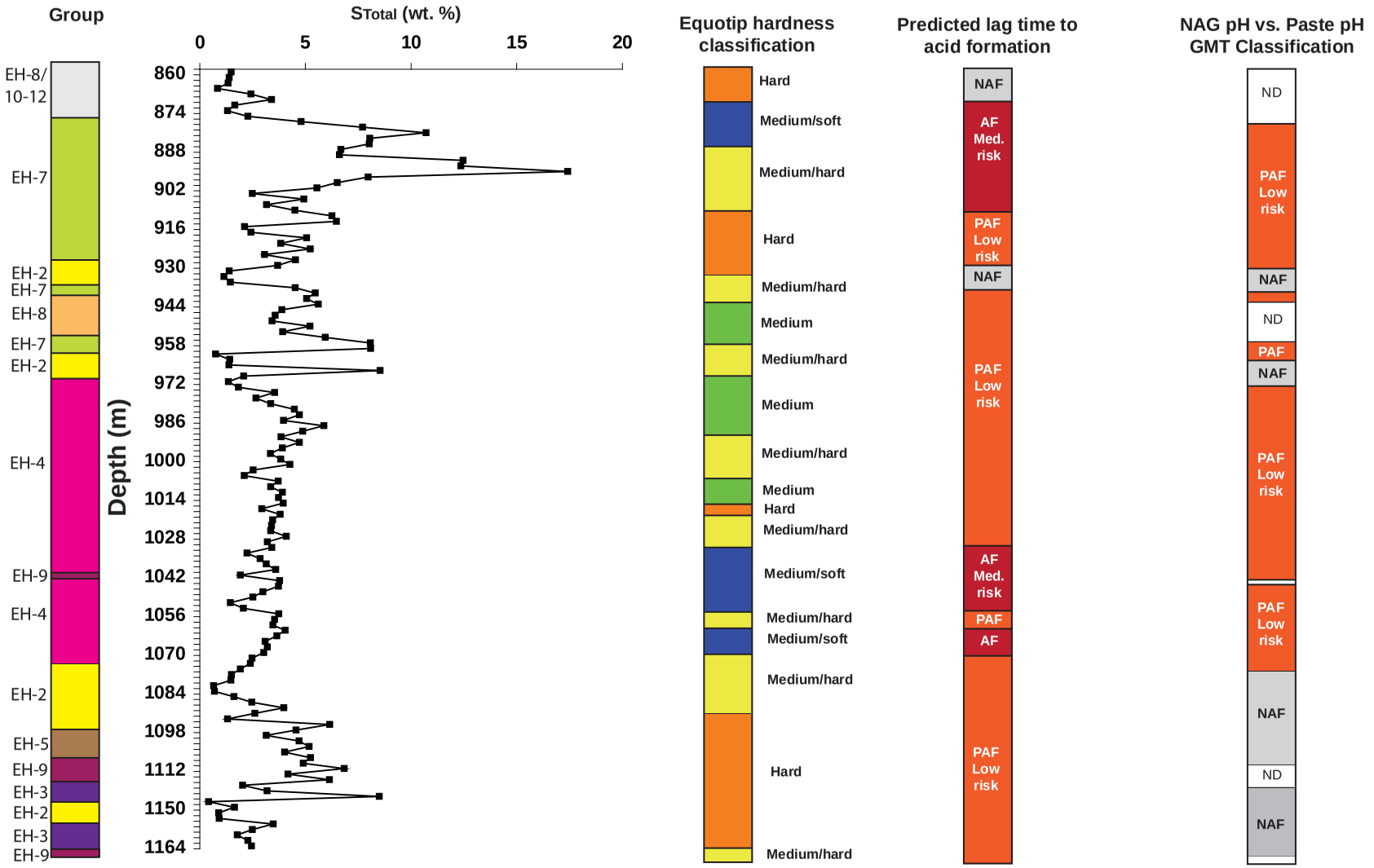

Figure 5.38 Domaining of lag time to acid formation in Ernest Henry drill hole EH 633 based on S_{Total} values (obtained from assay) and EQUOtip hardness (measured by Keeney, 2008). Abbreviations: AF, acid forming; PAF, potentially acid forming; Med, medium.

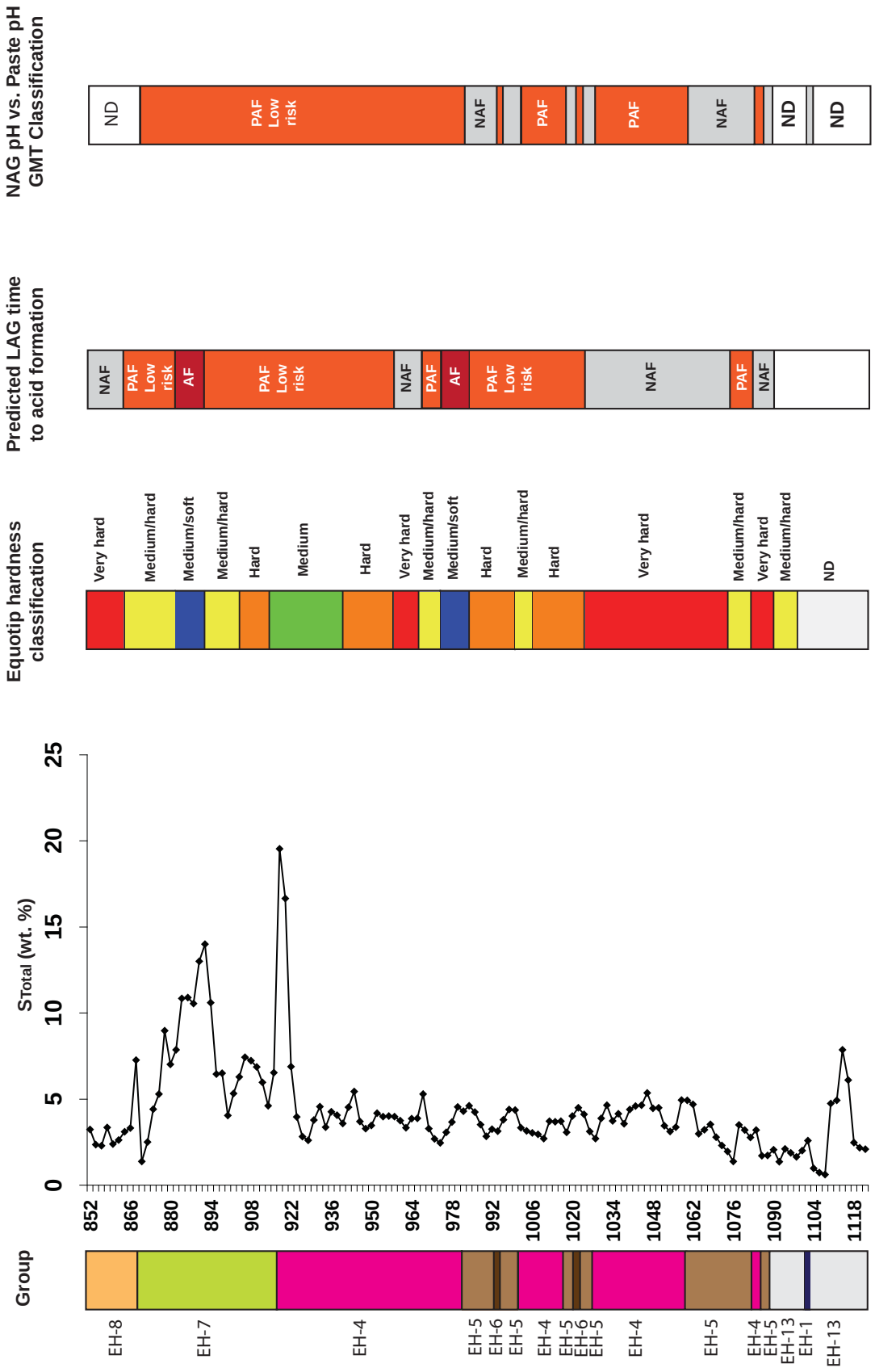

Figure 5.39 Domaining of lag time to acid formation in Ernest Henry drill hole EH 635 based on S_{Total} values (obtained from assay) and EQUOtip hardness (measured by Keeney, 2008). Abbreviations: AF, acid forming; PAF, potentially acid forming; Med, medium.

Table 5.15 Proposed classification criteria for the modal mineralogy weathering index (MMWI).

Classification	Score (/100)
Dissolving	100
Fast weathering	41 to 99
Intermediate weathering	2 to 40
Slow weathering	1
Very slow weathering	1
Inert	0.4 to 0. 9

5.4.5.5 Automated ARDI logging

The ARDI may be regarded as subjective and limited by the fact that only a small number of grains (n=20) are recommended for evaluation. However, the ARDI in its current form satisfies the research objective listed in Section 1.5 to develop a textural method of evaluating acid forming potential. This first required the identification of key textural parameters, with a ranking system subsequently developed. Now the ARDI has been tested, automation is the next logical step. This will increase the number of grains analysed making the calculated ARDI values statistically valid, and limit subjectivity. This section outlines how the ARDI could be automatically performed using geometallurgical data rather than by manually evaluating drill core, petrographic thin sections or MLA images frame-by-frame.

As postulated in Section 5.2.3.3, core photographs collected by a GEOTEK logger could be utilised for *Me*-scale ARDI evaluation. Whilst unprocessed core images could be used at a site with relatively uncomplicated geology and mineralogy (i.e., Croydon), it would not be possible at operations such as Ernest Henry. Instead classified images are required, which can be created using Definiens software (Berry and McMahon, 2008). An example is presented in Figure 5.41 where pyrite is located in a fine-grained magnetite-potassium feldspar-carbonate-quartz matrix (Figure 5.41a). If the unclassified image alone was used, some difficulties in assigning values for parameters D and E would be incurred as discriminating between felsic minerals and quantifying mineral associations may prove challenging. Using the classified image overcomes this, as the mineralogy is better discriminated as each mineral is assigned a distinctive colour (Figure 5.41b). Thus, if *Me*-scale ARDI evaluations are going to be performed manually by a site geologist, then classified images are given preference for use providing they exist.

Using classified GEOTEK logger images from EH 635, Bonnici (2012) demonstrated the possibility of extracting modal mineralogy information, as well as specific textural data from chalcopyrite (i.e., area, length and width, minerals association, distribution) using Definiens software. Bonnici (2012) collected information for >10,000 chalcopyrite grains from EH 635. Chalcopyrite was dominantly associated (>70 %) with potassium feldspar (i.e., a non-acid forming mineral), and pyrite (~10%; net-acid formation anticipated). Bonnici (2012) reported multiple chalcopyrite size populations, however, the equivalent circle diameter was >150 µm for >80% of measured grains. This type of analysis should also be performed on other identified acid forming sulphides (i.e., pyrite), and general trends observed for each textural group reported in a similar manner.

Similarly, *Mi*-scale ARDI evaluations can be performed using data collected from an optical microscopy (i.e., Leica DM6000) or the MLA SPL-Lite function (Section 5.2.3.5). Berry and MacMahon (2008) collected and classified >100 images using the Leica DM6000 optical microscope from EH 633 and 635, however, this was on particulate samples (i.e., not intact). Bonnici (2012) undertook an SPL-Lite MLA study on chalcopyrite grains. This data could be reinterpreted to extract ARDI relevant data as indicated in Table 5.16. Of the two possible *Mi*-scale data sets, SPL-Lite data are likely to be the most statistically sound. Extracting ARDI data in this manner on both scales was not undertaken (due to time limitations), thus the opportunity remains to undertake this analysis.

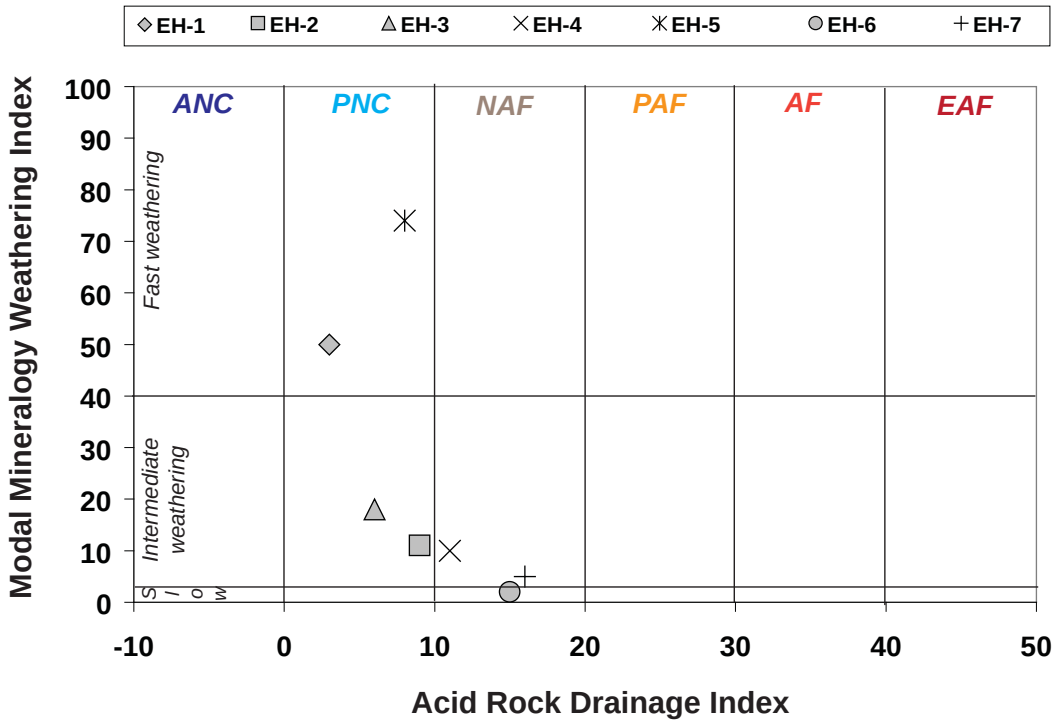

Figure 5.40 Lag-time to acid formation assessment based on modal mineralogy weathering index values plotted against the acid rock drainage index for one sample from each Ernest Henry group (EH-1 to EH-7) identified in EH 633 and 635.

Table 5.16 Potential links between textural data extractable from classified images (collected by a GEOTEK logger (Me-scale), classified optical microscope images (Me-scale) and MLA-SPL-Lite analysis) and acid rock drainage index (ARDI) parameters.

ARDI Parameter	Description	Retrievable from MLA and GEOTEK data?	Relevant MLA parameter
A	Size (max. diameter of sulphide)	Yes	Equivalent Area
B	Alteration of sulphide	No	Development required
C	Sulphide morphology	Yes	PSSA
D	Content of primary neutralisers	Yes	XMOD/ modal mineralogy
E	Sulphide mineral association	Yes	Mineral extraction & association

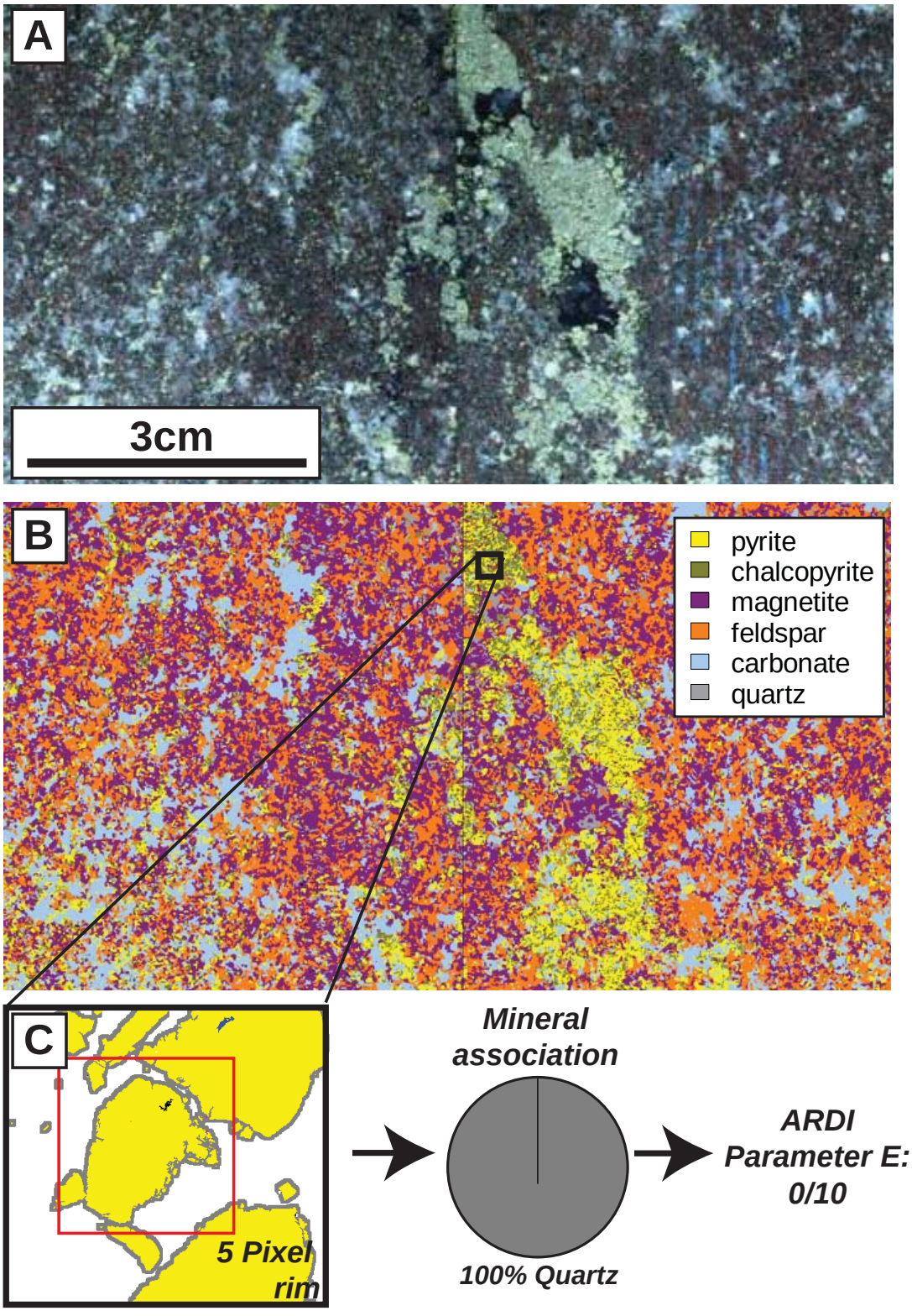

Figure 5.41 (A) GEOTEK Multi Sensor Core Logger images of drill core tiles (3 cm x 6 cm) in Bonnici et al. (2009), taken from EH 633, group EH-7; **(B)** Classified mineral map of the drill core image showing pyrite present as both clots (in the centre-right of the image) and disseminated towards the border. Pyrite clots do not appear directly rimmed by carbonate; **(C)** Extracted pyrite grains with a 5-pixel rim shown which was 100% quartz. Parameter E of the ARDI thus scored this as as 0/10.

5.5 Discussion

5.5.1 GMT classification of ARD potential

Whilst this study was not a full GMT classification of the two drill holes sampled at Ernest Henry, some general observations with respect to acid forming characteristics can be made. First, these results demonstrate that sample mineralogy influences the potential for acid formation or neutralisation more so than texture. Second, disseminated sulphide textures (i.e., group EH-4) and clotted sulphide textures (i.e., EH-7) are more acid forming than massive (i.e., group EH-2) or clast dominated (i.e., EH-1) textures. This proves that the *Me*-scale ARDI criteria selected for parameter C (Table 2.10) is adequate. Breccias with a carbonate matrix (i.e., EH-5) offered the most effective acid neutralising capacity, followed by coarsely clotted carbonate textures (i.e., EH-1, EH-3).

Whilst all samples contained both chalcopyrite and pyrite, the relative reactivity and contribution to acid producing potential of these sulphides were not determined. However, by the ranking given in Moncur et al. (2009), pyrite is likely more reactive, thus samples containing higher pyrite to chalcopyrite can be assumed to form acid at a greater rate. No alteration products of either sulphide were identified by QXRD or SEM studies, which was expected given the depth (<800 m) from which the sampled drill core material originated. Moncur et al. (2009) stated that there is potential for magnetite to influence ARD formation. However, samples containing high magnetite (i.e, groups EH-3, EH-4, EH-6 and EH-7), also contained significant sulphide quantities, thus it was not possible to determine the influence of magnetite.

A dominant mineralogical component of these samples was potassium feldspar, which offers no significant acid neutralising capacity (Jambor et al., 2002) and is considered inert by the ARDI. Thus, for groups dominated by potassium feldspar and with no significant quantities of calcite (i.e., EH-6), net acid formation is predicted. Geometallurgical data indicated that where carbonates were identified in these drill holes, calcite dominated, suggesting that the neutralising capacity predicted by the Sobek method is likely accurate.

The general waste classification scheme presented in Tredinnick and Tuesley (2000; Table 5.1) classified the ore body and its hanging wall margins as PAF, which is broadly in agreement with GMT results. In total, these zones represent 32% of the deposit, with the majority (64%) classified as acid consuming. In general, neutral mine drainage is more likely to originate from deposits which have been subjected to carbonate alteration (Plumlee, 1999), as is the case at Ernest Henry where a post-ore carbonate alteration stage was reported (Hunt and Clifford, 2008). Consequently, neutral mine drainage was identified as a concern at this operation (Dobos, 2008), and indeed for others in the Cloncurry district (Exco Resources Pty Ltd, 2010). In terms of metal and metalloid contents, no samples were considered to pose significant risks (Figures 5.16 and 5.17). On going waste management at this operations must continue to focus on managing neutral mine drainage. However, some consideration should be given to the fact that at depth in EH 633 and EH 635, the majority of sampled groups were classified as PAF by the GMT approach. Thus as the underground expansion continues into the next decade, an updated waste management strategy may need to be adopted.

5.5.2 Linking the GMT approach with geometallurgy

The GMT evaluation at this site demonstrated the importance for precise definition of mesotextural groups at the start of the investigation. Whilst sample grouping systems established on site may state that consideration is given to alteration and texture, they are fundamentally based on lithology. Developing new mesotextural groups or adhering to geometallurgical groups (i.e., as defined at Ernest Henry by Bonnici, 2012) will lead to effective GMT characterisation. Otherwise, groups such as EH-4 and EH-7, (in which both disseminated sulphide and clotted sulphides textures were observed) will return a spread of acid forming classifications. Consequently uncertainty will arise with regards to which samples to take forward for stage-two and stage-three testing. If geometallurgical studies are undertaken at a deposit, then ARD studies should aim to use the identical geometallurgical sampling protocol for stage-one of the GMT approach.

Defining modal mineralogy is the key to understanding acid forming potential, and the GMT approach recommends that one sample per mesotextural group is analysed by QXRD to provide a quantified indication of this. However, in a deposit such as Ernest Henry where there is considerable mineralogical variability, an alternative is required. In Bonnici's (2012) study, modal mineralogy estimates were obtained from both the GEOTEK logger and MLA-XMOD, thus quantified mineralogical data for a large number of samples were available. Additionally, assay data were routinely collected every 2m, thus both sulphur and metal/metalloid values were available at stage-one. The ARDI was undertaken on the *Me*-scale in this study at no extra financial cost (i.e., involved examination of drill core off cuts). However, to perform on site, appropriate training of the site geologists is required. Thus, the only additional stage-one GMT test required here in surplus to geometallurgical data is the paste pH test ($9; ALS 2010). Noble et al. (2012) reiterated that the paste pH test is of limited use for predicting ARD. However, as it is a measure of the current acidity of a sample, it provides a useful insight at the pre-screening stage as to whether a sample is already neutralising, or acid forming. This is illustrated when comparing the Croydon and Ernest Henry datasets, with two examples of samples containing similar sulphide-sulphur values (comprising pyrite and chalcopyrite) shown in Table 5.17. Lower paste pH values are reported for the Croydon samples, which reflect the mineralogy of these samples (quartz-pyrite). The Ernest Henry samples returned higher values as the paste pH was controlled by the presence of calcite, thus indicating that they currently have a higher acid neutralising capacity than the Croydon samples. As rock material is placed onto waste rock piles soon after they have been mined, this test remains of use, as the short-term drainage pH can be anticipated. Noble et al. (2012) reported that the paste pH test is best applied on weathered sulphidic samples following the disuse of the test in some US states (e.g., Pennsylvania). However, the results from Ernest Henry demonstrate that the paste pH test should not only be considered in terms of reflecting inherent acidity, but also neutralising potential. Thus, the benefit of spending the extra sum on paste pH testing is that the short-term ARD risk (either high or low) can be cost effectively determined using a combination of geochemical, mineralogical and textural data across a deposit. This practice is not currently undertaken, as risk is commonly defined based on chemical results alone (e.g., Broadhurst and Petrie, 2010).

Table 5.17 Sulphide-sulphur and paste pH values of four samples from the Ernest Henry and Croydon mining operations. Similar sulphide-sulphur values are shown in columns A and B, but the paste pH varies as a function of mineralogy.

	A		B	
	Ernest Henry	**Croydon**	**Ernest Henry**	**Croydon**
Sulphide-sulphur (%)	4.55	4.47	6.85	6.9
Paste pH	7.98	5.64	7.85	3.18

At stage-two, there is an opportunity to integrate HyLogger data to identify if the Sobek ANC is effective, as relative proportions of carbonates are reported. Whilst Quigley (2012) inferred that there may be methods to quantify HyLogger data, no further details or examples were presented. This study indicated that with a large quantity of paste pH and Sobek ANC values, their relationships with carbonate intensity as measured by HyLogger could be mathematically defined. Thus, if no geochemical data (e.g., paste pH, Sobek ANC) exists for parts of the deposit, carbonate intensity values could be collected, and estimates of paste pH and Sobek ANC calculated. EQUOtip data may have an application in indicating the relative hardness of PAF or ANC zones, thus lag-time to acid formation could be domained. For example, an acid forming rock group identified as hard (e.g., EH-4) would be predicted to weather slowly in a waste rock environment, indicating a significant lag-time to acid formation. Similarly, an acid neutralising group (e.g., EH-5) identified as soft would be anticipated to weather relatively quickly if being used as capping material to PAF material in a waste rock pile. Thus, there would be an initial stage of net-neutralisation, followed by acid formation. This study showed that by domaining in this manner more conservative classifications are returned than when compared against NAG pH versus paste pH values. It would therefore be more effective to use the modal mineralogy weathering index (MMWI) which could be undertaken at stage-one of the GMT approach.

At stage-three fewer ABCC tests (to define effective ANC) are required, if HyLogger data have been collected at stage-two (i.e., only validation samples required). At this stage, geometallurgical data to determine liberation potential collected from acid-forming sulphides by optical microscopy or MLA techniques should be re-evaluated in terms of the ARDI. Computer software to determine ARDI values should be developed to increase the statistical accuracy of this textural assessment. These values can then be used iteratively to improve Me-scale ARDI evaluations performed at stage-one of the GMT approach. This was undertaken here with ARDI values manually calculated based on interpretations of classified MLA images returning slightly higher values only (<9) which did not affect the overall sample classification. No further applications of geometallurgical data were identified at stage-three.

Geometallurgical data integration into the GMT approach is shown in Figure 5.42. Essentially, adopting the same sampling protocol as used in geometallurgical studies is recommended. However, if dealing with overburden or other areas of non-economic waste, geometallurgical sampling is unlikely to be performed. Thus, for these zones the sampling strategy outlined in Section 2.2.1 is recommended (i.e., with at least one sample every 50m). Adopting this methodology at a geometallurgically characterised

deposit should ultimately lead to an improved understanding of the ARD forming potential, and should reduce both environmental and rehabilitation costs associated with waste rock management. However, a larger case-study must be undertaken in order to develop and test this hypothesis further.

5.6 Summary

- The AMIRA P843 GeM project focussed on developing low-cost geometallurgical techniques using samples from a range of mining operations at the pre-feasibility/feasibility stages. The data accumulated have not been used for predicting ARD formation. Therefore, the aim of this chapter was to identify the links between the GMT approach and existing geometallurgical data at the operational Ernest Henry IOCG mine.
- Drill core off cuts (n=30) from drill holes EH 633 and 635 were subjected to the GMT approach. The sample grouping system (based primarily on lithology) developed on site was used, and seven groups (EH-1 to EH-7) were identified.
- The GMT approach classified groups EH-1 and EH-5 as having acid neutralising capacity. Groups EH-4, EH-6 and EH-7 were potentially acid forming, and all other groups were non-acid forming.
- Results indicate that the GMT approach can be effectively applied at an operational mine site, but only if adequate mesotextural grouping is performed at the start of the investigations, which has not performed at Ernest Henry (cf, Treddinick and Tuesley, 2000). As groups EH-4 and EH-7 were not mesotexturally uniform, some conflicting classifications from these groups were reported. Instead the mesotextural grouping proposed by Bonnici (2012) should have been adopted.
- Comparison of XMOD data with QXRD values showed strong positive correlation, thus modal mineralogy can be accurately determined using intact sampless. In a deposit such as Ernest Henry there is considerable mineralogical variability as result of hydrothermal alteration. Thus, using XMOD data collected routinely (i.e., every 2 m) and not using QXRD data collected from a representative sample(s) of each mesotextural group provided an improved understanding of acid forming potential with the inherent mineralogical variability better accounted for.
- Interpretation of Thermal Infrared (TIR) data regarding the relative contents of carbonate minerals allowed for effective ANC to be determined when compared against Sobek ANC values. This was given preference to undertaking ABCC tests.
- Mineral hardness data used in combination with sulphur assay values provided highly conservative estimates with regards to the lag-time to acid formation, when compared against NAG pH versus paste pH classifications. Instead, the proposed modal mineralogy weathering index (which considers the modal mineralogy and reactivity of each mineral at pH 5) provides a better estimate of lag-time to acid formation, particularly when considered against ARDI values.
- Automation of the ARDI may be possible on both the meso-scale and micro-scale using GEOTEK core images and SPL_Lite images with sulphide grains extracted and evaluated against the ARDI parameters using Definiens and Texture viewer software. However, this remains to be undertaken.
- There are several links between GMT approach and geometallurgical data sets, with a second version of the GMT approach developed which includes these (Figure 5.42). GEOTEK logger and MLA-XMOD values are of use in stage-one, HyLogger and EQUOtip at stage-two and computer-based ARDI evaluations of classified images at stage-three.

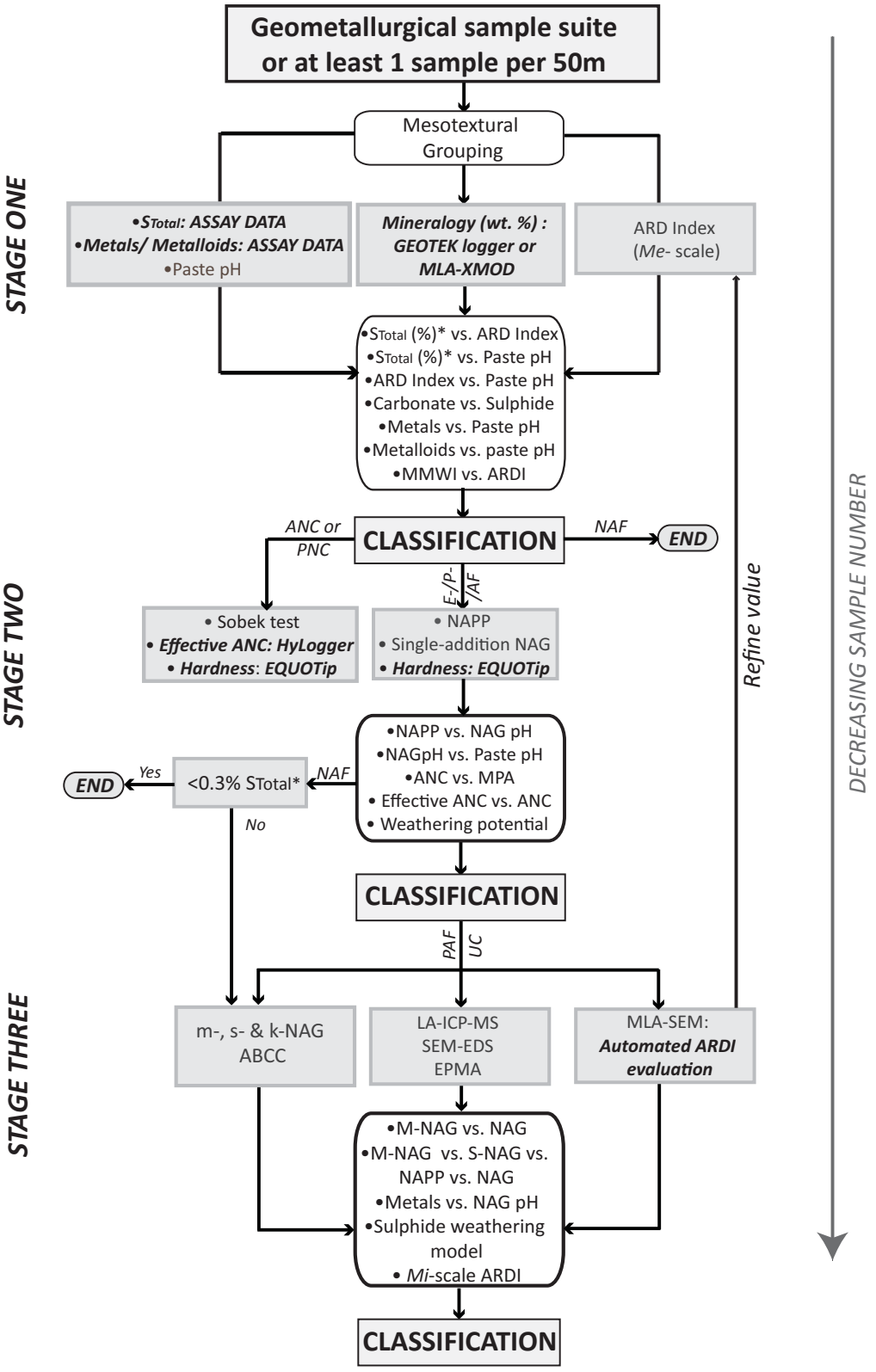

Figure 5.42 Proposed GMT approach at a geometallurgically characterised operational mine. Geometallurgical data is shown in bold and italic. Abbreviations: MLA-XMOD, mineral liberation analysis-modal mineralogy analysis; NAPP, net acid producing potential; ANC, acid neutralising capacity; NAG, net acid generation; MPA, maximum potential acidity; m-, s- and k- NAG, multi-, sequential and kinetic-NAG; LA-ICP-MS, laser ablation inductively coupled plasma mass spectrometry; μXRF, micro-XRF; SEM-EDS, scanning electron microscopy-energy dispersing spectrometry; EPMA, electron probe microanalysis; EAF, extremely acid forming; AF, acid forming; PAF, potentially acid forming; ANC, acid neutralising capacity (* indicates $S_{Sulphide}$ can be used instead).

- Further research efforts should focus on using rapid automated techniques (i.e., GEOTEK logger, HyLogger) to gather mineralogical and textural data which can be used to compute the ARDI automatically. This will provide a statistically significant repository of textural (and mineralogical) data of direct use in domaining and predicting ARD formation.

Chapter 6

Conclusions and further research

6.1 Introduction

A clear understanding of geochemical, mineralogical and textural characteristics of a mineral deposit are required in order to improve predictions of acid rock drainage (ARD) formation from solid mine waste. Considering this, the aim of this thesis was to establish geochemistry, mineralogy and texture in an integrated ARD predictive protocol in order to improve waste characterisation. The specific research objectives were: (a) to establish a protocol for predictive ARD testing of ores and waste rocks which has the potential for incorporation into resource block modeling; (b) to develop a simple scaled textural ARD evaluation scheme which can be used for deposit-scale ARD domaining; (c) to deduce a protocol by which samples are better identified for detailed microtextural sulphide characterisation and kinetic testing; and (d) to define the application of geometallurgical tools in ARD predictive studies. This chapter provides a synthesis of the results from each study site, and presents examples of how the GMT approach could be integrated into the pre-feasibility stages of operations. This chapter concludes with recommendations for future research.

6.2 The GMT approach

This thesis proposes the GMT approach whereby geochemical, mineralogical and textural assessments are undertaken in parallel over three stages, with results cross-checked to provide an accurate sample classification in terms of acid forming potential. Prior to undertaking the GMT approach, samples should be mesotexturally grouped based on mineralogical, textural and chemical similarities. All samples are subjected to simple pre-screening tests at stage-one (e.g., measurement of total-sulphur, paste pH), with the modal mineralogy and total element contents quantified for at least one representative sample per mesotextural group. A simple textural evaluation scheme termed the ARD Index (ARDI) was developed as part of this approach as a stage-one test. Iron-sulphide minerals are individually assessed by five categories (A to E), specifically chosen based on the direct influence on acid formation. Parameters A, B and C examine contents, degree of alteration, and morphology of sulphides; whilst parameters D and E evaluate the neutralising mineral content and the spatial relationship between acid forming and neutralising minerals. Based on these data, a general ARD forming potential classification is given. Only samples classified as acid forming, or as having neutralising capacity are recommended for stage-two testing.

Stage-two involves the use of routine geochemical tests (i.e., NAPP and NAG) in order to cross-check stage-one results, and also to quantify the acid forming/neutralising potential. Samples again classified as potentially acid forming are recommended for stage-three tests. Stage-three utilises advanced

geochemical tests (e.g., advanced NAG tests, acid-buffering characterisation curves) and microanalytical tools (e.g., laser ablation inductively coupled mass spectrometry: LA-ICP-MS, mineral-liberation analysis: MLA) to cross-check any ambiguous results from the previous stages, and for detailed mineralogical and textural characterisation of acid-forming sulphide phases. Based on the final GMT classification assigned at the end of stage-three, samples can be more appropriately selected for kinetic trials. The GMT approach was tested on waste material from the historic Croydon gold-lode mines (operational from 1880s to 90s and 1981 to 1991), and drill core samples from the operational Ernest Henry iron-oxide copper gold (IOCG) deposit. Both sites are located in Queensland, Australia. The geology differed between the two sites, allowing for the selection of the most effective tests and tools for use in the GMT approach, and the critical assessment of both the GMT approach and ARDI.

6.3 Application of the GMT approach at the historic Croydon operations

At the historic Croydon mine operations, ARD conditions (pH <4) were measured within 2 km downstream of two former site operations (Federation/ La Perouse and Glencoe) indicating that ARD sources remain onsite. Additionally, elevated Cd (80 µg/L; DME, 2008) was identified by the Queensland Government Department of Employment, Economic Development and Innovation (DEEDI) as impacting the local ecosystems downstream, particularly cattle livestock. At both former site operations, the dominant waste rock lithologies comprise hydrothermally altered rhyolites which host sulphide bearing quartz lodes. Sulphide mineralogy consisted of pyrite, arsenopyrite, galena and sphalerite. In terms of acid forming potential, the host rocks to mineralisation have little potential for buffering acid produced from sulphide oxidation, as carbonates are notably absent. Effective silicate neutralising minerals (e.g., biotite, chlorite and serpentine) as defined by Bowell et al. (2000) and Jambor et al. (2002) are also absent. Four waste rock piles are present across the operations, from which waste rock samples were obtained (c.2 kg; n=55).

Ten mesotextural groups (A to J) were recognised, with groups A to F and I identified as hydrothermally altered rhyolites (demonstrating a variety of textures); and groups G, H and J as semi-massive/massive quartz sulphides. Mesotextural groups were initially defined using routine geological logging methods. Field portable X-Ray fluorescence (FP-XRF) was trialed as a method to ensure samples within mesotextural groups were chemically similar, and to measure the trace element contents of each sample, as a low-cost alternative to XRF. This study showed that the FP-XRF data were only comparable to XRF analyses if pressed pellets (as used in XRF analyses) were prepared and analysed for each sample, as this homogenised the sample and reduced any matrix effects. Major (i.e., >1 wt. % or 10,000 ppm) mean concentrations of As were present in mesotextural groups H and J only, All groups except I contained minor mean concentrations of Pb, and groups E, G, H, I, and J contained minor mean Zn concentrations. An evaluation of two commonly used SW-IR instruments (PIMA and TerraSpec) to identify hydrothermal alteration minerals was undertaken. This study indicated that the TerraSpec produced better quality data and confirmed that rhyolite dominated mesotextural groups were extensively muscovite-altered.

At stage-one, elemental microanalysis (EA) was given preference to determine S_{Total} for waste rock samples, as the results were in strong agreement with XRF data, indicating its application as a low-cost

pre-screening tool. Mesotextural groups H and J contained the highest quantities of S_{Total} (maximum values 14.5 and 17. 4 wt. % respectively). Paste pH testing was undertaken on three grain size fractions (<75 μm, <5 mm and <20 mm). The <75 μm fraction returned the highest results, which was not expected when considering the higher exposed surface area of sulphide minerals in this fraction. This suggested potential uptake of protons in buffering reactions involving muscovite, iron hydroxide and potassium feldspar. Based on this, the GMT approach recommends that a range of size fractions are used in paste pH testing, as by pulverising samples (e.g., <75 μm), the exposed surface area of buffering minerals is also increased allowing for proton consumption, potentially leading to inaccuracies in classification. Samples from mesotextural group J consistently returned the lowest pH values (pH <4), indicating material from this group is currently acid forming.

An evaluation of computer programmes MINSQ (Berry and Hermann, 2002) and ModAn (Paktunc, 2001) used to calculate modal mineralogy from total element data was undertaken, and limitations were identified with both methods. Thus, mineralogy is best measured using QXRD, with at least one representative sample per mesotextural group subjected to analysis, and resulting mineralogical classifications assigned to all other samples within the particular mesotextural group. Rhyolite mesotextural groups were dominated by quartz, muscovite, potassium feldspar and kaolinite. Secondary iron-sulphates szomolnokite and rhomboclase were detected by QXRD analysis in the majority of mesotextural groups, and are both pyrite weathering products (Jambor, 2000). Scorodite, a weathering product of arsenopyrite was identified by QXRD analysis in groups A to C, E, G and H. Anglesite was identified in mesotextural groups A to F and I to J and is an early alteration product of galena (Diehl et al., 2008; Lottermoser, 2010). The ARDI classified groups A to D, F and I as non-acid forming (NAF), groups E and G were classified as potentially acid forming (PAF) and groups H and J as extremely acid forming (EAF). Based on extensive classification of data collected at stage-one, groups A, B, D, F and I were classified as NAF (and did not technically require further GMT analyses). Group C contained samples which were both classified as NAF and PAF; groups E and G were PAF, and groups H and J were acid forming (AF) and EAF respectively. These groups were identified by stage-one of the GMT approach as requiring stage-two analyses. However, in order to validate stage-one classifications, all waste rock samples were subjected to stage-two testing.

At stage-two, geochemical ANC results derived from the Sobek and Modified Sobek tests were compared against calculated mineralogical neutralising potential (NP) data, and indicated that Sobek results were more accurate for this sample suite. By routine geochemical NAPP versus NAG pH plots, all samples from group J and H were identified as potentially acid forming in addition to several samples from groups G and C. All other samples were non-acid forming. Maximum potentially acidity from groups H and J was calculated by NAPP and NAG methods as >400 kg H_2SO_4/t, indicating material representative of these groups are a significant source of acidity in the Croydon waste rock piles. Classification of data by NAG pH and paste pH confirmed that group J and several samples from group G are high risk, with ARD predicted to form immediately. Group H was also identified as high risk. Based on final stage-two classifications, groups C and E were classified as PAF, group G as AF and groups

H and J as EAF, and therefore were recommended for stage-three testing. All other groups were non-acid forming and therefore were not advanced to stage-three. These stage-two classifications indicated that stage-one pre-screening classifications were accurate.

Advanced mNAG and sNAG geochemical testing results performed at stage-three did not change the classification assigned at the end of stage-two. Of the two advanced geochemical tests, preference is given to the mNAG test for routine use (i.e., to replace NAG testing) when undertaking future geochemical testing at Croydon, or indeed for any waste rock sample with $S_{sulphide}$ contents >0.3 wt.%. Group H was identified by kNAG tests to be the most acid forming, with pH <2 recorded after 5 minutes, followed by group J. Kinetic trials performed on group H material confirmed its highly acid forming nature.

Detailed MLA and SEM analyses indicated the influence of texture on acid formation. In general, (semi)massive sulphide textures were more acid forming than disseminated sulphide textures but this correlated to sulphide contents. In groups C and E, pyrite associated with the fine-grained muscovite-quartz groundmass appeared to have oxidised faster than grains located in quartz veinlets, which is in agreement with observations made by Smuda et al. (2007). SEM analyses showed skeletal grains remained, with secondary sulphate phases having extensively developed around weathered anhedral grains. Generally in groups C and E, larger sulphide grains appeared more weathered than smaller grains, possibly due to an increased concentration of microfractures and galena microinclusions observed in SEM studies. LA-ICP-MS mapping indicated that group C pyrite is As-rich and therefore is more suceptible to oxidation than As-poor pyrite. Secondary Fe-sulphates precipitated around pyrite grains in groups C and E were likely rhomboclase and szomolnokite, and appeared relatively enriched in Zn.

Samples from mesotextural group G contained intergrown sphalerite and galena, with both either associated with each other, pyrite, or quartz. Where galena and sphalerite were intergrown, oxidation progressed at a greater rate as a result of galvanic interactions with sphalerite preferentially weathering as a result of its lower rest potential (-0.24 V) relative to galena (0.28 V; Kwong et al., 2003; Lottermoser, 2010). Generally, larger sphalerite grains (>500 μm) appeared more weathered than smaller grains (<100 μm). Electron microprobe spot analyses revealed that sphalerite in group G is iron rich, containing on average 8.4 wt. % Fe and 0.19 wt. % Cd, indicating that it is more susceptible to oxidation than trace-element poor sphalerite. Sphalerite in this group demonstrated chalcopyrite disease, another factor likely to increase rate of sulphide oxidation. A slight decrease in Zn concentration at the grain boundary was observed in LA-ICP-MS element maps, and provided evidence for the dissolution of sphalerite to form a Zn-deficient layer (Weisner et al., 2004; Cook et al., 2009). Secondary electron images of galena grains revealed the presence of two galena microtextures, with one showing partial alteration of galena with a well-developed reaction front between the primary grain and dull-grey, fine-grained porous secondary anglesite. Diehl et al. (2008) suggest that at this reaction interface, metals are likely to enter solution. Galena was much less weathered in the second microtexture, which was characterised by larger grains with an anhedral morphology and serrated grain boundary with anglesite yet to develop. Galena was also

subjected to LA-ICP-MS element mapping and spot analyses. Both larger (>200 μm) and smaller (<200 μm) grains were analysed and indicated that higher maximum concentrations of As, Ag, Bi, Cd and Cu were measured in larger grains, with similar concentrations of Sb measured in both grain sizes. Overall, galena is considered trace-element rich, and therefore susceptible to weathering (cf. Diehl et al., 2007). Thus, grain size is likely a dominant control on galena oxidation in this group.

Mesotextural group H displayed a massive arsenopyrite-pyrite-quartz texture with scorodite extensively precipitated at the interface of these minerals, and within fractures. Pyrite appears relatively unweathered when encapsulated in scorodite, with euhedral grains well preserved. When intergrown with arsenopyrite, quartz-associated pyrite was weathered to a greater degree. Scorodite was relatively thick within arsenopyrite, with a dendritic texture observed. Smaller quartz-associated arsenopyrite grains (<200 μm) appear unfractured and unweathered. Electron microprobe spot analyses of both larger (<200 μm) and smaller (<200 μm) arsenopyrite grains showed it was trace element poor (Cd, Cu, Co, Ni, Pb, Sb and Zn were below detection limit).

Pyrite was observed as both grains and very fine (<100 μm) veinlets in mesotextural group J. Larger euhedral-subhedral pyrite grains appeared slightly more weathered than smaller grains, with serrated grain boundaries displayed; however, secondary products had yet to develop. Pyrite was occasionally intergrown with galena and demonstrated anhedral morphology. Pyrite veins in quartz and the muscovite-quartz groundmass appeared to have weathered along grain boundaries with secondary sulphates and HFO formed. Like mesotextural groups C and E, pyrite within the volcanic groundmass appears more weathered than grains encapsulated in quartz. Larger pyrite grains appeared more fractured, and therefore more appeared more weathering. Additional factors increasing oxidation rate of pyrite in this group included the presence of galena micro-inclusions, and LA-ICP-MS element mapping also indicated these grains as As-rich. Secondary products were relatively poorly developed, indicating that material representative of this waste rock group is in the early-intermediate stages of weathering by the general mine waste paragenesis proposed in Jambor et al. (2000).

Final GMT classifications were in agreement those assigned at the end of stage-one, and classified two groups as extremely acid forming (H: arsenopyrite-pyrite-quartz, and J: quartz-pyrite), and three as potentially acid forming (C: potassium feldspar-quartz-muscovite-pyrite; E quartz-potassium feldspar-muscovite-pyrite-chalcopyrite-galena; and G: quartz-sphalerite-galena-pyrite). The remainder of groups were classified as non-acid forming, and did not require GMT testing beyond stage-one. These results demonstrated the potential of using stage-one pre-screening tests to rapidly, and cost effectively characterise historic sites such as Croydon, rather than undertaking a protocol which exclusively uses geochemical testing (e.g., AMIRA P387A Handbook, Smart et al., 2002). Based on full GMT analyses, groups G, H and J were identified as requiring column leach testing. Based on these findings, a final GMT approach for application at an abandoned mine site is shown in Figure 6.1.

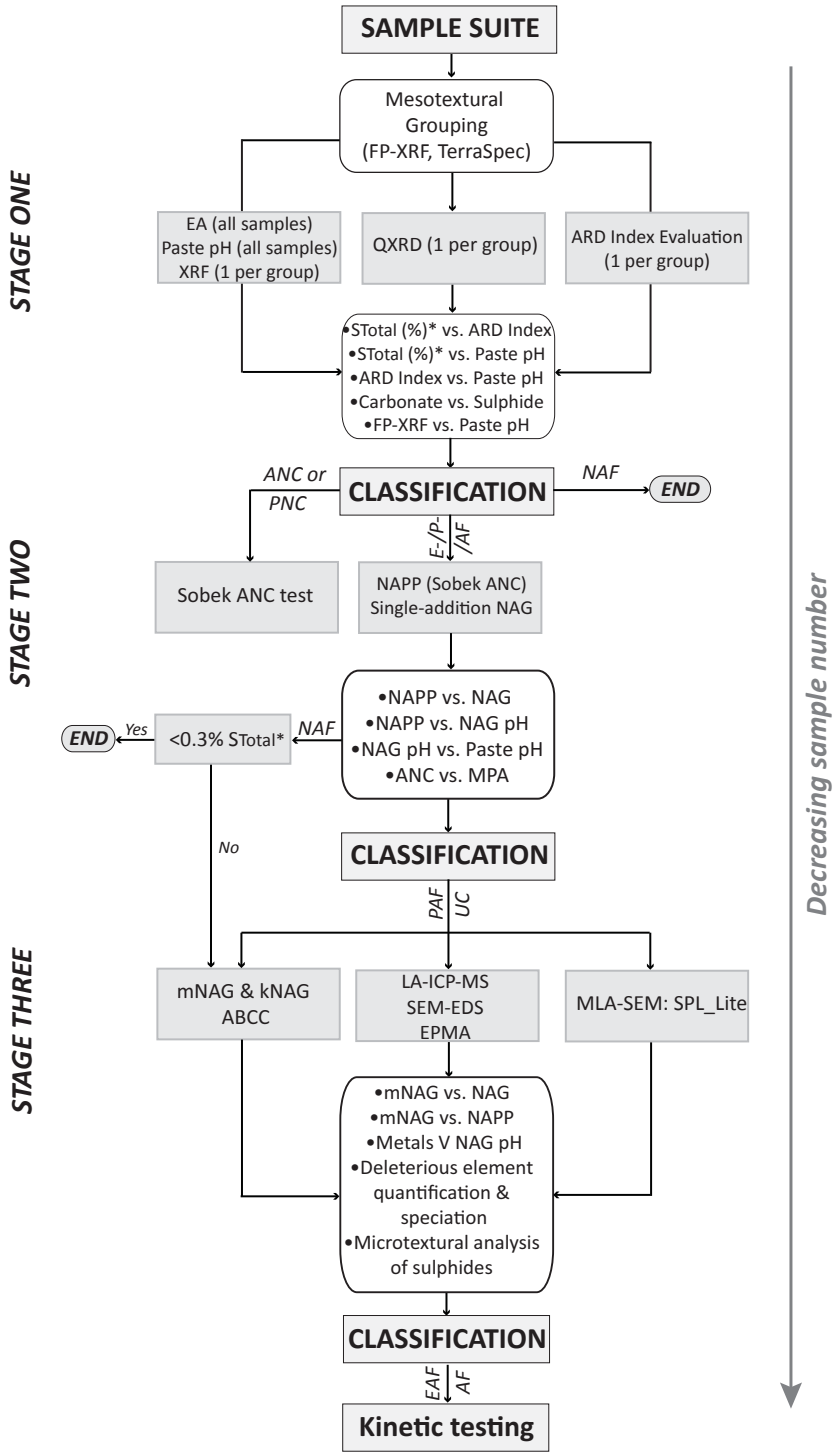

Figure 6.1 Final GMT approach developed primarily for application at historic mine sites with tests/analysis shown in rectangular boxes and evaluations shown in round cornered boxes. Abbreviations: PIMA, portable infrared mineral analyser; EA, elemental microanalysis; (FP) XRF, (field portable) X-ray fluorescence; QXRD, quantitative X-Ray diffractometry; NAPP, net acid producing potential; NAG, net acid generation; MPA, maximum potential acidity; m-, s- and k- NAG, multi-, sequential and kinetic-NAG; LA-ICP-MS, laser ablation inductively coupled plasma mass spectrometry; μXRF, micro-XRF; SEM-EDS, scanning electron microscopy- energy dispersing spectrometry; EPMA, electron probe microanalysis; MLA, mineral liberation analyis; SPL_Lite, sparse phase liberation_lite; EAF, extremely acid forming; AF, acid forming; PAF, potentially acid forming; PNC, potential neutraising capacity; ANC, acid neutralising capacity. *$S_{Sulphide}$ values are preferred however, S_{Total} values can be used in place.

6.4 Mineralogical and chemical evolution of Croydon sulphidic mine wastes

Following the GMT approach classification of Croydon mine waste, material representative of mesotextural groups G (sphalerite-galena-pyrite-quartz), H (arsenopyrite-pyrite-quartz) and J (quartz-pyrite) were selected for kinetic testing. In addition, material from mesotextural group E (porphyritic rhyolite with disseminated pyrite) was also chosen in order to confirm its classification as potentially acid forming. Two grain sizes were used as column feed, with approximately 1 kg of a coarse fraction (-10 mm) and 1 kg of the recommended fine fraction (-4 mm) used to examine the control of grain size on leachate chemistry. Twelve free-draining column leach samples were kinetically leached for thirty weeks following the AMIRA P387A Handbook (Smart et al., 2002). One sample each from groups E, G and H and three from group J were selected for use. Initial geochemical and mineralogical characterisation of these samples confirmed their acid forming potential. An integrated approach to mineralogical analysis was trialled in these experiments in order to understand the temporal controls on leachate chemistry. Modal mineralogy (QXRD) of -4 mm column feed material was measured every 5 weeks. Additionally, particles obtained from the -10 mm column were subjected to microtextural studies (i.e., SEM and LA-ICP-MS) at this time.

Results demonstrate that mesotextural group H was the most acid forming sample of those tested, with pH values below 4 from the start of the column leach tests. Lower pH and high release rates of elements were measured from the -4 mm column, showing a clear grain size control for this group. Mineralogical data indicated extensive replacement of arsenopyrite to scorodite in both columns, a reaction which forms acidity and high quantities of sulphate and iron (both of which were significantly high in the leachate). Two scorodite micro-textures were observed, spherules and acicular grains. Scorodite had significant trace element contents including Cu, Pb and Zn. In later weeks, scorodite weathering (to amorphous ferric arsenates) was observed, and a net decrease in its trace element contents was measured over time. Further research is required to understand the composition of the two scorodite microtextures, and in order determine their crystallinity as a means of understanding their solubility. This information is required for the purpose of site rehabilitation, as then the most appropriate pH conditions can be established to keep scorodite insoluble, thus controlling elution of As and Pb into creeks downstream of the site.

The sulphide mineralogy identified in columns E and J were dominated by As-rich pyrite. Mineralogical data indicated that oxidation progressed in both the -10 mm and -4 mm fraction columns, with ARD conditions (pH <4) measured. Sulphide (pyrite and galena) weathering textures were observed in particles from the -10 mm columns. In the -4 mm columns, a general decrease in pyrite content was measured from week 5 to 30, with minor (<1 wt. %) contents of secondary weathering minerals (e.g., rhomboclase, jarosite, alunite) identified. For two samples (sample 15: group E, and sample 6: group J) lower pH values were consistently measured from the -4 mm column. For the two other columns (sample 6 and 19: group J), there was a less distinct trend until towards the end of the experiment, when lower pH values were consistently measured. The leachate element content from both columns was significantly lower than first-flush results (and indeed the bulk-elemental contents measured at the

start of the experiments). This indicates that whilst textural and mineralogical evidence for sulphide weathering was observed in this group, elements liberated as a consequence were attenuated by fine-grained secondary HFO phases developed as rims and in grain fractures.

Material representative of mesotextural group G showed the most diversity in terms of sulphide mineralogy, but overall was acid forming as a result of the oxidation of pyrite observed in this group. In the -4mm column, effects of silicate neutralisation were realised, hence pH values oscillated over time, but generally were pH <4 from week 6 onwards. Whilst Zn was leached from this group as a result of sphalerite oxidation, very low quantities of Cd were leached from both grain size fractions. Sphalerite was observed to be the least weathered of all sulphides observed.

Through routine mineralogical analysis (i.e., LA-ICP-MS, SEM and QXRD performed every five weeks), a better understanding of sulphide weathering controls and resulting effects on leachate chemistry was gained. However, to further improvement this methodology more samples should be collected for QXRD analysis from each individual grain size fraction column. Furthermore, it may be more beneficial to prepare and characterise a range of polished laser mounts intially, place them in the columns, and systematically remove and characterise these at five week time intervals. This will allow for data to be directly compared, with mineralogical, textural and chemical changes better identified.

Comparison of grain size fractions tests confirmed that for the waste rock material tested, increasing the sulphide surface area (i.e., decreasing grain size) had the overall effect of decreasing pH in spite of the development of secondary sulphate and HFO coatings on these minerals. As there was a general absence of primary neutralising minerals in the Croydon waste materials, this relationship was uncomplicated (cf. Lapakko et al., 2006). These data suggest that the kinetic tests may not run for long enough with weathering of secondary phases such as scorodite and anglesite only starting to occur towards the end. Therefore, a 30 week test may not be appropriate to provide data to guide long term rehabilitation strategies.

These experiments indicate that the mineralogical and chemical evolution of mesotextural groups G, H and J are quite different, and therefore, should be treated as individual entities when undertaking site rehabilitation works, and not all generally considered as one collective unit of sulphide waste (cf. Harris et al., 2003). If such a blanket approach was adopted, then interactions between leachate generated from material representative of different groups may result in the liberation of potentially deleterious elements. For example, acidity generated from mesotextural groups H and J may react with galena and sphalerite in group H, causing the liberation of Cd and Zn. Thus, segregation of these mine wastes material representative of these mesotextures from those identified as NAF is recommended, with each placed in individual repositories. Such a strategy will remove the source of acidity and potentially deleterious elements which should prove more effective than treating acidic waters emanating from the sites (i,e., lime dosing) as was previously undertaken by the DME (2008) with limited success.

A geochemical study undertaken in the Croydon district showed elevated concentrations of As, Cu and Pb relative to ANZECC ISQG-high values at the mine sites, but as pH values increased >4.5 downstream of the sites, element concentrations declined. Around pH 4.5 to 5, As and Pb likely sorbed onto Fe-bearing precipitates (cf. Ashley et al., 2004; Hudson-Edwards and Edwards, 2005; Lottermoser, 2010). Copper sorbed onto Fe-bearing precipitates around neutral pH (cf. Hudson Edwards and Edwards, 2005). Cadmium and Zn concentrations correlate with Mn indicating coprecipitation of these elements with manganese oxides. At the confluence of both creeks draining the sites (c.10km downstream of both operations), neutral pH was measured, with metal (Cd, Cu, Pb and Zn) concentrations below ANZECC (2000) guideline values. The death of cattle livestock around the Croydon district was attributed to Cd-poisoning. However, kinetic test results indicate that the Cd elution from group G is very low (<0.05 mg/L^{-1}). Additionally, Cd concentrations are relatively low from 1km downstream of Glencoe. As the Croydon mine sites are currently designated grazing land, a more likely cause of death is through the consumption of the plant Calotrope observed around the Croydon mines (cf. Lottermoser, 2011).

6.5 Application of geometallurgical techniques for predicting ARD

The emerging discipline of geometallurgy focuses upon integrating geology, geostatistics and metallurgy, and fundamentally aims to provide constrained inputs that reflect inherent geological variability and its impact on metallurgical performance. Such an aim can also be adopted for ARD prediction at the early stages of mine operations. The Ernest Henry iron-oxide copper gold deposit was subjected to extensive geometallurgical characterisation as part of the AMIRA P843 GeM project. However, these data were not used for ARD prediction. Therefore, the opportunity arose to explore the links between existing geometallurgical data and the GMT approach.

Drill core off cuts (n=30) samples from drill holes EH 633 and 635 were subjected to the GMT approach. The sample grouping system (based primarily on lithology) developed on site was used, and seven groups EH-1 to EH-7 were identified. Groups EH-1 (matrix supported breccia with potassium feldspar clasts in a magnetite-calcite-quartz matrix) and EH-5 (crackle breccia with potassium feldspar clasts and a calcite matrix) were identified as having an acid neutralising capacity. Groups EH-4 (breccia with calcite and potassium feldspar clasts in a magnetite matrix containing fine-grained disseminated pyrite and chalcopyrite); EH-6 (breccia with coarse-grained intergrown pyrite-chalcopyrite in a calcite-quartz-magnetite-potassium feldspar matrix); and EH-7 (matrix supported breccia with potassium feldspar clasts hosted in a magnetite-calcite-quartz matrix containing coarse-grained disseminated pyrite and chalcopyrite) were classified as potentially acid forming. Groups EH-2 and EH-3 were classified as non-acid forming. These results indicate that the GMT approach can be effectively applied at an operational mine site, but only if adequate mesotextural grouping is performed at the start of the investigations. As groups EH-4 and EH-7 were not mesotexturally uniform, some conflicting classifications from these groups were reported. Thus, at operational mine sites, samples should not be selected for predictive ARD testwork based on lithology, but based on the mesotexture. At Ernest Henry, the geometallurgical grouping system proposed by Bonnici (2012) should have instead been used, as indicated through reevaluating GMT data using this method.

Comparison of MLA-XMOD data with QXRD from each group showed strong agreement, thus carbonate/ sulphide classifications can be performed accurately using these geometallurgical data (i.e., no additional costs need to be spent as part of the GMT approach for QXRD analysis if these data already exist). Additionally, in a deposit such as Ernest Henry there is considerable mineralogical variability as result of hydrothermal alteration. Thus, using XMOD data collected routinely (i.e., every 2m) and not using QXRD values from a representative sample(s) of a mesotextural group, an improved understanding of acid forming potential will be gained.

The Australia-developed HyLogging^{TM} systems are automated platforms to rapidly and systematically collect infrared spectroscopic reflectance data at dense sample spacing from drill core, chips or powders (Huntington et al., 2006; Quigley, 2012). Constituent mineralogy is determined based on the principles of reflectance spectroscopy, with mineral identification made possible based on the resulting 'spectral fingerprint' or 'signature' observed in the spectral response curve (Huntington et al., 2006; Quigley, 2012). Thermal Infrared (TIR) data generated by a HyLogger on the relative contents of carbonate minerals allowed for effective ANC to be determined for samples in these drill holes, when compared against Sobek ANC values. Results showed that Sobek ANC data accurately represents the effective neutralisation capacity of these samples, as the carbonate mineralogy is dominated by calcite. Cross-checking Sobek ANC data in this manner was given preference to using the ABCC test method.

An understanding of the susceptibility of a lithology to weathering is required to understand how rapidly potentially acid forming minerals will become exposed in a waste rock pile. This is qualitatively evaluated by the ARDI through parameter E, however, it is not directly measured. Therefore, the application of EQUOtip was explored. EQUOtip is a rebound hardness tester used in the AMIRA P843 GeM project as a routine non-destructive core-based measurement technique. Values (0 to 1000) are measured in Leebs (Ls) with higher values indicating greater hardness. Mineral hardness data used in combination with sulphur assay values provided highly conservative estimates with regards to the lag-time to acid formation (when compared against NAG pH versus paste pH classifications). Instead, the modal mineralogy weathering index proposed in this thesis (which considers the modal mineralogy and reactivity of each mineral at pH 5) provides a better estimate of lag-time to acid formation, particularly when considered against ARDI values.

Whilst it was not demonstrated in this thesis, the potential for automation of the ARDI was identified on both the meso-scale and micro-scale by using drill core images generated by a GEOTEK multi-sensor petrophysical core logger, and MLA-SPL_Lite images. Sulphide grains could be extracted from classified images produced by both techniques and evaluated against the ARDI parameters using modified Definiens and Texture viewer softwares. This would provide a signficant quantity of ARDI values improving the statistical robustness of this evaluation, and additionally would negate the potentially subjective nature of the evaluation. However, the ARDI should still be performed routinely as part of stage-one during drill core logging, as data from this study showed that accurate classifications were made based on *Me*-scale values alone. Furthermore, these data were crucially required when cross-check against paste pH and $S_{Sulphide}$ values in order to classify these samples at stage-one.

Based on this study, several clear links between the GMT approach and geometallurgical data sets were identified with a modified version of the GMT approach proposed for operational sites which have geometallurgical data available (Figure 5.42). GEOTEK logger, and MLA-XMOD values are of use at stage-one, Hylogger and EQUOtip at stage-two, and computer-based ARDI evaluations of classified images at stage-three.

6.6 Improving ARD risk assessment using the GMT approach

Risk management is a valuable tool in facilitating improved environmental planning and business outcomes (Lee, 1999; Broadhurst and Petrie, 2010). There are several published guidelines regarding ARD risk assessment, with the Guide to Leading Practice Sustainable Development in Mining (Australian Government, 2011) most commonly used in Australia. In this guide, it is recommended that risk assessment in ARD terms is undertaken at all stages of the mine life cycle, with the outcomes of these assessments used to drive decisions on the future direction of the project. The GARD Guide (2010) also adopts this principle. A significant part of the risk management procedure is adequately defining ARD sources (Table 6.1). It is by better identifying and characterising ARD sources that the GMT approach can improve risk assessment relative to more commonly used predictive protocols (i.e., the Wheel approach and the AMIRA P387A Handbook; Section 1.4).

Table 6.1 Risk management procedure for mine sites (modified from Lee, 1999). The GMT approach improves risk management through better identifying and characterising sources of acid rock drainage in step 2.

Step	Name	Description
1	Establishing the context	Define policy, purpose, objective, success criteria, assessment end points, receptors
2	Identify the risk	*Define sources*, pathways, concerns, and consequences
3	Analyse the risk	Calculations (identify concerns and possible outcomes); certainty and uncertainty
4	Assess and prioritise risks	Compare with criteria; prioritise
5	Manage (treat) the risks	Mitigation, communication; develop and implement contigency and management plans
6	Review and monitor	Risk management plan; continue reviewing and monitoring; assess effectiveness of treatment

One manner in which the GMT approach allows for improved ARD risk assessment is that the sample numbers required for stage-one are more aligned to best practice sample numbers recommended by the Australian government (i.e., several hundred samples tested at the pre-feasibility stage; Table 2.1). Various guidelines exist which offer methods by which to calculate the number of samples required for predictive ARD testing (e.g., Figure 2.2; SRK, 1989 in Downing, 1999). However, a review of the actual sample numbers used in ARD predictive studies for various deposits indicated that best practice is rarely achieved (Table 6.2). Inadequate ARD sampling may be explained by the high costs associated with ARD testing if either the wheel approach ($>280 AUD per sample) or the AMIRA approach ($>260 per sample) are used as illustrated in Figure 6.2 (NB. costs are calculated based on costs given by ALS, 2012; Mason Geoscience, 2012, and McKnight Mineralogy, 2011).

Table 6.2 Examples of samples numbers used for ARD testing for various mineral deposit types with best practice values (calculated from the SRK, 1989 hypothetical sample curve; Figure 2.2) NB. Deposits have not been named due to site confidentiality issues.

Deposit type, location and year of sampling	Estimated resource (Mt)	Actual sampling	Estimated best practice sample numbers
Epithermal-porphyry, Australia (2008)	200	217	250
Iron oxide copper-gold, Australia (2000)	500	118	300
Porphyry, South America (2010)	750	96	350
Porphyry Au-Cu, Australia (2009)	850	188	400
Epithermal porphyry, Asia Pacific (2010)	>1000	155	500

The predicted costs associated with ARD prediction at these various mine operations based on the actual sample number used (Table 6.2) and wheel approach costing indicate that approximately $20,000 to $65,000 AUD were likely spent (Figure 6.2). If best practice sample numbers had been used, this range increases to approximately $65,000 to $140,000 AUD (Figure 6.3). For example, at the epithermal-porphyry located in Asia-Pacific, the cost of ARD testing would increase significantly (i.e., $95,000 AUD) if best practice sample numbers hads been used (Figure 6.3). If stage-one of the GMT approach had instead been used, then the best practice number of samples could have been tested, as low-cost tests are utilised. Data presented in this thesis demonstrate that classifications assigned at the end of stage-one were accurate relative to those assigned after routine geochemical stage-two tests, and thus are approriate for use when undertaking deposit-wide ARD domaining.

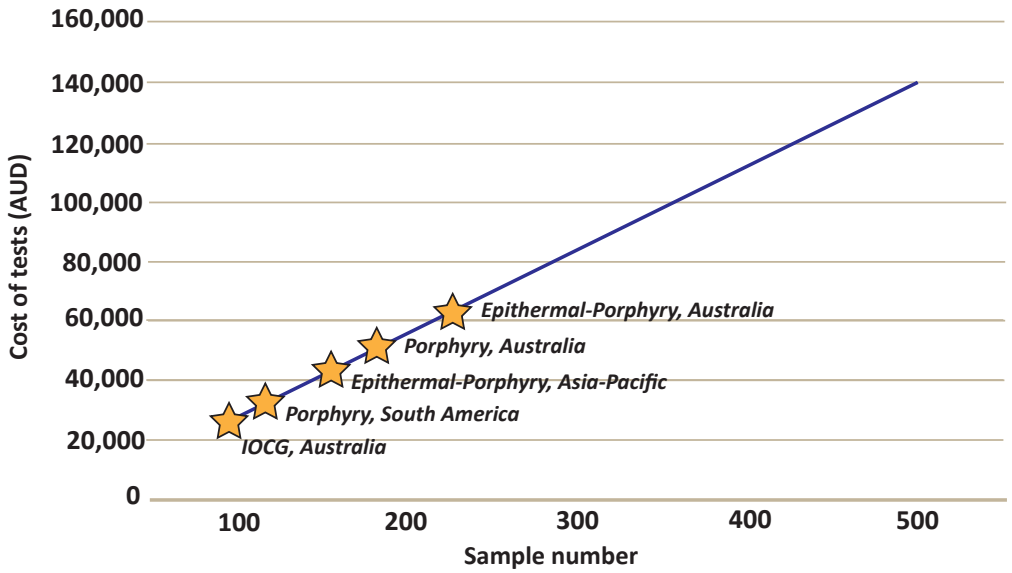

Figure 6.2 Predicted costs likely spent on ARD predictive testwork following the wheel approach, based on the actual sample numbers collected at the five deposits listed in Table 6.2.

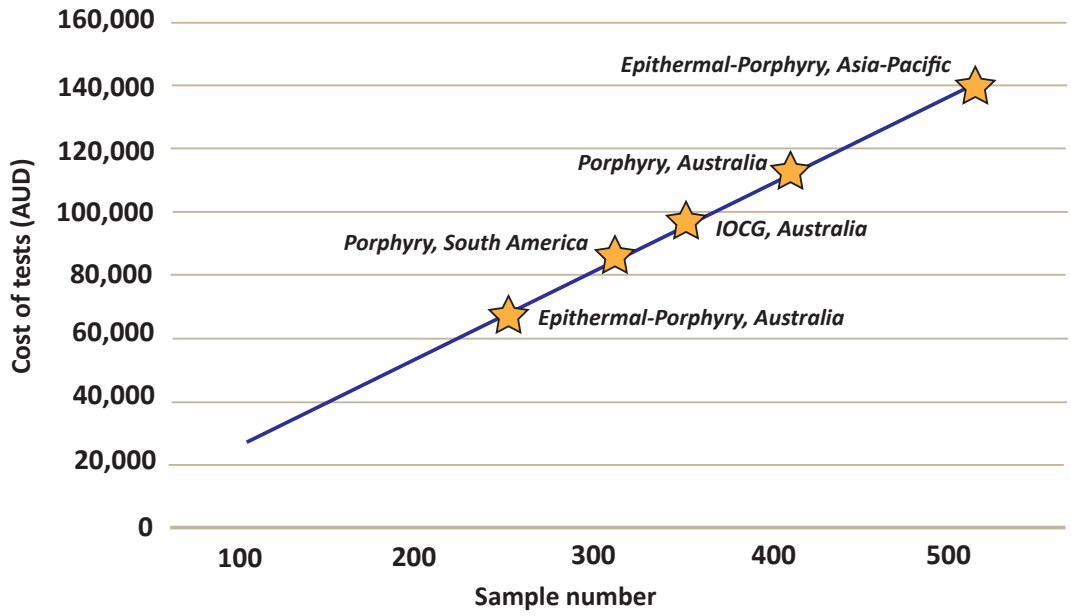

Figure 6.3 Predicted costs spent on ARD testwork using best practice sample numbers folllowing the wheel approach, for the five deposits listed in Table 6.2.

Using the calculated cost of stage-one tests (Appendix 6.1), an economic comparison of the GMT approach and the wheel approach costs based on best practice sampling is presented in Table 6.3 for the deposits listed in Table 6.2. Additionally, if geometallurgical characterisation of a deposit has been undertaken, then stage-one testing costs are further lowered as S_{Total} (or $S_{Sulphide}$), assay data and modal mineralogy data likely exist. Thus, only funds for paste pH testing are required, with the ARDI performed by site geologists. This is also shown in Table 6.3.

Table 6.3 Predicted GMT and wheel approach ARD testing costs using best practice sample numbers (calculated from the SRK, 1989 hypothetical sample curve; Figure 2.2) for the deposits listed in Table 6.2.

Deposit type, location and year of sampling	Wheel Approach costings (AUD)	GMT approach stage-one costing:s with geometallurgical data available (AUD)	GMT approach stage-one costings: without geometallurgical data available, but with mineralogy and or total element data required (AUD)
Epithermal-porphyry, Australia (2008)	65,000	2,250	50,000
Iron oxide copper-gold, Australia (2000)	78,000	2,700	60,000
Porphyry, South America (2010)	91,000	3,150	70,000
Porphyry Au-Cu, Australia (2009)	104,000	3,600	80,000
Epithermal porphyry, Asia Pacific (2010)	140,000	4,500	100,000

Considering the maximum estimate of stage-one costs (whereby all samples are identified as requiring mineralogical testwork and full assay elemental analysis, which would not be the case in practice as the GMT approach does not recommend this), the overall testing costs are lower than the wheel approach. For example, at the Epithermal porphyry, in Asia-Pacific, up to $40,000 AUD less spent would have been spent if this type of testing had been performed. In reality, the amount likely spent on stage-one characterisation would be between the values shown in last two columns of Table 6.5. Thus, through using stage-one of the GMT approach, effective domaining of an ore deposit in terms of ARD forming potential is possible. As operational mine sites start to implement geometallurgical characterisation protocols (e.g., Los Broncos porphyry-Cu-Mo, Chile, South America; Escondida porphyry Cu-Au, Chile, South America; Cadia East porphyry Au-Cu, Australia), the opportunity is presented to also integrate stage-one of the GMT approach, with the samples collected for geometallurgical studies also used for ARD characterisation. Adopting such an integrated approach is the best manner by which geostatistically sound deposit-wide ARD block models can be populated, and improved waste rock management plans developed.

Through stage-one testing, samples identified as NAF are not required for further testing, allowing for more funds to be spent on characterising acid forming samples (i.e., more stage-three detailed microanalysis could potentially be undertaken). For example, at Croydon, the majority of samples were classified as NAF, and did not require testing beyond stage-two. At a historic mine site under stewardship of the local government (such as Croydon) such cost-saving is benficial as budgets for site characterisation and rehabilitation works are often limited (Cottier, 2011, pers. comm). Thus, the GMT approach represents an improved site-specific protocol by which to undertake ARD risk assessment at both operation and historic mine sites as potential sources are cost effectively identified and subjected to appropriate testing in a more structured and logical manner relative to those most commonly used.

6.7 Advancement in knowledge

This section demonstrates how the research objectives (listed in Section 1.5.1 and Section 6.1) have been satisified, and how these findings contribute to improving the field of acid rock drainage prediction.

- The geochemistry-mineralogy-texture (GMT) approach proposed in this thesis is an improved protocol by which to systematically predict and classify acid forming potential of waste rock. The GMT approach comprises of three stages, and integrates the use of geochemical, mineralogical and textural tests and data. At the start of the GMT approach, samples are categorised into groups based on the texture demonstrated in hand specimen samples (i.e., mesotexture) and not by lithology. This thesis demonstrates applications of the GMT approach at both historic and operational mine sites. Stage-one of the GMT approach utilises simple and low-cost tests which can be effectively performed on best practice sampling numbers, ultimately improving ARD block modelling.
- The Acid Rock Drainage Index (ARDI) was developed as a method by which to evaluate both meso-scale (e.g., drill core) and micro-scale (e,g., petrographic thin section) samples to texturally assess acid forming potential. This thesis has demonstrated that at an operational mine site, meso-scale

ARDI evaluations alone can generate valuable data, which can be screened against geochemical and mineralogical results to accurately classify acid forming potential on a deposit-wide scale.

- Mesotextural groups identified as highly acid forming at the end of stage-two are recommended for detailed microtextural characterisation using techniques including LA-ICP-MS, MLA, SEM and EPMA. Such targeted microanalyses are performed to understand the sulphide oxidation controls of significantly acid forming groups, in order to improve waste management planning. By undertaking the GMT approach, highly acid forming groups are effectively identified and prioritised for kinetic testing.
- The application of geometallurgical tools and datasets in ARD prediction is demonstrated in this thesis, with datasets generated by HyLogger (relative carbonate abundance), MLA (modal mineralogy) and EQUOtip (mineral hardness) compared alongside GMT classifications, with the links identified. This thesis described the potential for utilising classified mineral maps produced over a range of scales (e.g., from a GEOTEK core logger and a LEICA DM6000 optical microscope) from which to compute ARDI evaluations, thus improving textural ARD assessment.

6.8 Further research

Based on the findings of this thesis, several areas for further research are listed in this final section:

- The GMT approach must be further tested and developed at additional operational mine case study sites. Ideally, the integration of stage-one tests into a geometallurgical characterisation protocol would be trialed to examine the possibility of collecting deposit-wide ARD data (using appropriate sample numbers at a lower initial cost) in order to develop and domain acid forming potential.
- The GMT approach should also be trialed at another historic mine with more complicated waste-rock mineralogy, to allow for the effectiveness of mesotextural grouping and the ARDI to be better evaluated.
- Computed software must be developed which can perform the ARDI on iron sulphide minerals identified in classified mineral maps generated from geometallurgical analytical instruments such as GEOTEK logger and MLA. This computer software should be further developed to simulate and predict the weathering rate and thus the lag-time to ARD formation and liberation of metals.
- Laser Raman spectroscopy was identified as a tool for use in mine waste characterisation (Table 2.16), however, its application was not explored in this thesis. Thus the benefits and limitations of this tool must be fully evaluated to resolve it has an application in the GMT approach. Preliminary work has since been undertaken by the author, particularly on scorodite identified in Croydon mesotexutral group H (arsenopyrite-pyrite-quartz). Indeed, LA-ICP-MS characterisation of scorodite from other deposits should be undertaken to determine the Pb content, and further analyses should be performed to resolve the manner by which Pb is incorporated in scorodite.
- A detailed chemical and mineralogical study of the effects of trace element contents in arsenopyrite and galena must be undertaken to determine more accurately the exact concentrations of such

elements which will cause significant acceleration of oxidation. Additionally, the potential effects of Co and Ni toxicity on arsenopyrite oxidising bacteria should be further investigated.

- Development of 'blended NAG' tests to more accurately evaluate the drainage chemistry of a waste rock pile should be pursued (this was intiated by the author and funded by the Society of Economic Geologists through a research grant). This test is designed to measure the interactions between material representative of different mesotextural groups, and characterise the resulting drainage chemistry. This test should be further developed, and correlated with long-term column leach kinetic tests in which mineralogical and microtextural analyses are routinely undertaken.
- The links between assay data and predicting mineralogy were here reviewed, however, this research demonstrated that the available computer methods have limited application for mine waste samples. Therefore, a new piece of software which can estimate mineralogy based on assay (or FP-XRF) data is required, and would significantly improve determination of mineralogy at stage-one.This has significant implications at both operational and historic sites. For example, at an operation site mineralogy would not need to be determined by XMOD.
- Further exploration of geometallurgical links and the GMT approach need to be established at Ernest Henry, particularly with respect to utilising GEOTEK petrophysical data, and examining how HyLogger data can be quantified.
- The acid forming potential of magnetite must be better documented, as whilst this was recently summarised in Moncur et al. (2009), a more detailed study is required to document with clarity its exact acid forming characteristics.

References

ABARE, 2008. Australian Mineral Statistics, September quarter 2008, Canberra, 10 December (http://adl.brs.gov.au/data/warehouse/pe_abarebrs99001588/ams_dec_08.pdf).

Abbassi, R., Khan, F., Hawbolt, K., 2009. Prediction of minerals producing acid mine drainage using a computer-assisted thermodynamic chemical equilibrium model. Mine Water and the Environment, v.28, p.74-78.

Abraitis, P., Pattrick, R., Kelsall, G., Vaughan, D., 2004. Acid leaching and dissolution of major sulphide ore minerals: processes and galvanic effects in complex systems. Mineralogical Magazine, v.68, p.343-351.

Adam, K., Kourtis, A., Gazea, B., Kontopoulos, A., 1997. Evaluation of static tests used to predict the potential for acid drainage generation at sulphide mine sites. Transactions of the Institute of Mining and Metallurgy, v.106, p.A1-A8.

Adams, F., Janssens, K., Snigirev, A., 1998. Microscopic X-Ray fluorescence analysis and related methods with laboratory and synchrotron radiation sources. Journal of Analytical Atomic Spectrometry, v.13, p.319-331.

Akabzaa, T.M., Benoeng-Yakubo, B.K., Seyire, J.S., 2007. Impact of mining activities on water resources in the vicinity of the Obuasi mine. West African Journal of Applied Ecology, v.11, p.101-109.

Al, T.A., Blowes, D.W., Martin, C.J., Cabri, L.J., Jambor, J.L., 2007. Aqueous geochemistry and analysis of pyrite surfaces in sulphide-rich mine tailings. Geochimica et Cosmochimica Acta, v.61, p.2353-2366.

Alruiz, O.M., Morrell, S., Suazo, C.J., Naranjo, A., 2009. A novel approach to the geometallurgical modelling of the Collahuasi grinding circuit. Minerals Engineering, v.22, p.1060–1067.

Alvarez, S.M., Ridolfi, B.A., 1999. Moon Creek reclamation project creative solution for an historic mine site, SME Annual Meeting March 1-3 1999, Denver Colorado, preprint 99-98, 7 pp.

Andrina, J., Wilson, G.W., Miller, S., Neale, A., 2006. Performance of the acid rock drainage mitigation waste rock trial dump at Grasberg mine, 7th International Conference on Acid Rock Drainage (ICARD), March 26-30, 2006, St. Louis MO. Published by the American Society of Mining and Reclamation (ASMR), 3134 Montavesta Road, Lexington, KY 40502, p.30-44.

ANZECC, 2000. Australian guidelines for water quality monitoring and reporting. National Water Quality Management Strategy Paper No 7, Australian and New Zealand Environment and Conservation Council & Agriculture and Resource Management Council of Australia and New Zealand, Canberra.

Aranda, C.A, Klein, B., Beckie, R.D., Mayer, K.U., 2009. Assessment of waste rock weathering characteristics at the Antamina Mine based on field cell experiments. In Securing the Future and 8th ICARD: Proceedings of the Conference, Skellefteå, Sweden.

Ashley, K.J, Callow, M.I., 2000. Ore variability: Exercises in geometallurgy. Engineering and Mining Journal, v.201, p.24-28.

Ashley, P.M., Lottermoser, B.G., 1999. Arsenic contamination at the Mole River mine, northern New South Wales. Australian Journal of Earth Sciences, v.46, p. 861-874.

Ashley, P.M., Lottermoser, B.G., Collins, A.J., Grant, C.D., 2004. Environmental geochemistry of the derelict Webbs Consols mine, New South Wales, Australia. Environmental Geology, v.46, p.591-604.

Australian Government Department of Industry, Tourism and Resources, 2007. Managing acid and metalliferous drainage, Leading Practice Sustainable Development Program for the Mining Industry, Canberra, 96p.

Australian Laboratory Services, 2010. Service Catalogue, p. 95-96.

Aykol, A., Budakoglu, M., Kumral, M., Gultekin, A.H., Turhan, M., Esenli, V., Yavuz, F., Orgun, Y., 2003. Heavy metal pollution and acid drainage from the abandoned Balya Pb–Zn sulfide Mine, NW Anatolia, Turkey. Environmental Geology, v.45, p.198–208.

Baker, B.J., Banfield, J.F., 2003. Microbial communities in acid mine drainage. FEMS Microbiology Ecology, v.44, p.139-152.

Barton, P.A., Jr., Bethke, P.M., 1987. Chalcopyrite disease in sphalerite: Pathology and epidemiology. American Mineralogist, v.72, p. 451–467.

Belcher, R.W., Rozendaal, A., Przybylowicz, W.J., 2004. Trace element zoning in pyrite determined by PIXE element mapping: evidence for varying ore-fluid composition and electrochemical precipitation of gold at the Spitskop deposit, Saldania Belt, South Africa, X-Ray Spectrometry, v.33, p.174-180.

Bernaus, A., Gaona, X., Esbri, J.M., Higueras, P., Falkenberg, G., Valiente, M., 2006. Microprobe techniques for speciation analysis and geochemical characterization of mine environments: the mercury district of Almadén in Spain. Environ. Sci. Technol., v.40, p.4090–

4095.

Berry, R., 2008. Automated mineral identification by optical microscopy, GeM (AMIRA P843) Technical Report 1, p.7.1-7.12.

Berry, R.F., McMahon, C., 2008. Automated mineral identification by optical microscopy: Ernest Henry, Aqqaluk. GeM (AMIRA P843) Technical Report 2 November, p.6.1-6.6.

Bethke, P.M., Barton, P.A., Jr., 1971. Distribution of some minor elements between coexisting sulfide minerals, Economic Geology, v.66, p.140–163.

Bezaazoua, B., Bussieré, B., Dagenais, A.M., Archambault, M., 2004. Kinetic tests comparison and interpretation for prediction of the Joutel tailings acid generation potential, Environmental Geology, v.46, p.1086-1101.

Blackburn, W.H., Schwendeman, J.F., 1977. Trace-element substitution in galena, Canadian Mineralogist, v.15, p.365–373.

Blake, D.H., Etheridge, M.A., Page, R.W., Stewart, A.J., Williams, P.R., and Wyborn, L.A.I., 1990. Mount Isa Inlier – regional geology and mineralization, in Hughes, F.E., ed., Geology of the mineral deposits of Australia and Papua New Guinea: Australasian Institute of Mining and Metallurgy, Melbourne, p. 915-925.

Blanchard, M., Alfredsson, M., Brodholt, J., Wright, K., Catlow, C.R.A., 2007. Arsenic incorporation into FeS2 pyrite and its influence on dissolution: A DFT study, Geochimica et Cosmochimica Acta, v.71, p.624-630.

Blowes, D., Moncur, M., Smith, L., Sego, D., Bennet, J., Garvie, A., Linklater, C., Gould, D., Reinson, J., 2006. Construction of two large-scale waste rock piles in a continuous permafrost region, 7th International Conference on Acid Rock Drainage (ICARD), March 26-30, 2006, St. Louis MO. Published by the American Society of Mining and Reclamation (ASMR), 3134 Montavesta Road, Lexington, KY 40502.

Blowes, D.W., Jambor, J.L., 1990. The pore-water geochemistry and the mineralogy of the vadose zone of sulphide tailings, Waite Amulet, Quebec, Canada, Applied Geochemistry, v.5, p.327-346.

Bluteau, M.C., Demopoulos, G.P., 2007. The incogruent dissolution of scorodite: solubility, kinetics and mechanism, Hydrometallurgy, v.87, p.163-177.

Bond, P. L., Druschel, G. K., Banfield, J. F., 2000. Comparison of acid mine drainage microbial communities in physically and geochemically distinct ecosystems, Applied and Environmental Microbiology, v.66, p.4962–4971.

Bonnici, N., 2012. The mineralogical and textural characteristics of Cu-Au deposits related to mineral processing attributes. Ph.D thesis, University of Tasmania.

Bonnici, N., Hunt, J., Walters, S., Berry, R., Kamenetsky, M., McMahon, C., Nguyen, K., 2009. Integrating meso- and micro- textural information into mineral processing: An example from the Ernest Henry Iron-Oxide Copper-Gold deposit, Queensland, Australia. In 41st Annual Meeting of the Canadian Mineral Processors, Ottawa, Ontario, Conference Proceedings. Canada, 2009, p. 259-278.

Borden, R.K., 2003. Environmental geochemistry of the Bingham Canyon porphyry copper deposit, Utah, Environmental Geology, v.43, p.752–758.

Bowell, R.J, Rees, S.B., Parshley, J.V., 2000. Geochemical predictions of metal leaching and acid generation: geologic controls and baseline assessment. Geology and Ore Deposits: The great Basin and Beyond Proceedings, 2, p.799-823.

British Columbia Acid Mine Drainage Task Force (BCAMDTF), 1989. Draft Acid Rock Drainage Technical Guide – Volume 1. Prepared by Steffen Robertson and Kirsten (SRK), Vancouver, BC.

Broadhurst, J.L., 2007. Generalised strategy for predicting environmental characteristics of solid mineral wastes – a focus on copper. PhD Thesis. University of Cape Town.

Broadhurst, J.L., Hesketh, A., Harrison, S.T.L., 2009. An Integrated Approach to the Management of Sulphide Tailings and Mitigation of Acid Mine Drainage, 8th International Conference on Acid Rock Drainage (ICARD 2009), June, 2009.

Broadhurst, J.L., Petrie, J.G., 2010. Ranking and scoring potential environmental risks from solid mineral wastes, Minerals Engineering, v.23, p.182-191.

Broughton, L.M., Robertson, A.M., 1992. Acid Rock Drainage from Mines - Where We Are Now. IMM Minerals, Metals and Environment Conference, February 4-6, Manchester, UK.

Brown, D., Salzsauler, K., Verburg, R., Sifuentes, R., Aranda, C., 2009. Geochemical characterization of waste rock using field kinetic testing at the Antamina mine, 8th International Conference on Acid Rock Drainage (ICARD) and Securing the Future: Mining, Metals & the Environment in a Sustainable Society, p. 311-321.

Brown, D., Verburg, R., Letient, H., Aranda, C., 2006. Geochemical characterization and water quality prediction at the Antamina mine. 7th International Conference on Acid Rock Drainage (ICARD), March 26-30, 2006, St. Louis MO. Published by the American Society of Mining and Reclamation (ASMR), 3134 Montavesta Road, Lexington, KY 40502, p. 291.

Bruckard, W.J., Davey, K.J., Jorgensen, F.R.A., Wright, S., Bew, D.R.M., Haque, N., Vance, E.R., 2010. Development and evaluation of an early removal process for the beneficiation of arsenic-bearing copper ores, Minerals Engineering, v.23, p.1167-1173.

Buckby, T., Black, S., Coleman, M.L., Hodson, M.E., 2003. Fe-sulfate-rich evaporative mineral precipitates from the Rio Tinto, southwest Spain, Mineralogical Magazine, v. 67, p.263–278.

Bucknam, C. H., 1997. Net carbonate value (NCV) for acid base accounting. http://www.bucknam.com/ncv.html

Bureau of Meteorology, 2012. www.bom.com.au

Cabri, L.J., Campbell, J.L., 1998. The proton microprobe in ore mineralogy (micro-PIXE technique). In Modern Approaches to Ore and Environmental Mineralogy in L.J. Cabri & D.J Vaughan (Eds). Mineral Association of Canada Short Course, v.27, p.181-198.

Cabri, L.J., Campbell, J.L., 1998. The proton microprobe in ore mineralogy (micro-PIXE technique), In: L.J. Cabri, (Ed), Modern Approaches to Ore and Environmental Mineralogy, Mineralogical Association of Canada Short Course, v.27, pp.181-198.

Capenema, L.X.L., Ciminelli, V.S.T., 2003. An investigation of acid rock drainage (ARD) occurrence in a gold mine located in a southeastern Brazil region, Revista Escola de Minas, v.56, p.201-206.

Carbone, C., Marescotti, P., Lucchetti, G., Cauzid, J., Chalmin, E., 2011. Application of synchrotron radiation-based techniques (μ-XRD, μ-XRF and μ-XANES) to study Fe-rich hardpans within waste rock dump, Neues Jahrbuch für Mineralogie, v.188, p.21-30.

Caruso, B.S., Bishop, M., 2009. Seasonal and spatial variation of metal loads from natural flows in the Upper Tenmile Creek Watershed, Montana, Mine Water and the Environment, v.28, p.166–181.

Chandra, A.P., Gerson, A. R., 2010. The mechanisms of pyrite oxidation and leaching: A fundamental perspective, Surface Science Reports, 65, p.293-315.

Changul, C., Sutthirat, C., Padmanahban, G., Tongcumpou, C., 2010. Assessing the acidic potential of waste rock in the Akara gold mining, Thailand, Journal of Environmental Earth Science, v.60, p.1065-1071.

Chapman, N.A., Shackleton, N.J., Maysiak, V., O'Connor, C.T., 2011. The effect of using different comminution procedures on the flotation of platinum group minerals, Minerals Engineering, v.24, p.731-736.

Chappell, D.A., Craw, D., 2002. Geological analogue for circumneutral pH mine tailings: implications for long-term storage, Macraes Mine, Otago, New Zealand, Applied Geochemistry, v.17, p. 1105-1114.

Chotpantarat, S., 2011. A review of static tests and recent studies, American Journal of Applied Sciences, v.8, p.400-406.

Ciccarelli, J. M., Weber, P.A., Stewart, W., Li, J., Schumann, R., Miller, S.D., Smart, R., 2009. Estimation of Long-term Silicate Neutralisation of Acid Rock Drainage, Securing the Future Mining, Metals & the Environment in a Sustainable Society, ICARD, 1-11, Sweden, 8th ICARD International Conference on Acid Rock Drainage, (Lars Lovgren Eds), 2009.

Comarmond, J., 1997. Chemical methods for predicting the acid mine drainage/acid rock drainage potential of mine wastes in Australia. Environmental division, ANSTO. http://www.environment.gov.au/ssd/publications/ssr/pubs/ssr125-appendices.pdf

Cook, N.J., Ciobanu, C.L., Pring, A., Skinner, W., Danyushevsky, L., Shimizu, M., Saini-Eidukat, B., Melcher, F., 2009. Trace and minor elements in sphalerite: a LA-ICP-MS study, Geochimica et Cosmochimica Acta, v.73, p. 4761-4791.

Corkhill, C.L., Vaughan, D.J., 2009. Arsenopyrite oxidation - A review, Applied Geochemistry, v.24, p.2342-2361.

Corriveau, M.C., Jamieson, H.E., Parsons, M.B., Campbell, J.L., Lanziorotti, A., 2011. Direct characterization of airborne particles associated with arsenic-rich mine tailings: Particle size, mineralogy and texture, Applied Geochemistry, v.26, p.1639-1648.

Craw, D, Falconer, D., Youngson, J H., 2003. Environmental arsenopyrite stability and dissolution: theory, experiment, and field observations, Chemical Geology, v.199, p.71-82.

Craw, D., 2000. Water-rock interaction and acid neutralisation in a large schist debris dam, Otago, New Zealand, Chemical Geology, v.171, p.17-32.

Craw, D., Falconer, D., Youngson, J.H., 2003. Environmental arsenopyrite stability and dissolution: theory, experiment and field observations, Chemical Geology, v.199, p.71–82.

Craw, D., Wilson, N., Ashley, P.M., 2004. Geochemical controls on the environmental mobility of Sb and As in mesothermal antimony and gold deposits, Applied Earth Sciences, v.113, p.B3–B10.

Croudace. I.W., Rindby, A., Rothwell, R.G., 2006. ITRAX: description and evaluation of a new multi-function X-ray core scanner, In: Rothwell, R.G. (ed.) New Techniques in Sediment Core Analysis, Geological Society, London, Special Publications, v.267, p.51–63.

da Silva, E.F., Bobos, I., Matos, J.X., Patinha, C., Reis, A.P., Fonseca, C., 2009. Mineralogy and geochemistry of trace metals and REE in volcanic massive sulfide host rocks, stream sediments, stream waters and acid mine drainage from the Lousal mine area (Iberian Pyrite

Belt, Portugal), Applied Geochemistry, v.24, p.383-401.

Danyushevsky, L., Robinson, P., Gilbert, S., Norman, M., Large, R., McGoldrick, P., Shelley, M., 2011. Routine quantitative multi-element analysis of sulphide minerals by laser ablation ICP-MS: standard development and consideration of matrix effects, Geochemistry: Exploration, Environment, Analysis, v.11, p.51-60.

Das, S., Hendry, M.J., 2011. Application of Raman spectroscopy to identify iron minerals commonly found in mine wastes, Chemical Geology, v.290, p.101-108.

David, C.P.C., 2003. Establishing the impact of acid mine drainage through metal bioaccumulation and taxa richness of benthic insects in a tropical Asian stream (the Philippines), Environmental Toxicology and Chemistry, v. 22, p. 2952–2959.

Denimal, S., Tribovillard, N., Barbecot, F., Dever, L., 2002. Leaching of coal-mine tips (Nord-Pas-de-Calais coal basin, France) and sulphate transfer to the chalk aquifer: example of acid mine drainage in a buffered environment, Environmental Geology, v.42, p.966-981.

DeSisto, S.L., Jamieson, H.E., Parsons, M.B., 2011. Influence of hardpan layers on arsenic mobility in historical gold mine tailings, Applied Geochemistry, v.26, p.2004-2018.

Di Benedetto, F., Bernardini, G.P., Costagliola, P., Plant, D., Vaughan, D.J., 2005. Compositional zoning in sphalerite crystals. American Mineralogist, v.90, p.1384-1392.

Diehl, S.F., Hageman, P.L., Smith, K.S., 2006. What's weathering? Mineralogy and field leach studies in mine waste, Leadville and Montezuma mining districts, Colorado, 7th International Conference on Acid Rock Drainage (ICARD), March 26-30, 2006, St. Louis MO. R.I. Barnhisel (ed.) Published by the American Society of Mining and Reclamation (ASMR), 3134 Montavesta Road, Lexington, KY 40502

Diehl, S.F., Hageman, P.L., Smith, K.S., 2008. What is weathering in mine waste? Mineralogic evidence for sources of metals in leachates, Chapter A., in P.L. Verplanck (ed.), Understanding contaminants associated with mineral deposits: U.S. Geological Survey Circular 1328, p. 4-7.

Diehl, S.F., Koenig, A.E., Hageman, P.L., Smith, K.S., Fey, D.L., Lowers, H.A., 2007. From the micro to the macroscale: a textural and chemical perspective of characterising waste-rock material. In: Proceedings of the 2007 Society for Mining, Metallurgy and Exploration (SME) Annual Meeting and Exhibit, and the 109th National Western Mining Conference, Denver, Colorado. Society for Mining, Metallurgy and Exploration Inc., United States, Preprint 07-021, 16 p.

Diehl, S.F., Koenig, A.E., Hageman, P.L., Smith, K.S., Fey, D.L., Lowers, H.A., 2007. From the micro to the macroscale: a textural and chemical perspective of characterising waste-rock material. In Proceedings of the 2007 Society for Mining, Metallurgy and Exploration (SME) Annual Meeting and Exhibit, and the 109th National Western Mining Conference, Denver, Colorado. Society for Mining, Metallurgy and Exploration Inc, United States, Preprint 07-021, 16 p.

Diehl, S.F., Smith, K.S., Desborough, G.A., Goldhaber, M.B., Fey, D.L., 2003. Trace-metal sources and their release from mine wastes: Examples from humidity cell tests of hard-rock mine waste and from Warrior Basin coal, National Meeting of the American Society of Mining and Reclamation Symposium, Billings, MT, June 3–6, CD ROM.

DME (Queensland Department of Mines and Environment), 2008. Report on Value Engineering Study, Remediaton of Abandoned Federation and Glencoe mines, Croydon.

Dobos, S.K., 2000. Potential problems with geologically uncontrolled sampling and the interpretation of chemical tests for waste characterisation and ARD prediction. In: Proceedings of the 4th Australian ARD Workshop on Acid and Metalliferous Mine Drainage, Townsville, ACMER, Australia, p.25-29.

Dold, B., Fontboté, L., 2001. Element cycling and secondary mineralogy in porphyry copper tailings as a function of climate, primary mineralogy and mineral processing, Journal of Geochemical Exploration, v.74, p.3-55.

Dold, B., 2003a. Dissolution kinetics of schwertmannite and ferrihydrite in oxidised mine samples and their detection by differential X-ray diffraction (DXRD). Applied Geochemistry, v.18, p.1531-1540.

Dold, B., 2003b. Speciation of the most soluble phases in a sequential extraction procedure adapted for geochemical studies of copper sulphide mine waste. Journal of Geochemical Exploration, v.80, p.55-68.

Dold, B., 2006. Element flows associated with marine shore mine tailings deposits, Environmental Science and Technology, v.40, p.752–758.

Dold, B., Wade, C., Fontboté, L., 2007. Water Management for Acid Mine Drainage Control at the polymetallic Deposit of Cerro de Pasco, Peru In Cidu, R., Frau, F., Water in Mining Environments. p.423-426.

Dold, B., 2008. Sustainability in metal mining: from exploration, over processing to mine waste management, Reviews in Environmental Sciene and Biotechnology, v.7, p.275-285.

Dold, B., 2010. Basic concepts in environmental geochemistry of sulphide mine-waste management. In Sunil Kumar (Ed.). Waste management, ISBN 978-953-7619-84-8. INTECH open access publications, p.173-198.

Dove, P.M., Rimstidt, J.D., 1985. The solubilty and stability of scorodite, FeAsO4.H2O, American Mineralogist, v.70, p.838-844.

Dowd, P.J., 2005. The business case for the prevention of acid drainage. Proceedings of the 5th Australian Workshop on Acid and Metalliferous Drainage, ACMER, Brisbane, Australia.

Downing, B.W., 1999. ARD sampling and sample preparation. http://technology.infomine.com/enviromine/ard/sampling/intro.html

Downing, B.W., Giroux, G., 1993. Estimation of a waste rock ARD block model for the Windy Craggy massive sulphide deposit, northwestern British Columbia, Exploration and Mining Geology, v.2, p.203-215.

Downing, B.W., Giroux, G., 1999. Acid rock drainage waste rock block modelling. www.enviromine.com/ard

Downing, B.W., Madeisky, H.E., 1997. Lithogeochemical methods for acid rock drainage studies and prediction, Exploration and Mining Geology, v.6, p.367-379.

Drahota, P., Filippi, M., 2009. Secondary arsenic minerals in the environment: A review, Environment International, v.35, p.1243-1255.

Dunham, S., Vann, J., Coward, S., 2011. Beyond Geometallurgy – Gaining Competitive Advantage by Exploiting the Broad View of Geometallurgy, The First AUSIMM International Geometallurgy Conference, Australia, p.1-10.

Edwards, K.J., Bond, P.L., and Banfield, J.F., 2000. Characteristics of attachment and growth of Thiobacillus caldus on sulphide minerals: a chemotactic response to sulphur minerals? Environmental Microbiology, v.2, p.324-332.

Egiebor, N.O., Oni, B., 2007. Acid rock drainage formation and treatment: a review, Asia-Pacific Journal of Chemical Engineering, v.2, p. 47–62.

Evangelou, V.P., Zhang, Y.L., 1995. A review: pyrite oxidation mechanisms and acid mine drainage prevention, Critical Reviews in Environmental Science & Technology, v.25, p.141-199.

Fandrich, R., Gu, Y., Burrows, D., Moeller, K., 2007. Modern SEM-based mineral liberation analysis, International Journal of Mineral Processing, v.84, p.310-320.

Feasby, D.G., Tremblay, G.A., 1995. New technologies to reduce environmental liability from acid generating wastes, In Proceeding of conference on Mining and the Environment, Sudbury, Ontario, 28 May-1 June 1995, Centre for Mining and Mineral Exploration Research, Sudbury, p.643-647.

Fey, D.L., 2003. Acid-base accounting. Billing symposium/ASMR annual meeting assessing the toxicity potential of mine-waste piles workshop.

Fillpek, L.H., Nordstrom, D.K., Ficklin, W.H., 1987. Interaction of acid mine drainage with waters and sediments of west squaw creek in the West Shasta mining district, California, Environmental Science & Technology, v.21, p.388-396.

Flemming, R.L., Salzsauler, K.A., Sherriff, B.L., Sidenko, N.V., 2005. Identification of scorodite in fine grained, high sulfide, arsenopyrite mine-waste using micro x-ray diffraction (MXRD), Canadian Mineralogist, v.43, p.1243-1254.

Foord, E.E., Shawe, D.R., 1989. The Pb-Bi-Ag-Cu- (Hg) chemistry of galena and some associated sulfosalts: A review and some new data from Colorado, California and Pennsylvania, Canadian Mineralogist, v.27, p.363-382.

Foster, A.L., Brown, G.E. Jr., Parks, G.A., Tingle, T.N., 1998. Quantitative speciation of arsenic in mine tailings using X-ray absorption spectroscopy, American Mineralogist, v.89, p.553–568.

Fox, D., 1997. Pyrrhotite and associated sulphides and their relationship to acid rock drainage in the Halifax Formation, Meguma Group, Nova Scotia, Atlantic Geology, v. 33, p.87-103.

Franco, S., Kadletz, O., Stevens, R., Nguyen, X., Reid, M., Scougall, J., McLean, R., Stutsel, M., Long, T., 2010. Strategic framework for managing abandoned mines in the minerals industry, Ministerial Council on Mineral and Petroleum Resources (MCMPR), pp. 44.

Frostad, S., Klein, B., Lawrence, R.W., 2002. Evaluation of laboratory kinetic test methods for measuring rates of weathering, Mine Water and the Environment, v.21, p.183-192.

Fujita, T., Taguchi, R., Abumiya, M., Matsumoto, M., Shibata, E., Nakamura, T., 2008. Effects of zinc, copper and sodium ions on ferric arsenate precipitation in a novel atmospheric scorodite process, Hydrometallurgy, v.93, p.30-38.

Garcia, O., Bigham, J.M., Tuovinen, O.H., 1995. Sphalerite oxidation by Thiobacillus fertooxidans and Thiobacillus thiooxidans, Canadian Journal of Microbiology, v.41, p.578-584.

Garcia-Sanchez, A., Alvarez-Ayuso, E., Rodriguez-Martins, F., 2002. Sorption of As(V) by some oxyhydroxides and clay minerals, Application to its immobilization in two polluted mining soils, Clay Minerals, v.37, p.187-194.

GARD (Global Acid Rock Drainage) guide, 2010. The International Network for Acid Prevention (INAP), http://www.gardguide.com/

Gasparon, M., Smedley, A., Jong, T., Costagliola, P., Benvenuti, M., 2007. Acid mine drainage at Mount Morgan, Queensland (Australia): Experimental simulation and geochemical modeling of buffering reactions, IMWA Symposium: Water in Mining Environments, R. Cidu and F. Frau (Eds) 27 – 31 May, Cagliari, Italy, p.433–436.

Gault, A.G., Cooke, D.R., Townsend, A.T., Charnock, J.M., Polya, D.A., 2005. Mechanisms of arsenic attenuation in acid mine drainage from Mount Bischoff, western Tasmania, Science of the Total Environment, v.345, p.219-228

Genna, D., Gaboury, D., Moore, L., Mueller, W.U., 2011. Use of micro-XRF chemical analysis for mapping volcanogenic massive sulfide related hydrothermal alteration: Application to the subaqueous felsic dome-flow complex of the Cap d'Ours section,Glenwood rhyolite, Rouyn-Noranda, Québec, Canada, Journal of Geochemical Exploration, v.108, p.131-142.

Ghorbani, Y., Becker, M., Mainza, A., Franzidis, J.-P. Petersen, J., 2011, Large particle effects in chemical/biochemical heap leach processes - A review, Minerals Engineering, v.24, p.1172-1257.

Giere, R., Sidenko, N.V., Lazareva, E.V., 2003. The role of secondary minerals in controlling the migration of arsenic and metals from high-sulfide wastes (Berikul gold mine, Siberia), Applied Geochemistry, v.18, p.1347-1359.

Gifkins, C., Herrman, W., Large, R., 2005. Altered Volcanic Rocks: a guide to description and interpretation, University of Tasmania, 275 pp.

Goldstein, J., 2003. Scanning Electron Microscopy and X-ray Microanalysis. Kluwer Academic/Plenum Publishers, 689 pp.

Gomez, M.A., Becze, L., Cutler, J.N., Demopoulos, G.P., 2011. Hydrothermal reaction chemistry and characterisation of ferric arsenate phases precipitated from $Fe_2(SO_4)_3$-As_2O5-H_2SO_4 solutions, Hydrometallurgy, v.107, p.74-90.

Goodall, W., 2008. Automated Mineralogy in the Prediction of Acid Rock Drainage: Accessible Mineralogy Using QEMSCAN®. In Proceedings of the 2008 Society for Mining, Metallurgy and Exploration (SME) Annual Meeting and Exhibit, Salt Lake City, Utah, Society for Mining, Metallurgy and Exploration Inc. United States, 2008.

Gore, D.B., Preston, N.J., Kirstie, A.F., 2007. Post-rehabilitation environmental hazard of Cu, Zn, As and Pb at the derelict Conrad Mine, eastern Australia, Environmental Pollution, v.148, p.491-500.

Gottlieb, P., Wilkie, G., Sutherland, D., Ho-Tun, E., Suthers, S., Perera, K., Jenkins, B., Spencer, S., Butcher, A., Rayner, J., 2000. Using quantitative electron microscopy for process mineral applications, Jounal of the Minerals, Metals and Materials Society, v.52, p.24-25.

Gray, N.F., 1997. Environmental impact and remediation of acid mine drainage: a management problem, Environmental Geology, v.30, p.62–71.

Gu, Y., 2003. Automated Scanning Electron Microscope Based Mineral Liberation Analysis – An Introduction to JKMRC/FEI Mineral Liberation Analyser. Journal of Minerals & Materials Characterization & Engineering, v.2, p.33-41.

Gunsinger, M.R., Ptacek, C.J., Blowes, D.W., Jambor, J.L., Moncur, M.C., 2006. Mechanisms controlling acid neutralization and metal mobility within a Ni-rich tailings impoundment, Applied Geochemistry, v.21, p.1301-1321.

Haffert, L. , Craw, D., Pope, J., 2010. Climatic and compositional controls on secondary arsenic mineral formation in high-arsenic mine wastes, South Island, New Zealand, New Zealand Journal of Geology and Geophysics, v.53, p.91-101.

Haffert, L., Craw, D., 2008a. Field quantification and characterization of extreme arsenic concentrations at a historic mine processing site, Waiuta, New Zealand. New Zealand Journal of Geology & Geophysics v.52, p.261-272.

Haffert, L., Craw, D., 2008b. Mineralogical controls on environmental mobility of arsenic from historic mine processing residues, New Zealand, Applied Geochemistry, v.23, p.1467-1483.

Haffert, L., Craw, D., 2010. Geochemical processes influencing arsenic mobility at Bullendale historic gold mine, Otago, New Zealand, New Zealand Journal of Geology and Geophysics, v.53, p.129-142.

Hakkou, R., Bezaazoua, M., Bussiere, B., 2009. Laboratory evaluation of the use of alkaline phosphate wastes for the control of acidic mine drainage, Mine Water and the Environment, v.28, p.206-218.

Hammarstrom, J.M., and Smith, K.S., 2002, Geochemical and mineralogic characterization of solids and their effects on waters in metal-mining environments, in Seal, R.R., II, and Foley, N.K., eds., Progress on Geoenvironmental Models for Selected Mineral Deposit Types: U.S. Geological Survey Open-File Report 02-0195, p. 8-54. Available online at http://pubs.usgs.gov/of/2002/of02-195/

Hammarstrom, J.M., Piatek, N.M., Seal, R.R., Briggs, P.H., Meier, A.L., Muzik, T.L., 2003a. Geochemical characteristics of TP3 mine wastes at the Elizabeth copper mine superfund site, Orange County, Vermont. United States Geological Survey Open-File Report 03-431, pp. 83.

Hansen , Y., Broadhurst, J.L., Petrie, J.G., 2008. Modeling leachate generation and mobility from copper sulphide tailings-An intergrated approach to impact assessment, Minerals Engineering, v.21, p.288-301.

Harries, J.H., 1997. Acid mine drainage in Australia: Its extent and future liability. Supervising Scientist Report 125, Supervising Scientist, Canberra, pp.10.

Harries, J.R., 1997. Acid mine drainage in Australia: its extent and potential future liability, Canberra, Supervising Scientist, pp.94.

Harris, D.L., Lottermoser, B.G., Duchesne, J., 2003. Ephemeral acid mine drainage at the Montalbion silver mine, north Queensland, Australian Journal of Earth Sciences, v.50, p.797-809.

Harris, K.E., Bunker, K.L., Stromeier, B.R., Hoch, R., Lee, R.J., 2007. Discovering the true morphology of amphibole minerals: complementary TEM and FESEM characterization of particles in mixed mineral dust, Modern Research and Educational Topics in Microscopy, p.1-8.

Harvey, M.C., Schreiber, M.E., Rimstidt, J.D., Griffith, M.M., 2006. Scorodite dissolution kinetics: implications for arsenic release. Environmental Science and Technology, v.40, p.6709-6714

Hayes, S.M., White, S.A., Thompson, T.L., Maier, R.M., Chorover, J., 2009. Changes in lead and zinc lability during weathering-induced acidification of desert mine tailings: coupling chemical and micro-scale analyses, Applied Geochemistry, v. 24, p.2234-2245.

Heidel, C., Tichomirowa, M., 2011. Galena oxidation investigations on oxygen and sulphur isotopes, Isotopes Environmental Health Studies, v.47, p.169-188.

Hermann, W., Berry, R.F., 2002. MINSQ- a least squares method for calculating mineral proportions from whole rock major element analyses. Geochemistry: Exploration, Environment, Analysis, v.2, p.361-368.

Herrmann, W., Blake, M. D., Doyle, M. G., Huston, D. L., Kamprad, J., Merry, N., Pontual, S., 2001. Short wavelength infrared (SWIR) spectral analysis of hydrothermal alteration zones associated with base metal sulphide deposits at Rosebery and western Tharsis, Tasmania, and Highway-Reward, Queensland, Economic Geology, v.96, p.939-955.

Hesketh., A.H., Broadhurst, J.L., Bryan, C.G., van Hille, R.P., Harrison, S.T.L., 2010, Biokinetic test for the characterisation of AMD generation potential of sulphide mineral wastes, Hydrometallurgy, v.104, p.459-464.

Higueras, P., Oyarzun, R., Iraizoz, J.M., Lorenzo, S, Esbri, J.M., Martinez-Coronado, A., 2012. Low-cost geochemical surveys for environmental studies in developing countries: Testing a field portable XRF instrument under quasi-realistic conditions. Journal of Geochemical Exploration, v.113, p.3-12.

Hita, R., Torrent, J., Bigham, J.M., 2006. Experimental oxidative dissolution of sphalerite in the Aznalcollar sludge and other pyritic matrices, Journal of Environmental Quality, v.35, p.1032-1039.

Hitzman, M.W., 1999. Routine staining of drill core to determine carbonate mineralogy and distinguish carbonate alteration textures. Mineralium Deposita, v.34, p.794-798.

Hofmann T., Schuwirth, N., 2008. Zn and Pb release of sphalerite (ZnS)-bearing mine waste tailings, Journal of Soils and Sediments, v.8, p.433-441.

Hudson-Edwards, K.A. and Edwards, S.J., 2005. Mineralogical controls on storage of As, Cu, Pb and Zn at the abandoned Mathiatis massive sulphide mine, Cyprus, Mineralogical Magazine, v.69, p.695-706.

Hudson-Edwards, K.A., 2003. Sources, mineralogy, chemistry and fate of heavy metal-bearing particles in mining affected river systems. Mineralogical Magazine, v.67, p.205-217.

Hudson-Edwards, K.A., Edwards, S.J., 2005. Mineralogical controls on storage of As, Cu, Pb and Zn at the abandoned Mathiatis massive sulphide mine, Cyprus, Mineralogical Magazine, v.69, p. 695-706.

Hudson-Edwards, K.A., Jamieson, H.E., Lottermoser, B.G., 2011. Mine wastes: past, present and future, Elements, v.7, p.375-380.

Hudson-Edwards, K.A., Macklin, M.G., Taylor, M.P., 1999. 2000 years of sediment-borne heavy metal storage in Yorkshire Ouse basin, NE England, UK, Hydrological Processes, v.13, p.1087-1102.

Hudson-Edwards, K.A., Wright, K., 2011. Computer simulations of the interactions of the (012) and (001) surfaces of jarosite with Al, Cd, Cu^{2+} and Zn, Geochimica et Cosmochimica Acta, v.75, p.52-62.

Hughes, J., Craw, D., Peake, B., Lindsay, P., Weber, P., 2007. Environmental characterisation of coal mine waste rock in the field: an example from New Zealand, Environmental Geology, v.52, p.1501-1509.

Hunt, J., Berry, R., Bradshaw, D., 2011. Characterising chalcopyrite liberation and flotation potential: Examples from an IOCG deposit, Minerals Engineering, v.24, p.1271-1276.

Hunt, J.A., Clifford, M., 2008. Ernest Henry deposit summary and GeM sampling strategy. GeM (AMIRA P843) Technical Report 2, November p.2.1-2.10.

Huntington, J.F., Quigley, M., Yang, K., Roache, T., Young, C., Roberts, I., Whitbourn, L.B., Mason, P., 2006. A Geological Overview of HyLogging 18,000 m of Core from the Eastern Goldfields of Western Australia. Proc 6th Int. Mining Geology Conf., Darwin, Australia, 21–23 August 2006. Aus IMM Publication Series No.6/2006, Ed. S. Dominy, pp. 45-50. ISBN 1920806504

Hustwit, C.C., Ackman, T.E., Erikson, P.E., 1992. The role of oxygen transfer in acid mine drainage (AMD) treatment, Water Environment Research, v.64, p.817-823.

Hutchinson, B.J., Brett, D., 2006. Savage river mine- practical remediation works. 7th International Conference on Acid Rock Drainage (ICARD), March 26-30, 2006, St. Louis MO. R.I. Barnhisel (ed.) Published by the American Society of Mining and Reclamation (ASMR), 3134 Montavesta Road, Lexington, KY 40502 p. 810-819.

Hutt, N.M., Morin, K.A., 2000. Observations and lessons from the International Static Database (ISD) on neutralizing capacity. In: Proceedings from the Fifth International Conference on Acid Rock Drainage, May 20-26, Denver, USA, V.I, p. 603-611

Irwin, R.J., Van Mouwerik, M., Stevens, L., Seese, M.S., Basham, W., 1997. Environmental contaminants encyclopedia cadmium entry, National parks service, Colarado, US. pp.88.

Jackson, J., McFarlane, A. J. and Olson Hoal, K., 2011. Geometallurgy - Back to the future: Scoping and communicating Geomet programs. In: Simon Dominy, The First AusIMM International Geometallurgy Conference 2011. Geomet 2011, Brisbane, QLD, Australia, p.125-131. 5-7 September 2011.

Jambor, J.L., 1994. Mineralogy of sulphide rich tailings and their oxidation products. In: Blowes, D.W. and Jambor, J.L. (Eds.), The Environmental Geochemistry of Sulphide Mine Wastes, Mineralogical Association of Canada, Short Course Series, v.22, p.59-102.

Jambor, J.L., 2003. Mine-waste mineralogy and mineralogical perspectives of acid-base accounting. In: Jambor, J.L., Blowes, D.W., and Ritchie, A.I.M. (Eds.), Environmental Aspects of Mine Wastes, Mineralogical Association of Canada, Short Course Series, v.31, p.117-145.

Jambor, J.L., Blowes, D.W., and Ritchie, A.I.M. (Eds.), 2003. Environmental Aspects of Mine Wastes. Mineralogical Association of Canada, Short Course Series, v.31, p.436.

Jambor, J.L., Dutrizac, J.E., Groat, L., Raudsepp, M., 2002. Static tests of neutralization potentials of silicate and aluminosilicate minerals. Environmental Geology, v.43, p.1-17.

Jambor, J.L., Dutrizac, J.E., Raudsepp M., 2006. Comparison of measured and mineralogically predicted values of the Sobek Neutralization Potential for intrusive rocks. In: Barnhisel, R.I. (Ed.), Proceedings of the 7th International Conference on Acid Rock Drainage (ICARD), p.820-832.

Jambor, J.L., Dutrizac, J.E., Raudsepp, M., 2007. Measured and computed neutralization potentials from static tests of diverse rock types. Environmental Geology, v.52, p.1019-1031.

Jambor, J.L., Nordstrom, D.K., Alpers, C.N., 2000. Metal-sulfate salts from sulfide mineral oxidation, Reviews in Mineralogy and Geochemistry, v.40, p.303-350.

Jamieson, H., 2011. Geochemistry and mineralogy of solid mine waste: essential knowledge for predicting environmental impact, Elements, v.7, p.381-386.

Jamieson, H.E., Robinson, C., Alpers, C.N., McCleskey, R., Blaine, R., Nordstrom, D.K., Peterson, R.C. 2005. Major and trace element composition of copiapite-group minerals and coexisting water from the Richmond mine, Iron Mountain, California. Chemical Geology, v.215, p.387-405.

Jamieson, H.E., Shaw, S.C. and Clark, A.H., 1995. Mineralogical factors controlling metal release from tailings at Geco, Manitouwadge, Ontario, In: Sudbury 95, Mining and the Environment, CANMET, v.1, p.405-413.

Kalinnikov, V.T., Makarov, D.V., Makarov, V.N., Oxidation sequence of oxide minerals in operating and out-of-service mine waste storage, Theoretical Foundations of Chemical Engineering, v.35, p.63-68.

Kamenetsky, M., 2008. MLA analysis: examples from Ernest Henry, GeM (AMIRA P843) Technical Report 2, November p.7.1-7.12.

Katsuta, N., Takano, M., Kawakami, S., Togami, S., Fukusawa, H., Kumazawa, M., Yasuda, Y., 2007. Advanced micro-XRF method to separate rhythm and event layers in sediments: its application to lacustrine sediment from Lake Suigetsu, Japan. Journal of Paleolimnology, v.37, p.259-271.

Keeney, L., 2008. EQUOtip hardness testing: Aqqaluk (including a guide on how to use EQUOtip). AMIRA P843 Technical Report 2, November p.17.1-17.20.

Keeney, L., Walters, S., Kojovic, T., 2011. Geometallurgical mapping and modelling of comminution performance at the Cadia East porphyry deposit. In: Simon Dominy, The First AusIMM International Geometallurgy Conference 2011. Geomet 2011, Brisbane, Australia, p.73-83.

Keith, C.N., Vaughan, D.J., 2000. Mechanisms and rates of sulphide oxidation in relation to the problems of acid rock (mine) drainage. In: Environmental Mineralogy: Microbial Interactions, Anthropogenic Influences, Contaminated Land and Waste Management, Mineralogical Society Series, v.9, p.117-139.

Koenig, A.E., 2008. Advances in quantitative element analyses by laser ablation ICP-MS, Microscopy and microanalysis the official journal of Microscopy Society of America Microbeam Analysis Society and Microscopical Society of Canada, v.14, p.1270-1271.

Korolay, T., Kadioglu, Y. K., 2008. Reasons of different colors in the ignimbrite lithology: Micro XRF and confocal Raman spectrometry method, Spectrochimica Acta, Part A. v.69, p.947-955.

Krause, E., Ettel, V.A., 1988. Solubility and stability of scorodite: new data and further discussion. American Mineralogist, v.73, p.850–854.

Kruezer, O.P., 2006. Textures, paragenesis and wall-rock alteration of lode-gold deposits in the Charters Towers district, north Queensland: implications for the conditions of ore formation, Mineralium Deposita, v.40, p.639-663.

Kruse, F.A., 1994. Identification and mapping of minerals in drill core using hyperspectral image analysis of infrared reflectance spectra. http://www.spectralcameras.com/files/Applications/Kruse_Core94.pdf

Kwong, J.Y.T., 1995. Thoughts on ways to improve acid drainage and metal leaching prediction for metal mines. US Geological Survey Water Resources Investigations Report 95-4227.

Kwong, Y.T., Swerhone, G.W., Lawrence, J.R., 2003. Galvanic sulphide oxidation as a metal- leaching mechanism and its environmental implications. Geochemistry: Exploration, Environment, Analysis, v.3, p.337-343.

Kwong, Y.T.J., 1993. Prediction and prevention of acid rock drainage from a geological and mineralogical perspective. MEND Report 1.32.1, Ottawa, ON (NHRI Contribution CS-92054).

Kwong, Y.T.J., Ferguson, K.D., 1997. Mineralogical changes during NP determinations and their implications, Proc. 4th International Conference on Acid Rock Drainage, Vancouver, BC, p.435-447.

Lane, G.R., Martin, C., Pirard, E., 2008. Techniques and applications for predictive metallurgy and ore characterization using optical image analysis. Minerals Engineering v.21, p.568-577.

Lapakko, K.A., 2002. Metal mine rock and waste characterization tools: An overview. Posted on the Acid Drainage Technology Initiative - Metal Mining Sector web page: www.mackay.unr.edu/adti

Lapakko, K.A., 2003. Developments in humidity-cell tests and their application. In: Jambor, J.L., Blowes, D.W. and Ritchie, A.I.M. (Eds.), Environmental Aspect of Mine Wastes. Mineralogical Association of Canada, Short Course Series, v.31, p.147-164.

Lapakko, K.A., Antonson, D.A., 2003. Pyrite oxidation rates from humidity cell testing of greenstone rock, 7th International Conference on Acid Rock Drainage (ICARD), March 26-30, 2006, St. Louis MO. R.I. Barnhisel (ed.) Published by the American Society of Mining and Reclamation (ASMR), 3134 Montavesta Road, Lexington, KY 40502, p.1007- 1025.

Lapakko, K.A., Engstrom, J.N., Antonson, D.A., 2006. Effects of particle size on drainage quality from three lithologies, In: 7th International Conference on Acid Rock Drainage (ICARD), St. Louis MO. Ed. R.I. Barnhisel. American Society of Mining and Reclamation (ASMR). United States.

Large, R.R., Danyushevsky, L., Holit, C., Maslennikov, V., Meffre, S., Gilbert, S., Bull, S., Scott, R., Emsbo, P., Thomas, H., Singh, B., Foster, J., 2009. Gold and trace element zonation in pyrite using a laser imaging technique: implications for the timing of gold in orogenic and Carlin-style sediment hosted deposits, Economic Geology, v.104, p.635-668.

Lawrence, R.W., Scheske, M., 1997. A method to calculate the neutralization potential of mining wastes, Environmental Geology, v.32, p. 100-106.

Leading practice sustainable development program for the mining industry, Australian Government, Continuing Opportunities Energy Efficiency Opportunities (EEO) Program, 2010. A look at results for the Energy Efficiency Opportunities Program 2006-2010, Taken from public reports of assessments undertaken during the period July 2006-June 2010. ISBN 978-1-921812-49-1.

Lee, M., 1999. Handbook on management of sulfidic mine wastes and acid drainage, Australian Centre for Mining Environment Research: Brisbane, ISBN 095853666X.

Lehner, S., Savage, K., 2008. The effect of As, Co and Ni impurities on pyrite oxidation kinetics: Batch and flow-through reactor experiments with synthetic pyrite, Geochemica et Cosmochimica Acta, v.72, p.1788-1800.

Lehner, S., Savage, K., Ciobanu, M., Cliffel, D.E., 2007. The effect of As, Co and Ni impurities on pyrite oxidation kinetics: an electrochemical study of synthetic pyrite, Geochemica et Cosmochimica Acta, v.71, p.2491-2509.

Lei, L., Watkins, R.T. 2005. Acid drainage reassessment of mining tailings, Black Swan Nickel Mine, Kalgoorlie, Western Australia, Applied Geochemistry, v.20, p.661-667.

Leichliter, S., Hunt, J., Berry, R., Keeney, L., Montoya, P. A., Chamberlain, V., Jahoda, R. and Drews, U., 2011. Development of a predictive geometallurgical recovery model for the La Colosa, Porphyry Gold Deposit, Colombia. In: Simon Dominy, The First AusIMM International Geometallurgy Conference 2011. Geomet 2011, Brisbane, Australia, p.85-92.

Lengke, M.F., Davis, A., Bucknam, C., 2010. Improving management of potentially acid generating waste rock, Mine Water and the Environment, v.29, p.29-44.

Li, X., Coles, B., Ramsey, M.H., Thornton, I., 1995. Sequential extraction of soils for multielement analysis by ICP-AES, Chemical Geology, v.124, p.109-123.

Lin, Z., Herbert Jr. R.B., 1997. Heavy metal retention in secondary precipitates from a mine rock dump and underlying soil, Dalarna, Sweden, Environmental Geology, v.33, p.1-12.

Linklater, C.M., Sinclair, D.J., Brown, P.L., 2005. Coupled chemistry and transport modeling of sulphidic waste rock dumps at the Aitik mine site, Sweden, Applied Geochemistry, v.20, p.275-293.

Liu, Y.G., Zhou, M., Zeng, G.M., Wang, X., Fan, T., Xu, W.H., 2008. Bioleaching of heavy metals from mine tailings by indigenous sulfur-oxidizing bacteria: Effects of substrate concentration, Bioresource Technology, v.99, p.4124-4129.

Longerich, H.P., Jackson, S.E., Gunther, D., 1996. Laser ablation inductively coupled plasma mass spectrometric transient signal data acquisition and analyte concentration calculation, Journal of Analytical and Atomic Spectrometry, v.11, p. 899-904.

Lottermoser, B.G., 2010. Mine Wastes: Characterization, Treatment and Environmental Impacts, 3rd edition, Springer-Verlag, Berlin Heidelberg, pp. 400.

Lottermoser, B.G., Ashley, P. M. and Costelloe, M. T., 2005. Contaminant dispersion at the rehabilitated Mary Kathleen uranium mine, Australia, Environmental Geology, v.48, p.748-761.

Lottermoser, B.G., 2011. Colonisation of the rehabilitated Mary Kathleen uranium mine site (Australia) by Calotropis procera: toxicity risk to grazing animals, Journal of Geochemical Exploration, v.111, p.39-46.

Lottermoser, B.G., Ashley, P.M., Lawie, D.C., 1999. Environmental geochemistry of the Gulf Creek copper mine area, north-eastern New South Wales, Australia, Environmental Geology, v.39, p.61-74.

Luís, A. T., Teixeira, P., Almeida, S. F. P., Ector, L., Matos, J. X., Ferreira da Silva, E. A., 2009. Impact of Acid Mine Drainage (AMD) on Water Quality, Stream Sediments and Periphytic Diatom Communities in the Surrounding Streams of Aljustrel Mining Area (Portugal), Water, Air, & Soil Pollution, v.200, p.147-167.

Lynch, G., Mendel, F., 1995. Metamorphism of arsenopyrite-pyrite-sphalerite-pyrrhotite lenses, Western Cape Breton Island, Nova Scotia, Canadian Mineralogist, v.33, p.105-114.

Ma, S., Banfield, J.F., 2011. Micron-scale Fe^{2+}/Fe^{3+}, intermediate sulfur species and O2 gradients across the biofilm–solution–sediment interface control biofilm organization, Geochimica et Cosmochimica Acta, v.75, p.3568-3580.

Marescotti, P., Azzali, E., Servida, D., Carbone, C., Grieco, G., De Capitani, L. Luccheti, G., 2008. Mineralogical and geochemical spatial analysis of a waste rock dump at the Libola Fe-Cu sulphide mine (Eastern Liguria, Italy), Environmental Earth Sciences, v.61, p.187-199.

Marescotti, P., Carbone, C., De Capitani, L., Greco, G., Lucchetti, G., Servida, D., 2007. Mineralogical and geochemical characterisation of open-air tailing and waste-rock dumps from the Libiola Fe-Cu sulphide mine (Eastern Liguria, Italy), Environmental Geology, v.53, p.1613-1626.

Margui, E., Salvado, V., Queralt, I. and Hidalgo, M., 2004. Comparison of three-stage sequential extraction and toxicity characteristic leaching tests to evaluate metal mobility in mining wastes, Analytica Chimica Acta, v.524, p.151-159.

Mark, G., Oliver, N.H.S., and Williams, P.J., 2006, Mineralogical and chemical evolution of the Ernest Henry Fe oxide-Cu-Au ore system, Cloncurry district, northwest Queensland, Australia: Mineralium Deposita, v.40, p.769-801.

Mark, G., Oliver, N.H.S., Williams, P.J., Valenta, R.K., and Crookes, R.A., 2000, The evolution of the Ernest Henry Fe-oxide-(Cu-Au) hydrothermal system, in Porter, T.M., ed., Hydrothermal Iron Oxide Copper-Gold & Related Deposits: A Global Perspective, volume 1: PGC Publishing, Adelaide, p.123-136.

Maslenikov, V.V., Maslennikova, S.P., Large, R.R., Danyuvshevsky, L.V., 2009.Study of trace element zonation in vent chimneys from the Silurian Yaman-Kasy volcanic hosted massive sulfide deposit (Southern Urals, Russia) using laser ablation inductively coupled plasma mass spectrometry (LA-ICPMS). Economic Geology, v.104, p.1111-1141.

Mason Geoscience Pty Ltd., 2012. Petrological Services for the Minerals Exploration and Mining Industry, Services and Fees January 2012.

Matthies, R., Bowell, R.J., Williams, K.P., 2011. Geochemical assessment of gold mine tailings proposed for marine tailings disposal. Geochemistry: Exploration, Environment, Analysis, v.11, p.41-50.

McGuire, M.M., Edwards, K.J., Banfield, J.F., Hamers, R.J., 2001. Kinetics, surface chemistry, and structural evolution of microbially mediated sulphide mineral dissolution, Geochimica et Cosmochimica Acta, v.65, p.1243-1258.

McKnight Mineralogy, 2011, Price list for analytical services.

McLemore, V.T., Sweeney, D., Dunbar, N., Heizler, L., Writer, E.P., 2009. Determining quantitative mineralogy using a modified modan approach on the Questa rock pile materials, New Mexico, SME Annual Meeting, preprint 09-020.

Melquiades, F.L., Appoloni, C.R., 2004. Application of XRF and field portable XRF for environmental analysis, Journal of Radioanalytical and Nuclear Chemistry, v.262, p.533-541.

Miller, S., Jeffery, J., 1995. Advances in the Prediction of Acid Generating Mine Waste Materials, Proceedings of the 2nd Australian Acid Mine Drainage Workshop, Australian Centre for Minesite Rehabilitation Research, pp. 33-43.

Miller, S.D., 1996. Advances in acid mine drainage prediction and implications for risk management. In: Proceedings of the 3rd International and 21st Annual Minerals Council of Australia, Environmental Workshop, v.1, p.14-18.

Miller, S.D., Robertson, A., Donahue, T., 1997. Advances in Acid Drainage Prediction using the Net Acid Generation (NAG) Test, Proc. 4th International Conference on Acid Rock Drainage, Vancouver, BC, p.533-549.

Miller, S.D., Stewart, W., Rusdinar, Y., Schumann, R., Ciccarelli, J.M., Li, J., Smart, R., 2010. Methods for estimation of long-term non-carbonate neutralisation of acid rock drainage, Science of the Total Environment, v.408, p.2129-2135.

Mills, C., Robertson, A., Shaw, S., 2011. Acid rock drainage at Enviromine: Infomine website. http://technology.infomine.com/enviromine/ard/home.htm.

Moncur, M.C., Jambor, J.L., Ptacek, C.J., Blowes, D.W., 2009. Mine drainage from the weathering of sulfide minerals and magnetite. Applied Geochemistry, v.24, p.2362-2373.

Monhemius, A.J., Swash, P.M., 1999. Removing and stabilising arsenic from copper refining circuits by hydrothermal processing, Journal of Metallurgy, p.30-33.

Montoya, P. A., Keeney, L., Jahoda, R., Hunt, J., Berry, R., Drews, U., Chamberlain, V. and Leichliter, S. (2011). Geometallurgical modelling techniques applicable to prefeasability projects - La Colosa case study. In: Simon Dominy, The First AusIMM International Geometallurgy Conference 2011. Geomet 2011, Brisbane, QLD, Australia, p.103-112.

Moon, Y., Song, Y., Moon, H-S, 2008. The potential acid producing capacity and factors controlling oxidation tailings in the Guryong mine, Korea, Environmental Geology, v.53, p.1787-1797.

Moricz, F., Walder, I.F., Madai, F., 2009. Characterisation of waste material from the Istos-Sn-Ag deposit, Bolivia. In: Securing the Future and 8th International Conference on Acid Rock Drainage (ICARD), Skelleftea, Sweden

Morin, G., Calas, G., 2006. Arsenic in soils, mine tailings, and former industrial sites. Elements, v.2, p.97-101.

Morin, K.A. 2010. The Science and Non-Science of Minesite-Drainage Chemistry, MDAG Internet Case Study #37, www.mdag.com/case_studies/cs37.html

Morin, K.A., Hutt, N.M., 1997, Environmental geochemistry of minesite drainage: Practical theory and case studies, MDAG Publishing, Vancouver, British Colombia, 1997, ISBN 0-9682039-0-6.

Morin, K.A., Hutt, N.M., 1998. Kinetic test and risk assessment for ARD. In: Proceedings of the 5th Annual BC Metal Leaching and ARD Workshop, Vancover, Canada.

Morin, K.A., Hutt, N.M., 1999. The international static database, Proceedings of Sudbury '99, Mining and the Environment II, v.1, p.363-370, Sudbury, Canada.

Morin, K.A., Hutt, N.M., 2009. On the nonsense of arguing the superiority of an analytical method for neutralising potential. www.mdag.com/case_studies/cs32.html.

Morin, N.M and Hutt, K.A., 1998. Comparison of NAG results to ABA results for the prediction of acidic drainage, Internet Case Study 10, http://www.mdag.com/case_studies/cs1-99.html

Moses, C.O., Herman J.S., 1991. Pyrite oxidation at circumneutral pH, Geochimica et Cosmochimica Acta, v.55, p.471-482.

Moses, C.O., Nordstrom, D.K., Herman, J.S., Mills, A.L., 1987. Aqueous pyrite oxidation by dissolved oxygen and by ferric iron, Geochimica et Cosmochimica Acta, 51, p.1561-1571.

Mudd, G. M., 2005. An environmental history of uranium mining in Australia : A scientific review, Proceedings of the Australian Uranium Conference, 2005, Fremantle, WA, October 2005, 19 p.

Mudd, G. M., Patterson, J., 2010. Continuing Pollution From the Rum Jungle U-Cu Project: A Critical Evaluation of Environmental Monitoring and Rehabilitation. Environmental Pollution, v. 158, p. 1252-1260.

Mudd, G.M., 2007. An assessment of the sustainability of the mining industry in Australia, Australian Journal of Multi-Disciplinary Engineering, v.5, p.1-12.

Müller, B., Axelson, M.D., Ohlander, B., 2002. Adsorption of trace elements on pyrite surfaces in sulphidic mine tailings from Kristineberg (Sweden) a few years after remediation, Science of the Total Environment, v.298, p.1-16.

Munksgaard, N.C., Lottermoser, B.G., 2011. Fertilizer Amendment of Mining-Impacted Soils from Broken Hill, Australia: Fixation or Release of Contaminants? Water, Air and Soil Pollution, v.215, p.373-397.

Munroe, E.A., McLemore, V.T., Kyle, P., 1999. Waste rock pile characterisation heterogeneity and geochemical anomalies in the Hillsboro Mining District, Sierra County, New Mexico, Journal of Geochemical Exploration, v.67, p.391-405.

Murceigo, A., Álvarez-Ayuso, E., Pellitero, E., Rodríguez, M.A., García-Sánchez, A., Tamayo, A., Rubio, J., Rubio, F., Rubin, J., 2011. Study of arsenopyrite weathering products in mine wastes from abandoned tungsten and tin exploitations, Journal of Hazardous Materials, v.186, p.590-601.

Murciego, A.M., Pascual, E.P., Rodríguez, M.A., Álvarez-Ayuso, E., García-Sánchez, A., Rubio, F., Rubio, J., 2009. Arsenopyrite weathering products in Barruecopardo mine tailings (Salamanca, Spain), Revista de la Sociedad Española de Mineralogía, v.11, p.133-134.

Murphy, D.M.K., Gilkes, R.J., 2010. Clay minerals in saprolite overlying hydrothermally altered and unaltered rocks Vera epithermal gold deposit, Australia, Clays and Clay Minerals, v.58, p.783-791.

Nesbitt, H.W., Jambor, J.L., 1998. Role of mafic minerals in neutralizing ARD, demonstrated using a chemical weathering methology. In: Cabri, L.J., Vaughan, D.J. (Eds.): Short Course Handbook on Ore and Environmental Mineralogy. Mineralogical Association of Canada, v.27, p.403-421.

Neuendorf, K.K.E., Mehl, J.P., Jackson, J.A., 2005. Glossary of Geology, American Geological Institute, Alexandria, Virginia, 779 pp.

Nguyen, K., 2009. Software-based textural analysis tools, GeM AMIRA P843 Technical Report 3. P.22.1-22.13.

Nicholson, R.V., Scharer J.M., 1994. Laboratory studies of pyrrhotite oxidation kinetics. In: Environmental Chemistry of Sulfide Oxidation. ACS Series 550, p.14-30

Noble, T.N., 2012. Predicting mine water quality, AMIRA P843A Sponsors Meeting, June 2012, Brisbane, Australia.

Noble, T.N., Lottermoser, B.G., Parbhakar-Fox, A., 2012. Evaluating pH tests for mine water prediction, In: Valenzuela, F. Wiertz, J. (eds), 3rd International Congress on Water Management in the Mining Industry, Santiago, Chile, p.504-512

Nordstrom, D.K., 2004. Modeling low-temperature geochemical processes, Chapter 5.02 in Drever, J.I., ed., Surface and ground water, weathering, and soils, Volume 5, H.D. Holland and K.K. Turekian, exe. eds., Treatise of geochemistry: Amsterdam, Elsevier Pergamon, p.37–72.

Nordstrom, D.K., 2009. Acid rock drainage and climate change, Journal of Geochemical Exploration, v.100, p.97-104.

Nordstrom, D.K., 2011. Mine waters: Acidic to circumneutral, Elements, v.7, p.393-398.

Nordstrom, D.K., Alpers, C.N., Ptacek P.J., Blowes, D.W., 2000. Negative pH and extremely acidic mine waters from Iron Mountain, California. Environmental Science & Technology, 34, p. 254-258.

Nordstrom, D.K.N., Alpers, C.N., 1999. Negative pH, efflorescent mineralogy, and consequences for environmental restoration at the Iron Mountain superfund site, California, Proc. Natl. Acad. Sci. USA, v.96, p.3455–3462.

Nugraha, C., Shimada, H., Sasaoka, T., Ichinose, M., Matsui, K., 2009. Waste rock characteristics at tropical coal mine area: A case study of PT. Kaltim Prima Coal, Indonesia, International Journal of the Japanese Committee for Rock Mechanics, v.5, p.77-82.

Ohlander, B., Müller, B., Axelsson, M., Alakangas, L., 2007. An attempt to use LA-ICP-SMS to quantify enrichment of trace elements on pyrite surfaces in oxidizing mine tailings. Journal of Geochemical Exploration, 92, p. 1-12.

Olympus Corporation, 2012. Olympus website: www.olympus-ims.com

Oyen, C.W., Fountain, K.B., McClellen, G.H., Eades, J.L., 1998. Thin-section petrography of concrete aggregates: alternative approach for petrographic number evaluation of carbonate aggregate soundness, Soils, Geology and Foundations, v.1619, p.18-25.

Özcelik, G.A.S., 2007. Prediction techniques of acid mine drainage: a case study of a new poly-metallic mine development in Erzincan-İliç, Turkey, PhD dissertation, Middle East Technical University.

Paktunc, A.D., 1999. Mineralogical constraints on the determination of neutralising potential and prediction of acid mine drainage, Environmental Geology, v.39, p.103-112.

Paktunc, A.D., 2001. MODAN a computer program for estimating mineral quantities based on bulk composition: Windows version, Computers and Geosciences, v.21, p.883-886.

Pappu, A., Saxena, M., Asolekar, S.R., 2006. Jarosite characteristics and its utilisation potentials. Science of the Total Environment, v.359, p.232-243.

Parbhakar-Fox, A., Lottermoser, B., 2011. Predictive Environmental Indicators in Mining: Review of the literature and current best practices, CRC ORE Technical Report 2, CRC for Optimising Resource Extraction, Brisbane, Australia, pp.1-142.

Payant, R., Rosenblum, F., Nesset, J.E., 2011. Galvanic interaction and particle size effects in self-heating of sulphide mixtures, Materials Science, p.359-379.

Pérez López, R., Macias, F., Caraballo, M.A., Nieto, J.M., Roman-Ross, G., Tucoulou, R., Avora, C., 2011. Mineralogy and geochemistry of Zn-rich mine-drainage precipitates from an MgO passive treatment system by synchrotron-based X-ray analysis, Environmental Science and Technology, v.45, p.7826-7833.

Petrunic, B., Al, T.A., Weaver, L., Hall, D., 2009. Identification and characterization of secondary minerals formed in tungsten mine tailings using transmission electron microscopy, Applied Geochemistry, v.24, p.2222-2233.

Pichler, T., Hendry, M.J., Hall, G.E.M., 2001. The mineralogy of arsenic in uranium mine tailings at the Rabbit Lake In-pit Facility, northern Saskatchewan, Canada, Environmental Geology, v.40, p.495-506.

Plumlee, G.S., 1999. The environmental geology of mineral deposits. In: Plumlee, G.S., Lodgson, M.J. (Eds.), The Environmental Geochemistry of Mineral Deposits Part A: Processes, Techniques and Health Issues, Reviews in Economic Geology, vol. 6B. Society of Economic Geologists, United States, Littleton, CO, p.71-116.

Plumlee, G.S., Nash, J.T., 1995. Geoenvironmental mod¬els of mineral deposits—Fundamentals and applications, In: du Bray, E.A., (ed), Preliminary compilation of descriptive geoenvironmental mineral deposit models: U.S. Geologi¬cal Survey Open-File Report 95–0831, chap. 1., http://pubs.usgs.gov/of/1995/ofr-95-0831/.

Posch, M., Kurz, D., 2007. A2M – A program to compute all possible mineral modes from geochemical analyses, Computers and Geosciences, v.33, p.563-572.

Price, W.A., 2009. Prediction Manual for Drainage Chemistry from Sulphidic Geologic Materials, CANMET Mining and Mineral Sciences Laboratories, 579p.

Price, W.A., Morin, K., Hutt, N., 1997. Guidelines for the prediction of acid rock drainage and metal leaching for mines in British Columbia: Part II- recommended procedures for static and kinetic testing, Proc.4th international conference on acid rock drainage, p.15-30.

Qiong-Li, Y., Chen, J., Chen, Y., Guo, J., 2011. Density function theory study of influence of impurity on electronic properties and reactivity of pyrite, Transactions of Nonferrous Metals Society of China, v.21, p.1887-1895.

Quigley, M. 2008. HyLogged mineralogy of selected drill holes from the Ernest Henry Cu-Au deposit, Queensland, GeM AMIRA P843 Technical Report 2, p.5.1-5.22.

Quigley, M., 2012. Geometallurgical Mineral Mapping, Domaining and Development of Predictive Processing Proxies using VNIR-SWIR + TIR Infrared Reflectance Spectroscopy (HyLogging) Data: Ernest Henry IOCG Deposit case study. Economic Geology, Article in Press.

Radcliffe, D., McSween, H.Y., 1969. Copper zoning in pyite from Cerro de Pasco, Peru: A discussion. The American Mineralogist, v.54, p.1216-1217.

Raudsepp, M., Pani, E., 2003. Application of Rietveld analysis to environmental mineralogy, Mineralogical Association of Canada, Short Course 31, p. 165-180.

Recio-Vazquez, L., Garcia-Guinea, J., Carral, P., Alvarez, A.M., 2011. Arsenic mining waste in the catchment area of the Madrid detrital aquifer (Spain). Water, Air and Pollution, v.214, p.307-320.

Redwan, M., Rammlmai, D., Meima, J.A., 2011. Application of mineral liberation analysis in studying micro-sedimentological structures within sulfide mine tailings and their effect on hardpan formation, Science of the Total Environment, v.93, p.480-493.

Rendell, P.S., Batley, G.E., Cameron, A.J., 1980. Adsorption as a control of metal concentrations in sediment extracts. Environmental Science and Technology, v.14, p.314–318.

Rimstidt, J.D., Vaughan, D.J., 2003. Pyrite oxidation: A state-of-the-art assessment of the reaction mechanism, Geochimica et Cosmochimica Acta, v.67, p.873-880.

Rizmanoski, V., 2011. The effect of microwave pretreatment on impact breakage of copper ore, Minerals Engineering, v.24, p.1609-1618.

Robertson, A.M., 2005. Leading practice in the design of waste rock dumps for acid drainage management: A case study, In Proceedings of the 5th Australian Workshop on Acid Drainage, p 29-41, ACMER, Kenmore, Queensland, Eds Bell L.C. and McLean R.W., August 29-31, 2005, Fremantle, WA, Australia.

Robinson P., 2003. XRF and Laser Ablation ICP-MS Analysis of Flux-Fused Discs, Geoanalysis, 5th International Conference on the Analysis of Geological and Environmental Materials., Rovaniemi, Finland.

Rollinson, H.R., 1993. Using Geochemical Data: Evaluation, Presentation, Interpretation, Longman UK, 352p.

Rossiter, A., Yani, S., Song, M.N., 2008. Dynamic pH testing as a means to predict acid rock drainage. 6th Australian acid mine drainage workshop, Australian Centre for Minesite Rehabilitation Research (ACMER), Burnie, Australia.

Rothwell, R.G., Hoogakker, B., Thomson, J., Croudace, I.W., Frenz, M., 2006. Turbidite emplacement on the southern Balearic Abyssal Plain (western Mediterranean Sea) during Marine Isotope Stages 1–3: an application of ITRAX XRF scanning of sediment cores in lithostratigraphic analysis. In: Rothwell, R.G. (ed.) New Techniques in Sediment Core Analysis. Geological Society, London, Special Publications, 267, p.79–98.

Ryan, A., 1998, Ernest Henry copper-gold deposit, in Australasian Institute of Mining and Metallurgy, Monograph 22, p.759-768.

Sampson, M.I., Phillips, C.V., 2001. Influence of base metals on the oxidising ability of acidophilic bacteria during the oxidation of ferrous sulphate and mineral sulphide concentrates, using mesophiles and moderate thermophiles, Minerals Engineering, v.14, p.317-340.

Sapsford, D.J., Bowell, R.J., Dey, M., Williams, K.P. 2008. Humidity cell tests for the prediction of acid rock drainage. Minerals Engineering, v.22, p.25-36.

Savage, K.S., Stefan, D., Lehner, S., 2008. Impurities and heterogeneity in pyrite: Influences on electrical properties and oxidation products, Applied Geochemistry, v.23, p.103-120.

Savage, K.S., Tingle, T.N., O'Day, P.A., Waychunas, G.A., and Bird, D.K., 2000. Arsenic speciation in pyrite and secondary weathering phases, Mother Lode Gold District, Tuolumne County, California, Applied Geochemistry, v.15, p.1219-1244.

Schaefer, M.O., Gutzmer, J., Beukes, N.J., 2004. Mineral chemistry of sphalerite and galena from Pb-Zn mineralization hosted by the Transvaal Supergroup in Griqualand West, South Africa, South African Journal of Geology, v.107, p.341-354.

Schippers, A., Kock, D., Schwartz, M., Böttcher, M.E., Vogel, H., Hagger, M., 2007. Geomicrobiological and geochemical investigation of a pyrrhotite-containing mine waste talilings damnear Selebi-Phikwe in Botswana, Journal of Geochemical Exploration, v.92, p.151–158.

Schwarz-Schampera, U., Herzig, P.M., 2002. Indium: Geology, Mineralogy and Economics. Springer-Verlag, Berlin Heidelberg, New York, 257p.

Servida, D., 2008. Innovative approaches to evaluate geochemical risk related to sulphide-bearing Abandoned mine lands. PhD dissertation, University of Milan.

Shaw, S.C., 2000. Geochemical characterization and water quality predictions for the Zortman/Landusky Reclamation Project. Proceedings of the Conference on Mine Design, Operations and Closure, MDOC'00, Robertson, Robertson GeoConsultants Inc., Vancouver, BC, Canada, p.1-16.

Shaw, S.C., Groat, L.A., Jambor, J.L., Blowes, D.W., Hanton-Fong, J., Stuparyk, R.A., 1998. Mineralogical study of base metal tailings with various sulphide contents, oxidized in laboratory columns and field lysimeters, Environmental Geology, v.33, p.209-217.

Shaw, S.C., Robertson, A.M., Maehl, W.C., 2000. Material characterization and prioritization of remediation measures at the Zortman/Landusky mine sites, Proceedings of the Billings Land Reclamation Symposium, BLRS'00, Billings, Montana, USA.

Sherlock, E.J., Lawrence, R.W., Poulin, R., 1995. On the Neutralization of Acid Rock Drainage by Carbonate and Silicate Minerals, Environmental Geology, v.25, p.43-54.

Siddharth, S., Jamal, A., Dhar, B.B., Shukla, R., 2002. Acid base accounting: a geochemical tool for management of acid drainage in coal mines. Mine Water and the Environment, v.21, p.106-110.

Simmons, S.F., Brown, P.R.L., 1997. Saline fluid inclusions in sphalerite from the Broadlands-Ohaaki geothermal system: a coincidental trapping of fluids evaporated due to dryness, Economic Geology, v.92, p.485-489.

Singhania, S., Wang, Q., Filippou, D., Demopoulos, G.P., 2006. Acidity, valency and third-ion effects on the precipitation of scorodite from mixed sulfate solutions under atmospheric-pressure conditions, Metallurgical and Materials Transactions, v.37, p.189-197.

Skousen, J., Renton, J., Brown, H., Evans, P., Leavitt, B., Brady, K., Cohen, L., Ziemkiewicz, P., 1997. Neutralization potential of over burden samples containing siderite, Journal of Environmental Quality, v.26, p.673-681.

Skousen, J., Simmons, J., Ziemkiewicz, P., 2002. Acid-base accounting to predict post-mining drainage quality on surface mines, Journal of Environmental Quality, v.31, p.2034–2044.

Smart, R., Skinner, W.M., Levay, G., Gerson, A.R., Thomas, J.E., Sobieraj, H., Schumann, R., Weisener, C.G., Weber, P.A., Miller, S.D., Stewart, W.A., 2002. ARD test handbook: Project P387, A prediction and kinetic control of acid mine drainage, Melbourne, Australia: AMIRA, International Ltd, Ian Wark Research Institute.

Smart, R.St.C., Weber, P., Thomas, J.E., Skinner, W.M., 2004. Improvements in acid rock drainage testing for short and long-term neutralisation kinetics. In: Rao, S.R., Harrison, F.W., Konzinski, J.A., Amaratunga, L.M., Cheng, T.C., Richards, G.G. (Eds.), Waste Processing and Recycling in Mineral and Metallurgical Industries V. Proceedings of the 5th International Symposium on Waste Processing and Recycling in Mineral and Metallurgical Industries. Canadian Institute of Mining, Metallurgy and Petroleum, p.525–540.

Smith, A., Robertson, A., Barton-Bridges, J., Hutchinson, I.P.G., 1992. Prediction of acid generation potential. In: Hutchinson, I.P.G., Ellison, R.D. (eds) Mine Waste Management, Lewis Publishers, Boca Raton, p.123-199.

Smith, L., Beckie, R., 2003, Hydrologic and geochemical transport processes in mine waste rocks. In: J.L Jambor, D.W. Blowes, A.I.M. Ritchie (Eds.), Environmental aspects of mine wastes. Short Course Series. 31, pp.51-72, Mineralogical Association of Canada, Canada.

Smith, L.J., Neuner, M., Gupton, M., Moore, M., Bailey, B.L., Blowes, D.W., Smith, L., Sego, D.C., 2009. Diavik waste rock project: From the laboratory to the Canadian arctic. In: Securing the Future and 8th International Conference on Acid Rock Drainage (ICARD), Skelleftea, Sweden.

Smith, L.J.D., Neuner, M., Gupton, M., Moore, M., Bailey, B.L., Blowes, D.W., Smith, L., Sego, D.C., 2009. Diavik waste rock project: from the laboratory to the Canadian Arctic, 8th International Conference on Acid Rock Drainage (ICARD) and Securing the Future: Mining, Metals & the Environment in a Sustainable Society, Skelleftea, p.40-50.

Smuda, J., Dold, B., Friese, K., Morgenstern, P., Glaesser, W., 2007. Mineralogical and geochemical study of element mobility at the sulphide-rich Excelsior waste rock dump from the polymetallic Zn–Pb–(Ag–Bi–Cu) deposit, Cerro de Pasco, Peru, Journal of Geochemical Exploration, v. 92, p.97–110.

Sobek, A.A., Schuller, W.A., Freeman, J.R., Smith, R.M., 1978. Field and laboratory methods applicable to overburden and minesoils, EPA 600/2-78-054, 203pp.

Song, Q., Yanful, E.K., 2011. Oxygen influx and geochemistry of percolate water from reactive mine waste rock underlying a sloping channelled soil cover, Applied Geochemistry, v.26, p.655-665.

Sracek, O., Choquette, M., Gelinas, P., Lefebvre, R., Nicholson, R.V., 2004. Geochemical characterization of acid mine drainage from a waste rock pile, Mine Doyon, Quebec, Canada. Journal of Contaminant Hydrology, v..69, p.45-71.

Stanton, M.R., 2005. Baseline laboratory studies of sphalerite (ZnS) dissolution: Effects on aqueous metal concentrations and solubilization rates in Barnhisel, R.I., ed., Proceedings 22nd National Conference, American Association of Mining Reclamation, Breckenridge, CO, June 19-23, p. 1155-1165.

Stanton, M.R., Gemery-Hill, P.A., Shanks III, W.C., Taylor, C.D., 2008. Rates of zinc and trace metal release from dissolving sphalerite at pH 2.0–4.0, Applied Geochemistry, v.23, p.136–147.

Stanton, M.R., Taylor, C.D., Gemery-Hill, P.A., Shanks III, W.C., 2006. Laboratory studies of sphalerite decomposition: applications to the weathering of mine wastes and potential effects on water quality. Paper presented at the 7th International Conference on Acid Rock Drainage (ICARD), March 26-30, 2006, St. Louis MO. R.I. Barnhisel (ed.) Published by the American Society of Mining and Reclamation (ASMR), 3134 Montavesta Road, Lexington, KY 40502.

Stanton, R., Gemery-Hill, P.A., Shanks, W.C., Taylor, C.D., 2008. Removal of zinc and trace metal release from dissolving sphalerite at pH 2.0 to 4.0, Applied Geochemistry, v.23, p.136-147.

Stevens, R.E., Carron, M.K., 1948. Simple field test for distinguishing minerals by abrasion pH, American Mineralogist, v.33, p.31-50

Stewart, W., Miller, S., Smart R. Gerson, A., Thomas, J.E., Skinner, W., Levay, G., and Schumann, R., 2003a. Evaluation of the Net Acid Generation (NAG) Test for Assessing the Acid Generating Capacity of Sulphide Minerals. p. 617-625. I: Proceedings of the Sixth International Conference on Acid Rock drainage (Cairns, 12-18th July 2003).

Stewart, W., Schuman, R., Miller, S., Smart, R.St.C., 2009. Development of prediction methods for ARD assessment of coal process wastes. Securing the future and 8th ICARD, June 22-26th, 2009, Skelleftea, Sweden.

Stewart, W.A., 2005. Development of Acid Rock Drainage Prediction Methodologies for Coal Mine Wastes, PhD Dissertation, University of South Australia.

Stewart, W.A., Miller, S.D., Smart, R., 2006.Advances in acid rock drainage (ARD) characterisation of mine wastes.Paper presented at the 7th International Conference on Acid Rock Drainage (ICARD), p.2098-2119.

Stomberg, B., Banwart, S., 1999. Weathering kinetics of waste rock from the Aitik copper mine, Sweden: scale dependent rate factors and pH controls in large column experiments, Journal of Contaminant Hydrology, v.39, p.59-89.

Strong, A., Flores, N.E., 2008. Estimating the economic benefits of acid rock drainage cleanup using cost shares, Ecological Economics, v.65, p.348-355

Sverdrup, H.U., 1990. The kinetics of base cation release due to chemical weathering: Lund University Press, Lund, 246 p.

Tarras-Wahlberg, N.H., Nguyen, T.L., 2008. Environmental regulatory failure and metal contamination at the Giap Lai Pyrite mine, Northern Vietnam, Journal of Environmental Management, v.86, p.712-720.

Tauson, V.L., Babkin, D.N., Parkhomenko, Y., Menshikov, V.I., 2004. On the mechanism of trace-element uptake during the hydrothermal growth of sulphide mineral crystals, Crystallographic Reports, v.49, p.149-157.

Tessier, A., Campbell, G.C., Bisson, M., 1979. Sequential extraction procedure for the speciation of particulate trace metals, Analytica Chemica, v.51, p.844-851.

Tipping, E., Hetherington, N.B., Hilton, J., Thompson, J.W., Bowies, E., Hamilton-Taylor, J., 1985. Artefacts in the use of selective chemical extraction to determine distribution of metals between oxides of manganese and iron. Analytical Chemistry v.57, p.1944–1946.

Thomas, H.V., Large, R.R., Bull, S.W., Maslennikov, V., Berry, R.F., Fraser, R., Froude, S., Moye. R., 2011. Pyrite and pyrrhotite textures and composition in sediments, laminated quartz veins and reefs at Bendigo Gold mine, Australia: Insights for ore genesis, Economic Geology, v.106, p.1-31.

Thompson, A.J.B., Hauff, P.L. Robitaille. A.J., 1999. Alteration mapping in exploration: application of short-wave infrared (SWIR) spectroscopy, Society of Economic Geology Newsletter, v.39, 13 p.

Thurston, R.S., Mandernack, K.W., Shanks, W.C., 2010. Laboratory chalcopyrite oxidation by Acidithiobacillus ferrooxidans: Oxygen and sulfur isotope fractionation, Chemical Geology, v.269, p.252-261.

Tran, A.B., Miller, S., Williams, D.J., Fines, P., Wilson, G.W., 2003. Geochemical and mineralogical characterisation of two contrasting waste rock dumps- the INAP waste rock dump characterisation project, Proceedings of the 6th ICARD, p.939-948.

Tredinnick, I., Tuesley, M., 2000. Acid rock drainage management at Ernest Henry Mining - A case study. Proceedings of Fourth Australian Workshop on Acid Mine Drainage (Eds. N.J Grundon and L.C. Bell), p.63-73.

Tremblay, G.A., Hogan, C.M., 2001. Mine Environment Neutral Drainage (MEND) Manual 5.4.2d: Prevention and Control, Canada Centre for Mineral and Energy Technology, Natural Resources Canada, Ottawa, 352 pp.

US EPA, 1994. Acid mine drainage prediction, EPA/530-R-94-036, US EPA Office of Solid Waste.

US EPA, 2003. Nationwide Identification of Hardrock Mining Sites. Report 2004-P-00005.

USDA Forest Service, 1992. A conceptual waste rock sampling program for mines operating in metallic sulfide ores with a potential for acid rock drainage. Written by Gene Farmer with the Department of Agriculture, Forest Service, Ogden, Utah.

USEPA, 1994. http://yosemite.epa.gov/R10/WATER.NSF/840a5de5d0a8d1418825650f00715a27/e4ba15715e97ef2188256d2c00783a8e/$FILE/ATT5YPWO/appendix%20c.pdf

Van Eck, M., Child, R., 1990. Croydon gold deposits. In: Hughes F.E. (Ed.) Geology and Mineral deposits of Australia and Papua New Guinea, the Australian Institute of Mining and Metallurgy, Monograph 14, p.979-982.

Vatandoost, A., Fullagar, P., 2008a. Multi-sensor petrophysical core logging: data acquisition, processing and preliminary interpretation for Ernest Henry. GeM (AMIRA P843) Technical Report 2, November p.3.1-3.42.

Vatandoost, A., Fullagar, P., Roach, M., 2008b. Automated multi-sensor petrophysical core logging. Exploration Geophysics, v.39, p.181-188.

Vik, E.A., Bardos, P., Brogan, J., Edwards, D., Gondi, F., Henrysson, T., Jensen, B.K., Jorge, C., Mariotti, C., Nathanail, P. and Papassiopi, N., 2001. Towards a framework for selecting remediation technologies for contaminated sites, Land Contamination & Reclamation , v. 9, p. 119-128.

Vink, L., 1997. Textures of the Hilton North deposit, Queensland, Australia, and their relationship to liberation, PhD dissertation, University of Queensland.

Volrath, S., 2012. Microbial Fe(II) oxidation at circumneutral pH: reaction kinetics, mineral products, and distribution of neutrophilic iron oxidizers in wetland soils, Ph.D thesis, Utrecht University, ISBN 978-90-6266-290-6.

Walker, S.R., Jamieson, H.E., Lanzirotti, A., Andrade, C.F., Hall, G.E.M., 2005, The speciation of arsenic in iron oxides in mine wastes from the Giant gold mine, N.W.T.: Application of synchrotron micro-XRD and micro-XANES at the grain scale, Canadian Mineralogist, v.43, p. 1205-1224.

Walker, S.R., Parsons, M.B., Jamieson, H.E., Lanzirotti, A., 2009. Arsenic mineralogy of near- surface tailings and soils: influences on arsenic mobility and bioaccessibility in the nova scotia gold mining districts. Canadian Mineralogist, v.47, p.533-556.

Walters, S., 2008. An overview of new integrated geometallurgical research, In: Ninth International Congress for Applied Mineralogy, ICAM Brisbane, Australia, 8-10 September.

Walters, S., Kojovic, T., 2006. Geometallurgical mapping and mine modelling (GEMIII) – The way of the future, in Proceedings SAG 2006, International Autogenous and Semi Autogenous Grinding Technology, p 411-425.

Weber, P.A., 2003. Geochemical investigations of neutralising reactions associated with acid rock drainage: Prediction, mechanisms, and improved tools for management, PhD dissertation, University of South Australia.

Weber, P.A., 2003. Geochemical investigations of neutralising reactions associated with acid rock drainage: Prediction, mechanisms, and improved tools for management. PhD dissertation, University of South Australia.

Weber, P.A., Hughes, J.B., Conner, L.B., Lindsay, P., Smart, R.St.C., 2006. Short-term acid rock drainage characteristics determined by paste pH and kinetic NAG testing: Cypress prospect, New Zealand, Paper presented at the 7th International Conference on Acid Rock Drainage (ICARD).

Weber, P.A., Thomas, J.E., Skinner, W.M, Smart, R.St.C., 2005a. A method to determine the acid-neutralisation capacity of rock samples, Canadian Mineralogist, v.43, p.1183-1192

Weber, P.A., Thomas, J.E., Skinner, W.M, Smart, R.St.C., 2005b. Improved acid neutralising capacity assessment of iron carbonates by titration and theoretical calculation, Applied Geochemistry, v.19, p.687-694.

Weber, P.A., Thomas, J.E., Skinner, W.M., Smart, R.St.C., 2004. Improved acid neutralisation capacity assessment of iron carbonates by titration and theoretical calculation, Applied Geochemistry, v.19, p.687-694.

Weisener, C.G., Smart, R.St. and Gerson, A., 2004. A comparison of the kinetics and mechanism of acid leaching of sphalerite containing low and high concentrations of Iron, International journal of Mineral Processing, v.74, p.239– 249.

Weisener, C.G., Weber, P.A., 2010. Preferential oxidation of pyrite as a function of morphology and relict texture, New Zealand Journal of Geology and Geophysics , v.53, p.22-33.

Weisner, C.G., Smart, R.St.C., Gerson, A.R., 2003. Kinetics and mechanisms of the leaching of low Fe-sphalerite, Geochimica et Cosmochimica Acta, v.67, p.823-830.

White, A., Robb, V.M., Robb, L.J., Waters, D.J., 2010. Portable infrared spectroscopy as a tool for the exploration of gold deposits in tropical terrains: A case study at the Damang deposit, Ghana, Society of Economic Geologists Special Publication 15.

White, W.W., Lapakko, K.A., Cox, R.L., 1999. Static test methods most commonly used to predict acid mine drainage: practical guidelines for use and interpretation. In: Plumlee, G.S., Lodgson, M.J. (Eds.), The Environmental Geochemistry of Mineral Deposits Part A: Processes, Techniques, and Health Issues, Reviews of Economic Geology, vol. 6A, pp.325-338.

WHO, 2006. Working Together for Health, The World Health Report 2006 (http://www.who.int/whr/2006/whr06_en.pdf).

Williams, P.J., Barton, M.D., Johnson, D.A., Fontboté, L., de Haller, A., Mark, G., Oliver, N.H.S., 2005, Iron oxide copper-gold deposits: geology, space-time distribution, and possible modes of origin: Economic Geology 100th Anniversary volume, Society of Economic Geologists Inc., p. 371-405.

Xstrata Copper, 2011, Xstrata PLC website: www.xstrata.com/operation/ernesthenry

Zhu, Y., Merkel, B.J., 2001. The dissolution and solubility of scorodite, Fe2AsO4.2H2O. Evaluation and simulation with PHREEQC2. Wiss.Mitt. Inst. für Geologie, v.18, p.1-12.